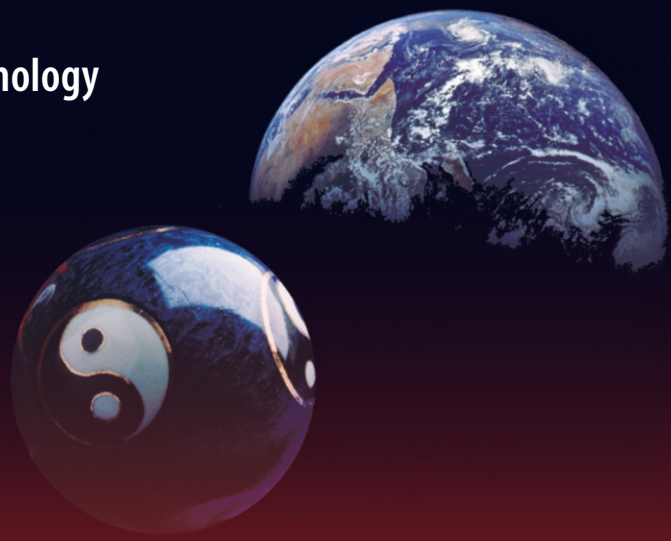Lin Chen *Editor*

Advances in Clean Energy Systems and Technologies

Springer

Green Energy and Technology

Climate change, environmental impact and the limited natural resources urge scientific research and novel technical solutions. The monograph series Green Energy and Technology serves as a publishing platform for scientific and technological approaches to "green"—i.e. environmentally friendly and sustainable—technologies. While a focus lies on energy and power supply, it also covers "green" solutions in industrial engineering and engineering design. Green Energy and Technology addresses researchers, advanced students, technical consultants as well as decision makers in industries and politics. Hence, the level of presentation spans from instructional to highly technical.

Indexed in Scopus.

Indexed in Ei Compendex.

Lin Chen

Editor

Advances in Clean Energy Systems and Technologies

Springer

Editor
Lin Chen
Institute of Engineering Thermophysics
Chinese Academy of Sciences
Beijing, China

School of Aeronautics and Astronautics
University of Chinese Academy of Sciences
Beijing, China

Paper in this product is recyclable.

Preface

The challenges of sustainable development and the climate emergency situate the goal of creating and deploying clean energy technologies as one of the most important for humanity right now. With this in mind, the 2023 8th International Conference on Advances on Clean Energy Research (ICACER 2023) was scheduled to be convened in Barcelona, Spain, on April 28–30, 2023, hosted in Universitat Politècnica de Catalunya BarcelonaTech (UPC), Spain and supported by Universitetet of Agder, Norway and Galati University 'Dunarea de Jos', Romania.

The objective of this conference is to present progressions in applied research of clean energy technologies and their system integration for 'Energy Transition' in moving towards sustainable societies. Applied research is needed to integrate the existing clean energy technologies for a low-carbon economy through focused and integrated efforts with the usage of smart network. The ICACER 2023 is an interdisciplinary clean energy research conference organized with objective of bringing together researchers, scientists, engineers, academics and graduate students in the fields of advances on clean energy technologies, energy economics and policy to share up-to-date research results.

ICACER 2023 proceedings span over created eight topic tracks including 'Solar Photovoltaic Power Generation Technology and Solar Energy Applications', 'Wind Power Generation and Marine Energy Development', 'New Power System Analysis and Power Grid Control Technology', 'Advanced Hydrogen Production System and Fuel Cell Technology', 'Renewable Energy Transformation and Energy Market Analysis', 'Clean Energy Combustion and Thermal Engineering', 'Building-Integrated Renewable Energy, Building Energy-Saving Design and Energy Efficiency' and 'Environmental Impact Assessment and Management of Different Power Generation Technologies'. As the program, we had three keynote speeches, three onsite sessions and four online sessions. It will be a golden opportunity for the researchers, scientists, engineers, academics and graduate students to interact among themselves to get better views on technical development and trends for the near future.

On behalf of the Organizing Committee, thanks are extended to the keynote speakers for their distinguished presentations and sharing. Thanks are also extended to the paper reviewers and the members of the organizing committee, for their contribution and commitment to putting together a program of paper presentations that conference participants should find beneficial in their professional development. Finally, we are grateful to all the authors and presenters of the papers as well as all the attendees for their contributions to this wonderful conference.

Barcelona, Spain   Conference Organizing Committees
ICACER 2023

Conference Committees

Advisory Committees
Jean Mahseredjian, Polytechnique Montreal, Canada
Le Yi Wang, Wayne State University, USA

Conference Chair
Mohan Lal Kolhe, Universitetet of Agder, Norway

Conference Co-Chair
Javier Contreras Sanz, Universidad de Castilla-La Mancha, Spain

Local Organizing Chair
Marc Alier, Universitat Politècnica de Catalunya, Spain

Program Chairs
Lin Chen, Chinese Academy of Sciences, China
Zhenzhi Lin, Zhejiang University, China

Program Co-Chairs
Qingguang Yu, Tsinghua University, China
James Marco, University of Warwick, UK
Eugen Rusu, Galati University 'Dunarea de Jos', Romania

Steering Committee Chairs
Adem Akpinar, Uludag University, Turkey
Stanislaw Szwaja, Czestochowa University of Technology, Poland

Technical Committees
Jinshun Wu, North China Institute of Science and Technology, China
Rafael C. F. Mendes, Universidade de Brasilia, Spain
Mahmoud Elgendi, United Arab Emirates University, UAE
Silvia Ruggiero, University of Sannio, Italy
Abdul Quader, Dubai Electricity and Water Authority (DEWA) Research and Development Center, UAE
José Manuel González Martín, Universidad de Burgos, Spain

Maisa El Gamal, Zayed University, UAE
Ameera Mohammad, United Arab Emirates University, UAE
Marianela Machuca Macías, Universidad de Cádiz, Spain
Ali Saberi Derakhtenjani, Dubai Electricity and Water Authority (DEWA) Research and Development Center, UAE
Tarek Safwat Kabel, University of Sadat City, Egypt
Marie Sawadogo, Institut International d'Ingénierie de l'Eau et de l'Environnement (2iE), Burkina Faso
Arta Babapour, Cukurova University, Turkey
Paweł Madejski, AGH University of Science and Technology, Poland
Sawsan Dagher, Abu Dhabi Polytechnic, UAE
Yanzhe Li, New York University, USA
Faezeh Bagheri Moghaddam, University of Strathclyde, UK
Imen Ben Salem, Zayed university, UAE
Wisam Al Saadi, Australian College of Kuwait, Kuwait
Kittipong Tissayakorn, Office of the National Economic and Social Development Council, Thailand
Roberto Garay-Martinez, University of Deusto, Spain
Wei He, Tianjin University of Commerce, China
Yulong Zhao, Hebei University of Technology, China
Manickam Minakshi, Murdoch University, Australia
Yang Han, University of Electronic Science and Technology of China (UESTC), China
Chengcheng Xia, University of Padova, Italy
Ottorino Veneri, National Research Council of Italy, Italy
Mohammad Golam Rasul, Central Queensland University, Australia
Angela Russo, Dipartimento Energia "Galileo Ferraris", Italy
Quan Li, The University of Edinburgh, UK
Nina Almasifar, Cukurova University, Turkey
Imane Belyamani, Zayed University, UAE
Benjapon Chalermsinsuwan, Chulalongkorn university, Thailand
Basil T. Wong, Swinburne University of Technology, Malaysia
Chaiyan Chaiya, Rajamangala University of Technology Thunyaburi, Thailand
Teerawat Sema, Chulalongkorn university, Thailand
Amit Sant, Pandit Deendayal Energy University, India
Piotr Olczak, Mineral and Energy Economy Research Institute, Polish Academy of Sciences, Poland
Liliana Rusu, Dunarea de Jos University of Galati, Romania
Poomiwat Phadungbut, Mahidol University, Thailand
Malligunta Kiran Kumar, Koneru Lakshmiah Education Foundation, India
Duong Minh Bui, Vietnamese-German University, Viet Nam
Chitrarekha Kabre, School of Planning and Architecture, India
Islam Al-Akraa, The British University in Egypt, Egypt
Masoud Taghavi, Technical and Vocational University (TVU), Iran
Krisztina Uzuneanu, "Dunarea de Jos" University of Galati, Romania
Cristian Paul Chioncel, UNIVERSITATEA "BABEŞ-BOLYAI", Romania

Sorin Ciortan, "Dunarea de Jos" University of Galati, Romania
Nilofar Asim, Universiti Kebangsaan Malaysia, Malaysia
Masita Mohammad, Universiti Kebangsaan Malaysia, Malaysia
Woraphon Yamaka, Chiang Mai University, Thailand
S. Suresh, Maulana Azad National Institute of Technology Bhopal, India
N. Balasubramanian, Anna University, India
Adel Younis, Australin University, Kuwait
Udara S.P.R. Arachchige, University of Sri Jayewardenepura Pitipana, Sri Lanka
Santanu Koley, Birla Institute of Technology and Science-Pilani, India
Alagappan Pandian, Koneru Lakshmiah Education Foundation, India
Abdul Waheed Badar, University of Bahrain, Bahrain
Ali Mohammadipour, Iranian Association for Energy Economies & Payame noor
    University, Iran
Ravishankar Sathyamurthy, KPR Institute of Engineering and Technology, India
Laveet Kumar, Mehran University of Eng. & Technology, Jamshoro, Pakistan
Yarrapragada K S S Rao, Aditya College of Engineering, India
Banza Bonaventure Wa Banza, University of Lubumbashi, Congo
Madhusudhanan J, Anand Institute of Higher Technology, India

Contents

**Part III New Power System Analysis
and Power Grid Control Technology**

Part IV Advanced Hydrogen Production System and Fuel Cell Technology

**Lee's Model and Determination of the Thermal Effect Zones
of an LNG BLEVE Fireball**   305

Abderraouf Guelzim, Aziz Ettahir, and Anas Mbarki

**Design Comparison for the Supercritical CO_2 Brayton Cycle
with Recompression and Thermal Regeneration: Numerical Results**   315

Jiaxiang Chen, Lin Chen, Jinguang Zang, and Yanping Huang

**Part VII   Building-Integrated Renewable Energy,
             Building Energy-Saving Design and Energy Efficiency**

**An Optimized Setpoint Framework for Energy
Flexible Buildings in Hot Desert Climates**   335

Ali Saberi Derakhtenjani, Juan David Barbosa,
and Edwin Rodriguez-Ubinas

**A State-of-the-Art Approach for Assessing
the Environmental Sustainability of Multi-renewable
Energy Systems in the Built Environment** 345

Joseph Akpan, Oludolapo Olanrewaju, and Rubén Irusta-Mata

**Realizing Visual Comfort Parameters and Adaptive
Thermal Comfort Models for Hot Climates** 367

Boshra Akhozheya, Sawsan Dagher, Maryam Akho-Zahieh,
Farhan H. Malik, Ariel Gomez, and Maisa El Gamal

Valentino Festa, Rosa Francesca De Masi, Antonio Gigante,
Michele Parrotta, Silvia Ruggiero, and Alessandro Russo

**Part VIII   Environmental Impact Assessment and Management
of Different Power Generation Technologies**

Abdulrahman Aleid, Amjad Ali, and Md Shafiullah

Part I
Solar Photovoltaic Power Generation Technology and Solar Energy Applications

Cloud Effects on Photovoltaic Power Forecasting: Initial Analysis of a Single Power Plant Based on Satellite Images and Weather Forecasts

Franko Pandžić (iD)**, Ivan Sudić** (iD)**, Tomislav Capuder** (iD)**, and Amalija Božiček** (iD)

1 Introduction

The growing demand for clean and sustainable energy sources has accelerated the adoption of renewable energy systems. Among these systems, photovoltaic (PV) technology has gained significant popularity due to its cost-effectiveness and environmental benefits. However, PV systems' performance is subject to weather conditions, making it challenging to accurately forecast their power output. The ability to forecast PV production is crucial for optimal grid integration, efficient energy management, and trading activities. Accurate forecasting also helps to minimize the uncertainty associated with renewable energy production, reducing operational risks and costs.

This chapter presents a study on PV production forecasting for a single solar power plant, with a goal to explore the effect of local cloud cover through satellite imagery on the plants' production. The study's primary motivation is to gain insights in data most important for accurate production forecasting along with validating sources of data. The authors distinguish the following papers of importance: Benavides Cesar et al. [1], Hong et al. [2], and Yang et al. [3] provide extensive research foundation as review papers regarding solar forecasting and forecasting energy quantities in general. Qin et al. [4] focus on enhancing PV output forecast by integrating satellite and ground data. They capture cloud motion patterns which they use to forecast PV output forecasts. Holland et al. [8] go a step further and incorporate numerical weather models along with satellite images and ground measurements for large power plants (>500 MW). Contrarily, this study focuses on a

F. Pandžić (✉) · I. Sudić · T. Capuder · A. Božiček
Faculty of Electrical Engineering and Computing, University of Zagreb, Zagreb, Croatia
e-mail: franko.pandzic@fer.hr

3.5 MW power plant which can pose an issue if following the aforementioned paper. Yu et al. [10] focus on PV forecasting using cloud images as well; first they forecast the amount of cloud coverage and consequently PV output using a convoluted LSTM. Son et al. [5] devise a solution without forecasts of solar irradiance, using only cloud cover images for ultra-short-term and short-term PV forecasting. These papers give foundation for the inclusion of satellite images in order to enhance PV output forecasting, but they mostly use sources of satellite data which may not be easily accessible. Consequently, the authors believe that the source of cloud satellite images in this study is a possible solution to that issue.

The findings of this study have practical implications for any operator in charge of a solar power plant enabling them to make informed decisions based on accurate PV production forecasts generated with the help of satellite images.

1.1   Showcase: Vis Solar Power Plant

For this chapter, the showcased power plant is the solar power plant of island Vis, Croatia. HEP Group, which is the national energy company of Croatia, constructed the Vis solar power plant in 2020, with an investment of 31 million kunas (approx. 4.1 million euros), leading to the successful establishment of the plant. The design and construction were done by Končar – Power Plant and Electric Traction Engineering Inc. At the time of its commissioning, SE Vis (from Croatian: *Sunčana elektrana*) was the highest-capacity solar production sight in Croatia with the capacity of 3.5 MW. SE Vis contains 11,200 modules with an individual power of 340 Wpp. Next to SE Vis, a battery tank with a power of 1 MW and a capacity of 1.44 MWh is installed, the first of its size in Croatia at that time. The battery tank is used to provide power system balancing services and for the purpose of preserving the stability of the network on the island, capable of powering up to 1600 households. The total area on which the facility is located is 5.5 ha (13.6 acres) [11]. The coordinates of the power plant are 16.141 longitude and 43.038 latitude, and its layout can be seen using Google Maps.

2   Data

Available data includes production measurements from Vis solar power plant, weather forecasts for the location of the plant obtained by Weather Research & Forecasting Model (WRF) [9] and EUMETSAT satellite imagery [6].
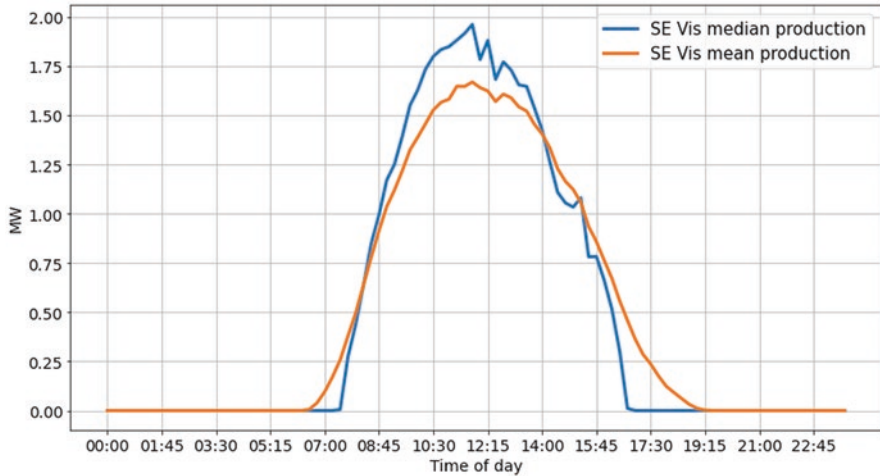
Fig. 1 SE Vis **mean** and **median** production through time of day

2.1   SE Vis Historical Production

Production measurements of SE Vis are available in 15-minute intervals from 03.09.2020. 02:00 UTC until 14.07.2022. 06:45 UTC (almost 2 years of data). Figure 1 shows the **mean** and **median** photovoltaic production for SE Vis for the aforementioned period. The median peak production (1.96 MW) is higher than the mean peak production (1.67 MW). This discrepancy implies that there are non-insignificant number of days when the production levels, which are expected to be at their highest, are impeded by factors such as local cloud cover.

2.2   WRF Forecasts

WRF forecasts are available every 6 hours for the next 72 hours starting from midnight UTC every day for SE Vis location. Specifically, new forecasts are available at 00:00, 06:00, 12:00, and 18:00 UTC every day. Forecasts of 7 meteorological phenomena are available to the authors:

- Wind speed (m/s)
- Wind direction (°)
- Composite reflectivity (dBZ)
- Air temperature (°C)
- Air pressure at sea level (hPa)
- Relative humidity (%)
- Solar irradiance (W/m²)

Table 1 Color meaning on *clm* images

Pixel color	Description
	Clear sky over land
	Cloud
	Clear sky over water

2.3 EUMETSAT Satellite Imagery

The *European Organisation for the Exploitation of Meteorological Satellites* (EUMETSAT) was created through an international convention agreed by a current total of 30 European Member States. Their primary goal is to establish, maintain, and utilize the European system of meteorological satellites. They offer multiple weather products such as images of cloud masks, microphysics models, etc. For the purpose of this chapter, the simplest product will be investigated – *clm* (Cloud Mask) which is obtained via Meteosat Second Generation (MSG) Geostationary (GEO) satellites. These satellites use an optical spinning enhanced visible and infrared imager (SEVIRI) sensor to obtain cloud mask images.

clm products categorize surfaces into four classes, one of which is *not processed surfaces*, leaving three classes that offer valuable information. Table 1 explains the three classes and their representation on an image.

Images were retrieved via EUMETSAT API for latitudes between 41° and 45° and longitudes between 14° and 18°. In other words, the images cover an area of approximately 444.4 km × 444.4 km. This area was chosen to have the island of Vis in the middle and have enough of the surrounding area for further research (forecasting cloud movement, etc.). *clm* image resolution is approximately 2.2 km (one pixel covers an area of approximately 2.2 km × 2.2 km). Figure 2 shows examples of *clm* images. The red ellipsoid highlights the island of Vis. Figure 2a features a clear day without much cloud coverage (few white pixels) while Fig. 2b shows a cloudy day over the Mediterranean. Although *clm* images are available in 5-min intervals, they were retrieved at 15-min intervals for times corresponding to those of SE Vis production measurements for easier data manipulation and analysis.

3 Analysis

To represent satellite images as a time series variable, a simple transformation was done. Only pixels part of the bounding box encompassing the entirety of the island of Vis were taken into consideration (Fig. 2c). Information from images was converted to cloud coverage (*cc*). For every time step *t* (image), the following was calculated:

$$cc_t = \frac{P_c}{P_{tot}} \tag{1}$$
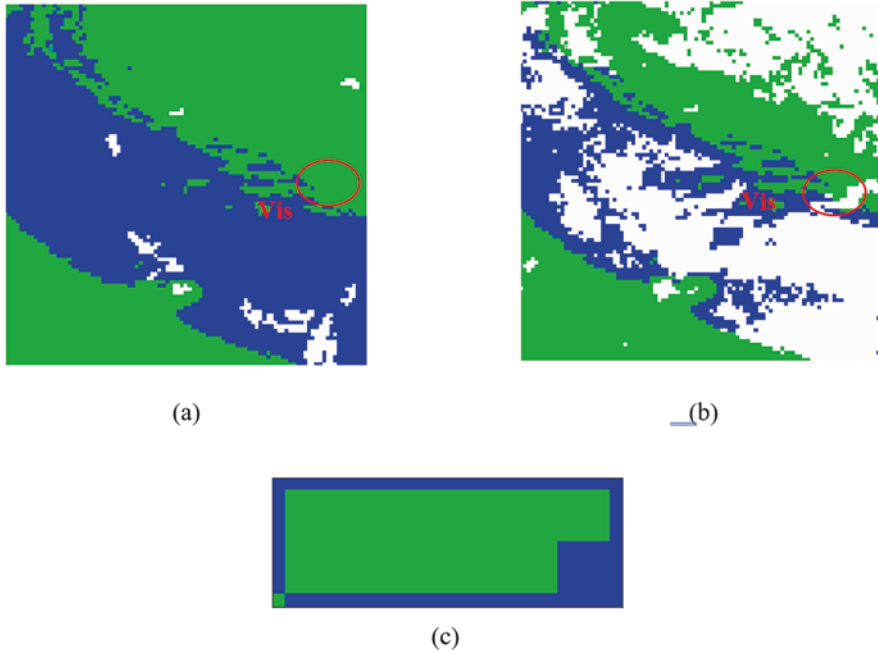
Fig. 2 (**a**) *clm* image for 05.09.2020. 08:15 UTC – clear day (**b**) *clm* image for 14.09.2020. 05:00 UTC – cloudy day (**c**) key pixels for determining cloud coverage

P_c is the number of cloud pixels and P_{tot} is the number of total pixels. If relied solely on the global Pearson's correlation coefficient (singular value for the entire time series), which stands at $\rho = -0.28$, the relationship between cloud coverage and production would be considered weak. Figure 3 displays the correlation coefficient calculated for each 15-minute interval of the day (00:00–23:45). The results indicate that during the night hours when there is no production, the correlation is weak. In other words, the night hours reduce the global correlation significantly. On the other hand, for hours when there is irradiance and thus production, the dependence between cloud coverage and production is relatively strong ($\rho \sim -0.7$).

To isolate the impact of cloud coverage, only the most significant WRF forecast will be utilized hereafter. To effectively merge the 15-minute interval production data with the forecast data, which is recorded in hourly intervals, the production data needed to be averaged over hourly intervals. Figure 4 shows the correlation between all available meteorological parameters and SE Vis production. As expected, forecasts of solar irradiance have the highest positive linear dependence with production ($\rho = 0.89$). As the goal of this chapter is to explore the effect of local clouds on production forecasting, and not specifically the optimal production forecast, other meteorological phenomena are disregarded. If developing an optimal forecast of production, exploring other meteorological variables would be necessary. In the next subsection, simple regression models are used to determine the effect of cloud coverage on production forecasting.
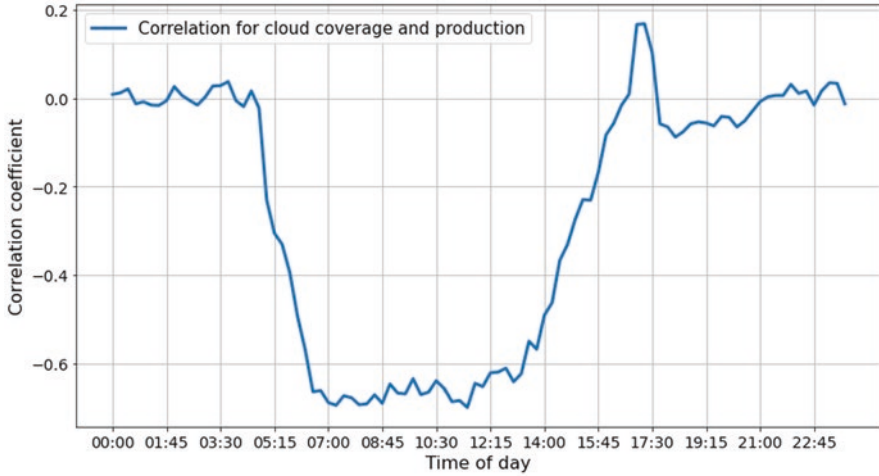
Fig. 3 Pearson correlation coefficient for cloud coverage and SE Vis production
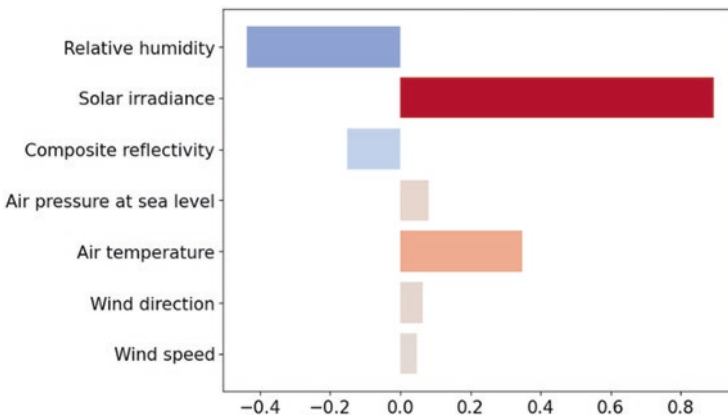
Fig. 4 Bar plot of correlations of meteorological parameter forecasts SE Vis production

4   Model Training and Results

To determine the impact of cloud coverage acquired from cloud mask satellite images on power production, two simple regression models based on the same architecture were trained. One is a ***base*** model as it only uses solar irradiance forecasts as inputs while ***cloud*** model uses cloud coverage and irradiance forecasts as inputs. Comparing errors of both models can clearly show if the inclusion of cloud coverage helps improve production forecasting.

Ridge regression with the same level of regularization was used for both *base* and *cloud* models. Samples (*input*, *target*) for every timestep *t* were created as:
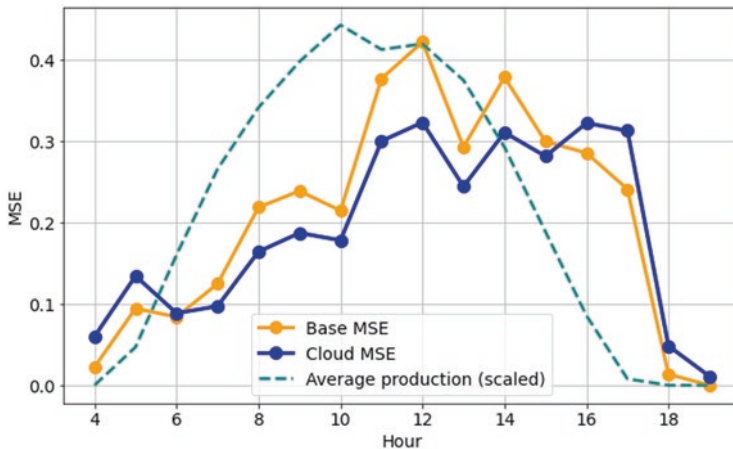
Fig. 5 MSE (*base* and *cloud*) for each hour of the day with **scaled average production** for reference of error significance

$$sample_t^{base} = \left(irradiance_t, \ production_t\right) \qquad (2)$$

$$sample_t^{cloud} = \left(\left[irradiance_t, \ cloud\,coverage_t\right], \ production_t\right)$$

Only the most recent WRF irradiance forecasts were considered. Seventy percent of the samples were used for training, 15% for validation, and the remaining 15% for testing. Models were trained, validated, and tested only for hours of the day for which production was measurable (night hours were disregarded). Figure 5 shows the mean squared error (MSE) for *base* and *cloud* models for each hour of the day of the test set. Scaled average production is also shown as the errors for peak production hours (7th to 14th hour UTC) are more important than the ones which have less production. *cloud* model outperforms the *base* model for almost all hours based on MSE.

 cloud model performs even better when observing only peak production hours, with the 12th hour exhibiting the largest MSE discrepancy (0.322 vs 0.421, 24% difference). Table 2 condenses information from Fig. 5 and shows the improvements made using *clm* images in one-hour ahead forecast production.

5 Conclusion and Future Work

It was shown in this chapter that the simple inclusion of EUMETSAT satellite images, specifically the cloud mask product, can greatly improve one-hour ahead production forecasting. The findings of this research can be implemented by any solar power plant operator to optimize management. Still, it needs to be mentioned

Table 2 Average MSE for total and peak hours

	MSE (total)	MSE (peak hours)
base	0.206	0.283
cloud	0.191	0.225
Improvement	**7.3 %**	**20.5 %**

that satellite images are taken in real-time and not available in advance (an hour before). As this chapter is considered as an initial case study, cloud images were regarded as perfect forecasts. Consequently, results of this work can be considered as best-case scenarios (having perfect forecast of cloud coverage). The authors recognize three important factors that can be improved upon and potentially greatly improve one-hour ahead production forecasts:

 (i) Image representation as a single value to models resulted in information loss. To improve upon this, more advanced transformations need to be explored.
 (ii) A simple linear architecture was used to investigate the effect of cloud information on production forecasting. More advanced architectures need to be explored, namely, deep neural networks which can extract key information from original images directly.
(iii) *clm* product does not differentiate between clouds. More advanced EUMETSAT products can address this limitation. Namely, a microphysics product (*mphys*) [7] categorizes clouds into five possible classes which extends available information.

To create a viable model, cloud forecasts must be developed. This can be done using advanced algorithms such as deep neural networks using consequent images or with motion estimation algorithms. However, the next step before cloud forecasting would be determining the most adequate EUMETSAT product (possibly *mphys*) for tackling this issue.

References

1. Benavides Cesar, L., Amaro e Silva, R., Manso Callejo, M.Á., Cira, C.I.: Review on spatio-temporal solar forecasting methods driven by in situ measurements or their combination with satellite and numerical weather prediction (NWP) estimates. Energies. **15**(12), 4341 (2022)
2. Hong, T., Pinson, P., Wang, Y., Weron, R., Yang, D., Zareipour, H.: Energy forecasting: a review and outlook. IEEE Open Access J. Power Energy. **7**, 376–388 (2020)
3. Yang, D., Kleissl, J., Gueymard, C.A., Pedro, H.T., Coimbra, C.F.: History and trends in solar irradiance and PV power forecasting: a preliminary assessment and review using text mining. Sol. Energy. **168**, 60–101 (2018)
4. Qin, J., Jiang, H., Lu, N., Yao, L., Zhou, C.: Enhancing solar PV output forecast by integrating ground and satellite observations with deep learning. Renew. Sust. Energ. Rev. **167**, 112680 (2022)
5. Son, Y., Yoon, Y., Cho, J., Choi, S.: Cloud cover forecast based on correlation analysis on satellite images for short-term photovoltaic power forecasting. Sustainability. **14**(8), 4427 (2022)

6. EUMETSAT.: https://www.eumetsat.int/. Accessed 14 Mar 2023
7. SEVIRI Day Microphysics RGB Quick Guide.: https://www.eumetsat.int/media/41625. Accessed 14 Mar 2023
8. Holland, N., Pang, X., Herzberg, W., Karalus, S., Bor, J., Lorenz, E.: Solar and PV forecasting for large PV power plants using numerical weather models, satellite data and ground measurements. In: 2019 IEEE 46th Photovoltaic specialists conference (PVSC), pp. 1609–1614. IEEE (2019)
9. Skamarock, W.C., Klemp, J.B., Dudhia, J., Gill, D.O., Liu, Z., Berner, J., … Huang, X.-yu: A description of the advanced research WRF model version 4.3 (No. NCAR/TN-556+STR) (2021)
10. Yu, D., Seowoo, L., Sangwon, L., Wonik, C., Ling, L.: Forecasting photovoltaic power generation using satellite images. Energies. **13**(24), 6603 (2020)
11. HEP.: https://www.hep.hr/u-rad-pustena-suncana-elektrana-vis-najveca-suncana-elektrana-u-hrvatskoj/3549. Accessed 14 Mar 2023

Enhancing the Performance of Photovoltaic Panels by Evaporative Cooling in Hot and Arid Climates

Waleed M. Alharbi (ID)**, Ahmed M. Alshwairekh** (ID)**,
and Ahmed Alaa Mahfouz** (ID)

1 Introduction

Photovoltaic (PV) panels are the most commonly used method of electricity production using solar energy due to its ease of use and long life. Moreover, it directly converts solar radiation into electrical energy. A solar cell or photovoltaic (PV) converts only a small portion of incident sun insolation to a power source, while the remainder is converted into heat. Najaf et al. [1] proved numerically that a rise in cell temperature will lead to a decrease in the produced power at various irradiation levels. Osarumen O. et al. [2] stated that the operations that cause a cell temperature of 43–63 °C or higher are critical and cause the most damage to the solder connection. However, according to Royo et al. [3] the application of cooling methods to PV panels could increase the lifespan from a 25–30 years to 48 years. Many different cooling methods have been used by several researchers to cool solar PV panels.

W. M. Alharbi (✉)
Renewable Energy Program, College of Engineering, Qassim University,
Buraydah, Saudi Arabia
e-mail: 421114489@qu.edu.sa

A. M. Alshwairekh
Department of Mechanical Engineering, College of Engineering, Qassim University,
Buraydah, Saudi Arabia
e-mail: a.alshwairekh@qec.edu.sa

A. A. Mahfouz
Department of Electrical Engineering, College of Engineering, Qassim University,
Buraydah, Saudi Arabia
e-mail: A.Mahfouz@qu.edu.sa

Nomenclature

A	Module area (m^2)	MPP	Maximum power point
PV	Photovoltaic	FF	Fill factor
V	Voltage (V)	Isc	Short-circuit current (A)
P	Power	Vsc	Open-circuit voltage (V)
I	Current (A)	STC	Standard Test condition
T	Temperature	TC	With cooling
PVC	Polyvinyl Chloride	TU	Without cooling
ω	The uncertainty of several parameters	A_c	Cross section area

1.1 Cooling Solutions for PV Modules

Most of the previous work on PV panels cooling was divided into two main sections, passive and active cooling. Nižetić et al. [4] used active cooled PV panels, which is using the water spray method on the front and backside of the PV panel which resulted in reducing the PV temperature from 54 to 24 °C, in return increasing the electrical efficiency of the panel by 2%. Bahaidarah et al. [5] used a back surface water cooling technique. Their results showed about a 9% increase in electrical efficiency. Hadipour et al. [6] studied the performance and economic effects of the active cooling for the PV panel. The researchers have used three cooling methods, steady-flow, spray cooling system, and pulsed-spray water cooling systems. Their results showed an increase in the electrical power output of the photovoltaic panel by about 33.3%, 27.7%, and 25.9%, respectively. Hernández et al. [7] have evaluated the performance of photovoltaic (PV) panels by using a forced air stream to improve the output performance of the PV module. According to their results, the temperature of the PV panels dropped by 15 °C, and the power output increased by up to 15%. Hasan et al. [8] performed many experiments with various Phase Change Materials (PCMs) and dropped the maximum temperature to 21 °C. Hussam et al. [9] carried out both experimental and numerical studies utilizing a heat sink with improved plate fins. It was observed that the PV system's power output reached about 55% and a 35% increase in electrical efficiency. Chandrasekhar et al. [10] have developed a simple passive cooling system with a heat spreader and a cotton wick structured on the rear of the PV module to regulate the temperature of flat PV modules. Their experimental results showed a reduction in the module temperature by about 12%. Alami [11] investigated the incorporation of a layer of synthetic clay into the back of the module and allowed a thin film of water to evaporate. The result showed 19.10% improvement in the output power compared with the PV module without cooling. Chandrasekhar et al. [12] studied a passive cooling system with cotton wick structures to cool flat PV panels. Their study showed a 30% temperature decrease when cooling was used compared with the case without cooling. Mustapha Dida et al. [13] studied an evaporative cooling system that achieved a significant temperature reduction of 26%. The output power was improved from

58.11 to 65.07 W, which is equivalent to a 12% output power improvement. Furthermore, the cooling procedure consumed only 0.39 *L*/h of water. Agyekum et al. [14] presented a cotton wick-based dual surface cooling system for a photovoltaic panel. The average temperature difference between the cooled and referenced modules, according to their experimental work's preliminary findings, is 24 °C, and the overall electrical efficiency has increased by 12%. The goal of the current study is to improve the efficiency of the PV module by evaporative cooling system under actual outside surroundings over summer days.

2   Methodology

The experiment setup consists of two flat PV modules of polycrystalline with the same standard test conditions (STC). The modules' specifications are illustrated in Table 1. The burlap material of capillary action was directly attached to the module's back surface. A firm press is applied to ensure a permanent adhesion between the burlap and the rear surface of the module to keep the burlap material wet and avoid sagging. A metal grid is positioned on the material and timber roof with suitable sizes placed between the metal grid and the aluminum frame of the module. This assembly ensures a firm fixation of the burlap material on the backside to the PV panel as shown in Fig. 1. Waterproof paint is used to protect the grid and the wood rods from corrosion and decay. The water source of this system is a water tank that is placed above the PV panels with a manual control valve to allow the water to flow by gravity through a PVC pipe. The PVC pipe is longitudinally cut to allow the burlap material ends to be inserted. Hot melt glue is used between PVC and burlap cloth to avoid water leaks and flows through the burlap cloth only. By utilizing this method, the PV panel's temperature can be decreased and uniformly distributed throughout the module. The PV setup is tilted at an angle of 26° over toward the south, which is about the latitude of Buryadah city in the Kingdom of Saudi Arabia. The experiment was carried out during the summer of 2022 on clear hot days on the roof of the Engineering College at Qassim Universityas as shown in Fig. 2, starting from 9:00 to 15:00 local time for four consecutive days. The PV panel power and efficiency are calculated using the following two equations:

Table 1 PV module characteristics at am:1.5, 1000 W/m^2, and 25 °C

Parameter	Standard
Technology	Polycrystalline
Maximum power (w)	80
Maximum voltage (V)	18
Maximum current (A)	4.62
Open circuit voltage (V)	20.76
Short circuit current (A)	5.18
Dimension (mm^2)	$780 \times 675 \times 25$
Weight (kg)	6.2
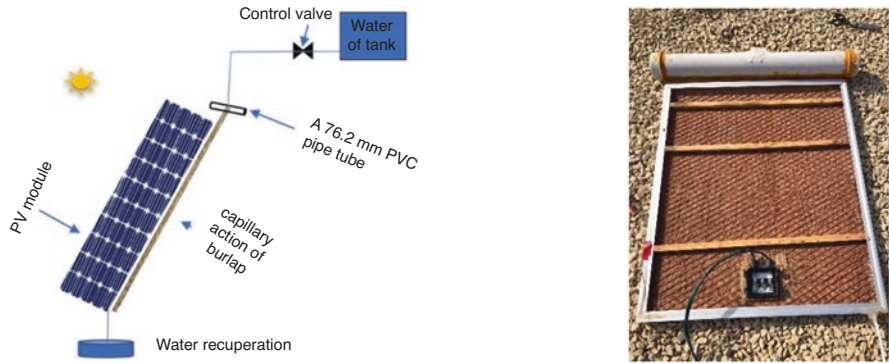
Fig. 1 Schematic view of the PV panel with evaporative cooling system and a rear side of panel
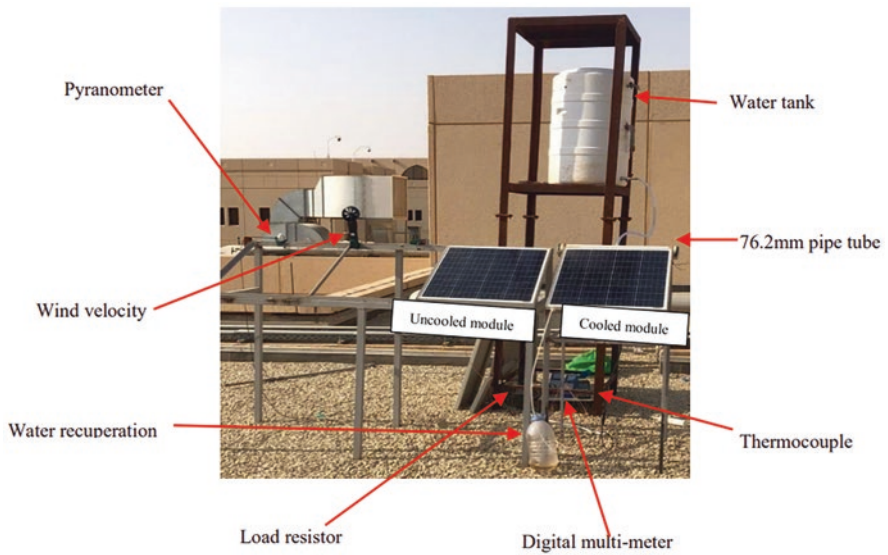
Fig. 2 The experimental test setup

$$P = V \times I \tag{1}$$

$$\eta = \frac{P}{A \times G} \tag{2}$$

where G is the solar irradiation incident on the PV panel.

Table 2 Specifications for measurement instruments

Measurement	Device construct	Range	Accuracy
Digital multimeter	PeakTech 3315	(0–20 A) (0–600 V)	±0.8%
Thermocouple (K-type)	HUATO (S220-T8)	−200 ~ 1800 °C	±1%
Pyranometer	LP02	0 ~ 2000 W/m²	±0.9%
Temperature	RHT20	0–70 °C	±1%
Humidity	RHT20	0–100%	±3%HR
Load resistor	LEYBOLD®	330 Ω	±0.8%
Wind velocity	Testo417	0 + 20 m/s	±0.01 m/s

2.1 Uncertainty Analysis

For each experiment, there is some level of uncertainty in the measurements. The measurement system's uncertainties in the experiment are indicated in Table 2. To evaluate the results' accuracy. The following calculation using Hadipour et al. [6]. calculate the measurement uncertainties of the efficiency of the PV module using the following equation:

$$\frac{\omega\eta}{\eta} = \sqrt{\left(\frac{\omega V}{V}\right)^2 + \left(\frac{\omega I}{I}\right)^2 + \left(\frac{\omega E}{E}\right)^2 + \left(\frac{\omega Ac}{Ac}\right)^2}$$

(3)

The calculations showed the uncertainty recorded of the efficiency of the PV module during the experiment is 1.41%.

3 Results and Discussion

3.1 Weather Conditions

The ambient temperature of the test days (August 29 to September 1, 2022) has been indicated in Fig. 3a. The peak ambient temperature at noon time was 43°C at 13:12, 45.1°C at 13:39, 42.8°C at 14.16, and 41.3 °C at 13.02. While the average was 41 °C, 41.4 °C, 40.1 °C, and 40.2°C for 4 days, respectively. Figure 3b showed the solar radiation over the test days with the highest irradiance was 874 W/m² at solar noon around 12:00 P.M. on Day 2, while the lowest amount was 565 W/m² at 15:00 P.M. on the first day. The hourly variation of humidity is illustrated in Fig. 4a. It is observed that a low humidity in summer-time promotes the adoption of water evaporation for the cooling of PV panels. According to the result of humidity, Days 1 and 2 were the lower days. Figure 4b showed variation of wind velocity during in the four test days.
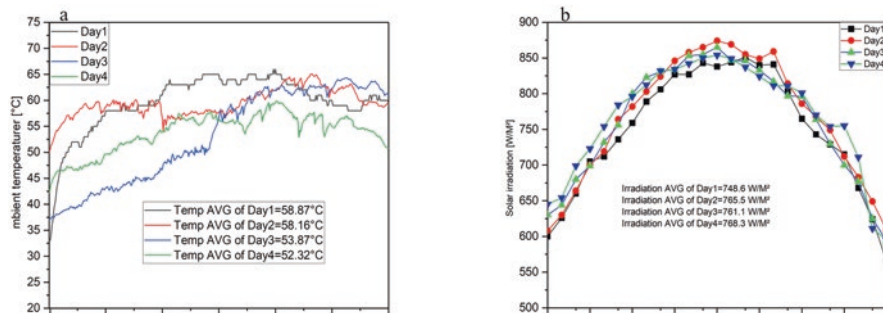
Fig. 3 (**a**) Ambient temperature during the four test days, (**b**) Horizontal radiation during the four test days
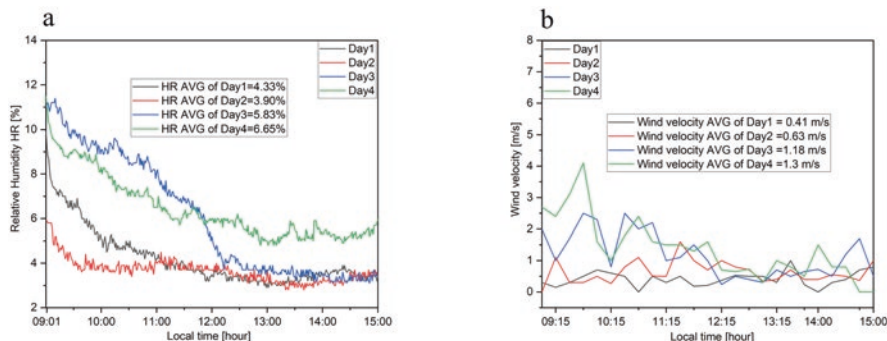
Fig. 4 (**a**) Humidity ratio during the four test days, (**b**) wind velocity during the four test days

3.2 Temperature of the PV Module

To evaluate the result of the two PV modules over the same period of time from 9:00 A.M. to 15:00 P.M. from August 29 to September 1, each module's back surface had four K-type thermocouples placed in different places (cooled and uncooled PV modules). The data was collected at intervals of 1-minute in order to investigate the impact of the evaporative cooling system on the temperature of the PV module and is depicted in Figs. 5 and 6. The temperatures as curves TU1, TU2, and TU3, TU4, are for the uncooled modules, while the TC1, TC2, and TC3, TC4 curves signify the temperature of the cooled modules. At the beginning of the experiments, the cooled PV panels' temperature drops rapidly due to the use of water, while the temperatures of the uncooled module continue rising. According to the results, the uncooled panel's temperature peaked from 12:00 P.M. to 1:30 P.M. for all days' tests and this could be explained by high radiation and low wind velocity below 0.5 m/s during the four test days depicted in Fig. 4a, b. The highest reported temperature of the uncooled module was 74.2 °C at 12:14 P.M. This was downgraded to 52.3 °C. It has been noted that the average temperature of the uncooled module over the days was
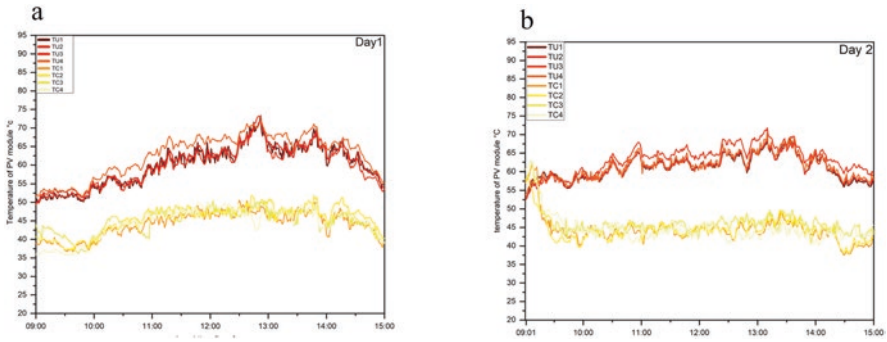
Fig. 5 (**a**) Temperatures of the cooled and uncooled PV module (August 29, 2022) (**b**) Temperatures of the cooled and uncooled PV module (August 30, 2022)
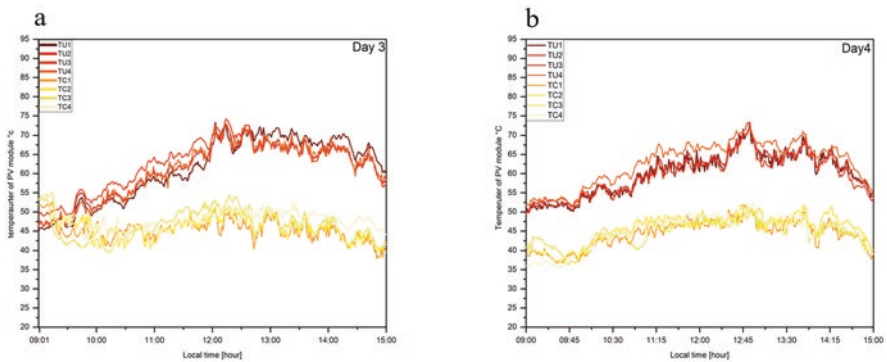
Fig. 6 (**a**) Temperatures of the cooled and uncooled PV module (August 31, 2022) (**b**) Temperatures of the cooled and uncooled PV module (September 1, 2022)

62.3 °C against 44 °C for cooled PV module. It results in an approximately 29.3% drop in operating temperature with the suggested cooling system.

Impact of Cooling on Electrical Characteristics In order to assess the influence of introducing the cooling system on solar-panel-generated electricity, I–V data was collected at intervals of 15 minutes throughout the duration of the test by comparing the measured outcomes. Figure 7a showed the difference between the uncooled and cooled PV modules. It can be observed in the curve of uncooled modules that V_{oc} decreases linearly by rising the cell temperature and the V_{oc} of cooled modules continues rising affected by the cooling system. The daily average of V_{oc} improvement was almost 5.5% because of the evaporative cooling system's utilization. The output power and electrical efficiency of the module will both be greatly improved by this increase in voltage. The two PV modules' output power comparison is provided in Fig. 7b. The average power generation of the cooled module was improved by about 10.8%. Figure 8a illustrates the I–V characteristic curves for the experiment. Figure 8b showed the effects of using the evaporative cooling system on the PV
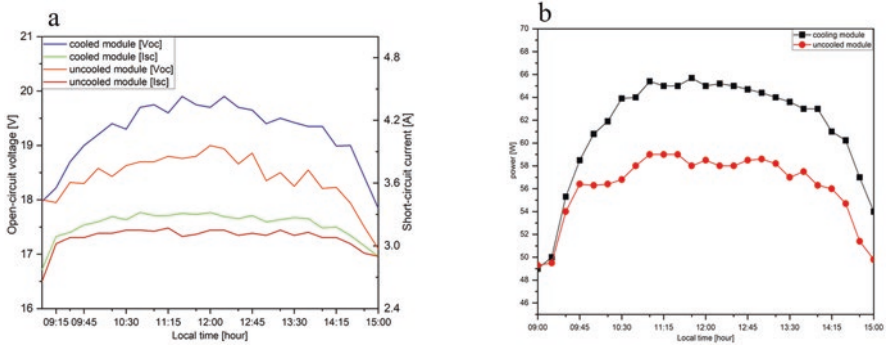
Fig. 7 (**a**) Variations in the tested PV modules of I_{sc} and V_{oc}, (**b**) Comparison of the power output for the two modules
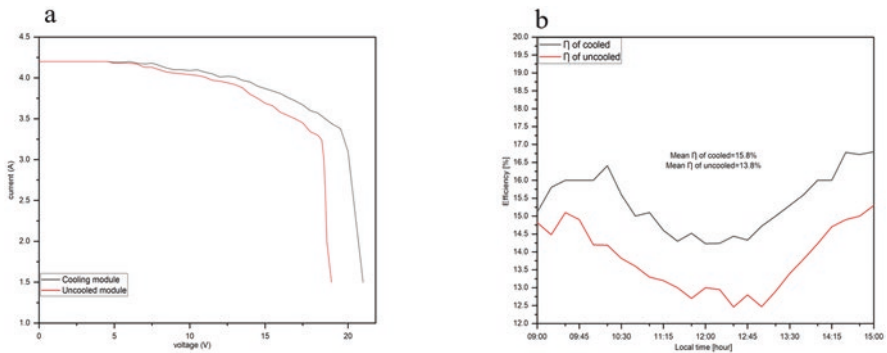
Fig. 8 (**a**) I–V characteristic curves, (**b**) differences in the electrical efficiency of the tested PV modules

module's efficiency and improved in efficiency. According to the experiment's test results the average electrical efficiency of the cooled module was 15.4% against 13.8% for an uncooled module which achieved a 12.7% increase in the efficiency of a cooling module.

Water consumption The water consumption was quantified during the experiment time approximately 0.30 L/h.

4   Conclusion

In this chapter, a passive cooling system is used to enhance the performance of PV modules based on the water evaporation process using a burlap material of capillary action. The study was carried out under real climate conditions. Each weather

parameter was taken into consideration in order to evaluate the effect based on the obtained outcome, and the following conclusions are drawn:

- Utilizing PVC pipe was longitudinally cut and hot melt glue could contribute to increase the water follow rate and avoid evaporating water from the PVC pipe where the minimal water consumption was just about 0.30 L/h.
- According to the result, the average V_{oc} improvement was about 5.5% because of the used evaporative cooling system.
- The average power output for the overall experimental period was improved by about 10.8%.
- According to the experiment results, the average electrical efficiency of the cooled module was 15.4% against 13.8% for an uncooled module where the cooling module achieved a 12.7% increase in efficiency.

References

1. Najafi, H., Woodbury, K.A.: Optimization of a cooling system based on Peltier effect for photovoltaic cells. Sol. Energy. **91**, 152–160 (2013)
2. Ogbomo, O.O., et al.: Effect of operating temperature on degradation of solder joints in crystalline silicon photovoltaic modules for improved reliability in hot climates. Sol. Energy. **170**, 682–693 (2018)
3. Royo, P., et al.: Hybrid diagnosis to characterise the energy and environmental enhancement of photovoltaic modules using smart materials. Energy. **101**, 174–189 (2016)
4. Nižetić, S., et al.: Water spray cooling technique applied on a photovoltaic panel: the performance response. Energy Convers. Manag. **108**, 287–296 (2016)
5. Bahaidarah, H., et al.: Performance evaluation of a PV (photovoltaic) module by back surface water cooling for hot climatic conditions. Energy. **59**, 445–453 (2013)
6. Hadipour, A., Rajabi Zargarabadi, M., Rashidi, S.: An efficient pulsed- spray water cooling system for photovoltaic panels: experimental study and cost analysis. Renew. Energy. **164**, 867–875 (2021)
7. Mazón-Hernández, R., et al.: Improving the electrical parameters of a photovoltaic panel by means of an induced or forced air stream. Int. J. Photoenergy. **2013**, 1–10 (2013)
8. Hasan, A., et al.: Energy and cost saving of a Photovoltaic-Phase Change Materials (PV-PCM) system through temperature regulation and performance enhancement of photovoltaics. Energies. **7**(3), 1318–1331 (2014)
9. Hussam, W.K., Khlefat, A.M., Sheard, G.J.: Energy saving and performance analysis of aircooled photovoltaic panels. Int. J. Energy Res. **46**(4), 4825–4834 (2021)
10. Chandrasekar, M., Senthilkumar, T.: Experimental demonstration of enhanced solar energy utilization in flat PV (photovoltaic) modules cooled by heat spreaders in conjunction with cotton wick structures. Energy. **90**, 1401–1410 (2015)
11. Alami, A.H.: Effects of evaporative cooling on efficiency of photovoltaic modules. Energy Convers. Manag. **77**, 668–679 (2014)
12. Chandrasekar, M., et al.: Passive cooling of standalone flat PV module with cotton wick structures. Energy Convers. Manag. **71**, 43–50 (2013)
13. Dida, M., et al.: Experimental investigation of a passive cooling system for photovoltaic modules efficiency improvement in hot and arid regions. Energy Convers. Manag. **243**, 114328 (2021)
14. Agyekum, E.B., et al.: Effect of dual surface cooling of solar photovoltaic panel on the efficiency of the module: experimental investigation. Heliyon. **7**(9), e07920 (2021)

Influence of Absorber Layer Thickness and Band Gap Tuning on the Optical and Electrical Properties of Semi-transparent Flexible Perovskite Solar Cells

Muhammad Noman (iD)**, Adnan Daud Khan** (iD)**, and Shayan Tariq Jan** (iD)

1 Introduction

With the advancement of technology, the demand for smart applications has also rapidly increased. One such application which is catching the attention of people are the semi-transparent windows used in building integrated photovoltaic (BIPV) technologies [1]. The smart windows not only allow a portion of the visible light to pass through for illuminating the room, but also harness the photons of the remaining light spectrum to produce electricity [2]. Thus, it provides dual functions. Obtaining high power conversion efficiency (PCE) with transparency simultaneously is one of the biggest challenges faced by this technology. This is due to the trade-off between efficiency and transparency in absorbing the sunlight spectrum [3].

Multiple materials have been tested as the photovoltaic (PV) material in these windows with different success rates. Some of the most promising results have been obtained with perovskite solar cells (PSC) because of its high absorption coefficient (5.7×10^4 cm^{-1} at 600 nm), good PCE (more than 20%), tunable band gap (1.3–2.2 eV), and fast carrier mobility (1–10 cm^{2}V^{-1}s^{-1}) [1, 2, 4, 5]. These outstanding characteristics make them an excellent contender to be considered for BIPV.

Two of the most feasible methods used to increase the transparency of the PV cell with acceptable PCE are (i) reducing the thickness of the PSC and (ii) tuning the band gap of the perovskite material [3, 6]. Both of these methods decrease the absorption of the light spectrum in the PSC, thus increasing the transparency. But the drawback is that lesser photons are absorbed, leading to lower PCE [4].

M. Noman (✉) · A. D. Khan · S. T. Jan
U.S.-Pakistan Center for Advanced Studies in Energy,
University of Engineering & Technology, Peshawar, Pakistan
e-mail: muhammad.noman@uetpeshawar.edu.pk

Therefore, it is very important to achieve a trade-off balance between efficiency and transparency.

Yaun et al. carried out a study on MAPbI$_{3-x}$Br$_x$ perovskite material in which band gap tuning was achieved by changing the ratio of I and B concentration [3]. The band gap was tuned between 1.5 and 1.8 eV. The results showed that as the band gap increased the material absorption reduced which in turn reduced the efficiency of the cell. Similarly, Mehran et al. in their work achieved higher optical transmittivity in the perovskite material by reducing the thickness from 700 nm to 300 nm but the efficiency of the cell also dropped to 4% [6]. Jan et al. in their work presented the relation of different materials' band gap with their optical transmittivity [7]. The study showed that materials with low band gap had low transmittivity with high absorption while materials having large band gap gave high transmittivity with reduced absorption.

In this study, the PSC structure FTO/TiO$_2$/MAPbI$_3$/PTAA/Au PSC is selected and modelled in SCAPS-1D software. A systematic methodology is designed to study the effect of band gap tuning and layer thickness on the absorption, transparency, quantum efficiency, energy band alignment, Jsc, Voc, and efficiency of the PSC [8].

2 Device Modelling

Figure 1 shows the architecture of the PSC [9]. It has 5 main layers [10]. In this work the FTO glass is used as the cathode and gold (Au) as the anode. For the n-type electron transport layer (ETL) titanium dioxide (TiO$_2$) is selected, while for the p-type hole transport layer (HTL) Poly[bis(4-phenyl)(2,4,6-trimethylphenyl)amine (PTAA) is selected. Methyl ammonium lead halide (CH$_3$NH$_3$PbI$_3$) is selected as the perovskite absorber material. The combination of all the layers makes the perovskite structure of FTO/TiO$_2$/MAPbI$_3$/PTAA/Au which is numerically modelled.

The PSC structure is modelled layer by layer using SCAPS. Intensive literature review of multiple studies was carried out after which the design parameters of each
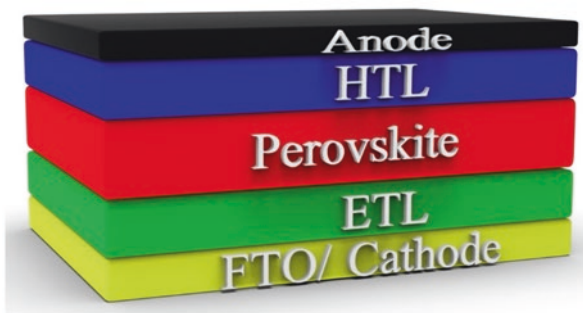
Fig. 1 PSC Layer Structure

Table 1 Design parameters for PSC [11–16]

Parameters	TiO$_2$	CH$_3$NH$_3$PbI$_3$	PTAA
Thickness (nm)	100	400	100
Bandgap (eV)	3.2	1.55	2.9
Electron Affinity (eV)	4	3.9	2.3
Dielectric Permittivity	10	6.5	9
CB Effective Density of State (cm^{-3})	2×10^{18}	2.2×10^{18}	1×10^{21}
VB Effective Density of State (cm^{-3})	1.8×10^{19}	1×10^{18}	1×10^{21}
Electron Thermal Velocity (cm/s)	1×10^7	1×10^7	1×10^7
Hole Thermal Velocity (cm/s)	1×10^7	1×10^7	1×10^7
Electron Mobility (cm^2/Vs)	20	2	1
Hole Mobility (cm^2/Vs)	10	2	40
Donor Density N$_D$ (cm^{-3})	1×10^{20}	–	–
Acceptor Density N$_A$ (cm^{-3})	–	1×10^{18}	1×10^{20}

material were identified and selected [11–16]. Table 1 presents the design parameters selected for the different materials. Standard test conditions were used to conduct all the simulations.

Defect densities (Nt) are introduced in the bulk of each layer and interface defects between them to obtain more realistic results close to the experimental ones. In this study Nt of 1×10^{14} cm^{-3} is modelled in the bulk of each layer including the perovskite and both charge transport layers (CTLs) while interface defect of 1×10^{11} cm^{-3} is selected for both interfaces between the absorber and CTL.

3 Results and Discussion

3.1 Band Gap Tuning

To analyze the effect of band gap tuning on the optical and electrical properties of the PSC, the band gap was tuned from 1.45 eV to 1.95 eV while keeping the thickness constant at 400 nm. The absorption, quantum efficiency, IV characteristics, fill factor (F.F), PCE, and energy band alignment were analyzed in detail.

Absorption and Quantum Efficiency Figure 2 shows the simulation results of absorption and quantum efficiency as a function of band gap. The results show that as the band gap of the PSC is increased and the absorption is reduced from 180 × 10^3/cm to 140 × 10^3/cm. This is because increasing the band gap energy increases the distance between the conduction and valance band of the perovskite material [3]. The increasing gap allows the light of higher wave lengths, which are low on energy, to pass through the cell without being absorbed [4]. Therefore, both the quantum efficiency and absorption wavelengths are affected. The quantum efficiency (at 400 nm) sees a decrease from 85% to 70% while the absorption wavelength is decreased from 870 nm to 650 nm.
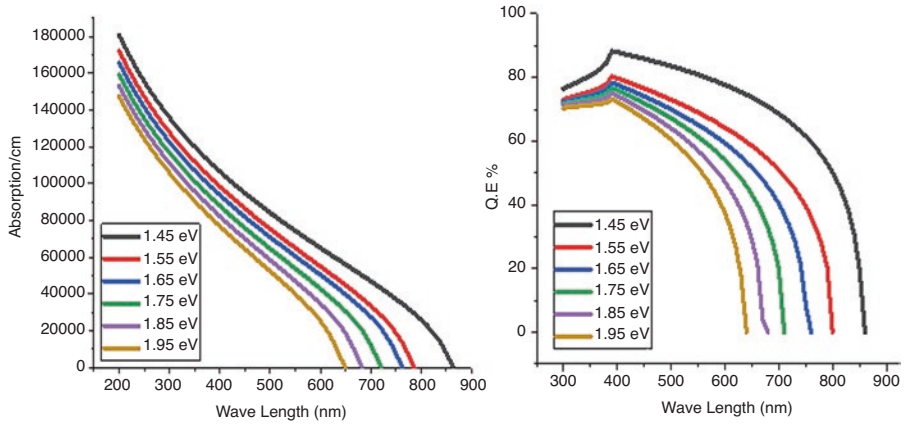
Fig. 2 Absorption and quantum efficiency of PSC with different band gaps
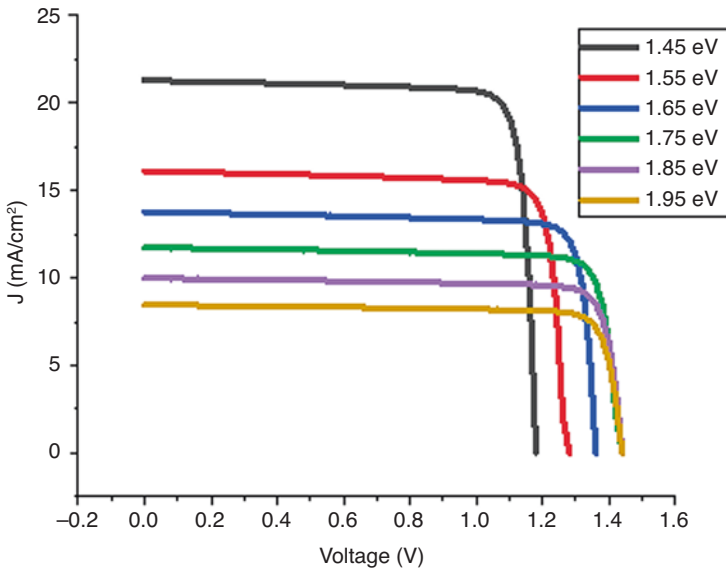
Fig. 3 IV curve of PSC with different band gaps

IV Characteristics The IV characteristic of all the PSC band gaps are shown in Fig. 3. Table 2 presents the electrical performance of the different band gaps.

From the results it can be seen that increasing the band gap increases the Voc of the cell from 1.17 v to 1.43 v. This is because increasing the Eg increases the minimum energy required for the electron in the valance band to make a successful jump to the conduction band, thus increasing the electric potential of the cell [17].

Table 2 Electrical output of PSC with different band gaps

B.G	1.45 eV	1.55 eV	1.65 eV	1.75 eV	1.85 eV	1.95 eV
Voc (v)	1.17	1.26	1.35	1.42	1.43	1.43
Jsc (mA/cm²)	21.29	16.11	13.77	11.74	9.98	8.47
F.F (%)	85.67	85.14	85.32	84.98	84.69	84.58
PCE (%)	21.49	17.34	15.95	14.25	12.16	10.31
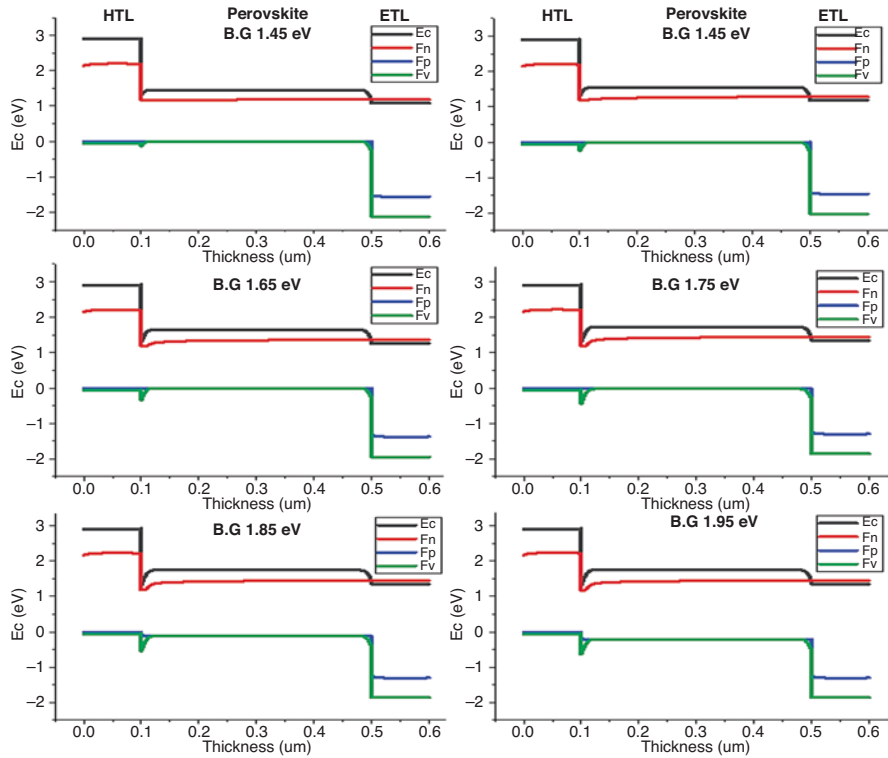
Fig. 4 Energy band diagram of PSC with different band gaps

Changing the band gap of the perovskite effects the valance band offset (VBO) between the absorber and CTL (Eq. 1). The bigger the VBO, the larger the spikes are produced at the interfaces of the structure as can be seen in Fig. 4 [18]. This produces a built-in potential (Vbi) at the interfaces. This in turn increases the Voc (Eq. 2):

$$\text{V.B.O} = \left(\chi_{\text{CTL}} - \chi_{\text{Per}} + \text{Eg}_{\text{CTL}} - \text{Eg}_{\text{Per}} \right) \tag{1}$$

$$\text{Voc} = \text{Vbi} - \frac{nKT}{q} \ln \frac{J}{J_l} \tag{2}$$

Here, "χ" is the electron affinity, "K" is Boltzmann constant, "T" is solar cell operating temperature, "J" is the reverse saturation current, and "J_l" is light-generated current.

The Jsc sees a significant reduction from 21.29 mA/cm^2 to 8.47 mA/cm^2 with increasing the band gap because less of the light spectrum is absorbed, which leads to less photons being absorbed and producing less charged particles [17]. The Jsc also reduces because of the larger spikes made at the interface due to large VBO [18]. The large spikes produced, impacts the flow of charge particles by making hurdles. The significant reduction of the Jsc reduces the PCE of the PSC from 21.49% to 10.31%.

3.2   Thickness Tuning

To analyze the thickness tuning effect on the optical and electrical characteristics of the PSC, the perovskite thickness was changed from 100 to 400nm for the PSC structures of different band gaps. The Jsc, PCE, and transparency of the PSC were analyzed in detail.

Effect on Short Circuit Current (Jsc) Figure 5 demonstrates the Jsc as a function of thickness for the PSC of different Eg. For each Eg as the thickness of the perovskite is increased, the Jsc produced also rises. This is because as the material thickens, the absorbing of light also increases [19]. This in turn increases the number of photons absorbed and more charge carriers are produced [20]. The increased Jsc increases the performance and PCE of the PSC [21].
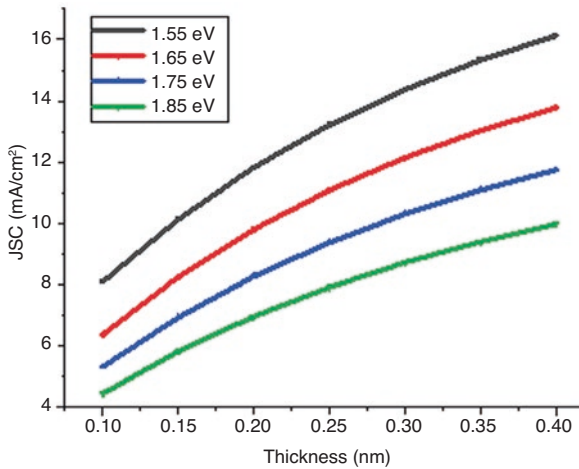
Fig. 5.   Jsc of PSC with different band gaps
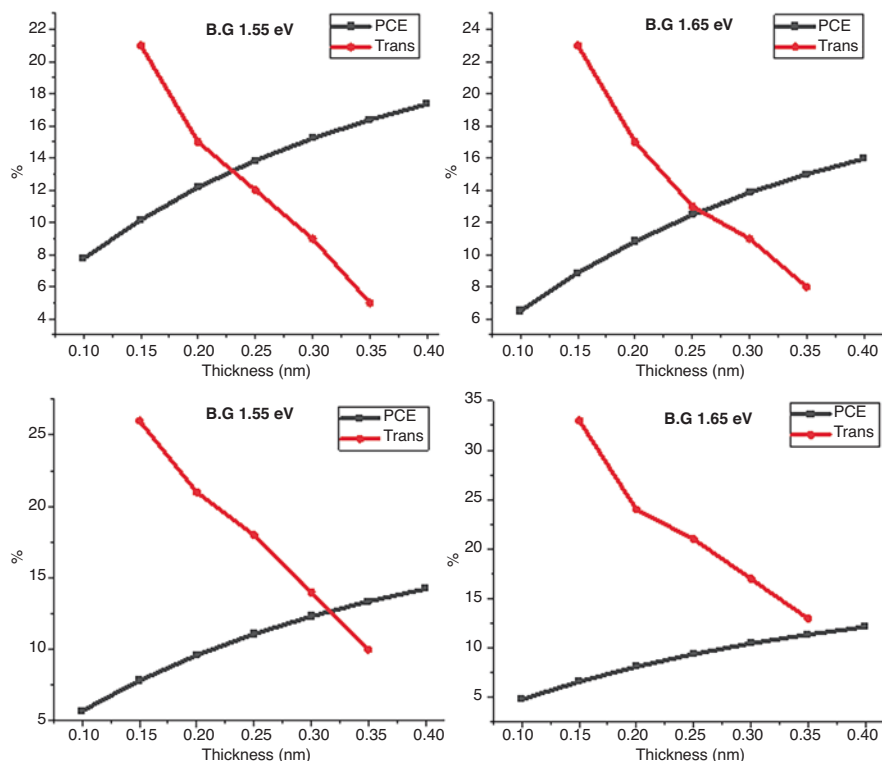
Fig. 6 Transparency vs. PCE of PSC with different band gaps

Transparency vs. PCE Figure 6 shows results of transparency vs. PCE as a function of thickness for the PSC of different band gaps. The results show that as the band gap rises the transparency of the PSC at 150nm thickness increases from 22% to 34%. But the PCE efficiency is reduced from 10% to 7%. When the perovskite thickness is increased from 100 nm to 400 nm, all the PSCs see an efficiency increase of more than 8%. But the transparency is reduced by more than 10%, with greater effect being on low band gap PSC. From the results it can be concluded that according to one's requirements, the desired transparency and efficiency of PSC can be achieved by tuning both the band gap and the thickness.

4   Conclusion

The PSC structure (FTO/TiO$_2$/CH$_3$NH$_3$PbI$_3$/PTAA/Au) is selected in this work to study the effect of band gap tuning and layer thickness on the absorption, transparency, quantum efficiency, energy band alignment, Jsc, Voc, and PCE of the PSC through SCAPS-1D. The study found that by tuning the band gap from 1.45 eV to

1.95 eV, the absorption is reduced from 180×10^3/cm to 140×10^3/cm, while the transparency increases from 22% to 34% because less of the light spectrum is used. The quantum efficiency (at 400 nm) sees a decrease from 85% to 70% while the absorption wave length is decreased from 870 nm to 650 nm. Because of this the Jsc sees a significant reduction from 21.29 mA/cm^2 to 8.47 mA/cm^2, which leads to the PCE to decrease from 21.49% to 10.31%. Although the Voc increases from 1.17 v to 1.43 v due to the Vbi of the cell increasing because of higher band gap and VBO. By tuning the thickness of the perovskite material from 150 nm to 400 nm the PCE increases more than 8% due to absorbing photons of higher wavelength. But the transparency is reduced by more than 10%. From the results it can be concluded that according to one's requirements, the desired transparency and efficiency of PSC can be achieved by tuning both the band gap and the thickness.

References

1. Batmunkh, M., Zhong, Y.L., Zhao, H.: Recent advances in perovskite-based building-integrated photovoltaics. Adv. Mater. **32**(31), 2000631 (2020)
2. Shen, L., Yip, H., Gao, F., Ding, L.: Semitransparent perovskite solar cells for smart windows. Sci. Bull. (Beijing). **65**(12), 980–982 (2020). https://doi.org/10.1016/j.scib.2020.03.014
3. Yuan, L., et al.: Semi-transparent perovskite solar cells: unveiling the trade-off between transparency and efficiency. J. Mater. Chem. A Mater. **6**(40), 19696–19702 (2018)
4. Rahmany, S., Etgar, L.: Semitransparent perovskite solar cells. ACS Energy Lett. **5**(5), 1519–1531 (2020). https://doi.org/10.1021/acsenergylett.0c00417
5. Shi, B., Duan, L., Zhao, Y., Luo, J., Zhang, X.: Semitransparent perovskite solar cells: from materials and devices to applications. Adv. Mater. **32**(3), 1806474 (2020)
6. Mahran, A.M., Abdellatif, S.O.: Optoelectronic modelling and analysis of transparency against efficiency in perovskites/dye-based solar cells. In: 2021 International Conference on Microelectronics (ICM), pp. 178–181 (2021). https://doi.org/10.1109/ICM52667.2021.9664924
7. Jan, S.T., Noman, M.: Influence of absorption, energy band alignment, electric field, recombination, layer thickness, doping concentration, temperature, reflection and defect densities on MAGeI $_3$ perovskite solar cells with Kesterite HTLs. Phys. Scr. **97**(12), 125007 (2022)
8. Tariq Jan, S., Noman, M.: Influence of layer thickness, defect density, doping concentration, interface defects, work function, working temperature and reflecting coating on lead-free perovskite solar cell. Solar Energy. **237**, 29–43 (2022). https://doi.org/10.1016/j.solener.2022.03.069
9. Shen, K., Sun, H.L., Ji, G.: Fabrication and characterization of organic–inorganic hybrid perovskite devices with external doping. In: Nanoelectronics & Materials Development. InTech (2016)
10. Khattak, Y.H., Baig, F., Shuja, A.: Numerical analysis guidelines for the design of efficient novel nip structures for perovskite solar cell. Solar Energy. **207**, 579–591 (2020)
11. Santos, I.M.D.L., et al.: Optimization of CH3NH3PbI3 perovskite solar cells: a theoretical and experimental study. Solar Energy. **199**, 198–205 (2020)
12. Hima, A., Lakhdar, N., Benhaoua, B.: An optimized perovskite solar cell designs for high conversion efficiency. Superlattices Microstruct. **129**, 240–246 (2019)

13. Husainat, A., Ali, W., Cofie, P., Attia, J., Fuller, J.: Simulation and analysis of methylammonium lead iodide (CH3NH3PbI3) perovskite solar cell with Au contact using SCAPS 1D simulator. Am. J. Optics Photon. **7**(2), 33 (2019)
14. Karimi, E., Ghorashi, S.M.B.: The effect of SnO2 and ZnO on the performance of perovskite solar cells. J. Electron. Mater. **49**(1), 364–376 (2020)
15. Azri, F., Meftah, A., Sengouga, N.: Electron and hole transport layers optimization by numerical simulation of a perovskite solar cell. Solar Energy. **181**, 372–378 (2019)
16. Raoui, Y., Ez-Zahraouy, H., Tahiri, N., El Bounagui, O., Ahmad, S., Kazim, S.: Performance analysis of MAPbI3 based perovskite solar cells employing diverse charge selective contacts: simulation study. Solar Energy. **193**, 948–955 (2019)
17. Shasti, M., Mortezaali, A.: Numerical study of Cu_2O, $SrCu_2O_2$, and $CuAlO_2$ as hole-transport materials for application in perovskite solar cells. Physica Status Solidi (a). **216**(18), 1900337 (2019). https://doi.org/10.1002/pssa.201900337
18. Khattak, Y.H., Baig, F., Toura, H., Beg, S., Soucase, B.M.: CZTSe kesterite as an alternative hole transport layer for MASnI3 perovskite solar cells. J. Electron. Mater. **48**(9), 5723–5733 (2019). https://doi.org/10.1007/s11664-019-07374-5
19. Mandadapu, U.: Simulation and Analysis of Lead based Perovskite Solar Cell using SCAPS-1D. Indian J. Sci. Technol. **10**(1), 1–8 (2017). https://doi.org/10.17485/ijst/2017/v11i10/110721
20. Adeyemi Owolabi, J.: Investigating the effect of ZnSe (ETM) and Cu2O (HTM) on absorber layer on the performance of pervoskite solar cell using SCAPS-1D. Am. J. Phys. Appl. **8**(1), 8 (2020). https://doi.org/10.11648/j.ajpa.20200801.12
21. Abdelaziz, S., Zekry, A., Shaker, A., Abouelatta, M.: Investigating the performance of formamidinium tin-based perovskite solar cell by SCAPS device simulation. Opt. Mater. (Amst). **101**, 109738 (2020). https://doi.org/10.1016/j.optmat.2020.109738

Evaluation of Energy Payback Time (EPBT) and Carbon Emission by a Medium-Sized PV Power Plant in Burkina Faso

Kodami Badza, Marie Sawadogo, and Y. M. Soro

1 Introduction

Like several African countries, Burkina Faso is facing the consequences of climate change. The country faces a very significant energy challenge with limited production capacities. The energy model of Burkina Faso highlights a strong dependence on electricity fossil fuels (56%), a total dependence on hydrocarbons, and a weak valuation of the national potentialities in renewable energies, such as solar. Solar energy is the most abundant source of renewable energy in Burkina Faso, with daily sunshine of 5.5 kWh/m² for 3000–3500 hours per year [1]. Solar energy has been the subject of significant development in Burkina Faso in recent years with the proliferation of PV power plants connected to the utility grid [2]. PV systems have long been considered a clean source of energy. Indeed, they are reliable, easy to install, and require low maintenance. From an environmental point of view, PV systems are silent and do not emit pollutants during the use stage [3, 4]. However, care must be taken not to displace pollution from one energy source from one stage to another. Analyzing the life cycle involves considering all product life cycle stages.

Life Cycle Assessment (LCA) is a tool for compiling and quantifying inputs and outputs and potential environmental impacts of a system throughout its lifetime from raw material extraction, manufacturing, transportation, operation, and end-of-life management [5]. Several studies have been conducted on LCA of PV systems worldwide [6–10]. These studies mainly assess the impacts of stand-alone and off-grid PV production systems. In addition, data on the impact of end-of-life management of PV systems in Africa is almost non-existent. This study evaluates the energy payback time and climate change indicator of a photovoltaic power plant in Burkina Faso by comparing different end-of-life scenarios and comparing it to the country's electricity mix.

K. Badza (✉) · M. Sawadogo · Y. M. Soro
Laboratoire Energies Renouvelables et Efficacité Energétique (LabEREE), Institut
International d'Ingénierie de l'Eau et de l'Environnement (2iE), Ouagadougou, Burkina Faso

33

2 Methodology

2.1 Description of the solar PV plant

The Ziga photovoltaic power plant is located 50 km from Ouagadougou (Burkina Faso), with a capacity of 1.1 MWp, it covers an area of nearly 2 ha. A partial view of the PV plant is shown in Fig. 1. There are 44 aluminum mounting structures (tables) distributed in this area, and each mounting structure is composed of 4 lines and 25 rows, making a total of 100 modules per mounting structure, inclined at 15° facing south. The 100 modules of the PV mounting structure are connected in series to form a string, which is connected to the input of a dedicated string inverter. The 44 mounting structures correspond to 44 string inverters and, therefore, to the same number of inverters whose AC output currents are combined before being fed into the plant's single transformer. This raises the voltage from the inverters to the level of the point of injection into the national interconnected grid. The Ziga power plant also has a meteorological station comprising a thermometer and an anemometer. The characteristics of the components of the PV plant are summarized in Table 1. The PV plant's total production over 25 years is estimated at 41.55 GWh.

2.2 Energy Payback Time (EPBT)

The EPBT is one of the most useful indicators for assessing the environmental performance of renewable energies. For an energy generation system to be sustainable, it must produce much more energy than is required to manufacture, install, and operate over its life cycle. The EPBT of a PV system expressed in years is the ratio

Fig. 1 Partial view of the Ziga photovoltaic power plant

Table 1 Characteristics of Ziga power plant components

Components	Characteristics
Module: 250 Wp Poly-Si	
Electrical characteristics	250 Wp, 31.2V/8.03 A, 15.51%
Dimensions	1620*987*40 mm
Weight/surface	19 kg/1,598 m^2
Number	4400 PV modules
Inverters: Sunny Tripower	
Electrical characteristics	25000 W/1000 V/33A/390–800 V
Number	44 inverters
Weight	61 kg
Transformer: DOTUL 1800 H/30	
Electrical characteristics	1800 kVA, 33kV/ 400V–50Hz
Number	01 transformer
Type of mounting structures	
Type of mounting structures	Fixed, aluminum, 15° facing south
Anchoring	metal piles
Cables	
14 mm^2 PVC-600V	3 km
200 mm^2 XPLE-600V	3 km
150 mm^2 PE-35kV	1 km

between the total primary energy used during its life cycle (manufacturing, assembly, transport, installation, maintenance, and recycling) and the energy generated annually. It is given by Eq. 1 [11]:

$$EPBT = E_{in} / E_{out}$$

(1)

E_{in} is the energy used by the PV system during the raw material extraction, manufacturing, transport, installation, and end-of-life stages, and E_{out} is the mean annual electricity generation during the operating stage.

2.3   Life Cycle Assessment

Goal and Scope Definition This study aims to determine the EPBT, assess the environmental impacts of a 1.1 MWp PV power plant installed in Burkina Faso, and compare it with the country's electricity mix. The study focuses mainly on assessing the climate change environmental indicator. The functional unit considered is 1 kWh of electricity generated and fed into the national grid.

The cradle-to-cradle assessment was carried out. Figure 2 presents a general description of the system boundaries and the associated geographical and temporal considerations. It includes the production, transport, installation, use, and their end-of-life stages.
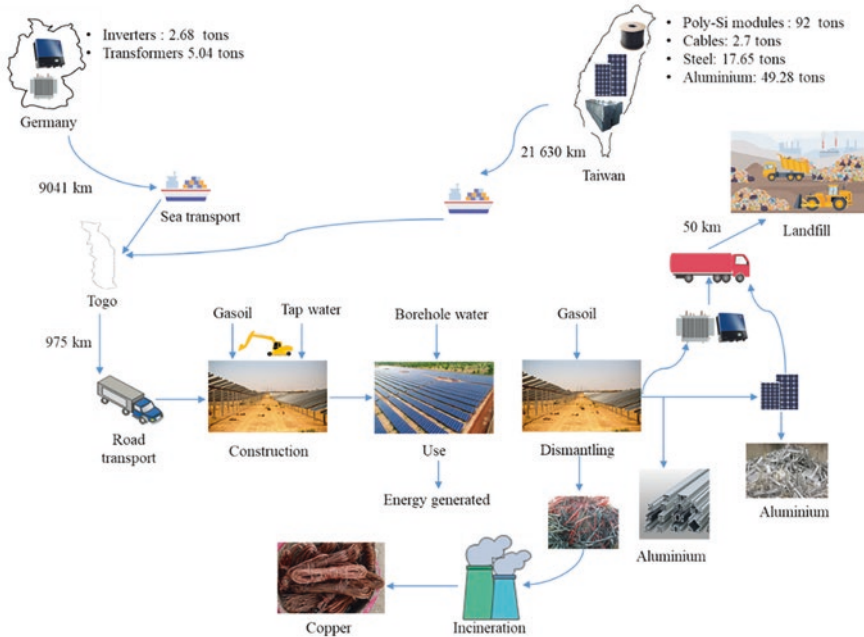
Fig. 2 System boundary studied

Three scenarios were created based on current trends in the end-of-life management of photovoltaic components (landfill and recycling). The scenarios are used to study the influence of the end-of-life stage on the overall carbon emission and the energy payback time. These three scenarios are then compared to a fourth scenario, which represents the national electricy mix of Burkina Faso.

- Scenario 1, the baseline scenario, is characterized by landfilling all PV system components at the end of their life due to the non-existence of a PV system waste treatment unit in the sub-region.
- In scenario 2, the aluminum frame of the PV module and the aluminum of the mounting structure are dismantled and recycled at 80% before sending the other components to the landfill.
- Scenario 3 considers a total recycling unit of the PV panels in addition to the recycling of the mounting structure. The PV power plant's production, transport, installation, and operation stages are identical in the 3 scenarios. The plant's production, transport, construction, and operation stages are identical in the 3 scenarios.

Finally, the discussed 3 scenarios are compared to the carbon emission from the national electricity mix of Burkina Faso.

Life Cycle Inventory The inventory data for this study was obtained from the ecoinvent database and data published in the literature. Data on manufacturing and

recycling PV panels are obtained from the studies of Bekkelund (2013), Fthenakis et al. (2011), Latunussa et al. (2016), Yu et al. (2017), and Yuan et al. (2011) [11–15], the inventory production of inverters, transformers, and recycling studies from the studies of Mason et al. (2006) and Tschümperlin et al. (2016) [16, 17].

The national electricity company of Burkina Faso (SONABEL) provided the construction and use phase data. The lifespan of the modules, transformer, inverters, and mounting structures is assumed to be 25 years. However, the parts of the inverters and the transformer must be replaced every 10 years, or 10% of their total mass, according to well-established data from the electrical industry on transformers and electronic components.

Environmental Impact Assessment The Cumulative Energy Demand (CED) method was used to determine the energy payback time of the PV plant. The climate change was calculated using the IPCC 2013 GWP 100 method. Climate change is frequently used in the literature to assess the environmental impact of an energy source [11, 18, 19]. The SimaPro 9.4 environmental modeling software and the Ecoinvent 3.6 database were used to perform the environmental impact calculations.

3   Results and Discussion

3.1   *Energy Payback Time (EPBT)*

Figure 3 illustrates the energy payback time of the Ziga photovoltaic power plant according to the end-of-life management of the components.
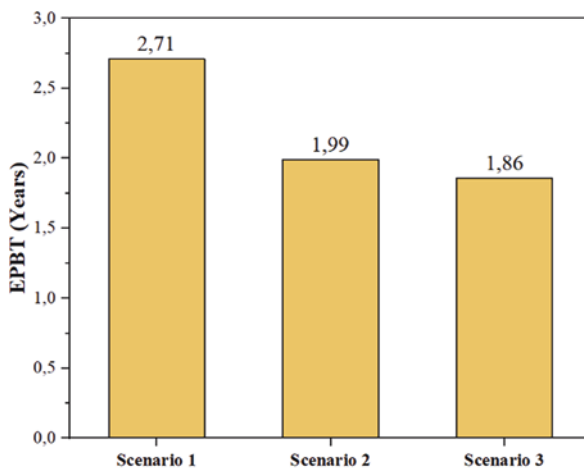
Fig. 3 Energy payback time of the PV plant

The Energy Payback Time of photovoltaics varies from 1.86 to 2.71 years, respectively, for the photovoltaic plant with a landfill of end-of-life components (scenario 1) and for the plant with recycling of the module plus the mounting structure (scenario 3). This reduction in the energy payback time of more than 31.3% is explained by the reduction in embodied energy linked to manufacturing system components. Indeed, recycled materials allow for a reduction in the consumption of materials during the manufacturing stage. However, considering the long lifespan of PV systems (25 years), the energy payback time values of these different scenarios are judged as acceptable. Indeed, the energy used by PV systemes over their entire life cycle will be recovered in less than 03 years. These energy payback times are similar to African literature studies [9, 18].

3.2 Climate Change

Figure 4 shows the contribution shares of the photovoltaic plant (scenarios 1, 2, and 3) and the electricity mix of Burkina Faso on climate change per kWh of electricity generated. The carbon emission by PV systems varies from 24.6 to 58.3 g CO_2 eq/
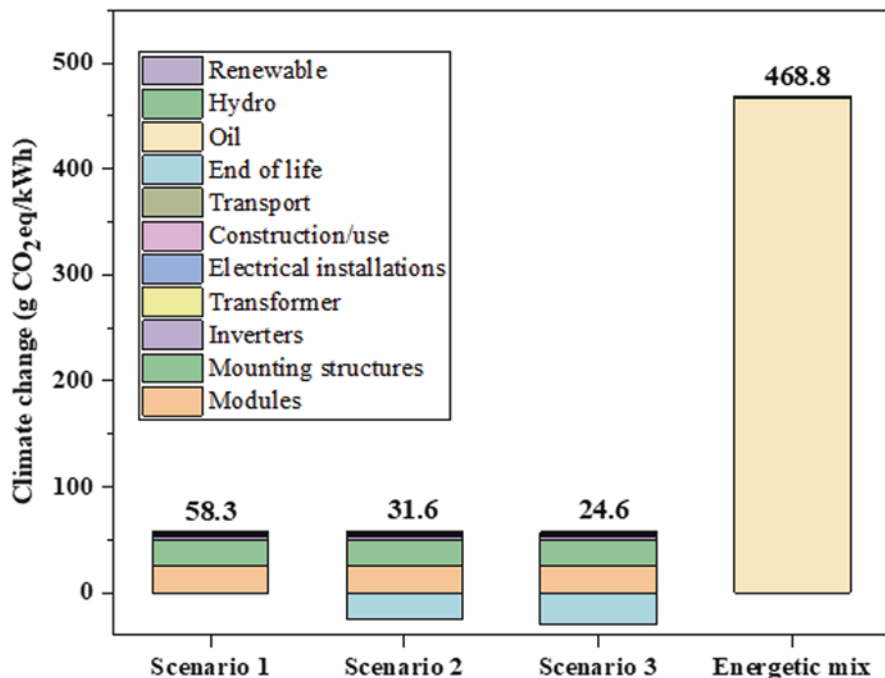
Fig. 4 Global warming potentials of PV systems plant

kWh, respectively, for a PV system with and end-of-life component landfill (scenario 1) and a recycling system for the PV module and mounting structure (scenario 3). The manufacture of the PV panels and the aluminum mounting structure are the main contributors to climate change indicators, with 42% and 43%, respectively. The carbon emissions come mainly from cokes and coal-fired thermal power plants in the production of high-voltage electricity used to manufacture solar-grade silicon and during the electrolysis stage of aluminum production.

The contribution of the mounting structure in this study contradicts with studies in the literature which have found a weak contribution of the mounting structure to the global impact on climate change [6, 17, 20]. This difference is partly explained by the fact that most studies have been conducted on power plants with steel mounting structures. The amount of aluminum used for the mounting structure can also explain these results. Indeed, for the construction of the Ziga power plant, 49.28 tons of aluminum were used.

Recycling the PV modules and the mounting structures reduces the rate of carbon emissions in the environment by more than 34%. Recycling significantly reduces environmental impacts.

A comparison of the PV production system (scenarios 1, 2, and 3) with the national electricity mix shows that the production contribution to the national electricity mix emits 8–19 times more carbon than the PV system when considering the entire life cycle of the PV system. Indeed, the national electricity mix is mainly dominated by diesel thermal power plants.

4   Conclusion and Recommendations

The analysis of the life cycle of energy production by a 1.1 MWp plant installed in Burkina Faso is used to determine the energy payback time and its impact on climate change while comparing it to the national electricity mix. The results show that the energy payback time of PV system is 1.86–2.71 years. Concerning climate change, the system's production of 1 kWh of electricity generates emissions of 24.6–58.3 g eq. CO_2, which is 8–19 times less than the emissions produced by the electricity mix. The end-of-life management strategy of the components influences not only the reduction of the energy payback time but also carbon emission. Energy production by PV plants has an environmental benefit compared to the national electricity mix. The results of this study could be improved if additional studies are carried out on the influence of the type of structural materials (steel, concrete) and the change of the manufacturing location of the components.

References

1. Azoumah, Y., Ramdé, E.W., Tapsoba, G., Thiam, S.: Siting guidelines for concentrating solar power plants in the Sahel: case study of Burkina Faso. Sol. Energy. **84**(8), 1545–1553 (2010). https://doi.org/10.1016/j.solener.2010.05.019

2. Abubakar, A., Vernyuy, A., Muhammad-sukki, F.: A review on the recent progress made on solar photovoltaic in selected countries of sub-Saharan Africa. Renew. Sustain. Energy Rev. **62**, 441–452 (2016). https://doi.org/10.1016/j.rser.2016.04.055

3. Todde, G., et al.: Embodied energy and environmental impact of large-power stand-alone photovoltaic irrigation systems. Energies. **11**(8), 2110 (2018). https://doi.org/10.3390/EN11082110

4. Tsoutsos, T., Frantzeskaki, N., Gekas, V.: Environmental impacts from the solar energy technologies. Energy Policy. **33**(3), 289–296 (2005). https://doi.org/10.1016/S0301-4215(03)00241-6

5. International Organization for Standardization 14044: Environmental management. Life cycle assessment. Requirements and guidelines.Ntc-Iso 14044. **3**(571), 16 (2007) [Online]. Available: http://tienda.icontec.org/brief/NTC-ISO14044.pdf

6. Desideri, U., Proietti, S., Zepparelli, F., Sdringola, P., Bini, S.: Life cycle assessment of a ground-mounted 1778kWp photovoltaic plant and comparison with traditional energy production systems. Appl. Energy. **97**, 930–943 (2012). https://doi.org/10.1016/j.apenergy.2012.01.055

7. Tannous, S., Manneh, R., Harajli, H., El Zakhem, H.: Comparative cradle-to-grave life cycle assessment of traditional grid-connected and solar stand-alone street light systems: A case study for rural areas in Lebanon. J. Clean. Prod. **186**, 963–977 (2018). https://doi.org/10.1016/j.jclepro.2018.03.155

8. Muteri, V., et al.: Review on life cycle assessment of solar photovoltaic panels. Energies (MDPI). **13**(1) (2020). https://doi.org/10.3390/en13010252

9. Akinyele, D.O., Rayudu, R.K., Nair, N.K.C.: Life cycle impact assessment of photovoltaic power generation from crystalline silicon-based solar modules in Nigeria. Renew. Energy. **101**, 537–549 (2017). https://doi.org/10.1016/j.renene.2016.09.017

10. Ma, L., Yu, Z., Ma, W., Qing, S., Wu, J.: Assessment and study on the impact on environment by multi-crystalline silicon preparation by metallurgical route. Silicon. **11**(3), 1383–1391 (2019). https://doi.org/10.1007/s12633-018-9937-6

11. Fthenakis, V., Kim, H.C., Frischknecht, R., Raugei, M., Sinha, P., Stucki, M.: Life cycle inventories and life cycle assessment of photovoltaic systems. Int. Energy Agency, 58 (2011) [Online]. Available: http://iea-pvps.org/index.php?id=315

12. Latunussa, C.E.L., Ardente, F., Blengini, G.A., Mancini, L.: Life Cycle Assessment of an innovative recycling process for crystalline silicon photovoltaic panels. Sol. Energy Mater. Sol. Cells. **156**, 101–111 (2016). https://doi.org/10.1016/j.solmat.2016.03.020

13. Bekkelund, K.: A Comparative Life Cycle Assessment of PV Solar Systems. Norwegian University of Science and Technology (2013)

14. Yuan, X., Zuo, J., Ma, C.: Social acceptance of solar energy technologies in China-End users' perspective. Energy Policy. **39**(3), 1031–1036 (2011). https://doi.org/10.1016/j.enpol.2011.01.003

15. Yu, Z., et al.: Life cycle assessment of grid-connected power generation from metallurgical route multi-crystalline silicon photovoltaic system in China. Appl. Energy. **185**, 68–81 (2017). https://doi.org/10.1016/j.apenergy.2016.10.051

16. Tschümperlin, L., Stolz, P., Frischknecht, R.: Life cycle assessment of low power solar inverters (2.5 to 20 kW) Authors. no. October, 2016

17. Mason, J.E., Fthenakis, V.M., Hansen, T., Kim, H.C.: Energy payback and life-cycle CO2 emissions of the BOS in an optimized 3.5MW PV installation. Prog. Photovoltaics Res. Appl. **14**(2), 179–190 (2006). https://doi.org/10.1002/pip.652

18. Tsuchiya, Y., Swai, T.A., Goto, F.: Energy payback time analysis and return on investment of off-grid photovoltaic systems in rural areas of Tanzania. Sustain. Energy Technol. Assessments. **42**(September), 100887 (2020). https://doi.org/10.1016/j.seta.2020.100887

19. Rajput, P., Singh, Y.K., Tiwari, G.N., Sastry, O.S., Dubey, S., Pandey, K.: Life cycle assessment of the 3.2 kW cadmium telluride (CdTe) photovoltaic system in composite climate of India. Sol. Energy. **159**(September 2017), 415–422 (2018). https://doi.org/10.1016/j.solener.2017.10.087

20. Beylot, A., et al.: Environmental impacts of large-scale grid-connected ground-mounted PV installations. Renew. Energy. **61**, 2–6 (2014). https://doi.org/10.1016/j.renene.2012.04.051

Conceptual Design for Active Solar Still with an Adsorption Unit

Mahmoud Elgendi, Maryam Nooman AlMallahi, Afra AlNuaimi, Sheikha AlKetbi, Wadima AlKaabi, and Wdeema AlKhyeli

1 Introduction

Many communities have been affected by natural freshwater scarcity due to rapid population increase and industrial development. By 2025, it is anticipated that 70% of the world's population will face freshwater scarcity [1, 2]. In addition, drinking brackish water is unsafe due to various health concerns, including skin cancer and black foot disease [3]. Therefore, the supply of fresh water in many parts of the world, particularly in remote and rural locations, is essential. Desalted water is the principal source of potable or fresh water; freshwater users must have enough water. Fresh water is used in various applications, including drinking, agriculture, and industry.

Various desalination systems have been suggested and explored; however, these procedures often require substantial energy and may have negative environmental consequences. Since solar energy is one of the most abundant renewable energy resources, solar desalination has become preferable without severely harming the environment, particularly in arid places with plentiful sunshine [4, 5]. Solar desalination may be divided into two types: direct and indirect. The direct approach

M. Elgendi (✉)
Department of Mechanical and Aerospace Engineering, College of Engineering, United Arab Emirates University, Al Ain, UAE

National Water and Energy Center, United Arab Emirates University, Al Ain, United Arab Emirates

Department of Mechanical Power Engineering and Energy, Faculty of Engineering, Minia University, Minia, Egypt
e-mail: mahgendi@uaeu.ac.ae

M. N. AlMallahi · A. AlNuaimi · S. AlKetbi · W. AlKaabi · W. AlKhyeli
Department of Mechanical and Aerospace Engineering, College of Engineering, United Arab Emirates University, Al Ain, UAE

combines the desalination process with solar radiation collecting simultaneously, whereas the indirect method divides the desalination unit into the solar collector and the desalination section. There are several solar desalination methods widely used, including solar still.

Solar still technology is simple, requires less maintenance, and is cost-effective. The basin is filled with impure water, evaporated by the sun through transparent plastic/glass. Pure water vapor condenses on the surface and falls to the side to be collected and discarded [6]. Although solar still is a simple method of distilling water powered by the sun's heat, solar stills are less productive than traditional desalination systems due to low efficiency [7, 8]. One of the causes for low productivity is inefficient utilization of released latent heat of condensation and challenges in harnessing the heat and mass transfer processes inside the solar still.

The distillation system is divided into two types: passive and active. Tiwari and Sahota [9] investigated the current state of research on passive and active solar distillation systems. In addition, the utilization of auxiliary subsystems to enhance freshwater productivity was widely studied [10–12]. Also, Anand et al. [13] addressed desalination systems that use different desalination systems coupled with photovoltaic thermal collectors as an energy source. In addition, desalination systems can be coupled with electrodialysis, forward osmosis, vapor compression, or adsorption desalination. Moreover, photovoltaic thermal collectors can be used as an energy source.

Adsorption is a phenomenon that develops at the interface surface of two phases, most often solid and liquid, in which cohesive forces, such as electrostatic forces and hydrogen bonding, operate between molecules of any material regardless of their aggregation state [14]. The system's main components are an adsorbent bed connected to a condenser and a water collector. This method generates water from moist air during the night. This method can use a variety of adsorbent materials. For example, silica gel has a higher adsorption capacity at low temperatures than alumina and zeolite, although it is less adsorbent than zeolite when moisture levels are low. Because of these properties, silica gel is suited for use in settings requiring low temperatures, moderate water vapor pressure, and high adsorption capabilities [15, 16].

Many researchers coupled adsorption desalination with solar thermal collectors to provide the needed thermal energy. Kannan et al. [17] developed a solar still integrated with a vapor adsorption bed. Also, sponges, gravels, sand, black rubbers, and some of their mixtures were utilized to increase the output of the solar still. Correspondingly, Abhishek and Baiju [18] developed, fabricated, and tested traditional solar still and an adsorption desalination system. The suggested hybrid system produced cooling and distilled water while in operation. Sharon and Reddy [19] examined innovative corrosion-free materials and long-life membranes required for improved and dependable functioning. As a result, effective methods for extracting minerals from brine and reusing brine for irrigation must be employed. Solar energy can potentially make the desalination sector more environmentally friendly, and any advancements in solar thermal collectors and PV panels would benefit the desalination industry [20, 21].

Since solar still requires solar energy to produce fresh water, it only operates during the day. The present chapter proposes several design alternatives for a solar still system integrated with an adsorption unit to enhance the nocturnal productivity of the system.

2 Materials and Methods

The conceptual design is the first phase in the design process that identifies the best design layout to enhance the effectiveness of the system [4, 8]. Initially, the authors selected a target market from which customer requirements were gathered through surveys. Following the determination of customer requirements, the design may be applied to product specifications, and the objective tree is determined. Next, customers in the target market define product requirements, customer requirements, or user needs. Then, based on the customer requirements, product specifications can be proposed. Several solutions for each subfunction in the system can be proposed and collected in a morphological chart. Combining these solutions suggests several alternatives. Finally, using the decision matrix, we can decide the best alternative.

3 Results and Discussion

Conceptual design is the first stage of the design process, mainly defined by consumer needs, focus groups, the team of experts, and the design team's critical thinking and creativity.

3.1 Target Market, Survey, and Customer Requirements

The target market is the most significant market in which the product may be promoted, and there is an actual need for the product. There are several categories for which the target market is classified, including people with no direct water supply in their locations, charities, and government entities or agriculture field with low water resources, or sailors.

The survey was distributed to engineers, students, and landowners in arid areas. The total number of participants in the survey was 100, addressing customers' needs and requirements. According to the assessment, 84% of participants consider that the most important specification for solar still is high quality, followed by 67% eco-friendly and 61% low cost. As a result of the questionnaire, the customers' requirements may be summarized as follows:

- Having access to potable water daily
- A device that works for long periods

- Low cost
- Low maintenance cost
- Safe
- A durable device that can last up to 4–5 years
- Ecofriendly
- Easy to handle

The product specifications may be summarized based on these customer requirements as yearly maintenance, efficiency, operating steps, life span, and production cost.

3.2 Quality Function Deployment (QFD)

QFD is one of the most widely used approaches for improving quality and meeting customer expectations. This tool collects all customer needs in every product element and develops them into technical requirements to match their expectations. Generally, the objectives may be determined through Quality Function Deployment (QFD), which conveys the customers opinions based on customer requests and products. The survey decides on ranking the importance of customer requirements; the most critical requirement was assigned to 5, and the least essential need was set to 1, as shown in Fig. 1. The technical score is calculated by multiplying the

Column #			1	2	3	4	5	6	7	
Preference			▲	▲	▲	▼	▲	▲	▲	
Row #	Customer Importance Rating	Design Specifications / Customer Requirements	Low Maintenance	High Efficiency	Eco-friendly Material	Operating Steps	Solar Energy	Life Span	Simple Operating Mechanism	weighted Score
1	3	Low cost	9	1	9	1	9	1	3	99
2	5	High Quality	9	9	1	3	1	9	1	165
3	4	Environmentally Friendly	1	1	9	1	9	1	1	92
4	1	Durable	9	3	1	1	1	9	1	25
5	2	Practical	3	1	1	9	3	3	9	58
		Units	Years	%	%	Steps	kWh	Years	Steps	
		Technical Importance Score	91	57	71	41	75	67	37	439
		Importance (%)	21	13	16	9	17	15	8	100
		Weight Chart								
		Priorities rank	1	5	3	6	2	4	7	

Relationship	
Strong	9
Moderate	3
Weak	1

Fig. 1 House of quality

customer importance rating by each customer requirement; the importance is calculated by dividing each technical importance score to the total weighted score (439). In addition, the technical score is calculated by multiplying the customer importance rating by each customer requirement. The importance is calculated by dividing each technical importance score by the total weighted score (439).

3.3 Objectives Tree

The objectives tree helps in expanding and clarifying the customer's requirements. These goals are divided into levels. The objective tree of the solar still and the adsorption unit is depicted in Fig. 2. For example, higher-level criteria such as low cost, high quality, eco-friendly, practical, and durable were prioritized. Lower-level objectives, on the other hand, are separated to describe how higher-level goals may be achievable.
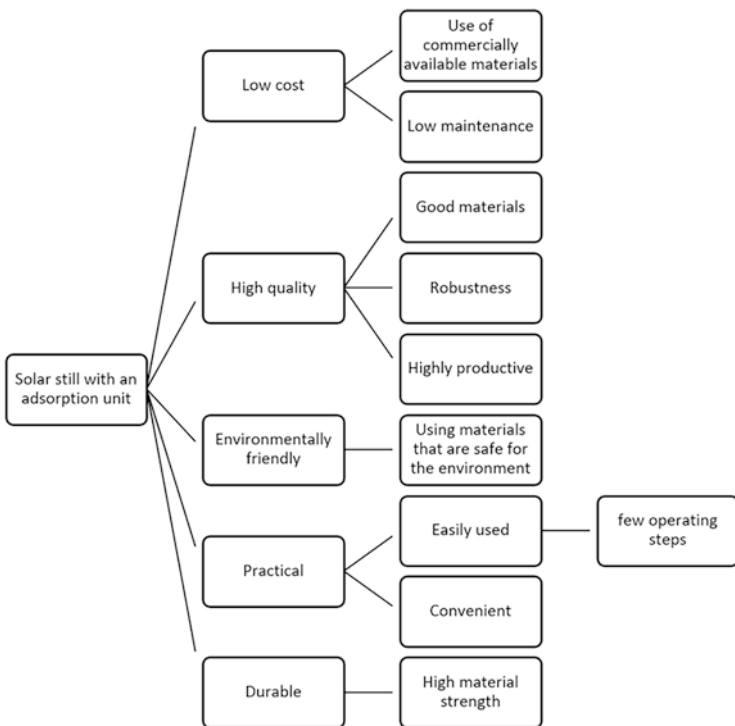
Fig. 2 Objectives tree

3.4   Morphological Chart

This strategy is critical for visualizing alternatives and developing new ideas during the development stages. Figure 3 shows the morphological chart that provides alternative design solutions for the proposed device. Each alternative was highlighted in alphabetical order. For example, the three subfunctions were holding water, heating, and cooling the adsorbent (blue beads silica gel), and adsorbent beds, as displayed in Figs. 4, 5, and 6.

Fig. 3 Morphological chart

Fig. 4 Alternative A: an inclined solar still coupled with a rectangular absorbent bed with a shell and tube heat exchanger
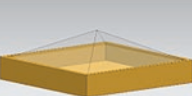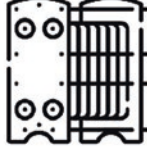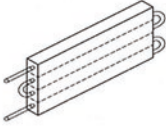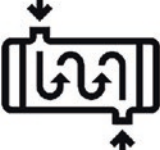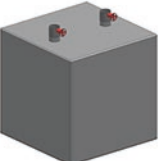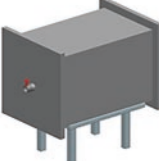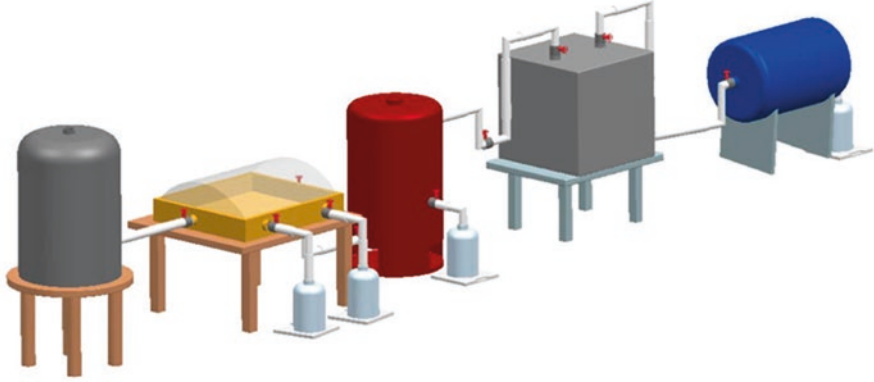
Fig. 5 Alternative B: a semi-cylindrical solar still coupled with a square-shaped absorbent bed with a plate heat exchanger

Fig. 6 Alternative C: pyramid solar still coupled with a cylindrical absorbent bed with a fin tube heat exchanger

Table 1 Decision matrix

Evaluation criteria	Weight	Alternative A		Alternative B		Alternative C	
		Rating	Score	Rating	Score	Rating	Score
Average cost	0.10	8	0.80	7	0.70	7	0.70
Low maintenance	0.10	8	0.80	6	0.60	7	0.60
Use recyclable material	0.13	7	0.91	7	0.91	8	0.78
Use green energy	0.20	10	2.00	8	1.60	8	1.60
Provide clean water	0.15	10	1.50	9	1.35	8	1.20
Endure high temperatures	0.10	7	0.70	6	0.60	5	0.50
Works for a long period	0.12	8	0.96	6	0.72	7	0.84
Easy to handle	0.10	8	0.80	7	0.70	7	0.70
Total	1.00		8.47		7.18		6.92

3.5 Decision Matrix

The three alternatives with different criteria were compared, and the weights were obtained from the QFD chart; each score was chosen considering the advantages and disadvantages of components in each alternative. The best alternative is then computed from the decision matrix. The three alternatives are compared using the objectives tree with the criteria indicated in Table 1.

4 Conclusion

The current study analyzed and applied the phases of the conceptual design process to the design of a solar still with an adsorption desalination unit. Researchers can construct a solar still and other products using these procedures. The target market is specified and surveyed. Moreover, the present study suggests three design alternatives for solar still combined with an adsorption desalination system and decides the best alternative using the decision matrix. Based on the decision matrix, Alternative A, with an inclined solar still coupled with a rectangular absorbent bed with a shell and tube heat exchanger, was chosen for embodied design and production. This design procedure eliminates various drawbacks of prior ideas before procurement and detailed design procedures. As a result, Alternative A is expected to be the most convenient for the end user and the most productive.

References

1. Li, C., Goswami, Y., Stefanakos, E.: Solar assisted sea water desalination: a review. Renew. Sust. Energ. Rev. **19**, 136–163 (2013)
2. Bajpayee, A., et al.: Very low temperature membrane-free desalination by directional solvent extraction. Energy Environ. Sci. **4**(5), 1672–1675 (2011)

3. Yadav, M.K., et al.: Status and management of arsenic pollution in groundwater: a comprehensive appraisal of recent global scenario, human health impacts, sustainable field-scale treatment technologies. J. Environ. Chem. Eng. **9**(3), 105203 (2021)
4. Elgendi, M., et al.: Design procedures for a passive pyramid solar still with an automatic feed water system. Alex. Eng. J. **61**(8), 6419–6431 (2022)
5. Elgendi, M., Kabeel, A., Essa, F.: Improving the solar still productivity using thermoelectric materials: a review. Alex. Eng. J. **65**, 963 (2022)
6. Elgendi, M., Selim, M.Y.: Determination of the effect of water depth on the yield of a solar still using an automatic feedwater system. Environ. Sci. Pollut. Res. **29**, 14595–14603 (2022)
7. Elgendi, M., et al.: Nanotechnology in solar still: conceptual design. In: 2021 6th International Conference on Renewable Energy: Generation and Applications (ICREGA). IEEE (2021)
8. Elgendi, M., et al.: Embodiment design and detailed design of a pyramid solar still with an automatic feedwater system. In: 2021 6th International Conference on Renewable Energy: Generation and Applications (ICREGA). IEEE (2021)
9. Tiwari, G., Sahota, L.: Advanced Solar-Distillation Systems: Basic Principles, Thermal Modeling, and Its Application. Springer (2017)
10. Mahmoud, A., Fath, H., Ahmed, M.: Enhancing the performance of a solar driven hybrid solar still/humidification-dehumidification desalination system integrated with solar concentrator and photovoltaic panels. Desalination. **430**, 165–179 (2018)
11. Sleiti, A.K., Al-Ammari, W.A., Al-Khawaja, M.: A novel solar integrated distillation and cooling system–design and analysis. Sol. Energy. **206**, 68–83 (2020)
12. Abdullah, A., et al.: Performance evaluation of a humidification–dehumidification unit integrated with wick solar stills under different operating conditions. Desalination. **441**, 52–61 (2018)
13. Anand, B., et al.: A review on solar photovoltaic thermal integrated desalination technologies. Renew. Sust. Energ. Rev. **141**, 110787 (2021)
14. Zhang, Y., Yang, Z., Jiang, J.: Insight into ions adsorption at the CSH gel-aqueous electrolyte interface: from atomic-scale mechanism to macroscopic phenomena. Constr. Build. Mater. **321**, 126179 (2022)
15. Strong, C., Carrier, Y., Tezel, F.H.: Experimental optimization of operating conditions for an open bulk-scale silica gel/water vapour adsorption energy storage system. Appl. Energy. **312**, 118533 (2022)
16. Essa, F., et al.: Extracting water content from the ambient air in a double-slope half-cylindrical basin solar still using silica gel under Egyptian conditions. Sustainable Energy Technol. Assess. **39**, 100712 (2020)
17. Kannan, R., et al.: Solar still with vapor adsorption basin: performance analysis. Renew. Energy. **62**, 258–264 (2014)
18. Abhishek, P., Baiju, V.: Modeling and performance analysis of a hybrid conventional solar still–adsorption desalination system. Proc. Inst. Mech. Eng. C J. Mech. Eng. Sci. **235**(24), 7934–7950 (2021)
19. Sharon, H., Reddy, K.: A review of solar energy driven desalination technologies. Renew. Sust. Energ. Rev. **41**, 1080–1118 (2015)
20. Assad, M.E.H., et al.: Desalination technologies: overview. In: 2022 Advances in Science and Engineering Technology International Conferences (ASET). IEEE (2022)
21. Obaideen, K., et al.: On the contribution of solar energy to sustainable developments goals: case study on Mohammed bin Rashid Al Maktoum Solar Park. Int. J. Thermofluids. **12**, 100123 (2021)

Heat Transfer and Collector Thermal Efficiency of Magnesium Oxide/Water Nanofluids in Solar Flat Plate Collector Under Thermosyphon Conditions

B. Deepanraj and L. Syam Sundar

1 Introduction

Worldwide energy consumption is a result of the depletion of fossil fuels. Renewable energy is merely a source of energy that can be used to replace fossil fuels; nevertheless, against conventional energy-based equipment, the renewable energy-based gadgets are less effective [1]. Using flat plate collectors, it is possible to transform solar energy into thermal (heat) energy. You can utilize the hot water for home purposes. Utilizing fluids with high thermal conductivity will increase the effectiveness of the solar water heating system. By distributing nanometer-sized solid particles in fluids referred to as nanofluids, which are achievable thanks to nanotechnology, their thermal conductivity is improved [2]. The effectiveness of the solar water heating system is improved by the circulation of nanofluids. Researchers use a variety of nanofluids in solar water heating systems, some of which are detailed here. Said et al. [3] used Al_2O_3-water nanofluids in a flat plate collector led to energy efficiency gains of 73.7% and 203%, respectively. In order to increase collector efficiency, Verma et al. [4] employed water mixed graphene, CuO, Al_2O_3, TiO_2, and SiO_2 nanofluids in flat plate collectors. In a square flat plate solar collector, Noghrehabadi et al. [5] employed water diluted SiO_2 nanofluids at 1 wt% and reported increased thermal efficiency. Cu-water nanofluids were utilized by He et al. [6] in a flat plate collector, and they discovered a 23.83% improvement in collector efficiency and a 24.52% increase in heat gain when compared to water. In a flat plate collector,

B. Deepanraj (✉) · L. Syam Sundar
Department of Mechanical Engineering, College of Engineering, Prince Mohammad Bin Fahd University, Al-Khobar, Saudi Arabia
e-mail: dbalakrishnan@pmu.edu.sa

Okonkwo et al. [7] employed hybrid nanofluids made of alumina-water and alumina-iron-water to increase exergetic efficiency from 5.7% to 6.9%. SiO_2/ethylene glycol nanofluid tests were carried out by Meibadi et al. [8], who discovered that the collector had a high thermal efficiency. When Al_2O_3-water nanofluids were used in flat plate collectors, Shojaeizadeh et al. [9] noticed improved thermal efficiency of the collector.

Fluid circulation, whether forced or free convection, improves the efficiency of the collector. According to the literature, there are no experimental data for MgO-based nanofluids in flat plate collector. This work is now being done in order to calculate the heat transfer, friction factor, and thermal efficiency of a flat plate collector for MgO-water nanofluids flow under thermosyphon circumstances. The experimental data is compressed to an equation to examine the Nusselt number and friction factor.

2 Experimental Study

We purchased the magnesium oxide (MgO) nanoparticles from Sigma-Aldrich. The volume concentration of 0.1%, 0.5%, and 1.0% were developed by mixing MgO with base fluid. In 15 liters of water, the MgO particles of 93.32, 281.10, and 470.4 g were dispersed to obtain 0.1%, 0.5%, and 1.0% vol. The MgO particles are uniformly dispersed in water using the mechanical stirring method.

The k_{nf} of MgO nanofluid was examined using apparatus made by Decagon Devices, USA. Nanofluids thermal conductivity is larger as temperature and particle loading are larger. A similar improvement in heat conductivity is suggested by Yoo et al. [10]. The equivalent increases in thermal conductivity for particle loadings of 0.1%, 0.5%, and 1.0% are 6.69%, 11.93%, and 15.13% at a temperature of 30 °C, and they further increase to 9.03%, 16.90%, and 22.86% at a temperature of 60 °C. With the aid of a Japanese AND vibro-viscometer, the viscosity of MgO nanofluid was determined. The viscosity of nanofluids increases with increasing temperatures, increased particle loadings, and increased viscosity of nanofluids. Cabaleiro et al. [11] noted the same pattern of growing viscosity for nanofluids. At temperatures of 30 °C and 60 °C, respectively, particle loadings of 0.1%, 0.5%, and 1.0% increase viscosity by 24.13%, 42.24%, and 60.34%, and by 45.83%, 62.5%, and 79.16%.

The density of the MgO nanofluid was determined using the Archimedes Principle. With increased temperatures and ϕ, density is raised. The largest density enhancement occurs at a nanofluid concentration of 1.0% vol. at a temperature of 60 °C, or 2.14%. A DSC 2920 modulated, TA instrument was utilized to measure the MgO nanofluid's specific heat. The specific heat is decreased up to 1.0088-times at 1.0% vol. in comparison to water.
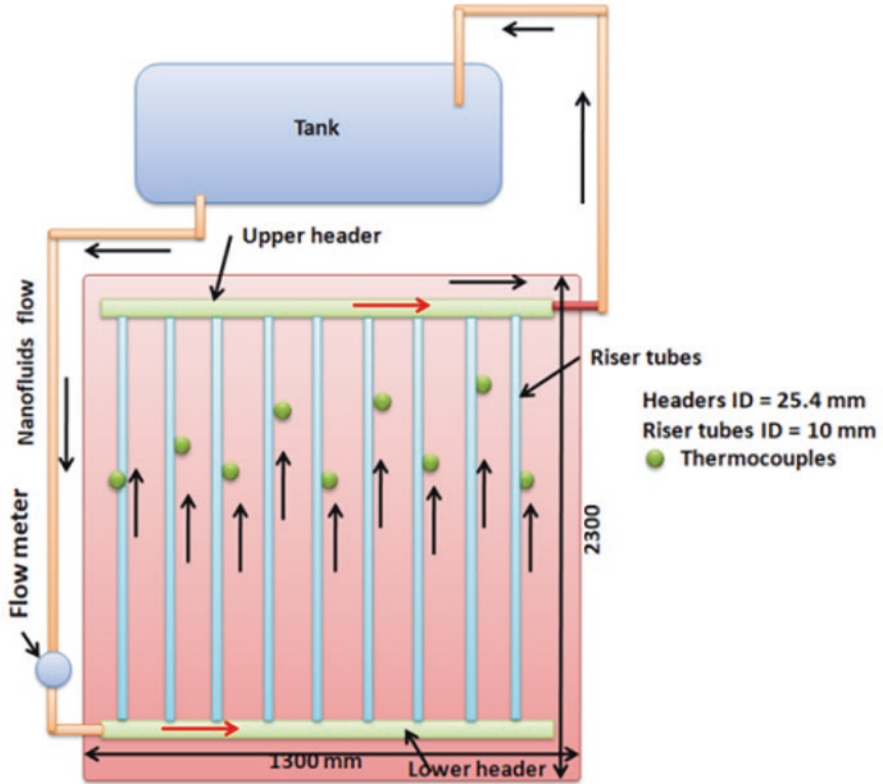
Fig. 1 Flat plate collector with thermocouple

3   Flat Plate Collector

A line diagram of SC, along with the locations and measurements of the thermo-couples is given in Fig. 1. The parts of an SC are an adiabatic tank, a water meter, an input and output header. Water is the substance being employed, and 15 liters of MgO/water nanofluids were initially added to a tank with a 100-liter capacity. When the SC is tilted 20° toward the south, the natural flow of nanofluid occurs in SC. The fluid initially flows intake header (ID = 25.4 mm), which is then uniformly dis-turbed by the riser tubes (ID = 10 mm; OD = 12 mm), before exiting through the outlet header and into the insulated tank. The copper riser tubes and headers are used. We employed 12 J-type thermocouples to measure the input, outflow, surface, and ambient temperatures. Nine thermocouples are brazed on the exterior of the riser tubes to measure the surface temperature, while two thermocouples were used to gauge the fluid's input (T_i) and outflow (T_o) temperatures. One thermocouple was used to gauge the ambient temperature.

To continuously record the values, a data acquisition system is linked to each thermocouple's needle. The buoyant force is what causes the flow circulation. To stop heat loss, glass-wool insulation is applied to the bottom surface of the collector and the inlet and exit headers. The studies were carried out from 09:00 to 16:00 during the day. Using the Pyranometer-Electro Mechanical Enterprises, UP, India, the sun radiation was measured. The Yokogowa differential pressure transducer was used to gauge the pressure drop inside the riser tubes. The sun radiation, temperatures, and mass flow rate are measured from 10:00 AM to 4:30 PM. The sun radiation is seen to have grown from 10:00 AM to 01:00 PM, reaching its peak at 01:00 PM, and then progressively decreasing from 01:00 PM to 16:30 PM. Two regions, commonly referred to as Region-1 (10:00 AM to 1:00 PM) and Region-2 (1:00 PM to 16:30), are separated by this nature.

4 Formulation

4.1 Nusselt Number

Water and MgO/water nanofluids receive their heat from:

$$Q = \dot{m}\, C_p \left(T_{out} - T_{in} \right) = U_o A_o \left(T_{surface} - T_{mean} \right) \tag{1}$$

$$\frac{1}{U_o A_o} = \frac{1}{h_i A_i} + \frac{\ln\left(\dfrac{D_o}{D_i}\right)}{2\pi kL} \tag{2}$$

$$\mathrm{Nu} = \frac{h_i D_i}{k} \tag{3}$$

$$\mathrm{Pr} = \frac{\mu C_p}{k} \tag{4}$$

$$Re = \frac{4\dot{m}}{\pi d\mu} \tag{5}$$

4.2 Friction Factor

From the drop in pressure of the fluid, the friction factor is estimated:

$$f_{\text{exp}} = \frac{(\Delta P)}{\left(\dfrac{L}{D}\right)\left(\dfrac{\rho v^2}{2}\right)}$$

(6)

4.3 Thermal Efficiency

Based on the Hottel–Whillier–Bliss [12] equation, the heat gained by fluid is calculated and the equation is given below:

$$Q = A_c F_R \left[G_T \tau\alpha - U_L \left(T_i - T_a \right) \right]$$

(7)

By using heat gain, collector area, and solar radiation, the collector efficiency is estimated:

$$\eta_i = \frac{Q}{A_c G_T} = \frac{\dot{m} C_p \left(T_o - T_i \right)}{G_T}$$

(8)

$$\eta_i = F_R \tau\alpha - F_R U_L \left(\frac{T_i - T_a}{G_T} \right)$$

(9)

where, Q is heat gain (W), A_c is collector area (m^2), F_R is heat removal factor, $\tau\alpha$ is absorptance–transmittance product, G_T is solar radiation (W/m^2), U_L is overall loss coefficient, T_i is inlet temperature (K), and T_a is ambient temperature (K).

By substituting collector efficiency calculated from Eq. (8) in Eq. (9), the terms $F_R \tau\alpha$ (heat removal factor-absorptance-transmittance) and $F_R U_L$ (heat removal factor-overall loss coefficient) were obtained by plotting the data η_i verses $T_i - T_a/G_T$.

5   Results and Discussion

5.1 Nusselt Number

The entire daytime data is split into two regions, as we mentioned in the operating conditions. Data for region-1 is available from 10:00 AM to 1:00 PM. The region-2 data covers the hours from 1:00 AM to 16:30 PM. With data from Sieder-Tate [13], the Nusselt number of water is determined for both regions:
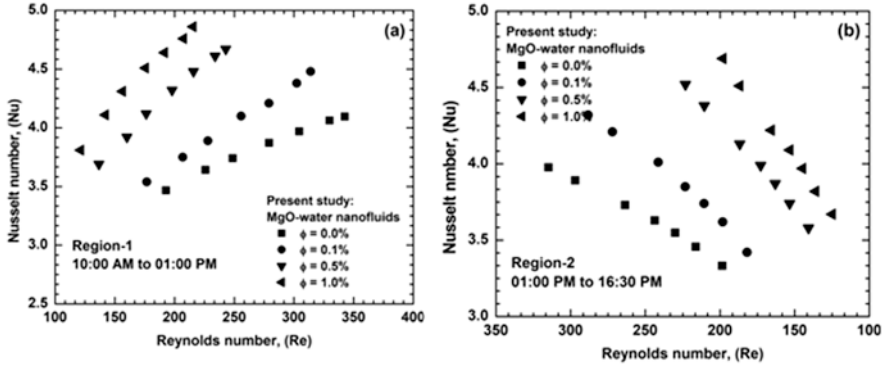
Fig. 2 Experimental Nusselt number of MgO/water nanofluids at different concentrations and Reynolds numbers (**a**) Region-1, and (**b**) Region-2

$$\text{Nu} = 1.86\,\text{Gz}^{1/3}\left(\frac{\mu_s}{\mu_w}\right)^{-0.14},\ \text{for Gz} > 10$$

(10)

where, Greatz number, Gz = $RePrD/L$, μ is the viscosity of the fluid (mPa.s).

As can be seen, the experimental Nusselt number shows a maximum 2.5% deviation from the values in the literature. The tests with MgO/water nanofluids are repeated when the confidence occurs with water data. The Nusselt number of MgO was assessed at zone −1, and the outcome is given in Fig. 2a. The Nusselt number data is displayed under the same Re for fluids. To calculate the Reynolds number, Eq. (5) is used. As particle loading rises, the Reynolds number falls, which is corrected in the mass flow rate. With increasing particle loadings and rising Reynolds numbers, the Nusselt number rises in water.

With particle loadings of 0.1%, 0.5%, and 1.0%, the Nusselt number rises to 5.93%, 12.26%, and 19.53%. When compared to water, it similarly rises to 15.71%, 27.40%, and 36.17% at Reynolds numbers of 140 and 345, respectively. In comparison with water, the Nusselt number increases with particle loadings of 0.1%, 0.5%, and 1.0% to 13.12%, 24.41%, and 33.94% and decreases with particle loadings of 6.51%, 14.88%, and 23.25% at Reynolds numbers of 317 and 215, respectively.

One of the factors that contribute to increasing Nusselt numbers is the increased particle thermal conductivity. The fluid absorbs less heat as a result of gradual reductions in solar radiation compared to daytime, which leads to a fall of outlet temperature.

A regression equation is developed based though the experimental Nusselt number for region-1 with deviation less than ±2%.

Region-1:

$$\text{Nu}_{\text{Reg}} = 1.657\,(\text{Gz})^{0.45}\,(1+\phi)^{0.1551}$$

(11)

$$5.14 < Pr < 7.41, 4.26 < Gz < 12.87, 0 < \phi < 1.0\%$$

Similarly, the experimental data in region-2 is developed by a regression equation to evaluate the Nusselt number with a maximum deviation of ±2%.

Region-2:

$$Nu_{Reg} = 1.551(Gz)^{0.4477}(1+\phi)^{0.1743} \tag{12}$$

$$4.87 < Pr < 6.95, 5.61 < Gz < 11.67, 0 < \phi < 1.0\%$$

5.2 Friction Factor

The full daytime data is split into two zones, as we indicated in the operating conditions. Data for regions 1 and 2 are available between 09:00 and 13:00 and between 13:00 and 16:00. Hagen-Poiseuille law [14] data are used in both zones to determine and validate the water's friction factor:

$$f = 64 / Re \tag{13}$$

As can be seen, there is a maximum 2.5% difference between the experimental friction factor and the values found in the literature.

Using Eq. (13), the *f* of MgO nanofluids for zone 1 is provided in Fig. 3a. The findings of *f* displayed at same *Re*. At greater particle loadings, the friction factor penalty is significant, however it becomes less severe as the Reynolds number increases. The *f* is 3.23%, 9.56%, and 14% larger for particle loadings of 0.1%, 0.5%, and 1.0%, respectively. The fine rises to 7.16%, 14.33%, and 24.85% at Reynolds numbers of 140 and 345.
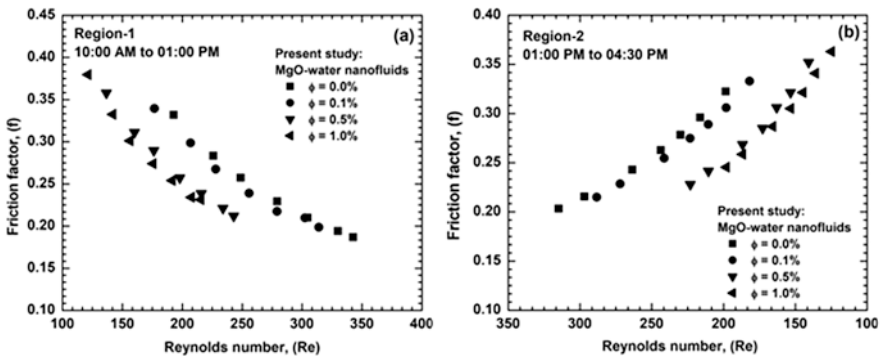
Fig. 3 Experimental friction factor of MgO/water nanofluids at different concentrations and Reynolds numbers (**a**) Region-1, and (**b**) Region-2

Equation (13) was used to estimate the data for region-2 of the MgO/water nano-fluids and the results are given n Fig. 3b. Findings of f were done at same Re. At greater particle loadings, the friction factor penalty is significant, but as the Reynolds number drops, it becomes less severe. The friction factor penalty is 6.57%, 13%, and 21.6% for particle loadings of 0.1%, 0.5%, and 1.0%, respectively. The fine increases to 4.17%, 9.44%, and 16.1% at Reynolds numbers of 317 and 215, respectively. With a maximum deviation of 2.5%, a developed equation fit was created using the measured data in region-1.

Region-1:

$$f_{\text{reg}} = 46.02 \left(Re \right)^{-0.9392} \left(1 + \phi \right)^{0.2367} \tag{14}$$

$$143 < Re < 345, 0 < \phi < 1.0\%$$

Similarly, from the experimental data, a regression fit was made to analyze the friction factor in region-2 with a maximum deviation of ±3%.

Region-2:

$$f_{\text{reg}} = 41.64 \left(Re \right)^{-0.9226} \left(1 + \phi \right)^{0.2325} \tag{15}$$

$$317 < Re < 217, 0 < \phi < 1.0\%$$

5.3   Collector Efficiency

The collector efficiency with water and MgO/water nanofluids is assessed using Eq. (9). Figure 4 displays the collector efficiency versus daylight hours. The effectiveness of the collection improved progressively from 10:00 AM to 01:00 PM, as is understood, before reaching its peak at 01:00 PM. The collector effectiveness continuously declined as the day length increased from 01:00 PM to 04:30 PM. The highest collector efficiency was attained at 1.0% volume concentration, and the thermal efficiency of the collector increases as particle loadings do. The efficiency of the water collector is 57.15%, but for nanofluid volume concentrations of 0.1%, 0.5%, and 1.0%, it rises to 60.25%, 64.25%, and 69.85%.

6   Conclusion

Thermophysical properties, heat transfer, friction factor, and thermal efficiency of different volume concentrations of MgO/water based nanofluids that circulate in flat plate collectors under thermosyphon conditions have been experimentally analyzed. The results show that at 1.0% vol concentration and 60 °C, the increase in k_{nf} and μ_{nf}
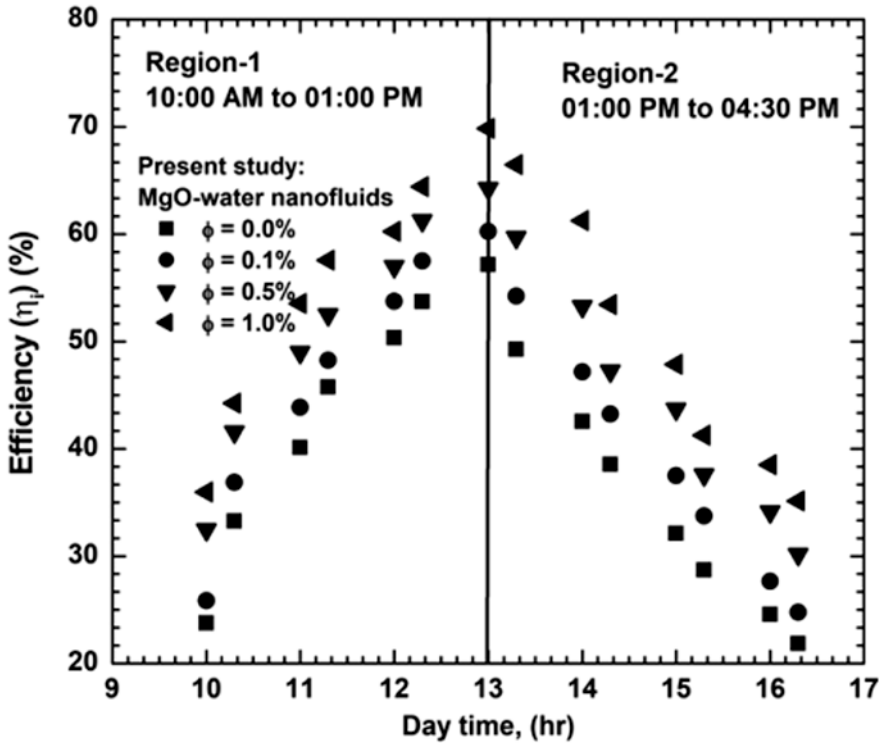
Fig. 4 Thermal efficiency of collector with water and MgO/water nanofluids at day time

are 22.8% and 79.2%, respectively. The Nusselt number at region-1 rises to 19.53% and 36.17% at $\phi = 1.0\%$ and at Re of 140 to 346, in contrast to water. Similar to this, region-2's Nusselt number increases to 33.94% and 23.25%, respectively, compared to water at $\phi = 1.0\%$ and Re of 317 to 214.

At $\phi = 1.0\%$ and at Re between 140 and 345, the f penalty at region-1 is 1.14 times higher compared to water. In comparison to water, region-2's friction factor penalty is 1.216 times larger than it is at 1.0% vol. concentration. In comparison to the Nu increment, the f penalty is inconsequential. Maximum efficiency of the collector is improved to 22.22% for particle loadings of 1.0% in water.

References

1. Sarsam, W.S., Kazi, S.N., Badarudin, A.: A review of studies on using nanofluids in flat-plate solar collectors. Sol. Energy. **122**, 1245–1265 (2015)
2. Zyla, G.: Thermophysical properties of ethylene glycol-based yttrium aluminum garnet (Y3Al5O12–EG) nanofluids. Int. J. Heat Mass Transfer. **92**, 751–756 (2016)

3. Said, Z., Saidur, R., Rahim, N.A.: Energy and exergy analysis of a flat plate solar collector using different sizes of aluminium oxide based nanofluid. J. Clean. Prod. **133**, 518–530 (2016)
4. Verma, S.K., Tiwari, A.K., Chauhan, D.S.: Experimental evaluation of flat plate solar collector using nanofluids. Energy Convers. Manag. **134**, 103–115 (2017)
5. Noghrehabadi, A., Hajidavalloo, E., Moravej, M.: Experimental investigation of efficiency of square flat-plate solar collector using SiO2/water nanofluid. Case Stud. Therm. Eng. **8**, 378–386 (2016)
6. He, Q., Zeng, S., Wang, S.: Experimental investigation on the efficiency of flat-plate solar collectors with nanofluids. Appl. Therm. Eng. **88**, 165–171 (2015)
7. Okonkwo, E.C., Wole-Osho, I., Kavaz, D., Abid, M., Al-Ansari, T.: Thermodynamic evaluation and optimization of a flat plate collector operating with alumina and iron mono and hybrid nanofluids. Sustainable Energy Technol. Assess. **37**, 100636 (2020)
8. Meibodi, S.S., Kianifar, A., Niazmand, H., Mahian, O., Wongwises, S.: Experimental investigation on the thermal efficiency and performance characteristics of a flat plate solar collector using SiO2/EG–water nanofluids. Int. Commun. Heat and Mass Transfer. **65**, 71–75 (2015)
9. Shojaeizadeh, E., Veysi, F., Kamandi, A.: Exergy efficiency investigation and optimization of an Al2O3–water nanofluid based Flat-plate solar collector. Energ. Buildings. **101**, 12–23 (2015)
10. Yoo, D.-H., Hong, K., Yang, H.-S.: Study of thermal conductivity of nanofluids for the application of heat transfer fluids. Thermochem. Acta. **455**(1), 66–69 (2007)
11. Cabaleiro, D., Pastoriza-Gallego, M.J., Gracia-Fernández, C., Pineiro, M.M., Lugo, L.: Rheological and volumetric properties of TiO2-ethylene glycol nanofluids. Nanoscale Res. Lett. **8**, 1–13 (2013)
12. Whillier, A.: Design factors influencing collector performance, low temperature engineering. In: Application of Solar Energy. ASHRAE, New York (1967)
13. Sieder, E.N., Tate, G.E.: Heat transfer and pressure drop of liquids in tubes. Ind. Eng. Chem. **28**, 1429–1439 (1936)
14. Incropera, F.P., Dewitt, D.P.: Introduction to Heat Transfer, 3rd edn. Wiley, New York (1996)

Part II
Wind Power Generation and Marine Energy Development

Long-Term Wind Speed Evaluation for Romanian Wind Farms

Marin Romeo, Sorin Ciortan, Valentin Amortila, and Eugen Rusu

1 Introduction

In the frame of IRENA's 1.5 °C scenario – aiming to a 1.5 °C temperature increase limit until the end of the century [1] in Romania were also taken measures in this direction. Based on its availability in renewable energy resources, Table 1, a constant policy to increase the percentage of green energy is targeted by the Romanian government, mainly on wind energy harvesting.

Knowing that the power generated by a wind turbine is determined by the wind speed, Eq. 1 [3], it is obvious that the main parameter for choosing the turbine location is the wind speed value:

$$P_{av}\left(v\right) = \left(\rho\left(t\right)A\left(v\right)^{3}\right)/2 \qquad (1)$$

The best wind farms' locations will be not those where the wind speed has the maximum value but also those where this speed maintains this value for a longer period of times. Figure 1 presents the availability of wind energy over Romania. Even there, there are regions with high maximum values of wind speed (see Fig. 1a), and the period of time when this is available varies from region to region (see Fig. 1b). Today Romania produces 3014.91 MW from wind and 1394.1 MW from solar sources [4]. As can be seen in Fig. 1, the energy sources are not equally distributed over the country area, the regions with highest wind energy potential being located in South-East and East of the country. As consequence, the most of wind

M. Romeo · S. Ciortan (✉) · V. Amortila · E. Rusu
Department of Mechanical Engineering, Faculty of Engineering, "Dunarea de Jos" University of Galati, Galati, Romania
e-mail: sorin.ciortan@ugal.ro

Table 1 Renewable energy resources available in Romania [2]

Energy source	Total amount per year	Energy product
Solar	1200 GWh	Thermal, electricity
Wind	8000 GWh	Electricity
Biomass	7597x103 TEP	Thermal, electricity
Geothermal	167x103 TEP	Thermal
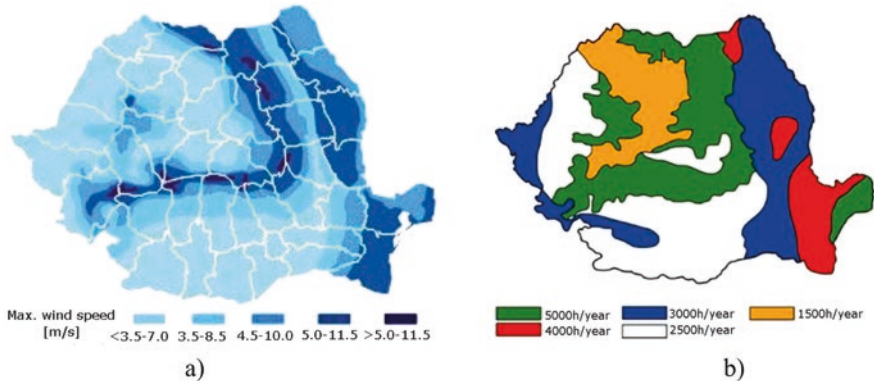
Fig. 1 (**a**) Maximum values of wind speed over Romania [2]; (**b**) Timely wind energy availability over Romania [6]

farms are placed there, getting the third position in European Top of biggest wind farms, with 240 wind turbines and an installed power of 600 MW [5].

Another important requirement for wind turbine efficiency is the stability of wind speed value over the turbine lifetime which is typically 20 years [7]. When is about a wind farm, including several turbines in different stages of working life, this aspect become essential. In this case, the farm developer must take into account the evolution of wind speed covering a much longer period of time. Based on this, the decision to continue the farm's development or to look for a new location can be made. As consequence, the prediction of wind speed evolution becomes an important research target. Studies on how the available resources, like databases and models, can be used in order to obtain more precise forecasts were a permanent subject of experts' studies [8]. Following the time interval considered, several approaches are proposed: ultra-short term (up to 30 minutes), short-term (up to 6 hours), medium-term (up to 1 day), and long-term (many days/years) [9]. In order to optimize the wind energy harvest using large wind farms, a long-term prediction, covering at least the working life of the wind turbines, is necessary. In this purpose, several methods can be used, such as statistical models, artificial neural networks-based models, etc. [10]. The present work proposes an analysis of long-term wind speed evolution in case of four wind farms, with the goal to assess the opportunity of possible future development. The analysis is based on two scenarios of the greenhouse gases evolution. The results emphasize the differences between the two

scenarios' forecasts and the opportunity to maintain or further develop the chosen wind farms.

2 Materials and Methods

2.1 Locations of Interest

Following the wind speed distribution shown in Fig. 1, four wind farms located in South-East and East areas of the country were taken into account, Table 2.

As can be seen in Table 2, several turbines are approaching the end-of-life limit. So, in order to decide to replace or install new ones, the wind speed evolution must be evaluated, at least for 20 years afore. In order to evaluate the future evolution of wind speed at selected locations, two RCP scenarios were used. Figure 2 presents the placement of the selected location on Romania's map.

2.2 RCP Scenarios

RCPs, standing for Representative Concentration Pathways, are a set of scenarios that evaluate the greenhouse gases concentration and emission pathways. Most used are RCP4.5 and RCP8.5 [11]. The RCP4.5 scenario stabilizes radiative forcing at 4.5 W/m^2, until the year 2100. This scenario assumes that a set of policies are applied with the goal of limiting emissions and radiative forcing [12]. The RCP8.5 scenario combines assumptions related to quick grow of the population doubled by a low income and with low energy improvements, leading to a radiative forcing of 8.5 W/m^2 until year 2100 [13]. This is a more aggressive scenario compared with RCP4.5 since it does not include climate mitigation targets. In the present work, the evaluation of wind speed over selected locations will be analyzed through both above-mentioned scenarios, for a period of 30 years, between 2021 and 2050. The data resolution was 6 hours/day/month/year. Analyzing the forecasted average wind

Table 2 Selected wind farm specifications and locations

Location ID	Farm name	Operational since	Equipment	Installed power [MW]	Latitude [°]	Longitude [°]
WF1	Nucări	2010	Micon NM 44	5.2	45.0644	28.9200
WF2	Cudalbi	2017	Gamesa 200	10	45.7727	27.7638
WF3	Vutcani	2014	Vestas 90/2000	24	46.5086	27.9194
WF4	Babadag	2011	Suzlon S88/2100	42	44.9016	28.6897

Fig. 2 Selected wind farms' locations, Google Maps (2023)

speed values for selected locations, over the specified years, one can conclude if the
wind farm will maintain its efficiency or not.

3   Results and Discussions

In order to evaluate the wind speed evolution during the specified period of time, the
predicted values obtained by RCP scenarios simulation were graphically repre-
sented. Analyzing the results, some comments on future situation in wind farms can
be made.

3.1   *RCP4.5 Scenario-Based Results*

The results obtained by RCP4.5 scenario are presented in Fig. 3. Looking into
Fig. 3, it can be observed that the wind speed values show differences between the
selected wind farms. In the WF3 farm area, the wind speed is lower than in the
other farms.

However, the values interval for all farms is tight, between 3.6 and 3.95 m/s.
Regarding the wind speed evolution, an important increase can be observed, from
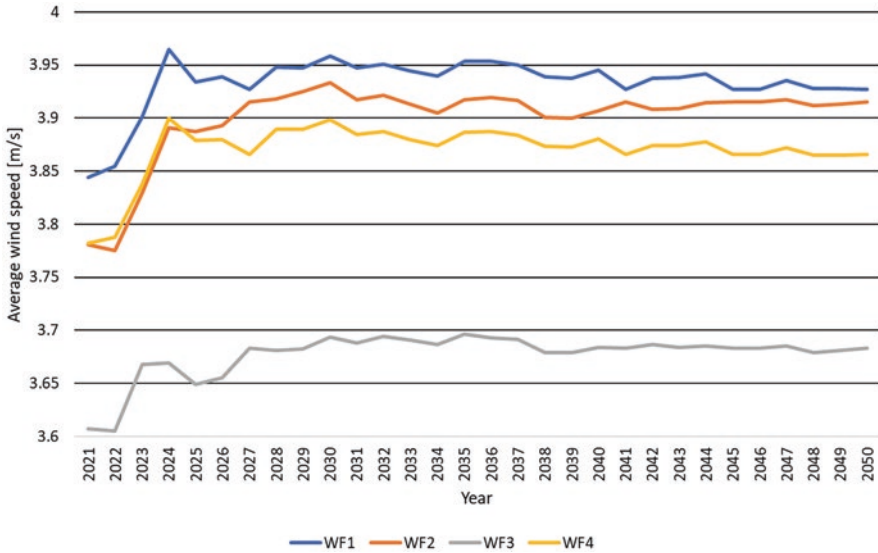
Fig. 3 Wind speeds evolution forecast based on RCP4.5 scenario

2021 to 2024, followed by a slight decrease, between 2025 and 2026. After this period of time, the wind speed value seems to be almost constant, until 2050 for farms WF1,2,4. In the WF3 case, the average wind speed rises again, from 2006 to 2031, showing very low oscillation after that, until 2050. From this scenario's point of view, all the investigated wind farms' locations offer valuable energy resources in the future. This is an important conclusion, especially in WF1 and WF4 cases taking into account that the wind turbines composing these farms are near the end of working life. As a consequence, more new turbines can be placed there, leading to an increased efficiency of wind energy harvesting.

3.2 RCP8.5 Scenario-Based Results

The results obtained by RCP8.5 scenario are presented in Fig. 4. There, the evolution of wind speed value into the future can be analyzed. Looking into Fig. 4, the same wind speed value differences between the selected wind farms, as were obvious in case of RCP4.5 scenario forecast, Fig. 3, can be observed. The interval where the values for all farms are contained is slightly larger in this case, between 3.55 and 4 m/s.

Regarding the wind speed evolution, same as in the RCP4.5 case, an important increase can be observed in the beginning of the considered period of time but the corresponding time interval is tighter, from 2021 to 2023. After this period, the wind speed value shows a drastic decrease until 2025. Then, the values' variation shows
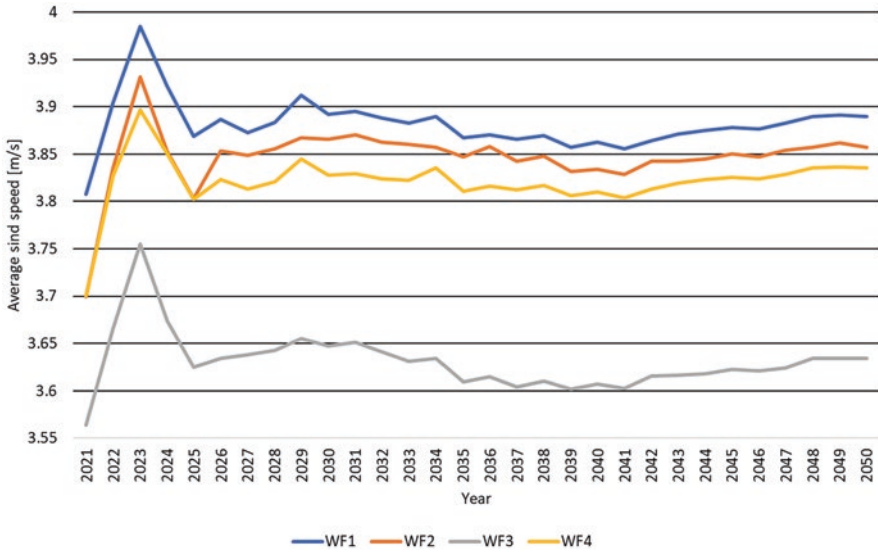
Fig. 4 Wind speeds evolution forecast based on the RCP8.5 scenario

a slight increase, followed by a constant decrease, with a minimum value in the year 2041. Since then, an increase is also observed, until 2050.

The RCP8.5 scenario also shows that, in the case of selected locations, the future available wind energy justifies the positioning of the wind farms in these places, during the considered period of time, until 2050. The period when an increase of the wind speed value is observed, from 2021 to 2023 years, is too short to be a reason for farms' expansion. As a consequence, based on these observations, some measures can be taken in order to maintain and improve the functionality of the considered farms.

3.3   RCP4.5-RCP8.5 Scenarios Compared Results

Looking at the results for wind speed forecasting obtained based on the RCP4.5 and RCP8.5 scenario simulations, one can observe that even though there is an obvious similarity in the general aspect (Figs. 3 and 4) there are few differences as well. Figure 5 presents a comparison of average wind speed values forecasted with these two scenarios. Here, one can observe that RCP4.5 offers higher values compared with RCP8.5. Another observation is that in both scenarios there is an increasing period of average wind speed value, about 2 years long, but in the case of the RCP4.5 scenario, the increase occurs between 2022 to 2024, while in the RCP8.5 scenario case, this increase occurs earlier, between 2021 and 2023. The behavior of the average wind speed evolution after year 2025 is also different in the RCP4.5 compared
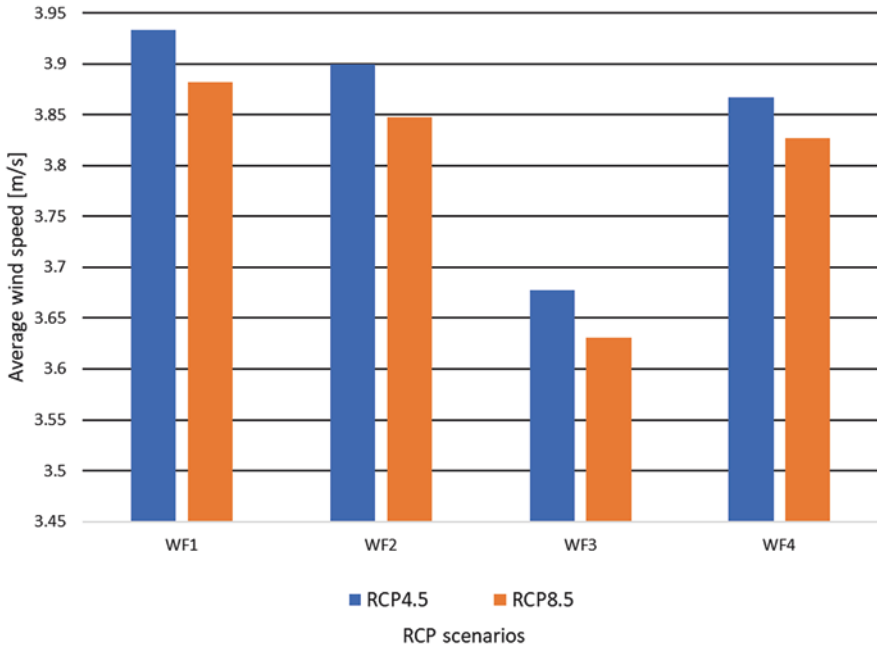
Fig. 5 Wind speed forecasted results obtained with RCP4.5/8.5 scenarios

Table 3 Differences between wind speed values obtained with RCP4.5 and RCP8.5

ID	Average values [m/s]		Difference		Maximum values [m/s]		Max-Min differences [m/s]	
	RCP4.5	RCP8.5	[m/s]	[%]	RCP4.5	RCP8.5	RCP4.5	RCP8.5
WF1	3.933	3.881	0.052	1.322	3.964	3.984	0.120	0.177
WF2	3.899	3.847	0.052	1.376	3.933	3.931	0.158	0.232
WF3	3.677	3.630	0.047	1.269	3.696	3.755	0.091	0.191
WF4	3.867	3.827	0.040	1.046	3.900	3.896	0.119	0.123

with RCP8.5 scenarios. While in RCP4.5 the evolution seems to be more stable, with few oscillations during 2032–2050 period of time, in RCP8.5 a more unstable evolution can be observed. In Fig. 4, it can be observed that there are increasing periods, during years the 2027–2030 and 2041–2049, alternating with decreases, during the years 2030–2040. Regarding the maximum and minimum values of the average wind speed during the considered period of time, it can be remarked that there also are differences between the RCP4.5 and RCP8.5 predictions, the last one giving higher a respectively lower value.

Table 3 summarizes the relevant differences observed between RCP4.5 and RCP8.5 predictions. There, one can observe both the differences between RCPs' results but also the differences in values for selected wind farms.

The observed differences between the results obtained with the RCPs are due to the length of time horizon considered. As the time range increases, the differences between the forecasts provided by the RCPs get more different, compared to short-term time intervals. This observation is in good concordance with others' researches findings [14].

4 Conclusions

Romania has large availabilities in wind energy and several wind farms built in regions where the wind speed provides enough energy and allows to obtain a large amount of green energy.

Taking that into account, due to continuous climate changes the wind conditions around the wind farm placement are also subjected to changes, an analysis of the evolution of wind speeds is needed, in order to design efficient wind farms. Also, because the working lifetime of the wind turbines is limited, the forecast should cover at least the corresponding time interval, in order to take appropriate decisions regarding the farm maintenance or development.

The average wind speed evolution for four Romanian wind farms, placed in regions with highest wind energy potential, was analyzed based on RCP4.5 and RCP8.5 scenarios, for the period of 30 years from 2021 to 2050. The chosen scenarios correspond both to medium climate changes, considering the application of mitigation measures (RCP4.5) and to high climate changes, with no mitigation measures (RCP8.5), with these scenarios covering a large area of possibilities of future weather evolution [15].

The obtained results show that all considered wind farms will be able to provide energy in an efficient way, during the analyzed period of time. However, some differences were observed between the predictions provided on RCP4.5/8.5, due mainly to the length of the time interval taken into account.

The analysis in the presented work allows the developers to establish the future development of the wind farms, taking into account that there are wind turbines that are getting close to the end of their working lifetime. This way, the decisions to replace the turbines and/or install new ones can be taken in order to increase the wind farm efficiency. Also, looking at the predictions, compensation measures for the national energy grid can be prepared for the periods of time when the average wind speed show decreases/increases.

References

1. IRENA: World Energy Transitions Outlook: 1.5°C Pathway, vol. 2021. International Renewable Energy Agency, Abu Dhabi (2021)
2. Center Regional Development Agency: Analysis of wind energy potential at the level center regions from the perspective of economic development sustainable REGIO 2010. www.regio.adrcentru.ro (2010)
3. Chen, Q., Folly, K.A.: Wind power forecasting. IFAC PapersOnline 51–28 pp. 414–419 (2018)
4. Romanian Agency for Regulation in the Field of Energy.: https://www.anre.ro/ (2023)
5. The largest wind farms in Europe.: https://cursdeguvernare.ro/ (2022)
6. Petrache, D.S.: Wind Energy. Polytechnic University of Bucharest, Bucharest, Romania (2021)
7. Ziegler, L., Gonzales, E., Rubert, T., Smolka, U., Melero, J.J.: Lifetime extension of onshore wind turbines: a review covering Germany, Spain, Denmark, and the UK. Renew. Sust. Energ. Rev. **82**, 1261–1271 (2018)
8. International energy Agency: 31st Meeting of Experts, Riso, Denmark (1998)
9. Perera, S.M.H.D., Putrus, G., Conlon, M., Narayana, M., Sunderland, K.: Wind energy harvesting and conversion systems: a technical review. Energies. **15**, 9299 (2022)
10. Lagos, A., Caicedo, J.E., Coria, G., Quete, A.R., Martinez, M., Suvire, G., Riquelme, J.: State-of-the-art using bibliometric analysis of wind-speed and-power forecasting methods applied in power systems. Energies. **15**, 6545 (2022)
11. Erickson, W.: Why ClimateCheck uses climate change scenarios RCP4.5 and RCP8.5. https://climatecheck.com, 22 July 2022
12. Thomson, A.M., Calvin, K.V., Smith, S.J., Kyle, G.P., Volke, A., Delgado-Arias, S., Bond-Lamberty, B., Wise, M.A., Clarke, L.E., Edmonds, J.A.: RCP4.5: a pathway for stabilization of radiative forcing by 2100. Clim. Chang. **109**, 77–94 (2011)
13. Riahi, K., Rao, S., Krey, V., Cho, C., Chirkov, V., Fischer, G., Kindermann, G., Nakicenovic, N., Rafaj, P.: RCP8.5 - a scenario of comparatively high greenhouse gas emissions. Clim. Chang. **109**, 33–57 (2011)
14. Barredo, J.L., Caudullo, G., Mauri, A.: Mediterranean habitat loss under RCP4.5 and RCP8.5 climate change projections. JRC Technical Reports. (2017)
15. Wayne, G.P.: The Beginner's guide to representative concentration pathways. https://skepticalscience.com, August (2013)

User-Defined Pitch Controller and Variable Wind Speed Turbine Aero-Dynamics Model in PSS/E

Qiumin Yu, Shimin Guo, and Qunneng Gao

Nomenclature

β	Wind turbine blade pitch angle
β_0	Initial value of pitch angle
β_{cmd}	Command value of pitch angle
$C_p(\lambda, \beta)$	Wind turbine power coefficient
V_t	Terminal voltage of the wind turbine generator
I_p, I_q	Active and reactive current
I_{pcmd}, I_{qcmd}	Command value of active and reactive current
K_a	Coefficients for the gain controller
$K_{pw}, K_{iw}, K_{pc}, K_{ic}$	Coefficients for the proportional-integral controller
T_p	Blade response time constant
ω_r, ω_t	Turbine shaft and generator rotor angle speed
ω_{r_max}	Generator rotor angle speed rated value
ω_r^*	Reference value of generator rotor angle speed
P_e, Q_e	Active and reactive power
P_e^*, Q_e^*	Reference value of active and reactive power
P_{ord}	Command value of active power
P_{e0}^*	Initial value of P_{ord}
P_m	Mechanical power
P_m^*	Reference value of mechanical power
P_{aero}	Aerodynamic power
ρ	Air density
R	Wind turbine blade radius

Q. Yu · S. Guo
Wind Power Bussiness Unit, CRRC Zhuzhou Electric Locomotive Research Institute Co., Ltd., Zhuzhou, China

Q. Gao (✉)
School of Electrical Engineering, Southwest Jiaotong University, Chengdu, China

V_w	Wind speed
λ	Wind turbine tip-speed ratio
GenSpeSynrad	Synchronous speed
GenboxRatio	Gearbox ratio
N	Number of wind turbines in wind farm
MBASE	Wind farm capacity

1 Introduction

As a rapidly developing clean energy, the installed capacity of wind turbines in the world is increasing year by year. However, due to the inherent volatility and randomness of wind power generation, the power electronics of grid-connected equipment and other new features, it will have a significant impact on the power quality and operation scheduling of the grid, which to some extent limits the overall consumption level of new energy in the grid [1]. To study the impact of large-scale wind power injection on power system operation and stability, a scientific and accurate wind turbine model needs to be established.

PSS/E is a commercial power system analysis tool developed by Siemens, which can accurately perform electromechanical transient simulation analysis of power system, and PSS/E contains accurate electromechanical transient models of wind turbine generator (WTG) [2], so it is often used as a simulation tool in the analysis of large-scale power system with wind power access. However, since the aerodynamic model of the generic wind turbine models in PSS/E is a linearized model [3], ignoring the change of wind speed, they are only applicable to cases where the wind speed remains constant for ~5–30 s after a disturbance occurs on the grid side [4]. Therefore, the generic wind turbine models cannot meet the requirements of studying the stochastic and intermittent wind power [5].

This chapter will describe the PSS/E 2nd-generation generic WTG, and use the PSS/E user-defined function [6] to establish a variable wind speed aerodynamic model and the corresponding pitch controller model for this variable wind speed WTG, and then verify the effectiveness of the user-defined variable wind speed WTG in this chapter through an example.

2 PSS/E Generic Wind Turbine Generator Model

According to different structures, the International Electrotechnical Commission (IEC) classifies WTG into four categories [7]: Conventional Induction Generator (Type1 WTG), Variable Rotor-Resistance Induction Generator (Type2 WTG), Doubly-Fed Asynchronous Generator (Type3 WTG), and Full-Converter Unit (Type4 WTG). Four types of equivalent simplified WTG models are developed by model researchers, that is, the 2nd-generation generic WTG model, which ignores
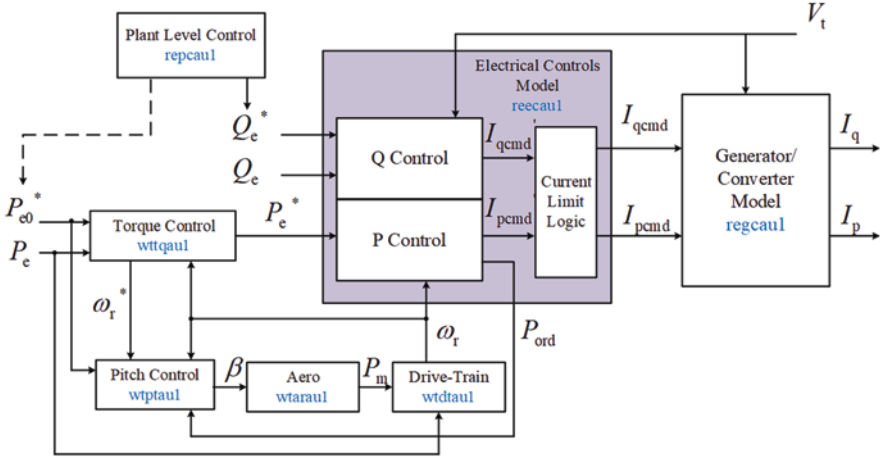
Fig. 1 Overall block diagram of PSS/E 2nd-generation generic DFIG model

the simulation of fast dynamic characteristics, such as the stator and rotor transient processes of the generator and the converter DC capacitance voltage.

The model library of PSS/E contains the 2nd-generation generic WTG model, which is shown in Fig. 1. The model has seven parts [8]: the generator/converter model (REGCAU1), the electrical controls model (REECAU1), the drive-chain model (WTDTAU1), the pitch-controller model (WTPTAU1), a simple linear model of the turbine aero-dynamics (WTARAU1), the torque control model (WTTQAU1), and the wind power plant controller model (REPCAU1).

As is shown in Fig. 1, the initial values of P_e, Q_e, and V_t are calculated from power flow; Q_e^* is sent from REPCAU1 to REECAU1, and P_{e0}^* is calculated and processed by WTTQAU1 and sent to REECAU1; WTPTAU1 calculates β based on ω_r, and passes it to WTARAU1 to obtain P_m; WTDTAU1 calculates ω_r and ω_t based on P_e and P_m; I_{qcmd} and I_{pcmd} are derived from REECAU1 based on P_e^*, Q_e, Q_e^*, and V_t through the current limiting logic and reactive/active power control within the model; REGCAU1 further processes I_{qcmd} and I_{pcmd}, and finally obtains I_p and I_q injected into the grid.

2.1 Mechanism of the Generic Turbine Aero-Dynamics Model

Figure 2 shows the structure of the generic turbine aero-dynamic model (WTARAU1), which is a simple linear wind turbine aerodynamic model [4]. The main function of this model is to output P_m and can be described as:

$$P_m = P_m^* - K_a \beta (\beta - \beta_0) \tag{1}$$
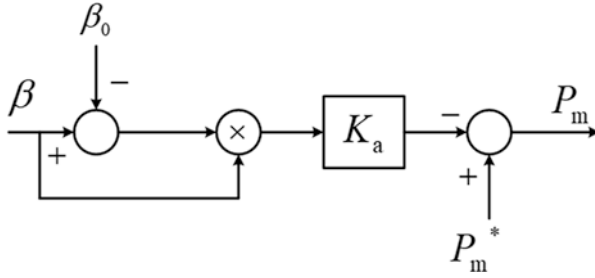
Fig. 2 Block diagram of the simple turbine aero-dynamics model

The wind speed is assumed to be constant during the transient simulation in the generic turbine aero-dynamics model and a one-dimensional linear relationship is used to describe the mechanical power versus pitch angle, bypassing the need for the curve of $C_p(\lambda, \beta)$.

The value of $P_m{}^*$ is calculated from the initialization of power flow in PSS/E and is equal to the actual active power output of WTG if β_0 is 0. Although $P_m{}^*$ can be considered as the aerodynamic power captured by the turbine blades, the model does not directly reflect the relationship of the wind speed and aerodynamic power. Therefore, in order to meet the needs of variable wind speed study in PSS/E, a user-defined variable wind speed turbine aero-dynamics model is established in this chapter.

2.2 Mechanism of the Generic Pitch Controller Model

The structure of the generic pitch controller model (WTPTAU1) is shown in Fig. 3 and can be described as:

$$
\begin{cases}
\beta_{cmd} = \left(K_{pw} + \dfrac{K_{iw}}{s} \right)\left(\omega_r - \omega_r{}^* + K_{cc}\left(P_{ord} - P_{e0}{}^* \right) \right) + \left(K_{pc} + \dfrac{K_{ic}}{s} \right)\left(P_{ord} - P_{e0}{}^* \right) \\[2ex]
\beta = \beta_{cmd} \dfrac{1}{1 + sT_p}
\end{cases}
\tag{2}
$$

An output lag for blade response and two PI controllers are consisted in this model. The inputs of the PI controllers are speed deviation and power deviation.

The input variable $\omega_r{}^*$ is derived from WTTQAU1, obtained by looking up the MPPT (Maximum Power Point Tracking) curve according to the current value of P_e. For variable wind speed turbine aero-dynamics model, the deviation with ω_r is the rated value of generator rotor angle speed ω_{r_max}. Therefore, a pitch controller model is established in this paper to suit the needs of the simulation of variable wind speed WTG model.
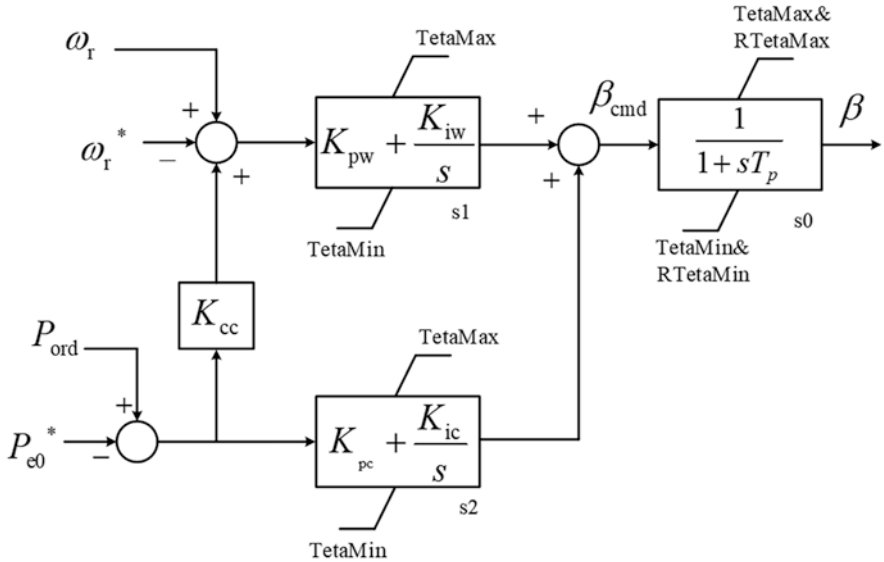
Fig. 3 Block diagram of the pitch controller model

3 PSS/E User-Defined Variable Wind Speed WTG Model

3.1 The User-Defined Modeling Function of PSS/E

When performing dynamic simulation in PSS/E, each model has some parameters and variables, such as gain coefficient, time constants, state variables, input and output variables. There are four general purpose storage arrays: CON (contains constants), STATE (contains state variables), VAR (contains algebraic variables), and ICON (contains integer variables). In addition, PSS/E sets up special arrays to contain some input and output variables. For user-defined WTG models, the common ones are ETERM (terminal voltage), WTRBSP (wind turbine rotor speed deviation), WPITCH (pitch angle), PELEC (active power), PMECH (mechanical power), etc.

The PSS/E UDM is independent of the PSS/E main program. It is only associated with the main program through the interface variables of the internal storage array and the FORTRAN code describing the UDM.

A complete program of UDM should be divided into eight subroutines, and the functions of each subroutine are shown in Table 1.

MODE 1–4 are essential in the program of UDM. The difficulty of UDM mainly lies in MODE 1 and MODE 2 subroutine writing, how to properly select state variables and correctly initialize and derive them is the key to user-defined modeling [6]. In addition, users can realize the calls of PSS/E power flow results and intermediate variables between different transient models by using the application program interface (API) provided by PSS/E in user-defined modeling [9].

Table 1 Function of each MODE flag in PSS/E

MODE	Function
1	The initialization of arrays and variables
2	Calculate the time derivatives of the state variables
3	Calculate the outputs of each models after state variables update
4	Update the number of model integrators
5	Output of model data reports (DOCU)
6	Output of model data records (DYDA)
7	Check model parameters
8	Describe the CON arrays of each models
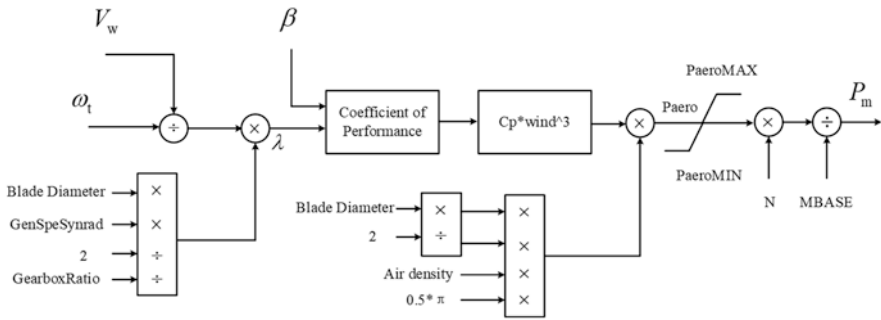
Fig. 4 Block diagram of the variable wind speed turbine aero-dynamics model

3.2 User-Defined Modeling of a Variable Wind Speed Turbine Aero-Dynamics

Figure 4 shows the structure of the user-defined turbine aero-dynamics model, which is established on the basis of aerodynamic physical relations.

P_{aero} is the mechanical power generated by a single wind turbine, which depends on the efficiency of the wind-blade interaction in the energy conversion process, that is, $C_p(\lambda, \beta)$, which can be expressed as:

$$P_{\text{aero}} = \frac{1}{2} \rho \pi R^2 V_w^3 C_p (\lambda, \beta) \tag{3}$$

Since the speed variable in PSS/E is in per unit and the famous value is needed to calculate $C_p(\lambda, \beta)$, it is necessary to convert the unit of ω_t at first, which can be described as:

$$\lambda = \frac{R\omega_t}{V_w} \times \frac{\text{GenSpeSynrad}}{\text{GearboxRatio}} \tag{4}$$

P_{aero} is the famous value of the aerodynamic power of a single turbine and P_m is the value of wind farm mechanical power in per unit for PSS/E transient simulation calculation, which can be described as:

$$P_m = \frac{P_{aero} \times N}{\text{MABSE}}$$

(5)

3.3 User-Defined Modeling of a Pitch Controller

Through the analysis of the generic pitch controller model in Sect. 2.2, a pitch controller model for the variable wind speed turbine aero-dynamics model is established, which is shown in Fig. 5.

The difference between the generic and user-defined pitch controller model is that the UDM ignores the PI controller of power deviation and keeps the PI controller of speed deviation by referring to the strategy of pitch controller model in variable wind speed turbine model [10, 11]. The user-defined pitch controller model can be described as:

$$\beta = K_{pw}\left(\omega_r - \omega_{r\_max}\right) + \frac{K_{iw}\left(\omega_r - \omega_{r\_max}\right)}{s}$$

(6)

β is set to $0°$ to maximize the wind turbine power coefficient when the wind speed is lower than the rated value, so that the air kinetic energy can be captured to the maximum extent, and ω_r is changed accordingly when the wind speed changes; when the wind speed raises to above the rated value, β is adjusted to reduce the output power of the wind turbine P_m, to make the output power of WTG P_e be rated power.

In summary, Fig. 6 shows the overall block diagram of the variable wind speed WTG model with a user-defined variable wind speed turbine aero-dynamics and the corresponding pitch controller model which can be used to research wind power volatility.
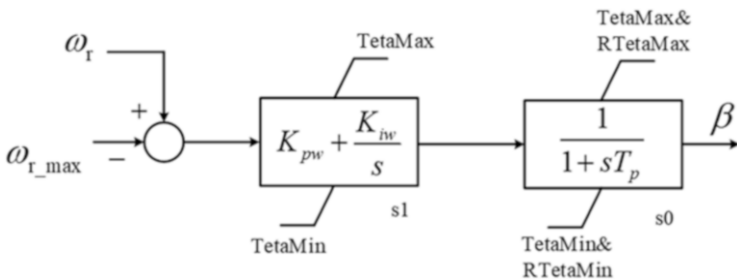
Fig. 5 Block diagram of the user-defined pitch controller model
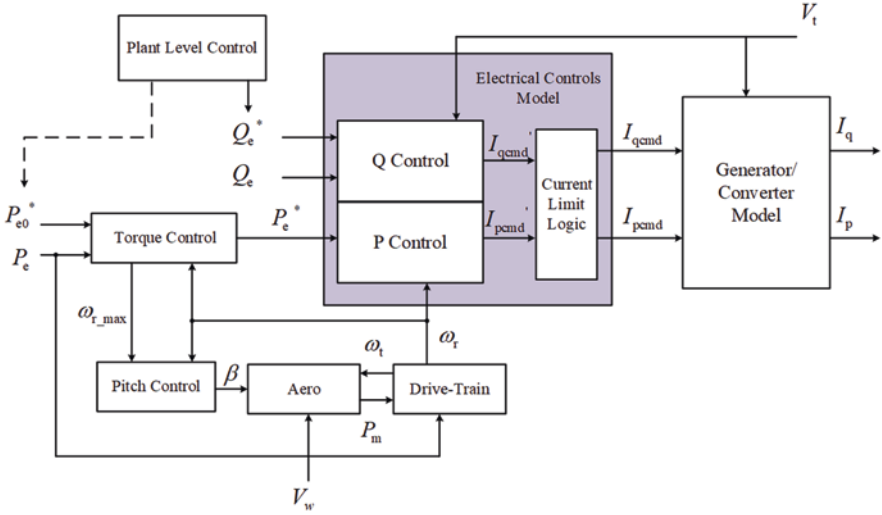
Fig. 6 Block diagram of the user-defined variable wind speed WTG model
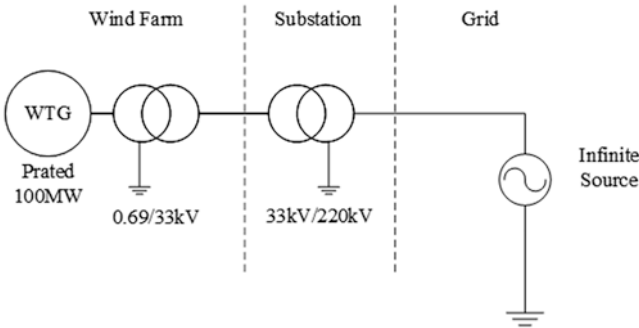
Fig. 7 A single machine infinite bus system

4 Study Cases of the User-Defined Variable Wind Speed WTG Model

A single machine infinite bus system for power flow and dynamic simulation is established based on [12], which is shown in Fig. 7, to simulate the step change in wind speed for the UDM. It is assumed that the wind farm has a rated active power of 100 MW, consisting of 67 wind turbines, each with a rated power of 1.5 MW. A step increase of wind speed occurs at 0.5 s and the result is shown in Fig. 8.

It can be seen from Fig. 8, as the wind speed rose, P_m and P_e increased accordingly. When P_e increased above the rated value, ω_t and β increased to reduce P_m by decreasing $C_p(\lambda, \beta)$. V_t did not return to its initial state as the user-defined WTG
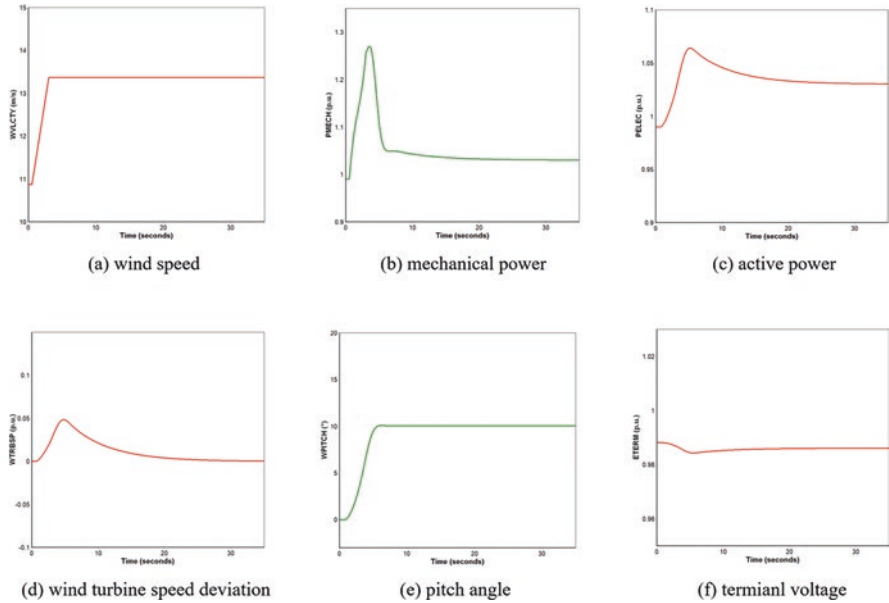
Fig. 8 The dynamic characteristic of user-defined variable wind speed WTG

reached a new stable operating point after a few seconds, but the deviation from the initial value is small. In addition, ω_t restored to the rated value at the new stable operating point. Due to the inability of the pitch controller to respond instantly when the wind speed rises, the mechanical power has overshoot.

5 Conclusions

This chapter introduces the 2nd-generation generic WTG model of PSS/E and focuses on the analysis of generic turbine aero-dynamics and pitch controller model, followed by the establishment of a user-defined variable wind speed turbine aero-dynamics and the corresponding pitch controller model in PSS/E. The UDM is tested in a single machine infinite bus system through a step change of wind speed, and the results show that the user-defined variable wind speed WTG model can perform properly in response to wind speed changes and restore stability after a period of time, which is consistent with the actual situation.

The PSS/E transient model library is further enriched through the research of this chapter. Moreover, the establishment of the user-defined variable wind speed WTG model makes it possible to research the stochastic and intermittent wind power generation in the dynamic analysis of large-scale renewable energy grid-connected power generation.

References

1. Zhigang, Z., Kang, C.: Challenges and prospects for constructing the new-type power system towards a carbon neutrality future. Proc. CSEE. **42**(8), 2806–2819 (2022)
2. Hiskens, I.A.: Dynamics of type-3 wind turbine generator models. IEEE Trans. Power Syst. **27**(1), 465–474 (2011)
3. Siemens, P.T.I.: PSS/E Model Library of PSS/E-33.4, Schenectady, NY, USA (2013)
4. Price, W.W., Sanchez-Gasca, J.J.: Simplified wind turbine generator aerodynamic models for transient stability studies. In: 2006 IEEE PES Power Systems Conference and Exposition, pp. 986–992. IEEE, Atlanta (2006)
5. Zhang, L., et al.: Review on Generic Model for Wind Power Generation. Autom. Electric Power Syst. **40**(12), 207–215 (2016)
6. Zhang, D., et al.: User-defined modeling in PSS/E and its applicability in simulations. Power Syst. Protect. Control. **44**(5), 82–87 (2016)
7. IEC 61400-27 Working Group: Wind Turbines-Part 27-1: Electrical simulation models for wind power generation–Wind turbines. Final Draft International Standard (2014)
8. Pourbeik, P.: Technical update-generic models and model validation for wind turbine generators and photovoltaic generation. Palo Alto, USA (2013)
9. Wang, Y., et al.: Dynamic process simulation system based on power flow API of PSS/E. Power Syst. Protect. Control. **42**(15), 136–141 (2014)
10. De, P.G.M., Sumper, A., Gomis-Bellmunt, O.: Modeling and control of a pitch-controlled variable-speed wind turbine driven by a DFIG with frequency control support in PSS/E. In: 2012 IEEE Power Electronics and Machines in Wind Applications, pp. 1–8. IEEE, Denver, Colorado, USA (2012)
11. Pan, X., et al.: Discussion on model structure of DFIG-based wind turbines. Autom. Electric Power Syst. **39**(5), 7–14 (2015)
12. Seyedi, M.: Evaluation of the DFIG wind turbine built-in model in PSS/E. Chalmers University of Technology, Göteborg (2009)

Expected Performances of WEC Systems Operating Near the European Offshore Wind Sites

Florin Onea and Eugen Rusu

1 Introduction

The European wind sector (EU-27) represents an important source of energy, being defined by an installed capacity of 236 GW, from which 28 GW are located offshore (12%). Nevertheless, the offshore sector is developing more rapidly, and compared to the year 2012 is expanding on a rate of 5.6x compared to the onshore one, where only a 2.2x ratio is noticed. More than this, the new offshore projects are expected to have capacity factors in the range of 42–55%, compared to a maximum value of 35%, which is related to the onshore ones [1]. The use of the wave energy is an attractive one considering that the power density is significantly higher compared to other renewables. This is the reason why in 1799, the Frenchman Pierre-Simon Girard patented the first concept of wave energy converter (or WEC). Since than almost 150 projects were developed on a global scale, more than 50% being found in Europe. From the existing solutions, the ones involving a point absorber (similar to a buoy) are considered to be the most promising, being expected to see them in future wave farms. At this moment, the wave sector is still in the early stages of development, the main reasons behind this situation being summarized as: (a) large number of concepts; (b) higher initial costs; (c) failure due to extreme marine events – storms; (d) low efficiency; (e) limited to particular coastal areas [2].

During the recent years, the idea of developing mixed wind-wave farms was advanced. Basically, by using the infrastructure of an existing offshore wind project it is possible to accelerate the development of a wave farm by reducing the initial investments and by using the established logistic supply chain. For example, in the work of Astariz and Iglesias [3] a theoretical wave farm was associated to the Alpha

F. Onea (✉) · E. Rusu
Department of Mechanical Engineering, Faculty of Engineering, "Dunarea de Jos" University of Galati, Galati, Romania
e-mail: florin.onea@ugal.ro

Ventus and Horns Rev 1 wind projects. The results indicate that the downtime period can be significantly reduced obtaining at the same time lower operation costs (up to 5%). In terms of energy production, a combined wind-wave project will be suitable for an island environment or for a developing country, which heavily depends on the fossil fuel imports [4, 5]. There are plans already to develop wave-wind projects, this being the case of Neptune 6 (Canada), P37 (Denmark), or DualSub (UK), the last one receiving a funding of €4.8 m for his development. Most of the research projects are currently developed in the UK, being invested funding that varies from 4.5 to €112 m per project [6].

In this context, the aim of the present work is to investigate the performances of various WECs by using as a reference the locations of several European offshore wind farms.

2   Materials and Methods

The marine sites considered for assessment are presented in Table 1 and Fig. 1, being associated to some relevant offshore wind projects from Europe. The selected projects are in different stages of developments, starting from a capacity of 25 MW (pilot project) and reaching a maximum one of 1000 MW, for the planned projects from Ireland and Norway, respectively. These sites are representative for the European coasts, starting from Iberian Peninsula and gradually reaching the northern areas.

The wave conditions in the vicinity of these sites were identified by processing the wave data related to the 10 years of ERA5 dataset (2012–2021), which are defined by a time step of 6 hours (00:06:12:18 UTC). Two wave parameters were considered for evaluation: (**a**) significant wave height (Hs); (**b**) wave period (Te). More details regarding the reanalysis date provided by the ERA5 project and the

Table 1 Details of the European offshore wind sites considered for evaluation. Information processed from [7]

ID	Project	Country	Lat (º)	Long (º)	Capacity	Status
P1	Mar de Agata	Spain	36.87	−1.89	300 MW	Early planning
P2	WindFloat Atlantic	Portugal	41.60	−9.06	25 MW	Operational
P3	Saint-Nazaire	France	46.53	−4.13	480 MW	Operational
P4	Saint-Brieuc	France	48.87	−2.47	496 MW	Under construction
P5	Clarus	Ireland	52.49	−10.35	1000 MW	Early planning
P6	Neart na Gaoithe	UK	56.26	−2.19	448 MW	Under construction
P7	Trollvind	Norway	60.52	3.57	1000 MW	Early planning
P8	Kriegers Flak	Denmark	55.00	13.23	605 MW	Operational
P9	Tender 1	Lithuania	55.94	20.02	700 MW	Early planning
P10	Tahkoluoto	Finland	61.55	20.95	720 MW	Early planning
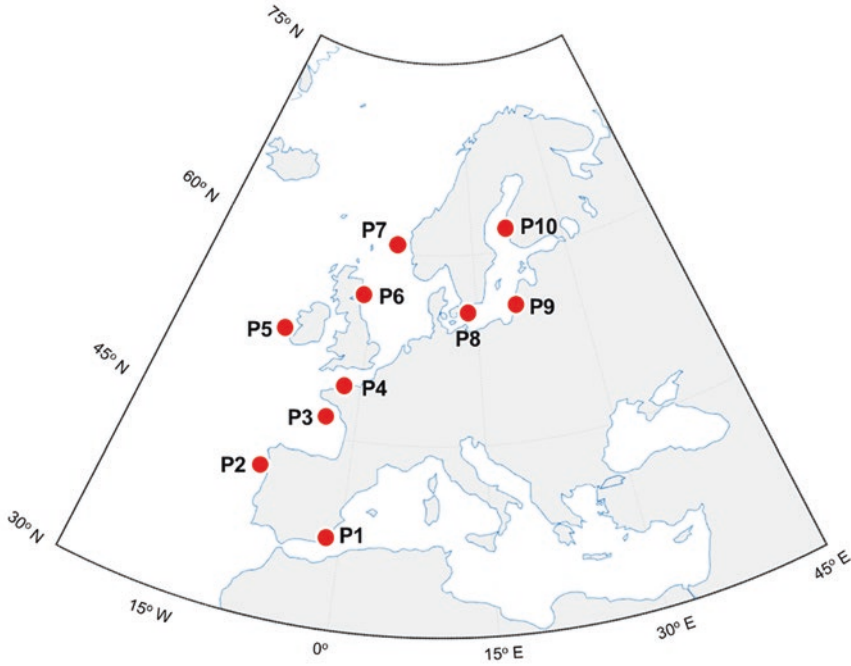
Fig. 1 The European coastal environment and the location of the reference sites (P1-P10)

practical use of these types of information for the wave energy sector can be found on the existing literature review [8, 9].

The wave power (in kW/m) can be defined as [10]:

$$P_{\text{wave}} = \frac{\rho_{\text{water}} \cdot g^2 \cdot T_e \cdot H_s^2}{64 \cdot \pi} \cong 0.49 \cdot H_s^2 \cdot T_e \tag{1}$$

where: $\rho_{\text{water}} = 1025$ kg/m³ (sea water density); $g = 9.81$ m/s² (gravitational acceleration).

Beside the evaluation of the wave resources, another purpose of the present work is to investigate the performances of several WECs that are representative for this industry. In this case, a total of five systems were considered, namely: (1) Wave Dragon – 7000 kW (rated power); (2) Pontoon Power Converter (or PPC) – 3619 kW; (3) Pelamis – 750 kW; (4) Aqua Buoy – 250 kW; (5) Seabased – 15 kW. Each system is defined by a particular power matrix, this information being presented in more details in Rusu and Onea [11]. The expected power output of a particular WEC can be expressed as [11]:

$$P_{\text{WEC}} = \frac{1}{100} \cdot \sum_{i=1}^{n\text{Te}} \sum_{j=1}^{n\text{Hs}} \text{PW}_{ij} \cdot \text{PM}_{ij} \tag{2}$$

where: PW_{ij}– sea state percentage associated to a particular *Hs* (line *i*) and *Te* (column *j*) combination; PM_{ij}– expected power output from a WEC associated to the same *i* and *j* combinations; *nHs* and *nTe* – number of wave heights and period intervals.

3   Results

A first evaluation of the wave resources is provided in Fig. 2, by considering the full time distribution (or total time) and also the main seasons: (a) Winter – December/January/February; (b) Spring – March/April/May; (c) Summer – June/July/August; (d) Autumn – September/October/November. The sites P2, P3, P5, and P7 are defined by more consistent values, a maximum peak of 86.9 kW/m being observed at site P5 (Clarus, Ireland). Much lower resources are expected in the case of the points from the enclosed seas (ex: P1 or P8), and also for the sites sheltered by particular land areas (ex: P4 and P6). The summer season is defined by much lower values that do not exceed 10 kW/m, and an expected peak of 12.15 kW/m in the case of P5.

Fig. 3 presents the distribution of the wave classes (from C1 to C7), as are mentioned in Rusu and Onea [2]. A site defined by a higher wave class can be considered a suitable candidate for the implementation of a wave project.

By looking on the first classes (ex: C1) a clear distinction can be made between the sites P2, P3, P5, P7, and the rest of the sites. For the first group points a significant percentage of the values (from 70% to 90%) is accounted by class C1,
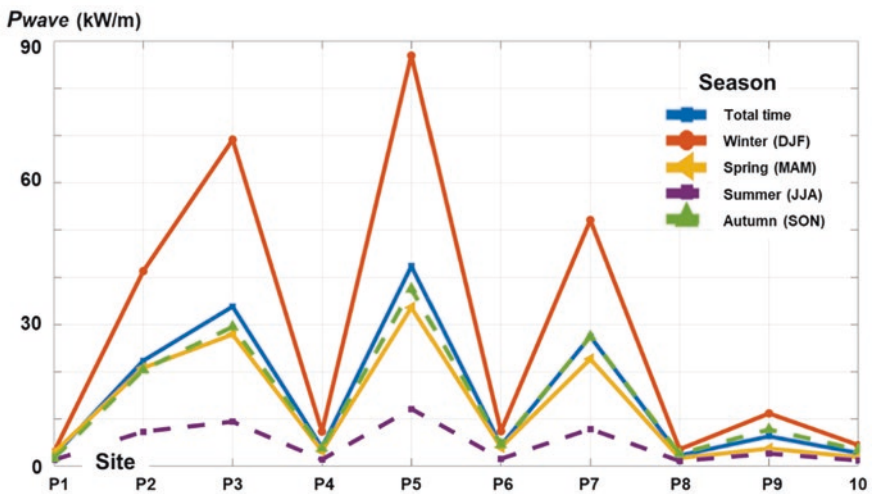
Fig. 2 Distribution of the wave power (*Pwave*) associated to the sites P1–P10. The general and seasonal evolutions are related to the 10-year time interval (2012–2021) of ERA5 data
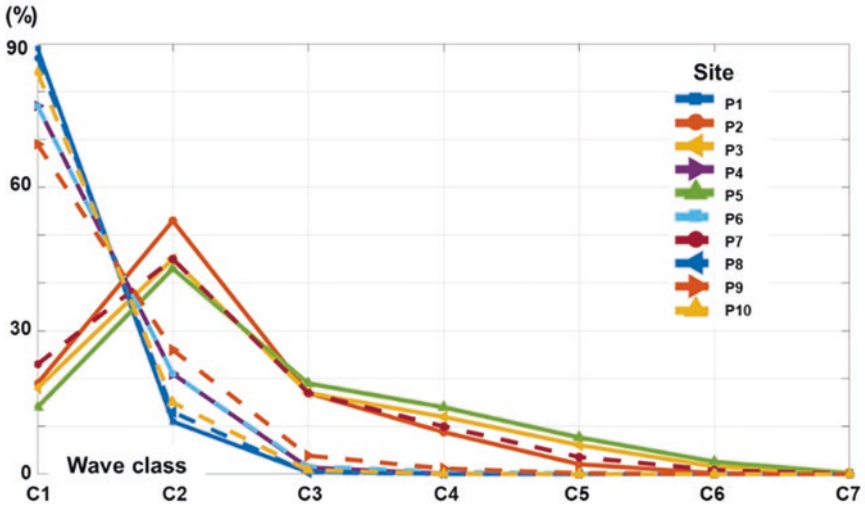
Fig. 3 Wave power classification according to each reference site
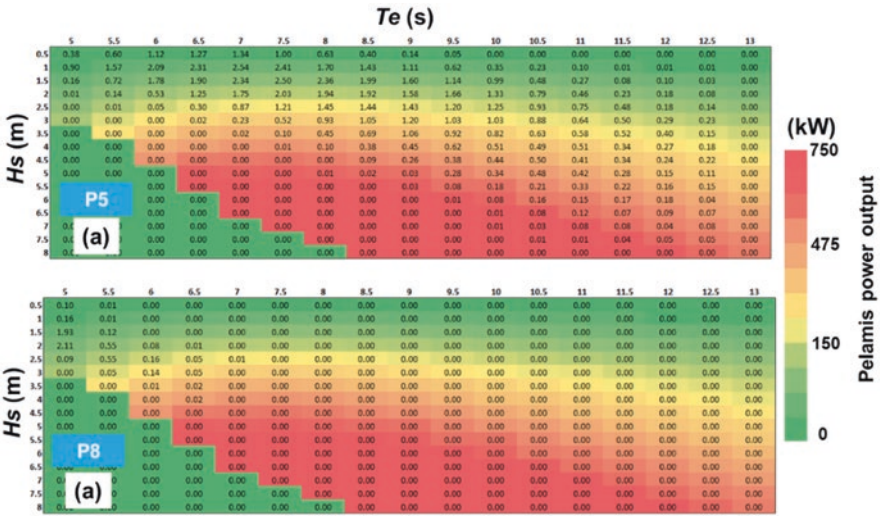
Fig. 4 General sea-state distribution expected for the sites: (**a**) P5, (**b**) P8. The values from the matrix indicate the percentage of occurrences for a particular Hs/Te combination, while the color scale is related to the expected power output from a Pelamis system

compared to only 20% that is expected for the site P2. The more energetic sites equally distribute their values in the upper wave classes, with values being noticed in class C6 (ex: P5–2.6%).

The bivariate distribution Hs/Te is presented in Fig. 4, by considering the full time distribution of the P5 (energetic) and P8 (less energetic) sites.
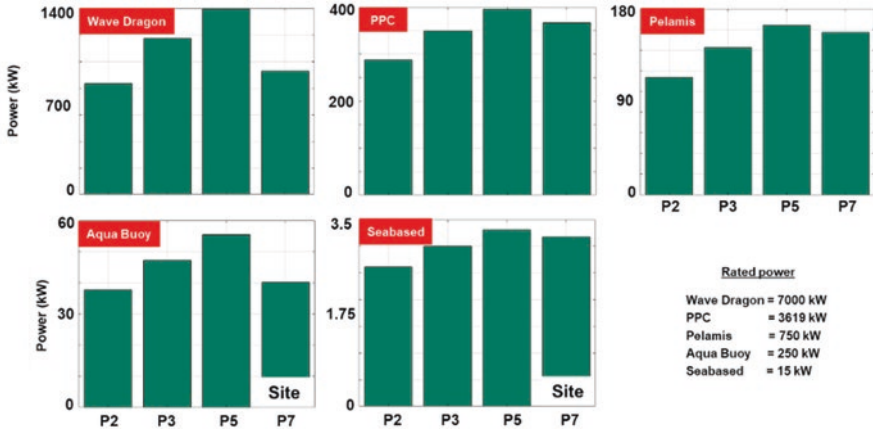
Fig. 5 Expected power output of the considered WECs processed for the sites P2, P3, P5, and P7, respectively

By matching these distributions with the power matrix of the Pelamis wave energy converter (see color scale), we can expect a lower performance since this system operates on a rated capacity for waves higher than 5 m and periods that does not exceed 10 s. In the case of the site P8, most of the values are close to zero and by summing the existing percentages we will obtain a total of 6.25%, compared to 97.10 expected from the site P5. This means that for the site P8, this type of WEC is not suitable for implementation, and it is expected that in the near future the available WECs are tuned according to the local resources in order to obtain better performances.

As a next step, only the sites defined by more consistent wave resources (P2, P3, P5, and P7) will be considered for the evaluation of several WEC generators. This is done in Fig. 5, where the expected power output is illustrated. The generated power is directly related to the rated capacity of each system, better performances being related to the site P5 (Ireland) that is directly located on the coastal area facing the North Atlantic. For example, the differences between the sites P2 and P5 are close to: Wave Dragon - 40%; PPC – 27.40%; Pelamis – 30.7%; Aqua Buoy – 32%; Seabased – 20.90%.

The capacity factor represents another important indicator for the efficiency of a particular WEC, being defined as the ratio between the rated power of a particular wave convertor and the expected power output associated to a particular site. Figure 6 presents the evolution of this indicator, where a maximum of 20% is expected for the site P5. Although the system Seabased is defined by the lowest rated capacity (15 kW), this generator presents much better values compared to the other WECs, reaching a minimum of 17.43% near the site P2.

Since the site P5 presents more energetic wave resources, Fig. 7 presents the expected monthly evolution of the capacity factor. This evolution is directly related to the seasonal distribution, being noticed that during the winter time there are systems (e.g., Wave Dragon, Aqua Buoy, and Pelamis) that obtain better performances than in the case of the Seabased generator.
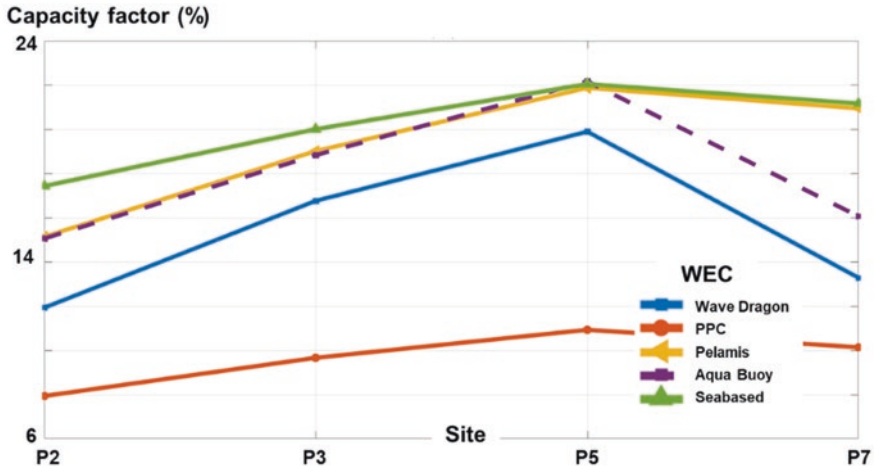
Fig. 6 WECs capacity factor (in %) expected for the sites P2, P3, P5, and P7, respectively
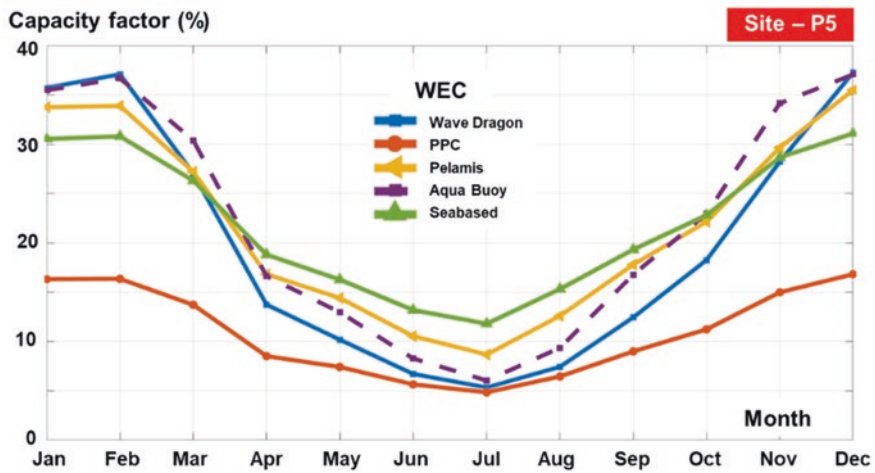
Fig. 7 WECs capacity factor – monthly values related to the site P5

4 Conclusions

The marine areas are defined by numerous opportunities, being expected to have a major impact in the consolidation of the energy market. The wave industry can benefit from the know-how accumulated by the offshore wind industry in order to accelerate the development of the wave farms and also to reduce the costs required to operate such projects. In the present work, based on the wave data related to the ERA5 project, it was possible to highlight the main differences that occur between

the sites facing the ocean environment and the ones located in enclosed or semi-enclosed sea areas. The performances of the considered WECs are directly related to wave energy profiles associated to a particular site, indicating the point P5 (project Clarus, Ireland) as the main candidate for the development of a mixed wind-wave farm. The capacity factors of the present WECs can be considered to be quite low compared to the offshore wind turbines. Nevertheless, this issue can be solved by adjusting the power matrix of a particular generator to the dominant sea state expected for a particular site.

References

1. Wind energy in Europe: 2021 Statistics and the outlook for 2022–2026. https://windeurope.org/data-and-analysis/product/wind-energy-in-europe-2021-statistics-and-the-outlook-for-2022-2026. Last accessed 18 May 2022
2. Rusu, L., Onea, F.: The performance of some state-of-the-art wave energy converters in locations with the worldwide highest wave power. Renew. Sust. Energ. Rev. **75**, 1348–1362 (2017). https://doi.org/10.1016/j.rser.2016.11.123
3. Astariz, S., Iglesias, G.: Output power smoothing and reduced downtime period by combined wind and wave energy farms. Energy. **97**, 69–81 (2016). https://doi.org/10.1016/j.energy.2015.12.108
4. Rusu, E., Onea, F.: Estimation of the wave energy conversion efficiency in the Atlantic Ocean close to the European islands. Renew. Energy. **85**, 687–703 (2016). https://doi.org/10.1016/j.renene.2015.07.042
5. Rusu, E., Onea, F.: Joint evaluation of the wave and offshore wind energy resources in the developing countries. Energies. **10**, 1866 (2017). https://doi.org/10.3390/en10111866
6. Jin, S., Greaves, D.: Wave energy in the UK: status review and future perspectives. Renew. Sust. Energ. Rev. **143**, 110932 (2021). https://doi.org/10.1016/j.rser.2021.110932
7. Global Offshore Renewable Map | 4C Offshore. https://www.4coffshore.com/offshorewind/. Last accessed 16 Jan 2023
8. Guillory, A.: ERA5. https://www.ecmwf.int/en/forecasts/datasets/reanalysis-datasets/era5. Last accessed 31 May 2019
9. Rusu, E., Onea, F.: Evaluation of the adverse weather conditions associated to some significant European marine renewable energy projects. Energy Rep. **8**, 185–193 (2022). https://doi.org/10.1016/j.egyr.2022.10.205
10. Silva, K., Abreu, T., Oliveira, T.C.A.: Inter- and intra-annual variability of wave energy in Northern mainland Portugal: application to the HiWave-5 project. Energy Rep. **8**, 6411–6422 (2022). https://doi.org/10.1016/j.egyr.2022.05.005
11. Rusu, E., Onea, F.: A parallel evaluation of the wind and wave energy resources along the Latin American and European coastal environments. Renew. Energy. (2019). https://doi.org/10.1016/j.renene.2019.05.117

Design and Performance Analysis of a Bio-Inspired Small Wind Turbine with Maple Seed Aerodynamics

Amr Khedr and Francesco Castellani

Nomenclature

AoA	Angle of attack
CFD	Computational fluid dynamics
HAWT	Horizontal axis wind turbine
MRF	Moving reference frame
NTNU	Norwegian University of Science and Technology
RANS	Reynolds Average Navier–Stokes
Re_C	Reynolds number based on the chord length
TSR	Tip speed ratio
UAV	Unmanned air vehicle

1 Introduction

Bioinspiration, also known as biomimicry, refers to the method of innovation that aims to address human challenges sustainably by emulating nature's proven strategies and mechanisms. Maple seeds, more commonly known as "Samaras" (shown in Fig. 1), are of significant interest for aerodynamic research inspired by nature. These seeds exhibit remarkable aerodynamic properties, inspiring researchers and aviators for years [1]. Maple seeds have been observed to travel distances of up to 6 kilometers from the parent vine [2]. The aerodynamic efficiency of these seeds is estimated to be in the range of 3–4 at low Reynolds numbers ($Re = 49103$) with a magnitude of 0.34 for lift coefficient [3]. The analysis of maple seeds in autorotation has resulted in new insights for wind turbine design and other aerodynamic applications. Early research on maple seed flight focused on understanding the

A. Khedr (✉) · F. Castellani
University of Perugia, Department of Engineering, Perugia, Italy
e-mail: amr.khedr@studenti.unipg.it

Fig. 1 A maple seed "Samara". (Taken by the author at Perugia University, Italy)

physics and stability, which has now advanced to mimicry with the goal of powered flight [2]. The blade element momentum theory was used by Rosen and Seter [4] to provide a quantitative evaluation of the aerodynamic effects in 1991. Leading-edge vortices were identified as the main source of lift for maple seeds in 2009, as studies by Lentink revealed the three-dimensional flow around scaled models [5].

During autorotation, the maple seed transforms potential energy into kinetic energy, which is then converted back into lift to maintain flight. The seed functions like a wind turbine or a propeller during descent. In 2017, Zhe Ning and Hui Hu [6] experimented a bio-inspired UAV propeller using the external shape of a maple seed with an E63 airfoil, comparing it to a conventional propeller. The results showed that the bio-inspired propeller produced equal thrust with less noise compared to the baseline, with a smaller wake region and faster decay of tip vortex strength.

A physical analysis of a maple seed with a comparison to wind turbine blades published in 2015 [7] side by side with a recent, 2022 [8], experimental measurement of the power coefficient of a Mapel seed emphasized that the power coefficient of a maple seed wind turbine blade can exceed the Betz's limit even in practical conditions. Betz's limit gives the coefficient of the maximum power, in perfect theoretical conditions, that can be extracted by a wind harnessing machine from the kinetic energy of the wind that passes through the projected area of the machine and equals 0.592. The excessive power that can be extracted by a maple seed was claimed to be due to its ability to harness the energy from the wind also outside its projected area [8]. However, no work has dealt with the design and analysis of an actual wind turbine that mimics the maple seed.

In this study, a small wind turbine of 2 blades and 1 m diameter has been designed using the exact external contour of a maple seed with the same swept-back angle provided in the work of Lee et al. [9] who analyzed the mechanism of autorotation flight of a specific maple seed. The high-lift airfoil S826 is the base airfoil of the designed turbine. This airfoil has shown very good performance for the small wind turbine developed by the Norwegian University of Science and Technology (NTNU) team [10]. The turbine is optimized at a low tip speed ratio of 3, as that is a requirement for small wind turbines to guarantee low noise and vibration levels especially because they are supposed to be used in residential areas. The turbine is studied numerically using computational fluid dynamics (CFD). The power and thrust performance are plotted and the performance of the turbine is explained via the numerical flow visualization.

2   Maple Seed Turbine Design

There are over 132 species of maple trees on the earth. The shape of the seeds is dependent on the species of the maple tree. Most of them are distinct with the autorotation phenomena. In the current study, the external contour and the swept-back angle of the maple seed studied by Lee et al. [9] are used to design a small wind turbine. The contours of the maple seed wind turbine designed in this study are shown in Fig. 2. The high-lift airfoil S826, which has shown very good performance for the small turbine developed by NTNU team [10], is used as the base section profile of the turbine. The turbine specifications are summarized in Table 1.

Based on design TSR of 3, the Re_C distribution along the current maple seed blade of 0.5 m radius has been found to be between 100, 000 and 200, 000. Analyzing the airfoil S826 experimental lift and drag data provided by Bartel et al. [11], it has been known that the best efficiency point of the airfoil in this Re_C range is at the attack angle of around 7. Therefore, the twist of the current maple seed blade has been optimized in order to provide an angle of attack of 7 at each blade section when it works at the design TSR of 3. The twist distribution of the present maple seed turbine blade is plotted in Fig. 3. Finally, the computer-aided design software SOLIDWORKS was used to create the blade geometry.

3   Numerical Methods

A half-cylindrical domain has been created around the blade model. It has a radius of 15R, an upstream distance of 15R from the blade, and a 20R downstream. The computational domain has been discretized using polyhedral conformal cells. Refined cell size has been used on the blade surface and 24 inflation layers have been made on the blade with a 1.2 growth ratio guaranteeing a Y+ less than 1 on the blade. The rotating wind turbine was modeled utilizing the MRF technique. Eltayesh

Fig. 2 Blade contours of
the present maple seed
wind turbine
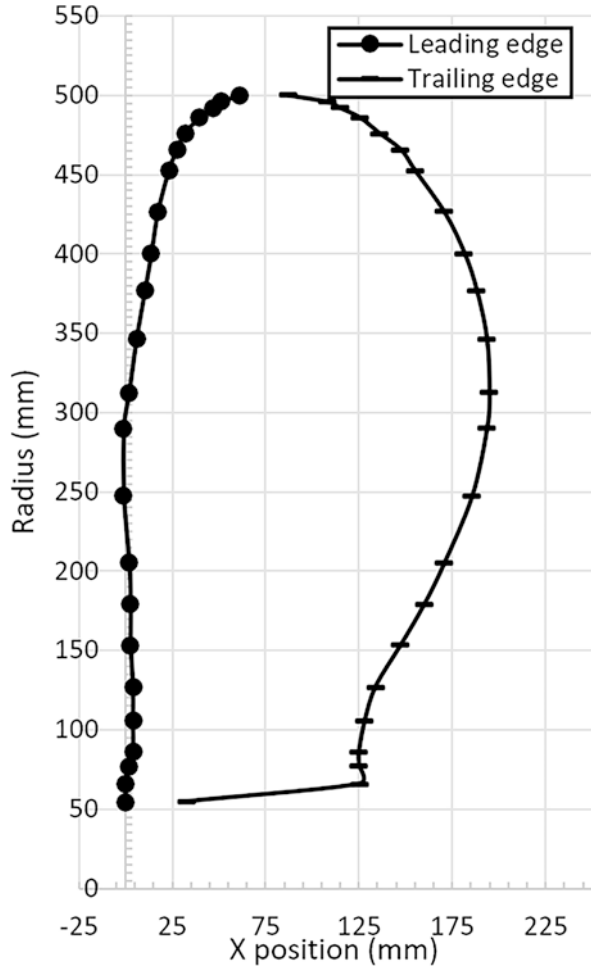
Table 1 Maple Seed Turbine specifications

Number of blades	2
Airfoil	S826
Rotor diameter	1 m
Hub diameter	0.082 m
Swept back angle	19.4°
Design TSR	3

et al. [12] provide further information regarding MRF. Many researchers have
adopted this approach, which has been shown to be accurate for predicting flow in
HAWT. Steady RANS equations are solved for the whole domain using the finite
volume code ANSYS Fluent. SST $-K\omega$ has been used for modeling the turbulent
flow, and the coupled scheme for the pressure-velocity coupling.
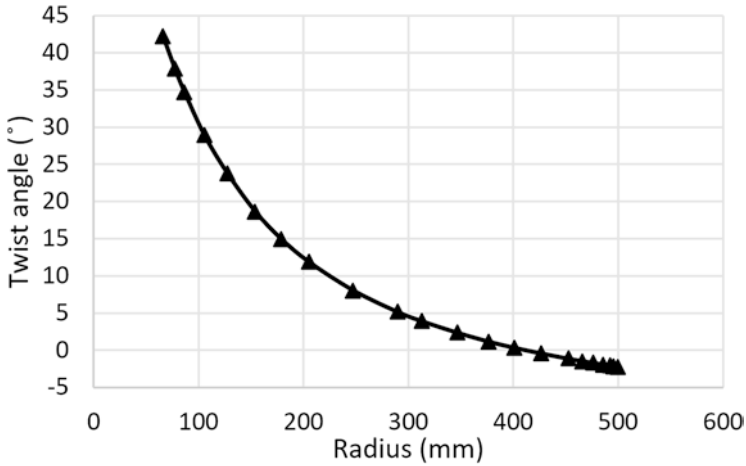
Fig. 3 Twist distribution along the present maple seed wind turbine blade
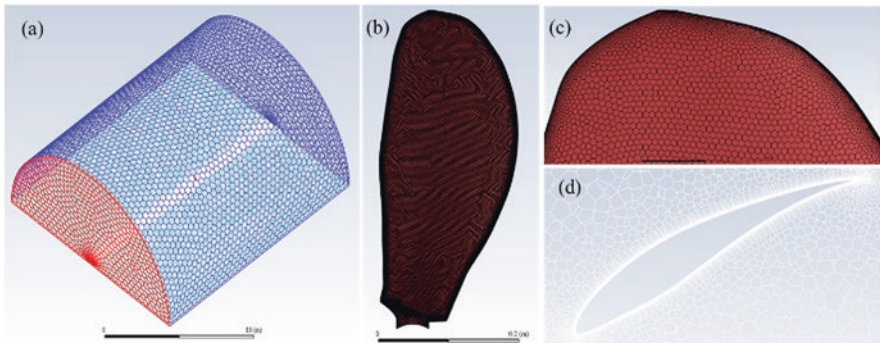
Fig. 4 (**a**) The computational domain, (**b**) the details of the mesh on the blade, (**b**) near the tip, and (**c**) the boundary layers on a blade section

A 10 m/s is specified as a velocity inlet, a zero-pressure outlet on the downstream boundary, a slip wall on the top and bottom half cylinder surfaces, periodic boundaries for the two lower faces, and no-slip boundary condition on the blade surface. The solution is converged when the change in C_P after 10 iterations is less than 0.05% and all the residuals drop at least five orders of magnitude. These conditions are achieved after more or less 4000 iterations. Details of the model and the mesh are shown in Fig. 4 Adapting the mesh sensitivity study on the C_P shown in Fig. 5 at TSR3, the mesh M2 has been selected for the study.

For the purpose of validation, the CFD model with the same mesh size is used to simulate the NTNU turbine [10] that has almost the same diameter size and the
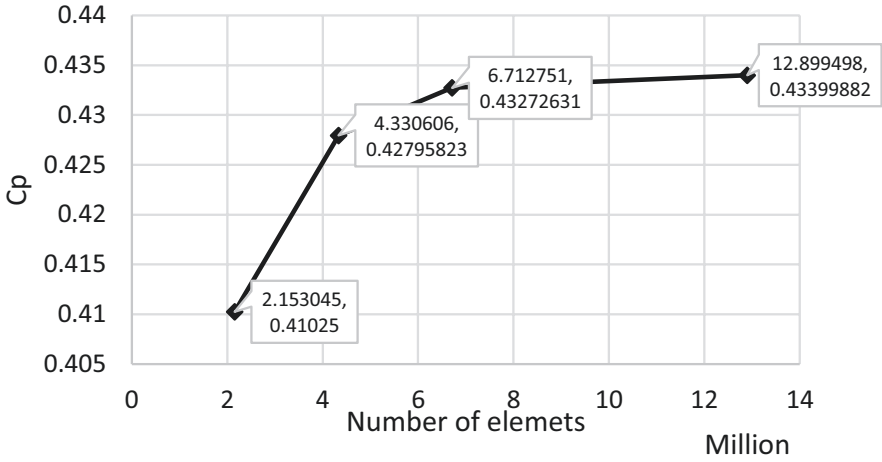
Fig. 5 Mesh sensitivity study
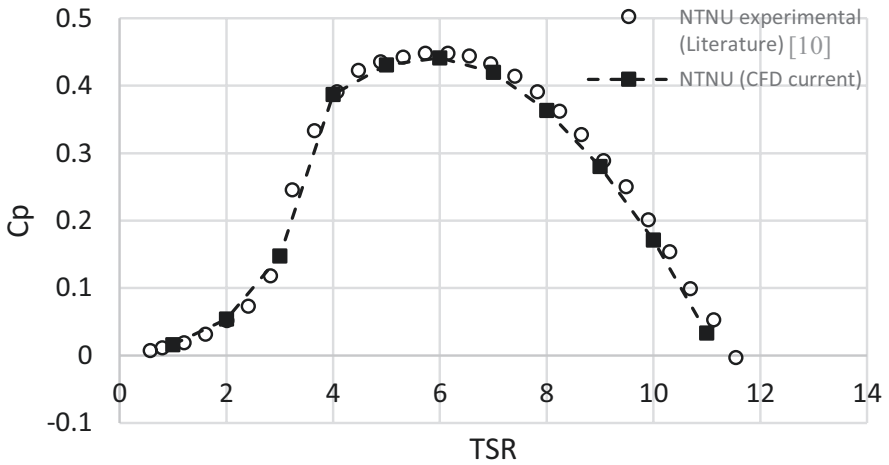
Fig. 6 CFD model validation

same airfoil used in the current study. The obtained power coefficient curve versus TSR compared to the experimental data shown in Fig. 6 shows the validity of the used CFD model. However, it should be mentioned that the provided experimental data are not corrected against tunnel blockage and it was supposed to be insignificant in the work of Krogstad et al. [10].

4   Results and Discussion

Figure 7 shows the power and thrust performance of the maple seed small wind turbine at a wind speed of 10 m/s. The turbine produces the maximum power at TSR = 3 with a power coefficient of 0.38. It can produce power until the TSR reaches 5. At TSR = 6 the power coefficient is negative means that the turbine will stop before arriving at this point. At the low TSR range, there is a sharp drop in the power curve starting from TSR 2.5. After that, from TSR 2 to TSR 1 the power drop is linear. The thrust performance of the turbine increases with an ascending slope over the whole TSR range except for between TSR 2 and TSR 1, referring gain to the sharp drop in the turbine performance. At the best design point, the turbine suffers a thrust coefficient of 1.16. Figure 8 illustrates the torque per unit area distribution along the span of the Maple seed wind turbine blade, obtained at the design tip speed ratio of 3 and a wind speed of 10 m/s, as investigated in this study. As shown in the figure, the chord distribution of the Maple seed contours employed to design the blade features a considerable chord distribution at the mid-sections of the blade, which results in a significant contribution to the torque production at the middle of the blade.

Examining the friction lines on the suction side of the blade is another approach to observe the flow conditions on the turbine blade which is shown in Fig. 9. The neat, straight lines at TSR = 4 illustrate that the flow is fully attached. The flow visualization at TSR = 2 says that the blade is fully stalled. The illustration at TSR = 3, where there is the maximum power coefficient, makes it very evident that the stall starts at the blade's root, however, on the upper section the flow is attached and at its maximum lift angle (the stall angle).
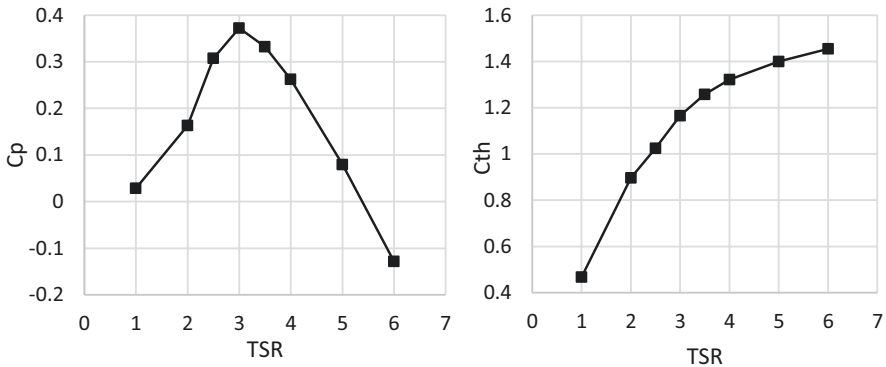
Fig. 7 Cp and Cth versus TSR for 2-blade maple seed small wind turbine of 1 m diameter at a wind speed of 10 m/s
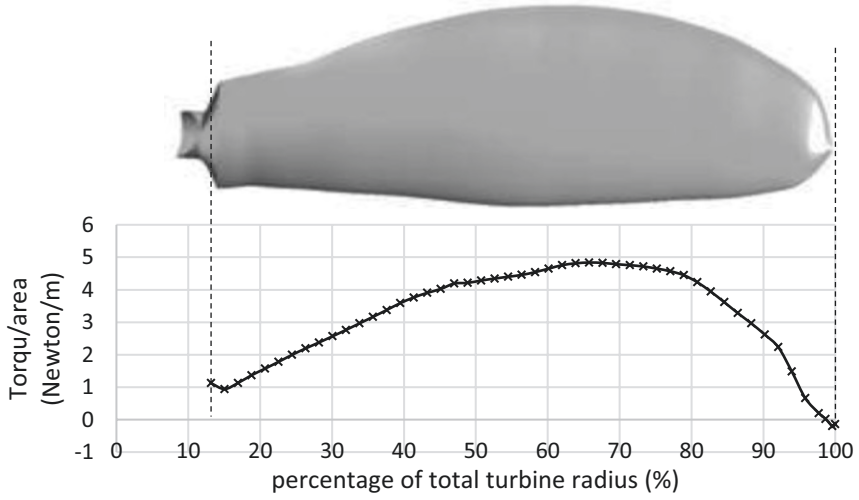
Fig. 8 Torque per unit area distribution along the present maple seed turbine blade at the design TSR of 3
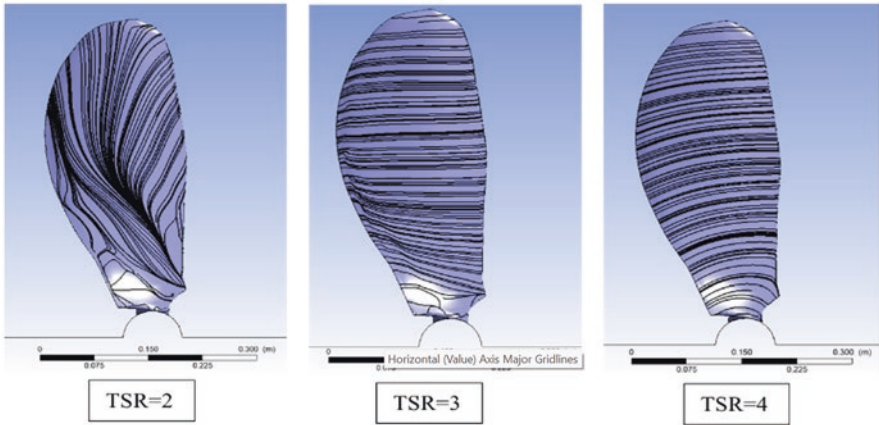
Fig. 9 Friction lines on the suction side of the turbine blade at different TSRs

5   Conclusions

The design of a small wind turbine inspired by the autorotating maple seed has been successfully implemented using the high lift airfoil S826 and optimizing the blade twist using the airfoil experimental data. The computational model developed for the turbine has been validated using experimental data from a small wind turbine that utilizes the same airfoil. Numerical simulations have shown that the turbine

exhibits good power performance at a small TSR range with a maximum Cp of 0.38 at TSR = 3 where the thrust coefficient Cth is 1.16. Here it should be mentioned that small wind turbines are recommended to be designed to work better at small TSRs to avoid high noise and vibrations in the residential area where they are supposed to be used. The results have shown also that the power coefficient drops at TSRs smaller than 2.5 due to the sudden separation on the suction side of the blade. NTNU turbine, which uses the same airfoil, suffers from the same sudden drop in power coefficient at a TSR of less than four. These findings suggest that further modifications are needed for the used airfoil in order to enhance the turbine performance at low TSRs. For future work, different airfoils will be investigated to determine their impact on the maple seed turbine power output, and the performance of the turbine at different wind speeds will be studied to further improve its efficiency. The investigation conducted in this study indicates also that the blade design employing the Mapel seed contours with a large chord distribution at the mid-sections of the blade results in a significant variation of toque along the blade span, particularly producing more torque at the mid-section of the blade. This finding highlights the importance of further investigations to assess the impact of these loads on the blade and the potential implications for fatigue loads. Ultimately, the successful implementation of this novel design holds promises for the development of highly efficient and cost-effective small wind turbines.

References

1. Hirschel, E.H., Prem, H., Madelung, G.: Aeronautical Research in Germany: From Lilienthal Until Today, vol. 147. Springer Science & Business Media, Germany (2004)
2. Kulfan, B.: Dr. john mcmasters: following the foot steps of a creative paleoaerodynamicist. In: 47th AIAA AerospaceSciences Meeting Including the New Horizons Forum and Aerospace Exposition, p. 869 (2009)
3. Rose, J., Natarajan, S.G., Gopinathan, V.: Biomimetic flow control techniques for aerospace applications: a comprehensive review. Rev. Environ. Sci. Biotechnol. **20**(3), 645–677 (2021)
4. Rosen, Seter, D.: Vertical autorotation of a single-winged samara (1991)
5. Lentink, D., Dickson, W.B., Van Leeuwen, J.L., Dickinson, M.H.: Leading-edge vortices elevate lift of autorotating plant seeds. Science. **324**(5933), 1438–1440 (2009)
6. Ning, Z., Hui, H.: An experimental study on the aerodynamic and aeroacoustic performances of a bio-inspired UAV propeller. In: 35th AIAA Applied Aerodynamics Conference, p. 3747 (2017)
7. Holden, J.R., Caley, T.M., Turner, M.G.: Maple seed performance as a wind turbine. In: 53rd AIAA Aerospace Sciences Meeting, p. 1304 (2015)
8. Molteno, T.: Nature's wind turbines: the measured aerodynamic efficiency of spinning seeds approaches theoretical limits (2022)

9. Lee, S.J., Lee, E.J., Sohn, M.H.: Mechanism of autorotation flight of maple samaras (Acer palmatum). Exp. Fluids. **55**, 1–9 (2014)
10. Krogstad, P., Karlsen, J., Adaramola, M.: Performance of a model wind turbine. In: 17th Australasian Fluid Mechanics Conference (2010)
11. Bartl, J., et al.: Performance of the NREL S826 airfoil at low to moderate Reynolds numbers— a reference experiment for CFD models. Eur. J. Mech. B. Fluids. **75**, 180–192 (2019)
12. Eltayesh, A., et al.: Experimental and numerical investigation of the effect of blade number on the aerodynamic performance of a small-scale horizontal axis wind turbine. Alex. Eng. J. **60**(4), 3931–3944 (2021)

Wind Climate Analysis at the Future Wind Farm Positions in the Mediterranean Sea

Ana-Maria Chirosca and Liliana Rusu

1   Introduction

In Europe, the exploitation of energy potential through renewable energy sources (wind energy, solar energy, hydropower, ocean energy, geothermal energy, and others) has increased considerably in recent years due to their many advantages. Given the general situation existing in Europe, which has had a strong impact on the energy market, European countries have accelerated the transition to renewable energy in response to the effects of war and increasing fossil fuel prices.

Wind energy is one of the least expensive renewable energy sources in terms of construction and is the most sustainable. Unfortunately, this type of energy is sensitive to climate change. However, climate studies carried out so far show that the variability of wind parameters is unlikely to be more than 15% in Europe [1].

In recent years, the leader in offshore wind energy has remained Northern Europe [2], and although there are currently no wind farms in production in the Mediterranean, the energy potential of this sea has been investigated in several studies [3–5]. Based on information provided by The European Marine Observation and Data Network (EMODnet) [6] regarding the future wind farms expected to be developed in the Mediterranean Sea, an analysis was carried out in terms of their position, their status (approved, planned, or under construction), and the estimated power they would develop. Having wind farm positions, mean wind speed values were evaluated at their positions using ERA5 datasets [7] for the 2001–2020 period and projections of the wind fields simulated under the RCP4.5 scenario [8] for the 2071–2100 period.

A.-M. Chirosca (✉) · L. Rusu
Dunărea de Jos" University of Galati, Galati, Romania
e-mail: ana.chirosca@ugal.ro

2   Wind Farms in the Mediterranean Sea

Offshore wind farms are more complex than onshore wind farms, and although the Mediterranean Sea has good energy potential, due to the depths of the water more complicated technologies and more expensive installations are needed to be anchored to the seabed, unlike in the North Sea. In addition to sea depth, several other important parameters that have delayed the implementation of wind farms are environmental and marine life issues and the impact they may have on tourism or other activities such as fishing.

In the Mediterranean Sea, currently, according to [6], we are talking about a total of 36 wind farms (as we can see in Fig. 1) of which one is under construction, 4 are approved, and 31 are planned. The estimated power of these wind farms is about 8000 MW, and the distance from the coast is from 1 to 53 km, depending on the region in the Mediterranean Sea.

Out of the wind farm positions identified, the majority are in Greece, with 53%, followed by Italy with 25%, France, and Spain, with only 2 wind farms being planned. Although the number of wind farms in Italy is about half the number to be installed in Greece, the turbine's estimated power is 4.5 times higher.

However, there is still a need to implement more wind farms in Italy, as it is one of the largest consumers of gas in Europe, and the conflict situation between Russia and Ukraine has accelerated the implementation of renewable energy technologies, as 40% of the natural gas [9] consumed by Italy came from Russia.

According to the position of the identified wind farms, 12 main working zones were chosen and the area where they are located is specified in Table 1.

Fig. 1 Wind farms positions in the Mediterranean Sea [6]

Table 1 Position of wind farms

P1	Spain	P7	Mathraki, Greece
P2	France	P8	Gulf of Manfredonia, Italy
P3	South Sardinia, Italy	P9	Taranto, Italy
P4	Sicily, Italy	P10	Methoni, Greece
P5	Rimini, Italy	P11	The Sea of Thrace, Greece
P6	Venice, Italy	P12	North Aegean Islands, Greece

3   Analysis of Wind Climate

The Mediterranean Sea has a weather climate characterized by hot, dry summers and mild, wet winters [10]. Given the characteristic regional wave and wind circulation in this area, a study is needed to see if similar wind characteristics to those of the currently prevailing will also be maintained in the near future so that the investment can be recovered as soon as possible, and the wind farms will be as efficient or perhaps even more efficient in the future.

For this study, wind data from the ERA5 database [7] and those simulated under the RCP4.5 (Representative Concentration Pathways) scenario [8] were considered for the wind climate analysis. ERA5 is a reanalysis dataset produced by the European Centre for Medium-Range Weather Forecasts for global climate and weather over the last 4–7 decades and provides hourly estimates for a large number of quantities, while the wind data under RCP 4.5 are provided by SMHI (Swedish Meteorological and Hydrologic Institute) in the framework of the EURO-CORDEX experiment.

Considering that the efficiency of wind farms depends on the wind climate and its evolution over time, a comparative study was carried out to analyze the wind climate in the period 2001–2020 using the ERA5 database and for the period 2071–2100 using wind fields simulated under RCP4.5 scenario.

Figure 2 shows the average values according to the season for the period 2001–2020 and the estimated average values for the near future. As expected, the highest average wind values for the Mediterranean Sea area are during the winter season, both for the 2001–2020 period and the 2071–2100 period.

The coastal area of France recorded the highest values, followed by the coastal areas of Italy and Greece. Both the average maximum values for the whole year and the average values for the winter season in the French area have an increase of about 10% in the near future. In contrast, a substantial increase of 25% is estimated for the near future for wind farms in Greece.

For wind farms to start up and produce energy, a wind speed of at least 2.5 m/s is required depending on the specifications of the wind turbines. To this end, for the near future, it has been estimated how much of the time they will operate during the years 2071–2100. The results are presented in Table 2 and it can be seen that except for the Taranto area and the Sea of Thrace area, wind farms will operate at least 75% of the time.

The wind power density (Pw) produced by a turbine installed at 100 m height was calculated based on wind speed, using the relationship [11]:
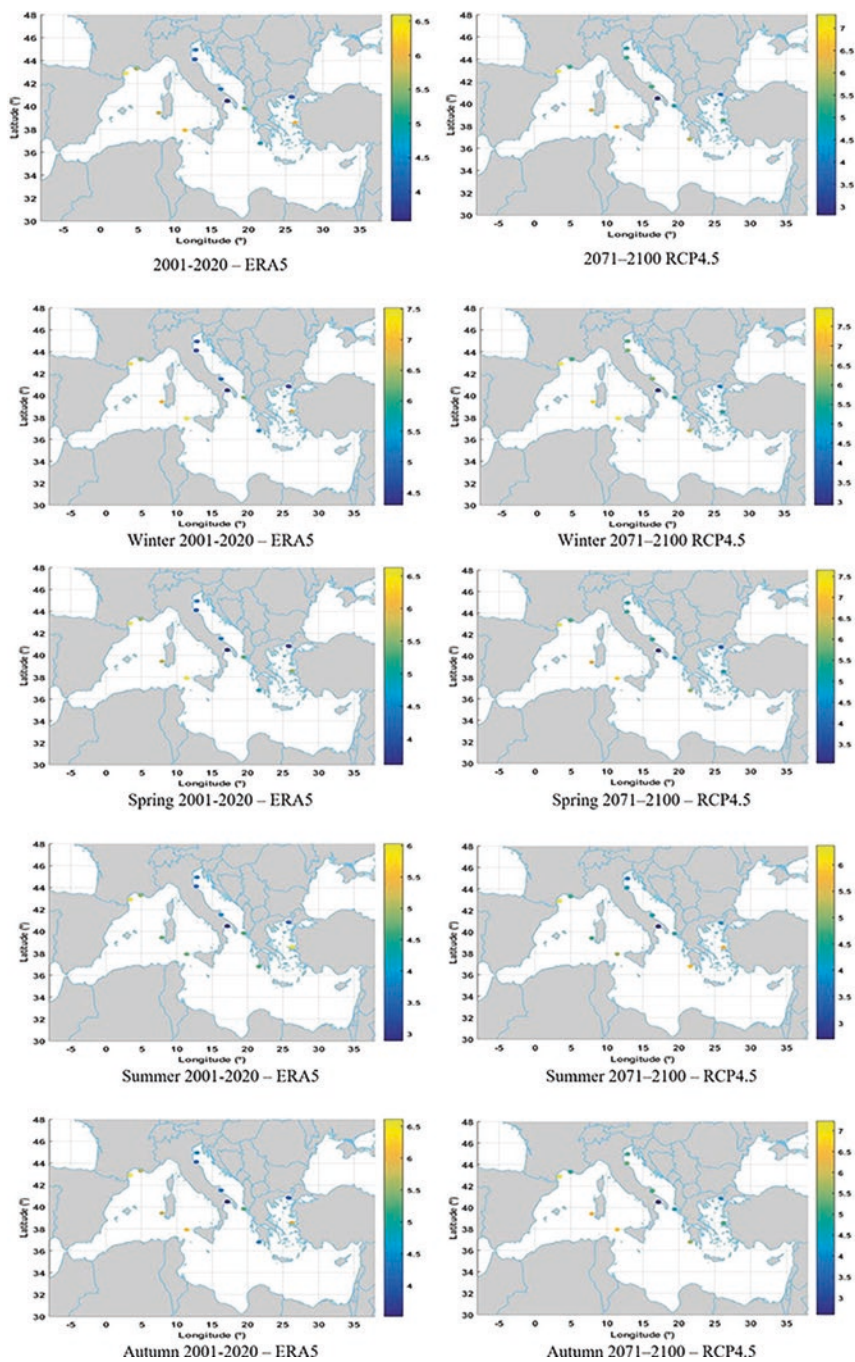
Fig. 2 Seasonal variability of the mean wind speed at the selected locations

Table 2 Wind farms operability

Zone	Percentage	Zone	Percentage	Zone	Percentage
P1	88.40%	P5	81.79%	P9	49.79%
P2	78.16%	P6	76.08%	P10	90.76%
P3	86.25%	P7	75.65%	P11	68.35%
P4	90.97%	P8	83.49%	P12	82.93%
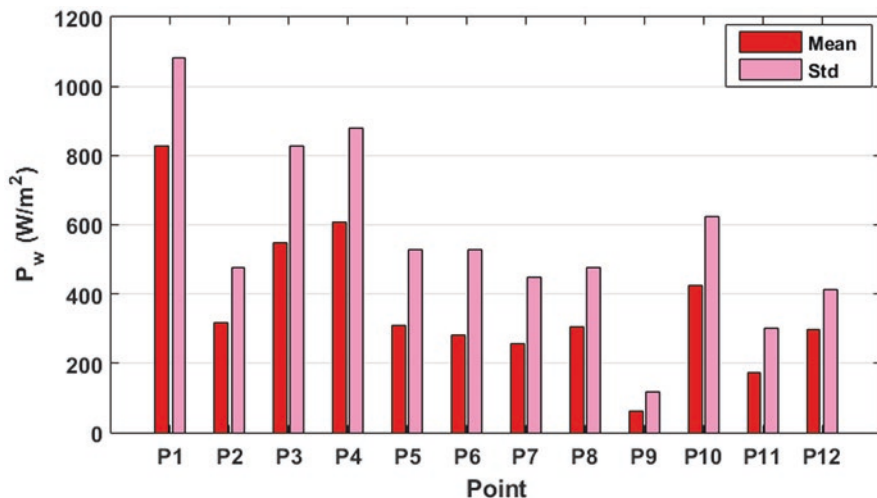
Fig. 3 Wind power at the selected locations

$$P_w = \frac{1}{2} \rho_{air} U_{100}^3$$

(1)

where ρ_{air} is the air density and has a value of 1.225 kg/m³.

In most cases, the wind speed value provided by the database is at a height of 10 m, so the wind speed at 100 m, at which the wind turbines are expected to operate, will have to be extrapolated. The wind speed at 100 m (U_{100}) can be computed using a logarithmic law [12], as follows:

$$U_{100} = U_{10} \frac{\ln\left(100/z_0\right)}{\ln\left(10/z_0\right)}$$

(2)

where U_{10} is the known wind speed at the height of 10 m, while the value of the sea surface roughness length z_0 is taken 0.0002 m over the sea.

From the obtained time series, the mean and standard deviation energy was extracted and presented in Fig. 3. As can be seen, in the Mediterranean Sea, the highest values are found in wind farms near the coast of Spain, followed by wind farms in Sicily and South Sardinia.

4 Conclusions

Offshore wind energy is one of the fastest-growing renewable energy sectors. Rising fossil fuel prices and the need to reduce greenhouse gas emissions contribute to the accelerated development and deployment of technologies for wind power generation.

According to Wind Europe [13], Europe has 236 GW of wind power capacity, and about 12% of new wind installations from 2012 to 2021 will come from offshore wind. There has been a gradual increase in this type of energy, year after year, but Germany remains the leader in terms of installed capacity, followed by Spain, the UK, France, and Sweden.

In the Mediterranean Sea, these factors have had a positive influence on the implementation of wind farms, although there are currently no wind farms in operation, in the future years at least 36 wind farms are expected to operate in the area. Assuming that wind turbines start at a speed of at least 2.5 m/s, depending on the specifications of each turbine, in the near future they will be operating an estimated 79% of the time, considering the wind climate for the 2071–2100 period.

Considering that climate changes can affect the functionality and efficiency of wind farms, the wind climate study for the future demonstrates that wind farms are feasible in the coming years, supporting Europe's trend to move toward green energy as soon as possible.

References

1. Pryor, S.C., Barthelmie, R.J.: Climate change impacts on wind energy: a review. Renew. Sust. Energ. Rev. **14**(1), 430–437 (2010). https://doi.org/10.1016/j.rser.2009.07.028
2. Chirosca, A.-M., Rusu, L., Bleoju, A.: Study on wind farms in the North Sea area. Energy Rep. **8**(16), 162–168 (2022). https://doi.org/10.1016/j.egyr.2022.10.244
3. Cottura, L., Caradonna, R., Ghigo, A., Novo, R., Bracco, G., Mattiazzo, G.: Dynamic modeling of an offshore floating wind turbine for application in the Mediterranean Sea. Energies. **14**(1), 248 (2021). https://doi.org/10.3390/en14010248
4. Onea, F., Rusu, E.: A spatial analysis of the offshore wind energy potential related to the Mediterranean islands. Energy Rep. **8**(16), 99–105 (2022). https://doi.org/10.1016/j.egyr.2022.10.249
5. Lira-Loarca, A., Ferrari, F., Mazzino, A., Besio, G.: Future wind and wave energy resources and exploitability in the Mediterranean Sea by 2100. Appl. Energy. **302**, 117492 (2021). https://doi.org/10.1016/j.apenergy.2021.117492
6. European Marine Observation and Data Network (EMODnet). Available online: https://www.emodnet-humanactivities.eu/. Accessed on 10 Nov 2022
7. ECMWF Reanalysis v5 (ERA5). Available online: www.ecmwf.int/en/forecasts/dataset/ecmwf-reanalysis-v5. Accessed on 15 Nov 2022

8. Thomson, A.M., Calvin, K.V., Smith, S.J., et al.: RCP4.5: a pathway for stabilization of radiative forcing by 2100. Clim. Chang. **109**, 77 (2011). https://doi.org/10.1007/s10584-011-0151-4

9. Gross imports of natural gas in Italy in 2021. Available online: https://www.statista.com/statistics/787720/natural-gas-imports-by-country-of-origin-in-italy/. Accessed on 7 Dec 2022

10. Lionello, P., Malanotte-Rizzoli, P., et al.: The Mediterranean climate: An overview of the main characteristics and issues. Develop. Earth Environ. Sci., vier. **4**, 1–26 (2006). https://doi.org/10.1016/S1571-9197(06)80003-0

11. Boyle, Godfrey ed. (2012). Renewable Energy: Power for a Sustainable Future (3rd ed.). Oxford: Oxford University Press and Open University, ISBN0-19-954533-2, 978-0-19-954533-9

12. Stull, R.: Practical Meteorology: an Algebra Based Survey of Atmospheric Science. The University of British Columbia, Canada (2016)

13. Wind energy in Europe, 2021 Statistics and outlook for 2022-2026, February 2022. Available online: https://windeurope.org/intelligence-platform/product/wind-energy-in-europe-2021-statistics-and-the-outlook-for-2022-2026/. Accessed on 7 Dec 2022

A Computational Platform to Assess the Coastal Impact of the Marine Energy Farms

Eugen Rusu and Florin Onea

1 Introduction

The human evolution is driven by the accessibility to a water source, starting from basic needs (e.g., domestic use) to more advanced levels involving transportation or energy production, respectively. Almost 71% of the earth surface is covered by water, from which a significant part is found in the oceans, which represent in fact the biggest ecosystem of the planet [1]. The coastal areas are considered to be very dynamic environments, being shaped by the natural forces and by anthropogenic activities, being estimated that almost 40% of the global population lives in these areas [2].

In terms of renewable energy, the marine areas seem to present some advantages compared to the onshore ones, the European offshore wind market being considered a successful one with an installed capacity of 28.4 GW. Nevertheless, in the European Union (EU) there are plans to increase this capacity up to 160 GW (by 2030), which will involve the use of floating platforms, as in the case of Hywind Tampen from Norway. Also the inclusion of new areas will make a difference, starting with the ones from France (e.g., project Saint-Nazaire, 480 MW) and gradually extending to coastal areas from the Mediterranean or the Black seas [3, 4]. Among the marine resources, the tidal and wave energy is expected to make a significant contribution to the EU's future, although at this moment there are 13 MW of devices tested on various levels. On a European level, during 2007 and 2019 a total of €3.84 billion was allocated to this sector, with an expected capacity production of 3 GW by the end of 2030 and 60 GW in 2050 [5].

E. Rusu (✉) · F. Onea
Department of Mechanical Engineering, Faculty of Engineering, "Dunarea de Jos" University of Galati, Galati, Romania
e-mail: eugen.rusu@ugal.ro

The recent progress related to the evolution of the marine renewable sector brings new possibilities, such as the development of combined wind-wave projects [6, 7], or the use of an array of energy convertors to provide a suitable coastal protection [8–10]. As a consequence, besides the analysis of the natural resources or the performances of a particular energy convertor, another important aspect is related to the expected impact of a particular farm layout onto the surf area of a particular coastal sector. These are very sensitive areas, the balance between accretion and erosion being influenced by multiple factors, such as the attenuation of the wave height, sediment transport rate, or even the type of breaking waves.

2 Materials and Methods

The proposed computational model involves the CSIAM and ISSM interface (Interface for SWAN and Surf Models), which was extensively used by the authors for various case studies [11, 12]. The ISSM system combines the SWAN (Simulating Waves Nearshore) wave model with the NSSM (Navy Standard Surf Model) model [13, 14]. In this way, it is possible to provide a more complete picture of the wave transformation in the coastal areas, including the transformations associated to the surf area and the evolution of the longshore currents. In Fig. 1 the workflow associated to this computational platform is illustrated, from which we can notice that the CSIAM section is used in the early stages of analysis.

Based on the configuration of the target area, a preliminary marine farm is proposed for evaluation and based on the preliminary results obtained throughout the ISSM interface; the scenarios can be refined or completely redesigned. A library of
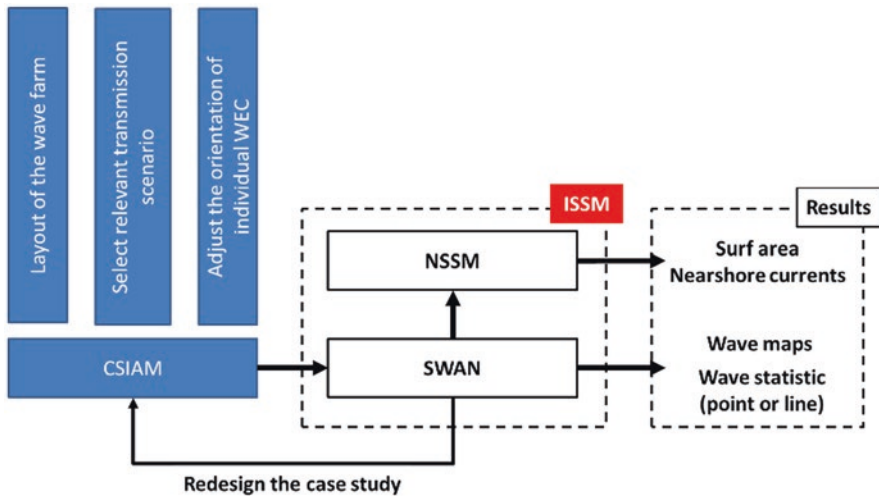
Fig. 1 Workflow presenting the CSIAM computational platforms

Fig. 2 Coastal environments considered for evaluation
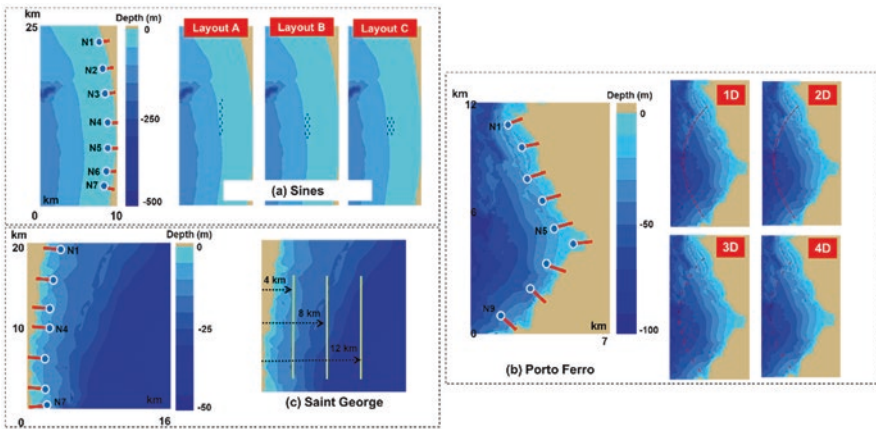
Fig. 3 Set-up of the SWAN computational domains, where: (**a**) Sines, Portugal; (**b**) Porto Ferro, Sardinia; (**c**) Saint George, Romania

scenarios is available, ranging from the transmission indexes available on the market, throughout the general orientation of the farms according to the shoreline, or eventually the layout (and orientation) of individual systems.

Several geographical areas were considered for assessment, as it can be noticed from Fig. 2. This includes a coastal area facing the ocean environment (Sines, Portugal), and island sector (Porto Ferro, Sardinia) and an enclosed sea region associated to the Saint George coastal sector, Romania.

Furthermore, in order to highlight the versatility of this system, several scenarios were developed as presented in Fig. 3. These involve different spatial layouts (CS1) based on the characteristics of the Wave Dragon system [15, 16], or the absorption properties of the Wave Cat system (CS2) [17] grouped in different wave farm configurations. Finally, a generic wave farm defined by either moderate (20%) or high absorption (40%) properties was proposed for the Saint George area (CS3). The N-points will be used to process the wave parameters, while the associated lines will be considered for the evaluation of the nearshore currents.

Table 1 Identification of the extreme sea states for each target area, based on the 10-year time interval of ERA5 data (from 2012 to 2021)

Reference area	Time frame	Hs (m)	Tm (s)	Dir (°)
Pinheiro da Cruz (PT)	2014.02.10-h00	8.02	11.56	300
Saint George (RO)	2012.02.07-h18	5.83	8.75	60
Porto Ferro (IT)	2017.12.28-h06	6.84	9.93	300
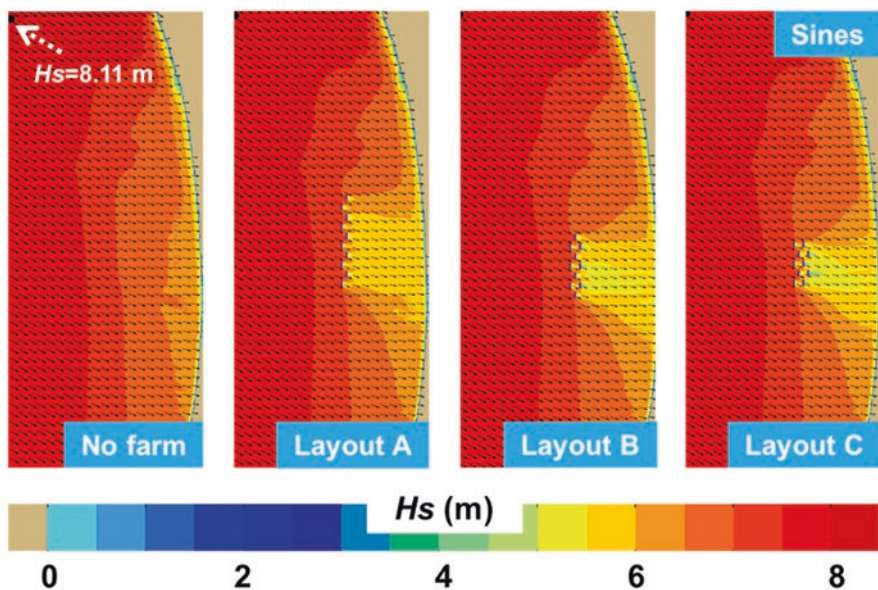
Fig. 4 Spatial distribution of the wave conditions (*Hs* scalar fields and wave vectors) related to the Sines area

The wave conditions in the vicinity of these coastal areas were identified by using the ERA5 data [18] that were processed for the 10-year time interval from January 2012 to December 2021. Table 1 presents the relevant statistics for the main wave parameters, namely: significant wave height (*Hs*), wave energy period (*Te*), and mean wave direction (*Dir*). Only the extreme values were considered for evaluation, since this will better reflect the expected impact of a particular case study.

3 Results

Figure 4 illustrates the wave distribution from the Sines target area. Although the proposed layouts cover a small percentage from this target area, the shielding effect is visible, being directly related to the direction of the waves heights that are occurring usually from the north-west sector. The expected changes near the shoreline are
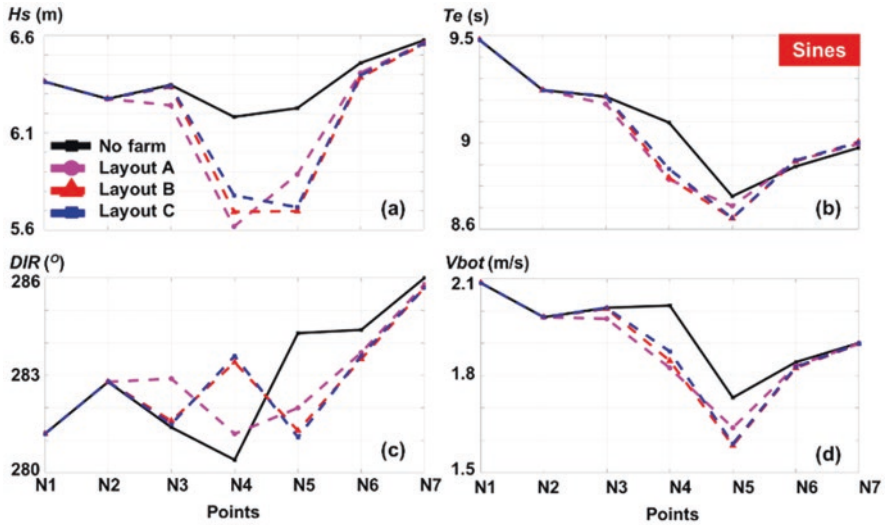
Fig. 5 Sines area – evolution of the main wave parameters associated to the N-points, where: (**a**) *Hs*; (**b**) *Te*; (**c**) *Dir*; (**d**) *Vbot*

better reflected by the N-points (see Fig. 5), where besides the well-known wave parameters, the orbital velocity at the bottom (*Vbot*) that is directly related to the sediment transport was included. The presence of the farms starts to become visible near the point N3, which is located above the Wave Dragon systems, presenting maximum values near the site N4. In this case, the waves are decreasing from 6.18 m (no farm) to a minimum of 5.62 m (layout A).

A similar analysis is performed in Fig. 6 for the Porto Ferro coastal sector, from which it can be noticed that a 1D layout can provide a better coastal protection compared to a 4D scenario that indicates values close to a no farm situation. Finally, related to the Saint George coastal area, Fig. 7 presents the evolution of the wave fields in the presence of the generic wave farm, and as expected a high absorption wave farm (40%) will provide a significant impact. The sheltering effect is visible regardless of the distance from the coast taken into account (4, 8, or 12 km), the wave heights decreasing near the shoreline from 3 m (no farm) to minimum 2.4 m (L4–40%), depending on the location.

The nearshore currents (maximum velocities) in the three target areas are provided in Fig. 8, for some of the case studies considered.

For example, in the case of the Sines region the velocity can increase in the presence of the wave farm near the points N3 and N4, while a decrease is expected for the sites N5 and N6 (e.g., 1.56 m/s). For the Porto Ferro, the wave farm will decrease the velocity in most of the cases, while for the Saint George an increase is expected.
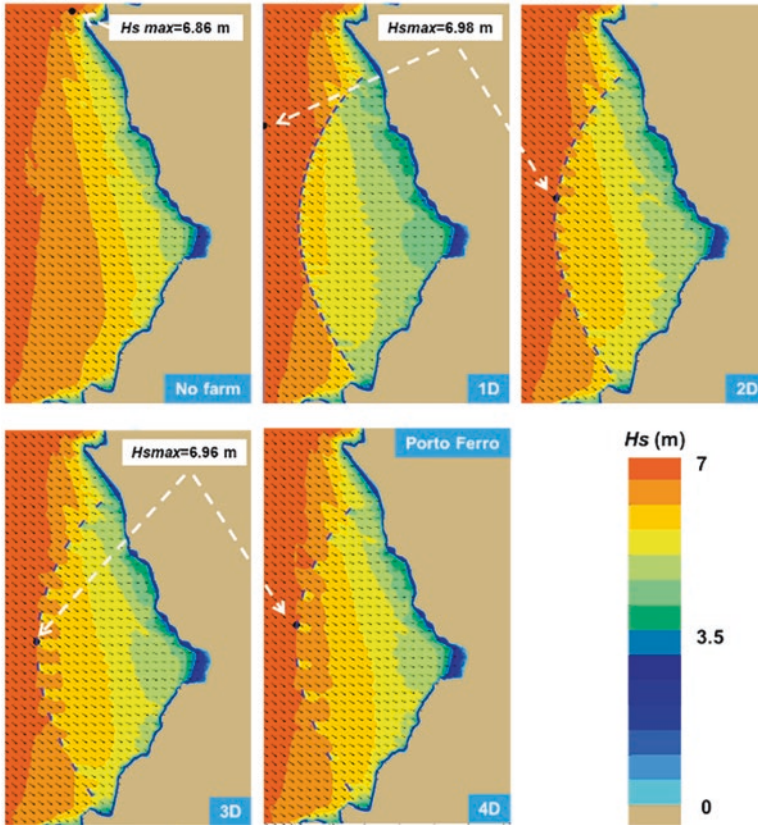
Fig. 6 Spatial distribution of the wave conditions (*Hs* scalar fields and wave vectors) related to the Porto Ferro coastal area

4 Conclusions

The nearshore areas are very sensitive environments and any intervention can trigger domino effects that may significantly influence the coastal stability. A sustainable energy future is possible to be obtained through the use of the renewable sources, in particular those from the marine areas. The chapter presents an interactive computational platform denoted as CSIAM, which is associated with the assessment of the down wave effects of the marine energy farms. This includes SWAN model for the waves and Surf model for the nearshore currents. By using this computational platform a more complete picture of the expected transformation induced by a marine energy farm can be obtained, making it possible to analyze in a short period of time various configurations that can be tailored to particular shoreline environments. As an example, three case studies have been considered. The first is Sines area in the Atlantic Ocean on the continental Portuguese nearshore, south of
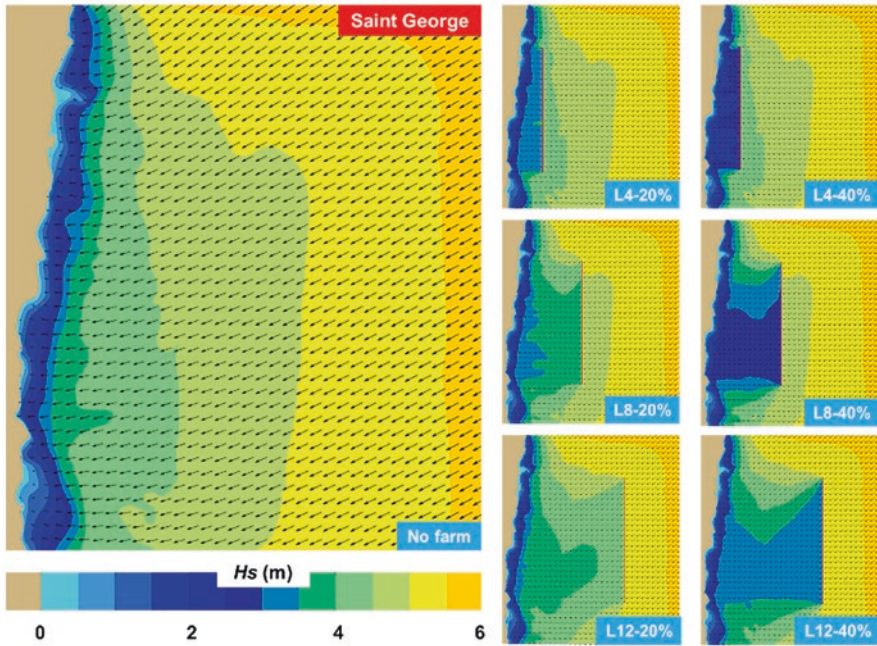
Fig. 7 Spatial distribution of the wave conditions (*Hs* scalar fields and wave vectors) related to the Saint George area
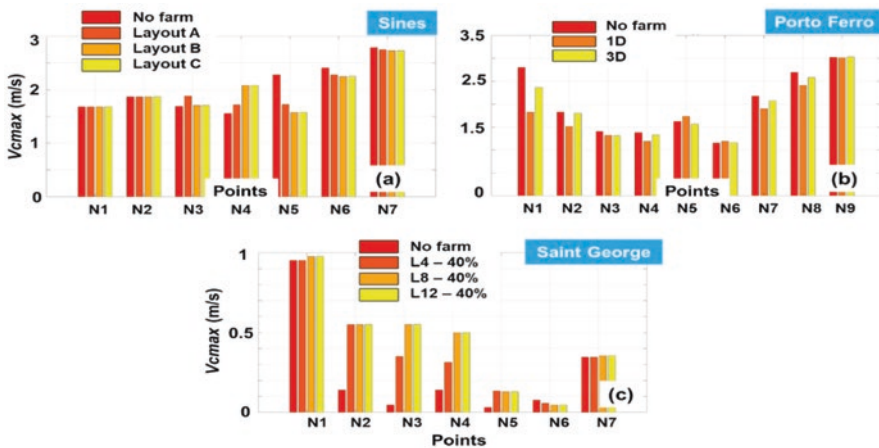
Fig. 8 Maximum velocity of the nearshore currents in the presence of the wave farms, where: (**a**) Sines; (**b**) Porto Ferro; (**c**) Saint George

Lisbon, the second is Porto Ferro in Sardinia the Mediterranean Island, and the third close to the Saint George arm at the Danube River outflow in the Black Sea. Taking into account that at this moment there is interest to accelerate the development of

marine energy sector, the proposed system can be considered to be opportune. Further development of this computational platform should include the design of a graphical user interface and also a post-processing routine that could simplify the processing of results.

References

1. Fava, M.F.: How much of the Ocean have we explored to date. https://oceanliteracy.unesco.org/ocean-exploration/ (2022). Last accessed 4 Jan 2023
2. Baztan, J., Chouinard, O., Jorgensen, B., Tett, P., Vanderlinden, J.-P., Vasseur, L.: Introduction. In: Baztan, J., Chouinard, O., Jorgensen, B., Tett, P., Vanderlinden, J.-P., Vasseur, L. (eds.) Coastal Zones, pp. xxi–xxiii. Elsevier (2015). https://doi.org/10.1016/B978-0-12-802748-6.02001-5
3. Offshore wind energy 2022 mid-year statistics.: https://windeurope.org/data-and-analysis/product/offshore-wind-energy-2022-mid-year-statistics. Last accessed 4 Jan 2023
4. Onea, F., Rusu, L.: A study on the wind energy potential in the Romanian coastal environment. J. Mar. Sci. Eng. **7**, 142 (2019). https://doi.org/10.3390/jmse7050142
5. Simon, F.: EU aims for "massive change of scale" on tidal, wave energy. https://www.euractiv.com/section/energy/news/eu-aims-for-massive-change-of-scale-on-tidal-wave-energy/. Last accessed 4 Jan 2023
6. Saenz-Aguirre, A., Saenz, J., Ulazia, A., Ibarra-Berastegui, G.: Optimal strategies of deployment of far offshore co-located wind-wave energy farms. Energy Convers. Manag. **251**, 114914 (2022). https://doi.org/10.1016/j.enconman.2021.114914
7. Rusu, E., Onea, F.: Joint evaluation of the wave and offshore wind energy resources in the developing countries. Energies. **10**, 1866 (2017). https://doi.org/10.3390/en10111866
8. Onea, F., Rusu, L.: Coastal Impact of a Hybrid Marine Farm Operating Close to the Sardinia Island. IEEE, New York (2015)
9. Abanades, J., Greaves, D., Iglesias, G.: Coastal defence through wave farms. Coast. Eng. **91**, 299–307 (2014). https://doi.org/10.1016/j.coastaleng.2014.06.009
10. Bento, A.R., Rusu, E., Martinho, P., Guedes Soares, C.: Assessment of the changes induced by a wave energy farm in the nearshore wave conditions. Comput. Geosci. **71**, 50–61 (2014). https://doi.org/10.1016/j.cageo.2014.03.006
11. Conley, D.C., Rusu, E.: The middle way of surf modeling. Presented at the Proceedings of the Coastal Engineering Conference (2007)
12. Raileanu, A., Onea, F., Rusu, E.: An overview of the expected shoreline impact of the marine energy farms operating in different coastal environments. JMSE. **8**, 228 (2020). https://doi.org/10.3390/jmse8030228
13. Booij, N., Ris, R.C., Holthuijsen, L.H.: A third-generation wave model for coastal regions: 1. Model description and validation. J. Geophys. Res. **104**, 7649–7666 (1999). https://doi.org/10.1029/98JC02622
14. Mettlach, T.R., Earle, M.D., Hsu, Y.L.: Software Design Document for the Navy Standard Surf Model Version 3.2. Defense Technical Information Center, Fort Belvoir (2002). https://doi.org/10.21236/ADA411576

15. David, D.R., Rijnsdorp, D.P., Hansen, J.E., Lowe, R.J., Buckley, M.L.: Predicting coastal impacts by wave farms: a comparison of wave-averaged and wave-resolving models. Renew. Energy. **183**, 764–780 (2022). https://doi.org/10.1016/j.renene.2021.11.048
16. Onea, F., Rusu, L., Carp, G.B., Rusu, E.: Wave farms impact on the coastal processes—a case study area in the Portuguese nearshore. JMSE. **9**, 262 (2021). https://doi.org/10.3390/jmse9030262
17. Rusu, L., Onea, F., Rusu, E.: The expected impact of marine energy farms operating in Island environments with mild wave energy resources—a case study in the Mediterranean Sea. Inventions. **6**, 33 (2021). https://doi.org/10.3390/inventions6020033
18. Guillory, A.: ERA5, https://www.ecmwf.int/en/forecasts/datasets/reanalysis-datasets/era5. Last accessed 31 May 2019

Part III
New Power System Analysis and Power Grid Control Technology

Directional Relay for Outlet Ground Faults Based on Zero Sequence Voltage Comparison

Tao Jiang, Minghao Wen, Kun Qian, and Xiang Zeng

1 Introduction

Due to the high speed development of wind, solar, and other new energy generation access to the power system, the grid fault characteristics are different from the traditional grid dominated by synchronous generators [1, 2]. The new energy sources are mostly connected to the grid via power electronics, and their fault current characteristics are determined by the fault control strategy, which may have an adverse effect on the reliability of the traditional grid relay protection action [3–6].

Distance protection is less affected by the system operation mode and is widely used for line protection [7]. The phase-based distance protection has a series of adaptation problems when applied to new energy access systems [8–12], which may appear to act incorrectly. The R-L model-based time domain differential equation algorithm has the advantages of not needing to filter out the non-periodic components and not being affected by the system frequency [13–16], which has better applicability in the new energy access system. However, when the fault point is near the line outlet, it is difficult to accurately distinguish between forward and reverse faults, which means that there is a "voltage dead zone" problem. For new energy transmission line outlet faults, the traditional fault direction discrimination method is no longer applicable because the new energy power supply cannot be considered as a voltage source model like the traditional synchronous machine power supply.

In view of the above problems, for asymmetric ground faults at the line outlet (single-phase ground faults occur with a much higher probability than other fault types), this chapter proposes a directional relay that is based on zero-sequence voltage comparison. The measured values of the zero sequence voltage are obtained directly from the protection. The calculated values of the zero sequence voltage are

T. Jiang (✉) · M. Wen · K. Qian · X. Zeng
State Key Lab of Advanced Electromagnetic Engineering Technology, Huazhong University of Science and Technology, Wuhan, China

obtained indirectly using the zero sequence current and topological parameters. When an outlet fault occurs on the transmission line, there is a large difference in the characteristics of the fault current provided by the new energy source and the AC system. As a result, the trend of the measured and calculated values of the zero sequence voltage varies for different fault locations. Due to this, it is possible to effectively determine the fault direction of an outlet ground fault.

2 Line Outlet Ground Fault Characteristic Analysis

A typical AC system with a new energy source is shown in Fig. 1, where the new energy source is connected to the AC system via a transformer and a 110 kV transmission line. The neutral point on the high voltage side of the transformer is directly grounded and the power supply of the AC system is mainly synchronous motors. M and N are the busbars on the new energy side and the AC system side of the line, respectively, with protection devices P and Q on each side.

Taking the transmission line as the study object, the AC system containing the new energy source is simplified and metallic ground faults are set at the line outlet, as shown in Fig. 2.
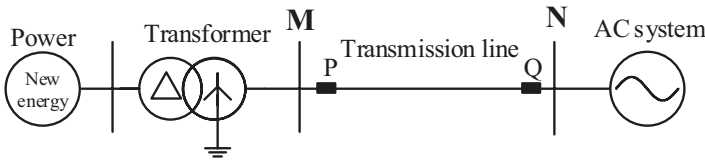
Fig. 1 Schematic diagram of an AC system with a new energy source
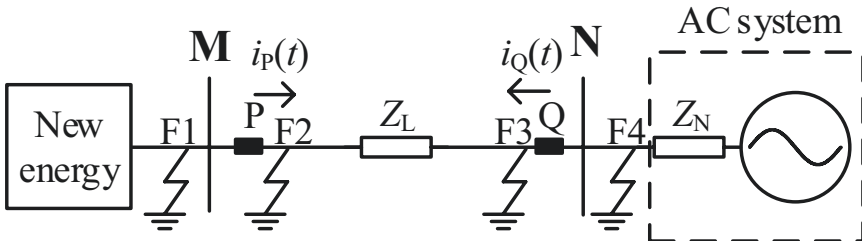
Fig. 2 Diagram of the fault of the new energy delivery line

$i_P(t)$ and $i_Q(t)$ are the currents flowing through the protection device P and Q, respectively, prescribing the positive direction of current flow from the busbar to the line. Z_L is the line impedance and Z_N is the AC system equivalent impedance. F1 and F2 are the reverse outlet fault point and forward outlet fault point of protection device P, respectively. F3 and F4 are the forward outlet fault point and reverse outlet fault point of protection device Q, respectively.

2.1   Fault in the New Energy Side of the Line Outlet

The situation when an asymmetrical ground fault occurs near the protection device P is shown in Fig. 2. Define the calculated value of the zero sequence voltage $u^0_{P-cal}(t)$ at the protection device P as:

$$u^0_{P\ cal}(t) = \left(R^0_L + R^0_N\right)i^0_P(t) + \left(L^0_L + L^0_N\right)\frac{di^0_P(t)}{dt}$$

(1)

where $i^0_P(t)$ is the zero sequence component of the current measured by the protection device P. R^0_L and L^0_L are the zero sequence resistance and inductance of the line, respectively. R^0_N and L^0_N are the equivalent zero sequence resistance and inductance of the system behind the busbar N, respectively.

Reverse faults: The fault point F1 is shown in Fig. 2. At this time, the fault current $i_P(t)$ at protection device P is supplied by the AC system. The measured value $u^0_P(t)$ and the calculated value $u^0_{P-cal}(t)$ of the zero sequence voltage satisfy the following relationship:

$$u^0_P(t) = u^0_{P-cal}(t)$$

(2)

Equation (2) shows the consistency of the measured and calculated zero sequence voltage trends after a reverse outlet fault on the new energy side of the transmission line.

Forward faults: The fault point F2 is shown in Fig. 2. At this time, the fault current $i_P(t)$ at protection device P is supplied by the new energy source, not the actual current flowing through the line impedance Z_L and the equivalent impedance Z_N of the AC system. Therefore, the measured value $u^0_P(t)$ and the calculated value u^0_{P-cal} (t) of the zero sequence voltage are not consistent with the change trend.

2.2 Fault in the System Side of the Line Outlet

When an asymmetrical ground fault occurs near the protection device P, the situation is shown in Fig. 2. Define the calculated value of the zero sequence voltage $u_{Q-cal}^0(t)$ at the protection device as:

$$u_{Q\ cal}^0(t) = -\left[R_N^0 i_Q^0(t) + L_N^0 \frac{di_Q^0(t)}{dt} \right] \tag{3}$$

where $i_Q^0(t)$ is the zero sequence component of the current measured by the protection device Q.

Forward faults: The fault point F3 is shown in Fig. 2. At this time, the fault current $i_Q(t)$ at protection device Q is supplied by the AC system. The measured value $i_Q^0(t)$ and the calculated value $i_{Q-cal}^0(t)$ of the zero sequence voltage satisfy the following relationship:

$$u_Q^0(t) = u_{Q-cal}^0(t) \tag{4}$$

Equation (4) shows the consistency of the measured and calculated zero sequence voltage trends after a forward outlet fault on the AC system side of the transmission line.

Reverse faults: The fault point F4 is shown in Fig. 2. At this time, the fault current $i_Q(t)$ at protection device Q is supplied by the new energy source, not the actual current flowing through the AC system equivalent impedance Z_N. Therefore, the measured value $u_Q^0(t)$ and the calculated value $u_{Q-cal}^0(t)$ of the zero sequence voltage are not consistent with the change trend.

3 Principle of Relay Protection

3.1 Outlet Ground Fault Direction Discrimination

When a metallic ground fault occurs near the protection installation, the direction of the outlet fault can be distinguished based on the consistency of the change trend between the measured and calculated zero-sequence voltage values. Taking the protection installation P as an example, based on the analysis in [17], the zero sequence voltage correlation coefficient r_P is defined as shown in Eq. (5), which is intended as a quantitative measure of the consistency of the measured and calculated zero sequence voltage values:

$$r_{\mathrm{P}} = \frac{\sum\limits_{i=1}^{W} f\left[u_{\mathrm{P}}^0(i), u_{\mathrm{P\ cal}}^0(i)\right]}{\sqrt{\sum\limits_{i=1}^{W}\left[u_{\mathrm{P}}^0(i) - \overline{u_{\mathrm{P}}^0}\right]^2} \sqrt{\sum\limits_{i=1}^{W}\left[u_{\mathrm{P\ cal}}^0(i) - \overline{u_{\mathrm{P\ cal}}^0}\right]^2}} \tag{5}$$

where W is the length of a data window. $u_{\mathrm{P}}^0(i)$ and $u_{\mathrm{P-cal}}^0(i)$ are the sampled values of the measured and calculated zero sequence voltage at moment i, respectively. $\overline{u_{\mathrm{P}}^0}$ and $\overline{u_{\mathrm{P-cal}}^0}$ are the average values of $u_{\mathrm{P}}^0(i)$ and $u_{\mathrm{P-cal}}^0(i)$ within a data window, respectively. The expression of $f\left[u_{\mathrm{P}}^0, u_{\mathrm{P-cal}}^0\right]$ is given by:

$$f\left[u_{\mathrm{P}}^0(i), u_{\mathrm{P\ cal}}^0(i)\right] = \begin{cases} \left[u_{\mathrm{P}}^0(i) - \overline{u_{\mathrm{P}}^0}\right]\left[u_{\mathrm{P\ cal}}^0(i) - \overline{u_{\mathrm{P\ cal}}^0}\right] & \text{if } u_{\mathrm{P}}^0(i) * u_{\mathrm{P\ cal}}^0(i) > 0; \\ -\left|\left[u_{\mathrm{P}}^0(i) - \overline{u_{\mathrm{P}}^0}\right]\left[u_{\mathrm{P\ cal}}^0(i) - \overline{u_{\mathrm{P\ cal}}^0}\right]\right| & \text{if } u_{\mathrm{P}}^0(i) * u_{\mathrm{P\ cal}}^0(i) \le 0; \end{cases} \tag{6}$$

r_{P} is within values of $[-1,1]$. When $r_{\mathrm{P}} = 1$, it implies that $u_{\mathrm{P}}^0(t)$ and $u_{\mathrm{P-cal}}^0(t)$ are fully positively correlated. When $r_{\mathrm{P}} = -1$, it implies that $u_{\mathrm{P}}^0(t)$ and $u_{\mathrm{P-cal}}^0(t)$ are fully negatively correlated. The directional criterion for grounding faults on the new energy side of the transmission line is shown in Eq. (7), which determines the direction of the fault by comparing the zero sequence voltage correlation coefficient r_{P} with the rectified value r_{setP}. When the criterion is satisfied, it is considered that a forward fault occurs on the new energy side of the line, and vice versa for a reverse fault:

$$r_{\mathrm{P}} \le r_{\mathrm{setP}} \tag{7}$$

Similarly, the directional criterion for grounding faults on the system side of the transmission line is shown in Eq. (8), and the direction of the fault is determined by comparing the zero sequence voltage correlation coefficient r_{Q} with the rectified value r_{setQ}. When the criterion is satisfied, it is considered that a forward fault occurs on the system side of the line, and vice versa for a reverse fault.

$$r_{\mathrm{Q}} \ge r_{\mathrm{setQ}} \tag{8}$$

3.2   Flow of Protection

After the initiating element of the protection has operated, the zero sequence current and three phase voltage at the protection installation are detected. Determine whether it is an outlet ground fault according to Eq. (9):

$$\begin{cases} I_0 > I_{set0} \\ U_\& < U_{low} \end{cases} \tag{9}$$

where I_0 is the zero sequence current amplitude at the protection installation. $U_\&$ is the fault phase voltage. I_{set0} is the zero sequence current threshold for ground fault and U_{low} is the low voltage threshold.

When Eq. (9) is satisfied, it is judged that an outlet ground fault has occurred and the subsequent steps are performed. The correlation coefficient between the measured and calculated value of the zero sequence voltage is calculated and then compared with the rectified value. If the criterion is satisfied, it is a forward fault, and vice versa for a reverse fault. The flow of protection is shown in Fig. 3.
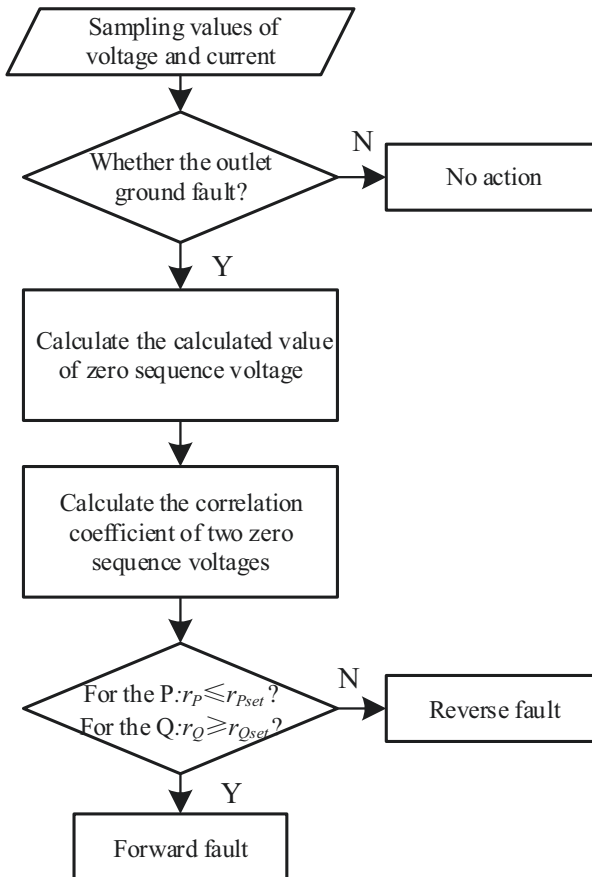
Fig. 3 Flow chart of directional relay

4   Simulation Validation

4.1   Build Simulation Models

For validation of the directional relays proposed in this chapter, a typical AC system model containing a new energy source is established in PSCAD/EMTDC as shown in Fig. 1. Main parameters of the model: AC bus rated at 110 kV; AC system positive sequence equivalent impedance $Z_N = (0.520 + 3.171)\,\Omega$, zero sequence equivalent impedance $Z_N^0 = (1.103 + 4.942)\,\Omega$; transmission line length of 15 km, using the Bergeron model, the detailed parameters are shown in Table 1.

4.2   Directional Relay Performance Test

In this simulation experiment, the system frequency $f = 50$ Hz, the sampling rate is 4 kHz, the second order Butterworth low-pass filter is used, and the cut-off frequency is 200 Hz. Set the fault conditions: the fault type is metallic single-phase ground fault, the initial time of the fault is 0.6 s, and the duration of the fault is 0.4 s. The data window length $W = 2$ ms, starting from 2 ms after the fault. A forward fault is considered to have occurred if the fault criterion is met at 8 consecutive points during the 8 ms calculation.

Considering the parameter errors of the line impedance and the AC system equivalent impedance, the rectified value of zero sequence voltage correlation coefficient is chosen as $r_{setP} = r_{setQ} = 0.5$.

Fault in the new energy side of the line outlet   When an outlet fault occurs on the new energy side of the transmission line, as shown in Fig. 2, the forward fault corresponds to fault point F2 and the reverse fault corresponds to fault point F1. Taking the new energy power capacity of 20 MW as an example, the simulation results are shown in Figs. 4 and 5.

The trend of the measured and calculated zero sequence voltage after the fault are obtained and the correlation coefficient r_P between them is calculated. It shows that if there is a forward outlet fault, the trend is obviously different and the correlation coefficient r_P is much smaller than the rectification value r_{setP}. If there is a reverse outlet fault, the trend is basically the same and the correlation coefficient r_P is much larger than the rectification value r_{setP}.

Table 1 Detailed parameters of AC line

	R [Ω/km]	X_L [Ω/km]	X_C [MΩ*m]
+ve sequence	0.085775076	0.295447415	215.1543
0 sequence	0.257325169	0.886342040	365.9286

(a)   (b)
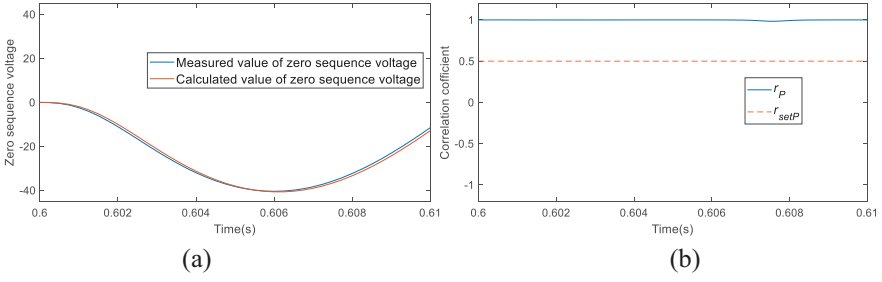
Fig. 4 Simulation results for fault point F1. (**a**) Measured and calculated zero sequence voltage values. (**b**) Zero sequence voltage correlation coefficient

(a)   (b)
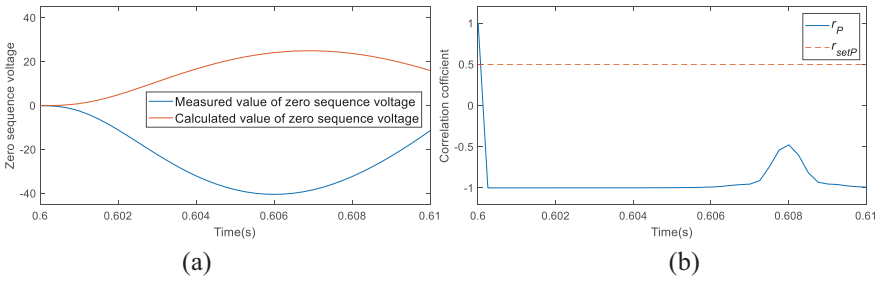
Fig. 5 Simulation results for fault point F2. (**a**) Measured and calculated zero sequence voltage values. (**b**) Zero sequence voltage correlation coefficient

(a)   (b)
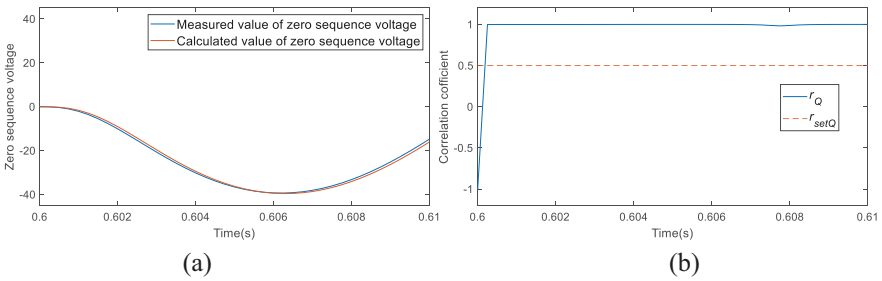
Fig. 6 Simulation results for fault point F3. (**a**) Measured and calculated zero sequence voltage values. (**b**) Zero sequence voltage correlation coefficient

Fault in the system side of the line outlet When an outlet fault occurs on the system side of the transmission line, as shown in Fig. 2, the forward fault corresponds to fault point F3 and the reverse fault corresponds to fault point F4. Taking the new energy power capacity of 20 MW as an example, the simulation results are shown in Figs. 6 and 7.

(a)   (b)
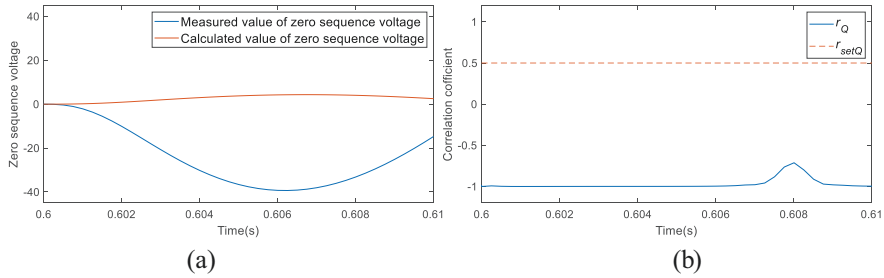
Fig. 7 Simulation results for fault point F4. (**a**) Measured and calculated zero sequence voltage values. (**b**) Zero sequence voltage correlation coefficient

Table 2 Operation characteristics when different new energy power capacity

Directional relay	Fault location	New energy power capacity (MW)	Action time (ms)
P	F1	5	NO
		20	NO
		40	NO
	F2	5	4.0
		20	4.0
		40	4.0
Q	F3	5	4.0
		20	4.0
		40	4.0
	F4	5	NO
		20	NO
		40	NO

The trend of the measured and calculated zero sequence voltage after the fault are obtained and the correlation coefficient r_Q between them is calculated. It shows that if there is a forward outlet fault, the trend is basically the same and the correlation coefficient r_Q is much larger than the rectified value r_{setQ}. If there is a reverse outlet fault, the trend is obviously different and the correlation coefficient r_Q is much smaller than the rectified value r_{setQ}.

Analysis of influential factors To further validate the dependability of the proposed directional relay, two factors that may affect the performance of the directional relay are analyzed below, in terms of the new energy power capacity and system equivalent impedance deviation.

New energy power capacity New energy power supply capacities of 5 MW, 20 MW, and 40 MW have been set up, respectively. The fault type is a metallic single-phase ground fault and the results are shown in Table 2.

Table 3 Operation characteristics at different system equivalent impedances

Directional relay	Fault location	System impedance (* Z_N^0)	Action time (ms)
P	F1	50%	NO
		200%	NO
	F2	50%	4.0
		200%	4.0
Q	F3	50%	4.0
		200%	4.0
	F4	50%	NO
		200%	NO

System equivalent impedance deviation Since the value of the system zero sequence equivalent impedance Z_N^0 is required in the process of obtaining the calculated value u_{P-cal}^0 (i), the effect of the change in system impedance on the directional relays requires analysis. Set the system zero sequence equivalent impedance to 50% and 200% of the original, respectively. The new energy supply capacity is 20 MW. The fault type is a metallic single-phase ground fault and the results are shown in Table 3.

To conclude, the directional relays proposed in this chapter for outlet ground faults are not affected by the capacity of new energy supply or changes of system equivalent impedance.

5 Conclusion

For the new energy power access system, this chapter proposes a directional relay based on the comparison of zero sequence voltages for the outlet metallic ground fault in the 110 kV transmission line.

When a reverse fault occurs on the new energy side or a forward fault occurs on the system side, the measured current at the protection is provided by the AC system. Using this feature, the measured zero sequence voltage at the protection is compared to the calculated zero sequence voltage based on the zero sequence current and topological parameters to distinguish the direction of the fault. The simulation results prove this directional relay is unaffected by the fault characteristics of the new energy supply and can accurately distinguish the direction of the outlet ground fault with a fast action.

References

1. Hooshyar, A., Azzouz, M.A., El-Saadany, E.F.: Distance protection of lines emanating from full-scale converter-interfaced renewable energy power plants—part I: problem statement [J]. IEEE Trans. Power Deliv. **30**(4), 1770–1780 (2015)
2. Bi, T.S., Liu, S.M., Xue, A.C., et al.: Analysis of fault transient characteristics of inverter-type new energy power supply [J]. Chin. J. Electr. Eng. **33**(13), 165–171 (2013)
3. Han, L., Li, F.T., Wang, C.Y., et al.: A survey on impact of wind farm integration on relay protection [J]. Power Syst. Prot. Control. **44**(16), 163–169 (2016)
4. Singh, M.: Protection coordination in distribution systems with and without distributed energy resources-a review [J]. Prot. Control Modern Power Syst. **2**(2), 294–310 (2017)
5. Jia, K., Gu, C.J., Xuan, Z.W., et al.: Fault characteristics analysis and line protection design within a large-scale photovoltaic power plant [J]. IEEE Transactions on Smart Grid, 2018, **9**(5): 4099–4108
6. Zhang, B.H., Wang, J., Yuan, B., et al.: Impact of wind farm integration on relay protection(4): performance analysis for wind farm outgoing [J]. Electric Power Autom. Equip. **33**(4), 1–5+11 (2013) (in Chinese)
7. Horowitz, S.H., Phadke, A.G.: Power system relaying 3rd editon[M]. John Wiley & Sons, (2008)
8. Wang, C.Q., Song, G.B., Tang, H.Y., et al.: Adaptation analysis of distance protection in wind power access systems [J]. Power Syst. Autom. **39**(22), 10–15 (2015)
9. Li, Y.B., Jia, K., Bi, T.S., et al.: Mechanistic analysis of the influence of inverter-type power supply on distance protection [J]. Power Syst. Prot. Control. **46**(16), 54–59 (2018)
10. Song, G.B., Tao, R., Li, B., et al.: Survey of fault analysis and protection for power system with large scale power electronic equipment [J]. Autom. Electric Power Syst. **41**(12), 2–12 (2017)
11. Yu, K.: Research on Novel Principles of Line Protection Adaptive Renewable Energy Integration and Extra-Long Distance Power Transmission [D], pp. 3–6. Huazhong University of Science and Technology, Wuhan (2017)
12. Zhang, L.Y., Ye, T.L., Xin, Y.Z., et al.: Problems and measures of power grid accommodating large scale wind power [J]. Proc. CSEE. **30**(25), 1–9 (2010)
13. Zhang, Y.X., Li, K.K.: Research on adaptive window long distance protection algorithm based on differential equation [J]. Chin. J. Electr. Eng. **07**, 25–28+34 (2000)
14. Chen, M., Zhang, T.: Research on distance protection based on R-L model algorithm and PSCAD simulation [J]. J. Electr. Power. **25**(02), 167–170 (2010)
15. Huang, S.F., Fei, B., Shen, H.M., et al.: Analysis of the impact of phase change failure on distance protection and study of preventive measures [J]. Power Syst. Prot. Control. **42**(20), 123–128 (2014)
16. Wen, M.H., Chen, D.S., Yin, X.G.: Fast distance protection of EHV lines with equal transmission [J]. Chin. J. Electr. Eng. **32**(04), 145–150+6 (2012)
17. Song, G.B., Wang, C.Q., Wang, T., et al.: A phase selection method for wind power integration system using phase voltage waveform correlation [J]. IEEE Trans. Power Del. **32**(2), 740–748 (2017)

Power Outages Quota Decomposition Method Based on Power Supply Mesh Reliability Comprehensive Evaluation

Feng Mingcan, Zheng Yuguang, Jin Oiang, Tian Ye, and Li Hongjun

1 Introduction

Reliability is an important indicator to measure the power supply capacity of distribution networks. To address the problem that the existing power supply reliability index system cannot accurately reflect the actual power reliability of users, reference [1] established an evaluation index system based on the concept of power reliability, and designed a comprehensive assessment method for power reliability of distribution networks based on the improved entropy weight method. Reference [2] proposes a nodal operational risk assessment metric based on the connectivity between generators and load nodes from a load perspective, combined with a data-driven approach – the nodal connectivity. Using hierarchical analysis to set different index weights for different assessment subjects, reference [3] proposes a comprehensive assessment method for the impact of power outages. Power grid enterprises in various countries attach great importance to the management and improvement of reliability. Reference [4] proposes a method to quantify the level of evaluation indicators for pre-scheduled outage management in distribution networks considering investment costs. Reference [5] proposes a power system outage risk assessment method based on outage risk assessment indicators, combined with ORNL-PSerc-Alaska (OPA) model. The development of distribution network in developed countries in Europe is relatively advanced and the reliability level is relatively high. The reward and punishment mechanism focusing on power supply reliability in foreign countries has been adopted in Britain, France, and Germany. The Ofgem of the United Kingdom stipulates the "Guaranteed Standards of Supply" to be observed by each distribution

F. Mingcan (✉) · Z. Yuguang · J. Oiang · L. Hongjun
State Grid State Power Economic Research Institute Co., Ltd, Beijing, China

T. Ye
State Grid Liaoning Electric Power Supply Co., Ltd, Beijing, China

company. If the distribution company fails to meet this standard, it shall make economic compensation to the affected users. France and Germany regard SAIDI index as the standard of power supply reliability rewards and punishments. Reference [6] proposes a method that fully considers the impact of various fault recovery methods on the reliability of AC/DC hybrid distribution networks, which can accurately evaluate the reliability of AC/DC hybrid distribution networks. Grid technology management can proactively identify and solve problems, and it utilizes digital management methods to improve management agility, accuracy, and efficiency. Power supply enterprises should quickly restore their power supply to users who owe fees after they have paid their electricity bills. For a power outage caused by a malfunction, when understanding the first emergency repair situation of the malfunction, inform the user of the approximate message of resuming power consumption. Through this approach, a good customer relationship between the enterprise and users can be achieved. For staggered and planned power outages, the best power outage plan should be analyzed to minimize the number of power outages and inform users accordingly.

2   Analysis on Reliability Factors of Distribution Grid

In order to ensure the comprehensiveness of the conceptual reliability analysis of functions, the influencing factors of reliability are analyzed from the aspects of grid structure, equipment level, distributed generation, energy storage (mobile energy storage), distribution automation level, uninterrupted power operation, management level, etc.

2.1   Grid Structure

The existence of the ring network enhances the connection between different lines. When a line fails or requires maintenance, the power supply can timely supply power to the load from other lines, or automatically switch the power supply of the load through the backup automatic switching device, so as to reduce the occurrence of power failure accidents. A reasonable grid structure can realize the effective transfer of power load when any component fails, and minimize the impact on production and people's life.

2.2   Equipment Level

Cabling rate   According to the equipment failure rate of overhead lines and cable lines, it can be calculated that the theoretical power supply reliability of overhead network can be improved after the cable transformation of various grid structures.

Insulation rate The insulation transformation of overhead lines mainly solves the failure power failure caused by foreign matter short circuit, thus improving the power supply reliability of overhead lines.

Line Distribution lines mainly include cable lines and overhead lines, which are divided into overhead insulated lines and overhead bare conductors.

Power distribution equipment Distribution transformer is an important part of distribution line, and its main faults include local short circuit of iron core, insulation damage, inter turn short circuit, and breakdown to ground.

2.3 Distributed Power Supply

The distributed power supply changes the traditional distribution network from the main network - distribution network - users of a single mode of power supply, in the event of a failure of the main substation or the grid, distributed power supply can continue to supply power to users in isolated operation, reducing the frequency and duration of power outages and improving the reliability of power supply to users.

2.4 Distribution Automation Level

After the implementation of distribution automation, the failure outage time is reduced.

Power supply reliability of typical power grid structure after distribution automation. According to the reduction ratio of failure outage time after the implementation of distribution automation, it can be calculated that the theoretical power supply reliability will be improved after the implementation of distribution automation for various power grid structures.

2.5 Operation Without Power Failure

Power failure operation is also one of the important influencing factors. If the power failure operation is properly planned, the time required can be greatly reduced, thus reducing its impact on power supply reliability.

2.6 Influence of Mobile Energy Storage on Power Supply Reliability

Mobile energy storage advantages. Mobile energy storage has the advantages of flexible operation mode, no installation, etc. It can effectively improve the reliability of power supply for different regions, different user levels, and characteristics.

Mobile energy storage emergency power supply. By moving the energy storage power supply to continuously supply power to users within the scope of influence of equipment outage maintenance, and then conduct outage operation after power transfer, it can make up for the shortage of live working mode.

Power failure is scheduled. As the pre-arranged outage can make targeted load adjustment, transfer, and other measures, minimize the outage range and shorten the pre-arranged outage time, which will effectively shorten the average outage time of users.

2.7 Power Grid Operation Management

It is clear that strengthening the distribution network management has a positive effect on the stability of power supply, and improve the reliability of power supply.

3 Analysis of Distribution Grid Reliability Evaluation

3.1 Two-Dimensional Analysis Method of Line Data

This chapter proposes a data analysis method of line operation and maintenance reliability based on vertical and horizontal dimensions. Combined with the type of relevant data and the topology characteristics of the power grid, the reliability assessment data can be classified and analyzed from two dimensions: vertical dimension and horizontal dimension. The dimensional classification and analysis structure of the big data of line operation and maintenance reliability is shown in Fig. 1.

3.2 The Theory and Method of Distribution Network Reliability Evaluation

Distribution network reliability evaluation is composed of evaluation system (show in Fig. 2) and evaluation system application method. The evaluation system includes selected evaluation indicators and their hierarchical structure, which determines the
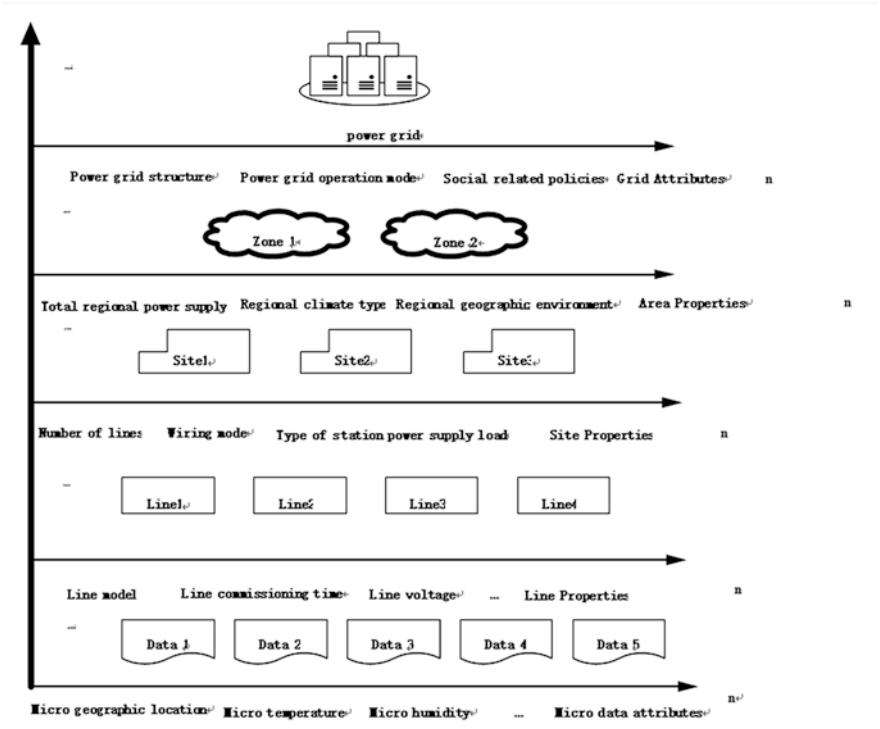
Fig. 1 Two-dimensional analysis framework for line operation and maintenance reliability data

direction and main content of evaluation, and answers the question "which aspect of the value of the object the evaluation subject is interested in". The application method includes the evaluation process (show in Fig. 3) and the determination of evaluation criteria, and indicator weights. It is an indispensable link in the application of evaluation indicators to specific practice.

4 Decomposition of Regional Outage Index

4.1 Construction Process of Regional Indicator System

The established distribution network reliability evaluation system needs to systematically and completely characterize the level of distribution network reliability related work. To this end, we must solve the problems of indicator selection, design, and relationship between indicators, and try to avoid or reduce the occurrence of overlapping indicator meanings, arbitrary selection of indicators, and too complex indicator system. Therefore, it is necessary to propose a methodological framework for
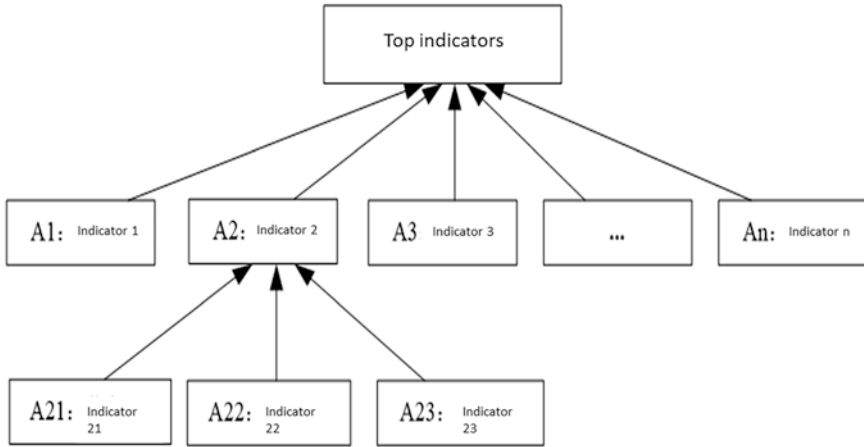
Fig. 2 Diagram of evaluation architecture
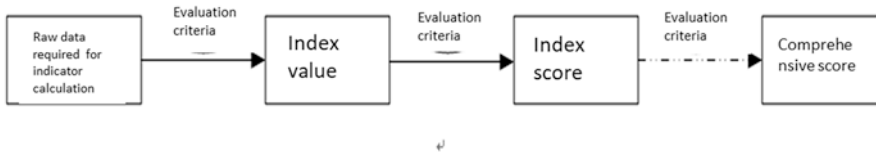
Fig. 3 Evaluation process

establishing the distribution network reliability evaluation system from the perspective of the generation mechanism and method of the index system, shown in Fig. 4.

4.2 Decomposition of Regional Outage Indicators

Load supply capacity The transformation of various distribution network equipment for the purpose of improving power supply capacity and the adjustment of operation mode and load switching for the purpose of adjusting line load can avoid the occurrence of power limitation, incomplete power transfer, and power failure in distribution network transformation caused by the distribution network itself, and ensure the smooth supply of load.

Continuous supply capability In the process of selecting power grid equipment, pay attention to whether it meets the requirements of uninterrupted power operation.

Power failure affects control capability Users of dual power supply, multiple power supply, or self-provided *power* supply can avoid the impact of power failure through automatic switching between different power supplies in the special distribution station.

Fig. 4 Evaluation process
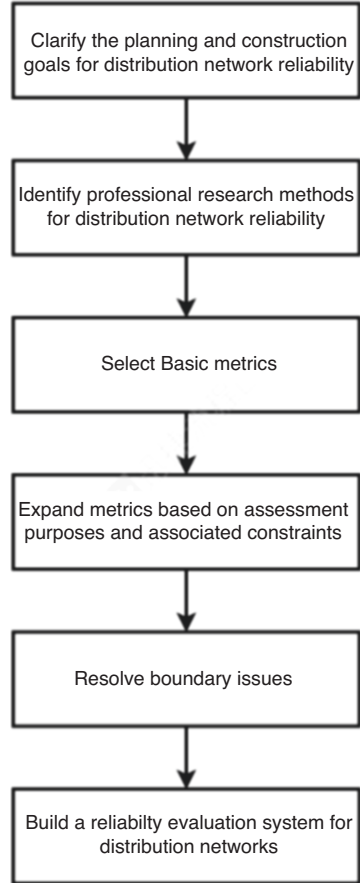
Power supply recovery capability Reasonably select the maintenance mode, and deal with the time-consuming online maintenance work with the unit replacement method when the maintenance time is significantly higher than the replacement time, which can shorten the scheduled outage time of maintenance.

4.3 Index Evaluation Standard and Its Combination with Power Supply Reliability

Considering the consistency between the evaluation criteria and the power supply reliability, the determination of typical scoring points must also be closely related to the power supply reliability, and combine the actual situation of the production and operation of power supply enterprises in China and the grid planning and design guidelines. The selection of the evaluation criteria of the grass-roots indicators in the power supply reliability evaluation system.

4.4   Index Weight and Its Combination with Power Supply Reliability

In order to ensure the consistency between the evaluation system and the power supply reliability rate, the determination of the weight must be based on the theoretical calculation of the power supply reliability rate, and the ratio of the change amplitude of the overall reliability rate after the same amplitude change of each index is taken as the basis for the determination of the weight.

5   Example

5.1   Analysis of Grid Reliability Index

Reliability index analysis of a grid is shown in Table 1.

5.2   Power Failure Type Analysis

The types of power failure include power failure and prearranged power failure. By analyzing the average outage time of users with failures and scheduled outages and the proportion of impacts, the weak links of power supply reliability are found.

5.3   Comprehensive Assessment and Analysis of Regional Reliability

The distribution network reliability evaluation index system is used to analyze and evaluate the reliability of an actual power grid. After basic data collection and grassroots index calculation, the set evaluation criteria and weights are used for statistics. The reliability score of this power grid is shown in Table 2.

It can be seen from the above assessment results that:

A: The load supply capacity scored 62.77 points, which was moderately good.
B: The uninterruptible power supply capability scores 57.21 points, which is moderately poor.

In terms of uninterrupted power supply capacity, the grid equipment level and overhead line protection level are both high, but all cables are directly buried, which is easy to be damaged by external forces. In addition, no other uninterrupted operation has been carried out. If the power grid needs to further control the occurrence of power failure, it is recommended to give priority to the protection of cable lines,

Table 1 Reliability index analysis of a grid

Power supply area	Power supply reliability (RS-3, %)	Average annual outage time of users (minute)	Annual average scheduled outage time of users (minute)	Average annual outage time of users (second)	Annual average scheduled outage time of users (second)
A+	99.9910	32.11	15.21	0.31	0.11
A	99.9893	41.10	15.27	0.41	0.15
B	99.9809	75.28	24.89	0.55	0.18
C	99.9642	91.24	97.19	0.55	0.25
D	99.9591	72.64	142.13	0.58	0.59

Table 2 Reliability scoring results of a power grid

Characteristic aspects	Level I indicators	Secondary indicators	Grass roots indicators and scores	Indicator value
A. Load supply capacity (62.77)	A1. Adequacy (47.7)	A11. Main network margin (58.8)	A111. Average load rate of substation (37)	72.49
			A112. Short-term development margin of main network (66)	3.33
		A12. Distribution network margin (44)	A121. Average line load rate (16)	66.33
			A122. Short-term development margin of distribution network (56)	1.82
	A2. Degree of limitation (72.8)	A21. Restricted primary network (80)	A211. Proportion of out of limit load of main network (100)	0
			A212. Proportion of heavy load substations (0)	100
		A22. Limited distribution network (69.8)	A221. Proportion of out of limit load of distribution network (73)	0.67
			A222. Proportion of heavy haul lines (0)	38.78
			A223. Proportion of power supply restricted lines (100)	0

(continued)

Table 2 (continued)

Characteristic aspects	Level I indicators	Secondary indicators	Grass roots indicators and scores	Indicator value
B. Uninterruptible power supply capability (57.21)	B1. Uninterruptible power supply capability of equipment (86.5)	B11. Maintenance free (less) capacity of equipment (——)	B111. Proportion of maintenance free (less) equipment (——)	——
		B12. Equipment quality (86.5)	B121. Proportion of old equipment (60)	10
			B122. Equipment availability (100)	100
			B123. Primary rate of equipment (85)	99.6
	B2. Line protection capability (67.2)	B21. Protection level of overhead lines (96)	B211. Proportion of lines not meeting lightning protection standards (96)	2
			B212. Proportion of lines that do not conform to anti-pollution standards (96)	2
			B213. Overhead insulation rate (96)	98.04
		B22. Protection level of cable line (0)	B221. Direct burial ratio (0)	100
			B222. Proportion of cables without compression resistance measures (——)	——

(continued)

Table 2 (continued)

Characteristic aspects	Level I indicators	Secondary indicators	Grass roots indicators and scores	Indicator value
	B3. UPS operation capability (22.9)	B31. Ability to carry out uninterrupted operation (42)	B311. Proportion of live working items (70)	70
			B312. Proportion of other uninterrupted operation items (0)	0
		B32. Coverage capability of uninterrupted operation (10.2)	B321. Coverage of live working projects (17)	17
			B322. Coverage of bypass operations (0)	0
C. Power failure affects control capability (68.6)	C1. Power control capability (89.5)	C11. Power configuration level (100)	C111. Multi power supply rate of substation (100)	100
			C112. Multi main transformer rate of substation (100)	100
		C12. Power switching capability (85)	C121. Proportion of interconnection lines between stations (86)	83.673
			C122. Average substation "N-1" distribution network power loss load ratio (85)	15.08
			C123. Power loss load ratio of average bus section "N-1" distribution network (84)	6.46

Table 2 (continued)

Characteristic aspects	Level I indicators	Secondary indicators	Grass roots indicators and scores	Indicator value
	C2. Distribution network control capability (67.7)	C21. Automatic isolation capability (85.8)	C211. Average automatic isolation capacity (79)	4127
			C212. Line coverage of automatic isolation technology (92)	51.852
			C213. Average sectional capacity of intelligent switch (100)	2789
		C22. Load isolation capacity (76.4)	C221. Average section length of load switch (92)	0.856
			C222. Average sectional capacity of load switch (96)	3180
			C223. Excessive proportion of sectional capacity of load switch (0)	52.459
			C224. Line accompanying stop rate (100)	0
		C23. Load transfer capacity (66)	C231. Average power loss ratio of "N-1" connecting line (0)	41.23
			C232. Proportion of connecting lines (78)	93.88
			C233. Temporary power capacity (0)	0
		C24. Switch control capability (98)	C241. Electric operation proportion of switch (100)	100
			C242. Switch remote control proportion (95)	74.19

(continued)

Table 2 (continued)

Characteristic aspects	Level I indicators	Secondary indicators	Grass roots indicators and scores	Indicator value
	C3. User control capability (56.3)	C31. User impact isolation capability (46.4)	C311. Average user failure influence range (46)	9419
			C312. Average user application influence range (47)	970
		C32. Guarantee level of users' electricity consumption (79)	C321. Ratio of double power supply automatic switching user capacity (79)	29.27
			C322. Proportion of self-contained power supply (——)	——
D. Power supply recovery capability (53.8)	D1. Fault handling capacity (76.8)	D11. Fault location (76.8)	D111. Proportion of automatic positioning lines (87)	51.852
			D112. Proportion of manual patrol lines assisted by fault indication (70)	71.697
	D2. Arrange processing capacity (0)	D21. Maintenance mode (0)	D211. Unit replacement maintenance proportion (0)	0
			D212. Online maintenance proportion (0)	100

the implementation of live working, and the development of other uninterrupted work projects.

C: The control ability affected by power failure scored 68.6 points, which was slightly better.

The power outage of the power grid has a strong influence on the control capability. In terms of power failure impact control, unreasonable line segmentation has affected load isolation, low passing rate of line "N-1," no mobile power supply has affected load transfer, and user power failure has a serious impact.

D: The power supply recovery ability scored 53.8 points, which was moderately poor.

There is still much room to improve the power supply recovery capacity of the grid. Although the power grid can quickly locate and handle faults (the installation of fault indicators and the proportion of automatic positioning are high), there is a lack of processing means for scheduling operations.

Summary: The four reliability characteristics of the power grid, such as load supply capacity, are basically equivalent, and the overall reliability of the distribution network is above the average level. It should be noted that the power distribution automation has been partially realized in this example grid, the live working technology is relatively mature, and the load development is not fast, but the load of power facilities is heavy. The statistical value of the power supply reliability rate of the grid this year is 99.93%, and the average number of power outages for users is 1.72 times per household. The assessment results are basically consistent with the actual situation.

6   Conclusion

This research pays attention to theoretical analysis and practical application at the same time. It not only summarizes all factors affecting reliability through upper level indicators, but also directly relates the actual production level and distribution network reliability through grass-roots indicators, and finds the relationship between actual production and distribution network reliability. Based on the previous research on reliability, a more complete index system for evaluating the reliability of distribution network is created.

References

1. Sen, O., Liyuan, L.: Reliability index system of distribution network for power consumer and its comprehensive assessment method. Power Syst. Technol. **41**(01), 215–222 (2017). https://doi.org/10.13335/j.1000-3673.pst.2016.0770
2. Hui, R., Genwang, W., Huanxin, T., et al.: Study on nodal outage risk evaluation index for transmission network based on data-driven method [J]. Proc. the CSU-EPSA. **33**(06), 51–59 (2021). https://doi.org/10.19635/j.cnki.csu-epsa.000583
3. Ruitao, L., Zhehao, L., Qinxing, Z., et al.: Impact index system and comprehensive assessment for the power outage of power users [J]. Power Syst. Technol. **44**(06), 2350–2360 (2020). https://doi.org/10.13335/j.1000-3673.pst.2019.1146
4. Liu, W.H., Yangtao, L., et al.: A quantitative method for evaluating management level of distribution network planned outages considering investment [J]. Power Syst. Technol. **43**(07), 2282–2291 (2019). https://doi.org/10.13335/j.1000-3673.pst.2018.2267

5. Lu En, L., Xiaojun, L.F., et al.: Indexes and method of power system outage risk assessment [J]. Electric Power Autom. Equip. **35**(03), 68–74 (2015). https://doi.org/10.16081/j.issn.1006-6047.2015.03.011
6. Zhang, L., Shunjiang, Y., Chen, W., et al.: Reliability evaluation of AC/DC hybrid distribution network considering VSC operation mode and fault recovery optimization [J]. Power Syst. Technol. **46**(01), 292–303 (2022). https://doi.org/10.13335/j.1000-3673.pst.2021.0169

A Harmonic Impact Assessment Method for Multiple Harmonic Sources Connected to Distribution Network

Chaoda Li and Zonghua Zheng

1 Introduction

Since the beginning of the twenty-first century, with the development of power electronic equipment and devices, a large number of nonlinear components have been widely used in the power grid. In particular, distributed systems represented by photovoltaic and wind energy are connected to the distribution network, which brings a series of harmonic problems while bringing clean energy [1, 2]. In addition, in the process of harmonic supervision and control, disputes often occur due to improper evaluation of harmonic responsibility, which has become a major obstacle to the commercialization of electric energy. Therefore, a "reward and punishment scheme" [3] has been proposed internationally. On the one hand, it provides economic compensation for users who actively control harmonics, and on the other hand, it provides corresponding economic punishment for users who produce excessive harmonics. The scheme reflects the common responsibility of power system and power users for power quality of power grid. However, the premise of the implementation of this scheme is the accurate division of harmonic responsibility.

At present, most of the related research on the division of harmonic responsibility made by scholars at home and abroad is based on the harmonic voltage responsibility evaluation index to estimate the harmonic impedance and background harmonic voltage [4]. However, in recent years, the power grid structure has become more and more complex, and a large number of distributed power sources have brought many new harmonic problems to the power grid, and the harmonic voltage responsibility evaluation index is difficult to reflect the above situation. Based on this, domestic and foreign scholars have proposed many indicators for measuring harmonic responsibility, including critical impedance determination method [5, 6], non-active power determination method [7], distortion power index [8], harmonic

C. Li (✉) · Z. Zheng
College of Electrical Engineering and Automation, Fuzhou University, Fuzhou, Fujian, China

power decomposition index [9], nonlinear current ratio index [10], and responsibility evaluation index based on superposition projection principle [11–13]. The responsibility evaluation index based on the superposition projection principle is the most commonly used responsibility division index. This index quantifies the responsibility by quantifying the harmonic contribution at the common connection point, but it also has defects in application. In special cases, the unreasonable division of responsibilities is different from the evaluation results when calculating the harmonic voltage and harmonic current responsibilities, and even the main harmonic judgment results are opposite [14, 15]. In addition, this method is mostly aimed at the responsibility division of a single public connection point and lacks the consideration of the responsibility division from the global perspective of the distribution network.

Therefore, this chapter proposes a harmonic impact assessment method based on power flow calculation, which takes into account the user's harmonic tolerance, network loss, and other factors. Combined with the harmonic power flow calculation results and the harmonic compatibility level of the distribution network, a comprehensive evaluation index is given for the impact of multi-harmonic sources on the distribution network to assist the division of harmonic responsibility.

2 Power Flow Calculation

Power flow calculation is a very important and basic calculation for the study of power system. At the mathematical level, the power flow calculation problem is a set of multivariate nonlinear equations. The Newton–Raphson method is a calibration method for solving linear equations in mathematics. Its main principle is to transform nonlinear equations into corresponding linear equations, and then solve linear equations. The actual solution process is to carry out Taylor expansion of the nonlinear equations ($f(x) = 0$) near the estimated value x0 near the initial value of a certain amount of x to be solved. Ignoring the second-order and second-order higher-order terms in the expansion term, simplifying and listing the corresponding equations, a set of equations linearized by the original nonlinear equations can be obtained. These kinds of equations are suitable for harmonic power flow calculation. These kinds of equations are generally modified equations. The modified equations are abbreviated as:

$$\Delta f = J \Delta x \tag{1}$$

In the formula: Δx is Variable correction value; J is a Jacobian matrix; Δf is correction value.

When using the Newton–Raphson method for power flow calculation, the choice of initial value should be closer to the value of the exact solution, otherwise nonconvergence will occur in the iterative process. The Newton–Raphson method can be directly used to solve the power flow equation of power system. The formula is as follows:

$$S_i = U_i \sum_{j=1}^{n} \left[\left(G_{ij} - jB_{ij} \right) U_j \left(\cos \delta_{ij} + \sin \delta_{ij} \right) \right] \tag{2}$$

In the formula: S is the node power; U is the node voltage amplitude; δ is the node voltage phase angle; G and B are is the line admittance.

The key to using the Newton–Raphson method to calculate the power flow problem is to construct a correction equation and solve it. Therefore, it is necessary to number each node in the distribution network, take the known node as the equilibrium node, and use its voltage and phase angle to establish a rectangular coordinate correction equation for Newton–Raphson method. The basic steps are as follows:

1. List the structural parameters of the distribution network, establish the corresponding node admittance matrix, bring the initial voltage value of the PV node and the balance node, and assume the initial voltage value of the PQ node.
2. The initial value and the assumed value of the node voltage are brought into the correction equation, and the correction of the equations is obtained and recorded.
3. Find the elements in the corresponding Jacobian matrix, that is, the power and voltage of each node are calculated for the voltage partial derivative.
4. Solve the correction equation to obtain the variation of each node.
5. The corrected value is brought into the correction equation again for iterative calculation. Until the convergence condition is satisfied, the final power flow calculation result is obtained.

3   Harmonic Compatibility Level

The pollution of power quality mainly comes from the electromagnetic disturbance phenomenon generated by various pollution sources and spread in the power grid. For example, harmonics and inter-harmonics generated by harmonic sources can overheat power transformers, motors, capacitors, and other equipment or cause misoperation of relay protection devices. From the perspective of power grid operation demand, the audience of power quality pollution is not a specific type of equipment, but the equipment group accessed by the power supply system. Therefore, the relationship between power quality pollution level and system access equipment can be embodied as power quality compatibility.

The compatibility of power system is mainly represented by the following four aspects: disturbance level, compatibility level, planning level, and anti-interference level. The disturbance level is the level of a given electromagnetic disturbance measured by a specified method; compatibility level is used to coordinate the reference value of emission and anti-interference degree of equipment composed of power supply network or powered by power supply network to ensure the electromagnetic compatibility of the whole system. The planning level is the level used to evaluate the impact of all user loads on the power supply system during planning; the

anti-interference level is the maximum level of given electromagnetic disturbance that is injected into a specific device or power supply system with a specified method without performance degradation. The schematic diagram is shown in Fig. 1.

The IEC standard provides four equipment performance states under the influence of harmonic pollution, which can explain the corresponding harmonic compatibility state. The performance status of devices corresponding to harmonic compatibility status is shown in Table 1. When the harmonic pollution level is lower than the equipment tolerance, the equipment performance state is M1, indicating that the equipment can work normally, and the harmonic effect is compatible with the equipment performance. When the harmonic pollution level exceeds the tolerance of the equipment, the equipment may fail. The harmonic effect is incompatible with the equipment and increases in turn according to the severity. When the equipment state is M2, it indicates that the equipment performance is temporarily reduced or the function is temporarily lost, but it has a self-recovery function. When the device state is M3, it means that the performance of the device is temporarily reduced or the function is temporarily lost, but the previous execution state needs to
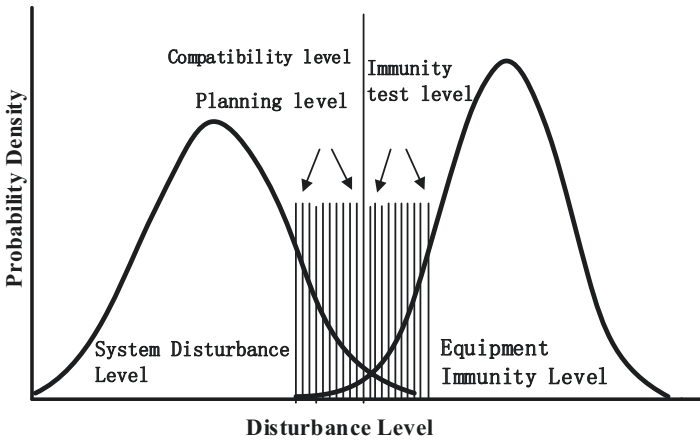
Fig. 1 Concept diagram of electromagnetic compatibility

Table 1 The Performance status of devices corresponding to harmonic compatibility state

Harmonic compatibility		Equipment characteristic
Compatible	M1	Normal performance and executive function
	M2	Temporary decline in performance or temporary loss of function, able to self-recover
Incompatible	M3	Temporary decline in performance or temporary loss of function, need operator intervention or system reset recovery
	M4	Permanent performance degradation or permanent loss of function, cannot be restored

be restored through manual operation or system reset. When the device state is M4, the device performance is permanently degraded or permanently lost, and the previous working state cannot be continued due to hardware loss or software data loss.

The power quality compatibility degree L is defined. The measured harmonic voltage containing rate HRU_h and the total voltage harmonic distortion rate THD_U are taken, and the CP95 value of the root mean square of its 10 min is taken as the compatibility index $HRU_{h.\ rms.\ CP95}$ and $THD_{U.\ rms.\ CP95}$. The compatibility index is compared with its corresponding IEC standard limits to obtain a series of harmonic normalized index values. The maximum value is combined to obtain the power quality compatibility degree L. The formula is as follows:

$$C_{h.rms} = \sqrt{\frac{1}{N}\sum_N C_{h.k}{}^2}\ N > 100;$$ (3)

$$\frac{\sum\limits_{-\infty}^{C_{h.rms.cp95}} f(C_{h.rms})}{\sum\limits_{-\infty}^{+\infty} f(C_{h.rms})} = 0.95$$ (4)

$$I_{Hx}\quad \frac{C_{h.rms.cp95}}{C_{h.Standard\_limits}}\quad x\quad HRU_h, THD_U\ ;$$ (5)

$$L\quad \max\ I_{H\_THD}, I_{H\_HRU_k}$$ (6)

In the formula: C_h refers to HRU_h, THD_U; N is the sampling amount of 10 min; $f(C_{h.\ rms})$ is the density distribution function composed of weekly 10 min values.

The power quality compatibility degree L is used to divide the equipment state M, and the tolerance of each user to harmonics is distinguished according to L. Because the users connected to each bus in the distribution network have different harmonic compatibility degrees, the influence of harmonic sources on the distribution network is also different.

4   Weighting Method Considering Harmonic Effects

The entropy weight method is an objective weighting method. In the process of specific use, according to the degree of dispersion of the data of each index, the entropy weight of each index response is calculated by using information entropy, and then the entropy weight is modified according to each index to obtain a more objective index weight. The entropy formula is:

$$H = -\sum_{i=1}^{m} f_i \cdot \ln f_i \tag{7}$$

Entropy value is a measure of system uncertainty and disorder degree, which can be used to determine the weight of each index in the multi-index evaluation system. Each evaluation index is taken as a random variable to calculate the entropy weight coefficient of the index. The greater the degree of change, the more disordered it is and the greater the amount of information it can provide, the more important the index is. The steps of entropy weight method are as follows:

1. Determine the evaluation object, establish the evaluation index system, and construct the evaluation matrix R.
2. The evaluation matrix R is standardized to R'. The standardized treatment is as follows:

   If the evaluation index j is a positive index, the following processing is performed:

$$r_{ij}' = \frac{r_{ij} - \min(r_{ij})}{\max(r_{ij}) - \min(r_{ij})} \tag{8}$$

If the evaluation index j is negative, the following treatment is performed:

$$r_{ij}' = \frac{\max(r_{ij}) - r_{ij}}{\max(r_{ij}) - \min(r_{ij})} \tag{9}$$

3. Calculate the entropy of each index according to Eq. (7).
4. Calculate the entropy weight w of each index, the calculation formula is as follows:

$$w_j = \frac{1 - H_j}{\sum_{j=1}^{n}(1 - H_j)} = \frac{1 - H_j}{n - \sum_{j=1}^{n} H_j} \tag{10}$$

5. The index entropy weight is modified according to the usage scenario.

5   Weighting Method Considering Harmonic Effects

The system can be adapted to all types of distribution networks. The example uses the IEEE14 node standard test system shown in Fig. 2, and the harmonic sources HL1, HL2, and HL3 are connected to the nodes 9, 13, and 14 of the system. The constant current source model is used to simulate the harmonic source emission characteristics. Table 2 shows the spectrum parameters of the harmonic source.
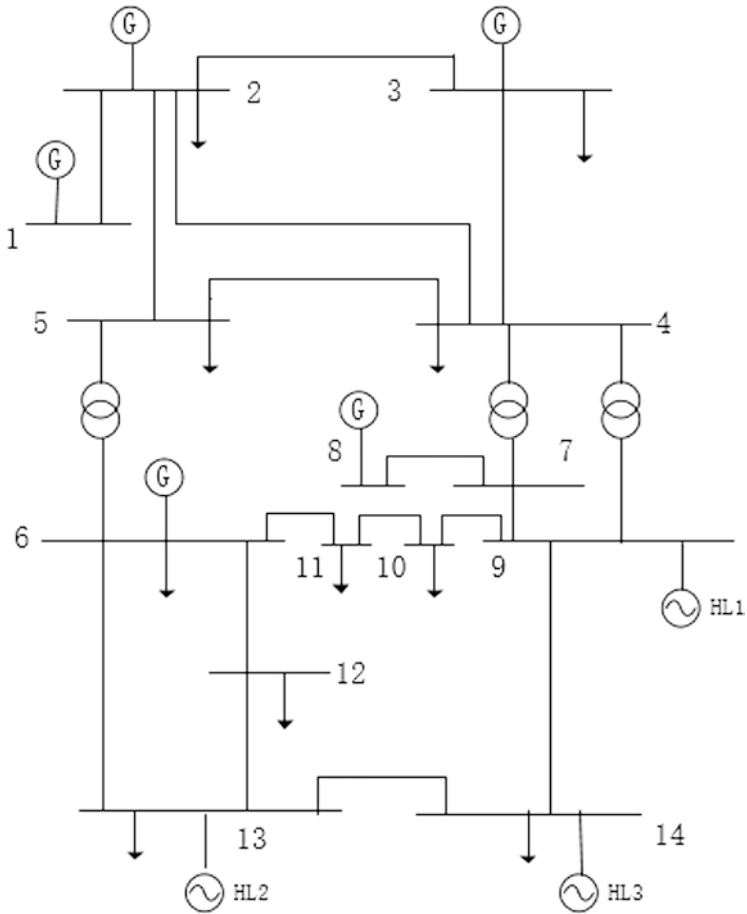
Fig. 2 IEEE14 node wiring diagram

Table 2 Harmonic source spectrum parameter table

Harmonic source	Harmonic number	Harmonic current containing rate %
HL1	5	10
	7	20
	9	30
HL2	7	20
	9	25
	11	30
HL3	5	15
	7	35
	11	20

The impact of multi-harmonic access is shown in Fig. 3.

Considering the harmonic tolerance of the load of the connected users in the distribution network, the harmonic compatibility level of each device is as shown in Table 3.

As shown in Table 3, the power quality compatibility of the devices connected to the 6, 7, 8, 9 buses is higher than that of the other buses, indicating that these buses are more susceptible to harmonic voltage fluctuations caused by harmonic sources. Therefore, the influence of harmonic voltage on these buses should be expanded.

The entropy weight method is used to analyze the weight of the harmonic influence of each harmonic source on each bus. The experimental results are shown in Table 4.
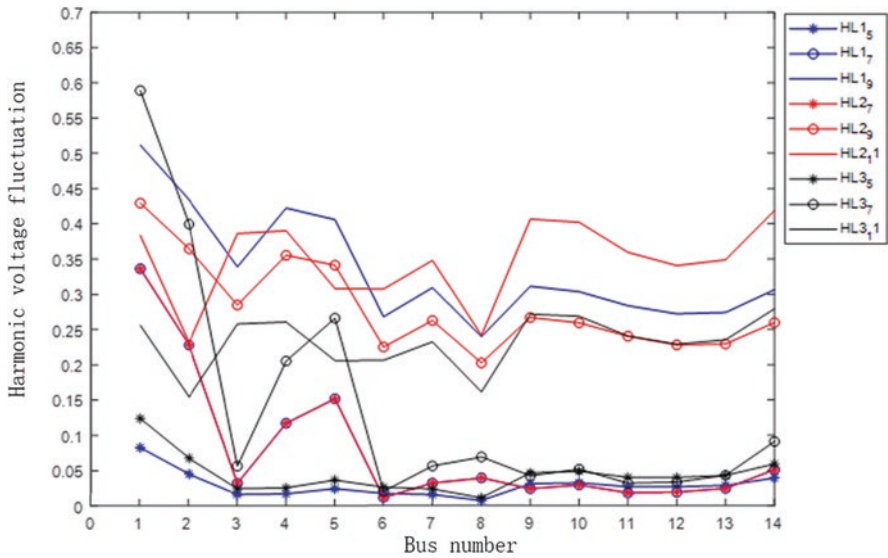
Fig. 3 A figure of each bus affected by multiple harmonic sources. The abscissa is the bus number, and the ordinate is the harmonic voltage fluctuation

Table 3 Compatibility level table for each bus

Bus	Harmonic number	Power quality compatibility L
6	5	2.25
	7	2.75
8	9	3.00
	11	4.25
The remaining buses (1, 2, 3, 4, 5, 7, 9, 10, 11, 12, 13, and 14)		1

Table 4 The influence proportion of harmonic source on distribution network

Harmonic source	Weight%
HL1	44.27
HL2	33.83
HL3	21.90

The above results are without considering the background harmonic shadow, only considering the influence proportion of distribution network under the interaction of harmonic sources HL1, HL2, and HL3. It can be seen from the results that there is only a small difference in the influence of the three harmonic sources on the power quality of the distribution network. The HL3 harmonic source has little effect on the distribution network. In the distribution of power grid rewards and punishments, the penalties for harmonic sources at HL3 can be appropriately reduced.

6 Weighting Method Considering Harmonic Effects

In order to study the impact of multi-harmonic sources on the distribution network, this chapter proposes a harmonic impact assessment method based on power flow calculation. Considering the possible electromagnetic compatibility level in the distribution network and the harmonic tolerance of users, the ieee14 node system network is taken as an example. The harmonic influence of multiple harmonic sources connected to the distribution network system is quantitatively analyzed and the influence weight of each harmonic source on the distribution network is obtained. The method in this chapter can be used to assist in judging whether the harmonic source can be connected to the distribution network and for the follow-up study of the power quality reward and punishment system.

References

1. Shao, Z., Haobo, X., et al.: Harmonic problems in a new energy power grid[J]. Power Syst. Prot. Control. **49**(4) (2021)
2. Aill, M., CaltalotiA, C.A., et al.: A self synchronizing instrument for harmonic source detection in power systems[J]. IEEE Trans. Instrum. Meas. **54**(1), 15–23 (2015)
3. Mceachern, A., Grady, W.M., Moncrief, W.A., et al.: Revenue and harmonics: an evaluation of some proposed rate structures[J]. IEEE Trans. Power Deliv. **10**(1), 474–482 (1995)
4. Liu, Z., Yonghai, X., et al.: Research status and prospect of harmonic responsibility quantitative evaluation method under new energy integration[J]. Electr. Power Autom. Equipment. **40**(11) (2020)
5. Liu, X., Wang, H., et al.: Application of critical impedance method in harmonic source detecting in distribution systems[J]. Autom. Electr. Power Syst. **31**(14), 76–80 (2007)
6. Balci, M.E., Hocaoglu, M.H.: Quantitative comparison of power decompositions[J]. EPSR. **78**(3), 318–329 (2008)

7. Ferrero, A., Menchetti, A., Sasdelli, R.: Measurement of the electric power quality and related problems[J]. ETEP. **6**(6), 401–406 (2006)
8. Wang, L., Xiao, X., et al.: A distortion power based assessment index and method of harmonic contribution of nonlinear loads[J]. Power System Prot. Contr. **45**(9), 41–47 (2017)
9. Dai, S., Yang, J., Li, Q.: An incentive energy measurement method based on harmonic power decomposition strategy[J]. Power Syst. Prot. Contr. **44**(1), 111–116 (2016)
10. Zhang, Y., Wang, Y., et al.: Determination method of user harmonic responsibility based on correlation analysis of monitoring data[J]. Autom. Electr. Power Syst. **44**(2), 189–197 (2020)
11. Wang, Y., Zang, T., et al.: Harmonic contribution partition of multiple harmonic sources considering background harmonic voltage fluctuation[J]. Autom. Electr. Power Syst. **39**(18), 55–61 (2015)
12. Wei, G., Qiu, H., et al.: Waveform matching based method for harmonic contribution determination[J]. Autom. Electr. Power Syst. **41**(2), 129–134 (2017)
13. Lin, S., Li, Y., et al.: System harmonic impedance estimation based on improved FastICA and partial least squares[J]. Power Syst. Technol. **42**(1), 308–314 (2018)
14. Ma, Z., Xu, Z., et al.: Harmonic contributions determination on condition of changing background harmonic impedance[J]. Electr. Meas. Instrum. **53**(23), 78–83+89 (2016)
15. Sha, H., Mei, F., Zhang, C., et al.: Multi-harmonic sources harmonic contribution determination based on data filtering and cluster analysis[J]. IEEE Access. **7**, 85276–85285 (2019)

Optimal Scheduling of an Islanded Multi-Energy Microgrid Considering Power-to-Gas and Carbon Capture Technologies

Seyed Ehsan Ahmadi, Mousa Marzband, Augustine Ikpehai, and Abdullah Abusorrah

Acronyms

BES/CES/HES/NGS/TES	Battery/Carbon/Hydrogen/Gas/Thermal Energy Storage
CHP	Combined Heat and Power
G2P/P2G	Gas-to-Power/Power-to-Gas
H2P/P2H	Hydrogen-to-Power/Power-to-Hydrogen
MT	Micro Turbine
MEMG	Multi-Energy Microgrid

S. E. Ahmadi
Northumbria University, Electrical Energy and Control Systems Research Group,
Newcastle upon Tyne, UK

M. Marzband (✉)
Northumbria University, Electrical Energy and Control Systems Research Group,
Newcastle upon Tyne, UK

Center of Research Excellence in Renewable Energy and Power Systems, King Abdulaziz
University, Jeddah, Saudi Arabia
e-mail: mousa.marzband@northumbria.ac.uk

A. Ikpehai
Department of Engineering and Mathematics, Sheffield Hallam University, Sheffield, UK

A. Abusorrah
Center of Research Excellence in Renewable Energy and Power Systems, King Abdulaziz
University, Jeddah, Saudi Arabia

Department of Electrical and Computer Engineering, Faculty of Engineering, Energy
Research and Innovation Center, King Abdulaziz University, Jeddah, Saudi Arabia

161

1   Introduction

Carbon capture and storage (CCS) technology is among many methods to decrease CO_2 emissions. CCS seeks to capture CO_2 and store it or apply it via conversion into productive items such as H_2 and CH_4 [1, 2]. With the growing penetration of power-to-gas (P2G), especially combined heat and power (CHP), coordinated scheduling of multi-energy microgrids (MEMGs) becomes a demanding operation [3, 4]. As shown in Fig. 1, the proposed MEMGs are composed of energy generation, storage, and conversion units [5]. Also, electrolyzer and steam methanation reactor (SMR) can be applied to convert P2H and H2G, as well as fuel-cell and natural gas reactor (NGR) to convert H2P and G2H. Also, post-combustion capture is valuable for separating CO_2 from the produced exhaust gases as the simplest method to capture CO_2 [6].

In recent years, some studies have been conducted on optimization problems in distribution networks, mainly combining power–gas or power–heat systems. Authors in [7] proposed a hydrogen-electric coupled compressed air energy storage and P2G taking into account the actual scheduling constraints. Authors in [8] proposed an optimal stochastic operation of an energy hub considering CHP, P2G
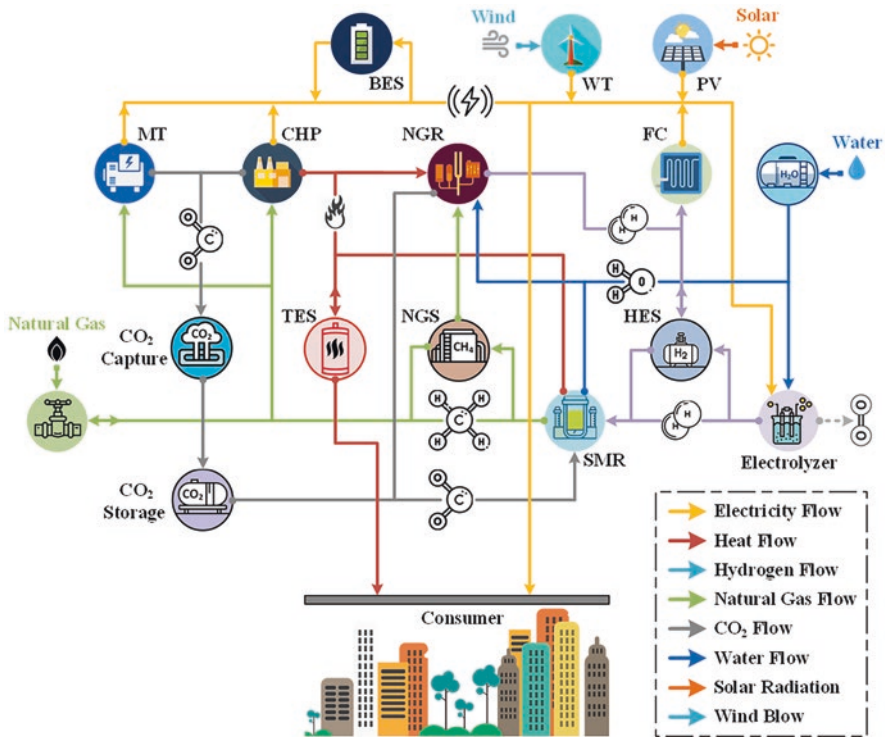
Fig. 1 Islanded MEMG with P2X technologies

storage, thermal storage, and wind turbine (WT) to supply the heat, gas, and power loads. Authors in [9] proposed a P2G combined heat and power microgrid to provide a two-stage distributionally robust optimization model to solve economic dispatch problem. However, in above-mentioned works, the investigation of CCS technology in energy networks is ignored. Authors in [10] studied carbon-to-power (C2P) virtual power plants with demand response and vehicle-to-grid combined by gas-power plant carbon capture. Authors in [11] proposed a hydrogen-based system combined with P2G function as a carbon recycling system to decrease carbon emissions and generate extra heat from its chemical reaction for consumers. However, the electrically islanded multi-energy network is not considered in the previous works.

To fill this gap, this chapter proposed an optimization framework for scheduling an islanded MEMG considering CCS and power-to-X (P2X) including power-to-hydrogen (P2H) and P2G to enhance the system flexibility. In the proposed system, five energy carriers of power, heat, hydrogen, natural gas, and CO_2 are considered. Besides, micro turbine (MT), CHP, WT, photovoltaic (PV), and multi-energy storage systems (MESS) including battery energy storage (BES), thermal energy storage (TES), hydrogen energy storage (HES), natural gas energy storage (NGS), and carbon energy storage (CES). The main contributions can be highlighted as follows:

- Proposing electrically islanded MEMG to schedule under fault-occurred conditions
- Presenting P2X technologies such as P2H and P2G along with HES and NGS.

2 Problem Formulation

The objective function of the proposed optimization problem is formulated by Eq. (1):

$$\min \sum_t \left(\wp_t^{MT} + \wp_t^{CHP} + \wp_t^{P2H} + \wp_t^{H2P} + \wp_t^{SMR} + \wp_t^{NGR} + \wp_t^{NGG} + \wp_t^{CCS} \right) \tag{1}$$

$$\wp_t^{MT} = \sum_m \left(a_m^{MT} . PO_{m,t}^{MT} + b_m^{MT} . \sigma_{m,t}^{MT,UC} \right) \tag{2}$$

$$\wp_t^{CHP} = \sum_n \left(\begin{array}{c} \varphi_n^{CHP,1} . \left(PO_{n,t}^{CHP} \right)^2 + \varphi_n^{CHP,2} . PO_{n,t}^{CHP} + \varphi_n^{CHP,3} + \\ \psi_n^{CHP,1} . \left(HE_{n,t}^{CHP} \right)^2 + \psi_n^{CHP,2} . HE_{n,t}^{CHP} + \psi_n^{CHP,3} \end{array} \right) \tag{3}$$

$$\wp_t^{P2H} + \wp_t^{H2P} = \mu_t^{H_2} . \left(\sum_e PO_{e,t}^{P2H} + \sum_f PO_{f,t}^{H2P} \right) \tag{4}$$

$$\wp_t^{\text{SMR}} + \wp_t^{\text{NGR}} + \wp_t^{\text{NGG}} = \mu_t^{\text{CH}_4} \cdot \left(\sum_v \text{NG}_{v,t}^{\text{SMR}} + \sum_w \text{NG}_{w,t}^{\text{NGR}} \right) + \mu_t^{\text{NGG}} \cdot \text{NG}_t^{\text{NGG}} \tag{5}$$

$$\wp_t^{\text{CCS}} = \sum_c \mu_t^{\text{CO}_2} \cdot \text{CO}_{c,t}^{\text{CCS}} \tag{6}$$

Equations (2) and (3) are the cost functions of MT and CHP. PO^{MT} and PO^{CHP}/HE^{CHP} are the power output of MT and power/heat generation of CHP unit. $a^{\text{MT}}/b^{\text{MT}}$, $\varphi^{\text{CHP,1}}$-$\varphi^{\text{CHP,3}}$, and $\psi^{\text{CHP,1}}$-$\psi^{\text{CHP,3}}$ are generation cost parameters of MT and CHP unit. $\sigma^{\text{MT,UC}}$ is the commitment state of MT. Equation (4) shows the costs of converting P2H and H2P. PO^{P2H} and PO^{H2P} are converted P2H and H2P [in kW], respectively. μ^{H_2} is the converting price of H_2. Equation (5) shows the costs of converting hydrogen-to-gas (H2G) and gas-to-hydrogen (G2H) and the cost of buying gas from the gas grid. NG^{SMR} and NG^{NGR} are gas produced and consumed in SMR and NGR [in m³]. μ^{CH_4} and μ^{NGG} are the converting price of CH_4 and the price of buying gas from the gas grid, respectively. Equation (6) shows the cost of the CCS. CO^{CSS} is the captured and stored CO_2 [in kg] and μ^{CO_2} is the cost of post-combustion capture. The constraints shown by Eqs. (7) and (8) ensure that the MT output is within its generation capacity:

$$PO_m^{\text{MT,min}} \cdot \sigma_{m,t}^{\text{MT,UC}} \leq PO_{m,t}^{\text{MT}} \leq PO_m^{\text{MT,max}} \cdot \sigma_{m,t}^{\text{MT,UC}} \tag{7}$$

$$\left| PO_{m,t}^{\text{MT}} - PO_{m,t-1}^{\text{MT}} \right| = PO_m^{\text{MT,RA}} \tag{8}$$

where $\text{PO}^{\text{MT,Min}}$/$\text{PO}^{\text{MT,Max}}$ and $\text{PO}^{\text{MT,RA}}$ are minimum/maximum power output and ramp limit of MT. The scheduling region of CHP units is formulated as Eqs. (9–14).

$$\text{PO}_{n,t}^{\text{CHP}} - \text{PO}_n^{\text{CHP,A}} - \frac{\text{PO}_n^{\text{CHP,A}} - \text{PO}_n^{\text{CHP,B}}}{\text{HE}_n^{\text{CHP,A}} - \text{HE}_n^{\text{CHP,B}}} \left(\text{HE}_{n,t}^{\text{CHP}} - \text{HE}_n^{\text{CHP,A}} \right) \leq 0 \tag{9}$$

$$\text{PO}_{n,t}^{\text{CHP}} - \text{PO}_n^{\text{CHP,B}} - \frac{\text{PO}_n^{\text{CHP,B}} - \text{PO}_n^{\text{CHP,C}}}{\text{HE}_n^{\text{CHP,B}} - \text{HE}_n^{\text{CHP,C}}} \left(\text{HE}_{n,t}^{\text{CHP}} - \text{HE}_n^{\text{CHP,B}} \right)$$
$$\geq -\left(1 - \sigma_{n,t}^{\text{CHP,UC}} \right) M \tag{10}$$

$$\text{PO}_{n,t}^{\text{CHP}} - \text{PO}_n^{\text{CHP,C}} - \frac{\text{PO}_n^{\text{CHP,C}} - \text{PO}_n^{\text{CHP,D}}}{\text{HE}_n^{\text{CHP,C}} - \text{HE}_n^{\text{CHP,D}}} \left(\text{HE}_{n,t}^{\text{CHP}} - \text{HE}_n^{\text{CHP,C}} \right)$$
$$\geq -\left(1 - \sigma_{n,t}^{\text{CHP,UC}} \right) M \tag{11}$$

$$0 \leq \text{HE}_{n,t}^{\text{CHP}} \leq \text{HE}_n^{\text{CHP,B}} \cdot \sigma_{n,t}^{\text{CHP,UC}} \tag{12}$$

$$0 \leq \text{PO}_{n,t}^{\text{CHP}} \leq \text{PO}_n^{\text{CHP,A}} \cdot \sigma_{n,t}^{\text{CHP,UC}} \tag{13}$$

$$\left| PO_{n,t}^{CHP} - PO_{n,t-1}^{CHP} \right| \leq PO_n^{CHP,RA} \tag{14}$$

where $PO^{CHP,A}$-$PO^{CHP,D}$ and $HE^{CHP,A}$-$HE^{CHP,D}$ are power/heat operation regions of CHP, $\sigma^{CHP,UC}$ is the commitment state of CHP, $PO^{CHP,RA}$ is ramp limit, and M is an adequately large number. Also, Eqs. (15–19) indicate the general constraints of MESS including BES, TES, HES, NGS, and CES. The level of energy stored at time t is shown by Eq. (15) and limited by Eq. (16). Equations (17) and (18) ensure that the amount of charging and discharging be within their allowed capacity limits:

$$SOC_{k,t}^{MESS} = SOC_{k,t-1}^{MESS} + \left(\begin{matrix} \eta^{MESS,ch}.ES_{k,t}^{MESS,ch} \\ -ES_{k,t}^{MESS,dch} / \eta^{MESS,dch} \end{matrix} \right) / ES_k^{MESS,Cap} \tag{15}$$

$$SOC_k^{MESS,min} \leq SOC_{k,t}^{MESS} \leq SOC_k^{MESS,max} \tag{16}$$

$$0 \leq ES_{k,t}^{MESS,ch} \leq ES_k^{MESS,Cap}.\sigma_{k,t}^{MESS,ch}.\left(1 - SOC_{k,t-1}^{MESS}\right) / \eta^{MESS,ch} \tag{17}$$

$$0 \leq ES_{k,t}^{MESS,dch} \leq ES_k^{MESS,Cap}.\sigma_{k,t}^{MESS,dch}.SOC_{k,t-1}^{MESS}.\eta^{MESS,dch} \tag{18}$$

where SOC^{MESS} is the state of charge (SoC) of the MESS and $SOC^{MESS, Min}$/$SOC^{MESS, Max}$ are minimum/maximum SoC. $ES^{MESS, ch}$ and $ES^{MESS, dch}$ are charged and discharged energy of MESS, $\sigma^{MESS, ch}$/$\sigma^{MESS, dch}$ are charge/discharge state, $ES^{MESS, Cap}$ is the storage capacity, and $\eta^{MESS, ch}$/$\eta^{MESS, dch}$ are charge/discharge efficiency. Equations (19) and (20) show the amount of natural gas consumed for generating energy in MTs and CHP units. Equations (21) and (22) show the amount of gas produced and consumed in H2G and G2H:

$$NG_{m,t}^{MT} = PO_{m,t}^{MT} / \left(10.55 \times \eta^{MT}\right) \tag{19}$$

$$NG_{n,t}^{CHP} = PO_{n,t}^{CHP} / \left(10.55 \times \eta^{CHP,EL}\right) + HE_{n,t}^{CHP} / \left(10.55 \times \eta^{CHP,TH}\right) \tag{20}$$

$$NG_{v,t}^{SMR} = 0.0225 \times \eta^{SMR}.\left[\left(HY_{v,t}^{SMR} / 0.27\right) + \left(CO_{v,t}^{SMR} / 44.01\right)\right] \tag{21}$$

$$NG_{w,t}^{NGR} = \left(0.0225 / \eta^{NGR}\right).\left[\left(HY_{w,t}^{NGR} / 0.27\right) + \left(CO_{w,t}^{NGR} / 44.01\right)\right] \tag{22}$$

where NG^{MT} and NG^{CHP} are consumed gas in MT and CHP, respectively, η^{MT} is the efficiency of MT and $\eta^{CHP, EL}$/$\eta^{CHP, TH}$ are electrical/thermal efficiency of CHP, HY^{SMR} and CO^{SMR} are H_2 and CO_2 consumed in SMR, respectively, HY^{NGR} and CO^{NGR} are H_2 and CO_2 produced in NGR, respectively, and η^{SMR}/η^{NGR} are efficiencies of H2G/G2H. Equation (23) shows the CO_2 that can be proposed in the CCS:

$$CO_{m,t}^{MT} + CO_{n,t}^{CHP} = \eta^{CO_2}.EM^{NG}.\left(NG_{m,t}^{MT} + NG_{n,t}^{CHP}\right) \tag{23}$$

where CO^{MT} and CO^{CHP} are captured and stored CO_2 from MTs and CHP, EM^{NG} is the emission rate of natural gas, and η^{SMR} is the efficiency of the CCS. Equations (24–28) show the power, heat, gas, hydrogen, and CO_2 balance at MEMG, respectively:

$$\sum_i PO_{i,t}^{Load} = \sum_m PO_{m,t}^{MT} + \sum_n PO_{n,t}^{CHP} + \sum_r PO_{r,t}^{RES} \\ + \sum_b \left[PO_{b,t}^{BES,dch} - PO_{b,t}^{BES,ch} \right] + \sum_e PO_{e,t}^{H2P} + \sum_f PO_{f,t}^{P2H} \tag{24}$$

$$\sum_i HE_{i,t}^{Load} = \sum_n \eta^{TES}.HE_{n,t-1}^{TES} - \sum_n HE_{n,t}^{TES} + \sum_n HE_{n,t}^{CHP} \tag{25}$$

$$NG_t^{NGG} + \sum_g \left[NG_{g,t}^{NGS,dch} - NG_{g,t}^{NGS,ch} \right] + \sum_v NG_{v,t}^{SMR} \\ = \sum_w NG_{w,t}^{NGR} + \sum_m NG_{m,t}^{MT} + \sum_n NG_{n,t}^{CHP} \tag{26}$$

$$\sum_h \left[HY_{h,t}^{HES,dch} - HY_{h,t}^{HES,ch} \right] + \sum_e HY_{e,t}^{P2H} + \sum_w HY_{w,t}^{NGR} \\ = \sum_f HY_{f,t}^{H2P} + \sum_v HY_{v,t}^{SMR} \tag{27}$$

$$\sum_c CO_{c,t}^{CCS} = \sum_m CO_{m,t}^{MT} + \sum_n CO_{n,t}^{CHP} + \sum_w CO_{w,t}^{NGR} - \sum_v CO_{v,t}^{SMR} \tag{28}$$

where PO^{Load} and HE^{Load} are power and heat loads, and PO^{RES} is the RES output.

3   Illustrative Implementations

Figure 2 illustrates the derived MEMG. The total operating cost of MEMG is minimized over a 24-hour scheduling. Table 1 shows the techno-economic data of the model and the forecasted values of energy prices. The installed capacity of renewable units includes a 150 kW WT and a 100 kW PV [12]. The hourly forecasted multipliers of renewable units, power, and heat demands are presented in Fig. 3 [13]. Plus, the power and heat load of each node are assumed to be 75 kW and 28 kWth, respectively.

Figure 4 shows the power balance in the MEMG. The power is converted into H_2 in hours 6, 10, 11, and 23 and converted into power again in peak hours. Also, the BES is charged in hours 16–19 and the power output of MTs is enhanced between hours 9 and 24. Figure 5 shows the gas balance in the MEMG. To cover the consumed gas of CHP and MTs, gas is purchased from the gas grid. Besides, H_2 produced in hours 6, 10, 11, and 23 is converted into gas. Also, the NGS is charged in hours 5–8 and discharged in hours 17–21 to reduce the peak load cost. Figure 6
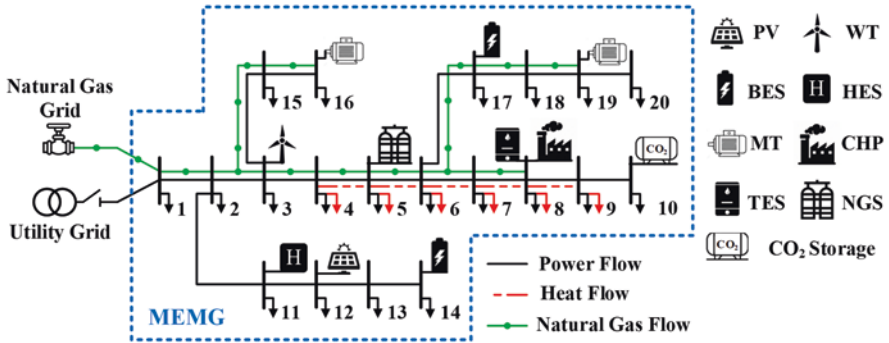
Fig. 2 MEMG test system

Table 1 Techno-economic input data of the proposed optimization model

Item	Value	Item	Value	Item	Value	Item	Value
a_1^{MT}	0.060	$\varphi^{CHP,1}$	4.35E-08	$PO^{CHP,A}$	494	$HE^{CHP,A}$	0
a_2^{MT}	0.024	$\varphi^{CHP,2}$	0.0145	$PO^{CHP,B}$	430	$HE^{CHP,B}$	360
b_1^{MT}	30	$\varphi^{CHP,3}$	26.5	$PO^{CHP,C}$	162	$HE^{CHP,C}$	209
b_2^{MT}	35	$\psi^{CHP,1}$	3E-08	$PO^{CHP,D}$	198	$HE^{CHP,D}$	0
$PO_1^{MT,max}$	450	$\psi^{CHP,2}$	0.0042	μ^{H_2}	0.15	μ^{NGG}	0.28
$PO_2^{MT,max}$	330	$\psi^{CHP,3}$	0.031	μ^{CH_4}	0.84	μ^{CO_2}	0.02
$PO^{MT,Min}$	0	EM^{NG}	1951.75	$SOC^{MESS,Min}$	0.2	$SOC^{MESS,Max}$	0.9
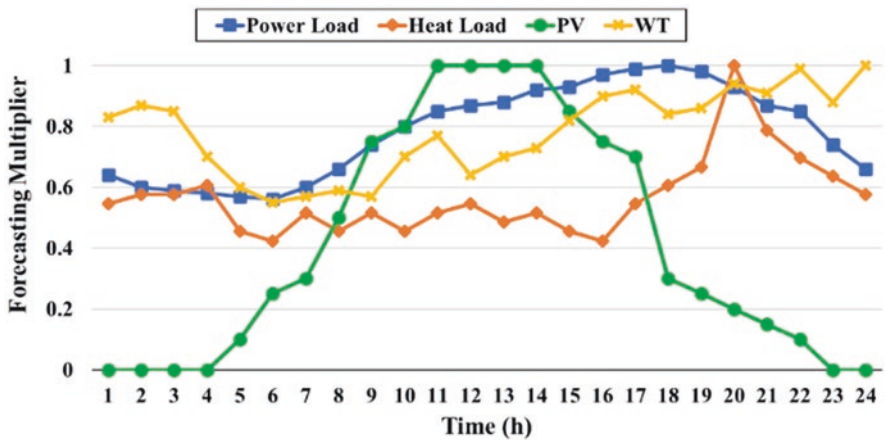
Fig. 3 Hourly forecasted multipliers of renewable units, power, and heat demands
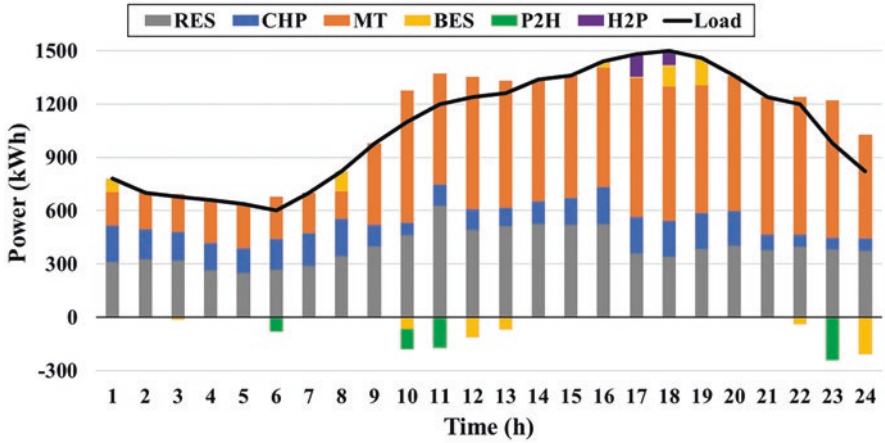
Fig. 4 Power balance in MEMG
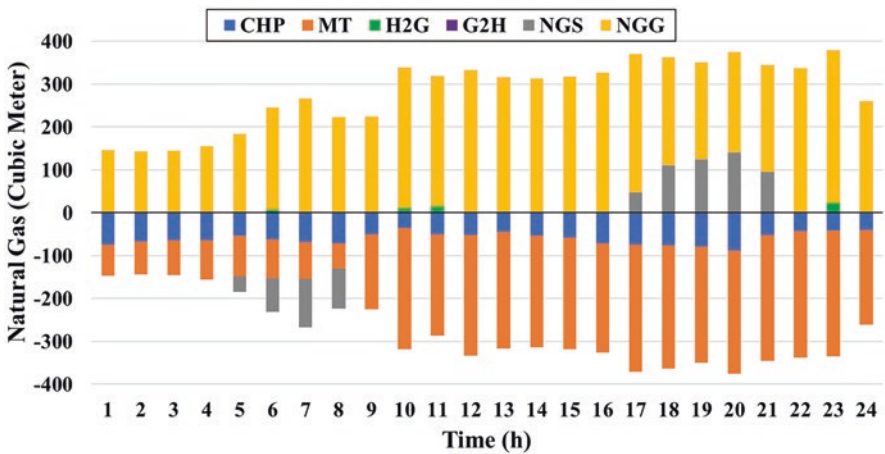
Fig. 5 Natural gas balance in MEMG

shows the CO_2 produced from CHP and MTs and stored in CES as well as the amount of CO_2 required in H2G.

Table 2 indicates the detailed cost results of the MEMG. It can be seen that although the prices of energy conversion in P2H, H2P, and H2G are high, their operating costs are much lower compared to other generation costs of CHP and MTs. However, if power network is connected to the upstream grid, the operating costs will decrease.
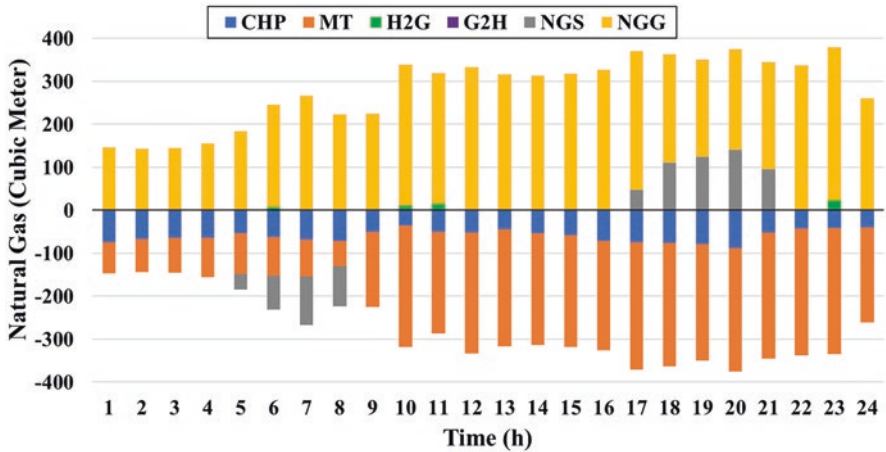
Fig. 6 CO2 balance in MEMG

Table 2 Detailed cost results of the MEMG

Cost	$\mathscr{C}^{MT}$	$\mathscr{C}^{CHP}$	$\mathscr{C}^{P2H}$	$\mathscr{C}^{H2P}$	$\mathscr{C}^{SMR}$	$\mathscr{C}^{NGR}$	$\mathscr{C}^{NGG}$	$\mathscr{C}^{CCS}$	Total Cost
Value ($)	1846.19	697.40	90.62	31.18	48.10	0.00	1738.00	196.00	4647.50

4   Conclusions

This chapter proposed an optimal operation of an electrically islanded MEMG considering CCS, P2H, and P2G along with the CES, HES, and NGS as the multi-energy storage systems. The derived model was simulated over an islanded MEMG with 20 buses minimizing the total operating cost. Analyzing the simulation results shows the advantage of the proposed CCS and P2G facilities. Despite the high cost and low efficiency of the P2G, applying this technology can be beneficial in an electrically islanded MEMG. The advantages of the proposed model are as follows:

- Can be applied in large energy systems, when the RESs' output is high.
- Can maintain continuous scheduling as a flexible multi-energy storage.
- Can be an acceptable opportunity to investigate the CO_2 via CCS technology to obtain required hydrocarbons via chemical reaction for P2G, which are being developed to mitigate growing air pollution.
- Finally, hydrogen production can contribute to the clean-mobility sector.

Furthermore, due to the architecture of MEMGs, the self-healing concept can be studied in future research to realize the related capabilities.

References

1. Madejski, P., Chmiel, K., Subramanian, N., Kuś, T.: Methods and techniques for CO2 capture: review of potential solutions and applications in modern energy technologies. Energies. **15**(3), 887 (2022)

2. Sadeghi, D., Ahmadi, S.E., Amiri, N., Satinder, M.M., Abusorrah, A., Rawa, M.: Designing, optimizing and comparing distributed generation technologies as a substitute system for reducing life cycle costs, CO2 emissions, and power losses in residential buildings. Energy. **253**, 123947 (2022)

3. Ahmadi, S.E., Kazemi-Razi, S.M., Marzband, M., Ikpehai, A., Abusorrah, A.: Multi-objective stochastic techno-economic-environmental optimization of distribution networks with G2V and V2G systems. Electr. Power Syst. Res. **218**, 109195 (2023)

4. Ahmadi, S.E., Sadeghi, D., Marzband, M., Abusorrah, A., Sedraoui, K.: Decentralized bi-level stochastic optimization approach for multi-agent multi-energy networked micro-grids with multi-energy storage technologies. Energy. **245**, 123223 (2022)

5. Ahmadi, S.E., Marzband, M., Ikpehai, A., Abusorrah, A.: Optimal stochastic scheduling of plug-in electric vehicles as mobile energy storage systems for resilience enhancement of multi-agent multi-energy networked microgrids. J. Energy Storage. **55**, 105566 (2022)

6. de Miranda, P.E.V.: Chapter 5.3.3-application of hydrogen by use of chemical reactions of hydrogen and carbon dioxide. In: Science and Engineering of Hydrogen-Based Energy Technologies, pp. 279–289. Academic Press (2019)

7. Zhao, P., Xu, W., Liu, A., Wu, W., Wang, J., Wang, X.: Assessment the hydrogen-electric coupled energy storage system based on hydrogen-fueled CAES and power-to-gas-to-power device considering multiple time-scale effect and actual operation constraints. Int. J. Hydrog. Energy. (2022)

8. Jiang, J., Zhang, L., Wen, X., Valipour, E., Nojavan, S.: Risk-based performance of power-to-gas storage technology integrated with energy hub system regarding downside risk constrained approach. Int. J. Hydrog. Energy. **47**(93), 39429–39442 (2022)

9. Siqin, Z., Niu, D., Wang, X., Zhen, H., Li, M., Wang, J.: A two-stage distributionally robust optimization model for P2G-CCHP microgrid considering uncertainty and carbon emission. Energy. **260**, 124796 (2022)

10. Ju, L., Yin, Z., Lu, X., Yang, S., Li, P., Rao, R., Tan, Z.: A tri-dimensional equilibrium-based stochastic optimal dispatching model for a novel virtual power plant incorporating carbon capture, power-to-gas and electric vehicle aggregator. Appl. Energy. **324**, 119776 (2022)

11. Yuan, Z., Wang, W., Li, J.: Carbon dioxide recycling in hydrogen-based energy systems using power-to-gas facility and stochastic multi-objective optimization. J. Clean. Prod. **135892** (2023)

12. Daramola, A.S, Ahmadi, S.E., Marzband M., Ikpehai, A.: A cost-effective and ecological stochastic optimization for integration of distributed energy resources in energy networks considering vehicle-to-grid and combined heat and power technologies. J. Energy Storage 57, 106203 (2023)

13. Ahmadi, S.E., Rezaei, N., Khayyam, H.: Energy management system of networked microgrids through optimal reliability-oriented day-ahead self-healing scheduling. Sustain. Energy Grids Netw. **23**, 100387 (2020)

The Coordination Control Strategy of Clustering PCS and Its Application

Daxing Li, Guilian Ma, Qingguang Yu, Yixiang Cheng, Sihui Li, Weixi Sun, YuTong Man, Zihao Wang, and Zitong Wang

1 Introduction

In recent years, there have been numerous cases of fire and other accidents in energy storage power stations. For example, on April 16, 2021, an explosion occurred at an energy storage power station located in Beijing. This was the most serious energy storage power plant safety accident in recent years, casting a heavy shadow over the booming energy storage industry. The reasons for the accident are that there are problems in the energy storage control system, so it is necessary to control the energy storage system to achieve stability inside the energy storage system, so as to avoid the occurrence of accidents. For the control of energy storage system, in fact, a lot of strategies have been proposed and a lot of technologies have been invented.

A research team designed a controller with the following characteristics: (1) The controller is the core coordination control device between the upper-level energy management system of the energy storage power station and the field equipment. Its hardware is based on the embedded architecture, and its software is based on the SOA architecture, which has very good versatility and scalability. (2) Combined with the user-side energy storage peak-valley arbitrage strategy of demand control and inverse power protection, the charge-discharge curve can be flexibly adjusted according to the price policy, and can be applied to the current peak-valley price and the future market price [1].

There are many similar studies, such as the research on the background of DC microgrid busbar voltage control is applied. From the DC microgrid bus voltage fluctuation reasons, resonant three-port bus voltage controller topology and control

D. Li · G. Ma
State Grid Jibei Electric Power Co. Ltd, Chengde Power Supply Co, Hebei, China

Q. Yu (✉) · Y. Cheng · S. Li · W. Sun · Y. Man · Z. Wang · Z. Wang
Tsinghua University, Beijing, China

methods, etc. [2], a research on the operation characteristics and control strategy of the in-phase power supply system with hybrid energy storage [3], distribution network coordinated control based on distributed power and energy storage, and distribution network coordinated control considering TOU price of two control methods [4], a research that improved variable parameter sagging control method [5], an energy storage controller based on backpull-Model predictive control [6].

Although these studies have put forward a lot of effective schemes, there are still some problems and they cannot meet the specific needs. Therefore, this chapter puts forward a brand new energy storage co-control controller to meet the special needs.

2 Generalization of System Function

The control system aims to accomplish accurate and rapid power scheduling. Depending on the innovative control algorithm of active power and reactive power, it can regulate the bidirectional flow of electric energy with millisecond precision under different operation modes, thus conforming the unstable and unbalanced characteristic of clean energy and guaranteeing the safety of the power grid. The controller also has the function of AI learning and the graphical user interface, which can relieve the contradiction between energy supply and requirement and increase the profit of energy storage.

2.1 System Composition

Figures 1 and 2 show the control strategy to cluster PCS. When the instructions are transferred to the energy storage system, the controller monitors the three-phase current and voltage of the bus bar. Then it distributes the target power to each PCS.

Figure 3 shows the hardware structure of the control system. The system determines the most appropriate and efficient active/reactive control algorithm automatically according to the priorities of different control policies. Considering the prepared strategy with the actual state of the power grid, the system generates control instructions to each energy storage system (ESS), which achieves economic benefit and sustainable development.
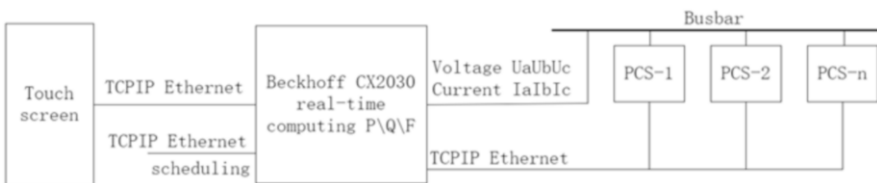
Fig. 1 Diagram of the control system composition
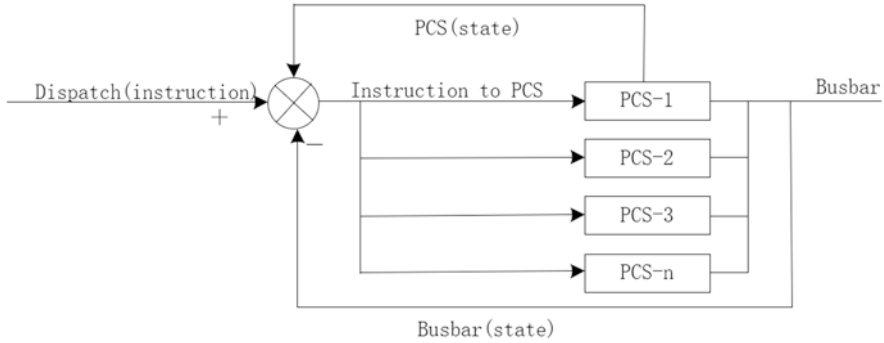
Fig. 2 Diagram of the control structure
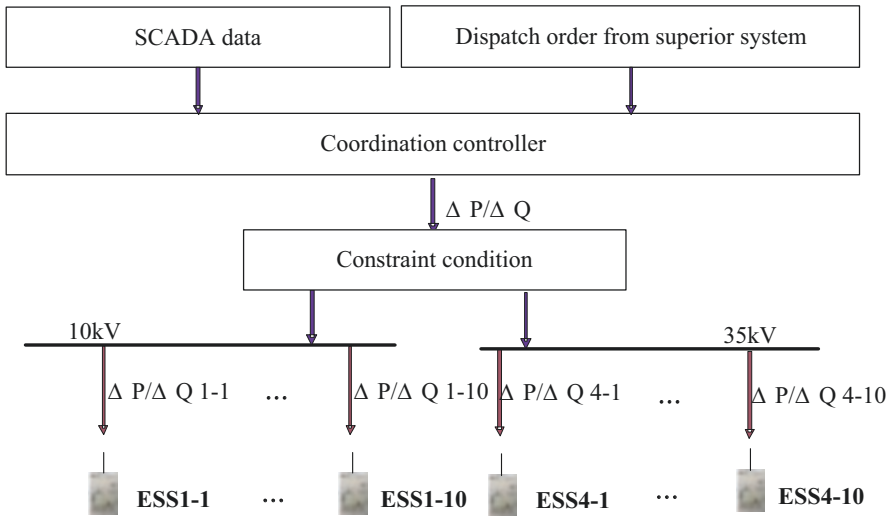
Fig. 3 Hardware structure

2.2   *Control Algorithm*

Once the frequency of the current deviates from the rated value, the controller calculates the active power target of each PCS. So, the increase or decrease of the active power can be limited and the active power can be restored.

After receiving the voltage control target of the bus bar, the system dynamically calculates the equivalent impedance of the energy storage station. As the result, the total reactive power can be allocated to each PCS. Moreover, the controller monitors the reactive power data in real time, thus realizing a closed loop automatic control pattern.

2.3   Artificial Intelligence Algorithm

The system monitors and collects PCS operating data such as the voltage, current, and active power in time. Under the condition of satisfying the system load requirements and the expected quality of the electric energy, the system achieves the power flow which can get the highest financial earnings by controlling the switch of the unit and distributing the active power of each unit.

As for the cluster of PCSs, the system uses greedy algorithm. After calculating the optimal solution of the economic function of each PCS in a short period of time, the total operating cost within the whole research reaches the overall minimum, thus realizing the optimization of dynamic control strategy [7].

3   The Coordinated Control Algorithm

Currently the optimization algorithm used is a multi-objective algorithm for composite energy storage. First, multiple sub-targets are aggregated into a single function by linear weighting method, and then the fitness difference sorting method of objective function is proposed to determine the weighting coefficient.

First, the objective function of compound energy storage is multiplied by a group of weight coefficient λ_j according to its importance, and then added to aggregate into a single objective function with a positive coefficient, and then the optimal solution is found on the constraint set X. The objective function in this article is:

$$\begin{cases} \min f_{(x)} = \lambda_1 f_1 + \lambda_2 f_2 + \lambda_3 f_3 + \cdots \\ \quad\quad s.t. \quad x \in X \end{cases} \tag{1}$$

Then, using the sorting method of the fitness difference of the objective function, the weighted coefficient of the expected value of the different target adjusts by numerical calculation.

The separation sorting procedure is as follows:

1. Suppose that there are m targets, find the optimal solution of each single target respectively, write as x_i.
2. Substitute the optimal solution of each objective function into different objective functions to obtain the corresponding objective function value f_i^j.
3. Calculate the deviation of each objective function δ_i^j when the optimal solutions x_i is different.
4. Calculate the average deviation of every target:

$$u_i = \frac{1}{m-1} \sum_{j=1}^{m} \delta_i^j \ i = 1, 2, \ldots, m \tag{2}$$

5. Calculation weight coefficient:

$$\lambda_i = \frac{u_i}{\sum_{j=1}^{m} u_j} \quad i = 1, 2, \ldots, m \tag{3}$$

Since the deviations are all non-negative, the weight coefficients calculated bythe above process are all positive, and $\sum_{i=1}^{m} \lambda_i = 1$.

6. In order to balance the range of effective solutions, the above weight coefficient is sorted according to the size. The objective function is reconstructed by multiplying the objective function with large mean difference by the small weight coefficient, and the objective function with small mean difference multiplied by the large weight coefficient [8].

After receiving the total allocated active power instruction, the system will regard the most economic and energy storage equipment life longer for the optimization goal, by obtaining the real-time SOC, active power output, and state parameters and update the constraint condition such as energy storage system SOC upper limits and lower limits, climbing speed, and so on to ensure that the energy storage response can meet the requirements of total active power index, and then the system will give the instruction of energy storage response to active power output. The specific process is shown in Fig. 4.

Fig. 4 Active power distribution algorithm system architecture
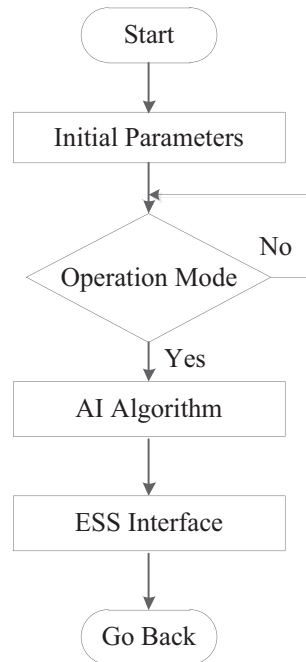
4   The Implementation of the System

4.1   Simulation Realization

Having the basic algorithm, the next step is to make a test, by using Matlab Simulink. It provides an integrated environment for dynamic system modeling, simulation, and integrated analysis. In this environment, a complex system can be constructed without a lot of writing programs, and just through a simple and intuitive mouse operation. Simulink model is usually composed of three parts: the input signal source, the system, and the receiving module. After building the three parts, run the model to make sure of its correctness [9]. This project developed the AI control technology based on the greedy algorithm, which can increase the intelligence and stability of the system energy distribution.

Having built a correct Simulink system, it is expected to get the desired result when we input real-time data. Further, our project demands to make the system achieve closed loop. So TwinCAT3.0 could meet our needs. Use Simulink coder to generate c code. In this way, a module is created in TwinCAT. To let it run normally and legally, an OEM license is needed to sign the generated model and add a whitelist in the registry to open the operating system test mode. Now the module could download on TwinCAT with permission. Then, create a Plc file and use ST programming language to connect the input and output variable. In this way TcCOM and PLC program closed loop can be achieved in Fig. 5.

Fig. 5 Control strategy from Simulink platform to TwinCAT platform
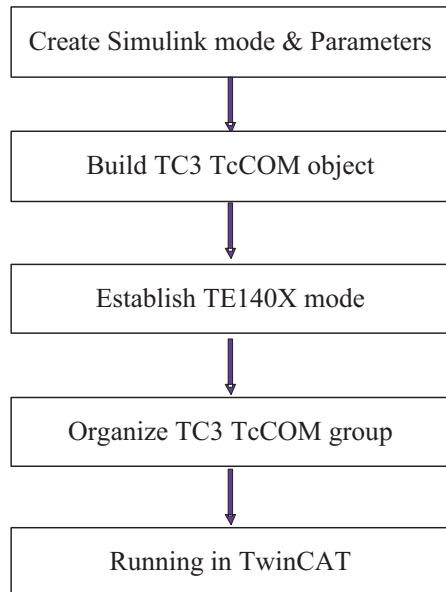
4.2   The Graphical User Interface Realization

The graphical user interface (GUI) designed by this project can support users to complete remote control of the system by touch screen. Users can choose to monitor or control the system based on account types. Only authorized users can get access to service and data, ensuring the security of GUI. The GUI is composed of system monitoring pages, historical query pages, and other parts, which can complete multiple functions such as independent data collection, alarm processing, event recording, and so on [10].

Users can access the PCS detection page through the link on the system overview page to monitor the specific operation of each PCS, and obtain clear and intuitive data that belongs to PCS on this page. The battery detection page allows users to monitor the running status of each battery set. When parameters such as temperature of the battery pack are abnormal, the battery detection page sends an alarm for users to find and maintain the battery pack in time, reducing the damage caused by accidents. In addition to the system monitoring page, users can also enter the historical query pages to query historical alarm information and historical control strategy. The system can accept clock synchronization to ensure the consistency of system time. Users can define various daily, monthly, and annual reports as needed, with precise timing, and the system has functions such as real-time/summon-to-print functions, which brings convenience for users in Fig. 6.
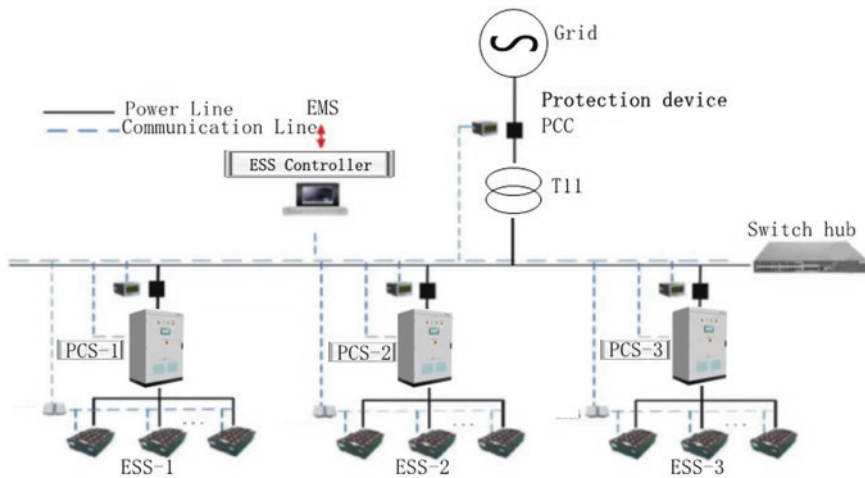
Fig. 6 System parameters page

Fig. 7 System implementation

5 System Implementation Installation

Figure 7 shows the realization of the system structure. With the reasonable system deployment and the efficient algorithm, the controller can realize the millisecond precision modulation and make the most accurate instructions to every element in the system, thus making the real-time and dynamic control strategy possible.

6 Conclusion

The controller can achieve rapid and accurate adjustment of all PCSs, thus greatly improving the performance of the energy storage station in the primary frequency modulation, dynamic reactive voltage response, and other aspects, ensuring to realize safe and stable operation of the power grid and ideal economic benefit. The function of the controller not only corresponds to the technical demand of the energy storage, its control strategy also boosts the construction of the new energy, which makes the energy structure of China more economic and environmentally friendly.

References

1. Li, H.: Design and implementation of user side energy storage controller based on embedded architecture. Zhejiang Electric Power. **39**(5), 27–34 (2020)
2. Wei, L.: Research on Bus Voltage Controller of Hybrid DC Microgrid with Three-port Energy Storage. 2021.01
3. Yilin, C.: Modeling and Coordinated Control Strategy Research of Inphase Power Supply System with Hybrid Energy Storage. 2022.05
4. Wen, C.: Research on Coordinated Control Method of Distributed Power and Energy Storage in Distribution Network. 2022.03

5. Ruizhi, W., Zhongxiao, C., Gang, Q., et al.: Research on coordinated control strategy of multi-energy storage in DC distribution network. Appl. Notes. **8**, 86–89 (2019)
6. Hong, L., Liwei, Z., Chenglong, Z., et al.: Design of energy storage controller based on backward pull-model predictive control. J. Nanjing Univ. Nat. Sci. **19**(3), 43–48 (2021)
7. Weizhong, B., et al.: The profit model and operation strategy of the energy storage station. China Acad. J. Electron. Publ. House. (2022)
8. Xingguo, T., Hui, W., Li, Z., et al.: Multi-objective optimization allocation method and evaluation index of microgrid complex energy storage. Power Syst. Autom. **38**(8), 7–14 (2014)
9. Hizkiel, N.A.: Energy management system for grid-connected solar photovoltaic with battery using MATLAB simulation tool. Cogent. Engineering. **7**(1) (2020)
10. Axel, G., et al.: First-principles modeling of electrochemical interfaces for energy storage[J]. Abstr. Pap. Am. Chem. Soc., 248 (2014)

Types of Grid Scale Energy Storage Batteries

Moses Jeremiah Barasa Kabeyi and Oludolapo Akanni Olanrewaju

Abbreviations

AIHBs	Aqueous ion hybrid batteries
BESS	Battery energy storage system
C	Charging costs
CAPEX	Capital expenditure
EEE	Electrical energy storage
EES	Electrical energy storage
ES	Energy storage
GLEES	Grid-level large-scale electrical energy storage
IQR	Interquartile range
LCBs	Lead-carbon batteries
LCOE	Levelized cost of energy
LCOS	Levelized cost of storage
Li-ion	Lithium-ion batteries
OM	Operation and maintenance

1 Introduction

Electricity is a dominant form of energy but limited by variations in instantaneous demand daily and seasonally. Energy storage is useful in balancing the demand and supply of electric power. The grid-level large-scale electrical energy storage

M. J. B. Kabeyi (✉) · O. A. Olanrewaju
Industrial Engineering Department, Durban University of Technology, Durban, South Africa
e-mail: mkabeyi@uonbi.ac.ke; oludolapoo@dut.ac.za

181

(GLEES) is a process used to convert energy from a grid-scale power network into a storable form for later conversion to electricity [1]. Many battery chemistries are either available or under investigation for grid-scale storage applications. They include lithium-ion, lead-acid, redox flow, and molten salt (including sodium-based chemistries). The use of utility-scale battery storage makes power systems more responsive to fluctuations in demand and supply and more flexible. Batteries support greater integration of variable renewable sources of energy to the grid, by storing energy from variable sources like solar and wind for later use. There is growing need for more flexible power systems to ensure more variable renewable sources are integrated efficiently and reliably. The battery storage systems have emerged as a potential solution to improve power system flexibility because of their ability to quickly absorb, hold, and then reinject electricity. Utility-scale battery storage systems' capacity ranges from a few megawatt-hours (MWh) to hundreds of MWh. Different battery storage technologies like lithium-ion (Li-ion), sodium sulfur, and lead acid batteries can be used for grid applications. Recent years have seen most of the market growth dominated by in Li-ion batteries [2, 3]. The global increase in use of small-scale and distributed generation, and use of variable renewable have led to high demand for electrical energy storage systems (ESS), which applies to different storage devices. They include electrochemical storages, super capacitors, gravity batteries, etc. The challenge is that we have no universally accepted economic indicator which for use in comparing compare different energy storage systems unlike in power plant planning where "Levelized Cost of Electricity (LCOE)" has been accepted [4]. Combining storage and renewable in a power system improves flexibility, which promotes adoption of renewable energy by ensuring security of the power grid. The future energy systems dominated by renewable energy will require large-scale and wide application of energy storage technologies [5].

Levelized cost of storage (LCOS) refers to the ratio between total costs of acquisition and operation costs of a storage system to the cumulated energy generated produced by the storage system or device. LCOS is applied in various investigations to assess different storage technologies, for example, pumped-storage hydroelectricity, compressed air energy storage, battery technologies like lithium-ion, lead, and vanadium redox flow batteries and power to gas [6, 7]. About 7200 gigawatts (GW) of electricity capacity must be built globally to keep pace with growing electricity demand and to replace retiring power plants by 2014. Future power systems are expected to have large proportions of intermittent power like wind, solar, and tidal generation and/or inflexible, nuclear, coal, etc. There is a need to scale-up energy storage to match the electricity supply with hourly, daily, and seasonal electricity demand profiles. According to the International Energy Agency, about 310 GW grid-connected electricity storage capacity will be needed by the USA, Europe, China, and India [8].

The main cause of growing use of energy storage is interest in small-scale and distributed generation, and use of renewable energy sources. There is however no generally accepted economic indicator for comparison of different energy storage systems, unlike in the planning of power plants which mainly use the "Levelized Cost of Electricity (LCOE)," which has now been modified. For application in

electrical energy storage systems, this derived indicator is called "Levelized Cost of Storage (LCOS)." However, the LCOS calculation procedure is not yet approved but its popularity has been growing [9]. Levelized cost (LCOS) quantifies discounted cost per unit of power discharged for a given storage technology and application. Therefore, the levelized cost of energy is used to account for the technical and economic parameters that affect the lifetime cost of discharging stored electricity. LCOS is equivalent to LCOE for generation technologies, but represents an appropriate tool used for comparing the costs of storage technologies [10].

1.1 Problem Statement

It is difficult to assess the cost of electricity storage technologies because of the diversity of technologies with different costs and performance characteristics as well as varying storage requirements. Studies on future costs have so far limited investment cost of storage technologies. The result of this is that the future role of electricity storage is seen as highly uncertain even with remarkable growth in deployment of storage technologies and applications [10].

The capacity of power generation by renewable energy like wind and solar is variable and intermittent, making it difficult to supply stable power for the system. Curtailment of solar and wind is costly, yet you cannot simply store electricity. This leads to insufficient renewable energy adoption. The combination of energy storage and renewable energy in power operation has significant advantages in improving the flexibility of a power system, promoting renewable energy adoption, and ensuring the security of the power grid [5].

Many studies have been carried out on the LCOS, but we are yet to have a common definition of LCOS. Some studies neglect parameters like replacement or disposal, cost, while others exclude specific performance parameters, like capacity degradation. Industry reports tend to hide their methodologies while academic studies tend to cover limited number of storage technologies and applications, with all focusing only on current LCOS. There is limited research analyzing the economics of large-scale electrical energy (EES) deployment. Therefore, it is necessary to employ the LCOS for evaluation of domestic EES projects [5].

1.2 Rationale of the Study

The transition to renewable energy supply requires significant storage capacity for electricity. Optimization requires a move beyond the electricity-only concentration to have a holistic energy system view for integrating renewable energy. Storage is not the optimum solution for integration of large intermittent and variable renewable energy as more efficient and cheaper options can be found through integration

of the power sector and other parts of the energy system through the creation of smart energy system [11].

Uncertainties around the future role of electricity storage can be reduced by increasing the transparency of and application of lifetime cost of various storage technologies and their competitiveness in diverse applications [10]. The electricity generation capacity of variable and intermittent renewable energy like wind and solar makes it difficult to provide a stable and reliable power supply for the system. It is difficult to simply store electricity while wind and solar curtailment is costly, leading to insufficient renewable energy adoption. By combining energy storage and renewable energy in power operation significantly improves power system flexibility, increases renewable energy absorption, and provides security of the power grid. With future power systems being dominated by renewable energy, energy storage demand is set to increase significantly [5, 12].

To achieve carbon neutrality, the establishment of a "near-zero emission" energy system based primarily on renewable energy is indispensable. Energy storage is the overriding technology that can accelerate energy transition and mitigate the mismatch between electricity supply and demand. Development of energy storage is mediated by the maturity of technology, capacity allocation optimization, system optimization, and scheduling of energy storage and energy storage policy. Reduction in energy storage technology cost will shorten the payback period of investment. The LCOS is considered as one of the international energy storage cost evaluation indexes [3, 5].

Energy storage can be classified into physical energy storage, electrical energy storage (EES), superconducting magnetic energy storage, super capacitors, and hydrogen energy storage used for three main applications, that is, large-capacity energy storage, transmission and distribution support services, and frequency regulation applications. Specific energy storage techniques include pumped storage systems, compressed air systems and chemical batteries, lead-carbon, lithium iron phosphate, and vanadium redox. Although electrical energy storage is developing rapidly, the economics of electrical energy technologies are quite ambiguous, which restricts the development of EES [5, 13].

1.3   Methodology

Although useful and actively applied, there is no generally accepted definition of a LCOE storage, which is a derivative of LCOE [14]. LCOS can facilitate the verification of the economic viability of some storage technologies for a given power system. The LCOS employs storage technology characteristics instead of generator characteristics in assessment. The process requires an understanding of the following:

(i) Absolute price at which electricity is discharged is of minor importance compared to average price spread between charged and discharged electricity to determine revenue.

(ii) Computed required price spread may not be directly comparable to available price spreads in the market because limited energy storage capacity can limit storage from charging and discharging based on optimal moments.

(iii) Obtainable arbitrage revenue may be lower than the possible obtainable price spread because of the cost of losses in efficiency.

(iv) The LCOS metric does not consider possible revenues earned by the investor due to assistance for ancillary services [14]

2 Storage Systems

Energy storage involves storing energy by means of equipment or media for release when needed. Energy storage facilitates temporal and spatial transfer electricity and effectively isolates generation and utilization of electricity. This will eliminate the peak valley difference of day and night power consumption, improve resource utilization efficiency, and enable large-scale connection of renewable energy sources to the grid. Energy storage application improves the peak shaving and frequency modulation ability of the power system, reduce the investment in development of peak-shaving power plants reserve capacity, and expansion of power transmission and distribution [5]. EES technology has wider applications in power systems due to their high-energy density, fast response, high specific power, flexible installation, high reliability, long life, etc. The most commonly used EES technologies are lead, lithium iron, flow batteries, Na-S, and super capacitors [5].

LCOS is the total lifetime cost of the investment in an electricity storage technology divided by its total or cumulative delivered electricity delivered. This reflects the internal average price that the electricity is sold for the project's net present value to be zero. The LCOS for various technologies and life cycle cost of energy (LCOE) for generation technologies can be compared directly but involves different concepts of providing electricity and leading to differences in cost calculation methods hence their different names [10].

2.1 The International Installed Capacity of Energy Storage and EES

By the end of 2020, about 191.1 GW of energy storage capacity had been put into operation globally with the proportion of EES being about 7.5%, exceeding 10 GW with lithium ion batteries having the largest capacity accounting for about 92% of the total installed capacity of EES [5]. The global installed capacity of storage is shown in Fig. 1.

Figure 1 shows the global installed capacity of storage between 2014 and 2020. It shows that capacity grew from 139 GW in 2014 to 191.1 GW in 2020.

Different storage technologies used globally right from electrical to thermal storage technologies. They are showed in Fig. 2.
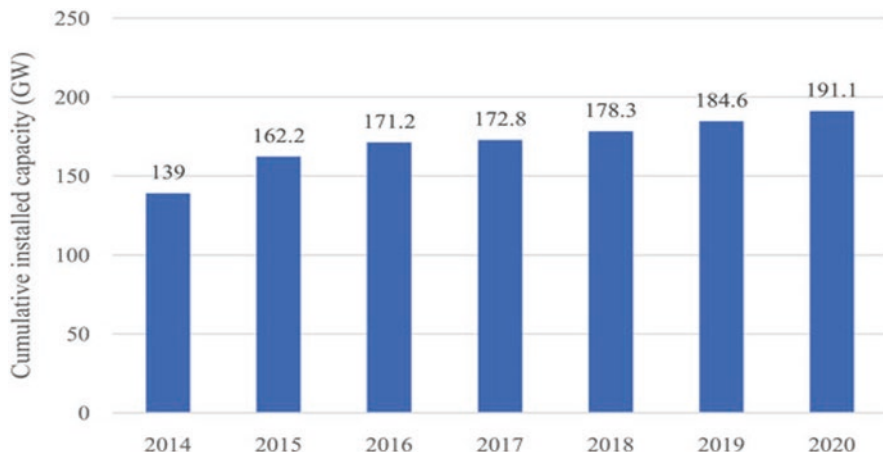
Fig. 1 Global installed capacity of storage
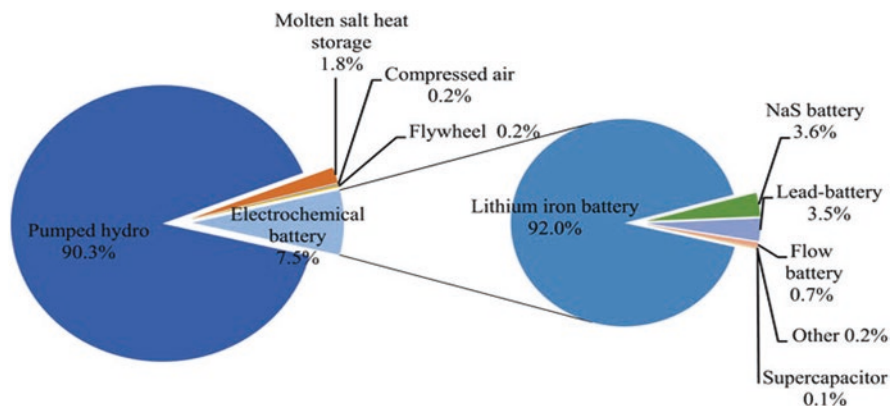
Fig. 2 Share of different storage technologies

In Fig. 2 it is noted that pumped storage is the most dominant technology used accounting for about 90.3% of the storage capacity, followed by EES. By the end of 2020, the cumulative installed capacity of EES had reached 14.2 GW. The lithium-iron battery accounts for 92% of EES, followed by NaS battery at 3.6%, lead battery which accounts for about 3.5%, flow battery 0.7%, supercapacitor 0.1%, and others 0.2%.

The cumulative installed capacity and growth rate of the global EES in 2014–2020 [5] are shown in Fig. 3.

From Fig. 3, it is shown that the cumulative storage capacity of EES grew from 893.5 GW in 2014 to 14.247.3 kW in 2020. The highest growth in capacity was realized between the year 2017 and 2018 at 126.39% and the least growth was realized between 2024 and 2015 at 30.02%.
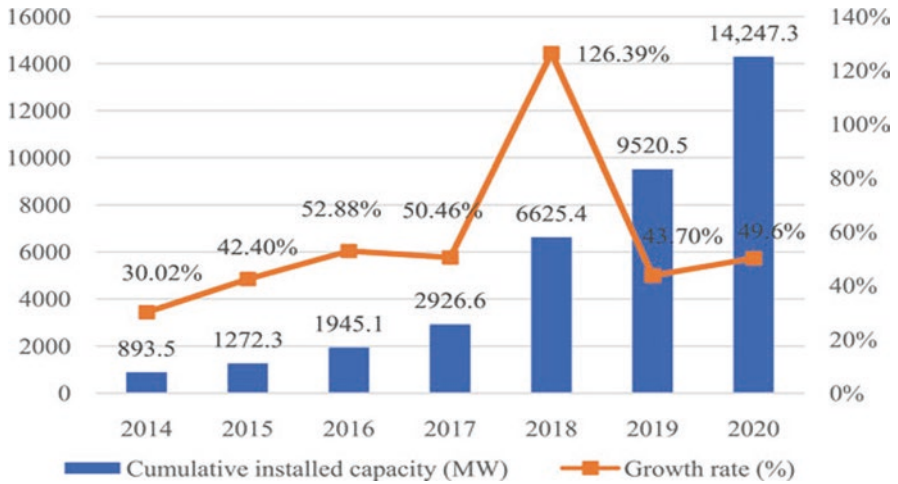
Fig. 3 Cumulative storage capacity of EES

3 Grid Scale Storage Battery Solutions

According to the Energy Storage Association of North America, market application of batteries is divided into front of the meter (FTM) and behind-the-meter (BTM) applications. Front of meter (FTM) batteries are systems connected to distribution or transmission networks or can be connected to the generation asset providing services like ancillary services or network load relief. Behind-the-meter (BTM) batteries are interconnected behind the utility meter of customers, aimed at electricity bill savings through demand-side management [2, 15]. There are many types of commercially available batteries globally, for example, lithium-ion (Li-ion), absorbed glass mat valve-regulated lead-acid (AGM-VRLA), gel valve-regulated lead-acid (Gel-VRLA), Lead-carbon (LCB), and Aqueous Ion Hybrid (AIHB) batteries [6]. The most extensively used rechargeable batteries are the lead batteries mainly due to their reliability, safety, and well-established worldwide supplier base [16].

3.1 Solid State Versus Flow Batteries

The solid-state batteries like lithium-ion store energy in solid electrode material like metal, while flow batteries store energy in electrolyte liquids. Many conventional energy storage batteries with flow batteries make use of two electrolyte liquids, with one at the node and the other at the cathode.

Solid State Batteries

A *solid-state battery* applies solid electrodes and a solid electrolyte, instead of a liquid or polymer gel electrolytes used in lithium-ion or lithium-polymer batteries. Solid electrolytes were first discovered in the nineteenth century, but their widespread development is limited by several drawbacks [17]. The solid-state batteries have potential solutions to many challenges facing liquid Li-ion batteries, like flammability, low voltage, unstable solid-electrolyte interphase formation, low strength, and poor cycling performance. Materials used in solid electrolytes include ceramics like oxides, sulfides, phosphates, and solid polymers. The solid batteries have applications like pacemakers, RFID, and wearable devices. They are generally safer, with higher energy densities, but expensive. The challenges facing the development of solid state batteries include limitations with respect to energy and power density, lower durability, high material costs, sensitivity, and stability [17, 18].

The solid-state batteries are proving to be a viable and cheaper option for next-generation traction batteries at high performance and safety. Liquid electrolytes are characterized by high ionic conductivity like $\sim 10^{-3}$ S cm^{-1} at room temperature with almost no electronic conductivity, can operate well over a wide range of temperature from tens of degrees below 0 °C to about 100 °C. The main disadvantages of liquid electrolyte batteries are high flammability, highly resistive at electrodes leading to capacity loss, electrolytic decomposition at high voltages which limit the use of high voltage cathode materials, formation of HF at thermal runaway, and the risk of leakage. Most of these weaknesses of liquid electrolyte batteries are addressed by solid state batteries like solid electrolyte lithium-ion cells that enable higher operating temperatures due to better thermal stability [18].

The future of solid-state batteries is that they will become real substitutes for lithium-ion batteries and are focused on applying a sulfur-based electrolyte to provide a more efficient power transfer. The use of solid-state batteries would reduce the risk of fires and increase the energy density. These next-generation batteries, like solid-state and metal-air batteries, are safer and have higher performance than lithium-ion batteries [19, 20]. All-solid-state batteries (all-SSBs) have emerged as an alternative battery strategy, with higher safety and energy density expected [1], because of substitution of flammable liquid electrolytes (LEs) with solid electrolytes (SEs). The possibility of bipolar stacking, and the use of high-voltage cathodes and a lithium metal anode will improve the energy density of solid state batteries (SSBs) compared to lithium ion batteries (LIBs) [17, 20].

Flow Batteries

Flow batteries have been explored since the 1970s, for application in electric utility storage in the USA and Japan. Flow batteries store energy in electrolyte solutions and contain two redox couples (e.g., V/V, Zn/Br2, V/Br2, S/Br2, Ce/Zn, Fe/Cr, and Pb/Pb) which flow through a power battery/reactor and involve a reversible chemical reaction [17]. Two electrodes of flow batteries are separated in different

electrolyte tanks. Unlike traditional energy storage battery technologies, the electrode and electrolyte of flow batteries are separated, and the energy capacity of the flow battery is influenced by the size of the electrolyte tanks, while the battery power depends on the size of the battery. For grid scale applications, we have three types of flow batteries.

Zinc–Bromine Flow Batteries

Zinc–bromine flow batteries offer several advantages, high specific energy density (75–85 Wh/kg), high flexibility, and low cost. The commercial development is limited by dendrite formation tendency of zinc, low energy efficiency, poor cycle life, and high solubility of bromine in the aqueous zinc bromide electrolyte.

Vanadium Redox Batteries

Vanadium redox batteries use sulfuric acid containing V5+/V4+ and V3+/V2+ redox couples as positive and negative half-cell electrolytes. The advantages of vanadium redox batteries include high battery efficiency of 75–85%, long lifetime of 12,000 to 14,000 cycles, high safety standards, are cheap to operate, and are easy to maintain. The vanadium redox batteries are capable of deep discharge and are good for stationary applications [1].

The limitations of these batteries include large space requirement due to relatively low energy density of 10–50 Wh/kg. The vanadium redox battery technology is mature GLEES, for example, 15 MW vanadium redox batteries were fabricated at Minamihayakita Transformer Station in Abira-Chou, Hokkaido, to supply power for 4 hours. Additionally, the China National Energy Administration approved a vanadium redox battery system of 200 MW capacity in Dalian, China, in 2016 [21].

Polysulfide Bromide Batteries

Polysulfide bromide batteries also operate based on the redox reaction using a cation-selective membrane like Nafon. Polysulfide bromide batteries generally have energy density of about 30 Wh/kg and are ideal for voltage and frequency regulation in GLEES because of their fast t response time. The batteries though have relatively low efficiency of ~60–75% mainly due to pumping requirements. The practical application of polysulfide bromide batteries faces challenges like high cost of carbon felt, the complicated preparation method of sodium polysulfide, and cross-contamination during long-term battery operation. The Regenesys technologies successfully commissioned the normal operation of a polysulfide bromide battery plant with 120 MWh, 15 MW power capacity at Innogy's Little Barford Power Station in the UK and in Columbus, Mississippi, in the USA [1].

3.2 AGM-VRLA Batteries (Lead-Acid (LA) Cells)

The lead-acid (LA) cells widely used BESS technologies in applications like solar traffic lights, telecommunications, automotive, uninterruptible power supplies (UPS), energy storage devices, and many others. There are three distinct designs of the lead-acid batteries having different structural and functional characteristics. The flooded or vented design has a large amount of liquid electrolyte (sulfuric acid) in which the electrodes are immersed and needs periodic watering to limit electrolyte depletion. The other two are sealed and valve-regulated (VLRA) lead-acid batteries, which contain minimal amount of electrolyte, and need no watering [6].

The main advantage of the VRLA batteries is their quick charge capabilities, high power density, and low maintenance requirements. Their basic components are the positive and negative plates, an electrolyte, and a separator used to immobilize the electrolyte. Separators are absorptive glass mat (AGM) or silica particles, which react with sulfuric acid to form a gel. The separators are made of glass microfibers obtained based on a paper-making process and wicked the sulfuric acid between the plates. This separator makes the AGM battery spill-proof and can make their shipping easy. The AGM batteries have a high discharge rate with low internal resistance and provide electrical reliability due to its low maintenance requirements. These batteries have between 500 and 2500 life cycles at a depth of discharge (DoD) of 30–50% and efficiency of 80–90%, and are widely used for household and industrial consumers [6].

3.3 Gel-VRLA Batteries (GEL-Batteries)

A gel battery has gelled electrolyte whose quality has a significant impact on its battery characteristics. Fumed and colloidal silica are the most widely used gelling agents with the first one being more reliable under deep-discharge conditions, but with shortcomings like an increased internal resistance and high production costs. The colloidal silica gels are simple to prepare and use lower material cost, but have a higher content of impurities like iron leading to high water consumption, and increased production costs [6].

The Gel-VRLA are superior to the AGM technology, in terms of higher reliability as a result of high deep-discharge performance, long service life of over 12 year, small self-discharge rate, good charge stability. The Gel-VRLA can reach 4500 cycles at 40% DoD with and efficiency of 90–99% [6].

3.4 Lead-Carbon Batteries (LCBs)

The lead-carbon batteries (LCBs) are a suitable replacement for conventional lead-acid technologies because of their longer cycle life under deep charge/discharge partial-state-of-charge operation conditions. Carbon and electrolyte additives can

be used to lower the hydrogen reaction rate in the batteries thus increasing lifecycle, and enhancing the reversibility of deep cell discharge. These batteries have between 500 and 2500 life cycles at 50–100% DoD, at charge/discharge efficiency of 90–99% [6].

3.5 Lithium-Ion Batteries (Li-Ion)

The first commercial Li-ion batteries were made in 1990 by Sony, but they are one of the most important types of batteries, leading the market in the field of energy storage. The Li-ion battery is operated by Li + moving back and forth between two electrodes by inserting or extracting from the interstitial space existing between atomic layers of electrode materials during discharge–charge processes. The battery construction comprises of positive and negative electrodes and a Li-ion-conducting electrolyte.

The concept of lithium-ion batteries was developed in the 1970s by the Exxon chemist Stanley Whittingham. This was followed by Sony and Asahi Kasei who created the first commercial product in 1991 [16]. The dominance of lithium-ion technology results from good parameters, like high round-trip efficiency, sufficient cycle life, and lower investment cost due to a high experience rate coupled with moderate levels of installed capacity for stationary systems, which explains the continuing dominance of first generation (crystalline silicon) solar cells with significant investments in alternative solar cell technologies initially expected to be significantly cheaper [22]. Like the crystalline silicon solar cells, the lithium ion range of technologies offers the possibility of chemistry or design improvements to ensure cost reductions for the technology group [10].

High experience rate for stationary lithium-ion systems is the technology's modularity that enables knowledge spillover from other markets, for example, lithium-ion batteries for electric vehicle applications. However, the lithium–ion batteries for transport, portable, and stationary applications may be inching closer to the performance limits than others as a result of significant recent research and deployment focus on lithium-ion thus offering an avenue for alternative technologies to become more competitive [10].

The positive electrode materials in the Li-ion batteries are metal oxides having layered or tunneled structures like lithium cobalt oxide [$LiCoO_2$], lithium manganese oxide [$LiMn_2O_4$], $LiFePO_4$ on an aluminum current collector. The battery's negative electrode usually consists of graphitic carbon on a copper current collector. The electrolytes can be liquid electrolytes or semisolid/solid-state electrolytes. The liquid electrolytes are generally lithium salts (e.g., $LiPF_6$, $LiBF_4$, $LiN[CF_3SO_2]_2$, and lithium bis-oxalato borate [LiBOB]) dissolved in organic carbonates like propylene carbonate, ethylene carbonate, dimethyl carbonate, ethyl methyl carbonate, and diethyl carbonate and their mixtures. For semisolid electrolyte, a polymer electrolyte which is ion-conducting material composed of lithium salts and high-molecular-weight polymer matrices like poly (ethylene oxide), polyvinylidene

fluoride, polyvinylidene fluoride-hexafluoropropylene) with or without solvents are used [1, 3].

The lithium-ion batteries (Li-ion) technically present the most BESS for residential consumers and commercial consumers because of the high flexibility in power and scalability. The anodes and cathodes are composed of different materials; with lithium iron phosphate and lithium nickel cobalt aluminum oxide being the most-used materials. Their advantage over the lead-acid are their higher power and energy density, higher charge/discharge efficiency of 90–99%, longer lifetime of 7 and 20 years, and over 6000 complete cycles based on operating conditions. However, the main disadvantage is that connecting them in parallel/series has risks concerning safety and balancing in operation due to high temperature, overload, short-circuits, which can easily lead to explosion and battery burns. These risks are minimized by the use of electronic circuits for each battery cell. High operating temperature and deep discharge can also limit the overall life cycle of the lithium-ion batteries [6].

The Li-ion batteries are characterized by a long cycle life bigger than 1000 cycles, low self-discharge of 2–8% per month, high efficiency of almost 100%, and wide operating temperature range, for example, commercial Li-ion batteries may charge between 0 and 45 °C and discharge between −40 and 65 °C. The batteries (Li-ion batteries) can be produced into a wide array of sizes and shapes, like fat or "stacked" prismatic, wound prismatic, spiral-wound cylindrical, and pouch cell designs in small (0.1 Ah) to large (160 Ah) sizes [1, 32].

However, major disadvantages of Li-ion batteries include their relatively low energy density (240 Wh/kg, 640 Wh/L), potential degradation potential when discharged below 2 V at high temperature, for example, 65 °C, and are dangerous when overcharged [1].

3.6 Sodium-Sulfur (Na-S) Batteries

Sodium-sulfur (Na-S) Batteries were developed originally by the Ford Motor Company in 1960, but the technology was sold to the Japanese company NGK which manufactures battery systems for stationary applications. Na-S operate at a high between 300 to 350 °C temperature range which can be a challenge in intermittent operations. The battery systems have round trip efficiency of about 90% making it an efficient energy solution [16]. Na–S battery was first invented by Ford in 1967 and is a serious candidate for GLEES. The Na-S batteries consist of molten Na anodes, molten S cathodes, and Na+ −conducting ceramic electrolytes (e.g., β''-Al2O3) and operate between 300 and 350 °C. The S cathodes are generally filled in a conductive porous carbon or graphite felt as current collectors. The casing for Na-S batteries is made of stainless steel. The Na-S battery has a theoretical energy density of 760 Wh/kg, while real or practical energy and power density is 150–240 Wh/kg and 150–230 W/kg.

Compared to Li-ion batteries, the Na-S batteries have a relatively long cycle life of about ~2500 cycles and efficiency of 75–90%. Additionally, the Na-S batteries

can handle pulse power for more than six times their continuous rating (for 30 s). This makes them ideal for energy storage devices for GLEES for applications like peak shaving and load leveling. The Na-s batteries operate with high specific energy and power density, high current and rate capacity, high self-discharge resistance, high electrical efficiency, low vibration, low noise, and high environment friendliness.

The main drawbacks of the of Na-S batteries is that they need a heat source and the reaction is highly exothermic between molten Na and S which increases fire risk. The initial capital cost of Na-S batteries is about ~$350/kWh, although it is expected to drop with increased production [1].

3.7 Aqueous Ion Hybrid Batteries (AIHBs)

The AIHBs are attractive due to high safety performances and ionic conductivity among all rechargeable batteries and are suitable for medium and large-scale applications. The AIHB technology employs similar electrodes to those used in Li-ion batteries. The electrolyte is based on an aqueous solution which reduces their environmental impact compared to the Li-ion batteries. The aqueous ion hybrid batteries (AIHBs) are however still under research and development stage though some commercially available solutions are available. The life of the AIHBs BESS is about 9 years which is approximately 3000 life cycles at a 70% DoD and a charge/discharge efficiency of about 90% [6].

Aqueous hybrid ion batteries (AHIB) are regarded as an environmentally friendly alternative to existing stationary battery technologies. The AHIB uses abundant and non-toxic materials, but has low energy density and requires more material to provide sufficient storage capacity. Analysis however shows that compared to lithium- or sodium-ion batteries they have significantly higher impacts under global warming and ozone depletion aspects. The AHIB have a high cycle life which compensates for the impacts partially as they require less battery replacements over the lifetime of the application. The AHIB has relatively high internal inefficiencies which becomes significant if charging is by fossil fuel–based electricity, making AHIB batteries unattractive [23].

3.8 Electrochemical Capacitors

Electrochemical capacitors (ECs) are also called the "electric double-layer" capacitors – or "Supercapacitor" or "Ultracapacitor." The phrase "double-layer" implies that they physically store electrical charge at a surface-electrolyte interface of high-surface-area carbon electrodes. Two main types of electrochemical capacitors are symmetric and asymmetric and have different properties that are suitable for different energy storage applications. The market for electrochemical capacitors is on

growth trajectory for applications in grid-scale electricity storage among others [21, 24].

Current flows when two electrodes of an electrochemical capacitor are connected in an external current path, until complete charge balance is achieved. The application of voltage returns the capacitor to its charged state. The process is fast and highly reversible with a limitless discharge-charge cycle since the charge is stored physically, with no chemical or phase changes taking place. The electrochemical capacitors have very high specific and volumetric capacitances due to their high surface area and the small thickness of the double layer. This enables a combination of a previously unattainable capacitance density with almost unlimited charge-discharge cycle life. One cell of an electrochemical capacitor has operational voltage which is limited by the breakdown potential of the electrolyte usually about 3 V or less. Higher voltage is obtained by connecting many cells in series [25, 26]. Figure 4 demonstrates the construction of the electrochemical capacitor.

Figure 4 shows the basic constriction of an electrochemical capacitor which has a porous carbon electrode at the cathode and a porous carbon electrode for the anode.

There are two types, namely, the symmetric designs, where both positive and negative electrodes are made of the same high-surface-area carbon and the asymmetric designs which have different materials used for the anode and cathode electrodes, with one having high-surface-area carbon and the other a higher capacity battery-like electrode. The symmetric electrochemical capacitors have specific energy values up to ~6 Wh/kg and higher power performance compared with the asymmetric capacitors which have specific energy values of about 20 Wh/kg [25].

The market for electrochemical capacitors has been growing mainly because of their high-power density, long cycle life, high reliability, etc. Their main applications are in portable electronics, transportation, and medical devices and are preferred for applications which require high cycle life and fast charge or discharge times of 1 second or less. The main limitation of electrochemical capacitors is a lack of understanding of the technology and limited ideal applications [26].

Fig. 4 Electrochemical capacitors
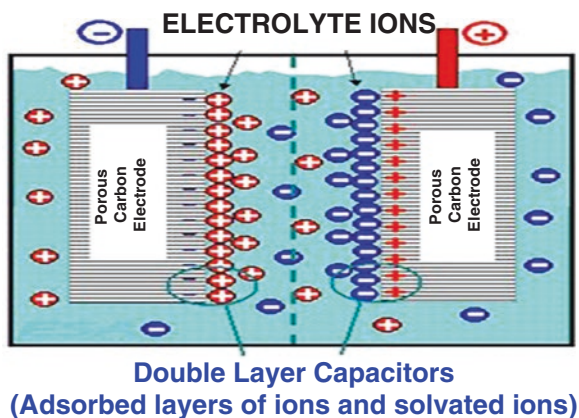
Their different requirements for energy storage in different grid electricity applications include voltage support, load following, integration of wind generation, and time-shifting. The symmetric electrochemical capacitors have a response time of the order of 1 second and are hence suitable for short duration high-power applications related to both grid regulation and frequency regulation. Asymmetric electrochemical capacitors are more suitable for energy storage applications with long duration, for example, charge-at-night/use-during-the-day storage which is bulk charge storage. Some asymmetric electrochemical capacitors are optimized for ~5-hour charge with ~5-hour discharge. The main advantages of electrochemical capacitors are long cycle life, good efficiency, low life-cycle costs, and adequate energy density [24, 25]. The electrochemical capacitors (ECs) are used to bridge the gap existing between batteries and solid-state and electrolytic capacitors. The high-power density makes them more attractive, since greater energy density is needed for the future [27].

3.9   Nickel-Metal Hydride (Ni-MH) Batteries

Ni-MH batteries were first studied in the 1960s and have been in the market for over 20 years as portable and traction batteries. Ni-MH batteries are made of metal hydride anodes like AB5-type [LaCePrNdNiCoMnAl], A2B7-type [LaCePrNdMgNiCoMnAlZr], or AB2-type [VTiZrNiCrCoMnAlSn] (metal hydride active materials), nickel hydroxide cathodes, and alkaline electrolytes (e.g., KOH, KOH/ LiOH, KOH/NaOH/LiOH). The batteries make use of a separator as an insulator between anodes and cathodes, and functions as the medium for absorbing electrolytes. It is composed of synthetic nonwoven material. The Ni–MH batteries have porous anode and cathode with a large surface area, which provide low internal resistance and high-rate performance capability. The cathode is made by impregnating or pasting nickel compounds into the foam nickel or a highly porous sintered substrate, while the anode is a hydrogen-storage-alloy-coated perforated nickel foil or grid. The Ni-MH batteries are generally used in telecommunications, for supply of uninterrupted power and to power hybrid electric vehicles because of their high energy and power (40–110 Wh/kg, 200–1200 W/kg),

The main advantages of the Ni-MH batteries are that they are environment friendly, have a wide range of operating temperatures (−30 to 70 °C), have a high degree of tolerance to abusive overcharge and over discharge, have long-life characteristics, are low maintenance, and are low cost [1].

4   BESS Input Data

Battery energy storage systems have different performance parameters and indicators, based on type of battery technology, the manufacturer, the operating environment, and conditions, that is, temperature, maximum current, voltage, and power

Table 1 Input parameters for the analyzed BESS technologies [6]

		AGM-VRLA	Gel-VRLA	LCB	Li-ion	AIHB
1	Normal voltage	6–12	2–12	6–12	12–600	48
2	Rated capacity [Ah]	22–460	17–3170	70–300	8.33–500	50
3	Rated energy [kWh]	0.264–3.48	0.204–14.4	0.84–3.264	0.3–25.6	2.4
3	Battery efficiency [%]	80–90%	80–95%	90–99%	90–99%	90%
4	DoD [%]	30–50%	30–60%	50–100%	50–100%	70
5	Cycles at DoD	400–2500	550–4500	500–2500	2000–7000	3000
6	Cycles/year	365				–
7	Calendar life (n)	2–7	2–13	2–7	6–20	9

and maintenance needs. The analysis of performance parameters assumes that for 24-hours period, the battery is fully charged and discharged at the various design like recommend DoD specified in the technical/commercial datasheets by the distributor, calendar life (n) and number of cycles considered per year i.e. (3 6 5 days).

From Table 1, it is noted that in terms of normal voltage, the Li-ion batteries are superior, LI-ion and LCB are superior in terms of efficiency. Batteries that exhibit lower or inferior DoD (depth of discharge) on average basis are the AGM-VRLA and Gel-VRLA. The AIHB and Li-ion have higher average useful life.

4.1 LCOS Calculation

The LCOS analysis determines the total cost for 1 kWh stored by each type of the analyzed BESS. It includes the capital expenditure (CAPEX), operation, maintenance (OM), and charging (C) costs over the entire lifetime (n) of the storage system divided by total energy generated by the storage system (W_{out}) in the entire lifetime. Annual costs and energy output are then discounted considering a discount rate i, for example, 8.5% [6].

The other cost parameters for consideration are annual operation and maintenance costs, which vary with storage technology. Values may be computed as percentages of CAPEX, that is, 0.5% for lead-acid/carbon technologies and 0.25% for Li-ion and AIHB batteries [6]. Charging costs per year (C) is price of electricity used for battery charging hence not injected into the grid. This represents the amount of money that a prosumer would receive if he decided to store the surplus for later instead of supplying to the grid and for demnistartetiion in this study for 2021 is 40.67 € for each MWh supplied to the grid [6].

CAPEX, OM, and C costs are established on the basis of market analysis. The analysis gives a wide range of values for each cost factor analyzed in the study. This implies that the same battery or system may have may have different costs, based on the manufacturer and distributor [6].

Identification of a representative value for each technology requires the use of an interquartile range (IQR) to remove outliers for each cost factor. The IQR

determines values between the first and third quartiles, spread out around the data median and indicates the middle (50%) of the series. Based on the median, the first and third quartiles are determined. The difference between the quartiles defines the *IQR*. The average (*Avg*) of *IQR* is computed to represent each cost factor's representative value. The range values, *IQR* and *Avg* for the primary cost parameters used to determine LCOS values are presented in Table 2.

From Table 2, five batteries are compared, i.e. aqueous ion hybrid batteries (AIHBs), lead-carbon batteries (LCBs), lithium-ion (Li-ion), absorbed glass mat valve-regulated lead-acid (AGM-VRLA), and gel valve-regulated lead-acid (Gel-VRLA), have different cost and performance characteristic. The Li-ion batteries exhibit superior technical properties.

4.2 LCOS Method Results and Discussion

Two values of LCOS were determined for the batteries. First, LCOS does not include subsidies while the second includes subsidies. The second LCOS, that is LCOS2, includes subsidies provided. The average values obtained are summarized in Table 3.

Table 3 shows LCOS1 and LCOS2. Based on average values, the lowest values for LCOS1 and LCOS2 are from the LCB battery technology at 39.04 to 29.39 c€/

Table 2 Main cost parameters of BESS technologies [6]

			AGM-VRLA	Gel-VRLA	LCB	Li-ion	AIHB
1	C_{BESS} [€/kWh]	Range	77.55–248.78	55.95–516.55	143.34–219.81	233.35–2397.68	470.40
		IQR	119.04–172.58	110.87–191.01	156.22–192.55	373.56–769.37	
		Average	146.59	142.03	180.01	568.89	
	VAT [€/kWh]	Range	14.73–47.27	10.63–98.14	27.23–41.76	44.34–455.56	89.38
		IQR	22.62–32.79	21.06–36.29	29.68–36.58	70.98–146.18	
		Average	27.85	26.99	34.20	108.09	
	DS [€/kWh]	Range	9.23–29.61	6.66–61.47	17.06–26.16	27.77–285.32	55.98
		IQR	14.17–20.54	13.19–22.73	18.59–22.91	44.45–91.55	
		Average	17.44	16.90	21.42	67.70	
	S_{BESS} [€/kWh	Range	30.45–97.70	21.97–202.85	56.29–86.32	91.64–941.57	184.73
		IQR	46.75–67.77	43.54–75.01	61.35–75.61	146.70–302.13	
		Average	57.56	55.77	70.69	223.40	
	OM [€/year]	Range	0.28–4.57	0.42–14.30	0.84–3.51	1.33–33.32	3.69
		IQR	1.08–2.10	1.09–2.20	1.48–2.63	3.17–12.98	
		Average	1.55	1.59			

Table 3 LCOS for the examined BESSs technologies [6]

		AGM-VRLA	Gel-VRLA	LCB	Li-ion	AIHB
LCOS$_1$ [c€/kWh]	*Range*	27.75–109.29	20.41–132.3	28.87–54.33	18.68–157.62	50.76
	IQR	41.79–80.39	36.28–65.98	31.6–42.95	25.96–76.57	
	AVR	54.58	48.13	39.04	45.6	
LCOS$_2$ [c€/kWh]	*Range*	22.23–79.76	17.01–95.6	22.78–39.49	14.5–112.9	37.64
	IQR	32.42–59.12	28.45–49.01	24.57–32.53	19.7–55.54	
	AVR	41.18	36.91	29.39	33.63	

kWh. They have high DoD of 50–100%, conversion efficiency higher than 90%, and low battery cost of 180.01 €/kWh, hence more electricity at low battery cost. The Li-ion battery which has an AVR of 45.6 for LCOS1 and 33.63 c€/kWh for AVR fort LCSO2 offer the second best LCOS Other studies have shown higher values of between 61.1 c€/kWh and 83 c€/kWh. Clearly the battery prices are on a decreasing trend mainly due to incentives and taxes.

In the third and fifth place of the LCOS ranking is the Gel- and AGM-VRLA batteries. The LCOS values for the two lead-acid batteries are lower generally 58.68 c€/kWh to 98 c€/kWh although in some values, 17 and 25 c€/kWh were established.

The fourth place lies with the AIHB battery with between 50.76 and 37.64 c€/kWh. It has high LCOS values, but is preferred by buyers due to its low environmental impact, and thus is considered to be an eco-friendly alternative of Li-ion batteries.

Although the LCB technology has a shorter life of 2–7 years compared to the Li-ion battery, it has a lower CAPEX of about 238 €/kWh, hence lower LCOS. The Li-ion batteries have the longest period of exploitation. The LCOS values may be close to Gel-VRLA battery, but the difference in life is about 7 years with the AGM-VRLA battery having shorter life and high LCOS values, which makes them inefficient [6].

5 Results and Discussion

The cumulative installed capacity of lithium-ion batteries is the highest among the chemical storage batteries accounting for about 88.8% of electrical energy storage (EES) in China for the year 2020. Lead-carbon batteries have highest safety due to a lack of combustibles during operation and are increasingly used for large-scale EES technology. The initial cost of vanadium redox flow is high, and the cost will reduce as the development of technology and industry progresses. The batteries have a very flexible scale design. The electrolyte capacity and concentration influence energy storage capacity, thus increasing the volume of the electrolyte increases energy storage capacity. This makes the vanadium redox flow the most promising large-scale electrical energy storage (EES) technology in the future [5]. The LCOS for the thermal energy storages are usually lower than that of the battery, at

23–47 USD ct/kWh [28]. Energy storage is essential for implementing the large-scale integration of renewable energy for the current and future transition to a 100% renewable energy supply. An electricity-only focus – as in a smart grid approach – leads to options primarily focused on electricity storage technologies in combination with flexible electricity demands and transmission lines to neighboring countries [29].

The grid-level large-scale electrical energy storage (GLEES), which entails converting electricity from a grid-scale power network to a storable form for later conversion to electricity, has an important role in delivery and plays an essential role in the balance of demand and supply of electricity. Many storage technologies are available like secondary battery technologies and supercapacitors, flow batteries, compressed air, flywheels, thermal energy storage, and pumped hydroelectric power. Battery technologies are considered as one of the most desirable electrochemical energy storage devices for grid-level large-scale electrical energy storage (GLEES) in terms of modularization, flexibility of installation, rapid response, and short construction cycles. The energy storage technologies serve the following functions:

 (i) Peak shaving and load leveling
 (ii) Voltage and frequency regulation
(iii) Emergency energy storage [1]

Peak shaving and load leveling is used to mitigate the peak-to-valley power demand gap between the night and the day when a renewable resource is available and when it is not available or is limited. Voltage and frequency regulation are applied in a nonuniform electrical load of the grid network for the realization of a real-time power system balance by providing power regulation to the grid by charging and discharging with a fast response time [1].

Electricity storage is approximately 100 times more expensive than thermal storage and much more expensive than storage for gases and liquids. It is therefore advisable to apply thermal and fuel storage since it is a cheaper and more efficient solution to utilize thermal and fuel storage technologies for integration of fluctuating renewable energy, such as wind and solar power, than rely on electricity storage which however requires strong integration across different energy sectors. The cross-sector smart energy systems approach leads to better and much cheaper options in terms of thermal, gas, and liquid fuel storage combined in a cross-sector energy conversion technology. Use of heat pumps, in each building in rural areas or in district heating system in the urban areas, can efficiently connect the electricity sector to thermal storage, while electric vehicles and electro-fuels can interconnect the electricity sector and storage in the transport sector. The use of more efficient and cheaper options eliminates the need for other options in the electricity sector required solely for the integration of renewable energy. Large electricity storage capacity is not economically viable within any of the steps between now and a future 100% renewable energy supply.

Large-scale integration of fluctuating renewable electricity sources, and electricity storage, should be avoided to encourage other storage types to provide optional

system balancing and flexibility at lower costs. Direct electricity storage can be put to other applications but should not be prioritized if its objective is to supply electricity to the grid.

Energy storage may not be the optimum solution to integrate large fluctuating renewable energy, since due to availability of more efficient and cheaper options for integration of electricity with other parts of the energy system and creation of a smart energy system. However, storage remains important for large-scale integration of variable renewable to the electric power systems.

For the case of the Chinese, studies established for application scenario of energy storage peak shaving, due to the abundant lead resources and mature lead-carbon battery recycling system, the initial cost of lead-carbon batteries is much lower than others while the LCOS of lead-carbon is about 0.84 CNY/kWh. The LCOS of lithium iron phosphate batteries is about 0.94 CNY/kWh mainly because of long life cycle but high end-of-life cost. As a result of high recycling value and high investment cost, the vanadium redox flow technology is still evolving but has LCOS of 1.21 CNY/kWh, which is the highest of the three common types of batteries.

A possible pathway to increase the business case for electricity storage is through multiple services using the same device which brings multiple revenue streams also called "benefit-stacking." The nominal power capacity is based on the largest service, that is, sequential stacking or the sum of all service provided at the same time, that is, parallel stacking. The discharge duration reflects the sum of durations required by all services for sufficient energy capacity when all services are needed in parallel or directly one after another. The full equivalent cycles also reflect the respective sum for all services provided by the system. Average electricity price could be the sum of prices captured during charging for individual services weighed by the full equivalent cycles attributed to them [10].

LCOS refers to the cost of kWh or MWh electricity discharged by a storage device when accounting for the entire costs incurred, and energy generated throughout the lifetime of the storage device. Energy storage is a high-quality flexible resource, with an important regulatory role in a high increasing the uptake of variable and intermittent renewable energy resources. The various elements of LCOS are the Capex, Opex, charging cost, tax cost, replacement cost, and end-of-life cost. From the cost breakdown, it is indicated that the proportion of *Capex* and charging cost is the largest, while the proportion of tax cost and Opex is the smallest. Batteries with a short life cycle and many replacements have the highest cost.

LCOS varies with different application scenarios, for example, for transmission and distribution applications LCOS is the lowest when lithium iron phosphate batteries are used because the batteries only need one replacement thus take advantage of the long life. Therefore, improving round-trip efficiency and storage duration, reducing the unit initial investment cost, and giving full play to the advantages of different technology types when laying out EES can be used to reduce costs.

The use of LCOS is dependent on economic storage characteristics, unlike the traditional levelized cost of energy (LCOE) which also depends on the temporal characteristics of the electricity price profile. Hence an analysis of the whole power system will provide more information than a single Levelized cost measure to compare different storage technologies in the electricity market.

6 Conclusions

The grid-level large-scale electrical energy storage (GLEES) plays an essential role in the balancing of the supply–demand of electricity generation, distribution, and consumption. Many types of energy storage approaches are available like secondary battery technologies and supercapacitors, solid and flow batteries, flywheels, compressed air energy storage, thermal energy storage, and pumped hydroelectric power. Energy storage technologies are needed for peak shaving and load leveling, voltage and frequency regulation, and emergency energy storage. The peak shaving and load leveling are applied to mitigate the peak-to-valley power demand gap between day and night. The voltage and frequency regulation are applied in nonuniform electrical load of the grid network to enable real-time power supply and demand balance when the battery is in use providing regulation power to the grid by charging and discharging with a fast response time.

The lead batteries have wide applications in telecommunications, uninterrupted power supply, electric traction, and energy storage for utilities, secure power, electric traction, and other domestic and commercial applications. The LCOS is a metric often applied to assess the economic competitiveness of different energy technologies. The lowest LCOS occurs when the system is designed for continuous operation, instead of peak shaving. Solar photovoltaics can guarantee output within economically feasible limits, although they are slightly currently expensive. An optimal storage solution must go beyond the lowest LCOS and consider other parameters like depth of discharge (DoD), number of cycles, etc., which define the technical capacity of storage technologies. The electro-chemical capacitors are used to store electrical energy from intermittent sources and for quick delivery when needed. The electrochemical capacitors (ECs) are used to bridge the gap existing between batteries and solid-state and electrolytic capacitors. The high-power density makes them more attractive, since greater energy density is needed for the future.

References

1. Fan, X., et al.: Battery technologies for grid-level large-scale electrical energy storage. Trans. Tianjin Univ. **26**(2), 92–103 (2020). https://doi.org/10.1007/s12209-019-00231-w
2. IRENA: Utility-Scale Batteries: Innovation Landscape Brief. International Renewable Energy Agency, Abu Dhabi (2019) [Online]. Available: https://www.irena.org/-/media/Files/IRENA/Agency/Publication/2019/Sep/IRENA_Utility-scale-batteries_2019.pdf
3. Kabeyi, M.J.B.: Challenges of Implementing Thermal Powerplant Projects in Kenya, the Case of Kipevu III 120MW Power Station, Mombasa Kenya, Masters, Department of Education Management, University of Nairobi, Nairobi, 5866, (2012) [Online]. Available: http://ereposi-tory.uonbi.ac.ke:8080/xmlui/handle/123456789/11023
4. Melnikov, V., Nesterenko, G., Potapenko, A., Lebedev, D.: Calculation of the levelised cost of electrical energy storage for short-duration application. LCOS sensitivity analysis. EAI Endorsed Trans. Energy Web. **6**(21), e2 (2018). https://doi.org/10.4108/eai.13-7-2018.155643

5. Xu, Y., Pei, J., Cui, L., Liu, P., Ma, T.: The levelized cost of storage of electrochemical energy storage technologies in China, (in English). Front. Energy Res. **10**, 873800 (2022). https://doi.org/10.3389/fenrg.2022.873800

6. Cristea, M., Tîrnovan, R.-A., Cristea, C., Făgărășan, C.: Levelized cost of storage (LCOS) analysis of BESSs in Romania. Sustain. Energy Technol. Assess. **53**, 102633 (2022). https://doi.org/10.1016/j.seta.2022.102633

7. Kabeyi, M.J.B., Olanrewaju, O.A.: Review and design overview of plastic waste-to-pyrolysis oil conversion with implications on the energy transition. J. Energy. **2023**, 1821129 (2023). https://doi.org/10.1155/2023/1821129

8. Smallbone, A., Jülch, V., Wardle, R., Roskilly, A.P.: Levelised cost of storage for pumped heat energy storage in comparison with other energy storage technologies. Energy Convers. Manag. **152**, 221–228 (2017). https://doi.org/10.1016/j.enconman.2017.09.047

9. Melnikov, V., Nesterenko, G., Potapenko, A., Lebedev, D.: Calculation of the levelised cost of electrical energy storage for short-duration application. LCOS sensitivity analysis. EAI Endorsed Trans. Energy Web Inf. Technol. **6**(21), 4 (2019) [Online]. Available: https://eudl.eu/pdf/10.4108/eai.13-7-2018.155643

10. Schmidt, O., Melchior, S., Hawkes, A., Staffell, I.: Projecting the future levelized cost of electricity storage technologies. Joule. **3**(1), 81–100 (2019). https://doi.org/10.1016/j.joule.2018.12.008

11. Lund, H., et al.: Energy storage and smart energy systems. Int. J. Sustain. Energy Plan. Manag. **11**, 3–14 (2016)

12. Kabeyi, M.J.B., Oludolapo, A.O.: Viability of Wellhead Power Plants as substitutes of Permanent Power plants. In: Presented at the 2nd African International Conference on Industrial Engineering and Operations Management, Harare, Zimbabwe, December 7–10, 2020, p. 77. [Online]. Available: http://www.ieomsociety.org/harare2020/papers/77.pdf

13. Kabeyi, M.J.B., Olanrewaju, O.A.: The role of electrification of transport in the energy transition. In: Presented at the Fifth European Conference on Industrial Engineering and Operations Management, Rome, Italy, July 26–28, 2022, p. 426. [Online]. Available: https://ieomsociety.org/proceedings/2022rome/426.pdf

14. Pawel, I.: The cost of storage – how to calculate the Levelized Cost of Stored Energy (LCOE) and applications to renewable energy generation. Energy Procedia. **46**, 68–77 (2014). https://doi.org/10.1016/j.egypro.2014.01.159

15. Kabeyi, M.J.B.: Potential and challenges of bagasse cogeneration in the Kenyan sugar industry. Int. J. Creat. Res. Thoughts. **10**(4), 379–526 (2022) Art no. IJCRT_218740, http://doi.one/10.1729/Journal.30042

16. American Clean Power. "Batteries" American Clean Power. https://energystorage.org/why-energy-storage/technologies/solid-electrode-batteries/ (Accessed 28 May 20223, 2023)

17. Reisch, M.S.: Solid-state batteries inch their way to market. C&EN Global Enterprise. **95**(46), 19–21 (2017). https://doi.org/10.1021/cen-09546-bus

18. Kurzweil, P., Garche, J.: 2 - Overview of batteries for future automobiles. In: Garche, J., Karden, E., Moseley, P.T., Rand, D.A.J. (eds.) Lead-Acid Batteries for Future Automobiles, pp. 27–96. Elsevier, Amsterdam (2017)

19. Toyota. "Solid state batteries." Toyoa Corporation. https://www.toyota.ie/company/news/2021/solid-state-batteries (Accessed 29 May 2023, 2023)

20. Huo, H., Janek, J.: Solid-state batteries: from 'all-solid' to 'almost-solid'. Natl. Sci. Rev. **10**(6), nwad098 (2023). https://doi.org/10.1093/nsr/nwad098

21. Chakraborty, M.R., Dawn, S., Saha, P.K., Basu, J.B., Ustun, T.S.: A comparative review on energy storage systems and their application in deregulated systems. Batteries. **8**(9). https://doi.org/10.3390/batteries8090124

22. Emblemsvåg, J.: On the levelised cost of energy of solar photovoltaics. Int. J. Sustain. Energy. **40**(8), 755–780 (2021). https://doi.org/10.1080/14786451.2020.1867139

23. Peters, J.F., Weil, M.: Aqueous hybrid ion batteries – an environmentally friendly alternative for stationary energy storage? J. Power Sources. **364**, 258–265 (2017). https://doi.org/10.1016/j.jpowsour.2017.08.041

24. American Clean Power. "Lithium-ion batteries" American Clean Power. https://energystorage.org/why-energy-storage/technologies/lithium-ion-li-ion-batteries/ (Accessed 29 July 2023, 2023)
25. Burke, A.: Capacitors | application. In: Garche, J. (ed.) Encyclopedia of Electrochemical Power Sources, pp. 685–694. Elsevier, Amsterdam (2009)
26. Simon, P., Gogotsi, Y.: Perspectives for electrochemical capacitors and related devices. Nat. Mater. **19**(11), 1151–1163 (2020). https://doi.org/10.1038/s41563-020-0747-z
27. Liu, L., Taberna, P.-L., Dunn, B., Simon, P.: Future directions for electrochemical capacitors. ACS Energy Lett. **6**(12), 4311–4316 (2021). https://doi.org/10.1021/acsenergylett.1c01981
28. Luerssen, C., Gandhi, O., Reindl, T., Sekhar, C., Cheong, D.: Levelised Cost of Storage (LCOS) for solar-PV-powered cooling in the tropics. Appl. Energy. **242**, 640–654 (2019). https://doi.org/10.1016/j.apenergy.2019.03.133
29. Kabeyi, M.J.B., Oludolapo, A.O.: Characteristics and applications of geothermal wellhead powerplants in electricity generation. In: 31ST Annual Southern African Institution for Industrial Engineering Conference, South Africa, H. Teresa, (ed.), 5–7th October 2020, vol. 2020, no. 31, pp. 222–235. South African Journal of Industrial Engineering, South Africa (2020). [Online]. Available: https://www.saiie.co.za/system/files/2021-11/SAIIE31%20Conference%20Proceedings.pdf. [Online]. Available: https://www.saiie.co.za/system/files/2021-11/SAIIE31%20Conference%20Proceedings.pdf

Part IV
Advanced Hydrogen Production System and Fuel Cell Technology

Techno-Economic Analysis of Solar and Wind Energy Systems for Power and Hydrogen Production

Mathna Salah Al-Sumri, Feroz Shaik, Nageswara Rao Lakkimsetty, and M. J. Varghese

1 Introduction

De-carbonization is an important step that countries throughout the world are doing to mitigate the risk of a global threat known as climate change. The impetus is on using renewable energy resources in place of fossil fuels to minimize the carbon emissions. With considerable reduction in greenhouse gas (GHG) emissions, the yearly global average rise in temperature could be maintained to 2 °C or less and without decrease in GHG, it may shoot up to 5 °C or beyond by the end of the century [1]. A lot of efforts are being made worldwide to utilize alternate renewable energy sources such as solar and wind for clean and environmental friendly energy production. The quantity of energy production by these resources is influenced by climatic factors such as solar radiation, wind speed, ambient temperature, and so on.

Sultanate of Oman has high potential to utilize renewable energy resources for the production of clean energy due to its geographical conditions. In order to achieve de-carbonization, the Sultanate of Oman has set a goal of gaining 10% of its energy needs from renewable sources by 2025. The Sultanate's total fixed power generation capacity from renewables was 159 MW by 2020. Out of this, solar power accounted for 68.6% and the remaining comes from wind resource.

Beside producing power from renewable energy resources, Sultanate of Oman is aiming toward being a global hydrogen (H_2) exporter. In the central part of the Middle Eastern country, an international consortium led by Omani oil is constructing a 25 GW wind-solar complex to manufacture green H_2 [2].

M. S. Al-Sumri · N. R. Lakkimsetty · M. J. Varghese
National University of Science & Technology (Al Hail Caledonian Campus), Muscat, Oman

F. Shaik (✉)
Prince Mohammad Bin Fahd University, Al Khobar, Saudi Arabia
e-mail: fshaik@pmu.edu.sa

Many hybrid renewable energy systems have been implemented globally with solar or wind energy serving as one source of energy. The complexity of the hybrid systems leads to many challenges for achieving reliable and efficient performance. One of the main challenges is to optimize the sizing of components for high performance with low capital investment. The installation of a hybrid solar system required extensive research due to its various designs and the uncertainty of solar parameters, such as the dynamic rate of solar irradiation. The complexity involved in solar parameters are due to its intermittent, seasonal and unpredictable nature. The HOMER (Hybrid Optimization of Multiple Energy Resources) model is used to solve these problems by establishing energy balancing schemes for every 8760 h in a year. It also compares the generated energy to the actual load demand for each hour. It also manages the battery's charging and discharging capabilities, as well as the project's installation and operating costs over its entire lifecycle [3, 4].

Various researchers investigated the optimum conditions for hybrid systems using HOMER simulation software [5–7]. The present study covers several optimization methodologies for comparing the energy production cost and performance of various hybrid system configurations using HOMER at various significant locations of Sultanate of Oman. The case study with respective Salalah is presented here.

2   Potential Use of Hybrid Solar-Wind Energy Systems

Oman has a talented geographic place for applying solar energy technologies. The climate in Oman is hot dry with temperatures shooting up to 50 °C in peak summer. Oman's solar energy situation is improving as more projects and research are completed in both the private and public sectors. Fresh ideas for optimizing photovoltaic (PV) systems in Oman are exposed every day. Subsidized power costs, natural gas, regulation, public reception, and education on solar energy concepts are the primary hurdles in the implementation of solar energy–based projects in Oman. These issues could be resolved over time as more of these systems are implemented. Public responsiveness will grow, and policy will follow. The yearly solar radiation in Oman varies between 2200 and 2500 kWh/m². Marmul receives the most solar radiation in Oman, followed by Fahud, Sohar, and Qairoon Hairiti [8].

Coastal and southern areas are evaluated as a potential resource of wind energy in the Sultanate of Oman. At 10 m height, the average wind speed for 28 distinct places ranges from 3.0 to 6.3 m/s. The most potential sites include Thumrait, Qairoon Hairiti, Masirah, and Sur located near the sea in Oman's southern areas. Thumrait has the highest projected energy of around 4.5 kWh/m² per year. Few sites, such as Marmul, Fahud, Thumrait, and Masirah, have both solar and wind energy potential, making them suitable targets for hybrid systems [4].

With a surface area of around 649 km² Masirah Island is Oman's largest island. The islands off grid or isolated system are entirely dependent on a diesel producing plant, with a total fitted capacity of 20.3 MW and a net existing size of 16.7 MW. The diesel power station, distribution, low network voltage, and a modest desalination water facility are all operated by the local power company. The substantial projected

growth in electrical demand on Masirah Island will place considerable limits on expensive, high-emission diesel-fuel usage. The choice of introducing energy via submarine cable and construction of gas power plant are considered to be not financially viable. As a result, using the island's natural solar and wind resources are evaluated as a feasible option for lowering energy generation costs, lowering emissions, and improving supply security [9].

Due to economic and rural improvements, the demand for energy in the Salalah community has been increasing. Salalah is situated in the southern governorate of Dhofar at latitude 17°3.0′N and longitude 54°6.4′E. The demand for energy is very high in Salalah especially during the Al-Khareef period, which runs from May to August every year. According to the metrological data, the maximum sunshine happens at Salalah city in June, July, and August. Salalah's average monthly radiation on surfaces ranges from 3.4 MJ/m^2 in August to 29 MJ/m^2 in May. While the monthly radiation on slope ($\beta = 0$–90) may decrease from June to August (during the summer), the decrease is minor [10]. The geographical location of Salalah provides high potential for the implementation of renewable energy–based power generation systems.

Hydrogen fuel created from renewable sources has recently gained much attention due to its broad applicability and ability to contribute for the de-carbonization drive. The excess power generated from the renewable resources after meeting energy demand can be utilized for H_2 production using electrolysis process.

3   Methodology

The methodology of solar photovoltaic-wind hydrogen production potential and cost assessment includes estimating the energy output of the PV and wind plant. The energy output evaluation depends on the site data, temperature variability effect, and wind speed. This is followed by quantifying hydrogen production, and performing an economic analysis. The hybrid energy system is optimized using HOMER software. The approach framework used in this study is as follows:

Step 1: Analysis of load demand, evaluation of renewable energy resources, hybrid system components and configuration.
Step 2: Development of hybrid system model in HOMER.
Step 3: Optimization of economic feasible hybrid system.
Step 4: Hybrid system selection.
Step 5: Load flow analysis of integrating proposed hybrid system in different scenarios.

The solar PV power plant's annual energy production, PV module's optimum working point current and voltage, the power output generated by a wind turbine, and the available battery bank capacity are evaluated as per the procedures mentioned in the literature [11]. The electricity provided by the renewable energy system would be sufficient to encounter the demand. If the generated power exceeds the load requirement, the electrolyzer can utilize the excess energy to manufacture hydrogen through a water electrolysis process.

4   Optimization

HOMER Software simulates and optimizes separate renewable energy systems. Thousands of combinations are possible due to the various extents of the system apparatuses. The best possible (or optimal) system configuration in HOMER is the one that meets the user-specified requirements at the lowest total net current cost. The loss of power supply probability (LPSP) and energy cost (COE) are minimized to ensure optimal system sizing. It should be noted that 100% renewable influence equates to a 0% chance for losing power supply. This implies that the hybrid system can fully refuge the load with renewable energy. Furthermore, the optimal configuration resembles the point at which the levelized cost of energy is the lowest.

The case study focused on assessing the possibility of renewable energy resources at Salalah in Oman for power generation and hydrogen synthesis is presented here. All of the power-generating components, including the wind turbines, produce DC power. As a result, the DC-bus configuration is appropriate in the current investigation.

5   Results and Discussion

PV arrays and wind turbines are employed to supply power for the load demand of a typical residence in Salalah (at latitude 17°3.0′N and longitude 54°6.4′E). The system is considered into two: the base case (system#1) (PV, hydrogen tank, electrolyzer, the battery bank is used as the storage) and the proposed case (system#2) (PV, wind turbine, electrolyzer, converter, hydrogen tank, and the battery bank). HOMER uses the Graham Algorithm to create synthetic hourly solar data from monthly averages. In addition, HOMER generates synthetic hourly wind data using the Weibull distribution. A detailed description and schematic diagram of a system are shown in the following subsections, followed by simulation and optimization results.

At night, solar energy is unavailable, and wind energy is unavailable when the local wind speed at the hub height is less than the wind turbine's cut-in wind speed. In this system, solar and wind energies are combined to compensate for the weaknesses of the other. The total cost of energy and the levelized cost of energy would both be reduced due to this arrangement. A schematic design of this system #2 is shown in Fig. 1.

Table 1 shows the average annual solar radiation and wind speed at Salalah location. According to this data, Salalah has the highest average solar annual radiation (5.65 kWh/m^2/day) and the highest yearly average wind speed (6.33 m/s). In May, Salalah has the most sun radiation (7.430 kWh/m^2/day). Hourly simulations are performed with hourly solar radiation and wind speed. Hybrid system section is examined in various sizes. The size of the PV array can range from 1 to 200 kW, while the no. of wind turbines ranges from 1 to 70, and the no. of batteries can range from 1 to 170. One of these systems includes an 80.8 kW PV array, 62 wind
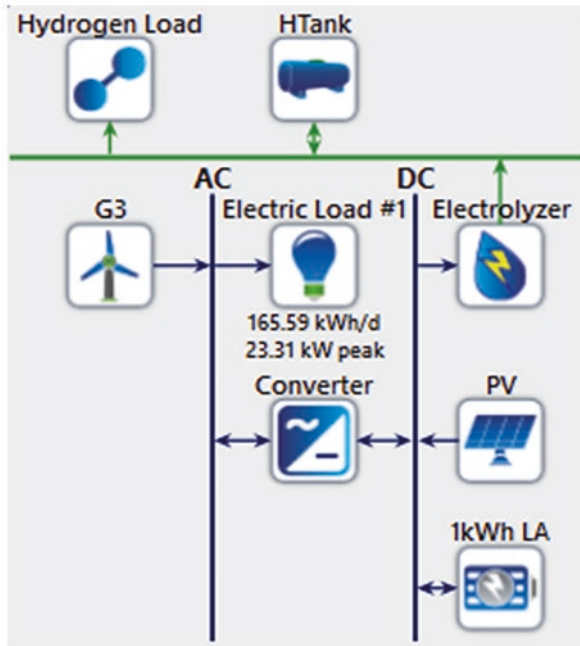
Fig. 1 Schematic design of system #2

Table 1 Average annual solar radiation and wind speed at Salalah location

City	Latitude	Longitude	Solar radiation (kWh/m² /day)	Wind speed, (m/s)
Salalah	17°3.0′ North	54°6.4′ East	5.65	6.33

turbines, a 20.5 kW converter, and 133 batteries, and has the lowest cost of energy. The net present of this system is 578,598 $ and the levelized cost of energy is 0.708 $/kWh. The hybrid system's monthly average electricity generation is indicated in Fig. 2.

The weather conditions (solar radiation, wind speed, and temperature) fluctuate by location, different system configurations are expected to meet the exact load requirements. The simulations carried out aim to discover the best system configuration location that meets the load while minimizing energy costs (COE). The optimal configuration has the lowest levelized cost while having a 100% renewable contribution (RF). Salalah's simulation findings in systems 1 and 2 are summarized in Table 2. The results show that for system #1 (without using wind turbine), the COE is 0.955 $/kWh with 187 kW PV, 165 batteries, and 22.5 kW converter. For system#2 that produces hydrogen and uses electrolyzer/hydrogen tank (PV-Wind-Battery) has the minimum COE of 0.708 $/kWh with 80.8 kW PV array, 62 wind turbine, 133 batteries, and 20.5 kW converter. The levelized cost of hydrogen is 10.2 $/kg.

The system#1 has 187 kW of PV and 165 kWh of battery capacity. The working costs for energy are presently $19,632 per year. Adding 186 kW of wind generation
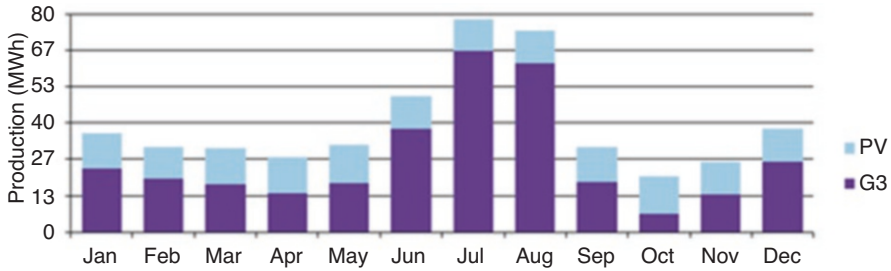
Fig. 2 Monthly average electricity production of the system

Table 2 Economic analysis of renewable energy systems at Salalah

	System 1	System 2
PV array (kW)	187	80.8
Wind turbine	–	62
Batteries	165	133
Converter (kW)	22.5	20.5
PV production (kWh/year)	346,590	149,888
Wind production (kWh/year)	–	324,212
Electrolyzer	100	100
Hydrogen tank	100	100
Initial capital ($)	514,588	615,635
Total NPC ($)	780,029	578,598
LCOE ($/kWh)	0.955	0.708
COH ($/kg H_2)	10.2	10.2
Operating and maintenance ($/year)	19,932	−2739
System lifetime (year)	25	25
RF	1	1

capacity in system#2 would decrease the effective costs to -$2739/year The asset has a payback of 4.59 years and internal rate of return (IRR) of 20.6%. The hybrid system, which consists of solar panels, wind turbine, and batteries provides the lowest cost of electricity.

6   Conclusion

This research gave a techno-economic study of creating green H_2 utilizing solar photo-voltaic power and wind turbines in Oman. The solar energy potential was first assessed with the bulk of the fields having a high radiation intensity of more than 2200 kWh/m². In Oman, the most substantial sun radiation is received by Marmul, Fahud, Sohar, and Qairoon Hairiti. Second, wind resources in Oman were explored, and a high-power density of 3.0–6.3 m/s was discovered at 28 different places.

With the help of HOMER software, two different renewable power generation systems are explored during the hourly base simulations. The power generation alternatives in this study are a PV array and wind turbines in a hybrid system. The energy created by the system covers the load demand, and any excess energy is directed to the electrolyzer, which produces hydrogen, and then to the hydrogen tank for later usage.

The research revealed that the Salalah area's hybrid renewable energy system, which integrates solar and wind resources via PV arrays and wind turbines with a battery bank storage system, results in a minimum cost of energy (COE) of 0.708 $/kWh. Due to the increased solar radiation and wind speed potential, the Sultanate of Oman's renewable energy potential (particularly in Salalah and Masirah Island) can develop PV-Wind Hybrid systems. A hydrogen production system may need to be constructed with a better electrolyzer utilization factor, reducing the size and cost of the system.

References

1. Climateknowledgeportal.worldbank.org. (2021)
2. Al-Falahi, A.K.S.: Solar energy in Oman: performance and efficiency. J. Stud. Res. (2020)
3. Ahshan, R.: Potential and economic analysis of solar-to-hydrogen production in the Sultanate of Oman. Sustainability. **13**(17), 9516 (2021)
4. Al Busaidi, A., Kazem, H., Al-Badi, A., Farooq Khan, M.: A review of optimum sizing of hybrid PV–wind renewable energy systems in Oman. Renew. Sust. Energ. Rev. **53**, 185–193 (2016)
5. Al-Sharafi, A., Sahin, A., Ayar, T., Yilbas, B.: Techno-economic analysis and optimization of solar and wind energy systems for power generation and hydrogen production in Saudi Arabia. Renew. Sust. Energ. Rev. **69**, 33–49 (2017)
6. Chisale, S.W., Eliya, S., Taulo, J.: Optimization and design of hybrid power system using HOMER pro and integrated CRITIC-PROMETHEE II approaches. Green Technol. Sustain. **1**(1), 100005 (2023)
7. Okedu, K.E., Uhunmwangho, R.: Optimization of renewable energy efficiency using HOMER. Int. J. Renew. Energy Res. **4**(2) (2014)
8. Alnaser, N., Alnaser, W.: The impact of the rise of using solar energy in GCC countries. Renew. Energy Environ. Sustain. **4**, 7 (2019)
9. Al Ghaithi, H., Fotis, G., Vita, V.: Techno-economic assessment of hybrid energy off-grid system – a case study for Masirah Island in Oman. Int. J. Power Energy Res. **1**(2) (2017)
10. Okonkwo, P., Barhoumi, E., Farhan, M.: Analysis of Hybrid Energy Power Arrangement for Salalah Community in Oman. 6th International Conference on Renewable Energy: Generation and Applications (ICREGA) (2021)
11. Rahman, F., Rehman, S., Abdul-Majeed, M.: Overview of energy storage systems for storing electricity from renewable energy sources in Saudi Arabia. Renew. Sust. Energ. Rev. **16**(1), 274–283 (2016)

Construction of a Prototype System for Hydrogen Production from Water Electrolysis with Homemade Materials

Ariana Koryn Casimiro Salazar, Dagner Lorenzo de la Cruz Laurente, Edelman Lepikov Castillo Curasma, and Jose Vladimir Cornejo Tueros

1 Introduction

Worldwide, global warming is causing concern among the population and its attention is increasing every year [1], according to IPCC (Intergovernmental Panel on Climate Change) studies, greenhouse gases (GHG) that are released by the burning of fossil fuels have irreversible effects on the climate, such as ocean warming, increased acidity in the oceans, melting of glaciers and others [2], and it is scientifically proven that greenhouse gases generate global warming. Carbon dioxide (CO_2) is the main GHG emitted by human activity, by altering and increasing the amount of CO_2 that natural sinks cannot capture [3]. The main human activity is the combustion of crude oil derivatives or fossil resources, due to the fact that the number of vehicles has increased worldwide and the number of vehicles has exceeded the limit allowed by the access roads [4]. On the other hand, air quality is in a vulnerable condition, with the presence of particulate matter (PM) and heavy metals, taking into account that gasoline is the main derivative of crude oil, its main characteristic is the octane number, which indicates the pressure and temperature to which the fuel must be subjected to be carbureted [5], confirming that one of the major pollutants is land transport.

Much of Latin America, especially Peru, is a place where energy solutions can be developed [6]; this is because it has a great variety of energy resources and so far only fossil resources have been exploited [6]. Hydrogen gas (H_2) considered as the fuel of the future and the main fuel for the generation of renewable energies [7], is the new fuel option and with the option of being able to access it in a homemade

A. K. Casimiro Salazar (✉) · D. L. de la Cruz Laurente · E. L. C. Curasma ·
J. V. Cornejo Tueros
Environmental Engineering Academic School, Engineering Faculty, Universidad Continental,
Huancayo, Junín, Peru
e-mail: 71066470@continental.edu.pe

way. For the above mentioned, the following research aims to build and implement a prototype hydrogen production system from water electrolysis, using homemade and easily accessible materials.

2 Materials and Methods

2.1 Methodology

Hydrogen gas is not found in its elemental form, but chemically combined with other elements, such as water and hydrocarbons [8]:

$$2H + 2e = H2 \tag{1}$$

Equation (1) 2 hydrogen molecules plus 2 electrons produce diatomic hydrogen [9]:

$$2H_2O = O_2 + 4H + 4e^- \tag{2}$$

Equation (2) 2 water molecules produce diatomic oxygen plus 4 hydrogen molecules + 4 electrons [9]:

$$2H + 2e = H2$$
$$2H_2O = O_2 + 4H + 4e^-$$
$$2H2O = 2H2 + O2 \tag{3}$$
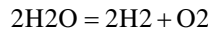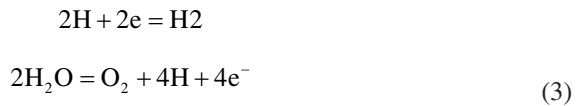
With the chemical reaction of water in the electrolysis processes of Eq. (3), we can identify the amount of hydrogen electrons present in the process [9]. The production of hydrogen reaches the anode, it is separated into electrons and protons. The protons are conducted through the membrane to the cathode, but the electrons are forced to travel through an external circuit (producing energy) this is because the membrane is insulated [10].

Electrolysis is an electrochemical process by utilizing the electrical conductivity derived from positively or negatively charged ionic conductors that are capable of transporting and generating electrical energy [11]. For electrolysis to be effective, water must not be in a pure state; in that state it is not conductive because it contains concentrations of salts or minerals [11].

Electrolysis is an electrochemical process using the electrical conductivity derived from positively or negatively charged ionic conductors, as shown in Eq. (4), which are capable of transporting and generating electrical energy [11].

$$Cathode: 2H_2O + 2e^- = 2OH^- + H_2$$

$$\text{Anode: } 2OH^- = H_2O + \frac{1}{2}O_2 + 2e^-$$

(4)

$$\text{Overall: } H_2O = H_2 + \frac{1}{2}O_2$$
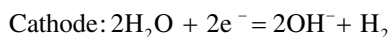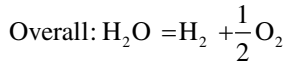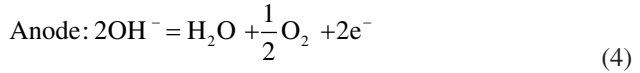
To achieve effective electrolysis, it is necessary that the water is not in a state of absolute purity, in that state it is not conductive because it has concentrations of salts or minerals [11], a continuous energy source is required and an electrolyte (water with a salt) that must be alkaline with 0.056 µS/cm of minimum electrical conductivity, in the scientific literature of the region there is an estimate of 275 µS/cm in drinking water and it is between 15 °C and 25 °C, which will transform the water into oxygen and hydrogen.

The prototype hydrogen production system is obtained from electrolysis with the help of sodium oxide. To obtain hydrogen from water is the electrolytic conversion. It combines reduction and oxidation reactions that produce oxygen gas separated from hydrogen gas [8]; for the process to be feasible, it requires a theoretical minimum of 237 kJ or 42 V of electrical energy input to dissociate each mole of water [8]. It is very important to note that the location, with coordinates 477,080 E and 8665907.2 N, which has an elevation of 3245 m.a.s.l., with an atmospheric pressure of 1012 hPa and average temperature of 20 °C, is the most important. Figure 1 shows the location of the testing site.

In order to carry out the development of the prototype, Fig. 2 shows the working diagram used, which begins with the search for accurate information according to
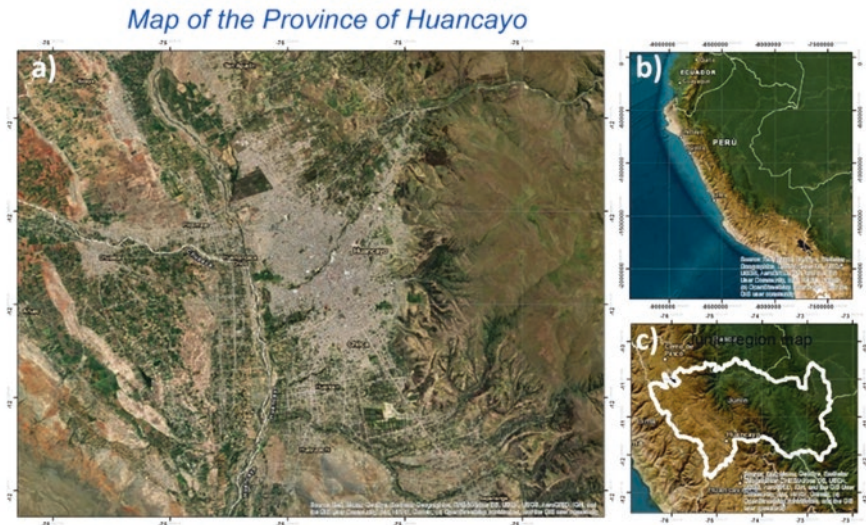
Fig. 1 (**a**) Map of the province of Huancayo, (**b**) Location map of Peru, and (**c**) Map of the Junín region
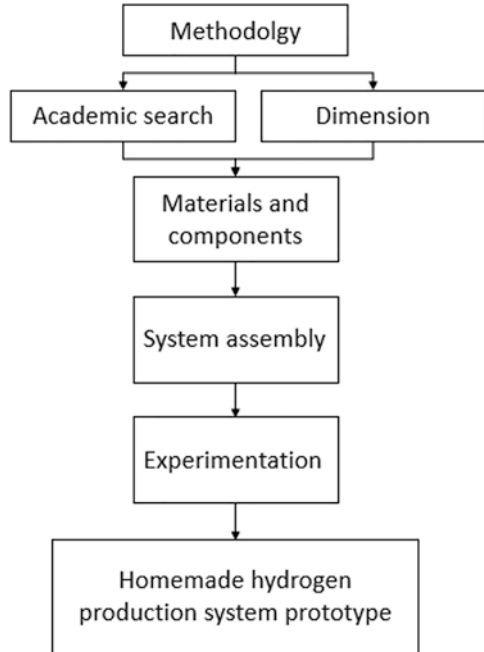
the prototype made, the integration of materials and components consists of an electrical system and a mechanical system, the materials and components used will be discussed later, after being assembled proceed to develop field tests and experiments in order to obtain the expected results.

2.2 Materials

We need a container with a wide screw lid and a capacity greater than 1 liter, in the lid of the container we coupled the stainless steel plates connected to each other, but separated with nylon insulators to have the cathode and anode. In the same lid a siliconized hose was conditioned through which the gas exits and enters a tank (container conditioned with a siliconized hose for the exit of the gas) that serves as a firewall – this more than anything when the hydrogen ignites, since it is very volatile, so the tank with water serves as a contingency plan. The container where the electrolysis is performed requires a water feeder, for this activity it is necessary that water enters the container; for the prototype to work optimally, it needs a power source of 42 volts (V) and it has to be of direct current.

The process starts by placing 1 liter of drinking water in the container, adding 7 grams of sodium oxide and mixing it with the water, also 7000 ppm mass concentration in solution can be considered as the minimum amount of hydrogen to be volatile. Then the stainless steel plates are placed and the tank is secured; once the

cables are secured to the plates, they are connected to the battery that generates the necessary amount of energy, the tank starts bubbling, which indicates that the gas is being produced. Inside the tank where the plates are located, sodium hydroxide is generated and hydrogen and oxygen come out of the tank. In the water electrolysis process, surgical steel plates are required, equipped with nylon insulators, which allow to have a positive electrode and a negative electrode. The electrodes are immersed in the electrolyte, which contains sodium oxide and drinking water.

2.3 Mass Balance

For the mass balance, potable water and sodium oxide enter the system. Through the electrolysis process, sodium hydroxide is generated and this allows oxygen and hydrogen to be obtained through the general balance of the system [12]. Figure 3 shows the mass balance – the input, the process, what is generated, and the output:

$$MW\ NaOH = 39.997\,g\,/\,mol$$

$$m\,NaOH = 10\,g$$

where MW is molecular weight, g/mol is grams per mole, m is mass, and g is grams:

$$m\,H_2O = 1000\,ml * 1\frac{g}{ml} = 1\,kg\,H_2O \tag{5}$$

$$m\,solution = m\,NaOH + m\,H_2O = 1010\,g\,Solution\ NaOH$$

Equation (1) represents the sodium hydroxide feed in the electrolysis tank, where the mass remains constant and only the distilled water feed enters. The ideal gas model will allow calculating the amount of gas produced, taking into account values such as temperature, atmospheric pressure, and the mass of the solution. When
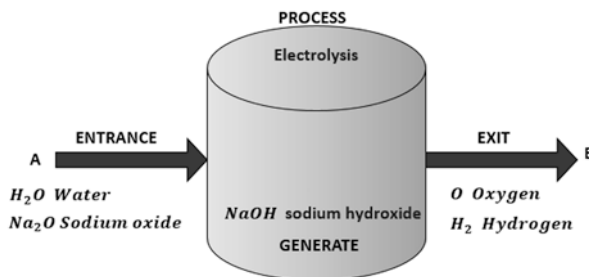
Fig. 3 Mass balance of the water electrolysis process to obtain hydrogen

clearing the equation, it is considered to find the mass, which is why the ideal gas model is feasible to determine the amount of gas produced.

Obtaining Oxygen The ideal gas formula [13] was used for this process, where the temperature variation was considered

$$P * V = n * R * T \tag{6}$$

For this purpose P is pressure, V is volume, n is the number of moles, R is the universal ideal gas counter, and T is temperature.

By solving Eq. (6):

$$n = \frac{m}{MW} \tag{7}$$

n is the number of moles, m is the mass of the gas and MW is molecular weight.

The final equation would be as follows:

$$m = \frac{P * V * MW}{R * T} \tag{8}$$

where m is the mass of the gas to be found, P is pressure, V is volume, MW is molecular weight, R is the universal ideal gas counter, and T is temperature.

m = mass of Oxygen gas, P = 1 atm, V = 0.05 l, MWO_2 = 31.99 g/mol,

$R = 0.082 \, \dfrac{\text{atm} * \text{l}}{\text{k} * \text{mol}}$, T = 15 °C - 288.15 K. For temperature of 15 °C:

$$m\left(\text{Oxygen}\right) = \frac{1\,\text{atm} * 0.051 * 31.99\,\text{g} / \text{mol}}{0.082 \, \dfrac{\text{atm} * \text{l}}{\text{k} * \text{mol}} * 288.15} = 0.068\,\text{g}\,O_2$$

According to the ideal gas formula [13] cleared to find the mass as presented in Eq. (8) and with a temperature of 15 °C or 228.15 K, we obtained 0.068 g O_2.

m = mass of Oxygen gas, P = 1 atm, V = 0.05 l, MWO_2 = 31.99 g/mol,

$R = 0.082 \, \dfrac{\text{atm} * \text{l}}{\text{k} * \text{mol}}$, T = 60 °C - 333.15 K. For temperature of 60 °C:

$$m\left(\text{Oxygen}\right) = \frac{1\,\text{atm} * 0.051 * 31.99\,\text{g} / \text{mol}}{0.082 \, \dfrac{\text{atm} * \text{l}}{\text{k} * \text{mol}} * 333.15} = 0.059\,\text{g}\,O_2$$

According to the ideal gas formula cleared to find the mass as presented in Eq. (8) and with a temperature of 60 °C or 333.15 K, 0.059 g O_2 was obtained.

Obtaining Hydrogen The ideal gas formula [13] was used for this process, as it was used in the case of oxygen, where the temperature variation was considered

$$P * V = n * R * T$$

(6)

For this purpose P is pressure, V is volume, n is the number of moles, R is the universal ideal gas counter, and T is temperature.

By solving Eq. (2):

$$n = \frac{m}{MW}$$

(7)

n is the number of moles, m is the mass of the gas, and MW is molecular weight.

The final equation would be as follows:

$$m = \frac{P * V * MW}{R * T}$$

(8)

where m is the mass of the gas to be found, P is pressure, V is volume, MW is molecular weight, R is the universal ideal gas counter, and T is temperature.

m = mass of gas Hydrogen, P = 1 atm, V = 0.1 l, MWH_2 = 2.016 g/mol,

$R = 0.082 \dfrac{atm * 1}{k * mol}$, $T = 15$ °C - 288.15 K. For temperature of 15 °C:

$$m(\text{Hydrogen}) = \frac{1 \, atm * 0.1 l * 2.016 \, g / mol}{0.082 \dfrac{atm * 1}{k * mol} * 288.15} = 0.011 \, g \, H_2$$

According to the ideal gas formula cleared to find the mass as presented in Eq. (8) and with a temperature of 15 °C or 228.15 K, we obtained 0.011 g H_2.

m = mass of Hydrogen gas, P = 1 atm, V = 0.1 l, MWH_2= 2.016 g/mol,

$R = 0.082 \dfrac{atm * 1}{k * mol}$, $T = 60$ °C - 333.15 K. For temperature of 60 °C:

$$m(\text{Hydrogen}) = \frac{1 \, atm * 0.1 l * 2.016 \, g / mol}{0.082 \dfrac{atm * 1}{k * mol} * 333.15} = 0.0074 \, g \, H_2$$

According to the ideal gas formula cleared to find the mass as presented in Eq. (8) and with a temperature of 60 °C or 333.15 K, we obtained 0.0074 g H_2.

2.4 Energy Balance

Based on the considerations made in the mass balance and with the parameters obtained, the following tests could be carried out.

For the energy yield it is necessary to know the energy consumption and this gave us the percentage yield [14]. The experiment was performed with two temperatures, and the results are detailed in the following explanation.

For the temperature of 15 °C, 0.068 g O_2 and 0.011 g H_2 were obtained:

$$0.068\,g\,O_2 * \frac{1\,mol\,O_2}{31.99\,g\,O_2} * \frac{1\,mol\,H_2O}{1\,mol\,O_2} * \frac{18\,g\,H_2O}{1\,mol\,H_2O} = 0.038\,g\,H_2O \tag{9}$$

$$\text{Yield percentage} = \frac{\text{Actual percentage}}{\text{Theorical percentage}} \frac{0.011}{0.038} = 0.289 * 100\% = 28.9\%$$

Equation (9) shows the percentage yield or efficiency.

To find the energy that the electrolysis uses for the reaction, Eq. (10) is used:

$$E = \frac{0.011\,g\,H_2}{0.038\,g\,/\,j} = 0.289\,J \tag{10}$$

To know what energy the electrolyzer provides:

$$E = \frac{0.0074\,g\,H_2}{0.011\,g\,/\,j} = 0.673\,J$$

Through Eq. (10), we can know the energy required for the electrolysis reaction and the amount of energy provided by the electrolyzer or power source:

$$Cp = 4.046 \frac{J}{g * °C}$$

$$T_i = 15°, T_f = 60°C, m = 1010\,g\,\text{solution NaOH}$$

$$E = CpNaOH * m\,\text{Solution} * \Delta°C$$

$$4.046 \frac{J}{g * °C} * 1010\,g * (60°C - 15°C) = 183,890.7\,J \tag{11}$$

Cp is heat capacity, T_i is initial temperature, T_f is final temperature, m is mass, and Δ °C is temperature difference.

By knowing the heat capacity of sodium hydroxide, through Eq. (11), we can know the amount of energy required by the prototype to achieve the efficiency

shown in the percentage yield and with the result of 183,890.7 J, it is certain that the minimum required energy is 273 kilojoule (kJ).

3   Results

Being a homemade prototype, which has a hydrogen production system by means of electrolysis, two tests were developed; the first test consisted of using 7 grams of sodium oxide and 1 liter of water, with a determined time of 15 minutes, after that time, the decrease of gas production is evidenced, even to obtain a non-flammable gas. Then the second part of the test consisted of using 10 grams of sodium oxide and 1 liter of water, with a determined time of 20 minutes, and after that time the decrease of gas production is evidenced; unlike the first test, the second one presents a volatile reaction as it is more dangerous to make a test with fire.

As it is necessary to use sodium hydroxide, it is obtained that the molecular weight is 39.997 g/mol and the mass of the solution is 1010 grams; thanks to the equation of ideal gases there was a production of 0.068 g of O_2 at 15 ° C and 0.059 g of O_2 at 60 °C. In the case of hydrogen production, a production of 0.011 g of H_2 at 15 °C and 0.007 g of H_2 at 60 °C was obtained. In addition, the energy balance demands 0.289 J by the electrolysis process, and 0.673 J supplied by the power source in the required time of 20 minutes; the whole process requires 183,890.7 J or 183.89 kJ, and this value is important, having other sources in the scientific literature, where it mentions that the minimum required is 273 kJ.

Figure 4 shows the proposed electrolysis prototype, which includes the components, the electrical and mechanical system through an assembly.
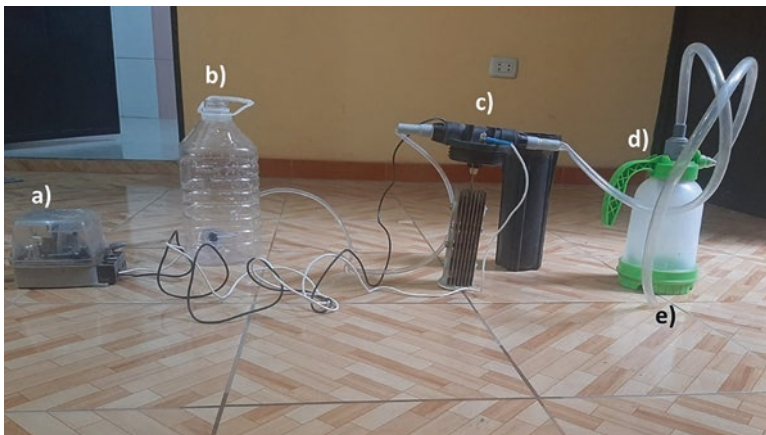
Fig. 4   (**a**) Power source with 220 v – 42 v transformer. (**b**) Water feeder to the electrolysis tank. (**c**) Tank with plates for electrolysis. (**d**) Short fire tank. (**e**) Oxygen and hydrogen gas outlet

4 Conclusion

The hydrogen and oxygen gas produced is related to the amount of sodium oxide used, which as a result was found to be more volatile as the concentration of sodium oxide increased. In addition, the developed system presents losses, after the temperature increase of the plates that perform the electrolysis, the water evaporates and that water vapor enters the tank of the hydrogen and oxygen gases, wetting the gases.

Hydrogen is considered as a potential source of renewable energy, this type of energy avoids and will avoid the deterioration of the environment; there is information in the scientific literature that supports this research, by mentioning that hydrogen is a clean fuel. The prototype has a production of 0.068 g of O_2 at 15 °C and 0.059 g of O_2 at 60 °C. Hydrogen had a production of 0.011 g of H_2 at 15 °C and 0.007 g of H_2 at 60 °C. Regarding the energy balance, demand of 0.289 joule J by the electrolysis process, and 0.673 J supplied by the power supply; for the whole process 183,890.7 J. With these results, we conclude that the prototype is efficient in the production of hydrogen.

Limits were found during the experimental development, the first limit was to measure the amount of gas produced, even with some advanced instruments, it was difficult to quantify the gas production. Another limit was to be able to separate the gases. By being able to continue developing research, they want to give multiple uses to oxygen and hydrogen. And finally, to know how efficient the hydrogen produced by the electrolysis system prototype is, an engine adapted and assembled for its operation with hydrogen is needed.

The production of hydrogen can replace fossil fuels, by adapting vehicle engines, the production of greenhouse gases can be reduced and global warming can be reduced, in addition to the fact that hydrogen can be used in the generation of electricity and not only depend on one type of production, such as hydroelectric. The hydrogen generated by the prototype can be used in a modified engine in order to initiate a reaction with said hydrogen, which makes it possible to determine the duration of time from the start of operation to the amount currently produced. In addition, the temperature influences the production, and for future research it will be considered to have a cooling system in the prototype, which has a constant temperature.

References

1. Marques, E., de Almeida Guimarães, V., de Azevedo-Ferreira, M., Boloy, R.A.M.: Renewable energy in sustainable supply chain: a review. Facul. Eng. Mag. **104**, 152–167 (2022). https://doi.org/10.17533/udea.redin.20210956
2. Concepción Martínez-Rodríguez, M., Campos-Villegas, L.E., Castillo-Monroy, J.J.: Baseline calculation of greenhouse gas emissions and future projections for the transportation sector in the state of Veracruz, Mexico Baseline calculation of greenhouse gases emissions and future projections for the transport sector in the state of Veracruz, Mexico. Tecnol. Marcha. **32**, 118–133 (2019). https://doi.org/10.8845/tm.v32.i1.4123

3. Fernández Santana, E., Rodríguez Muñoz, S., Ortega Viera, L., Franco Rico, R., Crespo Artigas, A., Bárcenas Pérez, L.: Purification of combustible gases, literatura review. Ann. Cuban Acad. Sci. **12**(2) (2022). ISSN 2304-01062

4. Muñoz Pérez, S., Salcedo Reátegui, J., Sotomayor Mendoza, A.: Environmental contamination produced by vehicular traffic and its effects on human health: literature review. Inventum. **16**(30), 20–30 (2021). https://doi.org/10.26620/uniminuto.inventum.16.30.2021.20-30

5. Campaña, G.R.C., Paredes, M.E.G., Guasgua, J.F.A.: Comparative study of emission of pollutant gases in vehicle M1, using fuel of the Andean Community. Enfoque UTE. **7**(3), 110–119 (2016). e-ISSN: 1390-6542 / p-ISSN: 1390-9363

6. Gómez-Ramírez, G.A., Meza, C., Morales-Hernández, S.: Opportunities and challenges for the integration of electrochemical storage in Central American electrical grids. Rev. Tecnol. Marcha. (2021). https://doi.org/10.18845/tm.v34i3.5352

7. Rodríguez Ramírez, Y.L., Sandoval Suárez, S.A., Santos Moreno, D.S.: Market analysis for a hydrogen generator adapted to a two (2) stroke engine on a bicycle in the city of Bogotá. Eng. Math. Inf. Sci. **9**(17), 77–91 (2022). https://doi.org/10.21017/rimci.2022.v9.n17.a113

8. Castiblanco, O., Cárdenas, D.J.: Hydrogen production and its perspective in Colombia: a review. Gest. Ambient. **23**(2), 299–311 (2020). https://doi.org/10.15446/ga.v23n2.86466

9. Rodríguez Ramírez, Y.L., Sandoval Suárez, S.A., Santos Moreno, D.S.: Design, construction and evaluation of a hydrogen generator adapted to a two (2) stroke engine on a bicycle in the city of BOGOTÁ. Eng. Mag. Math. Inf. Sci. **9**(18), 65–88 (2022). https://doi.org/10.21017/rimci.2022.v9.n18.a121

10. Kumar Baral, A., Choi, S., Kook Kim, B., Lee, J.: Processing and characterizations of a novel proton-conducting $BaCe_{0.35}Zr_{0.50}Y_{0.15}O_{3-d}$ electrolyte and its nickel-based anode composite for anode-supported IT-SOFC. Mater. Renew. Sustain. Energy. **3**(35), 3–9 (2014). https://doi.org/10.1007/s40243-014-0035-4

11. Tarazona-Romero, B.E., Sandoval-Rodriguez, C.L., Ascanio-Villabona, J.G., Quintero-Ruiz, A., Páez-Castro, R.E., Acosta-Cárdenas, O.A.: "Implementation of a prototype water electrolysis system as an alternative to produce hydrogen," IOP Conf Ser. Mater. Sci. Eng. **1154**(1), 012034 (2021). https://doi.org/10.1088/1757-899x/1154/1/012034

12. Contreras-Dioses, O., Lady Quezada-Correa, E., Quezada-Correa, Cuenca-Mayorga, F.: Equation operational model applying material balance in non-steady state // Operational model equation applying material balance in a non-stationary state. UNEMI Sci. **11**(28), 33–40 (2018). https://doi.org/10.29076/issn.2528-7737

13. Luis, G., Ríos, A., Iza, Y.M.: Ideal gases: thermodynamic diagrams. Sci. Tech. **XIII**(3), 449–454 (2007). ISSN 0122-1701

14. Calvo-Flores, F.G.: Parameters for the analysis of reactions in sustainable chemistry. Chem. Environ. **105**(1), 42–49 (2009)

Facile Electro-Oxidation of Methanol at Pd-Au/C Nanocatalyst

Abdelrahman Hosam, Yaser M. Asal (iD)**, Ahmad M. Mohammad** (iD)**, and Islam M. Al-Akraa** (iD)

1 Introduction

The heavy consumption and full dependence on fossil fuels led to many branched aspects of uncontrollable issues that eventually trapped heat and resulted in global warming, deficiency of fuel sources, and population growth resulting in ecological degradation and natural disasters. Recent studies suggested to start looking for renewable and/or clean replacements that can generate adequate amounts of energy without releasing indirect environmental emissions while at the same time remaining finitely available [1–7]. The use of fuel cells (FCs) was a good example and experimentally approved to supply enough energy without releasing any environmentally unfriendly emissions that might damage our ecosystem [8–15].

In this regard, the direct methanol FCs (DMFCs) as a class of the polymer electrolyte membrane FCs (PEMFCs) appeared highly promising where methanol was oxidized at the anodic side while oxygen from air was reduced at the cathodic side of the fuel cell, producing an electric current. Equations 1–3 describe the typical anodic, cathodic, and overall reactions in alkaline DMFCs [16]:

A. Hosam · Y. M. Asal · I. M. Al-Akraa (✉)
Department of Chemical Engineering, Faculty of Engineering, The British University in Egypt, Cairo, Egypt
e-mail: islam.ahmed@bue.edu.eg

A. M. Mohammad
Chemistry Department, Faculty of Science, Cairo University, Cairo, Egypt
e-mail: ammohammad@cu.edu.eg

$$\text{Oxidation Anode} : CH_3OH + 6OH^- \rightarrow 5H_2O + 6e^- + CO_2 \qquad (1)$$

$$\text{Reduction Cathode} : 1.5O_2 + 3H_2O + 6e^- \rightarrow 6OH^- \qquad (2)$$

_ _

$$\text{Redox overall} : CH_3OH + 1.5O_2 \rightarrow 2H_2O + CO_2 \qquad (3)$$
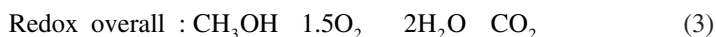
The small size, liquid nature, and the offered high theoretical energy density (4690 Wh L^{-1}) were the reasons behind the choice of methanol [13, 17]. However, a great weakness point which fades the performance of the DMFCs is the poisoning of the typical Pt and Pd anodes with oxidation intermediates such as CO released during the EOM that blocks the Pt and Pd active sites, decreasing the overall cell performance [18]. In this regard and because of the fascinating properties of AuNPs [19], the modification with AuNPs previously succeeded to mitigate such a poisoning impact via the "third body" (distorting the contiguity of the active Pt sites required for CO adsorption) and/or the "bifunctional" effects [13, 19, 20]. In the current investigation, we extended the use of AuNPs in preparing the Pd-Au/C catalyst by the simple sequential electrodeposition of PdNPs and AuNPs onto a GC electrode. Its further utilization in the catalytic EOM was studied and compared to that obtained at the conventional Pd/C catalyst. Moreover, the role behind the catalytic enhancement was elucidated and interpreted.

2 Experimental

A cleaned GC ($d = 5.0$ mm), an Ag/AgCl/NaCl (3 M), a spiral Pt wire were served, respectively, as the working, reference, and counter electrodes. The cleaning of the GC electrode was via the conventional cleaning procedures described previously [13]. All potentials in the current study were measured versus the Ag/AgCl/NaCl (3 M).

All chemicals used in the current study were of high purity and used without any further purification steps. The electrodeposition of PdNPs and AuNPs was carried out in 0.1 M Na$_2$SO$_4$ solutions containing, respectively, 2.0 mM Pd(CH$_3$COO)$_2$ and 2.0 mM HAuCl$_4$ by keeping the potential at 0.1 V allowing the passage of 10 mC for each case according to the following electrochemical equations:

$$Pd^{2+} + 2e^- \rightarrow Pd \qquad (4)$$

$$Au^{3+} + 3e^- \rightarrow Au \qquad (5)$$

All electrochemical experiments were conducted at room temperature (25 ± 1 °C) in a glass cell having two compartments with three electrode access using a Bio-Logic SAS Potentiostat (model SP-150) operated with EC-Lab software.

The surface morphology and composition of the proposed catalysts were obtained using a Zeiss Ultra 60 field emission scanning electron microscope (FE-SEM) equipped with an energy-dispersive X-ray spectroscopy (EDS).

3 Results and Discussion

3.1 *Characterization*

The surface morphology (Fig. 1) of the two prepared catalysts; Pd/C (unmodified, Fig. 1a) and Pd-Au/C (modified, Fig. 1b) was obtained using the FE-SEM. Figure 1a proved the deposition and the good distribution of PdNPs in ca. 16 nm well-distributed spherical lumps. These NPs became enlarged (ca. 44 nm) and a bit clustered in the Pd-Au/C catalyst (Fig. 1b). Such increase in size and the "no distinction in shape" behavior might infer about the possible combination/alloying of the PdNPs and AuNPs. Indeed, the real surface area was determined using a reference value of 420 μCcm^{-2} for both proposed catalysts where it was 0.46 and 0.79 cm^2, respectively, for Pd/C and Pd-Au/C catalysts.

To make sure that all active ingredients of the catalysts (Pd and Au) are deposited, and the prepared catalysts are successfully fabricated, the EDS analysis was performed. The Pd/C catalyst (Fig. 2a) showed all characteristic peaks of Pd, C, and O in their typical positions. Additionally, the Pd-Au/C catalyst (Fig. 2b) showed the other peaks corresponding to the deposition of Au.
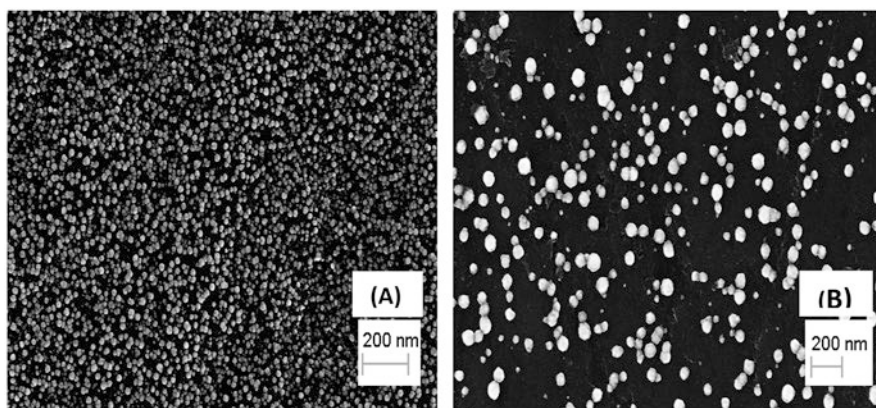
Fig. 1 FE-SEM images of (**a**) Pd/C and (**b**) Pd-Au/C catalysts

Fig. 2 EDS spectra of (**a**) Pd/C and (**b**) Pd-Au/C catalysts
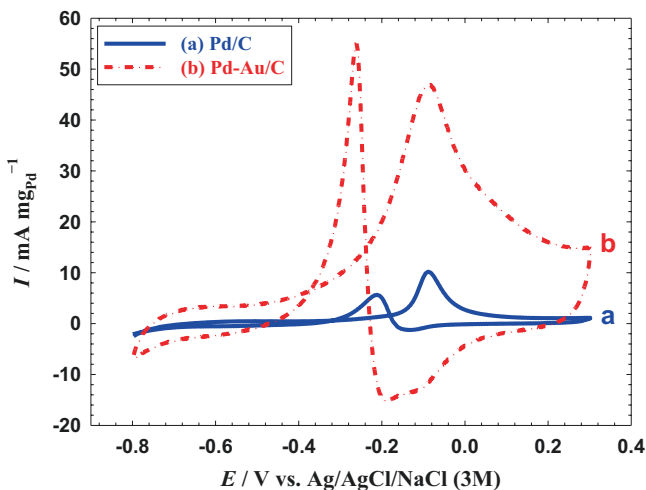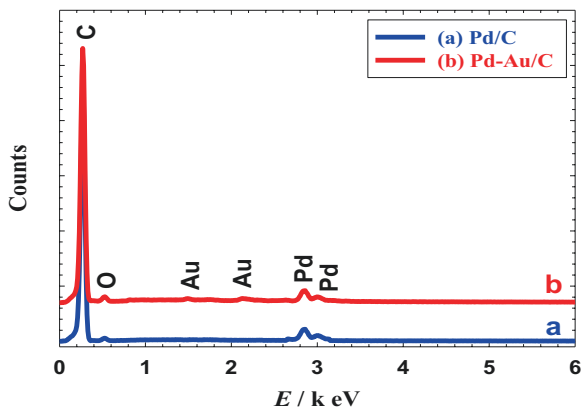
Fig. 3 CVs measured for MO at 100 mV s^{-1} in 0.3 M methanol (prepared in 0.1 M NaOH) at (**a**) Pd/C and (**b**) Pd-Au/C catalysts

3.2 Electrocatalytic Activities of the Catalysts Toward EOM

Figure 3 shows CVs for EOM at the unmodified Pd/C (Fig. 3a) and the modified Pd-Au/C (Fig. 3b) catalysts. As shown in Fig. 3a, the Pd/C catalyst acquired a low oxidation current (I_p, ca. 10 mA mg$_{Pd}^{-1}$ at ca. –0.1 V). The poisoning of the Pd surface with the oxidation intermediates which blocked most of its active sites was the reason behind this behavior [13]. Further modification of the catalyst with AuNPs could diminish such a poisoning impact by interrupting the contiguity of the Pd atoms responsible for the adsorption of such poisoning products [20]. Interestingly, the Pd-Au/C catalyst exceeded the Pd/C one in the catalytic performance toward EOM where it showed an I_p value of 47 mA mg$_{Pd}^{-1}$ (~ 5 times increase).
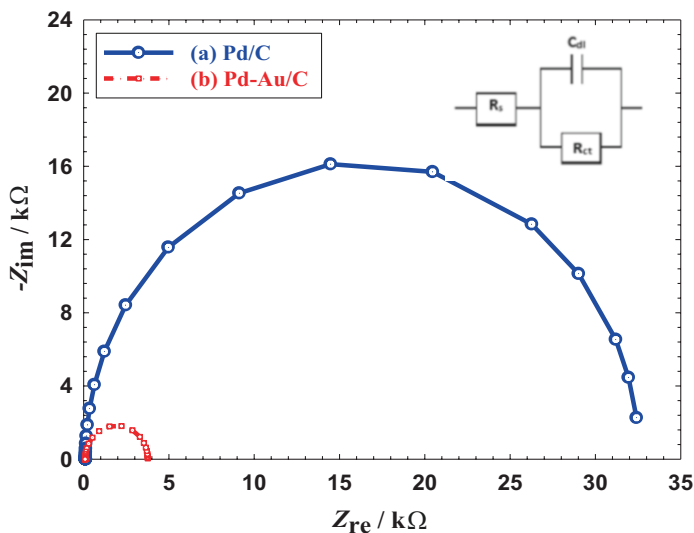
Fig. 4 Nyquist plots measured from 10 mHz to 100 kHz at open circuit potential (OCP) at the (**a**) Pd/C and (**b**) Pd-Au/C catalysts

From the other side, the enhancement in the catalytic performance may relate also to the enhanced kinetics of the electron transfer. To prove such a claim, the Nyquist plots were recorded for the two prepared catalysts. As is well known, the diameter of the semicircle could give us the value of the resistance of the charge transfer (R_{ct}). Compared with the behavior obtained at the Pd/C catalyst (Fig. 4a, 32.29 kΩ), the Pd-Au/C catalyst (Fig. 4b) acquired a much less R_{ct} value (3.67 kΩ). This confirms the data in Fig. 3 and implies the charge transfer enhancement of the Pd-Au/C catalyst toward EOM.

3.3 Parameters Affecting EOM

To achieve a better electrocatalytic EOM, the effect of changing the NaOH concentration and scan rate were examined.

Effect of NaOH Concentration Figure 5 shows the effect of changing the NaOH concentration on the I_p value of the EOM at the Pd-Au/C catalyst. It is clearly shown that as the concentration of NaOH increases, the I_p value increases with a linear dependence and a correlation coefficient of 0.98. It was concluded that increasing the OH$^-$ concentration facilitated the removal of the adsorbed intermediates and so the availability of higher number of active sites for the EOM [21].

Effect of Scan Rate Figure 6 shows the effect of changing the scan rate on the I_p value of the EOM at the Pd-Au/C catalyst. It is clearly shown that there was a slight
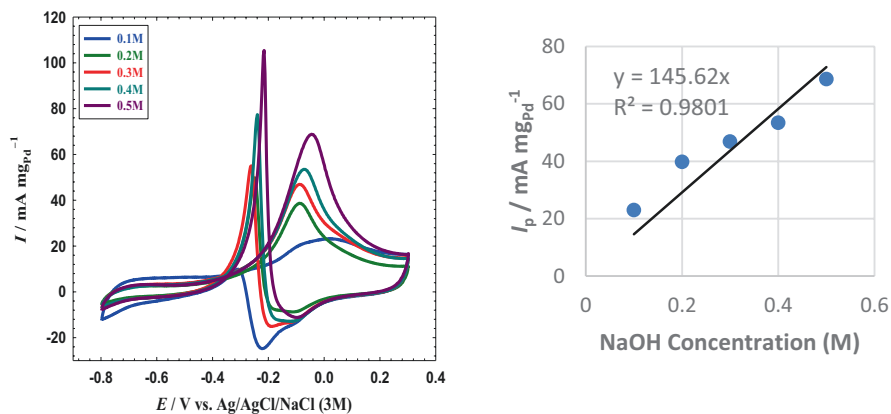
Fig. 5 CVs measured for EOM at 100 mV s^{-1} in NaOH with different concentrations containing 0.3 M methanol at the Pd-Au/C catalyst. A linear correlation between I_p and NaOH concentration is shown on the right side of figure
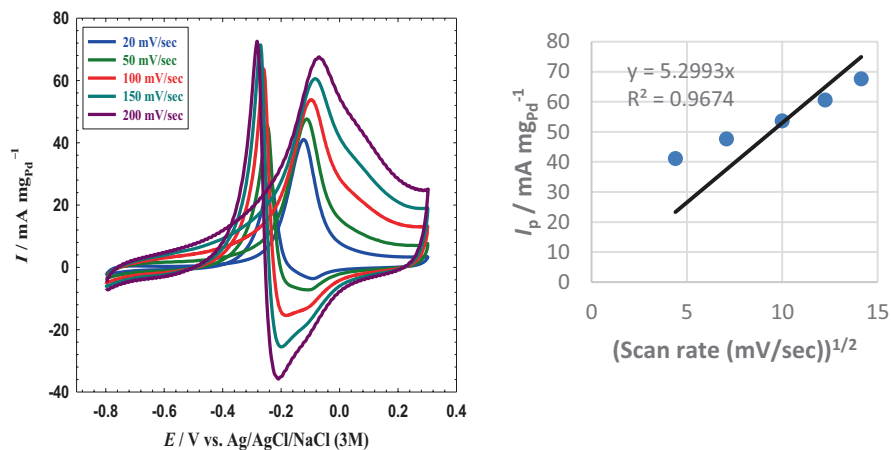
Fig. 6 CVs measured at different scan rates for EOM in in 0.3 M methanol (prepared in 0.1 M NaOH) at the Pd-Au/C catalyst. A linear correlation between I_p and square root of the scan rate is shown on the right side of figure

shift of the I_p to more positive values with increasing the potential scan rates, suggesting a kinetic limitation [22]. Moreover, as the scan rate increases, the I_p value increases with a linear dependence of the square root of the scan rate and the I_p with a correlation coefficient of 0.97 which confirmed the diffusion-controlled process [23].

4 Conclusion

A fabricated and characterized Pd-Au/C catalyst was recommended for the EOM. The Au modification step could enhance the catalysis of the EOM where a five-fold increase and a nine-fold decrease, respectively, in the I_p and R_{ct} values compared with the results obtained at the unmodified Pd/C catalyst. This suggested a decrease in the Pd surface poisoning and an enhancement in the charge transfer during the EOM. Moreover, the effect of NaOH concentration and scan rate was optimized to achieve a better electrocatalytic EOM. Linear relationships were obtained for both optimization steps suggesting, respectively, a facilitated removal of the adsorbed intermediates and a diffusion-controlled oxidation process.

References

1. Al-Akraa, I.M., Asal, Y.M., Arafa, A.M.: Fabrication of MnOx/MWCNTs-GC nanocatalyst for oxygen evolution reaction. Int. J. Electrochem. Sci. **13**(9), 8775–8783 (2018)
2. Al-Akraa, I.M., Asal, Y.M., Khamis, S.D.: Assembling of NiOx/MWCNTs-GC anodic nano-catalyst for water electrolysis applications. Int. J. Electrochem. Sci. **13**(10), 9712–9720 (2018)
3. Al-Akraa, I.M., Ohsaka, T., Mohammad, A.M.: A promising amendment for water splitters: boosted oxygen evolution at a platinum, titanium oxide and manganese oxide hybrid catalyst. Arab. J. Chem. **12**(7), 897–907 (2019)
4. Ayman, R., Asal, Y.M., Mohammad, A.M., Al-Akraa, I.M.: Castor oil conversion to biodiesel: a process simulation study. ARPN J. Eng. Appl. Sci. **17**(9), 964–968 (2022)
5. Hassan, H.E., Asal, Y.M., Mohammad, A.M., Al-Akraa, I.M.: Biodiesel production from castor oil: mixing optimization during transesterification. ARPN J. Eng. Appl. Sci. **17**(8), 844–848 (2022)
6. Bei, J., Wang, C.: Renewable energy resources and sustainable development goals: evidence based on green finance, clean energy and environmentally friendly investment. Resour. Policy. **80**, 103194 (2023)
7. Li, X., Raorane, C.J., Xia, C., Wu, Y., Tran, T.K.N., Khademi, T.: Latest approaches on green hydrogen as a potential source of renewable energy towards sustainable energy: spotlighting of recent innovations, challenges, and future insights. Fuel. **334**, 126684 (2023)
8. Al-Akraa, I.M., Mohammad, A.M., El-Deab, M.S., El-Anadouli, B.E.: Electrocatalysis by nanoparticle: enhanced electro-oxidation of formic acid at NiOx-Pd binary nanocatalysts. J. Electrochem. Soc. **162**(10), F1114–F1118 (2015)
9. Al-Akraa, I.M., Mohammad, A.M., El-Deab, M.S., El-Anadouli, B.E.: Fabrication of CuOx-Pd nanocatalyst supported on a glassy carbon electrode for enhanced formic acid electro-oxidation. J. Nanotechnol. **2018**, 3803969 (2018)
10. Al-Akraa, I.M., Mohammad, A.M.: A spin-coated TiOx/Pt nanolayered anodic catalyst for the direct formic acid fuel cells. Arab. J. Chem. **13**(3), 4703–4711 (2020)
11. Al-Akraa, I.M., Salama, A.E., Asal, Y.M., Mohammad, A.M.: Boosted performance of NiOx/Pt nanocatalyst for the electro-oxidation of formic acid: a substrate's functionalization with multi-walled carbon nanotubes. Arab. J. Chem. **14**(10), 103383 (2021)
12. Al-Akraa, I.M., Asal, Y.M., Darwish, S.A., Fikry, R.M., Mahmoud, R.H., Hassan, M., Mohammad, A.M.: Effect of palladium loading on catalytic properties of Pd/GCE for the electro-oxidation of methanol, formic acid, and ethylene glycol. Int. J. Electrochem. Sci. **17**, 220455 (2022)

13. Al-Akraa, I.M., Mohammad, A.M.: A spin-coated TiOx-modified Pt anodic catalyst for the direct methanol fuel cells. Energy Rep. **8**, 438–442 (2022)
14. Asal, Y.M., Mohammad, A.M., Abd El Rehim, S.S., Al-Akraa, I.M.: Co-electrodeposited PtPd anodic catalyst for the direct formic acid fuel cells. Energy Rep. **8**, 560–564 (2022)
15. Farrag, H.H., Al-Akraa, I.M., Allam, N.K., Mohammad, A.M.: Amendment of palladium nanocubes with iron oxide nanowires for boosted formic acid electro−oxidation. Arab. J. Chem. **16**(3), 104524 (2023)
16. Karimi, F., Akin, M., Bayat, R., Bekmezci, M., Darabi, R., Aghapour, E., Sen, F.: Application of quasihexagonal Pt@PdS$_2$-MWCNT catalyst with high electrochemical performance for electro-oxidation of methanol, 2-propanol, and glycerol alcohols for fuel cells. Mol. Catal. **536**, 112874 (2023)
17. Al-Akraa, I.M., Asal, Y.M., Khalifa, A.A.: A promising modification of Pt surfaces with CNTs for decreasing poisoning impact in direct methanol fuel cells. Int. J. Electrochem. Sci. **14**(1), 8276–8283 (2019)
18. Chandra Sekhar, Y., Raghavendra, P., Sri Chandana, P., Maiyalagan, T., Subramanyam Sarma, L.: Graphene supported Pd–cu bimetallic nanoparticles as efficient catalyst for electrooxidation of methanol in alkaline media. J. Phys. Chem. Solids. **174**, 111133 (2023)
19. Al-Akraa, I.M., Mohammad, A.M., El-Deab, M.S., El-Anadouli, B.E.: Self-assembling of gold nanoparticles array for electro-sensing applications. Int. J. Electrochem. Sci. **8**(1), 458–466 (2013)
20. Asal, Y.M., Mohammad, A.M., Abd El Rehim, S.S., Al-Akraa, I.M.: Preparation of co-electrodeposited Pd-Au nanocatalyst for methanol electro-oxidation. Int. J. Electrochem. Sci. **16**, 1–11 (2021)
21. Hassan, K.M., Hathoot, A.A., Maher, R., Abdel Azzem, M.: Electrocatalytic oxidation of ethanol at Pd, Pt, Pd/Pt and Pt/Pd nano particles supported on poly 1,8-diaminonaphthalene film in alkaline medium. RSC. Advances. **8**(28), 15417–15426 (2018)
22. Raoof, J.B., Ojani, R., Hosseini, S.R.: An electrochemical investigation of methanol oxidation on nickel hydroxide nanoparticles. S. Afr. J. Chem. **66**, 47–53 (2013)
23. Danaee, I., Jafarian, M., Mirzapoor, A., Gobal, F., Mahjani, M.G.: Electrooxidation of methanol on NiMn alloy modified graphite electrode. Electrochim. Acta. **55**(6), 2093–2100 (2010)

Part V
Renewable Energy Transformation and Energy Market Analysis

Renewable Energy and Economic Growth in "Next Eleven" Emerging Markets

Ismail Aremu Muhammed and Abdulbaki Teniola Ubandawaki

1   Introduction

So many nations have had fast economic expansion during the last four decades, mainly due to industrialization. The expansion of economic activity in both developed and developing nations has given rise to two major worries: first, the rapid depletion of non-renewable energy sources due to their constant consumption; and second, the effects of global warming brought on by the emissions of greenhouse gases like carbon dioxide (CO_2) and methane. Due to these energy issues, renewable energy is now receiving a lot of attention.

The international community has gradually realized that such development is not sustainable over the long term. Against this background, the 1997 Kyoto Protocol served as an avenue where attempts were made to cut the proportion of emissions caused by fossil fuels. The pact required the industrialized nations to cut greenhouse gas emissions, namely, CO_2 emissions. As a result, many industrialized and developing nations began to rely more on renewable energy and less on fossil fuels [1].

In 2013, it was projected that 19.1% of the final energy consumed worldwide came from renewable sources. Wind, solar PV, and hydropower have been driving the recent expansion of the electrical industry. The capacity for heating is expanding steadily, while the output of biofuels for transportation has lately increased after a decline in 2011–2012. According to the International Energy Agency's (IEA) most

I. A. Muhammed (✉)
Universiti Brunei Darussalam, Bandar Seri Begawan, Brunei

A. T. Ubandawaki
The American University in Cairo, Cairo, Egypt

optimistic scenario, renewable energy sources would account for 39% of power output by 2050, up from 18.3% in 2002. All these point to the growing consumption of renewable energy in order to yield a more sustainable environment and healthy living. However, the question of whether this trend will help fuel economic growth is becoming more and more pressing as there is a rise in the production and use of renewable energy in the overall energy mix.

There is, nevertheless, a lack of consensus on the mechanics of the link between renewable energy and economic growth. While some studies revealed that renewable energy promotes economic growth, others revealed that it hinders economic growth and others revealed no link between them. Looked at from another angle, the direction of causation between renewable energy and economic growth is mainly vague. An argument may support that improvement in economic growth leads to more renewable energy consumption, while another may support the other way round. Moreover, the emerging markets (most especially the countries categorized as "Next Eleven" emerging markets), which are now in the quest for economic prosperity more than ever, have received less attention in the investigation of the relationship between renewable energy and economic growth, leaving unanswered the question of how the increased use of renewable energy in this economies relates to their economic growth.

On this note, the key question raised is, what is the direction of causal relationship between renewable energy consumption and economic growth and how does the renewable energy promote economic growth in "Next Eleven" emerging markets?

In addition to this introduction section that highlights the policy problem and aims of the chapter, the second section provides the literature review and policy context, the third section highlights the hypothesis development, the fourth section gives details of the methodology and data, the fifth section presents the findings, and the sixth section provides the required policy recommendations.

2 Literature Review

2.1 The Impact of Renewable Energy Consumption on Economic Growth

Research on the renewable energy-economic growth nexus has gained attention from different climes of the world. Different researchers across the globe have explored the relationship between renewable energy and economic growth. The reason for this burgeoning attention given to this area of research might be attributed to the global campaign against fossil fuels and the need to contextualize the intertwined relationship between different energy sources and economic indicators.

Despite the numerous studies conducted along this line, there still needs to be a consensus on findings in the existing literature. Empirical findings from this discourse can be divided into two major schools of thought. The first and most prominent school opines that there is a relationship between renewable energy consumption and economic growth. (See, e.g., [2–17]).

The above school of thought which is undoubtedly the strongest in terms of empirical backing has three hypotheses within it: the feedback, conservation, and the growth hypothesis. The feedback hypothesis suggests a bi-directional causality between renewable energy consumption and economic growth, this implies that there is interdependence between the two constructs. Many studies have supported, including the work of [5], when they studied the impact of renewable energy on carbon emissions and economic growth in 15 major renewable energy-consuming countries. The authors of [4] also support the feedback hypothesis when they examined the impact of renewable and non-renewable energy consumption on economic growth using the Middle East and North Africa Net Oil Exporting Countries as a case study. The authors of [17] also found the feedback hypothesis to be valid in their study. The authors of [18] examined the heterogeneous impacts of energy efficiency, renewable energy consumption, and other factors on the economic growth of Brazil, Russia, India, China, and South Africa (BRICS) for 1990–2014 and the results also supported the feedback hypothesis.

The growth hypothesis suggests a uni-directional causality running from energy consumption to economic growth. This hypothesis has been supported by [3]. The authors of [11] also supported the growth hypothesis when they studied the effect of renewable energy consumption on economic growth across 38 renewable-energy-consuming nations covering the timeline of 1990–2018. The study adopted dynamic ordinary least squares (DOLS), fully modified ordinary least squares (FMOLS), and heterogeneous non-causality approaches.

Lastly, the conservation hypothesis suggests a uni-directional causality running from economic growth to renewable energy consumption. This hypothesis was supported by the work of [12] when they found a causality running from economic growth to renewable energy consumption among the 5 South Asian countries investigated. The study examined the long-run equilibrium relationship by adopting panel Fully Modified Ordinary Least Squares and panel Dynamic Ordinary Least Squares estimation techniques. The work of [19] has also supported the conservation hypothesis in the case of the Czech Republic.

The second school of thought opines that there is no relationship between renewable energy consumption and economic growth. This group supports the neutrality hypothesis, which is the fourth hypothesis found in the literature. This school reports that none of these constructs exert any effect on one another and they are independent totality. Even though this school of thought is the weakest due to the few studies that backed it, some studies have also supported the neutrality hypothesis. [7] studied the association between renewable energy consumption and economic growth in the nine Black Sea and Balkan countries, according to the st;

accordingutrality hypothesis was valid in the case of Turkey. Along this line, the authors of [19] also contributed to this school of thought by supporting the neutrality hypothesis in the case of Cyprus, Estonia, Hungary, Poland, and Slovenia when they investigated the role of renewable energy consumption in economic growth within the EU member countries.

2.2 Renewable Energy Policy in Nigeria

For instance, Nigeria set a target in its Renewable Energy Master Plan (REMP) to increase renewable electricity supply from 13% of total electricity generation in 2015 to 23% in 2025, consequently increasing the consumption of renewable energy to a large volume of total final energy consumption. The plan also includes a target to increase energy from small-hydro and biomass-based power sources from 600 megawatts and 50 megawatts in 2015 to 2000 megawatts and 400 megawatts in 2025, respectively, and also achieve 500 megawatts and 40 megawatts of energy from solar PV and wind energy sources, respectively, by 2025. The REMP also includes a variety of fiscal and market incentives to encourage the development of renewable energy. In the medium term, the strategy calls for a suspension of import taxes on renewable energy technology. Longer term, the strategy recommends the creation of further tax credits, capital incentives, and preferred lending alternatives for renewable energy projects. According to World Bank estimates, Nigeria already had its consumption of renewable energy as 81.4% of total final energy consumption in 2019. Even though this seems to ban outstanding achievement, there is more to how the consumption of renewable energy promoted economic activities in the country and how sustainable is the continuation of such consumption.

2.3 Renewable Energy Policy in Egypt

Egypt is working to increase the supply of electricity generated from renewable sources to 20% by 2022 and 42% by 2035, with wind accounting for 14%, hydropower accounting for 1.98%, photovoltaic (PV) 21.3%, wind accounting for 14%, and concentrating solar power (CSP) accounting for 5.52%. Conventional energy sources account for 57.33%. This plan is now being amended and awaits approval from the Supreme Council for Energy to represent 33% of the energy generated from renewable sources by 2025, 48% by 2030, 55% by 2035, and 61% by 2040. This is seen to be a highly hopeful strategy. The majority of this capacity is projected to be provided by the private sector. According to World Bank estimates, Egypt had its consumption of renewable energy as only 5.3% of total final energy consumption in 2019. This shows a very minimal proportion of total energy consumption being from renewable energy sources and equally shows the country has

a relatively long way to go to achieve its sustainable environment plans, despite its abundance of sunny weather and high wind speeds.

2.4   Renewable Energy Policy in Iran

According to Iran's Fifth Five-Year Development Plan, renewable resources must produce 5000 MW of power under green horizon scenarios. There is no scarcity of knowledge in Iran, which is positioned near the zero line (Earth's equator) and has around 300 bright sunny days per year, concerning developing regulations encouraging solar energy. According to recent figures, assuming current growth plans are carried out, the installed capacity of renewable energy systems will reach 2.8 GW by 2030. More than $2800 million in US dollars must be invested over 20 years, from 2010 to 2030. Despite the benefits of using solar energy, such as lowering greenhouse gas emissions, it is crucial to highlight that solar power is 2.5 to 5 times more expensive than electricity generated by existing conventional power sources, such as coal and other sources. According to World Bank estimates, Iran had its consumption of renewable energy as only 0.98% of total final energy consumption in 2019. This shows a very minimal proportion of total energy consumption from renewable energy sources and equally shows the country has a very long way to go to achieve its policy targets on renewable energy, despite having an impressive clear sunny number of days in a year.

2.5   Renewable Energy Policy in Bangladesh

The existing renewable energy policy for Bangladesh has as part of its objectives to scale up contributions of renewable energy both to electricity and to heat energy; scale up contributions of renewable energy to electricity production; develop sustainable energy supplies to substitute indigenous non-renewable energy supplies; enable, encourage, and facilitate both public and private sector investment in renewable energy projects; and harness the potential of renewable energy resources and dissemination of renewable energy technologies in rural, peri-urban, and urban areas. The government has continued to work in line with the policy in order to achieve these objectives. However, the country's renewable energy consumption as a proportion of total final energy consumption has been declining despite government policy to ensure a transition from the use of electricity from non-renewable energy sources to those from renewable energy sources. According to World Bank estimates, Bangladesh had its consumption of renewable energy as about 24.8% of total final energy consumption in 2019 down from 31.9% in 2015 which was also down from about 40.3% in 2010. This shows that the country is retrogressing in terms of renewable energy consumption.

3   Hypothesis Development

On the mechanics of the link between renewable energy and economic growth, there is, nevertheless, a lack of consensus. Some studies revealed that renewable energy promotes economic growth, other studies revealed that it hinders economic growth while a third group revealed that there is no link between them. In other words, the renewable energy- economic growth relationship is largely vague. An argument may support that improvement in economic growth leads to more renewable energy consumption while another argument may support the other way round. Moreover, the emerging markets (most especially the countries categorized as "Next Eleven" emerging markets), which are now in the quest for economic prosperity more than ever, have received less attention in the investigation of the relationship between renewable energy and economic growth, leaving unanswered the question of how the increased use of renewable energy in this economy relates to their economic growth.

On this note, this study tested the following stated research hypotheses for a clear understanding of the impact of renewable energy consumption on economic growth in "Next Eleven" emerging markets.

H1: There is a causal relationship flowing from renewable energy consumption to economic growth in "Next Eleven" emerging markets.

H2: There is a causal relationship flowing from economic growth to renewable energy consumption in "Next Eleven" emerging markets.

H3: Renewable energy promotes economic growth in "Next Eleven" emerging markets.

4   Methodology and Data

The study focuses on the "Next Eleven" emerging economies, which are a set of emerging markets comprised of two countries in Africa (Nigeria and Egypt), one country each in Central America, Europe, and Middle-East (Mexico, Turkey, and Iran, respectively), and six countries in Asia (Vietnam, South Korea, Philippines, Pakistan, Bangladesh, and Indonesia). The term "Next Eleven" was coined out by Goldman Sachs, referring to these countries which have potentials of rivaling the advanced economies. The choice of these countries rests on the increase in their renewable energy consumption in recent years, which has signaled a shift in their traditional energy consumption mix and opening up a potential of further enhancing their economies.

Secondary data was used in this study, covering a period between 1990 and 2019. The data was sourced from Word Development Indicators (WDI). The choice of the sample period stems from data availability from the secondary source. The data were collected for variables such as real GDP (RGDP), which was used to proxy economic growth, and gross fixed capital formation (GFCF), total labor force (LF),

and renewable energy consumption (RE), which are the explanatory variables. The natural logarithm transformation was taken for real GDP, gross fixed capital formation, and total labor force in order to bring down their large values.

In order to examine the causal relationship between renewable energy and economic growth, the Dumitrscu-Hurlin panel Granger causality procedure was employed. Dumitrescu and Hurlin (2012) proposed a test for Granger non-causality for heterogeneous panel based on the individual Wald statistics of Granger non-causality averaged across cross-sectional units. As for the impact of renewable energy on economic growth, the dynamic panel autoregressive distributive lag model was employed to estimate the model. The estimation procedure is capable of controlling for the likely endogeneity in the renewable energy-economic growth nexus. Stata 14 software was used to generate the panel data results for the effect of renewable energy on economic growth. Furthermore, E-views 9 software was employed to generate the time series results.

4.1 Summary of Variables

The panel summary of variables presented in Table 1 shows that real GDP is in billions and its average across the countries in the sample amounted to about US$415 billion. Similarly, gross fixed capital formation has an average of about US$113 billion. Labor force is averagely 42.3 million people among these countries and the proportion of renewable energy of total energy consumption is averagely 31.39%. The time series summary of these variables for each country is presented in Table 2. The summary for Turkey and Vietnam were not presented because of unavailability of data and this also influenced the decision to omit both countries from the panel and time series regression analyses.

4.2 Models

The empirical model to examine the causal relationship that exists between economic growth and renewable energy is presented as follows:

Table 1 Panel summary of variables

Variable	Mean	Std. Dev.	Min	Max
RGDP ($billion)	415.0	345.0	45.1	1640.0
GFCF ($billion)	113.0	183.0	−837.0	922.0
LF (millions of people)	42.3	24.3	14.3	136.0
RE (% of Total final energy consumption)	31.39	26.44	0.44	88.68

Table 2 Time series summary of variables

Country	Variable	Mean	Std. Dev.	Minimum	Maximum
Nigeria	RGDP	292.0	132.0	150.0	500.0
	GFCF	61.0	9.84	48.0	82.0
	LF	46.3	9.05	32.0	62.0
	RE	85.06	2.28	80.64	88.68
Egypt	RGDP	229.0	86.1	120.0	400.0
	GFCF	32.9	17.4	11.0	76.0
	LF	22.9	4.74	16.0	29.0
	RE	7.04	1.50	5.10	9.83
Mexico	RGDP	937.0	197.0	630.0	1300.0
	GFCF	209.0	46.4	130.0	270.0
	LF	42.9	8.17	29.0	57.0
	RE	10.95	1.67	8.97	14.41
Iran	RGDP	323.0	89.3	190.0	460.0
	GFCF	155.0	54.0	60.0	250.0
	LF	20.8	4.06	14.0	27.0
	RE	0.98	0.27	0.44	1.53
South Korea	RGDP	1010.0	386.0	400.0	1600.0
	GFCF	324.0	102.0	150.0	510.0
	LF	24.1	2.82	19.0	29.0
	RE	1.35	0.88	0.44	3.36
The Philippines	RGDP	200.0	86.2	110.0	400.0
	GFCF	39.9	23.5	19.0	100.0
	LF	33.4	7.01	22.0	45.0
	RE	34.94	6.73	26.73	51.96
Pakistan	RGDP	191.0	67.9	100.0	320.0
	GFCF	33.4	8.7	22.0	54.0
	LF	49.0	13.1	30.0	72.0
	RE	49.30	4.22	42.09	58.09
Bangladesh	RGDP	122.0	59.7	53.0	260.0
	GFCF	30.6	21.3	7.8	80.0
	LF	51.7	9.85	35.0	69.0
	RE	50.07	14.69	24.75	73.16
Indonesia	RGDP	563.0	225.0	270.0	1000.0
	GFCF	124.0	455.0	−840.0	920.0
	LF	104.0	17.1	77.0	140.0
	RE	40.49	11.04	19.09	58.60
Turkey	RGDP	556.0	226.0	289.0	997.0
	GFCF	–	–	–	–
	LF	24.4	4.14	19.4	33.4
	RE	17.01	4.54	11.40	24.51
Vietnam	RGDP	143.0	78.4	45.1	314.0
	GFCF	–	–	–	–
	LF	44.8	7.87	32.7	55.8
	RE	48.11	16.90	18.65	76.08

$$\ln\text{RGDP}_t = \alpha + \sum_{k=1}^{K} \beta_k \ln\text{RGDP}_{t-k} + \sum_{k=1}^{K} \gamma_k RE_{t-k} + \varepsilon_t \tag{1}$$

where lnRGDP is the natural log of real GDP and RE is renewable energy. The fundamental tenet is that if previous values of RE have significant impact on lnRGDP despite including past values of lnRGDP in the model, it is then said that RE has causal influence on lnRGDP. Given this equation, it is simple to test for causality using the following null hypothesis in an F-test:

$$H_0 : \gamma_1 = \ldots = \gamma_K = 0 \tag{2}$$

One can infer that causality flows from RE to lnRGDP if the null hypothesis is rejected. Naturally, the RE and lnRGDP variables can be swapped to test for causation in the opposite manner.

The model to examine the impact of renewable energy on economic growth is specified as follows:

$$\ln\text{RGDP}_{it} = \alpha_0 + \alpha_1 \ln\text{GFCF}_{it} + \alpha_2 \ln\text{LF}_{it} + \alpha_3 RE_{it} + \varepsilon_{it} \tag{3}$$

where: lnRGDP is the natural log of real GDP; lnGFCF is the natural log of gross fixed capital formation; lnLF is the natural log of total labor force; RE is renewable energy consumption, and ε is the disturbance term. The subscripts (it) indicate observation over a panel of eleven emerging markets. Although, the estimation was done for the countries together in a panel data analysis, a time series analysis was also carried out for each of the countries to verify the overall panel analysis.

5   Empirical Results

First, the study examined the time series properties of the panel data, as well as the time series data, through the unit root test. It further examined the cointegration of the non-stationary series employed in the study. The unit root test and cointegration test results are presented in Tables 3 and 4, respectively. The unit root results suggest that all the variables had unit root and are not stationary. Therefore, the test was conducted on their difference transformations which revealed that each of the variables became stationary after first difference. The result implies that estimation methods like the ordinary least squares would give spurious results in this situation. Therefore, this study resorted to employing the autoregressive distributive lag (ARDL) method in order to ensure the validity of the regression results. Prior to the ARDL results, the cointegration test result is presented. The result of the cointegration test conducted through the Westerlund (2007) error-correction-based test revealed that there is cointegration among the variables. The test shows four statistics and their respective low p-values indicate they are significant and hence guarantee long-run cointegration.

Table 3 Results of panel unit root test

	Fisher-ADF		Fisher-PP	
Variable	stat	p-value	stat	p-value
lnGDP	−1.599	0.945	−0.627	0.734
ΔlnGDP	9.257	0.000	19.29	0.000
lnGFCF	−2.023	0.978	−1.669	0.952
ΔlnGFCF	29.67	0.000	39.8	0.000
lnLF	−1.197	0.884	0.117	0.453
ΔlnLF	8.581	0.000	19.37	0.000
RE	0.225	0.410	−0.864	0.806
ΔRE	19.66	0.000	36.87	0.000

Note: Δ = difference notation

Table 4 Result of cointegration test

Statistic	Value	P-value
Gt	−6.178	0.000
Ga	−8.186	0.000
Pt	−4.852	0.000
Pa	−10.454	0.000

To verify the first and second hypotheses, Table 5 shows from the panel causality test result that a statistic value of −0.821 and p-value of 0.411 imply that there is no evidence of causal relationship flowing from renewable energy to economic growth. However, the table shows that there is causality running from economic growth to renewable energy consumption (with statistic value of 9.589 and p-value of 0.000). The table also shows that similar results were obtained for most of the countries in the sample individually. For Egypt, South Korea, Pakistan, Bangladesh, and Indonesia, respective statistics of 0.246, 0.010, 0.657, 1.066, and 0.081 and p-values of 0.783, 0.989, 0.527, 0.360, and 0.921 for the flow from renewable energy to economic growth and respective statistics of 3.025, 2.576, 5.248, 10.43, and 5.369 and p-values of 0.068, 0.097, 0.013, 0.000, and 0.012 for the flow from economic growth to renewable energy imply that there is evidence of causal relationship only flowing from economic growth to renewable energy for these countries.

For Nigeria, Mexico, Iran, and the Philippines, respective statistics of 1.186, 1.953, 2.133, and 0.133 and p-values of 0.323, 0.164, 0.141, and 0.875 for the flow from renewable energy to economic growth and respective statistics of 1.847, 0.011, 0.007, and 0.803 and p-values of 0.180, 0.988, 0.992, and 0.460 for the flow from economic growth to renewable energy imply that there is no evidence of causal relationship between renewable energy and economic growth for these countries.

The findings from these panel causality tests revealed that causal relationship mainly flows from economic growth to renewable energy consumption and not vice versa. In other words, it is an increase in economic growth that prompts an increase in the consumption of renewable energy in these economies, thereby supporting the conservation hypothesis that economic growth precedes renewable energy consumption. Specifically for individual countries, there is evidence of causal relation

Table 5 Causality test results

Sample	Direction	stat	*p*-value
Panel	RE to lnRGDP	−0.821	0.411
	lnRGDP to RE	9.585***	0.000
Nigeria	RE to lnRGDP	1.186	0.323
	lnRGDP to RE	1.847	0.180
Egypt	RE to lnRGDP	0.246	0.783
	lnRGDP to RE	3.025*	0.068
Mexico	RE to lnRGDP	1.953	0.164
	lnRGDP to RE	0.011	0.988
Iran	RE to lnRGDP	2.133	0.141
	lnRGDP to RE	0.007	0.992
South Korea	RE to lnRGDP	0.010	0.989
	lnRGDP to RE	2.576*	0.097
The Philippines	RE to lnRGDP	0.133	0.875
	lnRGDP to RE	0.803	0.460
Pakistan	RE to lnRGDP	0.657	0.527
	lnRGDP to RE	5.248**	0.013
Bangladesh	RE to lnRGDP	1.066	0.360
	lnRGDP to RE	10.43***	0.000
Indonesia	RE to lnRGDP	0.081	0.921
	lnRGDP to RE	5.369**	0.012

Notes: ***$p < 0.01$; **$p < 0.05$, *$p < 01$

flowing from economic growth to renewable energy consumption in Egypt, South Korea, Pakistan, Bangladesh, and Indonesia but there is no evidence of causal relation in Nigeria, Mexico, Iran, and the Philippines.

Verifying the third hypothesis and examining the impact of renewable energy on economic growth the panel ARDL method was applied to the panel data. The Hausman test was used to select the most preferred estimation procedure between the pooled mean group (PMG) estimator and each of the mean group (MG) and dynamic fixed effects (DFE) estimators. Its results in Table 6 revealed that the statistic of 1.54 for the choice between PMG and MG and the statistic of 0.001 for the choice between PMG and DFE, each with very high *p*-values, provide no evidence to reject the PMG as a better estimator to the other two alternatives. Considering the PMG result, log of gross fixed capital formation shows a significant positive coefficient both in the short and long runs (0.574 and 0.120, respectively). This connotes 1% increase in capital formation leads to an increase of 0.574% and 0.120% in economic growth in the short and long run, respectively. Renewable energy consumption reveals a negative and significant coefficient only in the long run (−0.028). This implies that 1% point increase in renewable energy consumption causes economic growth to decline by about 2.8%.

Therefore, the findings of this study revealed that renewable energy consumption have largely been detrimental to the growth pattern of "Next Eleven" emerging markets. In other words, renewable energy has not promoted economic growth but

Table 6 Results of panel regression for the effect of renewable energy on economic growth

	PMG		MG		DFE	
Variables	Coef.	z	Coef.	z	Coef.	z
Long run estimates						
lnGFCF	0.574***	5.71	0.061	0.06	0.441	1.65
lnLF	0.122	0.47	−0.558	−0.28	0.873	1.51
RE	−0.028***	−3.19	0.005	0.07	−0.021	−1.53
Short run estimates						
EC	−0.013	−0.79	0.072*	1.32	−0.023*	−1.9
ΔlnGFCF	0.120***	3.66	0.145***	7.53	0.089***	7.53
ΔlnLF	0.049	0.48	−0.068	−0.39	0.126	1.08
ΔRE	0.002	0.81	−0.001	−1.13	−0.001	−0.79
Constant	0.169	0.92	0.501	0.72	0.055	0.31
Diagnostic tests						
Hausman test			1.54(0.672)		0.001(0.999)	
Observation	250		250		250	

Notes: ***$p < 0.01$; **$p < 0.05$, *$p < 01$; Hausman test p-value in parentheses
PMG pooled mean group, *MG* mean group, and *DFE* dynamic fixed effects

affected it negatively by causing a decline in it in these economies. Specifically for each of these economies, the findings from results of Tables 7 and 8 revealed that renewable energy consumption causes a decline in economic growth both in the short and long runs in South Korea, but only in the short run in Indonesia and Pakistan. There is no evidence that renewable energy consumption affects economic growth in Nigeria, Egypt, Iran, and the Philippines. However, for Mexico and Bangladesh, there is short-run evidence that renewable energy consumption led to increased economic growth. While the effect was instantaneous in Mexico, the effect was only obvious after two-period lag in Bangladesh.

6   Conclusion

One of the major problems found with the existing renewable energy policies in the "Next Eleven" emerging market economies is the lack of consideration given to how and where the renewable energy sources are being produced. Most of the policies were focused on generating electricity from renewable energy sources at any cost, with very ambitious, if not overambitious, targets. For developing economies in which the production of equipment required to generate renewable energy is very minimal, it invariably becomes very costly to employ such energy efficiently in order to promote economic activities. Most of these countries resort to importing these equipment at very high cost, and in most cases, this high cost can only be affordable to the government and unaffordable to the private entities. One of the major elements to be included in the existing renewable energy policies is a harmony between the countries' capacity to produce the required equipment for

Table 7 Results of time series regression for the effect of renewable energy on economic growth in selected countries

Variable	Nigeria Coefficient	t	Egypt Coefficient	t	Mexico Coefficient	t	Iran Coefficient	t	South Korea Coefficient	t
Long run estimates										
lnGFCF	−2.354**	−2.622	0.690	1.203	0.651*	1.826	0.202*	1.991	0.615*	2.086
lnLF	4.067***	6.472	0.140	0.098	−0.079	−0.093	1.008***	4.877	1.743	1.575
RE	0.004	0.335	0.012	0.082	0.010	0.339	0.141	1.554	−0.070***	−3.015
Short run estimates										
EC	−0.191***	−4.323	0.032	0.485	−0.160*	−1.846	−0.211***	−2.998	−0.174*	−2.670
D(lnGFCF)	−0.162***	−3.519	0.086***	3.082	0.355***	10.06	0.143***	5.085	0.224***	7.313
D(lnLF)	0.656	1.646	0.189**	2.474	−0.257	−0.814	0.213**	2.394	1.145***	3.584
D(RE)	0.001	0.334	−0.000	−0.083	0.023***	3.820	0.030	1.665	−0.012*	−1.865
C	13.02	1.071	6.467	0.344	12.18	1.479	4.243**	2.141	−18.07	−1.578
Diagnostic test										
Autocorrelation	1.517(0.251)		2.683(0.100)		2.337(0.135)		1.571(0.232)		1.544(0.245)	
F-statistic	1799.5***		6686.4***		1005.9***		730.8***		6346.5***	

Notes: ***$p < 0.01$; **$p < 0.05$, *$p < 01$

Table 8 Results of time series regression for the effect of renewable energy on economic growth in selected countries

Variable	The Philippines		Pakistan		Bangladesh		Indonesia	
	Coefficient	t	Coefficient	t	Coefficient	t	Coefficient	t
Long run estimates								
lnGFCF	0.365***	7.613	−1.172	−0.264	−1.492	−0.338	0.007	1.090
lnLF	1.349***	10.95	1.033***	3.477	1.136	0.270	−0.562	−0.234
RE	0.000	0.030	−0.095	−0.335	−0.103	−0.546	−0.034	−1.106
Short run estimates								
EC	−0.249***	−2.905	−0.088	−0.351	−0.037	−0.498	−0.097	−0.886
D(lnGFCF)	0.101***	3.883	0.080*	1.893	0.116	1.168	0.002***	8.548
D(lnLF)	0.336***	2.959	−0.381*	−1.835	0.042	0.488	−1.755***	−4.253
D(RE)	0.000	0.030	−0.008***	−3.983	−0.002	−1.254	−0.011***	−3.823
C	−6.184***	−3.835	41.82	0.340	46.41	0.920	39.37	0.858
Diagnostic test								
Autocorrelation	0.337(0.717)		1.140(0.246)		0.132(0.876)		1.530(0.248)	
F-statistic	4106.0***		4095.1***		14954.6***		1160.7***	

Notes: ***$p < 0.01$; **$p < 0.05$, *$p < 01$
EC error correction

renewable energy and the proposed targets in terms of renewable energy consumption. It examined the causal relationship that exists between renewable energy and economic growth. It also examined the impact of renewable energy on economic growth in "Next Eleven" emerging markets. The study also presents some insights on the renewable energy policies in these countries.

The results revealed that in most of these countries, it is the increase in economic growth that precedes the increase in the consumption of renewable energy. In spite of the causal link, renewable energy has not really improved economic growth in most of these countries, but rather served has a detrimental force to economic growth in countries like South Korea, Indonesia, and Pakistan. Mexico and Bangladesh are the only countries that have experienced improvement in economic growth as a result of their increased consumption of renewable energy. Given this situation, it is recommended here that these economies should set a clear target about renewable energy consumption. Strategies and action plans must therefore be specified on how the goals and targets are met.

References

1. Venkatraja, B.: Does renewable energy affect economic growth? Evidence from panel data estimation of BRIC countries. Int. J. Sustain. Dev. World Ecol. **27**, 107–113 (2019)
2. Apergis, N., Danuletiu, D.C.: Renewable energy and economic growth: evidence from the sign of panel long-run causality. Int. J. Energy Econ. Policy. **4**(4), 578–587 (2014)
3. Inglesi-Lotz, R.: The impact of renewable energy consumption to economic growth: a panel data application. Energy Econ. **53**, 58–63 (2016)
4. Kahia, M., Aïssa, M.S.B., Charfeddine, L.: Impact of renewable and non-renewable energy consumption on economic growth: new evidence from the MENA Net Oil Exporting Countries (NOECs). Energy. **116**, 102–115 (2016)
5. Saidi, K., Omri, A.: The impact of renewable energy on carbon emissions and economic growth in 15 major renewable energy-consuming countries. Environ. Res. **186**, 109567 (2020)
6. Bhattacharya, M., Paramati, S.R., Ozturl, I., Bhattacharya, S.: The effect of renewable energy consumption on economic growth: evidence from top 38 countries. Appl. Energy. **162**, 733–741 (2016)
7. Koçak, E., Şarkgüneşi, A.: The renewable energy and economic growth nexus in Black Sea and Balkan countries. Energy Policy. **100**, 51–57 (2017)
8. Luqman, M., Ahmad, N., Bakhsh, K.: Nuclear energy, renewable energy and economic growth in Pakistan: evidence from non-linear autoregressive distributed lag model. Renew. Energy. **139**, 1299–1309 (2019)
9. Abbasi, K., Jiao, Z., Shahbaz, M., Khan, A.: Asymmetric impact of renewable and non-renewable energy on economic growth in Pakistan: new evidence from a nonlinear analysis. Energy Explor. Exploit. **38**(5), 1946–1967 (2020)
10. Dogan, E., Altinoz, B., Madaleno, M., Taskin, D.: The impact of renewable energy consumption to economic growth: a replication and extension of. Energy Econ. **90**, 104866 (2020)
11. Shahbaz, M., Raghutla, C., Chittedi, K.R., Jiao, Z., Vo, X.V.: The effect of renewable energy consumption on economic growth: evidence from the renewable energy country attractive index. Energy. **207**, 118162 (2020)
12. Rahman, M.M., Velayutham, E.: Renewable and non-renewable energy consumption-economic growth nexus: new evidence from South Asia. Renew. Energy. **147**, 399–408 (2020)

13. Soava, G., Mehedintu, A., Sterpu, M., Raduteanu, M.: Impact of renewable energy consumption on economic growth: Evidence from European Union countries. Technol. Econ. Dev. Econ. **24**(3), 914–932 (2018)
14. Qudrat-Ullah, H., Nevo, C.M.: The impact of renewable energy consumption and environmental sustainability on economic growth in Africa. Energy Rep. **7**, 3877–3886 (2021)
15. Pegkas, P.: The impact of renewable and non-renewable energy consumption on economic growth: the case of Greece. Int. J. Sustain. Energy. **39**(4), 380–395 (2020)
16. Doytch, N., Narayan, S.: Does transitioning towards renewable energy accelerate economic growth? An analysis of sectoral growth for a dynamic panel of countries. Energy. **235**, 121290 (2021)
17. Fu, Q., Álvarez-Otero, S., Sial, M.S., Comite, U., Zheng, P., Samad, S., Oláh, J.: Impact of renewable energy on economic growth and CO2 emissions—evidence from BRICS countries. PRO. **9**(8), 1281 (2021)
18. Akram, R., Chen, F., Khalid, F., Huang, G., Irfan, M.: Heterogeneous effects of energy efficiency and renewable energy on economic growth of BRICS countries: a fixed effect panel quantile regression analysis. Energy. **215**, 119019 (2021)
19. Alper, A., Oguz, O.: The role of renewable energy consumption in economic growth: evidence from asymmetric causality. Renew. Sust. Energ. Rev. **60**, 953–959 (2016)

Energy Configuration in the Ever-Changing Upheaval in the Health Sector in Our Era: Embracing Industrial Revolutions

Bantubenzani Nelson Mdlolo and Oludolapo Akanni Olanrewaju

1 Introduction

A growing number of industries depends on the availability of electricity to operate. According to historical statistics, electricity drives 99.98% of technological transformation around the world. Terashima et al. [7], for example, claim that a selection of photovoltaic (PV) module technologies differs depending on the capacity of the sector. Technological transformation is the most common form of industrial revolution currently taking place. Toktarova et al. [8] and Mora et al. [6] have noted that most types of energy still require coal-fired blast furnace technology. Technology transforms in many ways, but the most common element of technological transformation is that it brings the latest features available at that time to improve on older features.

Current energy output has proven insignificant at handling the high levels of technological transformation, given the deterioration in available power in recent years. Hospitals, for example, play major roles in society and depend mostly on electricity. However, the modern state of energy depends mostly on fossil fuels, although this has deteriorated over the past few years. Energy security, the adverse health impacts of unreliable air quality and shutdown costs have been hampered by potential legal noncompliance [1, 5]. When the major challenges come from the fossil fuel industry, all other sectors, including the health sector, feel the pain. If the ignorance of the damage caused by not changing to a new energy-generation system remains, the health sector will continue to suffer. Recently, a heat-transfer fluid which has temperature-controlling advantages, was recommended, but if it is not

B. N. Mdlolo · O. A. Olanrewaju (✉)
Department of Industrial Engineering, Durban University of Technology,
Durban, South Africa
e-mail: OludolapoO@dut.ac.za

improved, it might fail [7]. However, most sectors have backup systems, such as generators, which can be used only temporarily.

This article aims to address the gap between technological and energy revolutions. This should assist in overcoming the challenges faced by important sectors, such as health, banking and manufacturing, among others. Lovering et al. [4] argued that promoting nuclear is the best way to overcome the challenges that energy divisions in the US government face. However, the focus here is on the health sector because it is the most crucial sector for human health and has made only negligible technological advancements.

This study adopts quantitative techniques to analyse the end results of energy use in various critical sectors, such as health. It further takes a mathematical approach to address the depth of this challenge. Section 2 of this chapter focuses on the method used to address the current challenge of providing energy to the health sector. Section 3 reports and breaks down the results of the study for further analyses. Finally, Sect. 4 concludes.

2 Methodology

In this section, the research approach and techniques such as data gathering, data verification and data analysis are described in detail. The data gathering aimed at finding a more procedural way to achieve the obtained outcome and to obtain energy-consumption data from the health sector. The statistical approach used to analyse the obtain data is also thoroughly discussed to provide a better understanding of the results.

2.1 Data Gathering

Data were obtained from the annual financial statements of the health sector of South Africa. The authors approached the South African cement industry to obtain the necessary data (financial statements and energy consumption in the cement industry) used in the study. Data on daily production were also used to further analyse the energy consumption. Some of the daily production data used include the production time, machine breakdown time and teatime. The data were taken from the financial statements of the cement industry during a face-to-face interview with a senior cement industry representative.

The importance of energy consumption in the health sector was determined via statistical analyses. The health representative assisted by emailing electricity bills in that the bills yielded annual data for this study's analysis. The other data were obtained from research papers that contained relevant information on the health sector's energy consumption and on energy glitches that occurred during the absence of dependable sources of energy.

2.2   Analytical Approach

The study focused on energy consumption and the cost of energy in the health sector, where these values were used to determine the improvements still needed in the health sector. The division figures provided were used to visually analyse the energy consumption in the health sector before graphically displaying the data.

Statistical models, such as weighted average, were used to present this study's outcomes in a way an easily understandable way. It is a useful tool which allows analyses of historical data to be conducted. A further analysis led to the creation of a merging line by include a calculation of the average cost of all monthly energy costs.

The outcome of energy consumption in the health sector assisted in our conducting a cost–benefit analysis (CBA), which serves as a controlling tool that can assist the cement industry in reducing the energy costs of its processes, especially the grinding, proportioning, blending and kilning processes.

The calculated energy figures from the cement industry were put into Microsoft Excel to use its analytical techniques, such as creating bar graphs and pie charts. This kind of information is displayed in Sect. 3. However, the data on other types of energy consumption (such as lighting) were barely included because the study focused on the processes of cement manufacturing.

3   Results and Discussion

The results were divided into daily production data and energy performance. The health sector normally works all day because of ongoing societal demand. The statistical approach used to analyse the obtain data provided a better understanding of the results pertaining to the health sector. Fig. 1 shows the energy-consumption levels in the health sector.

On an ordinary day in a healthcare facility, average energy consumption was briefly calculated to identify level of electricity needed on a day-to-day basis. Because a week contains a maximum of seven days, every calculation was based on the weekly average. On day 1, the facility used the minimal amount of energy, but this was still critical because it shows that 56 kWh of energy is still being used to meet electricity demands. These data do not include lighting, because that is considered a household activity. New and returning patients are major contributors to the health sector's daily energy-consumption activity. Also, many returning patients are seen for several days: at days 1, 5 and 7, they require energy minima of 56 kWh, 32 kWh and 23 kWh, respectively.

On the other hand, days 2, 3, 4 and 6 reach especially high energy-consumption levels: 87 kWh, 98 kWh, 93 kWh, and 98 kWh, respectively. During the investigation, new admissions and long-stay patients both contributed to these high consumption levels. Because this article focuses on the unavailability of sufficient energy backup systems in the health sector, all the major sources of energy consumption in the health sector were analysed (Fig. 2).
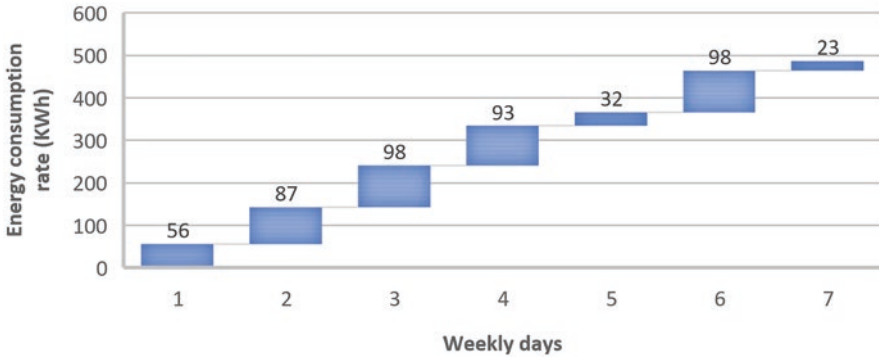
Fig. 1 Energy consumption in the health sector
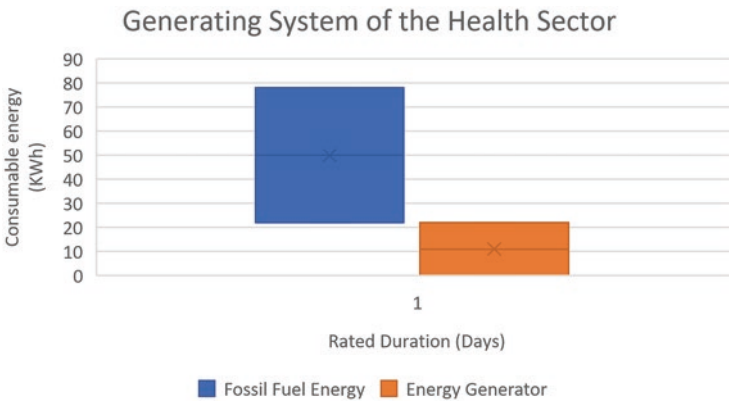
Fig. 2 Energy-generating system

Over the course of an unusual day, some of the average energy-consumption level may not be available for certain periods, even though the health sector operates 24 h a day. One-quarter of the day's energy consumption is saved by using the generator system, which immediately activates when it detects a dip in the electricity delivered from the electrical grid. If 22% of the day is unavailable and supplied by the health sector, then 22% of the day lacks consistent energy supply. This has huge impacts on human life in that the lack of energy hampers maintaining the wellbeing of patients in the health sector. However, if this 22% loss from the grid could be sustained full time with a normal solar system, it would be significantly better off. This sector has these expensive generators to save lives in emergencies, not to supplement daily electricity usage (Fig. 3).
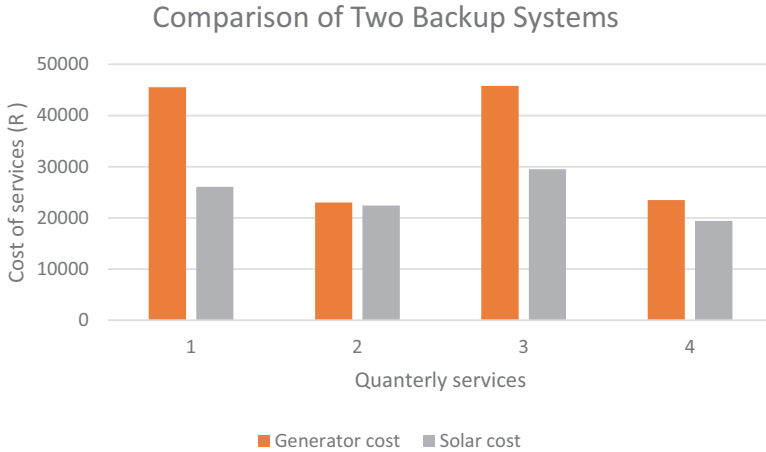
Fig. 3 Comparison of solar-power system and generator backup system

The percentage of daily sunshine is highest in the month of November, at 68.6%, and the lowest is in the month of August, at 32.9%. Harvesting solar energy would be much cheaper than maintaining consistent energy delivery from an electrical grid that is quickly deteriorating. Lopez Ferber et al. [3] claim that solar energy is hampered by the intermittency of sunlight. Also, LIU (2020) claim that it is difficult to develop other resources because of engineering and developmental costs, which makes solar less costly than other sources of electricity. The solar-power system does not wait for the unavailability of energy but instead generates energy for the electrical grid to maintain consistent energy output. Solar PVs have been used to improve the power supply from the recent load shedding [2].

According to this study's analysis, using solar energy is much more affordable than using generator systems. The cost–benefit analysis (CBA) conducted in this study clearly shows that electrical energy will become more affordable in the next decade, and it will more easily maintained moving forward. If energy savings of 42.8% have been realised in the first term, then the health sector needs to undergo a progression analysis to identify its other energy challenges. A low percentage of energy, such as the loss of 2.61% in quarter 2, should raise eyebrows because of the number of patients who would be affected.

4   Conclusion

This study focused on the health sector to address the impact of its energy generation and consumption. Numerous approaches were adopted to address these challenges in the sector, approaches such as the quantitative approach, cost–benefit analysis and the brainstorming approach. The results reflected that an immediate correctional procedure must be taken to compensate for the 22% annual energy loss

from the energy-generation system. However, the integration of human and machine in this energy transformation in the health sector still needs to be carried out. Finally, reducing the amount of energy used in this sector remains a major challenge.

References

1. (RSA), E. department: Integrated resource plan. Energy, 810 (2019)
2. Gira, N., Dahiya, A.K.: Solar PV-BES in distribution system with novel technique for DC voltage regulation. Eng. Sci. Technol. Int. J. **23**(5), 1058–1067 (2020). https://doi.org/10.1016/j.jestch.2020.01.004
3. Lopez Ferber, N., et al.: Development of an electric arc furnace steel slag-based ceramic material for high temperature thermal energy storage applications. J. Energy Storage. **51**(February), 104408 (2022). https://doi.org/10.1016/j.est.2022.104408
4. Lovering, J.R., Abdulla, A., Morgan, G.: Expert assessments of strategies to enhance global nuclear security. Energy Policy. **139** (2020). https://doi.org/10.1016/j.enpol.2020.111306
5. Mendiara, T. et al. (2018) Negative CO_2 emissions through the use of biofuels in chemical looping technology: a review, Appl. Energy, 232(October 2018), pp. 657–684. doi: https://doi.org/10.1016/j.apenergy.2018.09.201
6. Mora, J.C., et al.: on the use of reference areas for prospective dose assessments on populations of wildlife for planned atmospheric discharges around nuclear installations. Environ. Res. **182**(2019), 109057 (2020). https://doi.org/10.1016/j.envres.2019.109057
7. Terashima, K., Sato, H., Ikaga, T.: Development of an environmentally friendly PV/T solar panel. Sol. Energy. **199**(February), 510–520 (2020). https://doi.org/10.1016/j.solener.2020.02.051
8. Toktarova, A., et al.: interaction between electrified steel production and the north European electricity system. Appl. Energy. **310** (2022, 2021). https://doi.org/10.1016/j.apenergy.2022.118584

Europe's Post Pandemic Electricity Price Evolution

Fratita Michael [iD]**, Popescu Florin, and Eugen Rusu** [iD]

1 Introduction

Lately, Europe is going through a new energy crisis [1]. Fuel oil, natural gas, and electricity prices have been rising at an accelerating pace. All this has led to rising inflation and falling living standards. Member States of the European Union have followed different schemes to compensate for the increase in electricity, natural gas, and fuel prices. The compensations are made quantitatively, for vulnerable consumer groups. However, the balance sheet for 2022 shows unexpectedly high profits for energy and oil companies. So, the European Council has come up with a new plan of measure to stabilize electricity prices in Europe [2]. As we will see later in the chapter, most countries produce electricity using natural gas. This is why the wholesale price of electricity is closely linked to the trading price of natural gas. This chapter aims to analyze the evolution of electricity prices over the last 5 years. This theoretical study is based on statistics provided by electricity distribution systems in four countries of the European Union. These have been chosen according to the raw material used to produce electricity.

Statistically, there have been about four major events in the last 5 years with a major impact on the energy market.

Analyzing chronologically, in 2019 the Green Deal was presented. This plan foresees a gradual reduction of greenhouse gas emissions by 2050. Most greenhouse gases (75%) are produced by the energy system: cold, heat, gas, solid, and liquid fuel [3]. So, this sector is a priority for investment. There is a strong emphasis on financing renewable energy sources and closing coal-fired power plants as soon as possible. The closure of power plants and coal mines is planned to be phased in gradually between 2025 and 2030 for EU countries [4].

F. Michael (✉) · P. Florin · E. Rusu
"Dunărea de Jos" University of Galați, Faculty of Engineering, Galați, Romania
e-mail: michael.fratita@ugal.ro

In 2020, the COVID-19 pandemic will gradually close most of Europe's industrial sectors, causing electricity and fuel prices to fall due to lower demand [5]. In the meantime, the high demand for electronics due to remote working and remote education has caused a semiconductor crisis due to low raw material stocks [6].

The year 2021 brought up the recovery plan for Europe, the largest financial package in history to recover (reform) Europe along Green lines. Most of the energy sectors have been restarted [2], creating a raw material crisis. To supplement energy needs, most coal-fired power plants were run at full capacity to stabilize electricity prices [7].

Adding to the instability of the energy sector is the political instability in Eastern Europe. On February 24, 2022, Russia invaded Ukraine. The European Union reacted by introducing economic restrictions. Thus, with the introduction of the embargo, hydrocarbon and energy prices in the European economic area increased at an accelerated pace [8]. An upward trend is found in every country of the European Union, with differences depending on the country's own resources and sources of electricity production. The increases in electricity prices are expressed quantitatively in the second part of the chapter.

2   The Evolution of Electricity Prices in Europe

We will detail in this chapter the evolution of electricity prices in several European countries using different sources to produce electricity. To begin with, we analyze the evolution of electricity prices over the last 5 years in Spain. Spain is a country that relies heavily on green electricity generation. In 2021 it produced 23.28% of its electricity needs with wind turbines, 20.8% with nuclear power, 11.3% with hydropower, and 8% with solar power. Coal-fired power plants have a share of only 1.9% and diesel generators have a share of almost 1%. The rest of the percentages represent energy produced from natural gas and other green energy sources [9].

In Fig. 1, it can be observed that the price of electricity in Spain was around 48 euros/MWh until 2020. With the lockdown caused by the COVID-19 pandemic, the price dropped to a minimum of 10 euros/MWh.

At the same time, the easing of restrictions and the economic recovery have led to a gradual increase in electricity prices. The price per MWh increased until September 2021 when it reached more than 200 Euro/MWh.

The price averaged 200euro/MWh until June 2022, when electricity prices started to fall. Fluctuations are largely driven by energy input from wind turbines. Thus, due to the high availability of raw material for wind power plants, the electricity price reached a low of 6 Euro/MWh at the end of December 2022. Although a good part of the energy is produced from renewable sources, the effects of inflation are also clearly seen in Spain.

According to the latest updates of the Green Deal [4], electricity produced from natural gas and nuclear power is considered green energy. France is a country that relies heavily on electricity from nuclear reactors. Hence, the country's
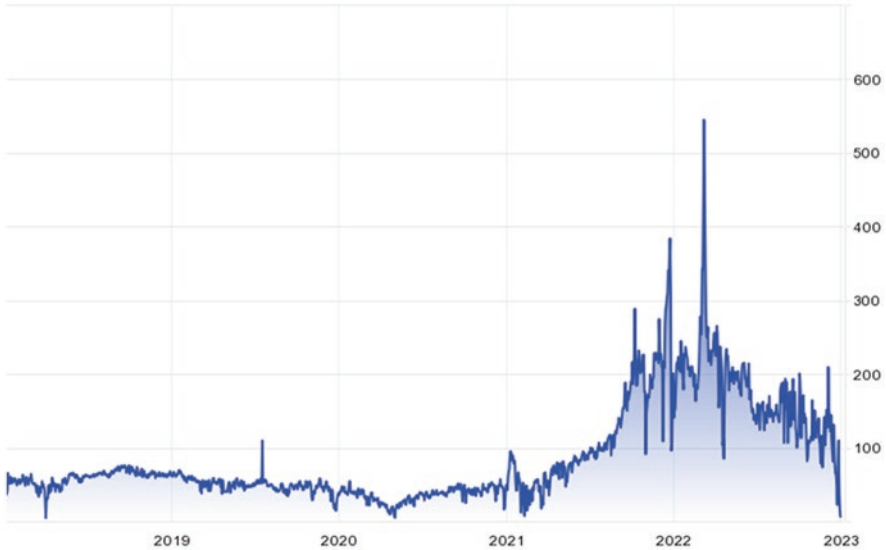
Fig. 1 Spain electricity spot price [10]

consumption is covered by 69%, followed by the hydropower sector with 12%, and wind turbines produced about 7% of the country's needs. The new Green Deal regulations clearly benefit France as electricity produced from hydrocarbons and coal only accounts for 7% of the total energy produced [9].

Nuclear power plants usually operate at constant power to stabilize the reactions inside the reactor and to achieve the lowest possible uranium consumption. Most nuclear reactors in France use enriched uranium. It can be seen in Fig. 2 that the price of electricity in France is stable at around 45 euro/MWh produced. However, the COVID-19 pandemic did not lead to a price decrease but to a price increase after the economic recovery. France is the largest exporter of electricity in Europe [11]. All this has led to the price of electricity in France rising in December 2021 to a maximum of 400 Euro/MWh. This price increase was momentary, in January MWh reached 126 euros. Due to political tensions in Eastern Europe, the electricity price started to increase again with an average of 370 Euro/MWh in 2022. Under these conditions a record price of 1130 Euro/MWh was recorded on August 26, 2022. In December, the price continued to fall to 245 Euro/MWh.

Another country benefiting from Green Deal completions is Italy. In 2021, 43% of Italy's electricity needs was generated by power plants using natural gas. Coal-fired electricity accounted for only 4%. As part of the Green Deal Italy has announced that it will phase out coal-fired power plants by 2025. This deadline is likely to be postponed due to dependence on natural gas from Russia. In 2021, Italy imported 29 million cubic meters of natural gas from Russia. This represents 29.2% of total natural gas imports. In second place was the import of natural gas from Algeria with 22.3% of the total volume [9]. The large capacity of electricity production based on
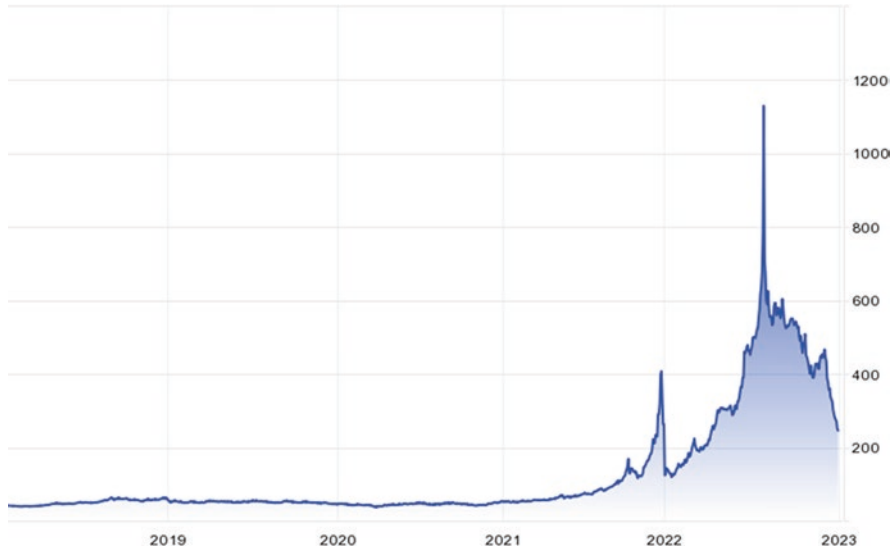
Fig. 2 France electricity spot price [10]

natural gas raises problems with the outbreak of the armed conflict between Russia and Ukraine. The embargo placed by the European Union on the import of Russian gas and oil directly affects the price of energy in Italy as well. However, the Trans Adriatic Pipeline (TAP) natural gas pipeline, opened in 2021, is a breath of fresh air for the country. So, the natural gas needs are supplied from Algeria and Azerbaijan. The cap on the price of Russian oil at USD 60 per barrel, which came into force in December 2022, is also intended to stabilize the energy market for maritime transport. EU ships are also banned from carrying Russian refined products from February 2022 [8].

Renewables accounted for only 18% of the total energy produced in Italy. Of this, hydropower and solar energy account for the largest share. However, solar energy is expected to be the dominant renewable energy source in Italy by 2030. As in the case of Spain, the COVID-19 pandemic has led to a drop in electricity prices due to the shutdown or reduced operation of the industrial sector. If before the pandemic the price of electricity was around 55 Euro/MWh produced, the economic recovery led to a gradual increase in the price to values above 200 Euro as shown in Fig. 3. Shortly after the invasion of Russia in Ukraine, the price of electricity reached 380 Euro/MWh. Further large price fluctuations between 250 and 650 Euro/MWh were recorded. In December 2022, a decrease in the price of electricity is observed. The price has stabilized at around 200 Euro/MWh, four times higher than the price before the COVID-19 pandemic.

Finally, we will discuss the evolution of electricity prices in Germany. In 2021, in Germany gross electricity production was 582.9 billion kWh. Of this, 39.7% was produced from renewable energy sources and 28.1% was produced using coal-fired power plants [12]. Coal-fired power plants are one of the most polluting sources of

Fig. 3 Italy electricity spot price [10]
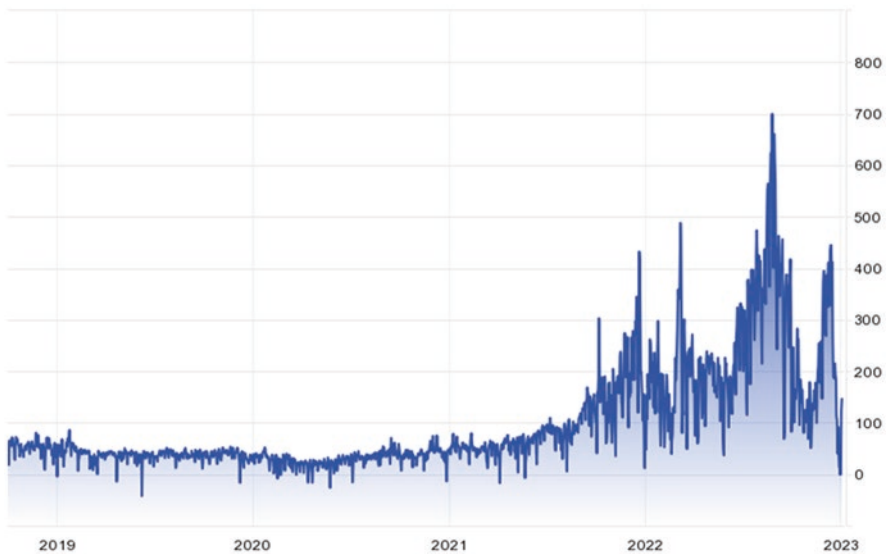
Fig. 4 Germany electricity spot price [13]

electricity production, producing twice as much CO2 as a natural gas-fired cogeneration power plant. As far as electricity production using natural gas is concerned, it is found to contribute 15.2% of the total energy produced.

An analysis of the evolution of the electricity price in Germany shows that in some cases the electricity price is negative as shown in Fig. 4. This means that an electricity producer pays to inject energy into the electricity grid. This solution is

often used because it is cheaper for the producer to pay for the injection of electricity into the grid than to switch off the equipment. This case is common in old coal or oil-fired power plants that cannot vary the electrical load on the turbo generator very much in relation to the overproduction of electricity from renewable sources over the forecast.

Given the variable profile of electricity generation from renewable sources, several algorithms have been developed that can predict the energy produced from renewable sources. For example, the Solcast database [14] can predict the electricity production of photovoltaic panels according to the installed power, the angle of the panels, the geographical position, the cloud movement, and the evolution of solar irradiance. An important role in electricity trading in Germany is played by the SMARD platform. It monitors the evolution of electricity production according to electricity generation sources and provides a prediction based on real-time data from electricity distributors in Germany. The platform provides prediction for renewable electricity (which is difficult to control) and prediction for electricity consumption. On December 30, the electricity price reached −0.78 Euro per MWh produced. Figure 5 shows in red the electricity consumption. The blue color shows electricity produced by onshore and offshore wind farms. The dotted line presents the electricity prediction. It is certain that the drastic drop in price is due to a mixed multiple of factors. Among these we can list the following:

- Errors in forecasting wind power generation. The forecast was exceeded during the day by about 10–15%, which represents about 1500 MW, when deviations from the usual forecast are less than ±5%.
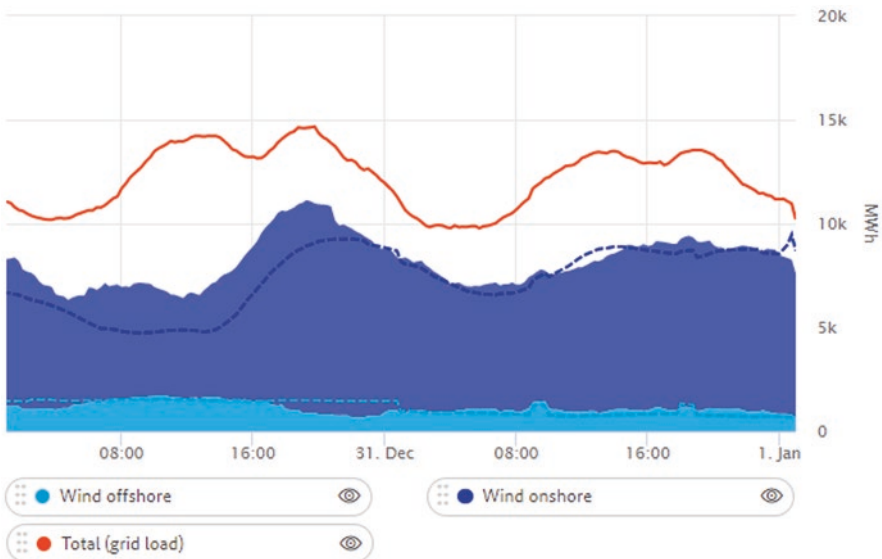
Fig. 5 Germany electricity production [13]

- The large amount of electricity produced by wind farms alone accounted for more than 70% of the country's needs.
- Electricity and gas/oil market transactions.

The electricity price at the beginning of December 2022 fluctuates (+-50Euro) around 350 Euro/MWh produced, whereas before the COVID-19 pandemic the electricity price had small variations around 40 Euro/MWh. Germany together with the Nordic countries benefits from a good productivity of onshore and offshore wind turbines due to high wind speeds throughout the year [15].

To avoid variations in the price of electricity, it is generally recommended to better balance the national energy system by achieving a correlation between consumer demand and production levels. Of course, not all electricity generation plants can operate at partial loads or can be always switched off and on safely. Different electricity storage options can also be used. It can be stored in its pure form using lithium-based electric accumulators with 85–95% efficiency or the electricity can be converted to another energy source.

For large energy storage options, Pumped-Storage Hydroelectricity (PSH) [16], Compressed Air Energy Storage (CAES), or green hydrogen can be used. Of these, PSH is the most widely used method. The principle of operation is that of hydro-power plants. When the energy produced in the power system exceeds consumption, pumps will take water from a reservoir/lake and pump it to a higher reservoir/lake. In general, the efficiency of such an installation is between 70% and 80%, and the same turbines operating as generators can be used for pumping. All these cycles are dependent on the energy requirements of the system. In addition, pumped storage hydroelectricity can mitigate the effects caused by intermittent power generation systems (wind and sun), but also in systems that cannot vary their output (nuclear).

3   Conclusions

Electricity is the purest form of energy that can be obtained from other forms of energy, transported, and then transformed into the desired form of energy. As we have seen in the graphics above, electricity has been affordable with small variations over the years. The COVID-19 pandemic has led to a decrease in electricity consumption and thus a decrease in price. The European economic recovery plan led to higher electricity prices and higher raw material prices. A normal phenomenon in a market economy is when demand is greater than supply. In addition to the rising price trend, the armed conflict between Russia and Ukraine and the EU's economic sanctions makes it impossible to make long-term forecasts with prices exploding from one day to the next.

All these factors are leading to the temporary closure of many economic sectors in Europe. As can be seen in the graphics above, the price of electricity has increased regardless of the source of electricity. At the same time, when renewable energy sources have produced significant amounts of electricity, the price per MW/h has dropped significantly (e.g., in December in Spain and Germany). Of course, this price drop is thanks to the electricity produced by wind turbines. Due to the

intermittent production of electricity from renewable energy sources, it is recommended to store it in order to stabilize the energy system and/or to obtain a higher profit by selling electricity at a higher price.

Analyzing the evolution of prices, it is clear that electricity produced from renewable sources is able to lower electricity prices due to free raw material. Thus, we can produce electricity from a source that for the moment is zero, and without operating costs. However, these energy sources can have a boomerang effect as we cannot control the amount of energy produced tomorrow but can only estimate it with some accuracy.

References

1. Agnès, B.Q., Beatrice, W.M.: European pandemic recovery: an opportunity to reboot. Intereconomics. **55**(4) (2020)
2. Grégory, C., Zsolt, D., Maria, D., Guntram, B.: The great COVID-19 divergence: managing a sustainable and equitable recovery in the EU. Intereconomics. **56**(4) (2021)
3. Sikora, A.: European Green Deal - legal and financial challenges of the climate change. ERA Forum Springer. **21**(1) (2020)
4. Dinçer, H., Uluer, G.S., Lisin, A.: The Role of European Green Deal for Carbon Emission Reduction, pp. 37–47. Springer (2022)
5. Peng, J., Yee, V.F., Jiri, J.K.: Impacts of COVID-19 on energy demand and consumption: challenges, lessons and emerging opportunities. Appl. Energy. **258** (2021)
6. Benjamin, F., Sylvia, S.: The "semiconductor crisis" as a result of the COVID-19 pandemic and impacts on the automotive industry and its supply chains. World Electr. Veh. J. **13**(10) (2022)
7. Li-Jing, L., Hong-Dian, J., Qiao-Mei, L.: Carbon emissions and economic impacts of an EU embargo on Russian fossil fuels. Nat. Clim. Change. (2023)
8. EU sanctions against Russia explained. Available online: https://www.consilium. europa.eu/en/policies/sanctions/restrictive-measures-against-russia-over-ukraine/ sanctions-against-russia-explained/
9. Statistical database. Available online: https://www.statista.com
10. Trading Economics database. Available online: https://tradingeconomics.com/
11. RTE is France's transmission system operator. Available online: https://www.rte-france. com/en/home
12. Germany electricity production. Available online: https://www.destatis.de/EN/Themes/ Economic-Sectors-nterprises/Energy/Production/Tables/gross-electricity-production
13. German Electricity Market. Available online: https://www.smard.de/
14. Solcast Database and Forecast. Available online: https://solcast.com/
15. European Environment Agency, Europe's onshore and offshore wind energy potential, EEA Technical report No 6/2009, ISSN 1725-2237 (2009)
16. Andrew, B., Matthew, S., Bin, L., Cheng, C.: A review of pumped hydro energy storage. Prog. Energy. **3**, 022003 (2021)

Can Community Energy Meet Distribution Network Operators' Expectations to Deliver Consumer Flexibility?

Simon Lawry-White, Abdul-Hadi G. Abulrub, and Chris McMahon

1 Introduction

The electricity distribution network in Great Britain (GB) is organised into 14 distribution licence areas [1]. These are managed by six distribution network operators (DNOs) each with the licence to operate in between 1 and 4 areas [2]. DNOs are monopoly suppliers within the United Kingdom's centralised power distribution system. They are regulated by the UK Office of Gas and Electricity Markets (Ofgem). The regulations set by Ofgem are designed to mimic conditions in an open, competitive marketplace.

Electricity demand in the United Kingdom is set to grow significantly and distribution networks will need to be reinforced to cope with peak loads. As DNOs enter a new price control period starting in April 2023, Ofgem requires them to minimize capital expenditure on the distribution networks so that consumers bills are kept as low as possible.

DNOs need to manage demand so that the peaks that place increasing stress on the distribution networks can be smoothed out. Distribution networks will have to accommodate many more decentralised energy resources (DERs) such as solar panels and electric vehicles. Unlike electricity supply companies, DNOs do not deal directly with customers, except over new connections or power cuts. Their new business plans for 2023–2028 see community energy as a principal means of reaching out to consumers to change consumer demand to reduce stress on the networks.

There are almost 500 community energy organisations in the United Kingdom. The growth of the community energy sector is held back by a lack of policy support and sustainable business models, as well as operational constraints, such as slow and expensive network connections. However, community energy is increasingly

S. Lawry-White (✉) · A.-H. G. Abulrub · C. McMahon
Cabot Institute for the Environment, University of Bristol, Bristol, UK
e-mail: simon.lawry-white@bristol.ac.uk

267

engaging communities in energy efficiency and in low carbon heat and transport. DNOs see community energy organisations' ability to engage with local communities as a route to achieving flexibility in domestic electricity demand.

2   Methodology

The research was carried out in two phases in 2021 and 2022. In phase 1, an extensive literature review was undertaken using academic research and industry documentation, including from community energy organisations and consultants. Nineteen semi-structured key informant (KII) interviews were undertaken with. After a period of analysis, a second phase of document review allowed the draft and final DNO business plans for 2023–2028 to be incorporated into the analysis. New policy debates have emerged as the external context continues to evolve, including in response to the energy crisis brought on by the war in Ukraine. A further 21 interviews were conducted in Phase 2, making a total of 40 key informant interviews across the two phases with community energy organisations, DNOs, consultants, academics, innovation projects, local authorities, trade and representative bodies, and other commentators from the energy industry. (Quotes from these interviews included below are marked KII.)

2.1   Trends in UK Electricity Distribution Network

The UK demand for electricity is expected to almost double from 330 Terawatt hours (TWh) in 2020 to over 600 TWh per annum by 2050. A large part of this increase in demand will come from electric vehicles and heat pumps. According to Ofgem, almost half of the final energy consumed in the United Kingdom is used to provide heat (760 TWh), with more than half going towards domestic space and water heating [3]. The UK government is committed to increase heat pump installations to 600,000 per year by 2028 [4]. As the Committee on Climate Change has observed, the greatest potential for emission reductions is through the uptake of low carbon heating systems and building refurbishment for improved thermal performance [5].

While demand is set to double, peak demand is set to increase more than three times from 60 to 190 Gigawatts (GW) over the same period [6]. Future distribution networks will need to integrate large numbers of DERs while balancing supply and demand. The current grid was not built for the bidirectional and unpredictable electricity flows that DERs can cause and the cost of balancing electricity supply and demand in the United Kingdom has already reached £1 billion per annum [7].

Modelling of electricity distribution networks by the UK Department for Energy Security and Net Zero shows electricity demand and generation increasing progressively to take up all the capacity in the distribution network by 2050. BEIS scenarios

assume that there is currently an average 60% spare thermal capacity across the distribution networks in GB, with wide variations in capacity between regions (Thermal capacity is the level of electricity current electricity cables and equipment can carry without overheating). Some parts of the network are already heavily constrained, but as the country moves to Net Zero, reinforcement will be needed across the whole of the network to accommodate increased demand and an estimated 80–140GW of additional generation capacity being added to the distribution network [8].

According to National Grid Electricity System Operator, 'energy system flexibility is the ability to adjust supply and demand to achieve that energy balance. It also allows us to keep the flows of energy through the networks within safe limits' [9]. Because the distribution networks are increasingly constrained, the electricity industry is focused strongly on flexibility as the first means of managing increased supply and demand while keeping reinforcement costs down. To this end, the DNOs have adopted the principle of 'flexibility first'. Major investment in network reinforcements will be required under any growth scenario. If more flexible management of DERs and of customer demand is not achieved, still greater investments in increased capacity of distribution networks will be required, leading consumer prices to increase more than they should [10].

The growth of decentralised energy means that DNOs need to employ more sophisticated technology and data management techniques to understand and manage demand in real time. Flexible technologies such as batteries, solar generation, electricity storage, combined heat and power, and electric vehicles can all enable the provision of flexibility services, to balance supply and demand, to help solve congestion issues on the grid and to release additional capacity, including the connection of more low carbon technologies. Domestic flexibility provides a huge opportunity to build a smart flexible energy system by enabling consumers to act as a new source of flexibility on the network. 'Unlocking end-consumer flexibility is fundamental to effectively managing a fully decarbonised energy system' [11] Distributed generation brings challenges to network congestion but also potential for new services, such as dynamic pricing, aggregation, peer-to-peer trading and various demand side management options that can help to overcome system balancing issues [12].

To reduce emissions to Net Zero at the least cost, more coordination will be needed between: sources of flexibility and electricity networks; transmission and distribution; the electricity and gas networks; and the electricity system and the heat and transport systems [13]. However, there is no UK body responsible for the strategic planning of the future evolution of the distribution networks towards Net Zero. 'It's no one's job, it's been left to the market' (KII). According to DNOs, they are not empowered to take major resource allocation decisions choices about strategic network upgrade investments. This function rests with government. DNOs are also not incentivized to work together across networks, rather the reverse, Ofgem wants them to compete. 'There is no coordination between DNOs, or even the motivation for it' (KII).

Aware of the current lack of coherence in the planning of the future of the transmission and distribution electricity networks, in 2022, the Government and Ofgem decided to create a new, independent, Future System Operator (FSO) to 'drive our overall energy transition and advise Government and Ofgem on the long-term requirements of the energy system' [14]. The absence of network strategic investment planning may be resolved, but as with any new body, it will take time for the FSO to become effective. In the meantime, there is a growing momentum towards energy planning at the local level. With support from Energy Systems Catapult, and with funding from the Prospering from the Energy Revolution programme, local authorities and Local Enterprise Partnerships are being supported to devise Local Area Energy Plans (LAEP), as a step towards delivering on their declarations of a climate emergency.

3   UK Government Policy

The UK Government's only Community Energy Strategy was published in 2014 [15]. This represented a high point in UK policy support for community energy, coinciding with the period of the sector's fastest growth. Since then, policy support has declined, with the progressive reduction of subsidy rates for low-carbon generation and the gradual closure of support schemes. However, since 2020 there has been a revival of interest in policy debate about local energy, including community energy. The Local Electricity Bill, which aims to enable electricity generators to become local electricity suppliers, was introduced to Parliament in June 2020 but did not progress. The campaigning group Power for People continues to promote the Bill, with many MPs and organisations in support. The Bill was reintroduced to Parliament as a Private Members Bill in November 2023, but key informants expressed doubt that it will advance.

Key informants agreed that there is currently insufficient momentum towards decarbonization: 'There is no consensus that we will get to Net Zero in time. We need an acceleration mechanism to get there' (KII). Official bodies have given their backing to community energy on several instances. The UK's independent Committee on Climate Change (CCC), an independent statutory body, stated that community energy has a role to play in getting to Net Zero; 'community-led delivery has an important local role in education and raising awareness of climate change, delivering energy saving and renewable energy often funded through charitable funds, crowdfunding or community shares and developing low-cost innovative projects' [16].

In April 2021, the UK Parliament Environment Audit Committee (EAC) held a debate on the role of community energy in decarbonisation and its benefits to local areas. The Committee expressed disappointment that there was not more focus on community energy in the Government's 2020 Energy White Paper and recommended that the Net Zero Strategy emphasise the importance of community energy

and that the Government develop a community energy strategy. The Committee's subsequent report made a series of recommendations regarding a greater role for local energy, including the reinstatement of community energy funds and changing regulations so that community energy could sell energy locally [17]. An MPs debate on Enabling Community Energy was held in Westminster Hall in July 2021 [18].

The CCC and EAC reports have brought no positive change in government policy regarding community energy so far, nor any sign that it is seen by government as a way to accelerate the United Kingdom towards Net Zero. It has not been possible to locate any UK government policy statement in favour of community energy from the period 2015 to present.

4   Status of Community Energy

Community Energy has diversified well beyond electricity generation. Figure 1 shows the various stated purposes of community energy gathered from across the literature and from key informants. While community energy organisations want to increase efficiency, reduce fuel poverty, and, in some cases, generate a financial surplus to reinvest in the community, reducing carbon emissions was cited most often by key informants as the primary motivators.
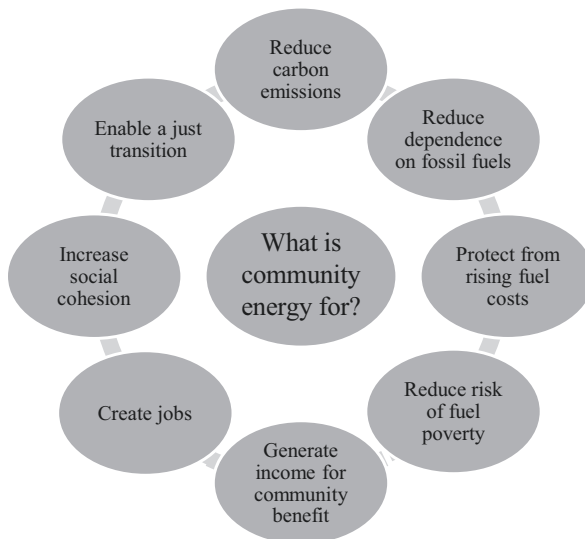
Fig. 1 Purposes of community energy

Following the introduction of the Feed-in-Tariff Scheme (FITS) in 2010, the 'largest single step forward for community energy', community energy grew rapidly in the period 2010–2016 and more gradually up to 2019 when entry to FITS was closed [19]. Key informants agree that, since then, it has been much more difficult for community energy generation projects to create a sustainable business model. A few community energy organisations have been funded to participate in government funded innovation projects. The Urban and Rural Community Energy Funds provided up to £140,000 of support per project towards feasibility and planning costs only. The urban fund closed in July 2016 and the rural in March 2022. A new £10 million Community Energy Fund for England was announced in August 2023. Scotland and Wales take a more supportive approach. In Scotland, the Community and Renewable Energy Scheme (CARES) provides financial and technical support to local community renewables generation and energy efficiency, with a target of 2GW of renewable energy generation to be locally or community owned by 2030 [20]. The Welsh government has set targets of 1GW of renewable electricity and heat capacity to be locally owned by 2030, and 100 Megawatts (MW) of renewable generation capacity to be added by public bodies and community groups by 2021–2026 [21].

According to the well-regarded Community Energy State of the Sector Report 2022, in 2021, there were 495 community energy organisations in United Kingdom, employing 644 full time equivalent staff. A total of £15 million was spent in local communities. 271 organisations were involved in renewable electricity, with a total of 331 MW capacity, generating 506 GWh in the year and powering 174,000 households. Generation capacity grew by 2% (7.6 MW). Also in 2021, there were 123 organisations delivering energy efficiency services, and 90 organisations working in low carbon transport. A total of £510,160 was spent on improving the energy efficiency of 20,843 households [22].

Nationally, total renewable energy capacity was 49.7GW in 2021, with total generation of 122.1GWh [23]. Community Energy represented, therefore, 0.67% of UK renewable capacity, 0.41% of UK renewable generation, and less than 0.2% of UK total electricity generation, given that renewables represent about 40% of total generation in the United Kingdom. By contrast, in Germany's decentralized energy management system, communities own 40% of renewable energy assets and can sell their electricity directly to local customers [24].

The principal barriers to any significant expansion of community energy are well documented and confirmed by key informants [25, 26]. The closure of FITS added to the challenges by making many new schemes non-viable. Problems include working with complex planning requirements, lack of finance, lack of subsidy, and limited human resource capacity, given the high dependence on the time and expertise of volunteers. Generation projects can face high startup costs, limited distribution network connection options, and lack of grid capacity. A surge in connection requests means that connection waiting times have grown still longer, up to 2–5 years, or even 8 years to connect larger projects over 1 MW capacity. (Connection times for smaller projects, say 100kW, can be as little as a few months.) New

planned schemes often end at the planning stage when they are informed of the likely network connection costs. Following the recent conclusion of the Access and Significant Code Review, the government has decided to change the way network connections are calculated by removing the cost of upstream network reinforcements, which will lower connections costs for some community energy projects. While community energy organisation acknowledge that DNOs now offer much better support regarding connections, procedures can still be very complicated to handle: 'There are so many codes and rule books, it's hard for community energy to stay plugged in' (KII). An increasingly high level of technical understanding and capacity is required for community energy to take part in demand side response (DSR) or other forms of flexibility. (Through DSR, businesses and consumers turn up, turn down, or shift their demand for electricity in real time in response to a signal from, for example, their DNO or electricity supplier.)

On the other hand, some research finds cause for optimism: the numbers of community energy groups and projects continue to grow (though slowly), established groups' revenues are generally secure, groups have become better at raising alternative financing, and local authorities are taking renewed interest in the energy system [27]. Interviews for this research show that a significant body of expertise now resides in the community energy sector, including with community energy projects themselves, supported by an ecosystem of intermediaries that has grown up to support community energy, including Community England, Scotland and Wales (three representative organisations) and a range of consultancies, project managers, think thanks, and academics.

The majority of communities have no community energy organisation and key informants saw no prospect of a major expansion of community energy in the near future. New community organisations launching new projects find it hard to raise finance as they are seen as both too small and too high risk. Fifty-three community energy generation projects are currently stalled, the majority for lack of either feasibility or early-stage development funding. However, 90 generation projects are in preparation, half of them with established groups [28]. The current energy crisis has given rise to a spike in the rates offered to community energy generators by energy companies. These increased rates make community energy projects appear financially viable that would not be at lower rates but key informants cautioned that a short-term spike in power prices does not provide a sound basis for schemes with a 20-year payback period.

According to key informants, two types of CE generation schemes are still viable without subsidy: (1) relatively small-scale roof top solar schemes (e.g., 50–100 kW capacity) that optimize the consumption of electricity in the school or other host buildings (so called 'behind the meter' usage) with any surplus exported to the grid and (2) large-scale solar farms of 5 MW capacity or more that have the scale to be profitable. 'You need to get the economies of scale in order to get the finances to work, especially now without the feed in tariff' (KII). The well-established community energy schemes in the United Kingdom now have 10–15 years of experience and a track record of successful projects that allows them to attract further finance

at reasonable rates. Crucially, they have another 10–17 years of subsidy from FITs, which makes their business models sustainable. A key to financial sustainability for these schemes is the agreement of a Power Purchase Agreement with an energy supplier, which gives certainty to the scheme by setting the purchase price over a fixed period of years.

Community energy is constrained by the inability to sell electricity generated locally in the United Kingdom but there are arrangements that allow customers to trade indirectly in a local market. For example, the Energy Local model allows a local group of domestic customers and a generator to form an Energy Local Club, legally a Cooperative, which partners with a licenced electricity supplier. The electricity from the local generator (for example, a wind turbine) is shared between club members who use the power when it is being generated, and at a cheaper tariff. As a result, it is claimed that consumers receive lower bills and generators receive a higher income [29]. There are currently nine Energy Local Clubs, with plans for further expansion. There are also solutions emerging to community energy providers having to sell their power into the national grid with no control over where it is used. New approaches use a distributed ledger system to create a Virtual Private Network that associates electricity from a renewable source with registered consumers who do not need to be in the same location as the local generator [30]. Some of the larger community energy generators sell their electricity to a large consumer such as a company, a local authority or a university, via a 'sleeved' Power Purchase Agreement, whereby an electricity supplier routes the equivalent power to the consumer across the grid based on a tripartite generator-supplier-consumer contract.

5   DNO to DSO Transformation

DNOs are about to enter new price controls for the period 2023–2028, known as RIIO-ED2 (hereafter ED2) [31]. Ofgem has stated that the changes DNOs are required to make during ED2 have the potential to save £10 billion for customers [32]. ED2 brings an unprecedented level of change for the DNOs. In the coming period, they must maintain security of supply and cope with rapid but unpredictable rates of growth in electricity consumption. They are also required to make significant changes to transform themselves into distribution system operators (DSOs), including a new role as 'a neutral facilitator of an open and accessible market, enabling competitive access to markets' [33]. As part of the DSO function, DNOs are required to achieve flexibility to ease the strain on distribution networks and avoid network reinforcements, wherever possible.

Twice a year, DNOs publish tenders for flexibility, requesting bids from contractors for flexibility services in zones where the network is already constrained. The total amounts tendered have grown quickly from 400 MW in 2018 to 4GW in 2022, with further growth expected as more zones become congested [34]. Scottish and Southern Energy Networks' (SSEN) plan for ED2 states that flexible connections in

its licence area alone will grow to 3.7GW by 2028, with customers avoiding £418 million in reinforcement cost as a result [35].

The Energy Networks Association (ENA) is the industry body representing DNOs. ENA's Open Networks Project works with all DNOs to provide a common approach to the DSO transition. In 2018, ENA published the 'Electricity Network Innovation Guide for Communities', which sets out how community groups can interact with their DNO and the innovations DNOs are looking for, including demand side response [36]. DNOs receive funding for innovation through the Network Innovation Allowance and Network Innovation Competition, a small portion of which reaches community energy organisations taking part in trials. For ED2, all DNOs have been obliged to create independent Customer Engagement Groups, including community energy representatives, which report to Ofgem [37]. There has been considerable consultation between DNOs and community energy in the run up to the agreement of plans for ED2. Some DNOs have organized periodic community energy consultations and ENA has also provided a series of Community Consultation Forums, with the support of Regen, a consultancy, including on flexibility [38].

The Open Networks project considers that community energy is a 'key player' in helping to expand local markets for flexibility services and to reach Net Zero [39]. According to Regen, community energy groups can enable flexibility because they are trusted by their local communities, can bring different types of stakeholders together, help to drive the concept of demand reduction or time-shifting existing demand, bring local knowledge and investment, and raise awareness [40].

Innovation projects have explored the potential for community energy flexibility projects. The Flex Community project led by Bath & West Community Energy is a pilot project exploring how 'flexible' households can be around the times they use electricity, with the aim of avoiding peak times and matching household demand to when there are more renewables available on the grid [28]. Wadebridge Community Energy Network, Cornwall, recruited 61 participants to trial Demand Side Response (DSR) time of use trial looking at shifting demand to when sunshine was generating from solar farms in Cornwall. The 6-month trial period was seen to be insufficient, and the most common reason for customers not signing up was that it did not make financial sense [41]. Project Leo's Smart and Fair Neighbourhood trials are testing different approaches to flexibility in six different areas in and around Oxford, working with their DNOs. Evaluation results are due in 2023 [42]. Despite these positive experiments, key informants noted that there has been little community energy engagement with DSR so far and they were not confident that the economics of DSR as a community project were viable. Community energy has engaged little with DNO tendered flexibility because it is too complicated, even though, according to one DNO, 'we have tried to make the flex services process easy for community energy'(KII). Some key informants considered that DNO flexibility does not contain sufficient value to make it worth engaging. A DNO interview confirmed that they have had no bids from community energy offering flexibility based on community-level demand side response, though such a bid would be considered.

In response to the winter 2022–2023 energy crisis, National Grid ESO introduced a Demand Flexibility Service for the period of November 2022 to March 2023, to reward customers for reducing their electricity use during the peak 4–7 pm period, given 24-hour advance notice [43]. This pilot service allowed energy supply companies to offer rebates based on customer flexibility over the winter period, for example, Octopus Energy's Saving Sessions and OVO Energy's Power Move. Both companies claim there is potential for each customer to save £100 during the winter. Consumers seem to have responded to these trials. Between 5–6 pm on 15 November 2022, 200,000 Octopus Energy customers provided 108 MW of flexibility [44, 45]. If these limited schemes are successful, there is potential for them to expand, if the Flexibility Service is extended for application in future winter periods.

6 Community Energy in DNO Business Plans

Most of the interaction between community energy projects and DNOs concerns connections, and most of the support being proposed by DNOs under ED2 is to continue to make community energy connections simpler and quicker. DNO's ED2 business plans place varying weight on community energy.

Most plans go beyond DNO's responsibilities to improve their technical advice and support to community energy network connections. Two business plans stand out as innovative in seeking to actively advance community energy as one of the routes to achieving Net Zero. National Grid Electricity Distribution (NGED) operates in four DNO licence areas that include 43% of community energy groups in the United Kingdom, with 100 MW of community-owned renewable electricity connected. According to NGED's ED2 plan, 'community energy has the potential to have a significant impact on the achievement of Net Zero', and 'community-led renewable energy, energy demand reduction and energy supply projects deliver collective social, environmental and economic benefits to the local community.' Further, 'Community-led renewable energy projects and energy demand reduction services have an essential role to play in the nation's efforts to tackle climate change'. The NGED plan commits to connecting at least 150 community energy schemes across the 5-year period, enabling 'extensive schemes of green, distributed generation to connect to the network'. Those with viable and ambitious low carbon schemes will be supported to secure funding. £540,000 per annum will go to installing solar PV on schools in areas of high economic deprivation. NGED will support community energy projects participating in flexibility and demand reduction schemes [46].

Similarly ambitious is the plan from Scottish Power Energy Networks (SPEN). It states that investment in community energy is 'essential to the green recovery', and 'community groups are uniquely placed to act as sources of network generation, demand and flexibility'. Community energy is 'critical to ensuring we achieve Net Zero'. SPEN's ED2 plan proposes the establishment of a Distribution Net Zero Fund of £30 million, through which it will have funded at least 50 low carbon

projects by 2028, 25% of them in community energy. SPEN's community energy strategy includes commitments to 'show how we will embed community energy thinking across our business', and to 'work in partnership with local support organisations to deliver community energy awareness campaigns at scale'. SPEN will 'deliver a step-change in support to local stakeholders for community energy and local green initiatives', 'deliver community energy campaigns', and employ community energy advisers [47]. 'We know that local, trusted groups will play an essential role in helping millions of individuals, including those in vulnerable circumstances, and accept low carbon technology and smart devices into their homes and day-to-day lives' [48].

According to the Energy Northwest's (ENW) ED2 plan, 'the green agenda will see more community-owned, renewable energy projects take shape'. Building on its track record of support to community energy, ENW is committed to establishing a new community fund with £150 k in 2023, £300 k in 2024, and £600 k in 2026, with up to £2 million in support to community projects in total over the plan period [49]. Northern PowerGrid commits to 'expand its community energy engagement offering', seeing community energy as a potential pathway to decarbonisation. A community energy panel has been established. A newly formed team of up to six community energy advisors will help to 'bring forward more community energy schemes', with a free advice and checking service for connection applications [50].

The ED2 plan from SSEN lists community energy amongst its 'hard to reach' customers. It commits to collaborate and coordinate with local authorities and community energy groups to assist them in local area planning and to reach their Net Zero ambitions, while implementing 'local community energy exchange markets' [51]. The plan includes £10.7 million in support for local authorities and community energy groups. For its part, UK Power Network's ED2 plan envisages no particular role for community energy and makes no commitments of support.

It is notable that it is in the achievement of flexibility that DNOs see the strategic importance of community energy. None of the DNO business plans mention community energy organisations as a potential source of additional decentralized generation or storage, even though National Grid ESO has stated that significant extra decentralized generation capacity is required for a Net Zero grid to be achieved by 2035 and Ofgem, in responding to the DNOs' draft business plans for ED2, stated that it requires DNOs to 'support an increase in the number of small-scale renewables connecting directly to the distribution grids' [52]. According to DNOs, 'we want a lot of small providers widely dispersed across the network'"; 'if we can match demand and generation [locally], then we don't need to transport that power' (KIIs). DNOs have no mandate to stimulate new providers to enter the market, only to respond to connection requests. Multiple small providers can also be problematic, causing more congestion in parts of the network that are already constrained.

7 Discussion

The community energy sector in the United Kingdom has limited scope for growth because of the various challenges discussed above. This means that civil society is missing opportunities to influence local engagement with climate change mitigation, decarbonization, behaviour change, and the adoption of low carbon technologies, even though the ability of community energy groups to do so is well established, as evidenced by their having engaged at least 57,600 people in energy efficiency measures in 2021 [53]. Meanwhile, five out of six DNOs have developed new business plans that assume, to some degree, that community energy, as a partner trusted by local people, will help them meet their goal of making the distribution networks fit for Net Zero. This gives rise to a few important questions:

Is There Sufficient Overlap Between the Agendas of DNO's and Community Energy for Cooperation to Work? Achieving a smart grid with flexible management of DERs and of demand is a common goal for DNOs and for the community energy sector, even if their motivations are different. Both parties want to see the decarbonization of the distribution network. They also share common ground in addressing the needs of vulnerable customers, for which DNOs have to meet obligations. Some community energy organisations earn income by providing flexibility services to DNOs through renewable DERs (though perhaps only a few, data was not found on this point).

Why Do Some DNO Plans for ED2 Go Far Beyond the Minimum Expected Support for Community Energy? Most of the ED2 plans are supportive of community energy, which is to be expected, given that community energy is one of the DNOs' key stakeholders and, in renewing their licences for another five years, Ofgem expects DNOs to demonstrate that they have listened and responded to stakeholders' feedback. However, some of the ED2 plans place more emphasis on community energy than might be expected. These DNOs are counting on the community energy sector as a delivery vehicle for flexibility. DNOs assigning an ambitious role to community energy might be the result of DNOs consulting with community energy organisations and informed intermediaries over a period of several years, and their plans may well have been shaped by their interactions with Community England, Scotland, and Wales, and with organisations such as Regen, the Centre for Sustainable Energy, and others. The DNO focal points for community energy are themselves often from the sector, which key informants see as key to successful dialogue.

How Well Have DNOs Articulated Their Intended Partnerships with Community Energy on DSR and Other Forms of Flexibility? In short, not at all well. DNO plans make strong, even lyrical, statements about the role of community energy. They also appear to assume that community organisations want to, and have the capacity to, deliver community education, messaging, and influence on DSR and the take up of DERs on a large scale. There is little movement on community energy responding to DNO flexibility tenders and there is little evidence the conditions for

successful cooperation in flexibility have been met. DNOs and Ofgem are placing great emphasis on achieving flexibility by working with community energy but without a clear strategy for achieving engagement at the level required. This bears the hallmarks of a high-risk strategy.

Can the Community Energy Sector Benefit from Its Anticipated Role as an Instrument of DNOs' Plans? Some DNOs' ED2 plans include technical support for community energy generation. Some go further to include modest levels of financial support, although given that community energy is framed in some plans as 'essential', with 'potential for significant impact on Net Zero', the sums allocated seem very modest. None of the ED2 plans state explicitly that financial resources will be allocated for community energy organisations engagement in domestic flexibility. There are also natural limits to the extent of cooperation between DNOs and community energy because DNOs only work on flexibility in the minority of zones where the network is constrained, and community energy organisations are not present in the majority of communities. Some community organisations will press ahead anyway with efficiency and demand management schemes but, given the resource constraints faced by community energy, they are not likely to meet the DNOs expectations on flexibility, as expressed in their ED2 business plans unless the DNOs come forward with the better incentives.

8 Conclusion

The community energy sector in the United Kingdom continues to diversify, innovate, and grow, albeit slowly. Community energy provides a small and declining proportion of electricity generation. Energy efficiency is already an area of growth for community energy in the in the United Kingdom, while engagement in demand side response is in its infancy.

In 2016, the Carbon Trust estimated that flexibility in UK networks could save between £17 and 40 billion cumulative between 2015 and 2050 [54]. If community energy could harness a small portion of this value for communities by helping to achieve these efficiencies and apply the income to local decarbonisation, it could change the trajectory of the sector significantly.

Unless DNOs come forward with more practical plans and incentives for community energy to engage in domestic flexibility, commercial electricity supply and technology companies will bypass the community level and work directly with individual consumers to capture the value from flexibility for their shareholders, if they get permission to expand their flexibility schemes following the winter 2022–23 piloting of the Demand Flexibility Service.

References

1. Electricity distribution networks in Northern Ireland are managed separately from GB, while government energy policy is set for the UK as a whole. The paper refers to GB and UK as appropriate
2. The six distribution network operator companies (DNOs) are: Electricity Northwest (ENW), Northern PowerGrid (NPG), National Grid Electricity Distribution (NGED), Scottish and Southern Energy Networks (SSEN), Scottish Power Energy Networks (SPEN), and UK Power Networks (UKPN). NGED, formerly Western Power Distribution, is separate from National Grid Electricity System Operator (NGESO), which manages the electricity transmission grid in England and Wales
3. Ofgem's Future Insights Series: The Decarbonisation of Heat, Ofgem, 2016, p. 3
4. Energy White Paper, Powering Our Net Zero Future, Department of Business, Energy and Industrial Strategy, December 2020, p. 79
5. Committee on Climate Change: Behaviour change, public engagement and Net Zero, October 2019, p. 38
6. Consultation Report: Future Smart - A Smart Grid for all: Our Transition to Distribution System Operator, UK Power Networks, 2017, p. 8
7. Electricity Networks, Report by the Comptroller and Auditor General, National Audit Office (NAO), January 2020, p. 15
8. Electricity Networks Strategic Framework Appendix 1: Electricity Networks Modelling, BEIS, August 2020, p. 14
9. Introduction to energy system flexibility, National Grid ESO, 2020, p. 1
10. Smart distribution networks, demand side response, and community energy systems: field trial experiences and smart grid modeling advances in the United Kingdom. In: Martınez, E., Mancarella, C. (eds.) Application of Smart Grid Technologies, p. 283. Academic Press (2018)
11. Bridging the Gap to Net Zero, National Grid ESO, March 2021,
12. Bray, R., Woodman, B., Connor, P.: Policy and Regulatory Barriers to Local Energy Markets in Great Britain, p. 11. Energy Policy Group, University of Exeter (2018)
13. NAO, January 2020, p. 25
14. Future System Operator: Government and Ofgem's response to consultation, BEIS/Ofgem April 2022, p. 4
15. Community Energy Strategy, Department of Energy and Climate Change, January 2014
16. Local Authorities and the Sixth Carbon Budget, Climate Change Committee, December 2020, p. 45
17. Empowering community energy schemes, House of Commons Library, November 2021, p. 13
18. https://commonslibrary.parliament.uk/research-briefings/cdp-2021-0108/, last accessed 24.11.2022
19. Braunholtz-Speight, T. et al.: The Evolution of Community Energy in the UK, Working Paper, UK Energy Research Centre, Manchester University, 2018, p. 4
20. https://www.gov.scot/policies/renewable-and-low-carbon-energy/local-and-small-scale-renewables/, last accessed 19.11.2022
21. Renewable energy in Wales, Welsh Parliament Climate Change, Environment, and Infrastructure Committee, May 2022, pp. 10, 26
22. Data in this paragraph from: Community Energy State of the Sector Summary Report 2022, Community Energy England, Community Energy Scotland, Community Energy Wales, 2022, pp. 4–6
23. https://www.gov.uk/government/statistics/energy-trends-section-6-renewables, last accessed 19.11.2022
24. Mirzania, P., Ford, A., Andrews, D., Ofori, G., Maidment, G.: The impact of policy changes: the opportunities of community renewable energy projects in the UK and the barriers they face. Energy Policy. **129**, 1282–1296 (2019)

25. Brummer, V.: Community energy – benefits and barriers: a comparative literature review of community energy in the UK, Germany and the USA, the benefits it provides for society and the barriers it faces. Renew. Sust. Energ. Rev. **94**, 192 (2018)
26. Braunholtz-Speight, T. et al., p. 31
27. Braunholtz-Speight, T. et al., p. 42
28. Community Energy State of the Sector Summary Report 2022, p. 12
29. https://energylocal.org.uk/, last accessed 19.11.2022
30. For example, https://www.urbanchain.co.uk/products, last accessed 19.11.2022
31. RIIO (Revenue = Incentives + Innovation + Outputs) ED2 (Electricity Distribution 2) taken from https://www.energynetworks.org/newsroom/what-is-the-riio-ed2-price-control-and-why-are-the-draft-business-plans-important, last accessed 24.11.2022
32. RIIO-ED2 Draft Determinations Overview Document, Ofgem, June 2022, p. 9
33. The Energy Networks Association (ENA) definition of the DSO function includes: 'securely operating and developing an active distribution system comprising networks, demand, generation and other flexible distributed energy resources (DER)'; 'acting as a neutral facilitator of an open and accessible market... enabling customer access, customer choice and great customer service'. https://www.smart-energy.com/regional-news/europe-uk/ena-role-uk-dso/, last accessed 19.11.2022
34. https://www.energynetworks.org/creating-tomorrows-networks/open-networks/flexibility-services, last accessed 21.11.2022
35. Powering Communities to Net Zero, Our Business Plan for RIIO-ED2, Scottish and Southern Energy Networks, December 2021, p. 99
36. Electricity Network Innovation Guide for Communities, Energy Networks Association, 2018, p. 5
37. https://www.ofgem.gov.uk/publications/reports-ofgem-riio-2-independent-customer-engagement-groups-and-user-group-energy-network-company-business-plans-riio-2, last accessed 28.11.2022
38. https://www.regen.co.uk/project/ena-community-energy-forums/, last accessed 20.11.2022
39. https://www.energynetworks.org/newsroom/open-networks-project-launches-community-energy-forums-to-build-an-all-inclusive-energy-system, last accessed 19.11.2022
40. Power to Participate a Specification for Community Energy to Participate in a Flexible Energy System, p. 25. Regen, Friends Provident (2019)
41. Rough Guide to Engaging Communities in Energy Network Innovation, ENA/Regen SW, February 2017, p. 12
42. https://project-leo.co.uk/our-trials/place-based-trials/, last accessed 19.11.2022
43. https://www.nationalgrideso.com/industry-information/balancing-services/demand-flexibility, last accessed 20.11.2022
44. https://www.current-news.co.uk/news/ovo-energy-launches-flexibility-scheme-to-reduce-energy-bills-this-winter, last accessed 20.11.2022
45. https://www.current-news.co.uk/news/octopus-energy-customers-provide-108mw-of-flexibility-during-first-saving-session, last accessed 24.11.2022
46. Our Business Plan 2023–2028, Final Submission, National Grid Energy Distribution, December 2021, pp. 10, 21, 23, 32, 60, 69, 73, 74
47. RIIO-ED2 Annex 1.1: Our Commitments, Scottish Power Energy Networks, December 2021, pp. 2, 10
48. RIIO-ED2 Business Plan, Scottish Power Energy Networks, December 2021, pp. 102, 134, 135
49. Our Plan to Lead the North West to Net Zero: 2023-2028, Energy Northwest, undated (likely December 2021), p. 72
50. Our Business Plan for 2023-28, Northern PowerGrid, December 2021, pp. 33, 38, 132, 138
51. Power Communities to Net Zero, Scottish and Southern Energy Networks, December 2021, pp. 113, 120
52. RIIO-ED2 Draft Determinations Overview Document, Ofgem, June 2022, p. 8
53. Community Energy State of the Sector Summary Report 2022, p. 11
54. The Carbon Trust, An analysis of electricity system flexibility for Great Britain (2016)

Part VI
Clean Energy Combustion and Thermal Engineering

Increasing Flow Rates of Air and Coconut Shell Producer Gas Mixed with PME20 for a Diesel Engine Generator

Pisak Chermprayong, Ekkachai Sutheerasak, Worachest Pirompugd, Sathaporn Chuepeng, and Surachai Sanitjai

1 Introduction

Greenhouse gas and particulate matter (PM) released from natural fires of plant-based materials, especially coconut shell, sugar cane, and wood chips, are nowadays causing the health and environmental impacts on farmers, living in the small village and wilderness. The Energy Ministry of Thailand suggests an electricity production policy for agriculturists by using engine generators to reduce the natural fire issues. Biomass cannot be ignited within a combustion chamber of reciprocating engines since it is in solid state. It can be converted to gases via gasifiers by gasification process; the thermal conversion of plant-based matters by partial oxidation into a gaseous product called producer gas (PG). This basically consists of carbon dioxide (CO_2), carbon monoxide (CO), hydrogen (H_2), methane (CH_4), and nitrogen (N_2) [1]. Downdraft gasifier is better than other gasifiers, due to the lowest tar production. It is applied for engine generators by carburation, injection, and dual fuel modes [2]. The carbureting and injecting techniques are applied with gasoline engines by an intake-manifold modification, but the engine performance fueling with PG is lower than original fuel [3]. Therefore, PG studies for diesel engines are considered due to the higher engine power and compression ratio than gasoline engines. PG cannot be directly ignited within diesel engines because it cannot ignite by itself under prevailing pressure. Dual fuel is a better procedure, since primary

P. Chermprayong · E. Sutheerasak (✉) · W. Pirompugd
Faculty of Engineering, Burapha University, Chonburi, Thailand
e-mail: ekkachai@eng.buu.ac.th

S. Chuepeng
Faculty of Engineering at Sriracha, Kasetsart University, Chonburi, Thailand

S. Sanitjai
Faculty of Engineering, King Mongkut's University of Technology Thonburi, Bangkok, Thailand

fuel is injected according to engine timing and PG is secondary fuel inducted through the intake manifold of reciprocating engines by a mixing box. This way is low cost and reduces the tar quantity, which damages engine parts [4].

Previous studies were focused on the fuel injection reduction of diesel engines under different speeds and loads [2, 4]. Dual fuel between diesel and PG produced from plant-based materials, such as wood pellet, unpressed jatropha seed, sugarcane bagasse, carpentry waste, sawdust, and cotton stalks, was compared with the neat diesel fuel [4–9]. This method consisted of compressing PG by limited air via a Y-type mixing box [2–5], modifying intake manifold for injecting PG [6, 7], and increasing compression ratio for mixing PG with air [8, 9]. The results of these techniques led to the reduction of diesel consumption, and diesel saving increased up to 65% from using the modified engine. Although diesel saving was escalated, engine performance parameters, particularly brake thermal efficiency (BTE) and brake-specific energy consumption (BSEC), were changed. The releases of carbon monoxide (CO), unburned hydrocarbon (UHC), and black smoke (BS) were extremely raised while nitrogen oxide (NO_x) was dropped according to PG flow rate increased. To improve exhaust emissions, the studies of oxygenated fuel and PG on the dual fuel mode were considered.

In cases of ethyl and methyl esters combined with PG, methyl ester of honge oil combined with constant PG flow rate led to the improvement of exhaust emissions. Nevertheless, the BTE and NO_x were lower and the CO, UHC, and BS were slightly higher than dual fuel between diesel and PG [7]. Contrarily, diesel blended with 50% ethyl ester of palm oil combined with increasing PG flow rate could increase BTE, but these emissions were changed by adding PG flow rate as applied with a turbocharging diesel engine generator [10, 11]. Additionally, several researchers [12–14] generated PG from renewable organic matters, such as calophyllum ino-phyllum, coconut shell, and jatropha seeds. This was combined with the diesel mixed with methyl ester, produced from calophyllum, jatropha, and palm oils, in ratios of 10–50%. As a result, BSEC and these pollutants were different. Fuel saving did not decrease to compare with these oils and diesel. Howbeit, pure esters had lower engine performance than its blends. Besides, the investigating pollutants by diesel blended with alcohols, such as ethanol, ethyl acetate, and butanol, combined with increasing PG flow rate were considered. Engine performance was improved, and fuel saving was increased with increasing alcohols. The releases of carbon monoxide (CO), unburned hydrocarbon (UHC), and black smoke (BS), notwithstanding, were highly increased according to enlarged PG flow rate, although the alcohols were added and the turbocharged diesel engine generator was applied with these blends [15–17]. Summarily, in combination with PG, the previous research work has shown that the diesel-ester-blended fuels can reduce the UHC and CO emissions greater than the diesel-alcohol-blended fuels.

In Thailand, palm oil methyl ester (PME) has been progressively studied as a renewable energy, due to a plenty of raw materials [18]. The diesel blended with 20% PME (PME20) is becoming an alternative fuel in local market to partially replace conventional diesel as engine performance fueled by PME20 is trivially lower than diesel [13]. Although earlier studies on PG produced from coconut shell

can be progressively founded, its usage as dual fuel combustion was rarely reported [19]. Additionally, the improvement of dual fuel mode by increasing air flow rate was rarely seen. Therefore, the present work aims to study the performance and exhaust emissions of a non-modified diesel engine coupled with a generator loaded, fueled by PME20 combined with increasing flow rates of air and PG generated from coconut shell. All operating parameters will be compared to those from PME20 and regular diesel at a constant speed of 3000 rpm and various loads.

2   Methodology

The overall project study comprises fuel property test, experimental design, and diesel engine operating parameter study. In the case of fuel baseline, regular diesel (RD) and PME20 were inspected under various ASTM methods before being operated with a generator-diesel engine unit. RD and PME20 properties, such as fuel density (ASTM D1298), kinematic viscosity (ASTM D445), and heating value (ASTM D240), were examined. They were by 832 and 849 kg/m^3, 3.19 and 4.18 mm^2/s, and 45.32 and 43.06 MJ/kg, respectively. These properties were under commercial fuel specifications, announced by the Energy Business Department, Thailand. PG was produced from coconut shell by a downdraft gasifier (maximum capacity at 75 kW_{th}) at equivalence ratio between 0.11 and 0.15. The PG components were characterized by a gas chromatographer, composed of $12.96 \pm 0.46\%$ CO_2, $5.48 \pm 0.64\%$ CO, $7.90 \pm 0.58\%$ CH_4, $14.20 \pm 0.67\%$ H_2, and $57.34 \pm 0.35\%$ N_2, and its calorific value was by 5.39 ± 0.16 MJ/m^3. Subsequently, the research protocol built a clean PG production system, consisting of a cyclone, a wet scrubber, and a sand-bed filter together with generator-diesel engine kit, as shown in Fig. 1. PG and air flow rates were increased by a blower attached with an inverter and a Y-shape mixing box. PG-air mixtures were inducted into the intake manifold, and PME20 was injected into a combustion chamber on a dual fuel mode. The experimental scheme was accomplished on a non-modified 5GF-ME Mitsuki engine [1-cylinder, 0.406 L displaced volume; 17.5:1 compression ratio; 5 kW at 3000 rpm maximum power]. Arrays of electrical lamp were used as a load of the generator-diesel engine unit. Electrical power was measured by a power meter and engine speed was monitored by a speed meter. Temperatures of PG, air, mixture, cylinder wall, and exhaust gas were recorded by K-type thermocouples combined with a temperature data logger; all data were stored in a computer. Flow rates of PG and air were managed by the flow conditioner before the mixing box, and a venturi tube and a digital manometer were applied in this experiment. The exhaust emissions (UHC, CO, NO_x, and PM) were recorded via an exhaust gas analyzer and a smoke meter.

The test engine was cranked and fired to its normal hot operating condition observed by steady cylinder wall temperature. The air temperatures were monitored in the range of 30 ± 5 °C. RD and PME20 were separately fueled in comparison on the usual mode (A). The engine was controlled to set the speed of 3000 ± 50 rpm. After stabilization of cylinder wall temperature, the electrical load was increased by
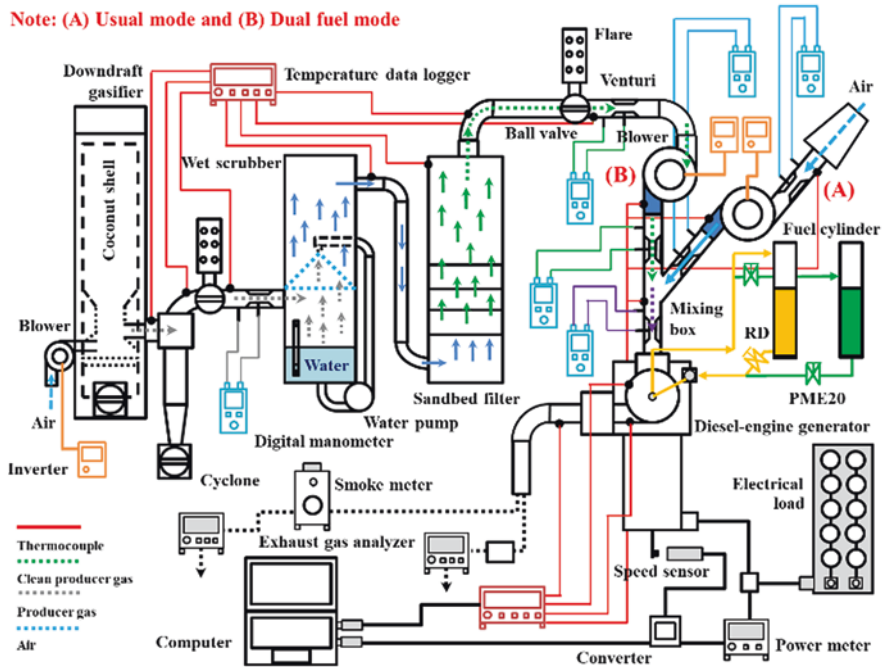
Fig. 1 Schematic diagram of the experimental setup

20, 40, 60, 80, and 100%. They generated the electrical power at 0.96 ± 0.02, 1.85 ± 0.07, 2.74 ± 0.03, 3.72 ± 0.06, and 4.62 ± 0.03 kW, respectively. Afterwards, the modes of dual fuel (A), dual fuel (B), dual fuel (C), dual fuel (D), and dual fuel (E) were investigated with regard to the air flow rates of 6.80 ± 0.28, 8.92 ± 0.75, 11.93 ± 0.54, 14.12 ± 0.46, and 16.21 ± 0.41 kg/h, respectively, under the PG flow rate of 9.74 ± 0.39 kg/h to replace the PME20 injection. They were studied under the same conditions for comparing with RD and PME20 on the usual mode. Finally, various parameters (flow rates, engine speed, electrical power, temperatures, and exhaust emissions) were investigated for three times in each condition. The tests were more than 100 h [15, 16, 18] to acquire for engine characteristics consisting of engine performance, explained in terms of BTE and BSEC, and exhaust emissions, in g/kW.h, referred from the literature [18].

3   Results and Discussion

Figure 2 shows the engine performance results of RD, PME20, and PME20 combined with adding flow rates of PG and air. Figure 2a indicates BTE raised with escalating electrical power, and Fig. 2b identifies BSEC reduced with expanding power generation. The best appropriate operating point was identified by the highest
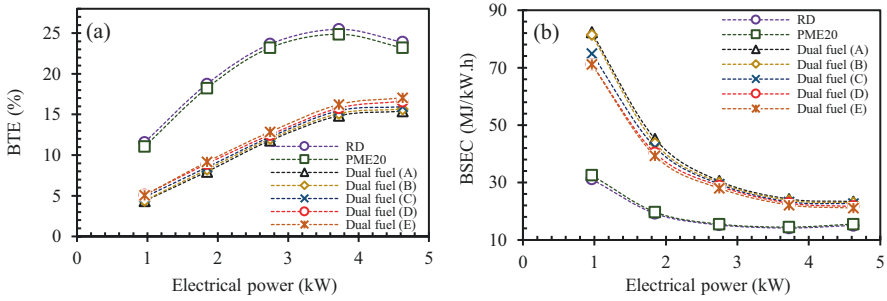
Fig. 2 Engine performance at different power

BTE and the lowest BSEC, at 3.72 kW, as the fuel was burnt and efficiently converted to the electrical power output [18]. Therefore, the engine characteristics were focused on this electrical load. BTE was defined by the ratio of the electrical power output to the total energy input and its values are shown in Fig. 2a. BTE of PME20 reduced 2.41% in comparison with that of RD. This is mainly due to the calorific value of PME20 lower than RD, leading to the subtle addition of fuel consumption at same load [12, 13, 18]. PME20 dual fueling with 9.74 kg/h PG limiting air at 6.80 kg/h (dual fuel (A)) caused the numerous reductions of BTE, by 41.73% and 40.29% compared with RD and PME20, respectively. These results correspond to the literature [6, 7, 13], due to the far lower energy value of PG than both fuels. When the electrical power was increasingly adjusted, the PME20 injection was increased with constant PG flow rate, affecting the escalation of total energy input, resulting in further reduction of BTE. However, PME20 combined with PG mixing with air flow rate increased from 8.92 to 16.21 kg/h (dual fuel (B) to dual fuel (E)), led to the improvement of BTE, increased from 1.81 to 9.34% compared with dual fuel (A). These results were similar to the earlier studies [2, 4, 15, 16], illustrated by the addition of air flow rate that improved the combustion reaction in diesel engine, leading to the upturn of BTE. As a result, the BTE of dual fuel (E) was relieved by 36.30% and 34.73% compared with RD and PME20, respectively.

BSEC was defined as the ratio of the total energy consumption to the electrical power output (Fig. 2b). At the best suitableness, the BSEC values of PME20 were greater than that of RD by 2.15% [16]. The mode dual fuel (A) was higher for BSEC, by 71.09% and 67.49%, respectively, than those of RD and PME20. These results were contrary to the previous studies [2, 4, 11, 15, 16] due to the difference in high PG addition to replace the PME20 injection. At the same electrical power output, PG was far lower in energy density value than PME20, resulting in the vast accretion of total energy consumption. Nevertheless, the mode dual fuel (A) can reduce the PME20 injection, leading to the reduction of PME20 consumption, and the PME20 saving increased by 42.12% compared with the usual mode. The increase of air flow rate from 8.92 to 16.21 kg/h improved the BSEC of PME20 combined with PG, declining in the range of 1.75–8.52% compared with the mode dual fuel (A). These results were similar to the earlier studies [15–17] since the
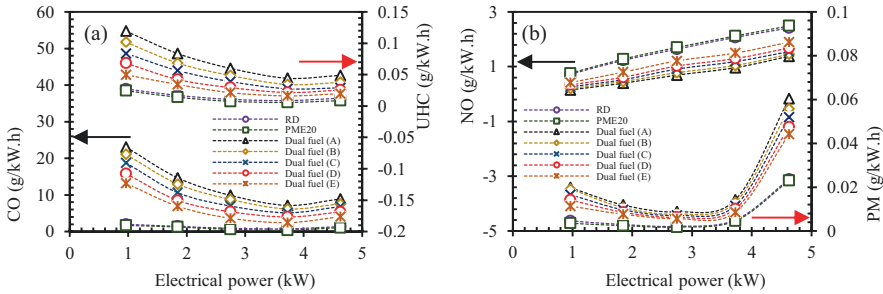
Fig. 3 Exhaust emissions at different power

more complete combustion from increasing air flow rate mixed with PG improves the PME20 combustion within diffusive region, the main combustion phase of diesel engine, and reducing the main injection of PME20. The total energy consumption was diminished corresponding to the increasing electrical power outputs. Outstandingly, the BSEC of the mode dual fuel (E) was higher by 56.53% and 53.23% than RD and POME20, respectively. PME20 saving was enlarged up to 50.57%. Therefore, the mode dual fuel (E) has better engine performance and higher fuel saving than the mode dual fuel (A).

Figure 3a shows the reduction of CO (left side) and UHC (right side) with increasing electrical power output. At the best appropriate operating point, the CO and UHC of PME20 were decreased by 47.39% and 33.73% compared with RD, respectively. These results were consistent with the previous studies [12, 13, 18] because the oxygenated PME20 led to more complete combustion than RD, resulting in the reduction of both emissions. Contrarily, the mode dual fuel (A) released more CO and UHC than RD by 6.75 g/kW.h and 0.04 g/kW.h, respectively. CO was beyond but UHC was lower than the Diesel Emissions Standards of Euro VI, determined at 1.50 g/kW.h and 0.13 g/kW.h, respectively. These results corresponded the literature [11, 15–17], since the PG consisted of CH_4, CO_2, and CO mixed with limited oxygen, leading to exceedingly incomplete combustion within the diffusion combustion zone. Although the combustion reaction was enhanced by the oxygen content in PME20, it was limited by the PG amount, resulting in the increase of both emissions. Outstandingly, the air flow rate increasing from 8.92 to 16.21 kg/h improved both pollutants. CO and UHC were reduced from 13.70 to 65.95% and 22.45 to 63.58%, respectively, compared with the mode dual fuel (A). These results have been improved from the previous studies [10–17] as the increasing air flow rate led to the escalation of oxygen content reacting with PG, resulting in better combustion in the diffusion combustion phase. As a result, both pollutants were lessened. Prominently, the mode dual fuel (E) emitted a slightly higher CO and UHC than RD and PME20.

Figure 3b shows the results of NO (left side) and PM (right side) over the range of electrical power output. NO is usually the main constituent of NO_x that forms in diesel engine exhaust [4, 18]. The NO emission levels were enlarged with electrical

power raised. The use of PME20 led to the increased NO by 2.57% over RD at 3.72 kW electrical power. The results were in line with those reported in [18] as the burning rate of increasing oxygen content in PME20 led to the higher flame temperature, resulting in the increased NO formation. The mode dual fuel (A) reduced NO by up to 53.46% and 54.63% compared to RD and PME20, respectively. These results correspond to the previous studies [4, 12, 13] due to the increase of PG combined with limited air entrancing a combustion chamber, resulting in incomplete combustion. As a result, the flame temperature was lower, and the NO formation was relieved. Oppositely, the addition of air flow rate from 8.92 to 16.21 kg/h enlarged NO formation, increasing from 8.43 to 55.56% compared with the mode dual fuel (A). It can be explained by the increase of air flow rate that improves the combustion reaction of PME20 combined with PG causes the escalated flame temperature, leading to the accretion of NO [6, 7]. The mode dual fuel (E) lowered the NO formation by 27.60% and 29.42% compared with RD and PME20, respectively, for the reasons described earlier. PM decreased with increasing power generation up to 3.72 kW. Afterwards, greater level of PM was released for greater load because of the fuel-rich combustion [4]. PM released for PME20 was dropped by 9.24% compared with RD. The attained results are consistent with the literature [18] due to the oxygen content of PME20, leading to complete combustion in diffusion combustion phase. The mode dual fuel (A) released greater PM than the RD and PME20 by less than 0.0097 g/kW.h. However, it was higher than the Diesel Emissions Standards of Euro VI. These results were similar to the studies [10, 11, 15–17], and they correspond to the increase of CO and UHC explained in the previous section. PG combined with limited air caused an entire fuel-rich combustion with burning zones, especially diffusion combustion period. As a result, the CO, UHC, and BS emissions were extremely accrued, leading to the vast formation of PM. Contrariwise, the increase of air flow rate from 8.92 to 16.21 kg/h can mitigate the PM formation, reduction in the range of 8.57 to 39.89% compared with the mode Dual fuel (A). The mode dual fuel (E) was slightly higher for PM than RD and PME20. Therefore, the mode dual fuel (E) improved the exhaust emissions better than the mode dual fuel (A).

4   Conclusions

PME20 combined with increasing flow rates of air and PG, generated from coconut shell, on a dual fuel mode led to the changes of performance parameters and exhaust emissions of the generator-diesel engine unit. The performances of the engine under dual fuel modes were lower than those of RD and PME20. Especially, the dual fuel (A) caused the reduction of BTE and the addition of BSEC up to 42% and 71%, respectively, compared with RD and PME20. However, PME20 saving were increased by 42%. Outstandingly, the addition of air flow rate (the modes dual fuel (B) to dual fuel (E)) had better engine performance than the dual fuel (A). Particularly, the dual fuel (E) led to the increase of BTE and the decrease of BSEC

up to 9% compared with dual fuel (A), and the PME20 saving accrued up to 51%. In term of engine emission, the dual fuel modes had extremely higher exhaust emissions, especially CO, UHC, and PM, over RD and PME20. The Dual fuel (A) released CO and PM greater than the Diesel Emissions Standards of Euro VI while UHC level was bounded by the standard. Eminently, NO was declined by 55% comparing between both fuels. Nevertheless, the increase of air flow rate from the modes dual fuel (B) to dual fuel (E) can decrease the CO, UHC, and PM releases up to 66%, 64%, and 40% compared with the dual fuel (A), respectively. In summary, the dual fuel (E) improved the engine characteristics, better than the dual fuel (A). Although the dual fuel (E) increased NO, it was lower than the Usual mode. Therefore, the research results recommend the use of PME20 combined with PG and increasing air flow rate. However, the increase of air flow rates is limited by a PG flow stream, and this technique leads to the augmentation of CO, UHC, and PM. Therefore, the injecting PG by engine modification and the exhaust gas recirculation are required for further research work.

Author Contributions Pisak Chermprayong is the first author who studied the instrument designs and measured the engine parameters. Ekkachai Sutheerasak is the corresponding author who conducted the research work, produced PME20 combined with PG-air flow rates, performed performance and exhaust emissions tests, and analyzed the experimental data of engine characteristics. Worachest Pirompugd studied the methods of PG-air flow measurement. Sathaporn Chuepeng explained the changes of engine characteristics and participated in research design, data analysis, as well as conclusion and recommendation. Surachai Sanitjai generated PG and reported the changes of fuel properties.

References

1. Teh, J.S., Teoh, Y.H., How, H.G., Le, T.D., Jason, Y.J.J., Nguyen, H.T., Loo, D.L.: The potential of sustainable biomass producer gas as a waste-to-energy alternative in Malaysia. Sustainability. **13**(3877), 1–31 (2021)
2. Sutheerasak, E., Pirompugd, W., Sanitjai, S.: Performance and emissions characteristics of a direct injection diesel engine from compressing producer gas in a dual fuel mode. Eng. Appl. Sci. Res. **45**(1), 47–55 (2018)
3. Authayarat, W., Sutheerasak, E., Pirompugd, W., Sanitjai, S.: Feasibility study of using producer gas from wood pellet operated with spark-ignition engine generators in different compression ratio. IEEE Xplore. **51686**(2021), 165–169 (2021)
4. Sutheerasak, E., Pirompugd, W., Ruengphrathuengsuka, W., Sanitjai, S.: Use of producer gas from wood pellet on dual fuel for a diesel-engine generator. Int. J. Mech. Eng. Robotic. Res. **9**(10), 1365–1370 (2020)
5. Monorom, R., Buenconsejo, B., Gonzaga, J.A., Gitano-Briggs, H.W., Lopez, N.S., Biona, J.B.M.: The combustion and emission characteristics of the diesel engine operated on a dual producer gas-diesel fuel mode. Eng. Appl. Sci. Res. **46**(4), 360–370 (2019)
6. Akkoli, K.M., Banapurmath, N.R., Shivashimpi, M.M., Soudagar, M.E.M., Badruddin, I.A., Alazwari, M.A., Yaliwal, V.S., Mujtaba, M.A., Akram, N., Goodarzi, M., Safaei, M.R., Venu,

H.: Effect of injection parameters and producer gas derived from redgram stalk on the performance and emission characteristics of a diesel engine. Alex. Eng. J. **60**, 3133–3142 (2021)

7. Akkoli, K.M., Banapurmath, N.R., Suresh, G., Soudagar, M.E.M., Khan, T.M.Y., Baig, M.A.A., Mujtaba, M.A., Hossain, N., Shahapurkar, K., Elfasakhany, A., Alsehli, M., Yaliwal, V.S., Goudadi, S.A.: Effect of producer gas from redgram stalk and combustion chamber types on the emission and performance characteristics of diesel engine. Energies. **14**(5879), 1–17 (2021)

8. Harmanpreet, S., Mohapatra, S.K.: Production of producer gas from sugarcane bagasse and carpentry waste and its sustainable use in a dual fuel CI engine: a performance, emission, and noise investigation. J. Energy Inst. **91**(1), 43–54 (2018)

9. Sohan, L., Mohapatra, S.K.: The effect of compression ratio on the performance and emission characteristics of a dual fuel diesel engine using biomass derived producer gas. Appl. Therm. Eng. **119**, 63–72 (2017)

10. Santasnachok, M., Sutheerasak, E., Chinwanitcharoen, C., Ruengphrathuengsuka, W.: The ability to use 50% biodiesel and supercharging syngas in dual fuel mode for a turbocharging diesel-engine generator. Int. J. Mech. Eng. Robotic. Res. **9**(1), 71–75 (2020)

11. Sutheerasak, E., Pirompugd, W., Chinwanitcharoen, C., Ruengphrathuengsuka, W.: Comparative performance and emissions of diesel engine using B50 and dual fuel between compressing producer gas and B50 for an alternative fuel. Burapha Sci. J. **24**(3), 1143–1159 (2020)

12. Hemanth, G., Prashanth, B., Benerjee, N., Choudhuri, T., Mrityunjay: Dual fuel mode operation and its emission characteristics in diesel engine with producer gas as primary fuel and jatropha biodiesel as pilot fuel. Int. J. Mech. Eng. Technol. **8**(4), 138–147 (2017)

13. Kumar, S.K., Mishra, P.C.: Emission from a dual fuel operated diesel engine fuelled with calophyllum inophyllum biodiesel and producer gas. Int. J. Automot. Mech. Eng. **14**(1), 3954–3969 (2017)

14. Mahgoub, B.K.M., Hassan, S., Sulaiman, S.A., Mamat, R., Adam, A.A., Hagos, F.Y.: Dual fuel combustion in a ci engine powered by blended diesel-biodiesel fuel and simulated gasification gas. ARPN J. Eng. Appl. Sci. **11**(22), 12947–12952 (2016)

15. Sutheerasak, E., Ruengphrathuengsuka, W.: Comparison of using DEE oil with supercharging syngas and DEE oil on dual fuel in a turbocharging diesel engine. Songklanakarin J. Sci. Technol. **42**(5), 991–999 (2020)

16. Sutheerasak, E., Pirompugd, W., Ruengphrathuengsuka, W., Sanitjai, S.: Comparative investigation of using DEB oil and supercharging syngas and DEB oil as a dual fuel in a DI diesel engine. Eng. Appl. Sci. Res. **46**(1), 26–36 (2019)

17. Sutheerasak, E., Chinwanitcharoen, Ruengphrathuengsuka, W.: Using diesohol and supercharging syngas on dual fuel in a turbocharging diesel-engine generator. Int. J. Mech. Eng. Robot. Res. **8**(6), 972–976 (2019)

18. Chinwanitcharoen, C., Ruengphrathuengsuka, W., Pirompugd, W., Sutheerasak, E.: Characterization of a high-speed compression ignition engine fueled with ethyl and methyl esters of palm oil. Energy Rep. **9**(1), 478–485 (2023)

19. Nayak, S.K., Mishra, P.C., Behera, G.R.: Characterization of coconut shell imitatived producer gas in a diesel engine. Energy Sources, Part A: Recovery, Util. Environ. Effect. **39**(16), 1718–1724 (2017)

Investigation on Combustion Processes of Gasoline Blended with Dissociated Methanol Gas

Chen Yexin, Xu Weihong, Zhang Yuchao, Zhang Beidong, and Jiang Yankun

1 Introduction

As a renewable energy, methanol is a type of alcohol-based fuel that can be used as a transportation fuel in engine [1]. People are looking for the improvement of engine thermal efficiency, and how to efficiently recycle exhaust heat is one of the key concerns. Renewable fuels are widely investigated [2]. Specifically, using methanol-dissociated technology to produce hydrogen is a promising solution [3]. Utilizing this approach, the waste heat generated by the engine serves to vaporize methanol within a methanol dissociation device. Consequently, in the presence of a catalyst, methanol undergoes dissociation, resulting in a composition comprising H_2 and CO. The dissociated methanol gas is added to the cylinder to improve combustion, as shown in Fig. 1. The gaseous methanol, post-dissociation, exhibits a high hydrogen content, contributing to an accelerated flame speed, an extension of the lean-burn threshold, and the attainment of uniform fuel combustion within the cylinder. By recycling part of the exhaust heat and improving the calorific value, the thermodynamic cycle process of the engine is closer to the ideal Otto cycle and the fuel burns more completely. All of these further improve the engine efficiency. Figure 2 shows that equivalent fuel consumption rate decreased with the increase of the dissociated methanol ratio [4].

C. Yexin · X. Weihong · Z. Yuchao · Z. Beidong
School of Energy and Power Engineering, Huazhong University of Science and Technology, Wuhan, China

J. Yankun (✉)
School of Energy and Power Engineering, Huazhong University of Science and Technology, Wuhan, China

State Key Laboratory of Coal Combustion, Huazhong University of Science and Technology, Wuhan, China
e-mail: jykhust@hust.edu.cn
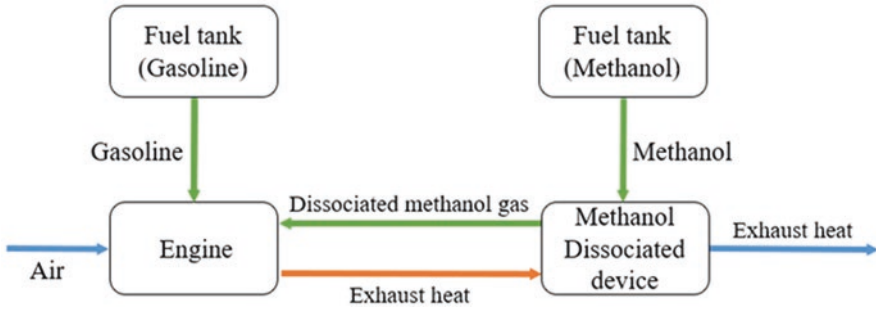
Fig. 1 Blending gasoline and dissociated methanol gas as a fuel for the engine
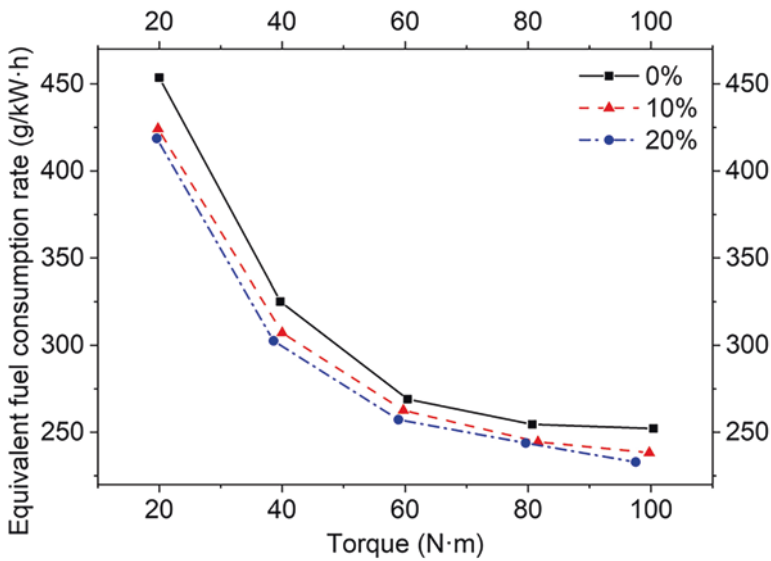
Fig. 2 Equivalent fuel consumption rate of engine at different working conditions

Regarding the effect of blending hydrogen-rich gases on flame speed, Mandilas et al. [5] conducted research on the flame speed of iso-octane/hydrogen blends, discovering that under stoichiometric conditions, an elevated mass proportion of hydrogen corresponded to an increase in the flame speed for these mixtures. Huang et al. [6] executed an empirical investigation to quantify the flame propagation rates of iso-octane/air combinations supplemented with reformer gas, revealing that incorporating methanol-derived reformed gas into hydrocarbon/air mixtures bolstered flame speed, primarily attributable to the presence of hydrogen within the blend. Nowadays, the improvement of hydrogen on gasoline combustion has been confirmed by constant volume chamber combustion tests with gasoline surrogate fuel [7] and gasoline [8] blended with hydrogen. Li et al. [9] carried out a sensitivity assessment which demonstrated that the flame speed of $i - C_8H_{18}/H_2$/air mixtures

was increased through chain branching reactions because of hydrogen instead of higher carbon species. Specifically, the concentration of H radical [10] and the concentration of H + OH + O [11] could significantly affect the flame speed.

2 Methodology

Laminar flame speed is an important characteristic of fuels. Simulation is conducted based on ANSYS CHEMKIN software. The premixed laminar flame speed is defined as the normal speed of a one-dimensional plane. The main governing equations are as follows:

The continuity equation is

$$\dot{M} = \rho u A \tag{1}$$

the conservation of species equation is

$$\dot{M}\frac{dY_k}{dx} + \frac{d}{dx}\left(\rho A Y_k V_k\right) - A\dot{\omega}_k W = 0 \qquad \left(k = 1, \ldots, K_g\right) \tag{2}$$

the conservation of energy equation is

$$\dot{M}\frac{dT}{dx} - \frac{1}{C_p}\frac{d}{dx}\left(\lambda A\frac{dT}{dx}\right) + \frac{A}{C_p}\sum_{k=1}^{K}\rho Y_k V_k C_{pk}\frac{dT}{dx} + \frac{A}{C_p}\sum_{k=1}^{K}h_k\dot{\omega}_k W_k = 0 \tag{3}$$

and equation of state is

$$\rho = \frac{P\bar{W}}{RT} \tag{4}$$

where $\dot{M}$ denotes the mass flow rate; Y_k corresponds to the mass fraction; W_k stands for the molecular weight; $\bar{W}$ is the average molecular weight of the mixture; C_{pk} represents the constant-pressure heat capacity; $\dot{\omega}_k$ signifies the molar production rate due to chemical reactions; h_k is the specific enthalpy; and V_k denotes the diffusion velocity.

The oxidation rate for the fuel was determined utilizing the Arrhenius equation. The rate constants corresponding to each elementary reaction can be described as follows:

$$k_{i,f} = A_i T^{b_i} \exp\left(\frac{-E_i}{RT}\right) \tag{5}$$

where $k_{i,f}$ represents the reaction rate constant; A_i denotes the pre-exponential factor; b_i corresponds to the temperature exponent; E_i indicates the activation energy. The self-design kinetic model is used in the simulation.

3 Results and Discussion

3.1 Validation of the Mathematical Model

A comparison between simulation outcomes and experimental data was performed to ascertain the accuracy of the mathematical model, with experimental data sourced from relevant literature [6]. Experiments were conducted to measure the flame speed of fuel consists of iso-octane, reformer gas, and air. The flame speed initially increased and subsequently decreased as the equivalence ratio grew at $p = 1$ atm and $T = 298$ K, reaching its peak at an equivalence ratio marginally above 1. When the equivalence ratio is fixed, the flame speed escalated as the molar percentage of reformer gas increased. As shown in Fig. 3, the simulation results generated by the model developed in this investigation generally align with the experimental data.
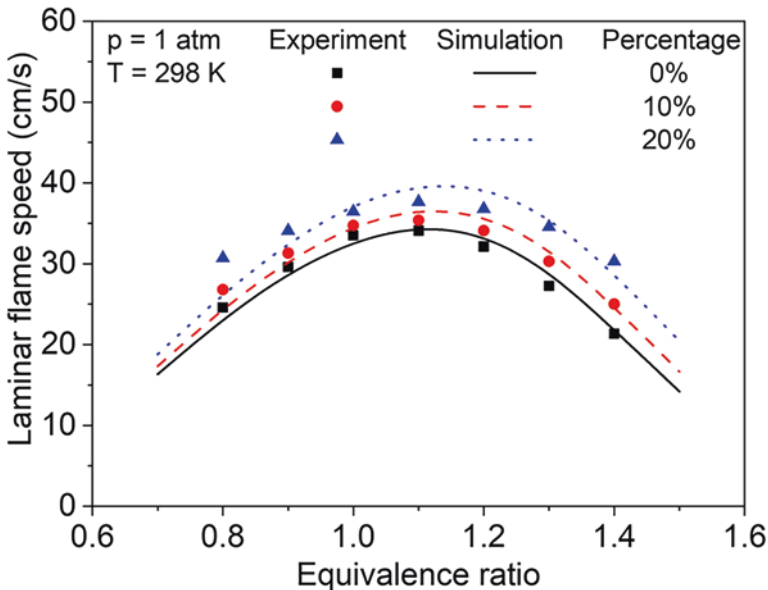
Fig. 3 A comparative analysis of laminar flame propagation rates was conducted. Symbols depict the experimental data [6]; lines illustrate the outcomes derived from simulated data

3.2 Effect on Flame Speed

Figure 4 shows the laminar flame speed of gasoline blended with dissociated methanol gas for different blend ratios at $T = 298$ K and $p = 1$ atm with different equivalence ratios. For gasoline, the laminar flame speed increases and then decreases with an increasing equivalent ratio, peaking near an equivalence ratio of 1.1.

The reason for this phenomenon was that the reactivity of dissociated methanol gas under rich fuel conditions was higher than the reactivity of syngas under lean fuel conditions. In addition, the equivalent ratio of the maximum flame speed gradually increased as the blend ratio increased.

In order to elucidate the effect of H_2 and CO on the flame speed, the adiabatic flame temperature and the maximum molar concentration of key active radicals (O, H, and OH) for various blended fuels with various blend ratios under $T = 298$ K, $p = 1$ atm and $\varphi = 1.0$ were calculated. Figure 5 shows the effect of blending dissociated methanol gas, H_2, and CO, respectively, on (a) laminar flame speed, (b) free radical concentration, and (c) adiabatic flame temperature at different blend ratios. The flame speed of the fuel increases with the increase of H_2 and dissociated methanol gas ratio, and increases more rapidly when blending H_2, but CO has little effect on flame speed. The sum of O, H, and OH concentrations is similar to the flame speed. The active radical concentration of the fuel increases with the blend ratio increasing when blending H_2 and blending dissociated methanol gas, and increases faster when blending H_2. However, blending CO has little effect on the concentration of active radicals. Because the active radical concentration of blending H_2 was
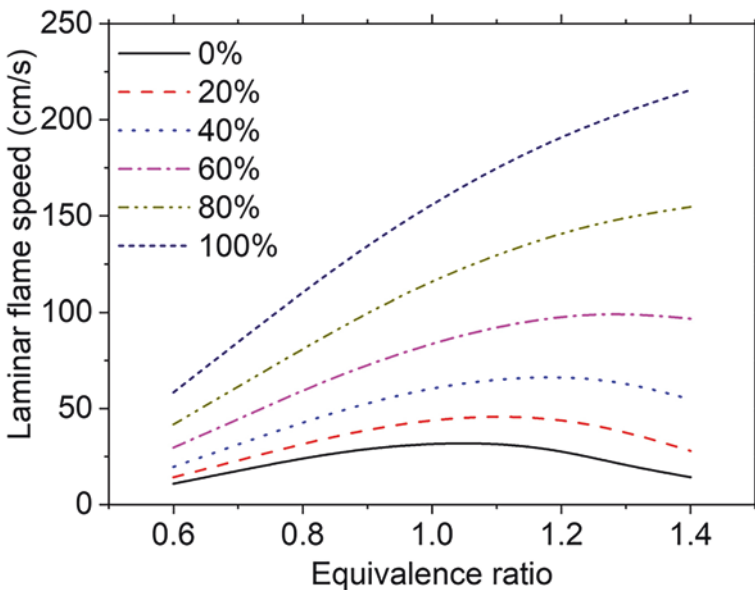
Fig. 4 Laminar flame speed of different blend ratios at 0%–100%
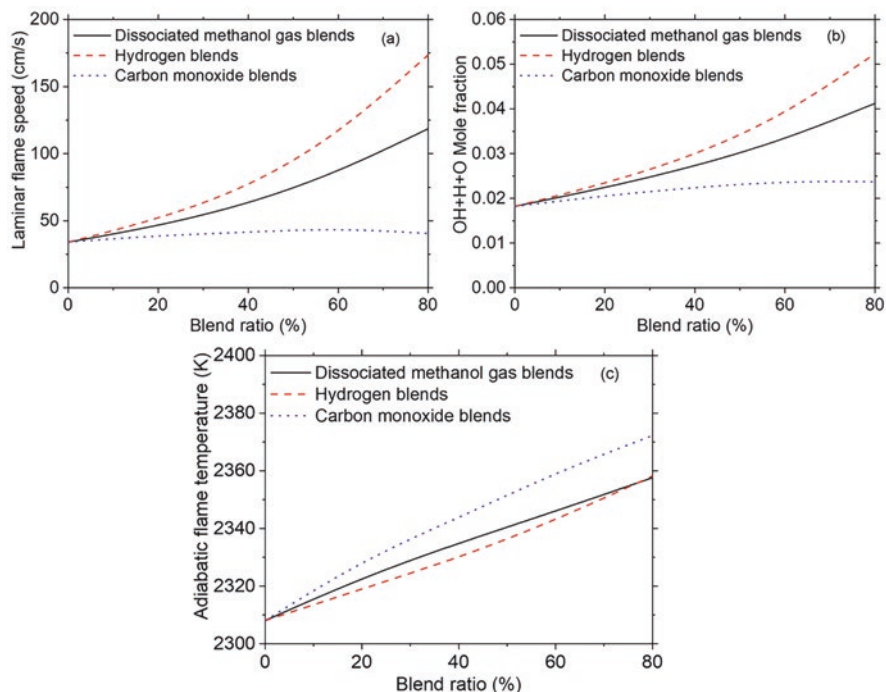
Fig. 5 Influence of blending dissociated methanol gas /hydrogen /carbon monoxide on (**a**) laminar flame speed, (**b**) mole fraction of radicals, (**c**) adiabatic temperatures, at $T = 298$ K, $p = 1$ atm and $\varphi = 1.0$

higher than that of blending dissociated methanol gas and CO, the chemical action of blending H_2 had the greatest influence on the flame speed. The flame temperature increased with increasing blend ratio, but the magnitude was small. Therefore, increase in flame speed after blending dissociated methanol gas with gasoline was mainly attributed to the chemical effects of H_2 in the gasoline.

3.3   Effect on Flame Structure

The heat release rate of combustion and flame structure of gasoline, gasoline/hydrogen blends, gasoline/carbon monoxide blends, and gasoline/dissociated methanol gas blends are given in Fig. 6. The analysis of the heat release rates showed that the combustion process mainly occurred in the range of 0.1–0.2 cm, and the addition of hydrogen or gasoline-carbon monoxide mixture resulted in a higher peak heat release rate and an earlier combustion process. The different initial concentrations of H_2 in the reactants led to different variations in H_2 concentration and different
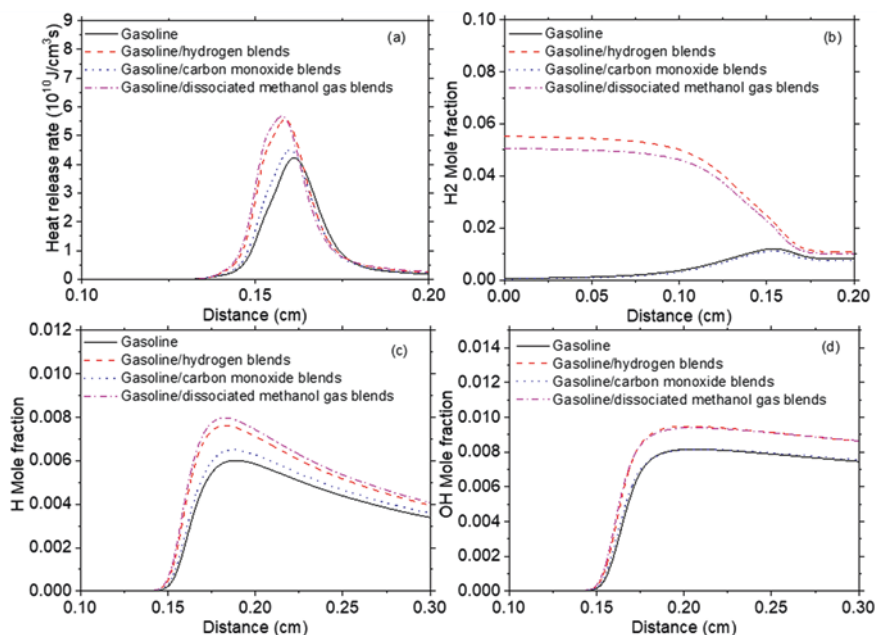
Fig. 6 Influence of blending dissociated methanol gas /hydrogen /carbon monoxide on (**a**) heat release rate, (**b**) mole fraction of H_2, (**c**) mole fraction of H, (**d**) mole fraction of OH, at $T = 298$ K, $p = 1$ atm and $\varphi = 1.0$

flame structures. In the initial stage of the reaction, $CH_2O + H = HCO + H_2$ (R79) and $HCO + H = CO + H_2$ (R87) produced H_2, while $H_2 + OH = H + H_2O$ (R5) consumed H_2. For the gasoline and gasoline/carbon monoxide blends, producing H_2 was the dominant reaction in the early stage, so the H_2 concentration increased at the beginning. With the acceleration of the reaction rate, H_2 began to be consumed rapidly and H_2 concentration decreased accordingly. For gasoline/hydrogen blends and gasoline/dissociated methanol gas blends, the initial high H_2 concentration could promote the forward reaction rate of R5 in the whole flame.

By analyzing the changes of H radical and OH radical, it was found that the addition of H_2 and CO changed the concentration and distribution of active radicals. When H_2 was added in gasoline and gasoline/carbon monoxide blends, the peak concentration of the radicals increased and the phase of the peak was correspondingly earlier. The addition of CO to gasoline and the gasoline/hydrogen blends only slightly increased the concentration of H radical but had little effect on the flame structure and concentration distribution of OH radical. Therefore, the H_2 in the blended fuel was the factor that determines the flame characteristics. The increase of the initial concentration of H_2 provided more free radicals to the flame, resulting in a higher heat release.
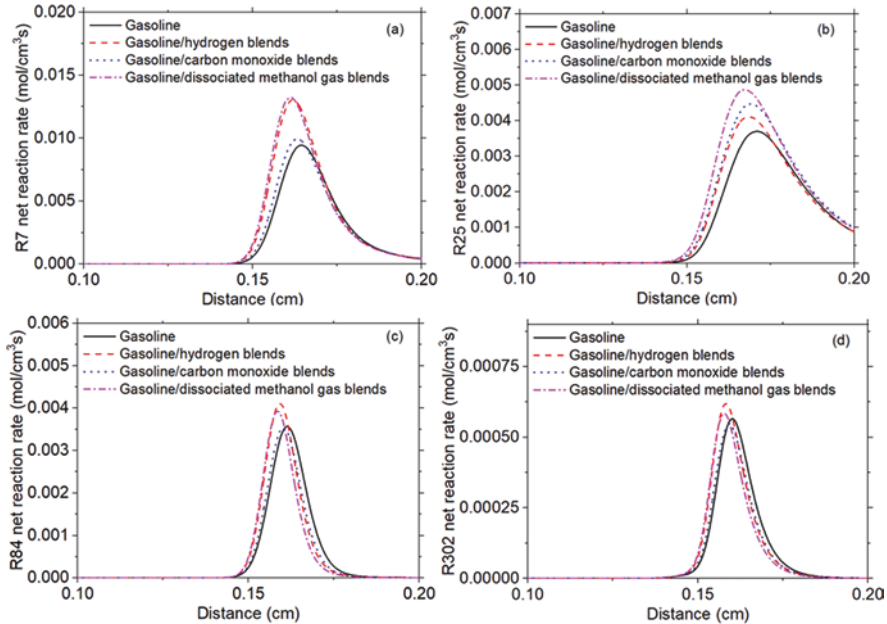
Fig. 7 Influence of blending dissociated methanol gas /hydrogen /carbon monoxide on the net reaction rate of (**a**) R7, (**b**) R25, (**c**) R84, (**d**) R302, $T = 298$ K, $p = 1$ atm and $\varphi = 1.0$

The effect of H_2 and CO on the net reaction rate of the elementary reaction is shown in Fig. 7. $O_2 + H = O + OH$ (R7), $CO + OH = CO_2 + H$ (R25), $C_6H_5 + O_2 = C_5H_5O + CO$ (R302), $HCO + M = H + CO + M$ (R84). The addition of H_2 enhanced the elementary reaction R7, while the addition of CO enhanced R25. Because the main reaction R7 started earlier than the consumption reaction R25, the molar fraction of OH increased in the early stage, while the molar fraction of OH decreased in the late stage with the consumption of R25 and other reactions. The most important reaction path of CO was R25, which was an important heat release reaction in the fuel oxidation stage and improves the temperature gradient and flame speed. The CO mole fraction was mainly controlled by the rate of HCO oxidation reaction R84, R87 and the rate of CO consumption reaction R25.

4   Conclusion

Employing the waste heat from the internal combustion engine for methanol disso-ciation to generate dissociated methanol gas, and subsequently introducing it into the cylinder alongside gasoline for combustion, constitutes a potential technique for enhancing engine efficiency. This study delved into the combustion dynamics of gasoline combined with dissociated methanol gas, arriving at the following primary conclusions.

(1) Blending gasoline with dissociated methanol gas as a fuel could improve flame speed. In addition, the equivalence ratio corresponding to the maximum laminar flame speed increased with the increase of the dissociated methanol ratio at 0.6–1.4 equivalence ratio.

(2) The addition of dissociated methanol gas enhanced the concentration of the O, H, and OH active radicals and the rate of some key elementary reactions and advanced the peak. The increase of flame speed in gasoline blended with dissociated methanol gas was mainly due to the chemical effects of H_2.

(3) The addition of H_2 increased the net reaction rates of all the elementary reaction rates and significantly enhanced the elementary reactions of $O_2 + H = O + OH$ (R7) and $H_2 + OH = H + H_2O$ (R5). The most important reaction path of CO was $CO + OH = CO_2 + H$ (R25), which was an important heat release reaction during fuel oxidation and improved the temperature gradient and flame speed.

References

 1. Shih, C.F., Zhang, T., Li, J., Bai, C.: Powering the future with liquid sunshine. Joule. **2**, 1925–1949 (2018)
 2. Abdudeen, A., Selim, M.Y.E., Sekar, M., Elgendi, M.: Jatropha's rapid developments and future opportunities as a renewable source of biofuel—a review. Energies. **16**, 828 (2023)
 3. Chen, Y., Jiang, Y., Wen, X., Liu, H.: An investigation of the kinetic modeling and ignition delay time of methanol—syngas fuel. Front Energy Res. **9** (2022)
 4. Jiang, Y., Chen, Y., Xie, M.: Effects of blending dissociated methanol gas with the fuel in gasoline engine. Energy. **247**, 123494 (2022)
 5. Mandilas, C., Ormsby, M.P., Sheppard, C.G.W., Woolley, R.: Effects of hydrogen addition on laminar and turbulent premixed methane and iso-octane–air flames. P. Combust. Inst. **31**, 1443–1450 (2007)
 6. Huang, Y., Sung, C., Eng, J.: Laminar flame speeds of primary reference fuels and reformer gas mixtures. Combust. Flame. **139**, 239–251 (2004)
 7. He, X., Hou, X., Yang, Q., Ma, X., Tian, G., Liu, F.: Study of laminar combustion characteristics of gasoline surrogate fuel-hydrogen-air premixed flames. Int. J. Hydrogen Energ. **44**, 13910–13922 (2019)
 8. Khan, F., Elbaz, A.M., Badra, J., Costanzo, V., Roberts, W.L.: A comprehensive experimental and kinetic study of laminar flame characteristics of H_2 and CO addition to oxygenated gasoline. Energ Fuel. **35**, 14063–14076 (2021)
 9. Li, Z., Han, W., Liu, D., Chen, Z.: Laminar flame propagation and ignition proper-ties of premixed iso-octane/air with hydrogen addition. Fuel. **158**, 443–450 (2015)
10. Xu, H., Liu, F., Sun, S., Meng, S., Zhao, Y.: A systematic numerical study of the laminar burning velocity of iso-octane/syngas/air mixtures. Chem. Eng. Sci. **195**, 598–608 (2019)
11. Liu, F., Liu, Z., Sang, Z., He, X., Liu, F., Liu, C., Xu, Y.: Kinetic study of the effects of hydrogen blending to toluene reference fuel (TRF) /air mixtures on laminar burning velocity and flame structure. Fuel. **274**, 117850 (2020)

Lee's Model and Determination of the Thermal Effect Zones of an LNG BLEVE Fireball

Abderraouf Guelzim, Aziz Ettahir, and Anas Mbarki (ID)

1 Introduction

The LNG value chain (exploration-production-processing-transport-liquidation-shipment-distribution) involves large quantities of fuel which, despite all the measures deployed for prevention, involves the risk of catastrophic accidents such as a BLEVE. A BLEVE corresponds to the sudden release of a mass of liquefied gas in a state of boiling under pressure, following the bursting or perforation of a storage envelope followed by an immediate general ignition. The fireball generated by the BLEVE is characterized by the emission of an intense thermal radiation, capable of causing lethal and irreversible damage to people and damage and destruction to buildings and constructions, located at significant distances from the center of the initial explosion [1–4]. Depending on atmospheric conditions, the thermal effects of such a fireball could produce third-degree skin burns and start fires several miles away [5].

The objective of this paper is to develop a fast calculation method for the rapid, but nevertheless reliable, estimation and delineation of thermal effect zones and corresponding safety distances for damage, degradation, and destruction effect doses with also the possibility to include distances from the center of the explosion and the radius of the fireball, to display all information in the same diagram.

In this chapter, we first present the radiative flux model (Lee's), the main thermal doses of lethality, and damage: minor effects (pain threshold, superficial burns) and major effects (irreversible effects, severe burns, property destruction, domino effect, lethality). Secondly, a methodological approach is developed to link the characteristic curves of thermal doses to the distances of effects on people and property.

A. Guelzim (✉) · A. Ettahir · A. Mbarki
Materials, Energy, Acoustics Team (MEAT), High School of Technology-Salé-Morocco,
Mohammed V University, Rabat, Morocco

2   Methods

The objective of this chapter is to propose a method or a means of rapid decision support (mnemonic or checklist type) for the first responders, during a particular intervention involving the presence of a storage or transport tank of pressurized liquefied natural gas and thus, to implement the first safety perimeters and zones to be evacuated necessary to minimize the thermal effects generated by the fireball following a BLEVE explosion.

In this perspective and from Lee's point source model [6], the analytical formulation distance-fraction-radiative-nature-weight of the fuel involved in the explosion and the formation of the fireball, called here characteristic curves, is thus deduced for each thermal dose. The conditions of the definition domains are realized with the application of the graphical calculator GeoGebra, while the final plotting is carried out by means of the software Matlab. The characteristic curves resulting from the same initial conditions at the time of the rupture (same stored product and same radiative fraction translating the pressure at the rupture) are grouped in the same graphical abacus with the addition of the characteristic curve of the fireball radius.

The graphical abacuses containing the characteristic curves drawn according to the LNG-breaking pressure-weight of the liquefied gas-thermal dose effect distance profiles are illustrated by Figs. 1 and 2. These charts will be used to determine the lethality and danger distances of the thermal effects of the fireball generated during a BLEVE phenomenon and according to the conditions of rupture of containment and ignition of the flammable cloud by their direct exploitation.

The reading of the projection of the intersection segment between the vertical line corresponding to the mass of the fuel contained in the tank (X = value, in kg), with the characteristic curves of the thermal doses pre-made on the axis of the Y,
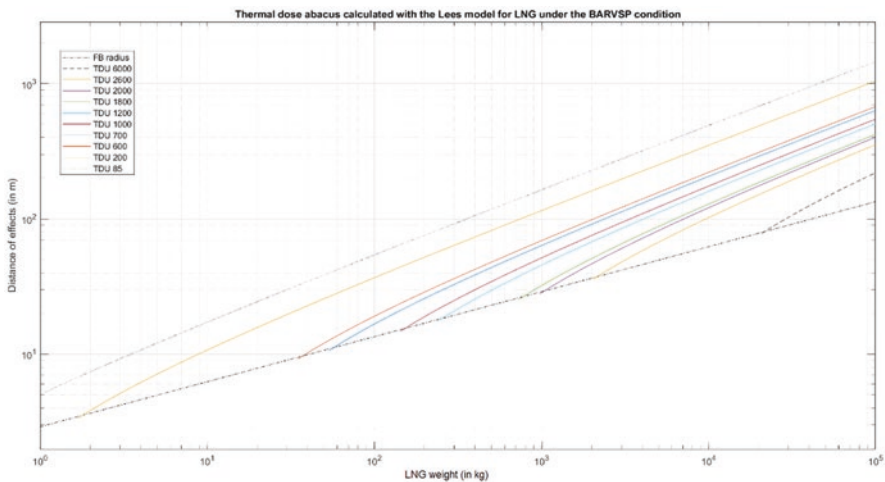
Fig. 1 Abacus of thermal doses deduced from the Lees model of the literature (BBRVSP)
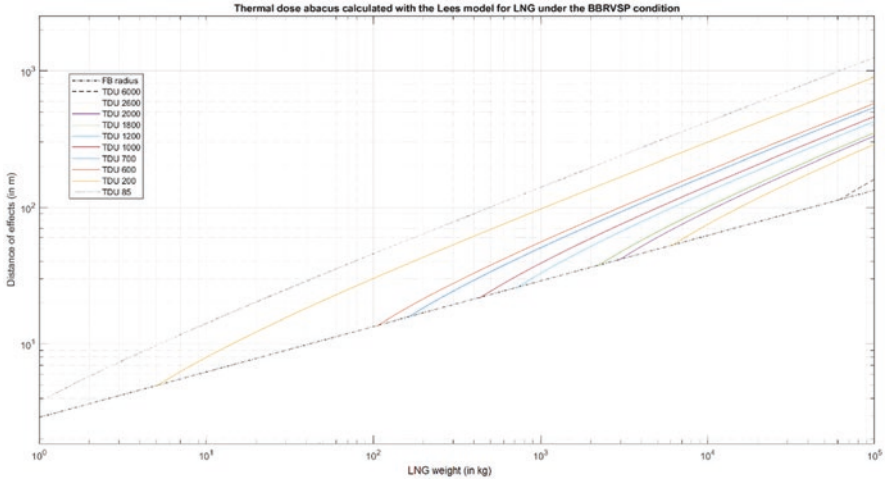
Fig. 2 Abacus of thermal doses deduced from the Lees model of the literature (BARVSP)

which corresponds to the intervals of the distances of effects, allows an almost instantaneous decision on the zones of potential dangers as well as on the distances of distance.

This part, in order to facilitate the assimilation of the various results, is subdivided into three sub-categories: calculation of the intensity of the thermal flux, realization of the graphic abacuses of the thermal doses, and finally comparison between the results obtained by our graphic abacuses.

3 Results

When the LNG storage or transport tank ruptures, a cloud of flammable vapor is formed, igniting the cloud in the form of a fireball. The energy released in the form of heat is transmitted to the surroundings either by convection or by thermal radiation. The intensity of the radiation felt by a target located at a certain distance describes the radiation power of the fire [7]. The intensity associated with the exposure time represents the thermal dose [8–10].

Our final objective is to draw graphical abacuses and to estimate the accuracy of the deduced results, for those three intermediate steps are necessary, namely:

- The determination of the lethal doses
- The analytical transformation of the thermal dose equation
- The realization of the abacus of the chosen model
- Exploitation and comparison

3.1 Determination of Lethal Doses

The effect of thermal radiation is measured in terms of intensity and duration of exposure or a combination of both [11]. Thermal effect thresholds are calculated using the thermal dose for the BLEVE fireball [12].

Thermal radiation hazards can manifest themselves as burns of varying degrees [13].

3.2 The Analytical Transformation of the Thermal Dose Equation

Lee's point source model is formulated as follows [6]:

$$I_{th} \quad q_s / 4 \quad L^2 \tag{1}$$

$$q_s = f_h \cdot M \cdot \Delta H_c / t_d \tag{2}$$

$$L^2 = X^2 + H^2 \tag{3}$$

The thermal dose represents the intensity of thermal radiation experienced during a certain period of time that coincides with the lifetime of the fireball or a fraction of that time [8–10]. The thermal dose is expressed as follows:

$$I_{dose} \quad t_{eff} \quad I_{th}^{\ 4/3} \tag{4}$$

where t_{eff} is the person exposure time to heat flux.

It is considered that the effect of the thermal dose corresponds to a given value "a," responsible for a certain degree of lethality or a certain degree of damage, degradation, and destruction of materials. The time of exposure to radiation corresponds to the life of the fireball of BLEVE:

$$a \quad I_{dose} \quad t_d \quad I_{th}^{\ 4/3} \tag{5}$$

$$t_d \quad c \ M^k \tag{6}$$

Finally, we find:

$$I_{th} \quad \frac{a}{c}^{\ 3/4} \quad M^{\ 3k/4} \tag{7}$$

Substituting the terms of Eqs. 2, 3, 4, 5, 6, and 7 into Eq. 1, we find:

$$\left(\frac{a}{c}\right)^{3/4} M^{3k/4} \cdot f_h \cdot M \cdot H_c / 4 \cdot X^2 \cdot H^2 \cdot c \cdot M^k$$

This implies:

$$X^2 \cdot H^2 = \frac{1}{4} \cdot f_h \cdot M \cdot H_c \cdot \left(c \cdot a^3\right)^{1/4} \cdot M^{k/4}$$

$$X = \left[\frac{1}{4} \cdot f_h \cdot M \cdot H_c \cdot \left(c \cdot a^3\right)^{1/4} \cdot M^{k/4} \cdot \left(4.35 \cdot M^{0.333}\right)^2\right]^{1/2}$$

(8)

3.3   The Realization of the Abacus of the Chosen Model

To carry out the graphic representation of the various abacuses, we proceeded to simplifications of the numerical calculations to carry out by adopting the following assumptions:

- The radiative fraction, 0.3 for fireballs bursting below the relief valve set pressure (BBRVSP) and 0.4 for fireballs bursting at or above the relief valve set pressure (BARVSP) [6].
- The thermal dose takes the values of Table 1.

Table 1 Reference threshold values for thermal effects on humans and structures [12]

Thermal dose [(kW/m2)4/3]·s	Effects on people	Effects on equipment
85	Pain threshold	
200	1st-degree burns	
600	Irreversible effects	
700	2nd-degree burns (superficial)	
1000	Beginning of lethality (100%)	Significant glass destruction
1200	2nd-degree burns (severe)	
1800	Significant lethality	Serious damage with domino effect
2000–2200	Lethal (100%)	
2600	3rd-degree burns (superficial)	
6000–7000	Lethal (100%)	

Table 2 Validity conditions on the LNG weight

a = Thermal dose[(kW/m2)4/3]·s	Validity conditions on the LNG weight	
	BBRVSP	BBRVSP
85	M > 0.484 kg	M > 0.167 kg
200	M > 5.167 kg	M > 1.791 kg
600	M > 108.592 kg	M > 37.411 kg
700	M > 167.211 kg	M > 57.371 kg
1000	M > 443.198 kg	M > 155.42 kg
1200	M > 741.862 kg	M > 255.01 kg
1800	M > 2294.9 kg	M > 793.222 kg
2000–2200	M > 3038.27–3974.79 kg	M > 1050.15–1385.9 kg
2600	M > 6194.33 kg	M > 2162.2 kg
6000–7000	M > 63737.4–94051.5 kg	M > 21628.5–34590.1 kg

- Two mathematical conditions are mandatory for the validation of the potential solutions, namely: the analytical term under the square root is positive and the value of X is strictly greater than the radius of the fireball. (The results are grouped in Table 2.)
- The input values of the analytical forms:

$$(c, k) = (0.900, 0.250).$$

– The heating value of LNG is ~38 MJ/kg [2, 14].

- Thermal dose corresponding to Lee's model:

$$X = 0.0817 \left[H_c \, f_h \, a^{3/4} \, M^{0.9375} \, 18.923 \, M^{0.666} \right]^{1/2} \tag{9}$$

Under the BBRVSP condition, Eq. 9 becomes:

$$X = 931.396 \left[a^{3/4} \, M^{0.9375} \, 18.923 \, M^{0.666} \right]^{1/2} \tag{10}$$

Under the BARVSP condition, Eq. 9 becomes:

$$X = 1241.861 \left[a^{3/4} \, M^{0.9375} \, 18.923 \, M^{0.666} \right]^{1/2} \tag{11}$$

The mandatory mathematical conditions for the validation of the potential solutions of equations n°10 and n°11 applied to LNG are grouped in the Table 2.

Table 3 Differences between the values calculated analytically and those read on the graphs

	BBRVSP				BARVSP			
	100	1000	10,000	100,000	100	1000	10,000	100,000
	Analytically calculated values Eqs. 10 and 11							
Radius FB	13.44	28.93	62.29	134.09	13.44	28.93	62.29	134.09
TDU 6000				161.44				219.70
TDU 2600			75.20	290.02			102.23	354.47
TDU 2000–2200			93.71	333.44			120.91	402.16
TDU 1800			101.10	351.64		32.17	128.62	422.36
TDU 1200		32.91	130.22	426.60		45.52	159.76	506.12
TDU 1000		38.96	143.97	463.27		51.49	174.75	547.35
TDU 700		50.60	172.50	541.13	16.67	63.58	206.36	635.53
TDU 600		55.73	185.67	577.65	19.02	69.06	221.08	677.05
TDU 200	30.11	97.41	299.59	901.32	36.67	115.24	350.12	1047.22
TDU 85	45.70	140.43	422.34	1256.87	54.04	164.09	490.65	1455.96
	Values deduced by the abacus Figs. 1 and 2							
Radius FB	14	29	63	130	14	29	63	130
TDU 6000				160				220
TDU 2600			75	290			100	350
TDU 2000–2200			92	330			120	400
TDU 1800			100	350		33	130	425
TDU 1200		34	130	420		46	160	500
TDU 1000		40	140	460		50	180	550
TDU 700		50	170	545	18	65	210	640
TDU 600		55	190	580	20	70	225	680
TDU 200	30	98	300	900	38	120	350	1050
TDU 85	45	145	425	1250	55	170	490	1450
Max difference ABS	6.87				6.12			

3.4 Exploitation of the Thermal Dose Abacus Calculated from Lee's Model

The usefulness of graphical abacuses comes from their predictive accuracies in the face of near-instantaneous deduction time. We have chosen to make a simulation of several LNG masses under the two conditions BBRVSP and BARVSP to estimate this usefulness and compare the results with those calculated numerically through equations n°10 and n°11. Table 3 summarizes the simulation and the comparison.

Reading the data summarized in Table 3, it can be seen that the absolute difference between the simulated values and those calculated analytically does not exceed 7 m for the effect distances of thermal doses.

We conclude that the values deduced from the graphical charts are very accurate, and therefore, their use will be very beneficial in terms of accuracy and speed of obtaining results.

4 Discussion

Despite all the preventive measures deployed in the storage or transport of liquefied natural gas (LNG), where large quantities are involved, the risk of catastrophic accidents such as a BLEVE remains. The proposed graphical method for first responders responsible for safety is based on a global and rapid analysis of the operational situation before any immediate reactions, including rescue actions, and allows integrating in a crisis resolution process as rational and well thought-out as possible the first safety perimeters to minimize lethal and irreversible damages to people and damages to buildings and constructions, located at significant distances from the center of the initial explosion, generated by the intense thermal radiation of the BLEVE's fireball [1].

The graphical charts, established by relatively simple equations, linking the properties of a fireball generated by an LNG BLEVE to the "doses" of thermal radiation, would be likely to systematize and homogenize quickly the safety of interventions, according to the different types and degrees of exposure.

The abacuses obtained and their patters show great similarities with the characteristic properties of the BLEVE phenomenon:

- The dimensions of the fireball generated by the ignition of the flammable vapor cloud during the rupture of the tank depend largely on the mass of the flammable product contained in the storage tank.
- For a rupture that occurs at a pressure level higher than or equal to the pressure of the safety valve, the simulation of the effect distances of the thermal doses is logically more extensive.
- The curves obtained are non-parallel lines; therefore, an intersection parallel to the ordinate axis will not necessarily intersect all the characteristic curves.

5 Conclusion

With the development of trade and advances in technology, each era has been marked by the emergence of new dangers and therefore new risks. Liquefied natural gas, which is the subject of this study, is today highly sought after for its ever-increasing energy needs. It can come from any producing country with a maritime coastline and ports equipped for LNG tankers and a liquefaction site. In spite of all the measures deployed for prevention, the risks of catastrophic accidents such as a BLEVE remain.

In this study the authors propose a new graphical approach, established on the basis of Lee's point source model [5] for the evaluation of the thermal doses generated by the intense thermal radiation of the BLEVE fireball and likely to cause lethal and irreversible damage to people and damage to buildings and constructions, located in the near and far environment of the initial explosion center.

This approach allows determining efficiently the danger zones of the effects of the thermal doses; its adequate exploitation is a means of decision support (mnemonic or check-list type) which would save, in the case of an LNG BLEVE, the time necessary for the implementation of the first safety perimeters and the zones to be evacuated as well as the traffic lanes to be forbidden to movements.

References

1. Prugh, R.W.: Quantitative evaluation of fireball hazards. Process. Saf. Prog. **13**, 83–91 (1994)
2. Makhviladze, G., Roberts, J., Yakush, S.: Modelling and scaling of fireballs from single -and two-phase hydrocarbon releases. Fire Saf. Sci. **6**, 1125–1136 (2000)
3. Roberts, T., Gosse, A., Hawksworth, S.: Thermal radiation from fireballs on failure of liquefied petroleum gas storage vessels. Process Saf. Environ. Prot. **78**, 184–192 (2000)
4. Center for Chemical Process Safety: Guidelines for Vapor Cloud Explosion, Pressure Vessel Burst, BLEVE, and Flash Fire Hazards, 2nd Edition: Free Download. Ebooks library. On-line books store on Z-Library (the American Institute of Chemical Engineers) (2010)
5. Hardee, H.C., Lee, O., Benedick, W.B., Lee, D.O.: Thermal hazard from LNG fireballs. Combust. Sci. Technol. **17**, 189–197 (1978)
6. Yang, S., Zhang, Y., Wu, H.: Comparison and validation of thermal radiation models for hydrocarbon jet fire and fireball. Appl. Mech. Mater. **204–208**, 3503–3512 (2012)
7. Bariha, N., Mishra, I.M., Srivastava, V.C.: Fire and explosion hazard analysis during surface transport of liquefied petroleum gas (LPG): a case study of LPG truck tanker accident in Kannur, Kerala, India. J.Loss Prevent. Proc. Indus. **40**, 449–460 (2016)
8. Papazoglou, I.A., Aneziris, O.N.: Uncertainty quantification in the health consequences of the BLEVE phenomenon. J. Hazard. Mater. **67**, 217–235 (1999)
9. Skřínská, M., Skřínský, J., Sluka, V., Senčík, J., Malý, S., Tetu, G.: Mathematical Models for the Prediction of Heat Flux from Fire Balls. WSEAS Transactions on Heat and Mass Transfer (2014)
10. Dhurandher, B.K., Kumar, R., Dhiman, A.: Impact assessment of thermal radiation hazard from LPG fireball. Proc. Earth Planet. Sci. **11**, 499–506 (2015)
11. Woodward, J.L., Pitblado, R.M.: LNG Risk Based Safety: Modeling and Consequence Analysis. John Wiley & Sons, Inc., Hoboken (2010)
12. Anon 2004 Guide technique relatif aux valeurs de référence des seuils d'effets des phénomènes accidentels des installations classées
13. Boot, H.: Developments in modelling of thermal radiation from pool and jet fires chemical. Eng. Trans. **48**, 67–72 (2016)
14. Bariha, N., Srivastava, V.C., Mishra, I.M.: Theoretical and experimental studies on hazard analysis of LPG/LNG release: a review. Rev. Chem. Eng. **33** (2017)

Design Comparison for the Supercritical CO₂ Brayton Cycle with Recompression and Thermal Regeneration: Numerical Results

Jiaxiang Chen, Lin Chen, Jinguang Zang, and Yanping Huang

Nomenclature

$\dot{m}$ [kg/s]	Mass flow
p [MPa]	Pressure
T [°C]	Temperature
h [J/kg]	Mass specific enthalpy
s [J/kg°C]	Mass specific entropy
c_p [J/kg°C]	Specific heat capacity at constant pressure
W [MW]	Work consumed by compressor or produced by turbine
Q [MW]	Cold/thermal energy supplied by cooler/heater
Q_h [MW]	Total heat load of heater 1 and heater 2

Special Characters

ρ [kg/m³]	Density
η [−]	Cycle efficiency of the sCO₂ Brayton cycle
η_s [−]	Isentropic efficiency of compressor or turbine

J. Chen
Institute of Engineering Thermophysics, Chinese Academy of Sciences, Beijing, China

L. Chen (✉)
Institute of Engineering Thermophysics, Chinese Academy of Sciences, Beijing, China

University of Chinese Academy of Sciences, Beijing, China

Innovation Academy for Light-duty Gas Turbine, Chinese Academy of Sciences, Beijing, China
e-mail: chenlin2018@iet.cn

J. Zang · Y. Huang
CNNC Key Laboratory on Nuclear Reactor Thermal Hydraulics, Nuclear Power Institute of China, Chengdu, China

η_{me} [−]   Mechanical efficiency
η_{mo} [−]   Motor efficiency
ΔT_{min} [°C]   Minimum heat transfer temperature difference of the recuperators

Subscripts

mc   Main compressor
re   Recompressor
com   Compressor
in   Inlet
T1   Turbine 1
T2   Turbine 2
c   Cooler
h1   Heater 1
h2   Heater 2
s   Isentropic

1   Introduction

Worldwide energy demand is increasing continuously due to the development of global economy. However, a great amount of CO_2 emission caused by fossil fuel–based energy consumption are worsening the greenhouse effect as well as our environment. Therefore, it is very pressing to break through certain revolutionary energy technology characterized by low-carbon and high efficiency to solve the severe problem of CO_2 emission [1–3]. Supercritical CO_2 (sCO_2) Brayton cycle power generation technology has the advantages of high thermal efficiency in a wide temperature range (350 ~ 800 °C) and simple and compact structure [4], and it can achieve high efficiency in various thermal utilization fields such as solar thermal power generation, waste heat recovery, and the fourth-generation nuclear reactor [5]. Especially in the field of solar thermal utilization, the sCO_2 Brayton cycle has been praised as a priority for the development of new generation solar thermal power generation technology [6]. As a result, the sCO_2 Brayton cycle is an important technology to solve the current carbon emission problem and has become the primary focus in the field of thermal power generation in recent years [7].

Also, sCO_2 has no gas-liquid phase transition process, and has strong nonlinear physical properties near the critical point. sCO_2 presents excellent heat transfer characteristics with the heat source, consumes lower compression power near the critical point, and achieves higher cycle efficiency [8, 9]. A previous study shows that, when the turbine inlet temperature exceeds 550 °C, the efficiency of the sCO_2 Brayton cycle is better than the steam Rankine cycle and the supercritical helium Brayton cycle, and the power generation cost is reduced by about 18% in contrast to the traditional steam Rankine cycle [10].

The study of the sCO_2 Brayton cycle began in the 1960s when Feher [11] first proposed a simple supercritical Brayton cycle. Dostal [12] proposed the recompression CO_2 Brayton cycle and changed the flow distribution in the regenerator, which improved the heat exchange effect, and finally a variety of optimized cycle layouts are put forward. The current key issues of the sCO_2 Brayton cycle are focused on the research of thermodynamic analysis and parameter optimization to obtain cycle efficiency as high as possible. Moullec [13] proposed a sCO_2 Brayton cycle for coal-fired power generation, and the optimal system cycle efficiency is 50% at designed temperature and pressure of 620 °C and 30 MPa, respectively. Al Sulaiman et al. [14] studied a variety of sCO_2 Brayton cycles for solar thermal power generation, the maximum thermal efficiency of the recompression cycle is 52%, and the corresponding turbine inlet temperature is about 830 °C. Wang et al. [15] analyzed the thermal efficiency of the solar thermal power generation system integrated with different sCO_2 Brayton cycle layouts, including the recompression cycle, intercooling cycle, etc., and the results revealed that the intercooling cycle could achieve the highest efficiency under thermal storage conditions using molten salt. Xin et al. [16] proposed the thermal cycle splitting analytical method, which can divide a complex sCO_2 Brayton cycle into a simple host cycle and one or several simple equivalent power cycles, to analyze the thermodynamic performance of a novel sCO_2 Brayton cycle. In the novel Brayton cycle configuration, the partial intercooling process was introduced for efficiently heat recuperating, and an optimum cycle efficiency of 53.58% was achieved. Du et al. [17] studied the thermodynamic design and off-design of the sCO_2 recompression Brayton cycle integrated with a nuclear power cycle, a two-stage recompression was introduced to improve the off-design performance, and the optimization mechanism was conducted and clarified.

Even though a lot of theoretical studies have achieved very high cycle efficiency for the sCO_2 Brayton cycle, the actual efficiency of the existing experimental systems is much lower than theoretical results. One main reason is that the performance parameters of key equipment in literatures for thermodynamic analysis are usually set at optimal value levels, including the isentropic efficiency of the compressors and turbines, the heat transfer temperature differences of thermal regeneration heat exchangers, etc. However, in the current status, the manufacture level and operation conditions in real power plants and equipment optimization show limit on the performance of actual operation in the sCO_2 Brayton cycle. In the study of Dostal [12], the re-compressing Brayton cycle and its related optimization analysis has been proposed. However, for real systems established in Sandia National Lab, Tokyo Institute of Technology, Korea Advanced Institute of Science and Technology (KAIST), and other research institutes and organizations, the overall efficiency generally falls below 30% [1, 18], which shows very large difference from the above-mentioned studies of theoretical efficiency (nearly 50%). In very recent developments in China, the Institute of Engineering Thermophysics, Chinese Academy of Sciences has built PCHE (Printed Circuit Heat Exchanger) for Brayton cycle tests [19]. And the compressor design and tests have also achieved MW level results in the Institute of Engineering Thermophysics, Chinese Academy of Sciences in 2021 [19]. Most recently, more designs about the unsteady input or thermal storage coupling have

also been proposed and tested in small-scale prototype systems [15, 20–23]. In 2022, the world-first 5 MW scale Brayton cycle has been put into test for 72 hours and claimed successfully the operation of large-scale system [24]. In that system, the first parameter calculation shows an efficiency below 30% at optimal, which gives two hints for further development: (1) apparatus construction of MW-scale Brayton cycle system has been successful for world R&D institutions; (2) overall efficiency is still a challenge for optimization studies. Though there are a lot of system designs and real prototype analyses already exist, there still need parameter analysis and cycle efficiency considerations for Brayton cycle development. One challenge is the high parameter compressing and expansion process and its stability control, and another is the near-critical compressor inlet and compressing challenge. For the second challenge, the compressor inlet parameters (pressure, temperature, and related viscosity, density, etc.) will show very large changes and deviations from optimal conditions, due to the critical fluid nature in the near-critical region [1, 18, 25–27]. In such cases, the crossing-critical or crossing-pseudo-critical line phenomena in the compressor will affect the performance of the Brayton cycle a lot in real applications [28, 29]. Especially in real system operations, it will be susceptible for two-phase or transient fluctuations of properties in the critical region, and if it is closer to the critical point, the deviations become larger; thus, one cannot keep the system too close to the critical point such that the efficiency loss will be seen [1, 30, 31]. To discuss such process, further parameter analysis and matching of the compressor, heater, and expansion end parameters are necessary to maintain reasonable efficiency.

Therefore, the current study mainly focuses on the effect of the equipment performance parameters on the overall system performance of a sCO$_2$ Brayton cycle, and the cycle is designed with recompression and thermal regeneration process, which can achieve relatively high efficiency in previous theoretical studies. Major efficiency-related parameters and the parameter matching analysis has been conducted in this study. In addition, the real application potential and challenging points on the overall efficiency have also been discussed into detail in the analysis. It is hoped that the current study can contribute to real system applications in the next step R&D.

2 System Description

2.1 Model Set-Up

Figure 1 is the schematic of the sCO$_2$ Brayton cycle system with recompression and thermal regeneration designs. The sCO$_2$ cooled by the cooler enters the main compressor to be pressured to a high-pressure state. The high-pressure sCO$_2$ first enters the low-temperature recuperator to be heated to medium temperature and then mixes with the sCO$_2$ coming from the outlet of the recompressor. The mixed sCO$_2$
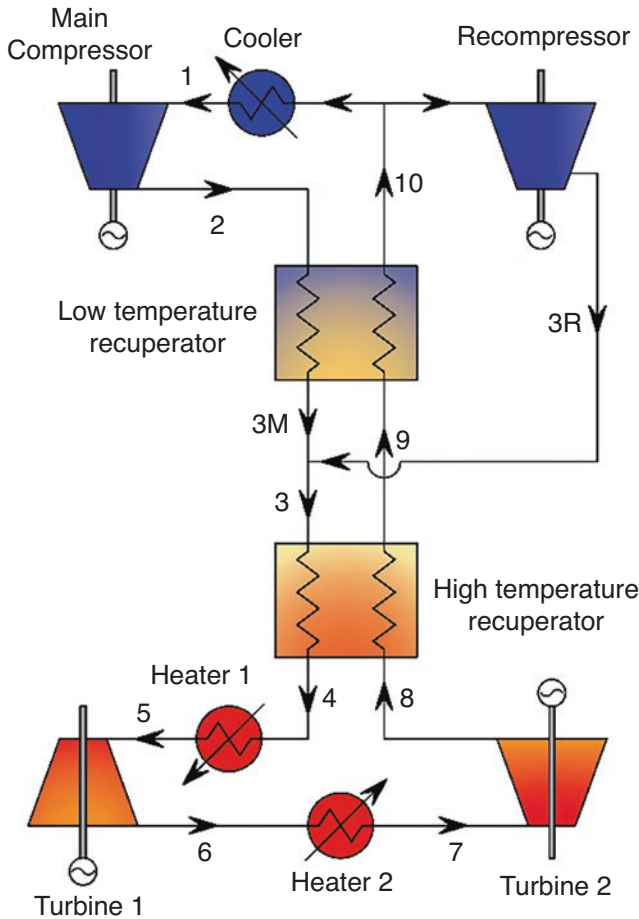
Fig. 1 Schematic of the sCO$_2$ Brayton cycle with recompression and thermal regeneration designs

enters the high-temperature recuperator to be heated to a relatively high-temperature state. The outlet sCO$_2$ successively enters turbine 1 and turbine 2 to release energy and produce work after being heated by heater 1 and heater 2, respectively. The sCO$_2$ from turbine 2 becomes a low-pressure state, and it still has a relatively high temperature; thus, it enters the high-temperature and low-temperature recuperators successively to further release its thermal energy, and then it is divided into two flows of which the first one enters the cooler, and the other one enters the recompressor. With this coupled design system of the Brayton cycle, the parameter analysis near the critical region and high parameter region matching have been tested and conducted in this analysis.

2.2 Thermodynamic Model

The thermodynamic model of the sCO$_2$ Brayton cycle mainly refers to the thermo-
dynamic calculation models of the key equipment in Fig. 1, including the compres-
sion work of the main compressor and recompressor, the output work of the two
turbines, and the heat exchange relation of the high-temperature and low-temperature
recuperators, etc. Also, the model picture of the current system has been shown in
Fig. 2. In the following equations, the numbers in the subscript of the variables have
the same meaning as shown in Figs. 1 and 2.

The compression work of the main compressor (W_{mc} [MW]) is calculated as Eqs.
(1) and (2), where $\dot{m}$ [kg/s] is the mass flow, h [kJ/kg] is the mass-specific enthalpy,
$h_{2,s}$ [kJ/kg] is mass-specific enthalpy at the outlet of the main compressor under
isentropic compression condition, η_s is the isentropic efficiency, η_{me} is the mechani-
cal efficiency, η_{mo} is the motor efficiency, and the subscript "mc" represents the
main compressor.

$$W_{mc} = \dot{m}_1 \left(h_2 - h_1 \right) / \left(\eta_{me,mc} \eta_{mo,mc} \right) \tag{1}$$

$$h_2 = h_1 + \left(h_{2,s} - h_1 \right) / \eta_{s,mc} \tag{2}$$

The compression work of the recompressor (W_{re} [MW]) can be calculated as
below, where the subscript "re" represents the recompressor.

$$W_{re} = \dot{m}_{3R} \left(h_{3R} - h_{10} \right) / \left(\eta_{me,re} \eta_{mo,re} \right) \tag{3}$$

$$h_{3R} = h_{10} + \left(h_{3R,s} - h_{10} \right) / \eta_{s,re} \tag{4}$$

The work produced by turbine 1 (W_{T1} [MW]) and turbine 2 (W_{T2} [MW]) is shown
as Eqs. (5) to (8), where the subscripts "T1" and "T2," respectively, represent tur-
bine 1 and turbine 2, and $h_{6,s}$ [kJ/kg] and $h_{8,s}$ [kJ/kg] are, respectively, the outlet-
specific enthalpy of turbine 1 and turbine 2 under isentropic expansion conditions.
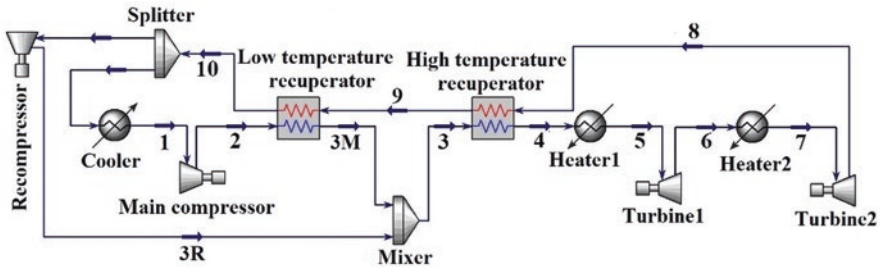
Fig. 2 Simulated model picture of the current cycle

$$W_{T1} = \dot{m}_5 \left(h_5 - h_6 \right) \eta_{me,T1} \eta_{mo,T1} \tag{5}$$

$$h_6 = h_5 - \left(h_5 - h_{6,s} \right) \eta_{s,T1} \tag{6}$$

$$W_{T2} = \dot{m}_7 \left(h_7 - h_8 \right) \eta_{me,T2} \eta_{mo,T2} \tag{7}$$

$$h_8 = h_7 - \left(h_7 - h_{8,s} \right) \eta_{s,T2} \tag{8}$$

The heat exchange process in low- and high-temperature recuperators satisfies the following expressions.

$$\dot{m}_2 \left(h_{3M} - h_2 \right) = \dot{m}_9 \left(h_9 - h_{10} \right) \tag{9}$$

$$\dot{m}_3 \left(h_4 - h_3 \right) = \dot{m}_9 \left(h_8 - h_9 \right) \tag{10}$$

The cold energy supplied by the cooler (Q_c [MW]) and the thermal energy supplied by heater 1 (Q_{h1} [MW]) and heater 2 (Q_{h2} [kW]) are shown as below.

$$Q_c = \dot{m}_1 \left(h_{10} - h_1 \right) \tag{11}$$

$$Q_{h1} = \dot{m}_4 \left(h_5 - h_4 \right) \tag{12}$$

$$Q_{h2} = \dot{m}_6 \left(h_7 - h_6 \right) \tag{13}$$

The mass flows of point 1, 2, and 3 M are the same, the mass flows of point 3 to point 10 are the same, and the mass flows of point 3 and point 10 satisfy the following expressions.

$$\dot{m}_3 = \dot{m}_{3M} + \dot{m}_9 \tag{14}$$

$$\dot{m}_{10} = \dot{m}_1 + \dot{m}_{3R} \tag{15}$$

The cycle efficiency is defined as below.

$$\eta = \frac{W_{T1} + W_{T2} - W_{mc} - W_{re}}{Q_{h1} + Q_{h2}} \tag{16}$$

The simulation is carried out by Aspen-HYSYS, and Peng-Robinson equation is selected for physical property calculation. Some assumptions should be made first, as shown below:

(1) Power consumption of the cooler is neglected for the reason that the cycle is operating above the critical point (7.38 MPa, 31.0 °C [9]); that is, the cooler can utilize natural cold sources (e.g., the cooling tower) which consumes very little power, and it is not considered in Eq. (16).

(2) Isentropic efficiency of the compressors and turbines are all 0.90 unless other-
     wise specified.
(3) The mass flow of the turbine is 100.0 kg/s.
(4) The pressure loss of any heat exchanger is 0.1 MPa.
(5) The mechanical efficiency and motor efficiency are 0.99 and 0.95, respectively,
     for all compressors and turbines.
(6) The expansion ratio of the two turbines is the same.
(7) The temperature of the cold sCO_2 at the outlet of the low-temperature recupera-
     tor (node 3 M) is the same as that of the sCO_2 at the outlet of the recompressor
     (node 3R).
(8) Heat loss of the overall system is neglected.

3   Results and Discussion

3.1   Compression Ratio

As shown in Eq. (16), it should increase the turbine's output work and decrease the
compression work and heat load of the heaters to improve the cycle efficiency.

The sCO_2 Brayton cycle utilizes the liquid-like properties of CO_2 near the critical
point to consume less compression work and obtain higher efficiency. Figure 3 is
the compression work (W_{com} [kW]) of a compressor under different inlet tempera-
tures (T_{in} [°C]) and pressures (p_{in} [MPa]), where (a) and (b) represent different com-
pression ratios. The variation of the inlet density (ρ_{in} [kg/m^3]) is also shown. The
mass flow is 100.0 kg/s, and the isentropic efficiency is 0.90 in this figure.

As can be seen in Fig. 3, the compression work increases with the inlet tempera-
ture under the same inlet pressure and compression ratio conditions, while the den-
sity curves show the opposite trend. At the same inlet temperature, the compression
work decreases with the inlet pressure in most cases, except when the inlet tempera-
ture is close to the critical value. From another aspect, the compression work has a
negative correlation with fluid density. In a word, the compressor can consume rela-
tively low power in cases with high pressure and temperature close to the critical
value, so the density in these cases is very high and sCO_2 is liquid-like.

The curves of W_{com} and ρ_{in} in Fig. 3 have inflection points when the p_{in} is 9.0 MPa
and 10.0 MPa; for that, these curves come across the pseudo-critical temperature of
sCO_2 (40.0 °C for 9.0 MPa and 45.0 °C for 10.0 MPa, calculated by the NIST-
REFPROP Database [32]).

The heat load can be lowered by the two recuperators, while the energy that can
be regenerated is related to the heat transfer process between the high pressure
(from the compressor) and low pressure (from the turbine) sCO_2, which is deter-
mined by the specific heat capacity (c_p [kJ/kg°C]). Figure 4 shows c_p varying with
pressure and temperature (accessed from the NIST-REFPROP Database [32]). The
results show that c_p is higher under high-pressure conditions for most cases. The
pressure of 7.5–10.0 MPa and 20.0–30.0 MPa are, respectively, the usually used low
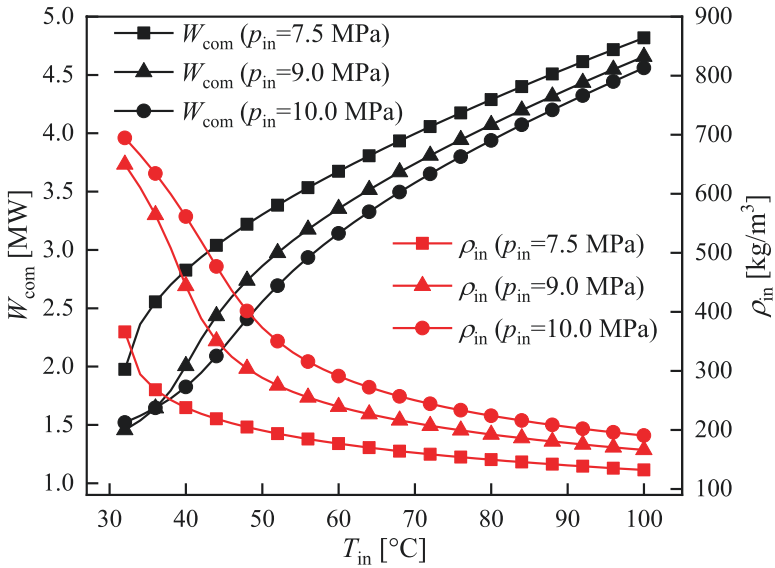
(a) Compression ratio is 2.0
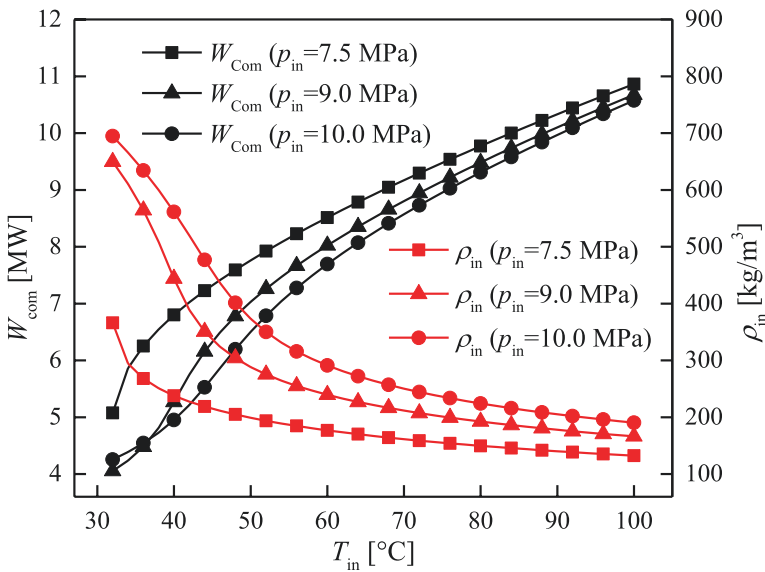
(b) Compression ratio is 4.0

Fig. 3 Compression work and density under different compressor inlet conditions
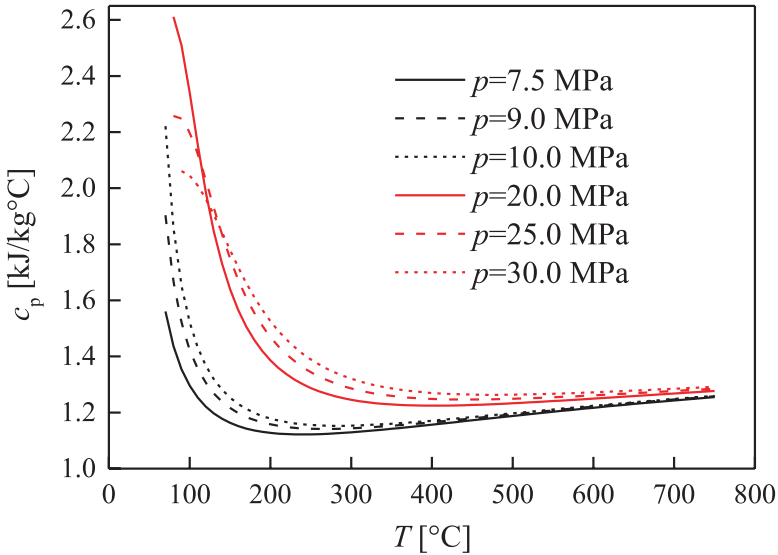
Fig. 4 Variation of c_p with pressure and temperature

pressure and high pressure in sCO$_2$ Brayton cycles. That is, the high-pressure sCO$_2$ (cold fluid) has higher c_p than the low-pressure sCO$_2$ (hot fluid), leading to the result that the temperature rising of the cold sCO$_2$ is smaller than the temperature decreasing of the hot sCO$_2$, and the thermal energy grade of the low pressure and hot sCO$_2$ is degraded. For such parameter operation conditions, the compressor and heat exchanger would experience fluctuations in parameters that go through those apparatus and the diploma of the expansion end parameter: close to critical point is necessary, but if too close to critical point, the compressing efficiency will be a big problem. Such process should be discussed more in future studies.

3.2   Recuperator Parameter

The heat transfer curve of a recuperator under some typical conditions is shown in Fig. 5. In the figure, the mass flows of the hot and cold sCO$_2$ are both 1.0 kg/s, the minimum heat transfer temperature difference (ΔT_{min}) is 5.0 °C, the hot sCO$_2$ inlet pressure is 8.0 MPa, the cold sCO$_2$ inlet temperature is 100 °C, $p_{cold,in}$ [MPa] is the cold sCO$_2$ inlet pressure, and $T_{hot,in}$ [°C] is the hot sCO$_2$ inlet temperature. The results show that the maximum heat transfer temperature difference occurs at the hot end of the recuperator, which is very large (about 100 °C) and is consistent with the analysis of c_p. Thus, the mass flow of sCO$_2$ in the recuperator should be redistributed to optimize the heat transfer process, increase the cold sCO$_2$ outlet temperature, lower the heat load of the heaters, and finally improve the cycle efficiency.
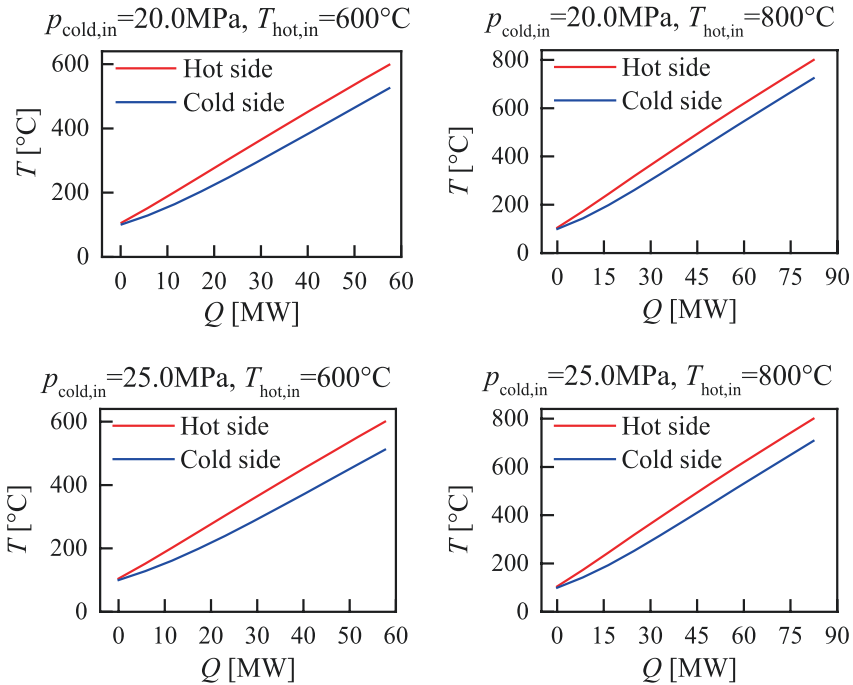
Fig. 5 Heat transfer curves of a recuperator under typical operating conditions

3.3 *Compressor Inlet Parameter*

Figure 6 is the variation of cycle efficiency with the inlet temperature of the main compressor ($T_{mc,in}$), along with the heat load and the compression work of the main compressor and recompressor. In this figure, the low pressure (main compressor inlet pressure) is 8.0 MPa, and the high pressure (main compressor outlet pressure) are respectively 20.0 MPa and 25.0 MPa for (a) and (b). As can be seen in this figure, the sCO₂ Brayton cycle has high efficiency when $T_{mc,in}$ is close to the critical point, while when $T_{mc,in}$ is far away from the critical point, the cycle efficiency decreases quickly. When increasing $T_{mc,in}$, the heat load decreases, but the compression work increases. Even though the former can help to increase the cycle efficiency, the latter is more prominent, leading to the decrease of the cycle efficiency when increasing $T_{mc,in}$. For such understanding, real applications should consider conditions close to the critical point, but real compressors will tend to have liquid state fluid near the critical point. As discussed in Sect. 3.2 about the compressor inlet conditions. In the current basic type of the Brayton cycle with recompression, the main compressor inlet parameter defines the critical distance toward the critical point and the crossing-pseudo-critical line. In previous studies [1, 18], the compressor inlet process has been considered a key process as the compressing efficiency
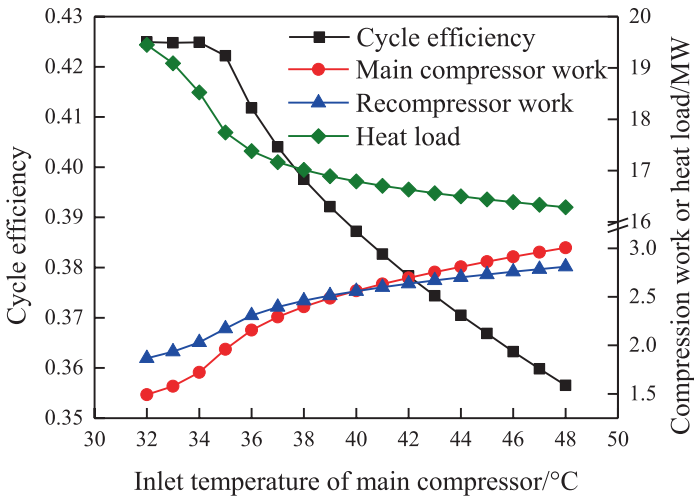
(a) The high pressure is 20.0 MPa
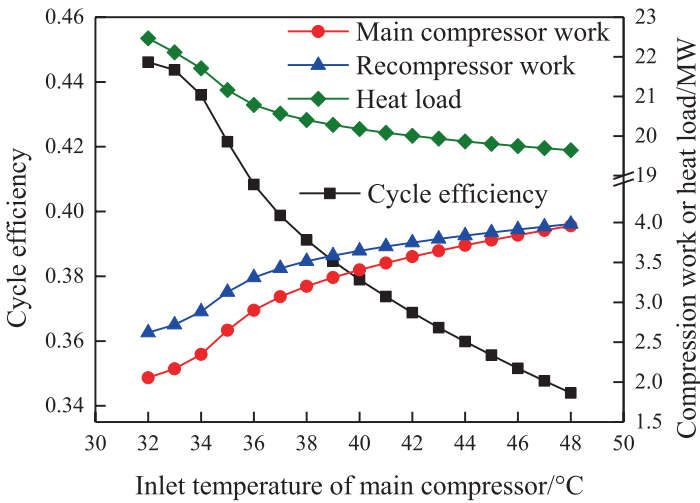
(b) The low pressure is 25.0 MPa

Fig. 6 Influence of $T_{mc,in}$ on the system performance
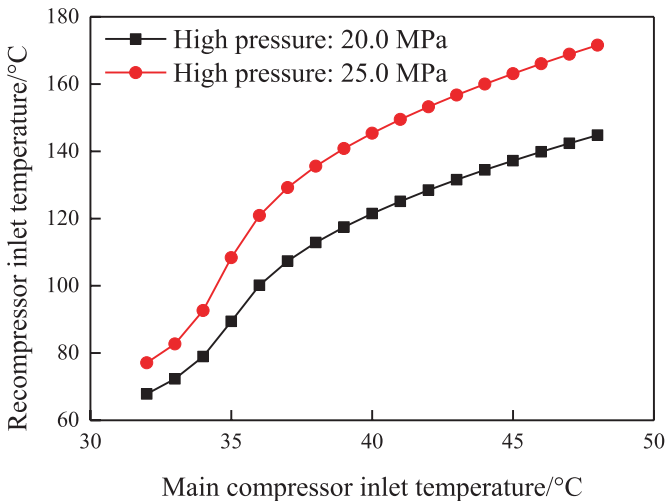
Fig. 7 Variation of $T_{re,in}$ with $T_{mc,in}$

will be achieved when the crossing-pseudo-critical line has large variations (such as density increase due to its status change of self-"shrink" with very small compressing work). And such cross-pseudo-critical compressing process will possibly lead to liquid-supercritical mixture region and the cross-pseudo-critical line process will need some amount of heat input. Otherwise, for the adiabatic compressing process, the end point will not be optimal as the adiabatic index γ fluctuates in the critical region. Thus, it should need very critical design and analysis for real applications of the Brayton cycle to achieve or get close to the high efficiency as found by theoretical analysis.

The mass flow of sCO$_2$ in the recompressor is about twice that in the main compressor. However, the recompressor output work is close to or even larger than the main compressor. The reason is that the recompressor inlet temperature ($T_{re,in}$) is higher than $T_{mc,in}$ and far away from the critical temperature. When increasing $T_{mc,in}$, $T_{re,in}$ is correspondingly increased to meet the heat transfer temperature difference of the recuperators, as shown in Fig. 7, with increased W_{re}.

The *T-s* diagram of the cycle is shown in Fig. 8, under conditions of that $T_{mc,in}$ is 34.0 °C, the high pressure is 20.0 MPa. The other conditions are the same in Fig. 6. The results in Fig. 6 show that the curves of the cycle efficiency have reflection points, and $T_{mc,in}$ is about 36.0 °C at the reflection point. In the following part, the influence of the isentropic efficiency of the compressors and turbines and the heat transfer temperature difference of the recuperators will be investigated under conditions of $T_{mc,in}$ equal to 36.0 °C.
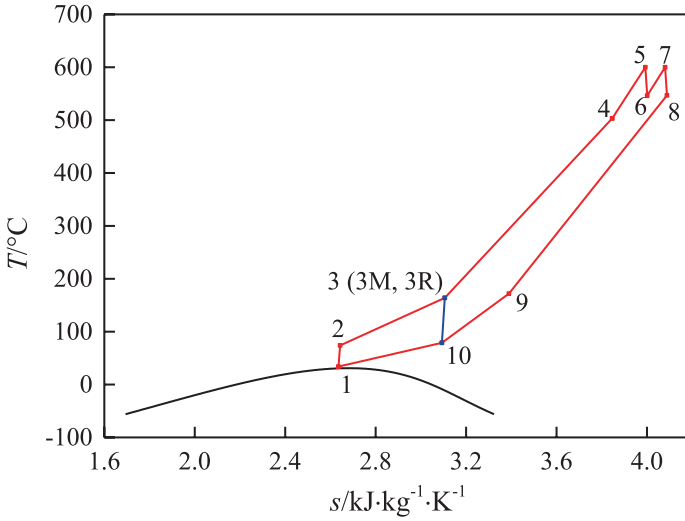
Fig. 8 *T-s* diagram under conditions of that $T_{mc,in}$ is 34.0 °C, and the high pressure is 20.0 MPa
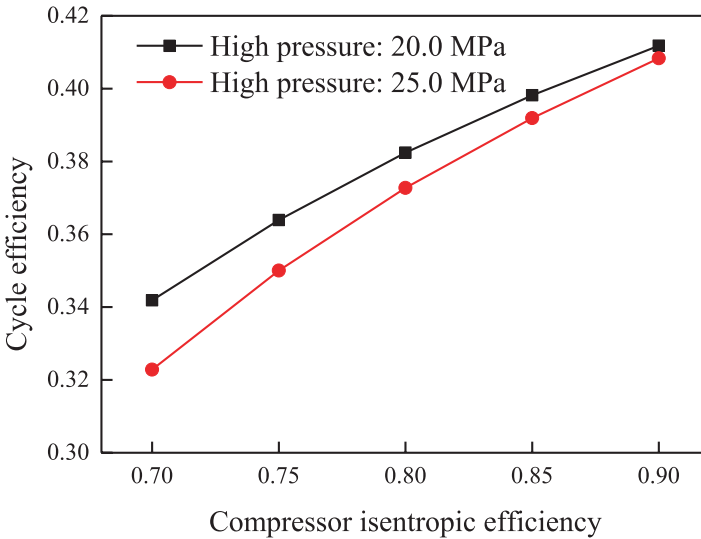
Fig. 9 Influence of the compressor isentropic efficiency on the cycle efficiency

3.4 System Efficiency Analysis

Figures 9 and 10 show the variation of the cycle efficiency with the isentropic efficiency of the compressors and turbines, respectively. In these two figures ΔT_{min} is 5.0 °C. The results show that the isentropic efficiency of the compressors and turbines has a significant influence on the cycle efficiency, lower isentropic efficiency
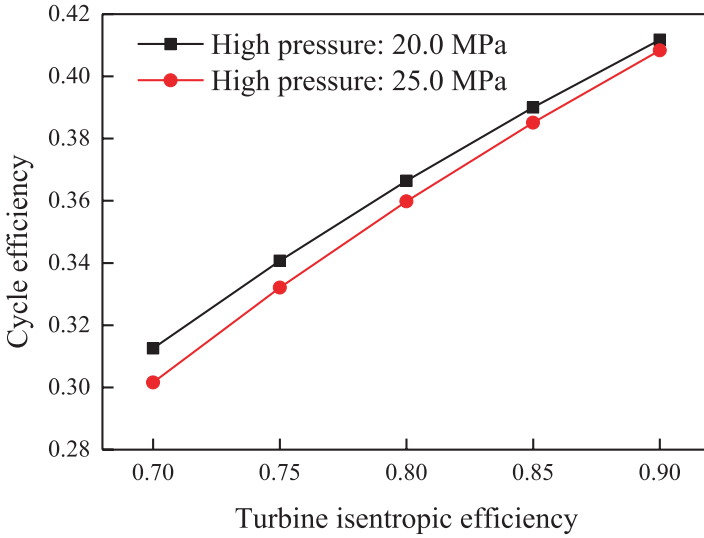
Fig. 10 Influence of the turbine isentropic efficiency on the system performance
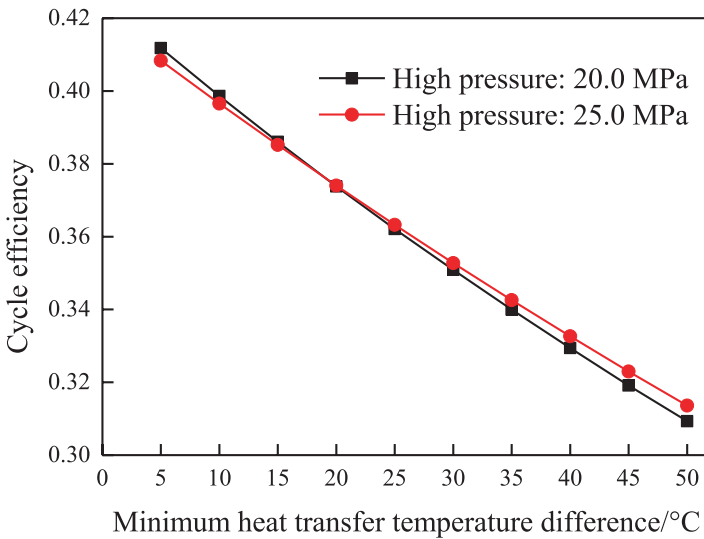
Fig. 11 Influence of ΔT_{min} on the cycle efficiency

can decrease the cycle efficiency, and the isentropic efficiency of the turbines has a more significant effect on the system performance than that of the compressors.

Figure 11 shows the variation of the cycle efficiency with ΔT_{min}, and in the figure the isentropic efficiency of the compressors and turbines are set as 90%. The result shows that increasing ΔT_{min} can almost linearly lower the cycle efficiency.

From the results shown in Figs. 9, 10, and 11, if the compressors or turbines' isentropic efficiency is decreased to 70%, or ΔT_{min} is increased to 50.0 °C. The sCO$_2$ Brayton cycle can only achieve the cycle efficiency a little larger than 30%, which has no advantages compared to the traditional Rankine cycle. While, for existing applications, the isentropic efficiency of real compressors and turbines is not yet very high, and ΔT_{min} cannot reach a lower value (e.g., 5.0 °C) to reduce the heat transfer area and the equipment cost, making the actual cycle efficiency of the existing sCO$_2$ Brayton cycle is relatively low.

4   Conclusion

This chapter proposed a recompression sCO$_2$ Brayton cycle with a heat regeneration process. Thermodynamic performance of the sCO$_2$ Brayton cycle was numerically tested, and the conclusions are obtained as follows.

(1) The main compressor inlet temperature has a significant effect on performance, and the system shows high efficiency only when the main compressor inlet temperature is close to the critical point. When the main compressor inlet temperature is below 36 °C, the cycle efficiency achieves a relatively high value of around 40%. This is very critical for real applications.
(2) The isentropic efficiency of the compressors and turbines and the heat transfer temperature difference of the recuperators have a significant influence on efficiency. Improving compressors and turbines' efficiency and decreasing the heat transfer temperature difference of the recuperators are very important. When the isentropic efficiency of the compressors or the turbines decreases to 0.7, or the minimum heat transfer temperature difference of the recuperators increases to 50.0 °C, the cycle efficiency drops close to 30.0%, which has few advantages compared with the traditional Rankine cycles.
(3) The compressing process involves cross-pseudo-critical line and the large parameter variations as preferred (density change and small compressing work needed) in the Brayton cycle system. However, it has been found that the real compressing parameter should be optimized by considering the phase process and energy cost in the critical region as the adiabatic compressing index fluctuates in that region. Also, the cycle efficiency depends on other apparatus efficiencies, which should be discussed more with real test results in future analysis and comparison studies.

References

1. Chen, L.: Handbook of Research on Advancements in Supercritical Fluids Applications for Sustainable Energy Systems. IGI Global, USA (2021)
2. Kumar, K.R., Chaitanya, N.V.V.K., Natarajan, S.K.: Solar thermal energy technologies and its applications for process heating and power generation – a review. J. Clean. Prod. **282**, 125296 (2021)
3. Yu, S.C., Chen, L., Li, H.X., Zhang, X.R.: A brief review study of various thermodynamic cycles for high temperature power generation systems. Energy Convers. Manag. **94**, 68–83 (2015)
4. White, M.T., Bianchi, G., Chai, L., Tassou, S.A., Sayma, A.I.: Review of supercritical CO_2 technologies and systems for power generation. Appl. Therm. Eng. **185**, 116447 (2021)
5. Crespi, F., Gavagnin, G., Sánchez, D., Martínez, G.S.: Supercritical carbon dioxide cycles for power generation: a review. Appl. Energy. **195**, 152–183 (2017)
6. Mehos, M., Turchi, C., Vidal, J., Wagner, M., Ma, Z., Ho, C., Kolb, W., Andraka, C., Kruizenga, A.: Concentrating solar power Gen3 demonstration roadmap. NREL/TP-5500-67464 (2017)
7. Chen, L.: Microchannel Flow Dynamics and Heat Transfer of Near-Critical Fluid. Springer, Singapore (2017)
8. Sarkar, J.: Review and future trends of supercritical CO_2 Rankine cycle for low-grade heat conversion. Renew. Sust. Energ. Rev. **48**, 434–451 (2015)
9. Ahn, Y., Bae, S.J., Kim, M., Cho, S.K., Baik, S., Lee, J.I., Cha, J.E.: Review of supercritical CO_2 power cycle technology and current status of research and development. Nucl. Eng. Technol. **47**, 647–661 (2015)
10. Dostal, V., Driscoll, M.J., Hejzlar, P.: A Supercritical Carbon Dioxide Cycle for Next Generation Nuclear Reactors. Advanced Nuclear Power Technology Program, the MIT Center for Advanced Nuclear Energy Systems (2004)
11. Feher, E.G.: The supercritical thermodynamic power cycle. Energy Convers. **8**, 85–90 (1968)
12. Dostal, V., Hejzlar, P., Todreas, N.E., Buongiorno, J.: Medium-power lead-alloy fast reactor balance-of-plant options. Nucl. Technol. **147**, 388–405 (2004)
13. Moullec, Y.L.: Conceptual study of a high efficiency coal-fired power plant with CO_2 capture using a supercritical CO_2 Brayton cycle. Energy. **49**, 32–46 (2013)
14. Al-Sulaiman, F.A., Atif, M.: Performance comparison of different supercritical carbon dioxide Brayton cycles integrated with a solar power tower. Energy. **82**, 61–71 (2015)
15. Wang, K., He, Y.L., Zhu, H.H.: Integration between supercritical CO2 Brayton cycles and molten salt solar power towers: a review and a comprehensive comparison of different cycle layouts. Appl. Energy. **195**, 819–836 (2017)
16. Xin, T., Xu, C., Yang, Y.: Thermodynamic analysis of a novel supercritical carbon dioxide Brayton cycle based on the thermal cycle splitting analytical method. Energy Convers. Manag. **225**, 113458 (2020)
17. Du, Y.D., Yang, C., Hu, C.X., Zhou, M.: Thermodynamic design and off-design investigation of nuclear power supercritical CO_2 recompression cycle. Nucl. Eng. Des. **369**, 110851 (2020)
18. Chen, L.: Microchannel Flow Dynamics and Heat Transfer of near-Critical Fluid. Springer, New York (2017)
19. The Institute of Engineering Thermophysics, Chinese Academy of Sciences. Successfully of Brayton cycle project and equipment development in IET-CAS. http://www.iet.cas.cn/news/kyjz/202005/t20200527_6209980.html; http://www.iet.cas.cn/news/kyjz/201912/t20191226_6209953.html; http://www.iet.cas.cn/hdzt/135zl/2016yisanwu/201912/t20191211_5451699.html
20. Osorio, J.D., Hovsapian, R., Ordonez, J.C.: Effect of multi-tank thermal energy storage, recuperator effectiveness, and solar receiver conductance on the performance of a concentrated solar supercritical CO_2-based power plant operating under different seasonal conditions. Energy. **115**, 353–368 (2016)
21. Calle, A.d.l., Bayon, A., Pye, J.: Techno-economic assessment of a high-efficiency, low-cost solar-thermal power system with sodium receiver, phase-change material storage, and supercritical CO_2 recompression Brayton cycle. Sol. Energy. **199**, 885–900 (2020)

22. Wang, X.H., Liu, Q.B., Lei, J., Han, W., Jin, H.G.: Investigation of thermodynamic performances for two-stage recompression supercritical CO_2 Brayton cycle with high temperature thermal energy storage system. Energy Convers. Manag. **165**, 477–487 (2018)
23. Zhao, Y.W., Li, P.W., Jin, H.G.: Heat transfer performance comparisons of supercritical carbon dioxide and NaCl-KCl-ZnCl2 eutectic salts for solar s-CO_2 Brayton cycle. Energy Procedia. **142**, 680–687 (2017)
24. Xi'an Thermal Power Research Institute Co. Ltd. The world first 5MW scale Brayton cycle has been put into test for 72 hours. http://www.tpri.com.cn/; http://www.tpri.com.cn/productinfo.html?artId=9371&catId=675
25. Chen, L., Zhang, X.R.: Heat transfer and various convection structures of near-critical CO_2 flow in microchannels. Appl. Therm. Eng. **72**, 135–142 (2014)
26. Chen, L., Zhang, X.R., Okajima, J., Maruyama, S.: Thermal relaxation and critical instability of near-critical fluid microchannel flow. Phys. Rev. E. **87**, 043016 (2013)
27. Chen, L., Zhang, X.R., Yamaguchi, H., Liu, Z.S.: (Simon), effect of heat transfer on the instabilities and transitions of supercritical CO_2 flow in a natural circulation loop. Int. J. Heat Mass Transf. **53**, 4101–4111 (2010)
28. Liu, H., Chi, Z., Zang, S.: Transient behaviour and optimal start-up procedure of closed Brayton cycle with high thermal inertia. Appl. Therm. Eng. **199**, 117587 (2021)
29. Du, Y., Yang, C., Wang, H., Hu, C.: One-dimensional optimisation design and off-design operation strategy of centrifugal compressor for supercritical carbon dioxide Brayton cycle. Appl Therm Eng. **196**, 117318 (2021)
30. Yang, J., Yang, Z., Duan, Y.: Novel design optimization of concentrated solar power plant with S-CO_2 Brayton cycle based on annual off-design performance. Appl. Therm. Eng. **192**, 116924 (2021)
31. Liu, X., Xu, Z., Xie, Y., Yang, H.: CO_2-based mixture working fluids used for the dry-cooling supercritical Brayton cycle. Thermodyn. Eval. **162**, 114226 (2019)
32. NIST Standard Reference Database-REFPROP, Version 9.1 (2013)

Part VII
Building-Integrated Renewable Energy, Building Energy-Saving Design and Energy Efficiency

An Optimized Setpoint Framework for Energy Flexible Buildings in Hot Desert Climates

Ali Saberi Derakhtenjani, Juan David Barbosa, and Edwin Rodriguez-Ubinas

1 Introduction

The building sector uses about 40% of primary energy worldwide and emits about 39% of carbon [1]. Decarbonizing the building sector is essential for achieving a carbon-neutral global society. Meanwhile, another challenge to address is climate resilience. With more frequent, intense, and longer-lasting extreme weather events, exacerbated by climate change such as heat waves, energy resilience of buildings and grids has become essential in providing the demand for electricity, cooling, and heating services to occupants to avoid excessively high or low indoor temperature or energy outage that threatens lives of citizens and causes illness and health consequences. Decarbonizing buildings and improving their climate resilience should be tackled together with evaluating technologies, design, and operation strategies to improve buildings' energy performance. Electrification of buildings has been creating growing dependence on buildings' energy provision and resilience on the capacity and reliability of power grids. Energy flexibility through demand side management and energy storage technologies is increasingly becoming critical in balancing the electric power supply and demand for buildings, especially considering the intermittent nature of the growing renewable energy production from solar photovoltaics (PV) and wind as well as increasing dynamics of electricity demand in buildings and EV charging.

IEA EBC Annex 67 developed a common definition of building energy flexibility as "the ability to adapt/manage its short-term (a few hours or a couple of days) energy demand and generation according to local climate conditions, user needs,

A. S. Derakhtenjani (✉) · J. D. Barbosa · E. Rodriguez-Ubinas
Dubai Electricity and Water Authority, DEWA R&D Center, Dubai, UAE
e-mail: ali.saberi@dewa.gov.ae

and energy network requirements without jeopardizing the technical capabilities of the operating systems in the building and the comfort of its occupants. The energy flexibility of buildings will thus allow for DSM/load control and thereby DR based on the requirements of the surrounding energy grids" [2]. Energy flexibility is often expressed as the power or energy that can be shifted, increased, or decreased in reaction to an external signal (price signal, for example) without scarifying indoor comfort over a specific time span. Energy flexible buildings (EFBs) are energy-efficient buildings capable of controlling their energy demand using elements such as smart building management systems (BMS), thermal mass, adjustable HVAC systems, thermal energy storage, renewables, batteries, electric vehicles, and plug-in loads shifting. Characterizing buildings' energy flexibility is quite challenging since it involves various aspects and it strongly depends on the boundary conditions and evaluation methods. Hence, energy flexibility quantification in buildings is one of the topics of most significant interest in current scientific research [3–5]. However, the majority of existing literature on energy flexible buildings is for heating-dominated climates. Therefore, there is a need to develop and study strategies and methodologies for buildings located in cooling-dominated climates.

In Dubai, the rapid increase in electricity demand calls for investment in developing more efficient and enhanced future energy networks. In the first 5 months of 2021, Dubai's demand for energy increased by 10% to 16,467 GWh compared to 14,988 GWh for the same period in 2020. Also, the peak load for the same period observed a 10% increase to 7966 MW, compared to 7248 MW for the same period in 2020, recording an extra 718 MW [6]. Hence, to accommodate the constant growth of energy demand and its related carbon emissions, Dubai is implementing an ambitious plan to increase its share of renewables. The Dubai Clean Energy Strategy aims to provide 25% of Dubai's power output from clean energy by 2030 and 100% by 2050 [7]. Dubai Electricity and Water Authority's initiatives, such as the Mohammed bin Rashid Al Maktoum (MBR) Solar Park and Shams Dubai distributed generation program, have significantly increased solar energy production. The MBR solar park is the largest single-site solar park in the world based on the Independent Power Producer (IPP) model, with a planned production capacity of 5000 MW by 2030 [8]. It will save over 6.5 million tons of carbon emissions annually when completed. Nevertheless, solar power is intrinsically variable and can affect the stability of the energy system, especially when it accounts for a high percentage of the total generation, and its share is expected to grow due to the Emirate's accelerated urbanization. Energy flexible buildings can respond quickly to the grid's dynamic needs. Therefore, it is crucial to evaluate their implementation feasibility and capability to support the stability of the power grid. In alignment with this need, the present study aims to quantify the thermal energy flexibility of a building in Dubai (cooling-dominated climate) utilizing two indicators and to evaluate the potential benefits of the model predictive control strategies in a dynamic marginal cost of electricity scenario.

2 Building Thermal Modeling

The thermal zone considered in this study is an office room with a floor area of 10 m². The walls, floor, and window U-values were selected to fulfill the requirements of the Dubai building code [9], presented in Table 1:

The floor is made of 10 cm of concrete and represents the main thermal mass in the zone. Cooling load is limited to 2000 W maximum. The modeling approach used for this study is based on the low-order, lumped-parameter RC models, which are practical for control studies [10]. Figure 1 shows the thermal network for the RC

Table 1 Dubai building code: envelope requirements

Building element	Thermal transmittance
1. External walls	2. $U \leq 0.57$ W/m²K
3. Roof	4. $U \leq 0.30$ W/m²K
5. Windows (WWR > 40%)	6. $U \leq 1.70$ W/m²K
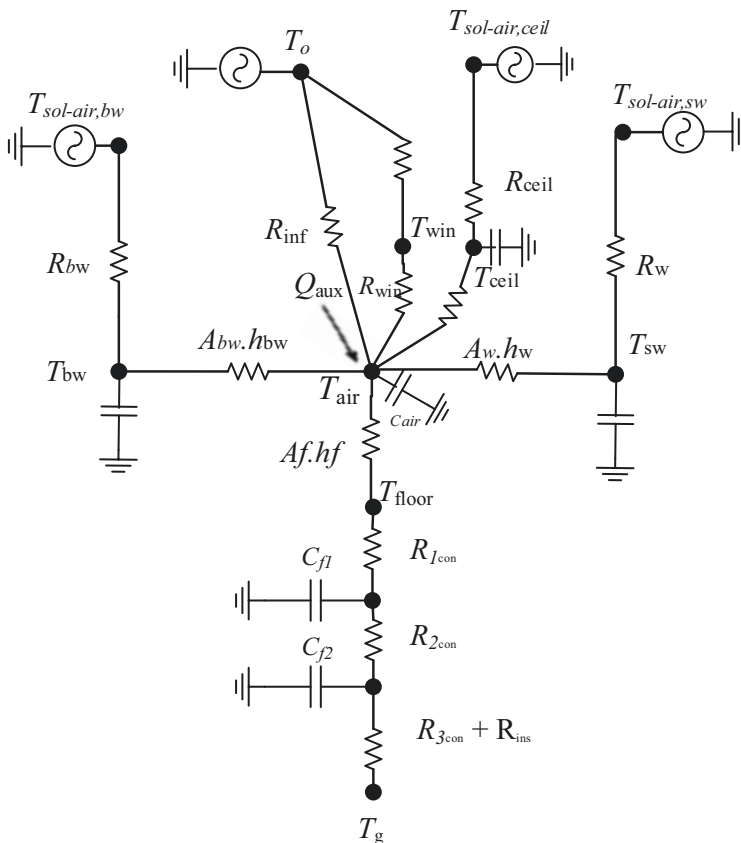
Fig. 1 Thermal network model of the zone

model of the zone. The main cooling source is convective and is controlled based on the desired room air temperature.

The sol-air temperature was assumed for the exterior surfaces to take into account the effect of solar radiation and is defined as:

$$T_{\text{sol}-\text{air}} = T_o + \frac{Q_{\text{sol}}}{h_o} + \tag{1}$$

where T_o is the outdoor (ambient) temperature, Q_{sol} is the incident solar radiation on each surface, and h_o is the outdoor heat transfer coefficient.

A detailed reference model developed in the EnergyPlus building simulation tool was used to calibrate and validate the RC model of the building. The geometry of the building can be seen in Fig. 2a, which has a single window covering 60% of the south-facing façade. Insulation layers of 4 m²K/W and 2 m²K/W are assigned to horizontal surfaces and walls, respectively. The HVAC system of the model assumes an ideal air load system that can provide the demanded load to achieve the desired setpoint. It should be noted that in both models it is assumed that internal gains are negligible.

The output from the EnergyPlus model is used as virtual experiment data to calibrate and validate the RC model. An optimization formulation was considered to minimize the error between the EnergyPlus and the RC models cooling loads by finding and assigning the effective values of the capacitances and resistances of the low-order RC model. The algorithm was based on the Euclidean norm or the second norm of the difference between the cooling loads calculated by EnergyPlus and the RC model. If the cooling load from the EnergyPlus is represented by QE and the cooling load from the RC model is represented by QRC, then the objective function JQ based on the second norm difference is defined as:

$$JQ = QE - QRC = \sqrt{\sum_i \left(QE_i - QRC_i\right)^2} \tag{2}$$
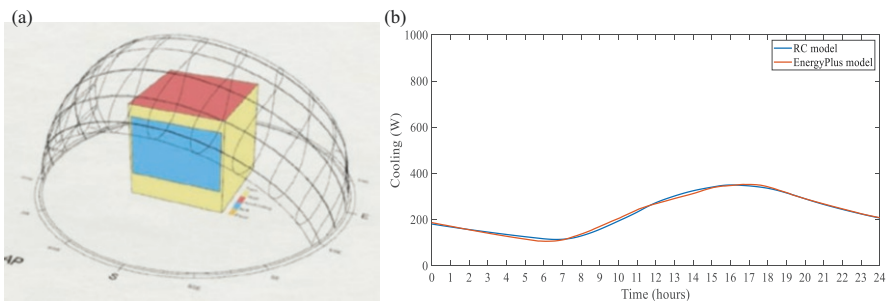
Fig. 2 (**a**) EnergyPlus model geometry; (**b**) cooling load for EnergyPlus vs. calibrated RC model

MATLAB Optimization Toolbox™ [11] was used here to solve the optimization problem. Figure 2b shows the calibration result.

3   Thermal Energy Flexibility KPIs

Within the research work done in the IEA EBC Annex 67, certain KPIs were introduced by [12] to quantify significant aspects of energy flexibility. These KPIs include the available storage capacity (C_{ADR}) and storage efficiency (η_{ADR}), which for an active demand response (ADR) event are defined as:

$$C_{\text{ADR}} = \int_0^{l_{\text{ADR}}} \left(Q_{\text{ADR}} - Q_{\text{Ref}} \right) dt \tag{3}$$

$$\eta_{\text{ADR}} = 1 - \frac{\int_0^{\infty} \left(Q_{\text{ADR}} - Q_{\text{Ref}} \right) dt}{\int_0^{l_{\text{ADR}}} \left(Q_{\text{ADR}} - Q_{\text{Ref}} \right) dt} \tag{4}$$

C_{ADR} is defined as the amount of cooling/heating that can be added to the structural mass of a building for an active demand response (ADR) event without jeopardizing indoor thermal comfort in a specific time frame. The storage efficiency (η_{ADR}) represents the fraction of the cooling/heating that is stored during the ADR event, which can be used subsequently to reduce the heating power needed to maintain thermal comfort. Figure 3 shows the schematic representation of the KPIs.
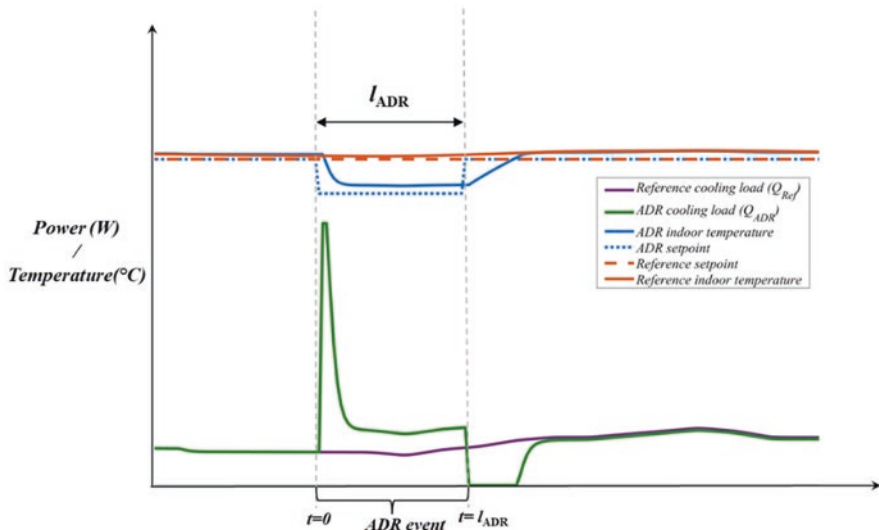
Fig. 3 Schematic representation of energy flexibility KPIs

4   Analysis of Energy Flexibility

The analysis performed here is based on changing the zone air temperature setpoint with which modulation of the cooling load happens. The mainly considered strategy to quantify the building energy flexibility is to precool the building by lowering the reference setpoint (which here is considered to be 24 °C) by 2 °C for a certain period of time before the peak demand period. Then, the KPIs are calculated from the reference and flexible load profiles.

Figure 4 shows the reference cooling load profile for several selected months of the year. As observed, the higher cooling loads are during the summer months.

The first strategy to evaluate energy flexibility was to reduce the setpoint by 2 °C from 24 °C to 22 °C. This change is implemented for 4 h from 7 am to 11 am just before the peak demand period, which happens between 12 pm and 6 pm. Figure 5 shows the change in the cooling load for a typical day in June. It is observed that the proportional controller uses the maximum system capacity (2000 W) to push the temperature toward the lower setpoint. This strategy shifts 100% of the cooling load outside the peak hours for this case. The calculated C_{ADR} for the 4-h event for this case is 485 Wh/m². The calculated efficiency for the rest of the day is 82%.

Table 2 shows the calculated C_{ADR} and η_{ADR} for the rest of the year for the months requiring a noticeable cooling load (April to November).

As observed from the table, the value of C_{ADR} remains almost constant throughout the year. This important observation shows that thermal flexibility is a fixed value and depends on the building's construction materials and their capacity to store energy. For η_{ADR}, we observe different values for each month with August being the highest. The reason for this is that since η_{ADR} is the ratio between the utilized stored energy after the ADR event to the energy stored during the ADR event, during warmer months like July and August, significant cooling is needed after the
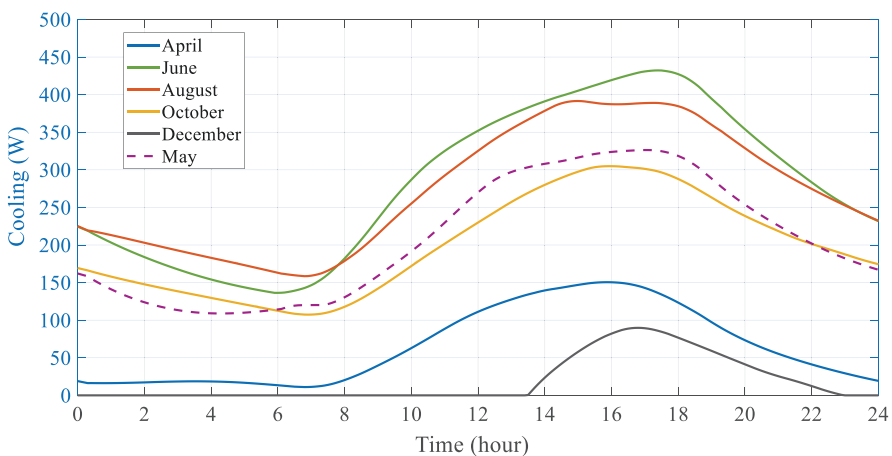
Fig. 4 Reference cooling load profiles for a day in different months
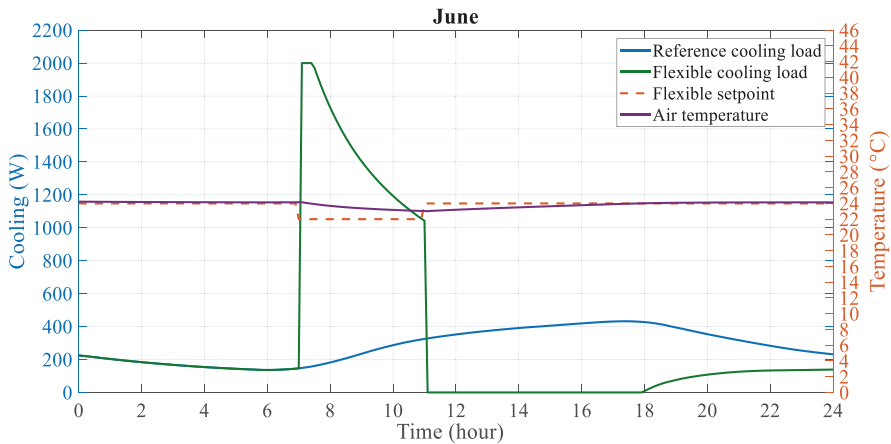
Fig. 5 Flexible cooling load profile for a day in June

Table 2 Calculated KPIs for different months of the year

Month	C_{ADR} (Wh/m^2)	η_{ADR} (Until the end of the day)
April	486	26%
May	485	72%
June	485	82%
July	485	77%
August	483	90%
September	484	77%
October	485	66%
November	486	38%

ADR event. Therefore, utilization of the stored energy after the ADR event is much higher compared to the cooler months, like April, where there is not much cooling needed after the ADR event for the rest of the day.

5 Predictive Control with a Dynamic Marginal Cost of Electricity

This section presents how a hypothetical dynamic marginal cost of electricity can be handled utilizing model predictive control techniques. These techniques permit the operation of the systems with minimum power and/or energy consumption during high-cost periods, utilizing weather and electricity marginal cost forecasting. In addition, an optimal setpoint can be found for the zone air temperature so that the indoor air temperature stays within the comfort range while minimizing the cost of electricity for the user. In this case, the objective function can be defined as:
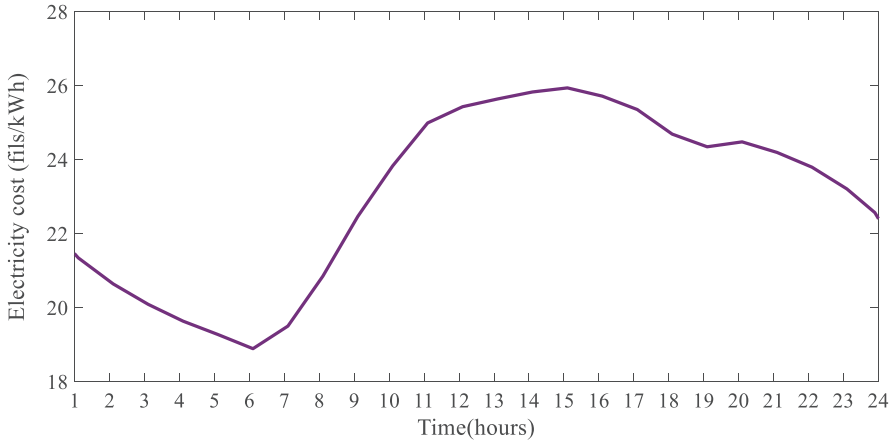
Fig. 6 Hypothetical dynamic marginal cost of electricity for a day in July (1fils = 0.1AED)
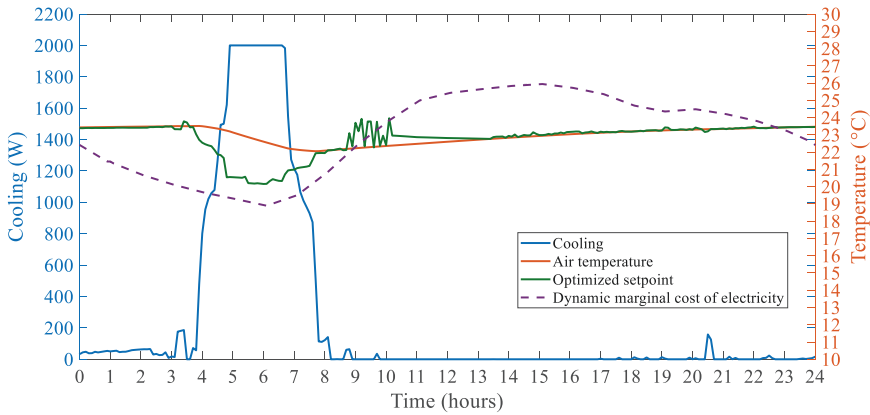
Fig. 7 Predictive control strategy

$$minimize \quad JC = \sum \left[\mathrm{Cost}(t) \times Q_{\mathrm{aux}}(t) \right] \rightarrow \text{so that}: 18°C \leq T_{\mathrm{air}} \leq 24°C \qquad (5)$$

where Cost(t) is the marginal cost of electricity at every time step. For example, Fig. 6 shows a hypothetical marginal cost of electricity profile for a day in July based on a typical daily demand profile. As observed, the cost fluctuates significantly during the day, with higher values from 11:00 to 18:00 and reaching its peak at 15:00 (3:00 pm).

The optimization was performed using MATLAB Optimization Toolbox to minimize the cost of electricity for this dynamic marginal cost signal. Figure 7 shows the results of the predictive control strategy for the case in July.

As observed in Fig. 7, the optimizer designs the setpoint so that precooling of thermal mass happens at the time of the lowest marginal cost from around 3:30 am to 8:00 am. Then, the stored cooling being released during the rest of the day makes the building stay in the thermal comfort range and there is no need for additional cooling. This strategy results in 11% cost saving compared to the normal operation and the reference profile.

6   Conclusion

This chapter presented a study of energy flexibility quantification and strategies for a typical building in Dubai. A low-order RC model was developed for a typical thermal zone in Dubai. A detailed model of the zone developed in EnergyPlus was used as the reference model to validate the RC model. The validated RC model was then used to study and quantify the energy flexibility of the zone during the months in which the building requires a significant cooling load (April–November).

The first strategy to evaluate energy flexibility was lowering the zone air temperature setpoint by 2 °C from 24 °C to 22 ° C for 4 h before the peak demand period. Then, the building energy flexibility was quantified by means of two indicators. It was observed that building thermal flexibility is mainly dependent on the building materials, allowed comfort temperature range, and the duration of the ADR event. On the other hand, flexibility is almost independent of weather conditions as long as there is a cooling demand. For the considered building and the ADR event of 4 h and changing the setpoint by 2 °C from 24 °C to 22 °C, the quantified flexibility was equal to 485 Wh/m^2 almost throughout the year. Therefore, when using a similar strategy for similar buildings, the same numbers for energy flexibility are expected.

In the next section, a model predictive control strategy was introduced for optimized building operation when dealing with a day-ahead prediction of dynamic marginal cost of electricity and ambient conditions. It was observed that the controller designs the zone air setpoint in a way that maximum consumption happens during the time of the lowest cost, and then the stored cooling is released during the day, eliminating the need for any cooling later during that day. This strategy provides the lowest bill for the building owner (cost saving of 11% compared to normal operation) while helping the grid reduce consumption during peak demand hours. Future works will include validating the predictive control strategies in a real building, including analyzing multiple zones.

References

1. Cao, X., Dai, X., Liu, J.: Building energy-consumption status worldwide and the state-of-the-art technologies for zero-energy buildings during the past decade. Energ. Buildings. **128**, 198–213 (2016). https://doi.org/10.1016/j.enbuild.2016.06.089
2. Jensen, S.Ø., et al.: IEA EBC annex 67 energy flexible buildings. Energ. Buildings. **155**, 25–34 (2017). https://doi.org/10.1016/j.enbuild.2017.08.044
3. Li, R., et al.: Ten questions concerning energy flexibility in buildings. Build. Environ. **223** (2022). https://doi.org/10.1016/j.buildenv.2022.109461
4. Saberi-Derakhtenjani, A., Athienitis, A.K., Eicker, U., Rodriguez-Ubinas, E.: Energy flexibility comparison of different control strategies for zones with radiant floor systems. Buildings. **12**(6) (2022). https://doi.org/10.3390/buildings12060837
5. Morovat, N., Athienitis, A.K., Candanedo, J.A., Delcroix, B.: Model-based control strategies to enhance energy flexibility in electrically heated school buildings. Buildings. **12**(5), 581 (2022). https://doi.org/10.3390/buildings12050581
6. Dubai Electricity and Water Authority (DEWA): Dubai records 10% energy demand growth and 10% peak load increase until end of May 2021. June 02, 2021. https://www.dewa.gov.ae/en/about-us/media-publications/latest-news/2021/06/dubai-records-10energy-demand-growth-and-10peak-load-increase-until-end-of-may-2021. Accessed 11 Nov 2022.
7. Dubai Electricity and Water Authority (DEWA): 100% clean energy in Dubai by 2050, May 05, 2022.
8. Government of Dubai: Mohammed bin Rashid Al Maktoum Solar Park (2022)
9. Government of Dubai: Dubai Building Code (2021)
10. Candanedo, J.A., et al.: Control-oriented archetypes: a pathway for the systematic application of advanced controls in buildings. J. Build. Perform. Simul., 1–12 (2022). https://doi.org/10.1080/19401493.2022.2063947
11. MathWorks: Optimization Toolbox (2018)
12. Reynders, G., Amaral Lopes, R., Marszal-P omianowska, A., Aelenei, D., Martins, J., Saelens, D.: Energy flexible buildings: an evaluation of definitions and quantification methodologies applied to thermal storage. In: Energy and Buildings, vol. 166, pp. 372–390. Elsevier (2018). https://doi.org/10.1016/j.enbuild.2018.02.040

A State-of-the-Art Approach for Assessing the Environmental Sustainability of Multi-renewable Energy Systems in the Built Environment

Joseph Akpan (ID)**, Oludolapo Olanrewaju** (ID)**, and Rubén Irusta-Mata** (ID)

1 Introduction

1.1 Background

The global energy grid could provide reliable and affordable energy that is environmentally friendly if the current energy system is restructured to be clean, adaptable and responsive to the Intergovernmental Panel on Climate Change (IPCC) recommended climate scenarios. Building such a resilient energy system would require energy efficiency and environmental sufficiency. The energy efficient process would mean less energy requirement and the sufficient implies least impact on the environment. Both energy efficiency and sufficiency are instrumental in helping deplete the world's "carbon budget" i.e., the amount of Carbon needed to limit global warming to below 2°C threshold. Carbon dioxide (CO_2) emissions resulting from the use of fossil fuels have a significant impact on the environment, hence, the preference for renewable energy systems over non-renewable ones. To accurately measure impact based on the activities throughout the entire life cycle of any system of choice, life cycle assessment methods have proven particularly useful for comparing the environmental impact of the energy systems.

J. Akpan (✉)
Industrial Engineering, Durban University of Technology, Durban, South Africa

Institute of Sustainable Processes, University of Valladolid, Valladolid, Spain
e-mail: 22176142@dut4life.ac.za

O. Olanrewaju
Industrial Engineering, Durban University of Technology, Durban, South Africa

R. Irusta-Mata
Institute of Sustainable Processes, University of Valladolid, Valladolid, Spain

An impact assessment is crucial for understanding the complete life cycle of a building integrated renewable energy system and facilitating comparisons among different production systems. As such, the more suitable renewable system of choice for building integration can be selected from an assessment using LCA methods. In this study, two key knowledge areas and their applicability in the built environment are presented. First, the energy efficiency process and the second is sufficiency (herein, referred to as the best availability techniques). An overview for both concepts is presented, with a discussion on the challenges with the achievement of both concepts in the built environment. Subsequently, the study centers on LCA, being one of the highly recognized assessment tools that aids in identifying BAT and in assessing the environmental sustainability of energy systems. Life Cycle Assessment (LCA) simulation tools are comprehensively examined, and specific criteria are proposed for use in dveloping unique tool for building integrated renewable systems LCA application.

1.2 The Energy Efficiency Process and Best Available Techniques for the Built Environment

The need for continuous improvement of clean energy supply chain operations, including those in the built environment, continues to be on the rise, given the increasing changes in legislation and policy redesign by countries and institutions. This reason has often been tied to the benefits of sustainability and growth in cutting-edge technology, which has given birth to new techniques to either eliminate or support existing methods. These techniques can be generic or specific to a particular sector, while some approaches can be applied across most or all sectors. Such sectors with the characteristic of presence in other sectors include energy efficiency and general production-related emissions from storage facilities and industrial cooling systems. The Best Available Techniques (BAT) are a definition of how industrial activities should be executed under the most optimal techniques attainable, and should not negatively impact the environment or, failing that, said impact should be the least possible [1, 2]. They are considered the most effective techniques to achieve a high general level of protection of the environment. In addition, the application of the techniques must be economically and technically feasible, considering the costs and benefits. The techniques and technologies for developing industrial energy efficiency have been well proven. The challenge for policy formulators is to speed up the adoption of techniques and technologies [3]. Energy efficiency needs to be improved in all sectors. International experience shows that the success of policies and programs depends on effective design, implementation, and ongoing evaluation.

As a means of introducing sophisticated environmentally sustainable technology in industrial sectors, a concept known as best available techniques (BAT) [4] is employed in the EU and 39 OECD countries [5], as well as Russia, Belarus, and China. The best available techniques are those that are most effective in reducing

and/or preventing emissions of pollutants into the atmosphere [6]. From the proceedings of the Sevilla Process [7], it is established that these techniques will be divided into general industrial sector and sector-specific best practices [8]. Techniques that apply to all or many of the industrial sectors are regarded as general BREFs, while ones that are unique to a particular industry sector-specific practices are seen as specific BREFs. For the former, issues related to energy efficiency, cooling in industrial processes and emissions from storage are commonly applicable. The latter includes practices in sectors such as food, water, electricity production, raw material, refining, and manufacturing. To achieve operational excellence, it then becomes imperative to develop the most suitable technique for each industrial sector-specific requirement towards achieving energy efficiency. In integrating energy-efficient approaches to meet standards and requirements for energy management of assets in an industrial sector, both new and existing systems, as well as their dynamic nature, should be taken into consideration. Asset life cycle conceptualization presents a significant challenge when it comes to taking a proactive stance on the functionality and regulation of interconnected engineering asset systems. The International Energy Agency (IEA) [9] highlighted some of the foreseen challenges with implementing energy efficiency measures. Among the challenges are the lack of technical capability, policy and regulatory obstacles, lack of public awareness and education, hurdles related to funding, investment, and technology constraints, which make it difficult to find, analyze, and implement energy efficiency measures. Many countries, regions, companies, and businesses have implemented asset management systems that include energy-efficient practices. A wide range of industries were examined in this study, and numerous criteria were identified.

For the study, an examination on energy efficiency measures in the built environment, including their limitations, capabilities, and impacts, is addressed through the discussion on BAT. In other respects, this research provides a foundation for evaluating energy efficiency measures through BAT to meet the global needs for sustainable asset operations in the built environment.

The term "energy efficiency"is a distinct one that can indicate several things depending on the case and the author. According to [10], a technical definition of energy efficiency is given, which is used to establish a link between energy output and input ratios. However, in practical applications, this definition can be unclear. Therefore, it becomes important to define energy efficiency by linking it to a precise level of activity or output in order to track the measures over time, using indicators based on defined parameters. With these considerations, energy efficiency can refer to using less energy to accomplish the same task and, in the process, reducing energy bills and pollution. In other words, it involves reducing the energy consumption needed to achieve the same output or achieving more output with the same energy input [11]. To enhance energy efficiency, a global and coordinated effort is necessary to implement all available measures and technologies for reduction [12]. Energy efficiency plays a crucial role in mitigating the increase in electricity demand. As a result, energy efficiency is included in the policy roadmap such as outlined in the Net Zero Emissions Scenario for 2050 [13]. Table 1 presents some additional definitions of energy.

Table 1 Selected energy efficiency definitions

Description	Ref(s)
The term "energy efficiency" simply refers to the concept of utilizing as little energy as possible to achieve the greatest feasible outcome.	[14]
Energy efficiency is referred to as the economical way of lowering emissions, increasing energy competitiveness, and reducing the cost of energy for users.	[15]
A very effective strategy to increase supply security, boost employment, reduce emissions and energy dependence while improving economic sustainability and competitiveness is energy efficiency.	[16]
Energy efficiency is a crucial energy policy strategy on a global scale, ensuring a reliable energy supply and lower greenhouse gas emissions.	[17]
Energy efficiency is a crucial resource for economic and social advancement, offering significant advantages to varying parties, from the organizations that create energy-saving technologies to all members of society.	[18]
Efficiency in the use of energy to promote economic growth, social development, and health and well-being of occupants, with little or no environmental impact.	[19]
Energy efficiency is the ratio of energy input to output in terms of performance, service, products, or energy.	[20]
Utilizing less energy while producing the same quantity of goods or useful output is referred to as energy efficiency.	[21]

Achieving energy efficiency in buildings requires a well-planned approach, where the overall coordination of the building system considers all relevant aspects to meet energy-saving objectives. This involves adopting a perspective that encompasses the entire life cycle of the building, including aspects of planning, design, construction, maintenance, operation, and disposal. Building systems should undergo thorough evaluations to ensure that energy efficiency measures can be effectively implemented.

Shao B, et al [22] delves into the thermal engineering calculation of buildings in accordance with national norms, standards, local standards, and the author's practical experience, focusing specifically on energy-saving technology promotion. The emphasis is on utilizing these calculations to optimize energy efficiency, effectively reducing energy consumption and ensure effective thermal performance.

1.3 The Challenge and Issues Related to BAT and Energy Efficiency in the Built Environment

As the economy grows, urban activities are intensified with the increased development of new building infrastructures to accommodate the growing population and industrial activities. Consequently, energy consumption also increases. Higher energy consumption results in higher operational costs for building consumers, who are the energy end-users. Using less energy leads to reduced operational costs and higher earnings. Furthermore, reducing energy imports can help alleviate foreign

exchange constraints and enhance the availability of crucial energy resources. Industries can promote economic growth through the implementation of appropriate management practices. Efforts are being made in this regard through the construction of energy-efficient buildings. However, there is currently no comprehensive and universally adopted global strategy to achieve these goals, as different regions have approached energy efficiency in their own ways. The reference document BREF [23], which focuses on energy efficiency, does not adhere to the typical format of the Integrated Pollution Prevention and Control (IPPC) Directive 96/61/EC [23, 24]. Instead, it takes a more general approach to energy efficiency due to the wide range of sectors and activities involved. It does not include sections on specific features, energy consumption and emissions, BAT, determination factors, or emerging techniques for achieving energy efficiency in specific sectors, especially in the context of the built environment. To determine the most effective methods for achieving energy efficiency using BAT in a particular sector, specific BREF documents are reviewed. The findings from these documents are intended to serve as a knowledge-based integrated approach to develop techniques for energy efficiency in the built environment.

The general issues to be considered in determining BAT as adapted from Ref. [23], include:

(a) The specific category of the built environment and its associated energy consumption, as well as the nature of the raw materials used (including water)
(b) The energy efficiency considerations at different levels of operations within the category of the built environment

- At the installation level, which includes individual components and, in the case of this study, renewable energy systems
- At the interaction level among processes, units, and systems

(c) The overall objective of protecting the environment and maximizing energy efficiency when assessing BAT and imposing BAT-related permit restrictions.

Specific considerations for selecting the best available procedures, as described in Article 2(12): [23] *having in mind the probable costs and benefits of a measure, as well as the ideals of precaution and prevention*

- Low-waste technology
- Use of less hazardous compounds
- Recovery and recycling of substances generated and used in the process and waste, if applicable
- Adoption of similar proven operational techniques on a large scale
- Consideration of advancements in scientific understanding resulting from technological breakthroughs, particularly in relation to the environmental impact of emitted pollutants
- Timing of the introduction or replacement of equipment, whether new or old

- Implementation timeline for the best available technology
- Efficient use of raw materials, including water, in the process, and emphasis on energy efficiency
- The necessity to reduce or prevent overall emissions' impact on the environment and to minimize associated risks
- Prevention of accidents and minimization of environmental consequences
- Insights derived from regular meetings among member states, held every three years

After reviewing both the general and specific requirements for implementing BAT, it is evident that the primary focus is on minimizing the environmental impact of production systems throughout the entire life cycle of the built environment. This objective is achieved by employing the best methods and energy technologies, as discussed in references [25–27]. As a result, the subsequent section will delve into a comprehensive and widely accepted tool for evaluating the environmental impacts of systems in the built environment.

2   Global Adoption of Life Cycle Assessment Concepts in the Built Environment

According to the literature, LCA is a flexible integrated management framework that encompasses concepts, techniques, and procedures incorporating environmental, economic, and social aspects of products, processes, and organizations. It is also a management concept that promotes a sustainability-oriented mindset throughout the life cycle [28, 29]. LCA adopts system thinking approach to assist organizations in effectively managing their products and services in an environmentally friendly manner [29] This integrated approach, inspired by the ChainNet project [30], involves utilizing multiple tools and approaches. Businesses employ LCA to ensure their products have a long-term positive environmental impact. This is evident in various areas such as product development, strategic planning, and public relations. Additionally, the public sector also uses life cycle thinking in stakeholder dialogues and policy implementation [31]. In policy-oriented environmental evaluations, LCA takes into account upstream and downstream trade-offs, ensuring a comprehensive analysis. To assess the adoption and adaptation processes of LCA, it is essential to understand the components that drive its implementation.

Within the framework of Sustainable Consumption and Production (SCP), LCA serve as scientific methods to environmental policy and decision-making in commercial settings. To effectively employ the LCA technique, it is crucial to have access to consistent data that has been independently validated, quality-assured, and customized to the specific circumstances [32]. For LCA to be successful, it must be tailored to the unique requirements of the organization implementing it [33]. It is important to note that the application of life cycle techniques may not be suitable in

every case [33]. This challenge presents an ongoing research question, and as a result, there is a lack of information and results regarding the specific procedures required to ensure widespread acceptance and implementation of life cycle approaches.

The built environment provides a compelling case for the application of LCA. With the growing recognition of cities as key players in addressing environmental challenges such as climate change, decision-makers are increasingly prioritizing long-term planning. In this context, researchers have examined various LCA methods in the construction sector, encompassing structural materials and urban regions, to determine the effectiveness of existing standards, indexes, and guidelines for assessing the sustainability of metropolitan cities or regions [34].

The use of LCA enables the comparison of cities and the establishment of reference flows for neighborhoods, cities, and urban regions. This facilitates the quantification of environmental impacts and plays a vital role in determining the boundaries of cities, which is essential for achieving long-term sustainability throughout their life cycles [35]. Figure 1 illustrates the progress made in LCA studies, showcasing how they contribute to the pursuit of sustainable cities and addressing the challenges posed by global climate change.

One thing to note from Fig. 1 is that many LCAs have been conducted at the product level. However, as the triangle moves toward the apex, the number of LCA
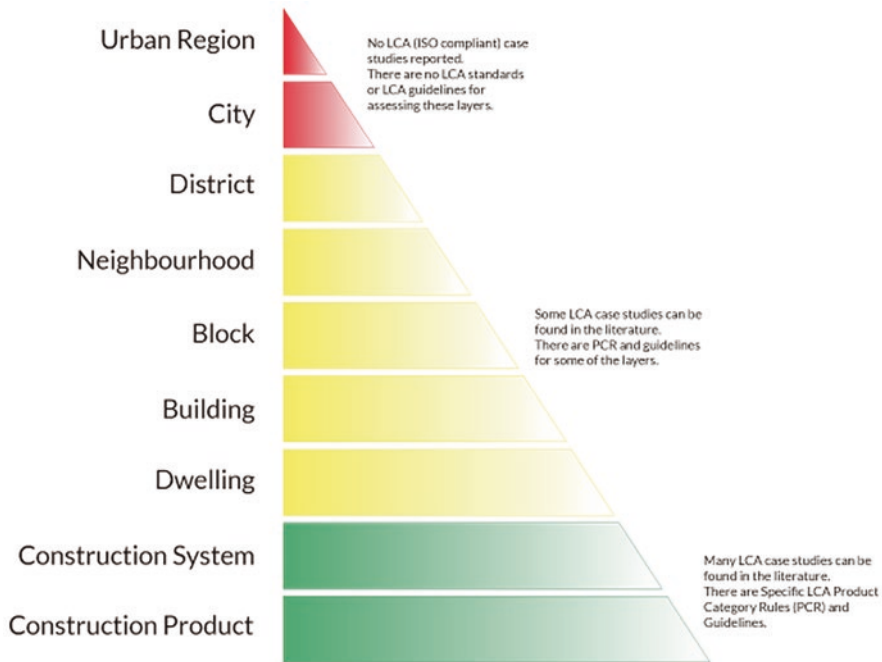
Fig. 1 Application of life cycle assessment in the built environment hierarchy, from products to urban regions [34]

studies decreases. In the case of buildings, some LCAs have been performed at the system or product level, and numerous LCA case studies can be found in the literature. However, when it comes to unique cases such as renewable energy systems integrated into buildings, there has been a growing interest in LCA research. Despite this, only a few studies focus on LCA of renewable energy systems integrated into buildings, even though renewable energy has been extensively examined from a life cycle perspective.

2.1 Renewable Energy System in the Built Environment and LCA Overview

Modern society relies on a diverse range of energy sources, including power generation and cooling systems, to sustain its functioning. However, these systems, despite their critical role and wide variability, have been demonstrated to have significant impacts on human health, ecology, and natural resources [36]. In the past two decades, several assessments approaches have been performed to determine and mitigate the environmental effects of energy systems. In the construction industry, sustainability assessments have become increasingly important for long-term success. Consequently, many renowned architects today are actively engaged in constructing buildings that are environmentally friendly and resource efficient. Such buildings can yield significant energy savings. Conservation strategies can be implemented in both new constructions and renovations. To further reduce the building's dependence on electric power, passive construction methods should be combined with well-established and proven renewable energy technologies [37, 38]. There are several examples of renewable energy technologies that can be integrated into building energy systems, including photovoltaic (PV) or solar electric systems, thermodynamic systems for solar hot water (domestic hot water heat and space heating) and preheating ventilation air, geothermal heating and cooling systems, biomass power plants, and wind turbines [39]. The successful integration of renewable energy technologies into architectural designs is best achieved during the building's conceptual phase, where technical features and potential application scenarios can be critically evaluated. Developing an optimal design approach for buildings that incorporate renewable energy technology involves formulating architectural schemes, implementing energy generation methods, and constructing the structure. The integration of renewable energy processes provides new design processes for building design that reflect the organic relationship between architectural design and renewable energy system design. The influencing factors for the different types of renewables systems and technologies in architectural-integrated designs are presented below in Table 2.

Economic gains, energy efficiency, and environmental benefits can all be improved through the use of a holistic approach. As people become more aware of the significance of energy and growing concerns about the sustainability of current

Table 2 Architectural design influence for selected integrated renewable energy technologies in building

S/N	Example	Influencing factors
1	Biomass	Total waste; equipment performance; emissions indicators
2	Solar PV system	Solar collector system type; collectible area; equipment efficiency
3	Geothermal system	Hydrogeology; room location and size; terminal device
4	Wind	Wind profile of the environment; noise management
5	Hydrogen	Existing renewable energy resources with surplus power generation, fuel cells, and storage systems
6	Co-generation	Building occupants' needs (cooling/heating) and other energy systems

Adapted from Ref. [40]

and future energy sources, questions arise about how much energy is required for energy production. Calculating the net energy consumption of a building-integrated energy system is an important application of LCA. According to the definition provided in [41], net energy refers to the energy remaining for consumer use after accounting for the energy associated with locating, producing, upgrading, and transporting it. If a new technology consumes more energy than it produces, it should be considered a net energy sink das it is not directly economically beneficial. However, even if a new energy technology may not be economically favorable, if it can generate a positive net energy output during periods of energy variability from other energy systems, it should be adopted for use. Analyzing all energy and material flows for the adoption of RES involves breaking it down into its component parts [42], followed by applying the phases of LCA and simulating the processes using appropriate tools.

LCA results in the building and construction sectors have shown significant variations in previous studies [43–45]. Several factors have shown to be responsible for some of these variations:

- Differences in the software/database, including different characterization factors, data sources, and location of case data, as well as the scope of assessment.
- Not considering the LCA for all the integrated external and internal building systems, such as building specific information and integrated energy systems.
- There have been scarcely any LCA comparison studies involving building-integrated renewable energy systems. Because of the lack of literature and open verifiable datasources on LCA for building-integrated energy systems, this may have been the case.

Given that the main objective of the majority of LCA studies is to identify the activities within each process of the energy systems that have the most significant environmental impacts, rather than the consequences of modifying these activities, an attributional LCA (ALCA) approach is commonly employed [46].

Other Life Cycle Inventory (LCIA) approaches, such as Eco-Indicator 99, Environmental Priority Strategies in Product Design 2000, and the Intergovernmental Panel on Climate Change (IPCC) 2013 method, are utilized to address the

limitations of alternative methods for assessing energy requirements and associated environmental impacts throughout the life cycle of energy systems. These additional LCIA methodologies enable evaluation of the potential environmental implications of each individual phase or overall life cycle of a multi-energy system. The goal and scope definition of the LCA, the life cycle inventory (LCI), the life cycle impact assessment (LCIA), and the interpretation of results are all interconnected components of the life cycle assessment, which must comply with ISO 14040:2006 [47]. As LCAs are also used for evaluating new technologies and promoting proactive action during technological development, upscaling, and applying LCA can have a positive environmental impact and contribute to a sustained increase in energy production with the least or no environmental impact. Figure 2 presents a proposed framework for the application of LCA in further reducing emissions throughout the life cycle phase of renewable energy systems. It is important to note that the framework currently includes only three building-integrated energy systems (Geothermal, PV, and Biomass) for demonstration. For full LCA studies, a variable number of energy systems (represented by "n") can be incorporated, depending on the systems being considered.

2.2 Materials and Energy Requirements for the LCA of Energy Systems in the Built Environment

It is important to highlight that the energy expended by a building can be separated into operational, embodied, and decommissioning energy during its life cycle. Every piece of equipment and appliance needs some level of operational energy to work properly. Embodied energy refers to the non-direct energy necessary to develop and maintain a structure. Energy (indirect energy) is necessary for the procurement, processing, and fabrication of building materials, as well as the energy required to transport them to the construction site and erect the building (direct energy). Over the course of their useful lifetimes, building materials, components, and systems must be serviced and repaired, costing more energy (recurring energy). The decommissioning energy of a structure is the energy required to demolish/deconstruct it and convey the demolished/salvaged materials to landfills or recycling facilities. Each of these can be evaluated independently if necessary to determine the amount of energy required at each of the five stages of the process or product life cycle. LCA will be useful in ascertaining this energy needed, and the four stages in a product's life cycle are material extraction, manufacturing, consumption, disposal, and recycling [47, 48]. Table 3 highlights the four stages and the definition of the energies needed at each point.

The energy requirements are incorporated as a process, while the assembly of each part will also require material input for each of the five stages of the process or product life cycle, which can be assessed separately. Table 4 highlights the four stages and the definition of the materials requirements at each point.
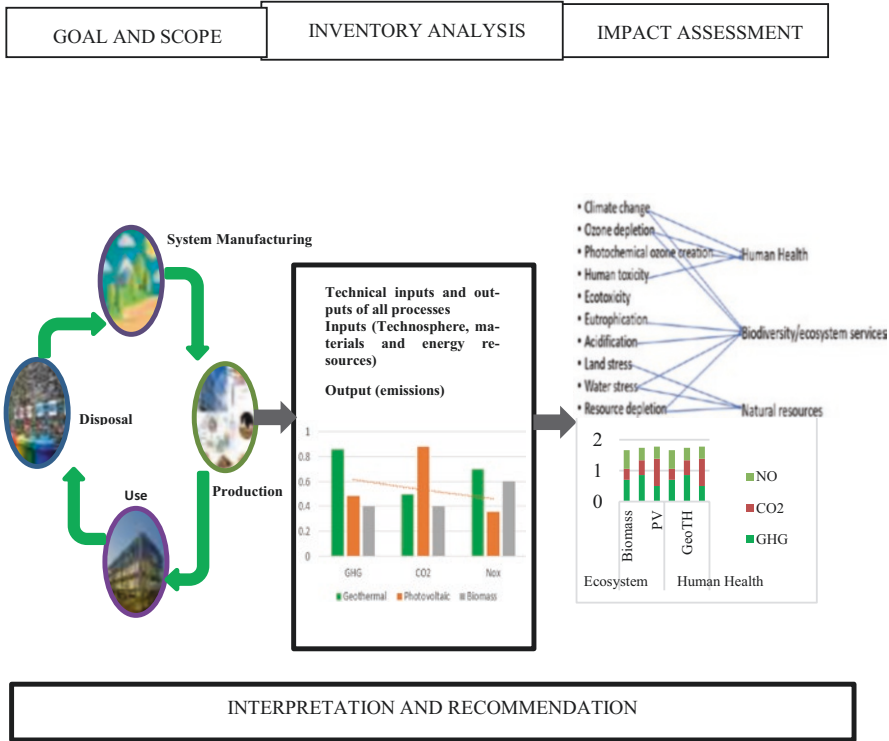
Fig. 2 Conceptual framework for the LCA of building-integrated renewable energy system

3   Comparative Study of the Tools for LCA of Energy Systems in the Built Environment

There are many modeling and simulation applications available for energy systems, each with varying complexity, usage conditions, input parameters, and outputs. In the study by Al Ka'bi, A. [53], ten commonly used energy modeling and simulation software applications for buildings were analyzed. These software applications include DesignBuilder, IDA-ICE, IES-VE, EnergyPlus, TRNSYS, eQUEST, Autodesk Green Building Studio, Ecotect, RIUSKA, and VIP-Energy. Except for DesignBuilder, eQUEST, RIUSKA, and VIP-Energy, all of these software applications allow for CO_2 modeling. However, the modeling is typically limited to the operational phase of the building and its associated energy systems. As a result, there is a growing interest in conducting life cycle assessments of the building-integrated energy systems throughout all stages of their life cycle. The selection of software for conducting LCA of building integrated energy production systems and processes can significantly impact the LCA results.

In this section, a comparison is made on LCA software packages that have been reviewed for buildings and the building integrated renewable energy systems. The

Table 3 Four stages and the definition of the energies needed at each point

Life cycle stage	Energy requirement definition	Units	Ref.
Material extraction	This term refers to how much energy it takes to make a given amount of a substance from its ore and feedstock. Raw material extraction, energy for materials transportation, and preparation for use are all included in this definition.	MJ/kg (or equivalent)	[49, 50]
Construction/ manufacturing	Energy used to achieve the manufacturing of a product or in the process of product development. The process energy requirement is dependent on the product type.	MJ/kg (or equivalent)	[50, 51]
Consumption (usage or operations and maintenance)	Energy dissipated during the operational phase of the product or process. This includes energy consumed during product installation, commissioning, operations, and maintenance.	MJ/kg (or equivalent)	[51]
Disposal	The energy required to dispose the product upon reaching its intended design useful life. The associated energy here can include the demolition, transportation requirement.	MJ/kg (or equivalent)	[52]
Recycling	The energy required to convert the undesired product to meet other functional requirements at a lower cost benefit analysis. The energy requirement depends on the waste hierarchy path chosen; refurbishment for reuse, incineration for by-product generation.	MJ/kg (or equivalent)	[52]

Table 4 Four stages and the definition of the materials needed at each point

Life cycle stage	Material requirement definition	Units
Material extraction	This term refers to how much materials it takes to make a given amount of a substance from its ore and feedstock. Material input for extracting raw materials, transportation, and preparation for use are all included in this definition.	Kg (or equivalent)
Construction/ manufacturing	Material input used to achieve the manufacturing of a product or in the process of product development. The physical material requirement is dependent on the product type.	Kg (or equivalent)
Consumption (usage or operations and maintenance)	Materials used during the operational phase of the product or process. This includes materials such as consumables during product installation, commissioning, operations, and maintenance.	Kg (or equivalent)
Disposal	The materials required to dispose of the product upon reaching its intended design useful life. The associated material here can include the disposal materials.	Kg (or equivalent)
Recycling	The material employed in the recycling process to convert the undesired product to meet other functional requirements at a lower cost benefit analysis. The material requirement depends on the waste hierarchy path chosen; refurbishment for reuse, incineration for by-product generation.	Kg (or equivalent)

selection of LCA applications for buildings and building energy systems varies depending on the assessment goals, scope, and availability of inventory data as discussed in the previous section of this study. To ensure a fair comparison of simulation programs, no specific energy system is used. The objectives of these comparisons are as follows:

- To identify differences between applications based on unified selection criteria. This involves understanding the modeling capabilities, strengths, weaknesses, and limitations of each software in relation to standards, benchmarks, databases, LCIA methods, generic usage, and applications in building-integrated renewable energy systems.
- To propose a classification and evaluation criteria for data and software sources that could help unify the differences between factors that influences variation in LCA results.

Recently, a list of software tools for LCA in building was mentioned and summarized in an EU joint study [54]. The study also provided an analysis and proposed general evaluation criteria that should be considered when selecting any of these tools for LCA in buildings. It is worth noting that these classification and evaluation criteria did not include specific information related to LCA applications for building-integrated energy systems. In order to address this gap and build upon previous works on LCA tools comparison and classification [55, 56], an improved new set of criteria is developed specifically for the application of LCA in building-integrated energy systems. These criteria are based on the ISO frameworks [47, 57] and takes into account the unique requirements and considerations associated with such systems. Before these criteria, a new list of software tools is compared in Sect. 3.1, which provides some alignment with specific criteria to be established in Sect. 3.2, providing a more targeted approach for LCA in building-integrated energy systems.

3.1   Comparison of Tools

Table 5 provides a summary comparison of tools that can be used in the LCA process, specifically for built environment multi-energy system LCA.

The tools in Table 5 have been categorized based on the employed criteria, and Table 6 presents the tools that are most suitable for conducting LCA of building-integrated energy systems.

As highlighted in Table 6 with additional green marks, SimaPro and Gabi appear to be most suitable for building-integrated energy systems LCA while Umberto and OneClick are promisingly gaining more EPDs in its data base but need the use of add-in tools to do analysis on building integrated systems. In [58], an LCA on building and associated building systems was carried out using both SimaPro and Gabi in comparison. The result found showed that for the fifteen environmental impact categories from building systems, for the most part, the estimates from GaBi and SimaPro/ecoinvent are within 20% of each other, except for complementary works.

Table 5 Comparison of tools for the built environment multi-energy system LCA

Tool Name	Database	LCIA	Follows ISO 14040 Guidelines	Generic	Building in General	Integrated Energy Systems	Country	Access
ECOSOFT				✓			Austria	http://www.ibo.at/en/ecosoft.htm
One Click LCA	✓	✓	✓		✓		Finland	http://www.oneclicklca.com/green-building-software
COCON				✓			France	http://eosphere.fr/COCON-comparaison-solutions-constructives-confort.html
ELODIE				✓			France	http://www.elodie-cstb.f/default.aspx
EQUER	✓	✓	✓	✓			France	http://www.izuba.fr/logiciel/equer
GaBi-Build-IT	✓	✓	✓	✓			Germany	http://www.pe-international.com/sweden/services-solutions/green-building/building-lca/
LEGEP	✓	✓	✓	✓			Germany	http://www.legep-software.de/
SBS	✓	✓	✓	✓			Germany	http://www.sbs-onlinetool.com
LEGEP Software GmbH	✓	✓	✓	✓			Germany	https://legep.de
Klimagassregnskap				✓			Norway	http://www.klimagassregnskap.no/
Arquimedes				✓			Spain	http://arquimedes.cype.es/
EcoEffect				✓			Sweden	http://www.ecoeffect.se/
Eco-bat				✓			Switzerland	http://www.eco-bat.ch/index.php?option=com_content&task=blogcategory&id=14&Itemid=30
GreenCalc+				✓			Netherlands	http://www.greencalc.com/
envest 2				✓			UK	http://envestv2.bre.co.uk/
Bilan Produit ADEME					✓		France	http://www.base-impacts.ademe.fr/bilan-produit
EIME				✓			France	http://codde.fr/en/our-software/eime-en/eime-presentation
TEAM	✓	✓	✓		✓		France	http://ecobilan.pwc.fr/en/team.html
Qantis suite					✓		France	https://quantis-suite.com/free_product.html
GaBi	✓	✓	✓		✓		Germany	http://www.gabi-software.com
OpenLCA					✓		Germany	http://www.openlca.org/
SULCA					✓		Germany	http://www.simulationstore.com/sulca
Umberto	✓	✓	✓		✓		Germany	http://www.umberto.de/en/
GEMIS	✓				✓		Germany	https://ghgprotocol.org/Third-Party-Databases/GEMIS
SimaPro	✓	✓	✓	✓	✓	✓	Netherlands	http://www.pre-sustainability.com
Carbon Footprint					✓		UK	https://www.carbonfootprint.com/
Athena Impact Estimator		✓		✓			Canada	
Athena EcoCalculator		✓		✓			Canada	http://www.athenasmi.org/our-software-data/impact-estimator/
BEES	✓	✓		✓			USA	http://www.athenasmi.org/tools/ecoCalculator/
Tally				✓			USA	http://www.nist.gov/el/economics/BEESSoftware.cfm/

Table 6 Software tools most suitable for building integrated energy system LCA

Tool Name	Database	LCIA	Follows ISO 14040 Guidelines	Generic	Building in General	Integrated Energy Systems	Highlights
GaBi	✓	✓	✓	✓	✓	✓	Database is from Ecoinvent, Gabi, and the US Input-Output
SimaPro	✓	✓	✓	✓	✓	✓	Database is more robust, it includes Ecoinvent, industry data, input-out data from the US, Japan, Switzerland, Netherlands, etc.
Umberto	✓	✓	✓	✓	✓		Database is from Ecoinvent, and Gabi Netherlands, etc.
OneClick	✓	✓	✓	✓	✓		Finnish data with growing addition of other Environmental Products Declarations (EPDs) from other countries

There was only one difference for climate change values, which may have been due to truncation errors in the software database and may be a basis for further investigation. Therefore, to avoid the truncation error and obtain more precise estimates of the actual emissions contained in buildings integrated systems, a hybrid LCA approach could be used as proposed by the same author [58]. In summary, the tool used in LCA of building-integrated energy systems will depend on the users' access to the needed database and EPDs, training capability, and preferences as the ones presented in Table 6 as most suitable are subject to the criteria used for the comparison. Therefore, in the Sect. 3.2, we propose criteria that any of the users' preferred tool is expected to possess.

3.2 Evaluation Criteria for the Adaptability in Developing Unified LCA Tool for Building Integrated RES

The LCA process for building-integrated energy systems requires certain essential features. Based on selected suitable software for LCA of related systems integrated into buildings, as discussed in Sect. 3.1, a set of criteria is summarized in Table 7, in line with related works [54] are presented that could be useful in developing a unique tool for building integrated RES LCA.

4 Conclusion

The improvement of the world's power grids could help achieve an energy supply that is sufficient, efficient, affordable, and sustainable for the built environment. The advantages of transitioning to renewable energy sources are widely debated, and it is believed that the benefits outweigh the costs. Environmental impacts of CO2 emissions resulting from the combustion of fossil fuels is significant and alarming.

Table 7 Classification and evaluation criteria for developing comprehensive building integrated energy systems LCA Tool

Criteria classification	Software tools	Databases
1. Comprehensiveness		
(a) Building-integrated energy system specificity	(a) Building-integrated energy system specificity (b) Generic	(a) Building-integrated energy system specificity (b) Generic
(b) Goals, scope, and system boundaries	The assessment approach should be applied. (a) Cradle-to-Grave method as in EN 15978. (b) Cradle-to-cradle method as in EN15978. (c) Further features such as scenario information modeling.	The assessment approach should allow. (a) Cradle-to-Grave method as in EN15804 and as may be applicable for EN 15978. (b) Cradle-to-Cradle method as in EN15804 and as may be applicable for EN 15978. (c) Incorporation of further features such as scenario information modeling.
(c) Indicators	(a) Both full and partial coverage of indicators set in EN 15978 + additional indicators. (b) GHG emissions only. (c) May allow further study such as LCC and SLCA.	(a) Both full and partial coverage of indicators set in EN 15978 + additional indicators. (b) GHG emissions only. (c) May allow further study such as LCC and SLCA.
(d) Modeling	Assessment options ranging from the most comprehensive to the most basic, for instance, covering: (a) Specific elements and components of the energy system. (b) The complete energy system, allowing for enough adaptability to meet the unique design and operational requirements of the system.	Assessment options ranging from the most comprehensive to the most basic, for instance, covering: (a) Specific elements and components of the energy system. (b) The complete energy system, allowing for enough adaptability to meet the unique design and operational requirements of the system.
2. Robustness		
(a) Compliance with EN standards and methodological level adherence	Assessment options ranging from the most comprehensive to the most basic, for instance, covering: In alignment with EN15978 with (a) Extension to fit with methodological levels. (b) Either external evaluation or self-declaration. (c) Aligned for general aspects.	Assessment options ranging from the most comprehensive to the most basic, for instance, covering: In compliance with EN15804 with (a) Extension to fit with methodological levels. (b) As a whole. (c) Aligned for general aspects.

(continued)

Table 7 (continued)

Criteria classification	Software tools	Databases
(b) Quality of data	The tool should facilitate: (a) Reliability assessment of the quality of the data input. (b) Sensitivity analysis (e.g., check the influence of parameters and datasets on results). (c) Uncertainty analysis (e.g., check variability of results). (d) Scenario analysis (e.g., check of alternative options). (e) Analysis of uncertainty (e.g., check variability of results).	Enabling data quality assessment, the following should be considered: (a) High-quality data (in terms of geography, time, manufacturing, operations, and system technology, and accuracy) should be made available. (b) In the case of adapting a dataset, specify whether the database provides data quality assessment or simply enables it.
(c) Transparency and verification	It is important to: (a) Keep track of the sources of information, data, and assumptions used in the modeling process, or to document them in detail in the software itself (data available and accessible at unit process level). (b) However, where there is no way to track or verify the data or assumptions used in the modeling, nor are they documented in any way within the software, the use of third-party verification and validation by the national government is strongly encouraged.	It is important to: (a) Keep track of the sources of information, data, and assumptions used in the modeling process, or to document them in detail in the software itself (data available and accessible at unit process level). (b) However, where there is no way to track or verify the data or assumptions used in the modeling, nor are they documented in any way within the software, the use of third-party verification and validation by the national government is strongly encouraged.
3. Operability and barriers		
(a) Accessibility	It is important that the tool should have the following properties: (a) The web interface should be easy to use, and maybe integrated into cloud-based platforms. (b) The tool should support statistical analysis. (c) Installation of software tools should be compatible with common operating systems and easy to install.	(a) Information at the unit level of specificity should be provided. (b) The use of specific design features to access data, easy to access, modify, transfer, and managed. (c) Basic flows and/or quantified indicators may be provided in system process datasets or external software.

(continued)

Table 7 (continued)

Criteria classification	Software tools	Databases
(b) Interoperability and data exchange	While the software tool is expected to work independently, and conversion factors between measurement units are provided as an additional service, the following should be included in the tool: (a) Design and LC inventory can be imported and exported. (b) Design information from building information modeling (BIM) tools can be imported or exported.	Design and LC inventory can be imported and exported. For specific energy system information, it should be accepting import and export to external software that will provide key supporting data. For instance, in Photovoltaic system LCA, real-time information on irradiation and energy production per period would help provide data on energy inputs or requirements during the system operational phase.
(c) Interoperability and data exchange	Tools may be available for free or at a commercial affordable rate. Availability for training supports should be available either at: (a) Demo or free trial. In addition to the demo, documentation and training. (b) In-person or distance learning options with customer support after product purchase.	Access to data should be available for free for research purposes.
(d) Training and capability support		Availability for training supports on accessing and usage of the database should be available either at: (a) Demo or free trial. In addition to the demo, documentation and training. (b) In-person or distance learning options with customer support after product purchase.

Hence, the growing preference for renewable energy sources. For the built environment, the importance of developing a unique approach for assessing the RES integrated into them is pertinent. This study presented a method for tracking and assessing the environmental impact of different building integrated RES from energy consumption, production, and waste throughout the entire life cycle of the system in order to effectively decide on the best choice of system and to monitor greenhouse gas emissions. Building Integrated RES renewable energy systems utilize land and material resources, and these resources are within limits. As a result, the proposed building integrated RES LCA evaluation criteria as presented in this study is useful to assess the impact of these resources so as to plan for the mitigation of consequences of the limits of the different resources of the RES on society and the built environment. This assessment helps determine the most suitable choice to adopt.

References

1. European Commission, 'Reference document on best available techniques for energy efficiency', European Commission BREF, February, pp. 1–430 (2009). Available Online. https://eippcb.jrc.ec.europa.eu/sites/default/files/2019-11/ENE_Adopted_02-2009.pdf

2. European Commission, 'Reference Document on BAT on emissions from storage', European Commission BREF, July 2006. Available Online. https://eippcb.jrc.ec.europa.eu/reference/emissions-storage

3. Fawkes, S., Oung, K., Thorpe, D.: Best Practices and Case Studies for Industrial Energy Efficiency Improvement. (2016). Available Online. https://c2e2.unepccc.org/wp-content/uploads/sites/3/2016/02/best-practises-for-industrial-ee-web.pdf

4. IGTIC, 'Experience of Transition to the Best Available Techniques in Electric Power Industry: Large Combustion Plants', International Centre for Green Technologies and Investment Projects (IGTIC) in Cooperation with the European Union's (EU) (2020). Available Online. https://wecoop.eu/news-kazakhstan-bat-in-power-industry/

5. OECD: Annual Report, Paris (2009). https://doi.org/10.1787/annrep-2009-en

6. Andew Pilipchul, Practical Aspects of BAT Implementation in Belarus Andew Pilipchul Republic of Belarus Law "on Atmospheric Air Protection" (2008). Available Online. https://unece.org/fileadmin/DAM/env/documents/2019/AIR/Capacity_Building/BAT_workshop_2019/5_2_BAT_good_practice_Belarus_Pilipchuk_eng_1_.pdf

7. European Commission. The Sevilla process: a driver for environmental performance in industry. April, 6–7 (2000). Available Online. https://eippcb.jrc.ec.europa.eu/about/sevilla_process

8. EU, 'BAT Reference Documents', Sevilla (2008). Available Online. https://eippcb.jrc.ec.europa.eu/reference

9. World Energy Outlook, International Energy Agency (2022). Available Online. https://www.iea.org/reports/world-energy-outlook-2022

10. IEA. Renewable Energy & Energy Efficiency Partnership, 'Energy efficiency technologies and benefits: Sustainable Energy Regulation and Policymaking for Africa', April, pp. 1–29 (2012). Available Online. https://www.unido.org/sites/default/files/2009-02/Module12_0.pdf

11. EU, Special Report Energy Efficiency in Enterprises (2022). https://doi.org/10.2865/986796

12. IEA, Energy Efficiency (2021). Available Online. https://www.iea.org/reports/energy-efficiency-2022

13. IEA. Net zero by 2050: a roadmap for the global energy sector. 1–224 (2021). Available Online. https://www.iea.org/events/net-zero-by-2050-a-roadmap-for-the-global-energy-system

14. Tatang, N., Ray, T.: Design and planning of energy efficient building : a critical review. Int. J. Eng. Res. Appl. **12**(2), 28–31 (2022). https://doi.org/10.9790/9622-1202012831

15. Malinauskaite, J., Jouhara, H., Egilegor, B., Al-Mansour, F., Ahmad, L., Pusnik, M.: Energy efficiency in the industrial sector in the EU, Slovenia, and Spain. Energy. **208** (2020). https://doi.org/10.1016/j.energy.2020.118398

16. Malinauskaite, J., Jouhara, H., Ahmad, L., Milani, M., Montorsi, L., Venturelli, M.: Energy efficiency in industry: EU and national policies in Italy and the UK. Energy. **172**, 255–269 (2019). https://doi.org/10.1016/j.energy.2019.01.130

17. Dunlop, T.: Mind the gap: A social sciences review of energy efficiency. In: Energy Research and Social Science, vol. 56. Elsevier Ltd (2019). https://doi.org/10.1016/j.erss.2019.05.026

18. Marchi, B., Zanoni, S.: Supply chain management for improved energy efficiency: review and opportunities. Energies. **10**, 10 (2017. MDPI AG). https://doi.org/10.3390/en10101618

19. Janíček, F., Perný, M., Šály, V., Váry, M., Breza, J., Chochol, P.: The role of smart grid in integrating the renewable energies in Slovakia. Energy and Environ. **29**(2), 300–312 (2018). https://doi.org/10.1177/0958305X17748156

20. Erbach, G.: Briefing understanding energy efficiency. EPRS | European Parliamentary Research Service (2015). Available Online. https://www.europarl.europa.eu/RegData/etudes/BRIE/2015/568361/EPRS_BRI(2015)568361_EN.pdf

21. Patterson, M.G.: What is energy efficiency? Concepts, indicators and methodological issues. Energy Policy. **24**(5), 377–390 (1996). https://doi.org/10.1016/0301-4215(96)00017-1

22. Shao, B., Liu, X.: Calculation of energy saving based on building engineering. In: Advances in Intelligent Systems and Computing, pp. 837–844. Springer Verlag (2020). https://doi.org/10.1007/978-3-030-14118-9_82

23. EU, 'Industrial Emissions Directive for Best Available Techniques for Energy Efficiency', Industrial Emissions Directive 2010/75/UE (IPPC), no. 2021, p. 429, 2021. Available Online. https://environment.ec.europa.eu/topics/industrial-emissions-and-safety/industrial-emissions-directive_en

24. Ieep, B.: Implementation of the IPPC Directive (96/61): Analysis and progress of issues, no. 01, 2003. Available Online. https://ieep.eu/wp-content/uploads/2023/01/ippcbriefing.pdf

25. Chu, L.K.: Environmentally related technologies, and environmental regulations in promoting renewable energy: evidence from OECD countries. J. Environ. Stud. Sci. **13**, 177–197 (2023). https://doi.org/10.1007/s13412-022-00810-9

26. Tontu, M., Sultan, A.: Energy and environment nexus: environmental impact mitigation strategies. Int. J. Glob. Warm. **27**(3), 213–236 (2022). https://doi.org/10.1504/IJGW.2022.124199

27. arc A. Rosen: Assessing energy technologies and environmental impacts with the principles of thermodynamics. Appl. Energy. **72**(1), 427–441 (2002., ISSN 0306-2619). https://doi.org/10.1016/S0306-2619(02)00004-1

28. Nilsson-Lindén, H., Diedrich, A., Baumann, H.: Life cycle work: a process study of the emergence and performance of life cycle practice. Organ. Environ. **34**(1), 99–122 (2021). https://doi.org/10.1177/1086026619893971

29. UNEP and L. C. Initiative: UNEP guide to life cycle management – a bridge to sustainable products. Front. Biosci. – Elite. **1**, 108 (2006). Available Online. https://wedocs.unep.org/bitstream/handle/20.500.11822/33072/BRUGLCM.pdf

30. Nicoline, W., Helias, A.U.d.H., Ursula, M.T., Peter, E., Roland, C.: Analytical Tools for Environmental Design and Management in a Systems Perspective: The Combined Use of Analytical Tools, 1st edn. Springer-Science+Business Media, B.V, Dordrecht (2002). https://doi.org/10.1007/978-94-010-0456-5

31. EU, European Platform on Life Cycle Assessment (LCA). https://ec.europa.eu/environment/ipp/lca.htm. Accessed 16 Apr 2022

32. Recchioni, M., Mathieux, F., Goralczyk, M., Schau, E.M.: ILCD Data Network and ELCD Database: Current Use and Further Needs for Supporting Environmental Footprint and Life Cycle Indicator Projects (2012). https://doi.org/10.2788/78678

33. Eva, H.: 'Managers' interpretations of LCA: enlightenment and responsibility or confusion and denial? Bus. Strategy Environ. **9**, 239–254 (2000). https://doi.org/10.1002/1099-0836(200007/08)9:43.0.CO;2-6

34. Albertí, J., Balaguera, A., Brodhag, C., Fullana-i-Palmer, P.: Towards life cycle sustainability assessment of cities. A review of background knowledge. In: Science of the Total Environment, vol. 609, pp. 1049–1063. Elsevier B.V (2017). https://doi.org/10.1016/j.scitotenv.2017.07.179

35. Petit-Boix, A., et al.: Application of life cycle thinking towards sustainable cities: a review. J. Clean. Prod. **166**. Elsevier Ltd, 939–951 (2017). https://doi.org/10.1016/j.jclepro.2017.08.030

36. Rosenbaum, R.K.: Application of LCA in Practice, Life Cycle Impact Assessment: Theory and Practice. Springer, Cham (2018). https://doi.org/10.1007/978-3-319-56475-3

37. Chel, A., Kaushik, G.: Renewable energy technologies for sustainable development of energy efficient building. Alex. Eng. J. **57**(2), 655–669 (2018). https://doi.org/10.1016/j.aej.2017.02.027
38. Chwieduk, D.: Towards sustainable-energy buildings. Appl. Energy. **76**(1–3), 211–217 (2003). https://doi.org/10.1016/S0306-2619(03)00059-X
39. Hayter, S.J., Kandt, A., Kandt, F.-A.: Renewable energy applications for existing buildings. In: 48th AiCARR International Conference, pp. 1–17, Baveno-Lago Maggiore (2011) [Online]. Available: http://www.osti.gov/bridge
40. Wei, S.: Renewable energy technologies applied in architecture and its innovative research. In: IOP Conference Series: Earth and Environmental Science. Institute of Physics Publishing (2018). https://doi.org/10.1088/1755-1315/186/4/012007
41. Hueti, D.A.: Net Energy Analysis – An Economic Assessment (1976). [Online]. Available: https://www.science.org/doi/10.1126/science.192.4235.101
42. Varun, I.K., Bhat, Prakash, R.: LCA of renewable energy for electricity generation systems – a review. Renew. Sust. Energ. Rev. **13**(5), 1067–1073 (2009). https://doi.org/10.1016/j.rser.2008.08.004
43. Cabeza, L.F., Rincón, L., Vilariño, V., Pérez, G., Castell, A.: Life cycle assessment (LCA) and life cycle energy analysis (LCEA) of buildings and the building sector: A review. In: Renewable and Sustainable Energy Reviews, vol. 29. Elsevier Ltd, pp. 394–416 (2014). https://doi.org/10.1016/j.rser.2013.08.037
44. Chau, C.K., Leung, T.M., Ng, W.Y.: A review on life cycle assessment, life cycle energy assessment and life cycle carbon emissions assessment on buildings. Appl. Energy. **143**(1) Elsevier Ltd, 395–413 (2015). https://doi.org/10.1016/j.apenergy.2015.01.023
45. Nwodo, M.N., Anumba, C.J.: A review of life cycle assessment of buildings using a systematic approach. Build Environ. **162**. Elsevier Ltd (2019). https://doi.org/10.1016/j.buildenv.2019.106290
46. Majeau-Bettez, G., et al.: Choice of Allocations and Constructs for Attributional or Consequential Life Cycle Assessment and Input-Output Analysis (2017). https://doi.org/10.1111/jiec.12604
47. ISO: Environmental Management – Life Cycle Assessment – Principles and Framework (ISO 14040:2006). British Standard. **3**(1), 32 (2004). [Online] Available. https://www.iso.org/standard/37456.html
48. Lee, K.-M., Inaba, A.: Life cycle assessment: best practices of International Organization for Standardization (ISO) 14040 series, Committee on Trade and Investment, no. February, p. 99 (2004). [Online]. Available. https://www.apec.org/docs/default-source/publications/2004/2/life-cycle-assessment-best-practices-of-international-organization-for-standardization-iso-14040-ser/04_cti_scsc_lca_rev.pdf?sfvrsn=a26bb391_1
49. Nieuwlaar, E.: Life Cycle Assessment and Energy Systems, Reference Module in Earth Systems and Environmental Sciences. Elsevier (2013. ISBN 9780124095489,). https://doi.org/10.1016/B978-0-12-409548-9.01334-8
50. Ciceri, N.D., Gutowski, T.G., Garetti, M.: A tool to estimate materials and manufacturing energy for a product. In: Proceedings of the 2010 IEEE International Symposium on Sustainable Systems and Technology, ISSST, p. 2010 (2010). https://doi.org/10.1109/ISSST.2010.5507677
51. Shrivastava, S., Chini, A.: Estimating energy consumption during construction of buildings: a contractor's perspective, pp. 18–21. Proceedings of the World Sustainable Building Conference, 18–21 October 2011 Helsinki, Finland, no. August 2017 (2011). [Online]. Available. https://www.researchgate.net/publication/273693109_Estimating_energy_consumption_during_construction_of_buildings_a_contractor%27s_perspective#fullTextFileContent
52. Ashby, M.: Materials and the Environment (Eco-Informed Material Choice), 2nd edn. Butterworth-Heinemann (2012). https://doi.org/10.1016/S1369-7021(09)70255-X
53. Al Ka'bi, A.H.: Comparison of energy simulation applications used in green building. Ann. Telecommun. **75**(7–8), 271–290 (2020). https://doi.org/10.1007/s12243-020-00771-6

54. Classification and evaluation criteria for assessing LCA software and data for buildings-draft 1.0 Parameter Software tools Databases Comprehensiveness. [Online]. Available: http://www.elodie-cstb.f/default.aspx

55. De Wolf, C., et al.: Criteria for Analysis of LCA Software Tools and Databases for Buildings-DRAFT 4.1. European Commission Joint Research Centre, Directorate B, Growth and Innovation, Unit 5 (2020). [Online]. Available. https://susproc.jrc.ec.europa.eu/product-bureau/sites/default/files/2021-10/UM3_Indicators_1-2_list_of_LCA_software_databases_v4.1.pdf

56. Olagunju, B.D., Olanrewaju, O.A.: Comparison of life cycle assessment tools in cement production. South African J. Ind. Eng. **31**(4), 70–83 (2020). https://doi.org/10.7166/31-4-2317

57. ISO, Environmental Management-Life cycle assessment-Goal and scope definition and inventory analysis (1998). [Online]. Available: https://www.sis.se/std-611594, Accessed June 3, 2022

58. Emami, N., et al.: A life cycle assessment of two residential buildings using two different LCA database-software combinations: recognizing uniformities and inconsistencies. Buildings. **9**(1) (2019). https://doi.org/10.3390/buildings9010020

Realizing Visual Comfort Parameters and Adaptive Thermal Comfort Models for Hot Climates

Boshra Akhozheya, Sawsan Dagher, Maryam Akho-Zahieh, Farhan H. Malik, Ariel Gomez, and Maisa El Gamal

1   Introduction

One of the main requirements that buildings must satisfy is the provision of a safe and comfortable indoor environment. In fact, the quality of the indoor environment, as defined by its three main axes—thermal, acoustic, and visual comfort—as well as the quality of indoor air, is a crucial factor for reasons related not only to health issues but also to the well-being and productivity of building occupants. As a result, the quality of the indoor environment is taken into account in the framework of all frequently applied practices and methods for evaluating the environmental performance of buildings. Comfort within buildings can be achieved using a wide variety of methods, including solar shading, thermal mass, natural ventilation, and insulation [1, 2]. The word "comfort" can be used to describe several states of physical and mental well-being as well as a happy or cozy sensation [3]. The study presented in this chapter focuses on the analysis of two significant axes defining comfort: thermal and visual comfort.

B. Akhozheya
Department of Building & Architectural Engineering, Polytechnic University of Milan, Milan, Italy

S. Dagher (✉) · F. H. Malik
Department of Electromechanical Engineering, Abu Dhabi Polytechnic, Abu Dhabi, UAE
e-mail: sawsan.dagher@adpoly.ac.ae

M. Akho-Zahieh
Department of Electrical Engineering, Applied Science Private University, Amman, Jordan

A. Gomez
Department of Architectural Engineering, United Arab Emirates Univeristy, Abu Dhabi, UAE

M. El Gamal
College of Natural and Health Sciences, Zayed University, Abu Dhabi, UAE

1.1   Thermal Comfort

The American Society of Heating, Refrigerating, and Air-Conditioning Engineers (ASHRAE) defines the term "thermal comfort"" as "the state of mind that reflects contentment with the thermal environment" [4]. The larger research community, which includes architects, engineers, quantity surveyors, and other professionals in the construction industry, accepts this idea of thermal comfort. It serves as the basis for thermal comfort standards from the International Standards Organization, including ISO 7730 and ASHRAE Standard 55 [3, 4]. Thermal comfort, as defined by the American Society of Heating, Refrigeration, and Air Conditioning Engineers (ASHRAE), is a psychological state of mind in which a person does not feel "too hot" or "too cold." It's a subjective response, or state of mind, in which a person demonstrates enjoyment with his surroundings. However, while determining what people regard as thermally pleasurable, a range of environmental or climatic as well as personal aspects must be considered [3].

The six fundamental components that directly affect thermal comfort, as defined by ASHRAE standards, can be separated into two categories: personal factors (occupant characteristics) and environmental factors (thermal environment conditions). The former are air temperature, mean radiant temperature, air speed, and humidity, while the latter are metabolic rate and level of clothing. Even though all of these factors may change over time, guidelines for assessing thermal comfort often refer to a stable state, with only slight temperature changes permitted [3].

To identify and develop design strategies for any climate, the determination of thermal comfort is fundamental. The bioclimatic design method for buildings mandates that designers use the surrounding environment throughout the year to achieve the appropriate level of thermal comfort for occupants. To develop thermal comfort standards, environmental scientists use models that can reach the neutral or optimal thermal comfort situation, focusing on the six components that affect thermal comfort that have been described. One of the most often employed thermal comfort models globally is the adaptive ASHRAE 55 thermal comfort model. The adaptive comfort model was created as a consequence of numerous field experiments conducted by various researchers over 20 years [1, 5–9]. Compared to occupants of centrally air-conditioned buildings, those who are more directly involved in maintaining their own indoor environment are more comfortable throughout a broader range of indoor temperatures. In addition to social interactions with indoor climates, the adaptive comfort theory is built on a psychological adaptation known as "occupant expectancy." [10]. Apart from the interactive nature of adaptive comfort and a wider range of thermal acceptability, the relationship between outdoor temperature and indoor comfort is another distinguishing feature of the theory [5]. The standard clearly indicates that this model is only to be used in naturally ventilated buildings because the database supporting ASHRAE's adaptive model did not include enough mixed-mode situations on which the model could be validated. The naturally ventilated mode of mixed-mode structures, which are typically seen in hot areas, is not mentioned. However, experience since Standard 55's release in 2004 demonstrates that practitioners are already utilizing that logical expansion to mixed-mode settings [11].

However, an arising issue is the adaptability of the ASHRAE model to hot climates. In hot climes, a lot of research has looked into the most appropriate comfort models that can be used in a new building [1, 10, 11]. There is currently a lot of debate regarding which thermal comfort standards should be used. Conventional regulations only recognize a small temperature range as potentially "optimal," i.e., a range of temperatures where the vast majority of a building's occupants would be comfortable. These traditional comfort criteria, such as the current ASHRAE and ISO standards, are still regarded as adequate anywhere in the world despite the wide range of climates, with just a little seasonal variation between summer and winter settings. Summer temperatures of nearly 22 °C, with the highest temperatures of about 26 °C, are appropriate for them. Numerous studies have considered this comfort range in literature [12, 13]. In warmer countries, where high electricity demand due to cooling loads is found [14], this would require the massive, in many circumstances long-lasting, use of air conditioning systems [15].

1.2 Visual Comfort

The European standard EN 12665 describes visual comfort as "a subjective condition of visual well-being caused by the visual environment" [16]. The human eye's physiology, the physical parameters indicating the amount of light and its distribution in space, and the spectrum emission of the light source are all factors. The assessment of certain factors that depict the connection between human needs and the light environment, such as (i) the amount of light, (ii) the uniformity of light, (iii) the quality of light in rendering colors, and (iv) the prediction of the risk of glare for occupants, has remained a joint method of studying visual comfort [17].

2 Methodology

Visual comfort parameters are reviewed, and an adaptive thermal comfort model that can be adopted in hot climates is selected. This technique will serve as a guideline for architects, designers, and engineers when designing a bioclimatic building.

2.1 Visual Comfort Parameters

From the point of view of comfort, visual capacity and visual comfort are extraordinarily important. The most common visual parameters are defined in multiple global standards. However, some studies have defined other parameters that could also be of significance when designing a buildings' interior space. The analysis presented in this chapter, outlines the distinct parameters adopted in the examined tools.

2.2 Adaptive Thermal Comfort Models

Based on the literature, there are several comfort models that are currently in use worldwide. In this study, the available comfort models were realized in different African countries to understand how the ranges of comfort temperatures, which are commonly used to design mechanical ventilation systems, differ from the different adaptive models. The realization of a comfort range more suitable to hot climates can help reduce cooling loads significantly.

3 Results

3.1 A Review of Visual Comfort Parameters in Literature

According to the overall evaluation context, structure, and system of each tool, the criteria used to evaluate visual comfort are grouped differently in each tool shown in the table below. The visual comfort assessment factors in BREEAM are categorized under the topic of "Visual Comfort" within the environmental category of "Health and Wellbeing" as shown in Table 1. While the majority of these criteria are mentioned under the subitem "Lighting and Illumination" in CASBEE, which is a part of the item "Indoor Environment," the corresponding credits in LEED each fall under the category of "Indoor Environmental Quality." The first three parameters in the SBTool fall under the performance issues of "Indoor Environmental Quality" and "Daylighting and Illumination," the fourth and fifth parameters are listed under the performance issue of "Service Quality," and the performance issue of "Social, Cultural and Perceptual Aspects," respectively. As specified in the following sections, glare-related issues in LEED are addressed in the context of "Daylight." It should be noted that various characteristics may be examined under several categories in these tools [18].

Additionally, additional parameters have been developed by researchers in multiple literature works [19, 20]. The visual comfort assessment methods are developed majorly in experimental setups under electrical lighting with few exceptions that address this phenomenon under daylight conditions. These methods rely on empirical models where subjective human response is correlated with a sophisticated relation of physical photometric quantities that represent perceived luminance contrast at the eye level. One of these models which addresses daylight-induced visual discomfort is Daylight Glare Probability (DGP) index. DGP is used to quantify the percentage probability of glare perception, developed for an office room under daylight conditions [21].

Table 1 Visual comfort parameters in different standards and literature

BREEAM	LEED	CASBEE	SBTool	[20]	[21]	[19]
Glare control	Interior lighting	Daylight	Appropriate daylighting in primary occupancy areas	Illuminance (lux)	Daylight Control	Daylight Glare Probability (DGP) index
Daylighting	Daylight	Anti-glare measures	Control of glare from daylighting	Daylighting autonomy (DA):	Glare protection	Glare impact (GI)
View out	Quality views	Illuminance level	Appropriate illumination levels and quality of lighting in non-residential occupancies	Useful daylighting index (UDI).	Control of illuminance	Vertical illuminance at the eye level
Internal and external lighting levels, zoning and control		Lighting controllability	Controllability (including several criteria regarding the degree of control for lighting systems)	Glare analysis		Relative contrast
		Perceived spaciousness and access to view	Access to exterior views from the interior			Relative contrast based on pixel illuminance

3.2 Adaptive Thermal Comfort Models in Hot Climates

There are a number of comfort models in use globally. In this study, the available comfort models were realized in different African countries to understand how the ranges of comfort temperatures used to design mechanical ventilations differ from the different models. The countries of North Africa have semiarid and arid desert climates, which are characterized by extremes in daily high and low temperatures, hot summers and cold winters, and little rainfall (roughly 200–400 mm per year for semiarid regions and less than 100 mm per year for desert regions) [22]. Maximum temperatures can be seen in Senegal, Mauritania and Mali, 90th where the percentile shows temperatures around 30 °C; on the other hand, cooler climates are found in Morocco and Tunisia on the uppermost North of the continent. Santy et al. adapted the comfort models in Table 2. in a hot and humid climate, Indonesia [13]. Their results of comfort temperatures align with the results found implementing the comfort models in the hot climates analyzed in Table 3.

Looking at Table 2, several models are created considering hot weather, with outdoor temperature limitations starting from 24–26 °C. Contrary to ASHRAE's [5], Humphreys and Nicol [9], and Toe and Kubota's [23] comfort models which demonstrate applicable ranges of temperatures starting at 10 °C which, reflecting on the 10th percentile temperatures in Table 3, are rarely observed in hot climates. Toe and Kubota instituted the ASHRAE RP-884 database to create an adaptive model for hot and humid climates by using mean daily temperatures, and they argue that the use of mean daily temperatures is better for predicting the comfort temperature rather than the mean monthly outdoor temperature [13]. Humphreys and Nicol's model follows a similar formula to that adopted by ASHRAE's, which is rational, knowing that their model is developed using data collected by De Dear and Brager [11] which was the basis of ASHRAE's model. Nguyen's adaptive comfort model

Table 2 Several adaptive comfort models in the literature

No	Source	Equation	Outdoor Temperature Limitation
1	ASHRAE 55-2004	$Tc = 0.31\ T_o* + 17.8$	10–33 °C
2	Humphreys and Nicol	$Tc = 0.54\ T_o* + 13.5$	10–34 °C
3	Nguyen	$Tc = 0.341\ T_o* + 18.83$	26–34 °C
4	Toe and Kubota	$Tc = 0.57\ T_o{}^\# + 13.8$	10–33 °C
5	Indraganti et al.	$Tc = 0.26\ T_{rm} + 21.4$	24.5–35.5 °C
6	Karyono	$Tc = 0.749\ T_d{}^\# + 5.953$	24–29 °C
7	Santy	$Tc = 0.61\ T_d{}^\# + 9.69$	24–30.8 °C
8	López-Pérez et al.	$Tc = 0.32\ T_{rm} + 18.45$	25.6–26.7 °C

Notes: *For ASHRAE Humphreys and Nicol, Nguyen, T_o is the mean monthly outdoor temperature; # for Toe and Kubota, Karyono and Santy, T_d are mean daily outdoor temperature; for Indraganti, T_{rm} is the running mean temperature

Table 3 Climate zoning of Northwestern African countries

Location	Characteristics		GH solar irradiation (kWh/m²)	Elevation (m)
	Air temperature (C)			
	90 percentiles	10 percentiles		
Algeria	27.4	18.3	5.92	558
Libya	23.8	20.9	6.13	416
Mauritania	30.1	25.3	6.04	263
Morocco	22.9	14.3	5.56	872
Tunisia	22.4	17.5	5.30	255
Western Sahara	26.3	20.5	6.10	252
Niger	29.6	25.8	6.26	460
Nigeria	28.8	25.4	5.44	329
Mali	30.1	27.3	6.02	320
Ghana	28.7	25.9	5.10	181
Senegal	30.2	26.8	5.80	53
Guinea	27.4	24.1	5.57	443

generated is applicable to naturally ventilated buildings under hot and humid conditions of South-East Asia [12]. Their research also revealed that adaptive activities do not appear to be particularly efficient at quite high temperatures and levels of humidity. As a result, the comfort range is a little bit smaller than it would be under more favorable circumstances [12]. López-Pérez et al. realized a model for educational buildings in Brazil, which has a hot and humid climate. However, the comfort range is narrow, which doesn't usually apply to the African countries selected; therefore, the application of this model was neglected for this study.

4   Discussion

To understand how these models perform at different comfort temperatures, the 90th percentile temperature in each country studied was input in the adaptive comfort temperatures. This will help realize differences from the ASHRAE's model. Fig. 1 demonstrates the comfort temperatures for each country following the adaptive models with the 90th percentile temperature; as expected the highest comfort temperatures can be designed for countries in Mauritania, Mali, and Senegal. The ASHRAE model gave comfort ranges between 24 and 27 °C, and the lowest comfort temperatures among other models in countries exhibiting higher outdoor temperatures more frequently. However, in countries where lower temperatures are more frequent, the Karyono and Santy model gave the lowest comfort ranges. Therefore, as reducing cooling loads is usually the target while maintaining well-being and comfort shouldn't be neglected, Santy and Karyono's models work best in hot climates, specifically in buildings with critical functions, such as schools, medical centers and clinics. According to Fig. 1, these models will provide short ranges between 24 and 28 °C. In offices or spaces where slightly higher comfort temperatures can be more tolerable and reducing cooling loads is a critical target, Indraganti, Nguyen, and Humphreys models can be best utilized in warmer
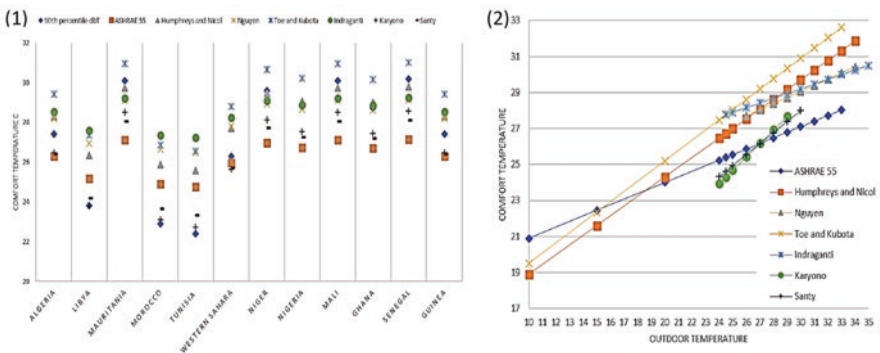

Fig. 1 (1) Comfort Temperatures in African Countries according to the different comfort models. (2) Comfort temperatures according to the limits of each thermal comfort model

climates. On the other hand, countries with lower temperatures can depend on ASHRAE; however, if reducing energy consumption is a significant target, Toe and Kubota's model is a more sustainable option in summer.

In the adaptive models by Nicol and Humphreys (when the outdoor temperature is above 20 °C), Toe and Kubota, Indraganti and Nguyen predict higher comfort temperature than the ASHRAE standard. This is comparable to saying that residents in hot, humid countries, where they are frequently exposed to outdoor temperatures exceeding 20 °C, tend to have greater preferred temperatures than people in other climates, where outdoor temperatures are lower. The adaptive models by Karyono and Santy, on the other hand, are much closer to ASHRAE and forecast a comfort temperature of roughly 27 °C, which is the same as the outdoor temperature. The remarkable argument lies in the fact that when the outdoor temperature is below 27 °C, these models predict lower than the ASHRAE standard, but in contrast, they predict higher when the outdoor temperature is above 27 °C.

5   Conclusion

To conclude, the demand for a secure and comfortable internal environment is one of the primary standards that buildings must meet. There are few reports on how occupant behavior adapts to changing thermal conditions in hot climates. The study discussed in this chapter focuses on the evaluation of two significant and critical axes that define comfort: thermal comfort and visual comfort. To provide thermal comfort for inhabitants, designers must utilize the surrounding environment year-round according to the bioclimatic design approach for buildings. The most typical visual parameters were identified as stated in international standards and other significant papers. The analysis in this work describes the specific parameters used in the tools under investigation and examines the climatic traits of several African locations using various thermal adaptation models. The available comfort models were realized on different countries in Africa to understand how the ranges of comfort temperatures, which are commonly used to design mechanical ventilation systems, differ from the different adaptive models. Significantly less cooling may be required if a comfort range more suited to hot regions can be achieved. The findings indicated that relying on the ASHRAE model in hot areas would necessitate the extensive, and in many cases, prolonged, use of air conditioning equipment. The models of Santy and Karyono performed well in hot environments. Indraganti, Nguyen, and Humphreys models are best used in warmer climates in offices or other buildings where somewhat higher comfort temperatures can be more tolerable. Decreasing cooling loads is a more significant aim. On the other hand, nations with lower temperatures can rely on ASHRAE, but if cutting energy use is a top priority, Toe and Kubota's approach is a better choice in the summer. This study can serve as a guideline when establishing a bioclimatic building, architects, designers, and engineers.

References

1. Dagher, S., Akhozheya, B., Slimani, H.: Energy analysis studying the effect of solar shading on daylight factors and cooling hours in an extreme weather. Energy Rep. **8**, 443–448 (2022). https://doi.org/10.1016/j.egyr.2022.10.231

2. Akhozheya, B., Dagher, S., Slimani, H.: Analyzing the impact of high thermal mass and natural ventilation strategies on indoor temperatures in an extreme climate. In: 2022 Advances in Science and Engineering Technology International Conferences (ASET), pp. 1–5 (Feb. 2022). https://doi.org/10.1109/ASET53988.2022.9734804

3. Efeoma, M., Uduku, O.: Assessing thermal comfort and energy efficiency in tropical African offices using the adaptive approach. Struct. Surv. **32**, 396–412 (2014). https://doi.org/10.1108/SS-03-2014-0015

4. ASHRAE HVAC 2001 Fundamentals Handbook.pdf | Carlos Martinez – Academia.edu., 2001. https://www.academia.edu/26602849/ASHRAE_HVAC_2001_Fundamentals_Handbook_pdf

5. ASHRAE 55-2013 | ASHRAE Store, 2021. https://www.techstreet.com/ashrae/standards/ashrae-55-2013?ashrae_auth_token=&gateway_code=ashrae&product_id=1868610

6. 14:00-17:00, "ISO 52000-1:2017." ISO. https://www.iso.org/cms/render/live/en/sites/isoorg/contents/data/standard/06/56/65601.html (2021)

7. Auliciems, A.: Towards a psycho-physiological model of thermal perception. Int. J. Biometeorol. **25**(2), 109–122 (1981). https://doi.org/10.1007/BF02184458

8. de Dear, R., Brager, G.S.: Developing an adaptive model of thermal comfort and preference. 1998, 2021. https://escholarship.org/uc/item/4qq2p9c6

9. Humphreys, M., Nicol, F.: Understanding the adaptive approach to thermal comfort. ASHRAE Trans. **104**, 991–1004 (1998)

10. Fountain, M., Brager, G., de Dear, R.: Expectations of indoor climate control. Energy Build. **24**(3), 179–182 (1996). https://doi.org/10.1016/S0378-7788(96)00988-7

11. de Dear, R.: Adaptive comfort applications in Australia and impacts on building energy consumption. In: IAQVEC 2007 Proceedings – 6th International Conference on Indoor Air Quality, Ventilation and Energy Conservation in Buildings: Sustainable Built Environment. Vol. 2, pp. 1–8 (2007)

12. Nguyen, A.T., Singh, M.K., Reiter, S.: An adaptive thermal comfort model for hot humid South-East Asia. Build. Environ. **56**, 291–300 (2012). https://doi.org/10.1016/j.buildenv.2012.03.021

13. Santy, H., Matsumoto, K.T., Susanti, L.: Bioclimatic analysis in pre-design stage of passive house in indonesia. Buildings. **7**(4), 24 (2017). https://doi.org/10.3390/buildings7010024

14. Akhozheya, B., Syam, M., Abdelghani, R., Aoul, K.A.T.: Retrofit evaluation of a residential building in UAE: Energy efficiency and renewable energy. In: 2018 5th International Conference on Renewable Energy: Generation and Applications (ICREGA), pp. 238–242 (2018). https://doi.org/10.1109/ICREGA.2018.8337615

15. Guedes, M.C., Lopes, L., Marques, B.: Bioclimatic project: general guidelines. In: Guedes, M.C., Cantuaria, G. (eds.) Bioclimatic Architecture in Warm Climates: A Guide for Best Practices in Africa, pp. 25–118. Springer International Publishing, Cham (2019). https://doi.org/10.1007/978-3-030-12036-8_3

16. EN 12665:2011 – Light and lighting – Basic terms and criteria for specifying lighting requirements. iTeh Standards Store, 2021. https://standards.iteh.ai/catalog/standards/cen/d7c62c9a-95ac-4ed8-9a40-862805aa5afc/en-12665-2011

17. Carlucci, S., Causone, F., De Rosa, F., Pagliano, L.: A review of indices for assessing visual comfort with a view to their use in optimization processes to support building integrated design. Renew. Sustain. Energy Rev. **47**, 1016–1033 (2015). https://doi.org/10.1016/j.rser.2015.03.062

18. Giarma, C., Tsikaloudaki, K., Aravantinos, D.: Daylighting and visual comfort in buildings' environmental performance assessment tools: a critical review. Proc. Environ. Sci. **38**, 522–529 (2017). https://doi.org/10.1016/j.proenv.2017.03.116

19. Hernández, F., Cejudo-López, J., Suárez, J., Muriano, M., Rueda, S.: Effects of louvers shading devices on visual comfort and energy demand of an office building. A case of study. Energy Proc. **140**, 207–216 (2017). https://doi.org/10.1016/j.egypro.2017.11.136

20. Persiani, S., Molter, P., Aresta, C., Klein, T.: Mapping of environmental interaction and adaptive materials for the autoreactive potential of building skins, 41st IAHS WORLD CONGRESSAt: Albufeira, Algarve, Portugal (2016)

21. Slipek, M., Sarey Khanie,M., Zukowska-Tejsen, D., Kolarik, J., Nielsen, T.: Visual Comfort Evaluation in Residential Buildings: A Simulation-Based Study (2017)

22. National Intelligence Council, North Africa: The Impact of Climate Change to 2030 (Selected Countries), 2022. https://www.dni.gov/files/documents/climate2030_north_africa.pdf

23. Toe, D.H.C., Kubota, T.: Development of an adaptive thermal comfort equation for naturally ventilated buildings in hot–humid climates using ASHRAE RP-884 database. Front. Archit. Res. (2017) https://www.scipedia.com/public/Chyee-Toe_Kubota_2013a

Assessment of the Potential of Commercial Buildings for Energy Management in Energy Performance Contracts

Antonio Garrido-Marijuan (ID)**, Roberto Garay-Martinez** (ID)**,**
Pablo de Agustín (ID)**, and Olaia Eguiarte** (ID)

1 Introduction

Building renovation is a key tool to decarbonize European households and businesses[1]. There is a clear potential linked to the improvement of the envelope [2] and smartness of the building itself [3]. This is strongly supported by the Energy Performance Building Directive (2018/844/EU), which encourages Member States to establish clear long-term renovation strategies, highlighting the value of energy renovation for both the envelope and the smart services application in buildings.

The potential of energy savings through envelope retrofitting has been largely demonstrated in the past decades for different climates. In this field, a number of systems have been developed over time, with external thermal insulation composite systems and ventilated façade systems being predominant [4, 5].

In building smartisation, the EC has focused on backing the EU housing market to use information and communication technologies based on their energy reduction potential. In this regard, the Smart Readiness Indicator (SRI) for buildings has been launched to rate buildings' capability of optimising energy efficiency and overall in-use performance, adapting their operation to the needs of the occupant and providing flexibility to the grid. Different studies show the potential for energy reduction linked to the increase in the SRI. [6] showed the positive effects of smart services on indoor environment quality and energy performance in the buildings,

A. Garrido-Marijuan (✉) · P. de Agustín · O. Eguiarte
TECNALIA, Basque Research and Technology Alliance (BRTA), Derio, Spain
e-mail: Antonio.garridomarijuan@tecnalia.com

R. Garay-Martinez
Institute of Technology, Faculty of Engineering, University of Deusto, Bilbao, Spain

while [7] demonstrated the positive influence of smart home tools and users' engagement to choose cost-effective solutions to provide thermal comfort.

Several studies show that the full exploitation of the smartness of the building is directly linked to ESCO market size, Demand Response (DR) market maturity, availability of Time-Of-Use (TOU), and explicit DR [8, 9]. In spite of the high potential, recent assessments show that the European building stock is far from being smart ready [10].

The aforementioned works have demonstrated the potential that energy renovation and energy management have for the reduction of the carbon footprint of the building stock. There is, however, a lack of works that effectively examine the cost-effectiveness linked to both the envelope retrofitting and the smartness of the building. The lack of research in this field could hinder the effective implementation and prevent building owners, occupants, and stakeholders from taking full advantage of these strategies.

This work tries to fill this gap, presenting an analysis method to assess the most suitable "target" market across Europe for energy renovation. The study focuses on different typologies of commercial buildings, assessing their potential for energy renovation under different boundary conditions such as climate, DR market maturity, and dynamic electricity tariffs. The assessment is performed in two stages. First the qualitative identification of those countries with the highest potential for renovation and energy management based on literature review such as public databases, statistics and surveys of the existing building stock and its performance. Second, the most suitable building typologies at specific regions are later modelled and simulated in different scenarios of renovation to assess the energy and monetary benefits from selected retrofitting scenarios, with a quantification of their potential. The study aims to serve as a decision-making process to explore and identify the potential for energy performance contracts (EPC) for different typologies at the European level.

2   Methodology

The proposed two-layered methodology based on the NOVICE project [11] and further developed under the SmartSPIN project [12] is divided into qualitative and quantitative assessment steps.

The qualitative analysis is built on a multi-criteria assessment to deal with the multiple factors that influence the potential and interest for EPC, such as building characteristics and legislative framework, which allows ranking the different typologies of commercial buildings based on their specific characteristics. Table 1 shows and describes the evaluation parameters and criteria proposed to choose the best candidates for EPC, as well as the scores associated to each parameter to determine their weight in the evaluation process.

Table 1 Building evaluation parameters

Parameter	Criteria	Score
Floor area	Floor area coverage is intrinsically linked to renovation potential. Large buildings have higher savings potential and therefore are more suitable for EPC.	Large (floor area >125% of the average value). Medium (floor area <125% and >75% of the average value). Small (floor area <75% of the average value)
Construction period	New or renovated buildings are highly efficient and have thus lower renovation potential than older buildings.	Old (built before 1990) → 3 points New (built after 1990) → 0 points
Energy consumption per m^2	Energy consumption is one of the key criteria for establishing the overall retrofitting potential of buildings, since large consumption should correspond to higher energy-saving potential.	Very high (>400 kWh/m^2) → 4 points High (>200 kWh/m^2; <400 kWh/m^2) → 3 points Medium (>100 kWh/m^2; <200 kWh/m^2) → 2 points Low (<100 kWh/m^2) → 1 point
SRI	Smart technologies are essential enablers for EPC since they allow for energy-efficient operation, adaptation to signals from the grid, and adapt the operation to variable requirements. Higher scores on the SRI are translated in higher potential for EPC.	High (>35%) → 2 points Medium (<35% and >15%) → 1point Low (<15%) → 0 points
ESCO market size	A well-established ESCO market increases the possibility of exploiting EPC.	Large → 2 points Medium → 1 point Small → 0 points
DR potential	The energy-saving and peak load shifting potential increases the interest in EPC.	High (>4%) → 2 points Medium (>2.5%; <4%) → 1 point Low (<2.5%) → 0 points
Availability of dynamic TOU tariffs	In order to fully exploit the potential through implicit DR strategies, a proper framework in the form of flexible tariffs must be available. A mature market increases the possibilities for the adoption of demand-side flexibility in the various building classes.	Dynamic TOU tariffs mainstream → 2 points Dynamic TOU tariffs emerging → 1 point No TOU tariffs or only static TOU rates → 0 points
Explicit DR	Some countries have commercially active markets regarding explicit DR, while others are still on early stages or have total lack of market instruments.	Commercially active → 3 points Partial opening → 2 points Preliminary development → 1 point Closed → 0 points
Incentives	Financial instruments for renovation projects are enablers for EPC.	3 instruments → 3 points 2 instruments → 2 points 1 instrument → 1 point No instruments → 0 points

It is important to highlight the differentiation between two types of parameters. On one hand, parameters (1)–(4) are directly linked to the EPC potential of the building itself. On the other side, the rest of the parameters (ESCO market size, DR market maturity, availability of dynamic TOU tariffs, explicit DR and incentives) are country-specific, and, therefore, independent of each commercial building's particularities within a country, providing essential information regarding the potential at different European regions and countries. Therefore, the qualitative analysis has as its outcome a two-layered classification, with the first layer being the score associated with the building type (size, SRI, age) and the second the score based on the geographical division.

The total score obtained for a specific building is the sum of the points obtained from the building characteristics and the points obtained from the country characteristics divided by two. The formula introduces a dimensionless weighting factor of 0.5 to reduce the impact of the country characteristics on the final score, fostering the interest in buildings in markets behind in terms of market maturity of DR or with lack of incentives. The application of the multi-criteria assessment to any building with sufficient information would give a score that ranks and benchmarks the building with similar buildings based on their potential for EPC. Nevertheless, specific typologies of buildings will rank high independent of the country. That is, large, nonrenovated buildings constructed before 1990 will have high potential even if the country lacks a mature DR market.

In the second step, buildings identified as highest interest are further evaluated in a quantitative manner. Building simulation is performed to assess the energy and economic impact of various renovation scenarios:

- Improvement of the energy-efficiency of building envelope.
- Improvement in the SRI, from SRI<15% to 15%<SRI<35%, was achieved by improvements in the management of the building (variable temperature control, controlled ventilation through variable air volume fans, artificial lighting control).
- Flexible, DR operation based on shifting the use of the HVAC system and other high consumption equipment for 3 h every day.

The proposed methodology is applied to the European market. The exploratory analysis is conducted at the country level, considering only relevant energy markets (countries with populations in excess of 5 million). Next, for the most interesting building typologies (3) and countries (3) of interest identified:

- Buildings: Medium office building, large mall, medium hotel
- Climates: Temperate oceanic (Dublin, Ireland), Temperate continental (Madrid, Spain), Warm Mediterranean (Athens, Greece)

The quantitative analysis is performed based on pre-existing, reference physics-based simulation models of commercial buildings found in the literature [13], adapted to the identified characteristics as the highest interest for EPC.

3 Results

3.1 Qualitative Outcomes

The following outcomes have been obtained (see Table 2).

For those parameters where data is unavailable for some countries, data has been taken as the value for the region (central Europe, etc.). In Figure 1 we present scores on the parameters for each country as a reference framework to understand the potential of different European countries based on the average values presented for these countries in each category.

Figure 1 shows that Nordic and West Mediterranean countries have the highest potential, with Eastern countries ranking among the least interesting ones. Furthermore, it can also be observed that specific typologies of buildings will

Table 2 Outcomes of the qualitative assessment

| Parameter	Criteria
Size of buildings	The average size across the EU shows that educational facilities have the highest size on average (1434 m^2) followed by hotels and restaurants (881 m^2), presenting the former the highest variability. The Netherlands and Denmark present the biggest buildings on average, being observed as a pattern that buildings get smaller from north to south.
Construction period	It can be observed that less than 20% of the stock was built after 1991 throughout Europe. In spite of some variability across regions, it can be concluded that building age distribution follows closely the average European pattern. Regarding the renovation rate, it ranges from below 0.5% (e.g. Spain) up to 8% or even greater (the Netherlands), with an average cost from less than 100€/m* (e.g. Poland) to over 1000 €/m^2 (e.g. Germany).
Energy consumption per m^2	In terms of energy consumption, the presented references show that most of the data is between 100 and 300kWh/m^2, with a very irregular distribution.
SRI	It can be observed that Nordic countries are front-runners, while southern and eastern countries are cautious adopters. Central European countries are in a middle position as followers.
ESCO market size	There is large diversity in Europe, with very well-developed markets in central and north-west countries (over 500 ESCOs in Germany, over 300 in France), and very small sizes in the rest of countries.
DR potential	The potential varies significantly per country. Malta and Greece (5%) present the highest numbers in relative terms, with the Czech Republic (0%) and Poland showing the lowest potential.
Availability of dynamic TOU tariffs	High diversity, with Nordic and Southern European countries presenting these tools for implicit DR.
Explicit DR	Central Europe has commercially active markets, with the countries of southern Europe behind on the development.
Incentives	Belgium, the Netherlands, and France present three instruments to foster EPC, being northern countries behind on this kind of incentives.
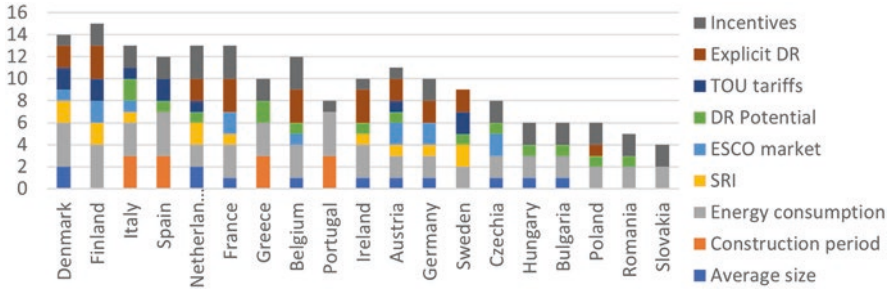
Fig. 1 Obtained results of the analysed European countries

rank high independently of the country. Large, nonrenovated buildings con-structed before 1990 will have high potential even if the country lacks a mature DR market.

3.2 Quantitative Assessment

Based on the countries and the scenarios of renovation previously defined, the simu-lations were performed based on the reference model and the characteristics identi-fied as most interesting for EPC. For each scenario, the following information is presented:

- Energy Consumption Per Conditioned Building Area in absolute terms [kWh/ m²·year]
- EPC potential, calculated as reduction of energy costs in €/year. To reach this number, the following equation is used:

$$\text{Savings}[C/\text{year}] = \left(C_{\text{baseline}} - C_{\text{scenario}}\right) \cdot \text{ Area} \cdot \text{Price}$$

(1)

- Payback of the intervention is calculated as the total investment divided by the total savings for each scenario. Being the energy price as follows (see Table 3):

Main outcomes are summarised in Table 4, Table 5, and Table 6:

4   Conclusions

This work presents a methodology to identify and properly quantify the most suit-able "target" market across Europe for EPC in commercial buildings. The explor-atory analysis is based on a two-stage analysis, hereby presented and applied to case studies. Different European countries and commercial building typologies have been qualitatively analysed to identify those with the highest potential for EPC and

Table 3 Prices of the different energy carriers per country. Source: Eurostat

Country	Electricity [€/kWh]	Gas [€/kWh]
Ireland	0.18	0.055
Greece	0.22	0.02
Spain	0.15	0.035

Table 4 Outcomes from the quantitative assessment for large offices in Ireland

Construction period	SRI	DR	Consumption [kWh/ m2·year]	EPC potential (€/year savings)	EPC payback
Before 1990	<15%	No	432	–	–
	>15%	No	183	224,106	4 months
		Yes	174	232,478	4 months
Renovated	<15%	No	213	196,636	5.3 years
	>15%	No	79	317,593	3.6 years
		Yes	74	322,263	3.6 years

Table 5 Outcomes from the quantitative assessment of a medium hotel in Greece

Construction period	SRI	DR	Consumption [kWh/ m2·year]	EPC potential (€/year savings)	EPC payback
Before 1990	<15%	No	415	–	–
	>15%	No	232	134,689	7 months
		Yes	193	164,246	6 months
Renovated	<15%	No	223	160,760	5.54 years
	>15%	No	104	235,135	4.13 years
		Yes	104	235,635	4.12 years

Table 6 Outcomes from the quantitative assessment of a mall complex in Spain

Construction period	SRI	DR	Consumption [kWh/ m2·year]	EPC potential (€/year savings)	EPC payback
Before 1990	<15%	No	413	–	–
	>15%	No	198	31,105	1.34 years
		Yes	189	32,530	1.28 years
Renovated	<15%	No	148	47,837	10.91 years
	>15%	No	101	54,753	10.3 years
		Yes	97	56,344	10.01 years

energy management based on a literature review (public databases, statistics…). The exploratory qualitative analysis particularly focuses on:

- Building-specific parameters to evaluate the EPC potential of different typologies.
- Country-specific parameters, which are independent among typologies and provide useful information in different European regions and countries.

Based on these parameters, the top candidates have been identified. In the next step, the EPC potential of three case studies from the top candidates has been assessed via simulation under different boundary conditions and scenarios of renovation. The analysis confirms the great potential of the identified candidates for both improvements in the envelope and the smartness of the building. This potential is higher than 75% if a complete upgrade of the building is performed, improving the performance of the envelope and increasing the SRI from <15% to 15%<SRI<35%.

The simulation outcomes suggest that active strategies have higher potential at lower cost, while the combination of active and passive strategies results in high-performing buildings with important revenues. On the other side, DR has very little impact when applied to high-performing buildings.

Regarding the economic potential of the evaluated retrofitting scenarios, active strategies present lower paybacks due to the relatively low investment needed for their implementation. On the other hand, the large investments needed for envelope renovation cause longer paybacks. In any case, medium-large offices and medium-large hotels present very attractive paybacks for all the considered retrofitting scenarios, as it's the case of SRI improvements on medium malls.

Results must be considered as a reference and not as a detailed calculation. This top-down approach, analysing a general case rather than specific case studies, is adequate for the present work, focusing on macro variables affecting the EPC market.

References

1. European Commission. A renovation wave for Europe – greening our buildings, creating jobs, improving lives (2020).
2. William, M.A., Suárez-López, M.J., Soutullo, S., Hanafy, A.A.: Building envelopes toward energy-efficient buildings: A balanced multi-approach decision making. Int J Energy Res, er.7166 (2021). https://doi.org/10.1002/er.7166
3. Eguiarte, O., Garrido-Marijuan, A., Garay-Martinez, R., Raud, M., Hagu, I.: Data-driven assessment for the supervision of District Heating Networks. Energy Rep. **8**(Supplement 16), 34–40 (2022) ISSN 2352-4847
4. Varela Luján, S., Viñas Arrebola, C., Rodríguez Sánchez, A., Aguilera Benito, P., González Cortina, M.: Experimental comparative study of the thermal performance of the façade of a building refurbished using ETICS, and quantification of improvements. Sustain. Cities Soc. **51**, 101713 (2019)
5. Fraga-De Cal, B., Garrido-Marijuan, A., Eguiarte, O., Arregi, B., Romero-Amorrortu, A., Mezzasalma, G., Ferrarini, G., Bernardi, A.: Energy performance assessment of innovative building solutions coming from construction and demolition waste materials. Materials. **14**(5), 1226 (2021). https://doi.org/10.3390/ma14051226
6. Ramezani, B., da Silva, M.G., Simões, N.: Energy Build. **249**, 111173 (2021)

7. Eguiarte, O., de Agustín-Camacho, P., Garrido-Marijuan, A., Vukovic, M., del Portillo, L., Romero-Amorrortu, A.: Engaging domestic users on demand response for heating cost reduction with a recommendation tool: case study in Belgrade. Energy Rep. **8**(Supplement 3), 325–331., ISSN 2352-4847 (2022). https://doi.org/10.1016/j.egyr.2022.01.069

8. Romero-Amorrortu, A., de Agustín-Camacho, P., Eguiarte, O., Huitema, G.B., Morcillo, L., Vukovic, M.: HOLISDER project: Introducing residential and tertiary energy consumers as active players in energy markets. Proceedings. **65**, 31 (2021). https://doi.org/10.3390/proceedings2020065031

9. Silva, C., Faria, P., Vale, Z.: Rating consumers participation in demand response programs according to previous events. Energy Rep. **6**, 195–200 (2020). https://doi.org/10.1016/j.egyr.2020.11.101

10. Buildings Performance Institute Europe. Is Europe ready for the smart buildings' revolution? Available online: http://bpie.eu/publication/is-europeready-for-the-smart-buildings-revolution/. Accessed on 22 Nov 2019

11. NOVICE PROJECT. https://cordis.europa.eu/project/id/745594

12. SmartSPIN PROJECT. https://www.smartspin.eu

13. Deru, M., Field, K., Studer, D., Benne, K., Griffith, B., Torcellini, P., Halverson, M., Winiarski, D., Liu, B., Rosenberg, M., Huang, J., Yazdanian, M., Crawley, D.: DOE Commercial Reference Building Models for Energy Simulation – Technical Report. National Renewable Energy Laboratory, Golden (2010)

The Incidence of Lighting System on Thermal Comfort Sensation: Experimental Evaluation

Nicoletta Del Regno, Rosa Francesca De Masi, Valentino Festa, Silvia Ruggiero, and Giuseppe Peter Vanoli

1 Introduction

The clean energy transition in the European Union goes through energy saving in building, considering that they are responsible for 36% of greenhouse gas emissions and 40% approximately of the European total energy consumption [1]. In 2022 the reduction of energy consumption in building is felt more due to the fossil fuel supply crisis. This has led to the implementation of a series of measures on energy saving at legislative level. For instance, in Italy for the winter 2022/2023 the switch-on period of the heating systems and the daily operating hours have been reduced [2]. In some companies or public buildings, the set point temperature has been lowered by $1 \div 2$ °C with respect the past seasons. According to Hoyt et al. [3] the reduction of the heating setpoint from 21 °C to 20 °C could saves averagely 34% of energy in an office building, considering seven different climate areas. One wonders, however, what can happen to the well-being conditions of the building occupants. In particular this study aims to investigate whether the thermo-hygrometric comfort conditions are influenced only by the ambient set-point temperature or also by other factors.

Buratti et al. [4] carried out an experimental campaign and showed that the importance of different environmental aspects was 34.5% for thermal, 35.7% for acoustical, and 30.1% for visual sensation. According to results from Frontczak and Wargocki [5], thermal comfort is considered more important than visual, acoustic comfort, and air quality. Frontczak et al. [6] also developed a study based on 2499

N. Del Regno · G. P. Vanoli
Department of Medicine and Health Sciences -Vincenzo Tiberio, University of Molise, Campobasso, Italy

R. F. De Masi · V. Festa · S. Ruggiero (✉)
Department of Engineering – DING, University of Sannio, Benevento, Italy
e-mail: sruggiero@unisannio.it

questionnaires on common house inhabitants. The responses indicated that manual control of the indoor environment is highly preferred for comfort satisfaction without a correlation with lighting or other parameters. Also Ricciardi et al. [7] developed a questionnaire for evaluating environmental comfort in 7 university classrooms in Italy providing 7-value and 13-value scales, finding that 55% of occupants overestimated the comfort condition using the 13-value scale. Krüger et al. [8] tested 16 males for 9 total days in a climate chamber, and they found that despite different daylighting configurations there were stable thermal conditions inside the room.

According to Xue et al. [9], luminous comfort depends on daylighting conditions and behavior patterns. In general, using artificial lighting for many hours per day could reduce luminous comfort. Castaldo et al. [10] highlighted that the levels of acceptance among occupants are greater than the standards of visual and thermal comfort point of view. For instance, even if the lighting levels were below 413 lux 74% of occupants declared neutral visual sensation. Considering the thermal comfort, the PMV calculated, around $0.44 \div 0.40$ is different from the thermal sensation resulting from questionnaires ($0.10 \div 0.11$). The authors conclude that this discrepancy could depend on the workplace's pleasant aesthetic and likable architecture that increase the workers' satisfaction. The study [5] highlights how characteristics of building users, such as psychological ones, thus factors unrelated to the indoor environment, can influence the indoor environment evaluation of comfort. Andargie and Azar [11] showed that both environmental conditions such as temperature, and relative humidity, illuminance and noise level than users personal characteristics affect occupants' comfort and cognitive abilities. In addition, demographical factors such as gender and age are determinants in the comfort metric. Laurentin et al. [12] demonstrated that thermal conditions do not influence visual comfort.

The study by Fakhari et al. [13] involved six office buildings and more than 100 people, showing that the correlation between lighting level and satisfaction with the microclimate has an R^2 value very low and equal to 0.015. The authors conclude that the level of illuminance has little significant impact on the thermal sensation. Furthermore, they conclude that occupants' responses to lighting conditions vary according to the age of people and not so much according to gender or time of day. In the present paper, on the other hand, with the same level of illuminance, the authors want to find a correlation between different lighting scenarios and the thermal sensation expressed by users in relation to the microclimate.

From the previous overview, it emerges that:

- There is a discrepancy between the assessment by means of standardized measures and that provided by users, since the standards do not also consider factors that come into play in the sensation of thermal comfort, such as the psychological aspect.
- There is a different feeling if the user can personally vary the thermal conditions of the surrounding environment.
- The physiological and psychological factors can affect the satisfaction of human thermal comfort sensations.

- The lighting system could interfere with the sensation of thermal comfort, given that the bright environment influences psychophysical well-being.

Even if investigated, these aspects are not easy to find in a single study with in-field measurements. The present paper aims to analyze how the possible lighting scenarios can influence the thermal sensation that the occupant has towards the microclimate, considering also different set-point ambient temperatures. In this context, the work deals with an experimental analysis inside a real-scale zero-energy building in Benevento Southern Italy. The building was designed to be the existing best practice of a new way of living, reducing the demands of active energy systems and covering the entire energy needs with deep use of renewable energies to close to zero the annual energy balance. The structure is a prototype of a detached house with a living area of approximately 70 m^2. The analysis was conducted for approximately one month between January and February 2022.

2   Methodology

The study is carried out in the living lab conceived as a home for two university students. The thermal zone in question is the bedroom, in which a male student of thirty years old carries out study work using the laptop in the afternoon. The occupant mostly sits at a desk facing the window from 3 pm to 7 pm.

All microclimate parameters are monitored to define the Predicted Mean Vote (PMV) and predicted percentage of dissatisfaction (PPD) following the international standard ISO 7730 [14] that implements the Fanger model. Surface temperatures, thermal flows through the various building components, and external climatic conditions are also measured. For the comfort index evaluation metabolic activity for all the days analyzed is set equal to 70 W/m^2. Considering that the man, for all measurement days, wore winter clothing consisting of trousers, sweater, shoes and socks, the thermal resistance of the clothing is evaluated as equal to 0.135 m^{2}K/W.

The study therefore involves the analysis of different lighting scenarios (color temperature and type of control) and different internal thermal conditions. In detail, the following have been implemented:

- Two different color temperatures for the lighting system
- Two different control logics
- Three different thermal conditions

The color temperature refers to warm or cold color temperature of the lights, called WARM or COLD respectively. The control logics used for the lighting system are also two: the first, called ON-OFF, in which the user switches on or off the lamps according to his needs; the second one, called LUX, provides for the switching on the lamp if the illuminance level, on the work plane, is below 250 lux. As regards the heating system, three set-point temperatures are chosen: 18 °C, 20 °C

and 22 °C. All the possible combinations of these scenarios are implemented and analyzed once a day, for 12 days of measurements.

The user is subjected to a questionnaire in which he expresses, for each hour, the thermal sensation on a 7-value graduated scale, going from very cold (−3) to neutral (0) to very hot (+3). The building occupant provides assessment results at every hour, both hourly averages and instantaneous.

3 Case Study

In 2018, in Benevento, a Mediterranean climate city [15], the University of Sannio inaugurated a full-scale living lab characterized by materials and technologies to be classified as nearly Zero Energy Building according to the law in force [1] (Fig. 1a). It is called BNZEB.

The building shows a pseudo-square plan of about 71 m^2 of conditioned floor, spread over one floor (3.6 m high) with a kitchen, a bathroom, a living room, two bedrooms, and a technical room (Fig. 1b). The windowed/opaque ratio is equal to 22.5% while the surface-volume ratio (S/V) is equal to 1.03 m^{-1}. The structure is characterized by Cross Laminated Timber structure (X-LAM) with wood fiber insulation (9.5 cm for the external wall and 12 cm for the roof). The thermal transmittance for external walls, roof, and the floor is 0.17 W/m^2 K, 0.23 W/m^2 K and 0.25 W/m^2 K, respectively. The windows are double glazing Argon filled and have a PVC frame.

The BNZEB is equipped with an air-to-air heat pump for heating, cooling, domestic hot water and mechanical ventilation services, with an electronic filtration. The nominal heat power is 3.18 kW and cooling power 2.14 kW. The HVAC system is integrated with a vertical geothermal field (2 m below ground) and an evacuated solar thermal collector (2.16 m^2). On the roof there is also a photovoltaic plant (5.3 kW$_p$) with electric storage of 6.5 kWh.

Fig. 1 External view (**a**) and room plan (**b**) of BNZEB

4 Sensor Setup and In-Field Monitoring

The four environmental parameters have been measured by means of a portable microclimatic station "400 IAQ and comfort kit" of Testo manufacturer (Fig. 2a). It is composed of a datalogger (Fig. 2b) and sensors of air temperature (called T_{a_in}), relative humidity (called RH_{in}), air speed (called AS), and globe temperature (T_g). The main technical characteristics are reported in Table 1.

The mean radiant temperature (T_r) is calculated based on T_g and T_{a_in} according to the Eq. (1).

$$T_r = \sqrt[4]{\left(T_g + 273\right)^4 + \frac{0.25 \bullet 10^8}{\varepsilon_g} \sqrt[4]{\frac{\left|T_g - T_{a\_in}\right|}{D}} \left(T_g - T_{a\_in}\right)} \, [°C] \tag{1}$$

where

D = globe diameter (150 mm)
ε_g = emissivity of the globe thermometer (0.95)
T_g = globe thermometer temperature
T_{a_in} = air temperature
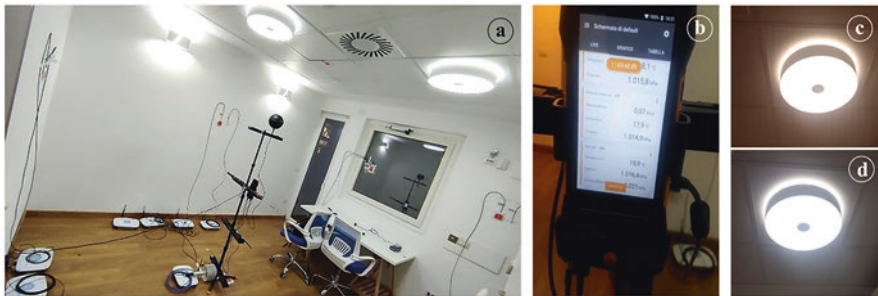
Fig. 2 Positioning of microclimate station (**a**); datalogger (**b**) lamp with color temperature warm (**c**) and cold (**d**)

Table 1 Technical data of used sensors

Probe	Range	Accuracy
T_{a_in}	0 ÷ 50 °C	±0.5 °C
RH_{in}	5 ÷ 95 %	±3% (10 ÷ 35% RH) ±2 % (35 ÷ 65 %RH) ±3 % (65 ÷ 90 %RH)
AS	0 ÷ 5 m/s	±(0.03 m/s + 4% of m.v.)
T_g	0 ÷ 120 °C	Tolerances Class 1, EN 60584-2

The monitoring period went from 18 January to 12 February 2022 with an acquisition step of 1 min. Different internal thermal and lighting scenarios are implemented, as described in the methodological section. In Fig. 2b, c the WARM and COLD lighting scenario is shown. The study considers only a single man in a single room; thus, it can lead to a sampling very small and without accurate conclusions. However, it is a preliminary study that will be repeated for other users and rooms.

5 Results

Figure 3 a depicts the average hourly microclimate rating provided by the user, with red dots, and the PMV calculated by means of field measurements, with green bars. The area highlighted in light green is the range in which, according to the UNI EN 7730 standard, the occupant feels a sensation of neutral thermal comfort. It corresponds to $-0.5 < PMV < 0.5$, with a maximum PPD value of 10%. In general, it can be seen that the user's votes are higher than those calculated with the numerical model, i.e., the user judges the environment warmer than it is described if a thermal comfort model is used. For the first four days of the test, when the set-point is 18 °C, for 75% of the hours the PMV values are lower than -0.5 ("quite cold"), while the occupant mostly rates the environment as thermally neutral. This shows that an indoor air temperature lower than 20 °C, in this case equal to 18°C, can guarantee thermal comfort for the occupant, and this condition is not always described by comfort models such as Fanger's. For the four days when the set point is 20 °C, the PMV is within the thermal neutrality zone for 80% of the hours, while the occupant expresses feeling "quite warm" or "warm" for 55% of the hours. Finally, for the last
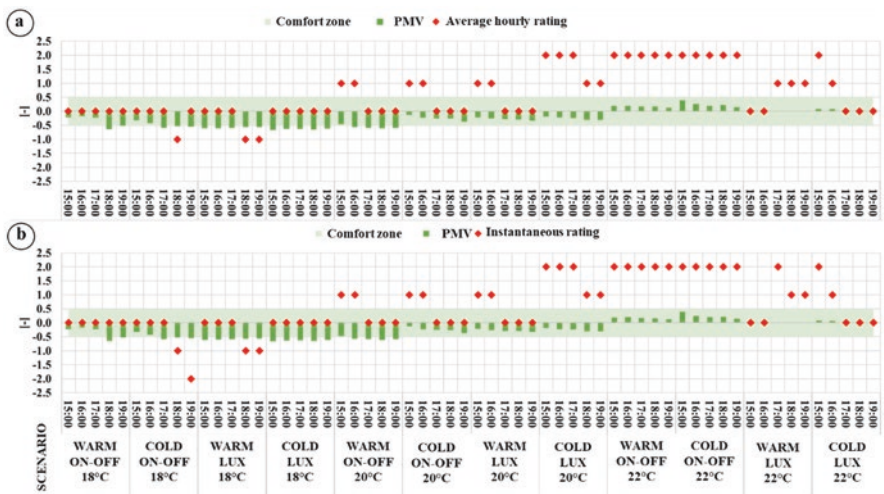

Fig. 3 PMV calculation and occupant vote average hourly (a) and instantaneous (b)

four days analyzed, the PMV values for all hours are within the comfort zone, while the occupant expresses "quite warm" or "warm" for 75% of the hours.

As regards the incidence of lighting scenarios, it has to be evaluated on subjective judgments, as the numerical comfort model does not take into account it. Considering the color temperature, by setting a control logic, e.g., ON-OFF, and with the same set-point, by varying only the color light, the thermal vote does not change, except for one hour of the second day, when he feels colder with cold light. In the case of LUX logic some small differences between WARM and COLD can be noted; in particular it would seem that the user feels colder when the light is warm. For instance, during days with LUX 20 °C, by varying the color temperature from WARM to COLD, the rating increases by one unit towards warmer sensation for 80% of the observations and by two units for 20% of the observations. This behavior is also found in the case of LUX 22 °C but only for the first two hours of analysis, after which cooler light gives a colder thermal sensation. The incidence of color temperature in the average hourly user judgments cannot be clearly and unequivocally deduced. Considering instead the incidence of the control logic, setting the other parameters equal, there is no unequivocal response in the thermal vote, which assumes no incidence of the lights control logic on the thermal sensation towards the environment.

Considering the instantaneous rating (Fig 3b), when the logic is ON-OFF at 20 °C and 22 °C by varying the color temperature, the judgment does not change while at 18 °C, for 40% of the observations, the user feels colder with cold lights. In the case of automatic logic, on the other hand, he feels warmer with cold lights, at 18 °C and 20 °C, while colder with cold lights at 22 °C. It is not possible to identify an unequivocal response by varying the lighting parameters, but if the occupant is in a lower temperature and has to choose when to activate the lighting system, he is more influenced by the color temperature in the instantaneous evaluation of the sensation of thermal comfort. By instead fixing the color temperature, for example, WARM and by varying the control logic, it is noted that at 18 °C with the LUX logic he feels colder than the ON-OFF logic; at 20 °C nothing changes and at 22 °C there is also a colder sensation. Setting the COLD scenario at 18 °C and 20 °C, the user feels colder with ON-OFF, while at 22 °C colder with LUX. It could be hypothesized that at low temperatures, if you have warm lights, it is preferable that they are controlled by the user, while if you have cold lights, they are controlled automatically.

6 Conclusions

The present work leads to some main conclusions. The building occupant judges the environment warmer than described if a static thermal comfort model is used. Thus, reducing the set point by 2 °C compared to the reference value (20 °C according to Italian law) still results in thermal comfort. A study on the same building during the previous winter showed that using a set point value of 18.7 °C reduces heating consumption by about 21% compared to using a set point value equal to 20 °C. Moreover,

if the occupant stays at a lower temperature (18 °C) and has to choose to activate the lighting system, he is more influenced by the color temperature in the instantaneous assessment of thermal comfort. Finally, if there are warm lights, it is preferable to be controlled by the user, while the cold lights are preferable to be controlled automatically.

The limit of the present study lies not significant number of subjects exposed to the test. Future developments will concern a greater number of users to be tested, varying their age and gender. Furthermore, the study conducted can be considered preparatory to the development of new numerical models for thermal comfort.

References

1. Directive 2010/31/EU of the European Parliament and of the Council of 19 May 2010 on the energy performance of buildings (recast)
2. Decreto del Ministro della Transizione Ecologica n. 383 del 6 ottobre 2022 (in Italian)
3. Hoyt, T., Arens, E., Zhang, H.: Extending air temperature setpoints: simulated energy savings and design considerations for new and retrofit buildings. Build. Environ. (2015). https://doi.org/10.1016/j.buildenv.2014.09.010
4. Buratti, C., Belloni, E., Merli, F., Ricciardi, P.: A new index combining thermal, acoustic, and visual comfort of moderate environments in temperate climates. Build. Environ. **139**, 27–37 (2018)
5. Frontczak, M., Wargocki, P.: Literature survey on how different factors influence human comfort in indoor environments. Build. Environ. **46**, 922–937 (2011)
6. Frontczak, M., Andersen, R.V., Wargocki, P.: Questionnaire survey on factors influencing comfort with indoor environmental quality in Danish housing. Build. Environ. **50**, 56–64 (2012)
7. Ricciardi, P., Buratti, C.: Environmental quality of university classrooms: Subjective and objective evaluation of the thermal, acoustic, and lighting comfort conditions. Build. Environ. **127**, 23–36 (2018)
8. Krüger, E.L., Tamura, C., Trento, T.W.: Identifying relationships between daylight variables and human preferences in a climate chamber. Sci. Total Environ. **642**, 1292–1302 (2018)
9. Peng Xue, C.M., Mak, H.D.C.: The effects of daylighting and human behavior on luminous comfort in residential buildings: A questionnaire survey. Build. Environ. **81**, 51–59 (2014)
10. Castaldo, V.F., Pigliautile, I., Rosso, F., Pisello, A.L., Cotana, F.: Investigation of the impact of subjective and physical parameters on the indoor comfort of occupants: a case study in central Iatly. Energy Procedia. **126**(2001709), 131–138
11. Maedot, S.: Andargie, Elie Azar, An applied framework to evaluate the impact of indoor office environmental factors on occupants' comfort and working conditions. Sustain. Cities Soc. **46**, 101447 (2019)
12. Laurentin, C., Bermtto, V., Fontoynont, M.: Effect of thermal conditions and light source type on visual comfort appraisal. Lighting Research & Technology. **32**(4) (2016)
13. Fakhari, M., Fayaza, R., Asadi, S.: Lighting preferences in office spaces concerning the indoor thermal environment. Front. Archit. Res. **10** (2021)
14. INTERNATIONAL STANDARD, ISO 7730:2005(E) Ergonomics of the thermal environment – Analytical determination and interpretation of thermal comfort using calculation of the PMV and PPD indices and local thermal comfort criteria
15. Kottek, M., Grieser, J., Beck, C., Rudolf, B., Rubel, F.: World Map of the Köppen-Geiger climate classification updated (2006)

Investigating the Effect of Distance Between Windows and Floor on Energy Losses in Residential Building Façades by Using Design Builder

SeyedehSara Yazdi Bahri, Marc Alier Forment, and Alberto Sanchez Riera

1 Introduction

One of the most difficult problems in the globe has been the supply of fuel and energy [1]. Energy and energy efficiency become increasingly crucial issues in Iran, especially with the removal of subsidies [2]. Energy consumption is unavoidable, according to the purpose of housing, which is to protect people from extreme heat and cold [3]. To capture more solar heat during the colder months of the year, architects used to design different types of openings [4, 5]. The lack of available energy sources is a recurrent issue in both industrialized and developing nations because the industry depends on fossil fuels [6]. According to the industrial activity of different nations, 30–35% of the total energy consumed is used in buildings and residences, and 50–60% of the energy spent by households is used for cooling and heating buildings during various times of the year [7, 8]. Because of this, 15–20% of all energy consumed is utilized to heat and cool interior spaces in homes [9, 10]. Following that, actions done to improve the building's quality [11] result in discernible reductions in energy utilization [12, 13].

Subsequently, approximately 99% of the energy used in these buildings comes from gas and oil production, according to data published in the energy balance sheet by the Deputy of Energy Affairs Ministry of Energy in 2005. The household and commercial sectors consume energy at 35% and 44%, respectively. Windows are the most crucial component of a building that absorbs solar energy and transfers heat, and the windows' placement affects how much light they transmit [14]. The second factor in a building's thermal dissipation is the thermal exchange and heat transfer that occurs inside and outside of it through its walls, windows, doors, roofs, floors, and seams and windows, which account for 20% of thermal dissipation [15].

S. Yazdi Bahri (✉) · M. Alier Forment · A. Sanchez Riera
Universitat Politècnica de Catalunya, Barcelona, Spain
e-mail: seyedehsara.yazdibahri@upc.edu

The most crucial component of a building is its windows [16, 17]. In other words, they give buildings light, heat, airflow, and aesthetic appeal [18]. The primary source of energy loss at any time of year may be windows placed carelessly [19, 20].

Moreover, initiatives to reduce the consumption of fossil fuels have increased in recent years due to rising prices and social concern over environmental deterioration [21]. The high amount of energy consumed for heating and cooling in Iran shows how important the issue of energy consumption to optimizations is in this country. The simulation software is used by designers to reduce energy consumption in a building. Hence, the present research aims to provide comfort by investigating the distance between window frames and the floor. That being the case, the following questions are posed for appropriate answers to be obtained:

– How much does the distance between window frames and the floor affect the amount of air tension in the hot seasons?
– How much does the distance between window frames and the floor affect the energy loss?

The hypothesis in this research is that airflow and natural ventilation are needed strongly according to the under-studied area's climate. As the distance between window frames and the floor decreases, natural ventilation in mild and humid climates decreases.

2 Theoretical Framework

2.1 Natural Ventilation and Thermal Comfort

The term "thermal comfort circumstances" refers to a range of temperature and humidity when the body's natural mechanism for regulating temperature is least active [22]. The thermal comfort range can be determined by many variables, including temperature, garment insulation, relative humidity, airflow speed, average radiant temperature, and metabolism [23]. According to the psychometrics' standard thermometric comfort range, the thermal comfort range is between 21 and 27.7 °C, and the humid comfort range is between 30% and 65%. [24]. In this research, the dry temperature and daily relative humidity (0, 3, 6, 9, 10, 15, 18, and 21 O'clock) were measured to evaluate these criteria. By placing these phenomena in the building-bioclimatic chart and connecting them, the following zones resulted (Fig. 1):

1. Heating facilities are required in December, January, February, and March.
2. No heating facilities are needed in April, May, August, September, October, November, and December.
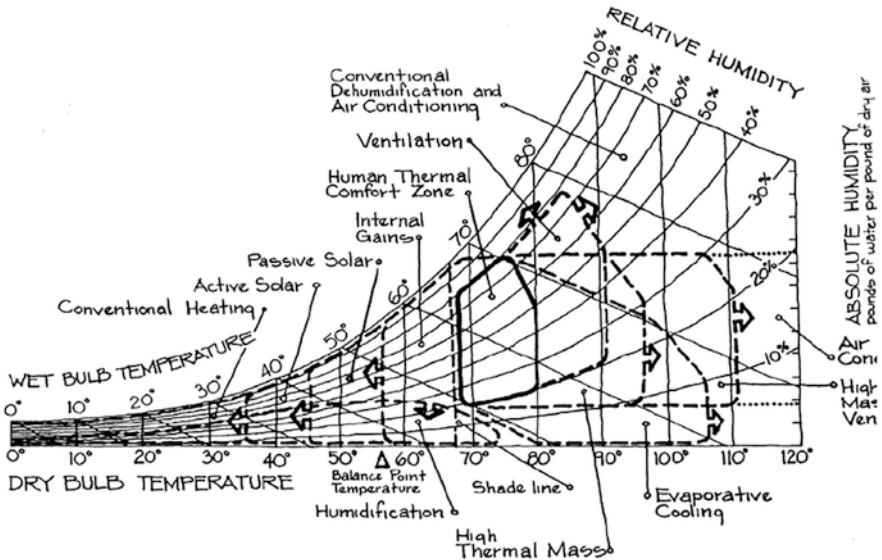3. In June and July, there is comfort in shades.

Fig. 1 Givoni's bioclimatic chart of Bandar-e-Anzali

The comfort zone can be determined on this chart. In Iran's meteorology calendar, relative humidity is usually recorded three times (6.5, 12.5, 18.5 O'clock) daily. Since the clock changes in relative humidity are opposite of the round-the-clock changes in temperature, the maximum humidity is before sunrise, and the minimum humidity is just after midday. Hence, the relative humidity at 6.5 and 12.5 O'clock of the day can be considered as maximum relative humidity and minimum relative humidity. If the information on relative humidity is not available, it can be calculated using dry and wet temperature and a psychometrics chart.

2.2 Natural Ventilation and Thermal Comfort

The seams of the building, which allow air to enter and exit, are another crucial element in thermal dissipation. In actuality, as warm air rises, cold air seeps into buildings through their seams, increasing energy consumption [25, 26]. Energy dissipation may be exacerbated by additional elements such as openings, high roofs, chimney openness, and wind speed [27]. Moreover, air cooler channels and air conditioning valves cause hot air to leave the room and cold air to enter [28, 29]. The direct correlation between air penetration in buildings and energy use indicates that air penetration must be avoided to reduce energy use [30].

3 Methodology

In this study, at first, the importance of natural ventilation in the interior of buildings in mild and humid climates is evaluated using library resources. After that, the energy consumption rate is analyzed using a computer simulation method for 12 months of the year in the study area. Hence, a residential building, which has windows with a different distance between window frames and the floor, is modeled by Design Builder. Finally, the conducted studies and the relation between them are analyzed. There are various formulas and methods to calculate the thermal load of the building. One of the best methods is to use energy modeling software because energy consumption simulating software is an efficient tool that can consider all complex interactions of the building indoors and outdoors. And so they can be one of the useful calculation techniques which are in relation to energy saving in a building. One of these software is Design Builder, a more comprehensive and advanced version of Energy Plus which can estimate the heating and cooling loads of buildings by having hourly climate data in any region.

In accordance with the process of this software, firstly, the desired building is drawn by using drawing instructions and by having information about materials of walls and openings, installation system, uses of the building, etc. At last, the thermal load of the building will be calculated. Since the time of energy consumption is different based on the uses of the building, determining the uses of the building is important. Residential buildings work full time. This software is capable of calculating energy consumption efficiently by having the working time of the installation system and lighting.

3.1 Case Study

The case study is in Bandar-e-Anzali city located in the north of Iran, which has a mild and humid climate. To provide comfort in warm seasons of the year, shade and ventilation should be used as much as possible, and airflow should be in the interior of the building to prevent it from stabilizing humid (Fig. 2). The source of damage to the exterior of buildings and a significant element in endangering the health and comfort of residents is humidity. Wet walls become less thermally resistant due to the presence of water, which lowers their internal surface temperature and increases the likelihood of perspiration [20]. This phenomenon is the reason for thermal discomfort or increasing the fuel by a mechanical system, etc.
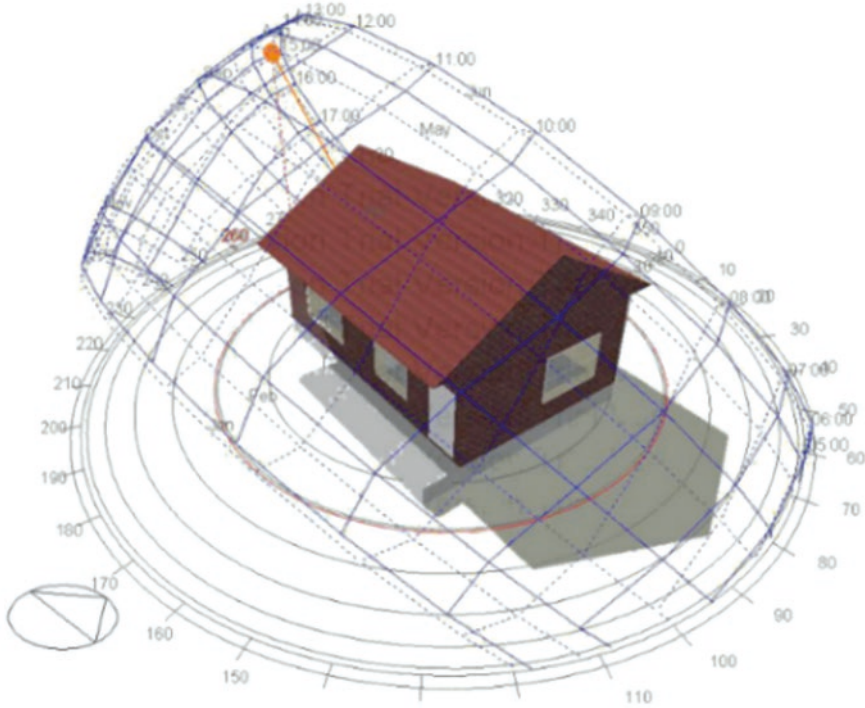
Fig. 2 The simulated sample

3.2 *Climatic Characteristics of the Study Area*

In this research, some conditions are considered a presupposition. According to the information of the meteorological organization of Gilan province, the annual average wind speed in Bandar-e-Anzali is 1.4 m/s². The minimum wind speed is in July, which equals 1.1 m/s², and the maximum wind speed is in January and February and equals 1.7 m/s². The total sunny hours of a year in Badar-e-Anzali is 1621, with minimum sunny hours occurring in December and 89 and maximum sunny hours occurring in July which equals 220. The average relative humidity per year is 81.9%. The average relative humidity is 85% in winter and decreases by approaching spring. In a way, that from 80% in April decreases to 76% in June. The seasonal average of relative humidity in spring is 78% and 78.5% in summer, increasing from 75% in July to 83% in September. Cold air inflow from the high-pressure centers of the North to Gilan province and humid absorption by this cold air cause vast rain falling in autumn. Consequently, humidity increases in this season compared to other seasons. Thus, autumn is the wettest season in Gilan province in which its relative humidity is 86% and the driest month is July, with a relative humidity of

Table 1 General climate information of Bandar-e-Anzali, Iran

Source	WMO	ASHRAE climate zone	Koppen classification	Latitude (°)	Longitude (°)	Elevation (m)	Standard pressure (kPa)
ASHRAE	407180	3A	Cfa	37.463909N	49.47986E	22.86 below sea level	1030
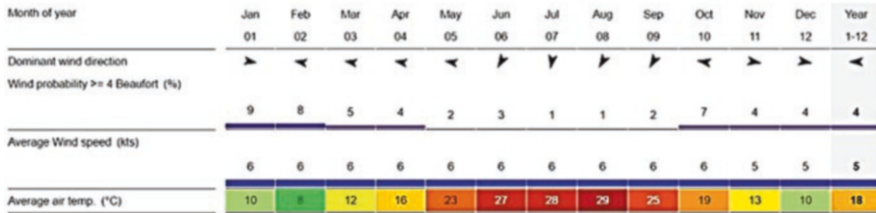
Fig. 3 Observations are conducted basis from 7 am to 7 pm. (https://www.windfinder.com/forecast/bandar-anzali)

75%. The difference in the humidity of these months is 12% which indicates that this city is humid in all seasons of the year. The annual average temperature of Bandar-e-Anzali is 15.9 °C. The maximum annual average temperature is 20.6 and the minimum is 11.3 °C. The difference between the maximum and minimum temperature per year is 9.3 °C. The average temperature in the coldest month, January, is 6.8 °C and in the warmest month, July, is 25.2 °C. The average temperature per season is 18.8 for spring, 24 for summer, 13 for autumn, and 7.6 for winter. General climate information of Bandar-e-Anzali is demonstrated in Table 1.

Regarding these conditions and the severe impact of humidity on thermal comfort in such a climate, the distances between window frames and the floor with 70 cm, 90 cm, and 110 cm are modeled, and their results are compared. Wind speed inside the building creates a pressure field around the building. The level of the pressure field is based on wind speed. Furthermore, the most determinant factor in airflow's path through a building is the direction of wind blowing (Fig. 3). A positive or negative pressure field is created while wind passes through a building. Then, air flows from areas with positive pressure to areas with negative pressure. When temperature increases, the air density decreases; consequently, air flows above the building, and at last, cooler air takes its place (Fig. 4). This phenomenon is known as the chimney effect. The temperature difference between the inside and outside of a building and among various parts of it causes pressure differences and as a result air replacement (Ahadi, 2015). Factors including radiation, wind, and the direction of the building's establishment effectively control the interior atmosphere.
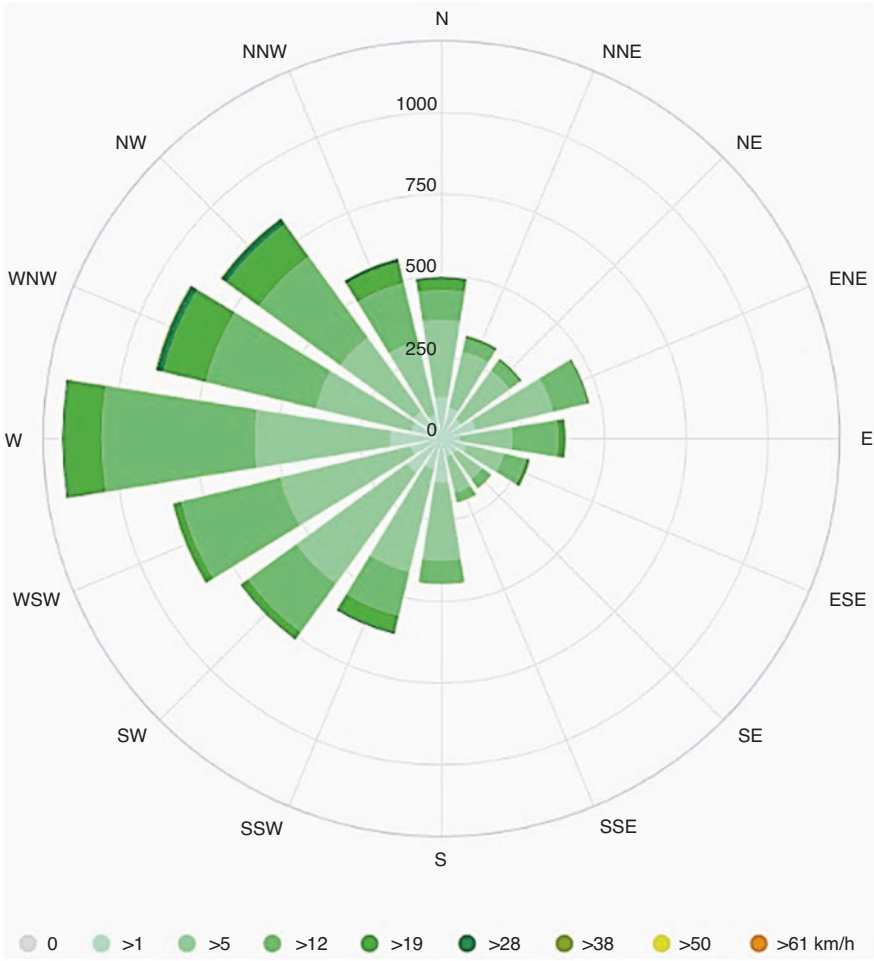
Fig. 4 Wind rose with 16 directions of Bandar-e-Anzali. (https://www.meteoblue.com/en/weather/historyclimate/climatemodelled/bandar-e-anzali_iran_141679)

4 Findings and Simulations

According to the effect of humidity on the thermal convenience of residents in this climate, the distance between window frames and the floor with 70 cm, 90 cm, and 110 cm have been modeled. The simulations of the Design Builder software and the extracted charts show the thermal exchanges. These charts present the thermal changes according to the distance between window frames and floor (Table 2). Simulations done in Design Builder and charts extracted from this software include airflow and natural ventilations which indicate a decrease in thermal exchange by the increase in the distance between window frames and the floor. The data in this table is collected in May.

Table 2 Thermal exchanges in the assumed openings using Design Builder software

Thermal exchange of the openings	Distance between window frames and the floor
−0.37 Kw	70 Cm
−0.35 Kw	90 Cm
−0.35 Kw	110 Cm
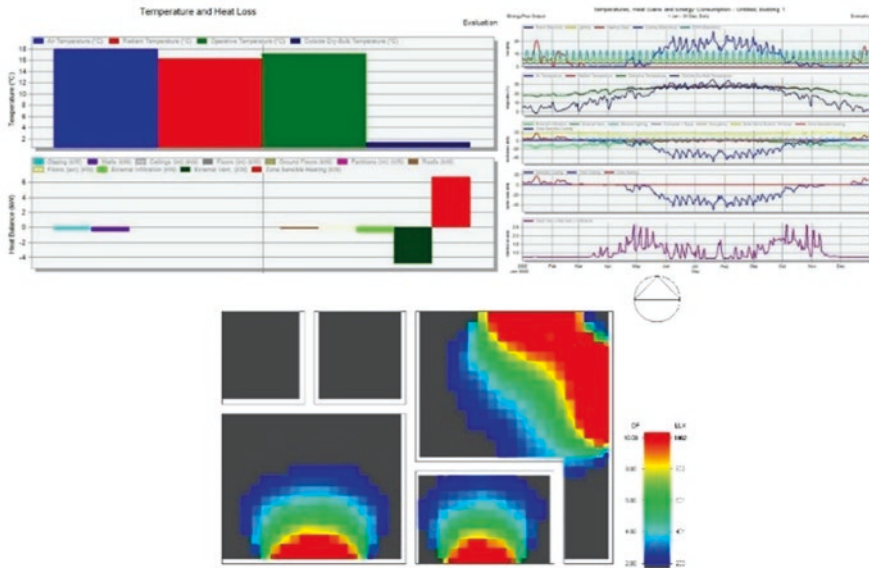
Fig. 5 Thermal exchange (cooling and heating) of the building by Design Builder software, H = 70 cm/rate of light entrance into building by Design Builder software, H = 70 cm

Thermal exchanges of the opening with a distance between the window and floor of 70 cm are −0.37 KW. As shown in Table 2, the entrance of coldness in cold seasons into the building is more than the exit of heat in hot seasons. The southern part of the building is the best location for those rooms which are used mostly. Based on their need to direct light and heat, the main rooms should be placed in the south, southeast, and southwest of the building. In other words, the route of designed spaces should be matched with the route of the sun. As shown in Fig. 5, rooms with a distance between the window frame and floor of 70 cm have high lighting.

Airflow is analyzed in the opening with H = 70 cm (Fig. 6) and the thermal exchange of such opening is −0.37 KW (Table 2). When wind flows through a window with H = 70 cm into the building, it passes and impresses the whole path quickly. As shown in Fig. 6, airflow is higher near the floor than the roof and warm air, due to its lower density, inhabits near the roof. As a consequence, the airflow does not go well. Regarding the limited airflow of such openings in a building, this distance between window frames and the floor is less appropriate than other designed models.
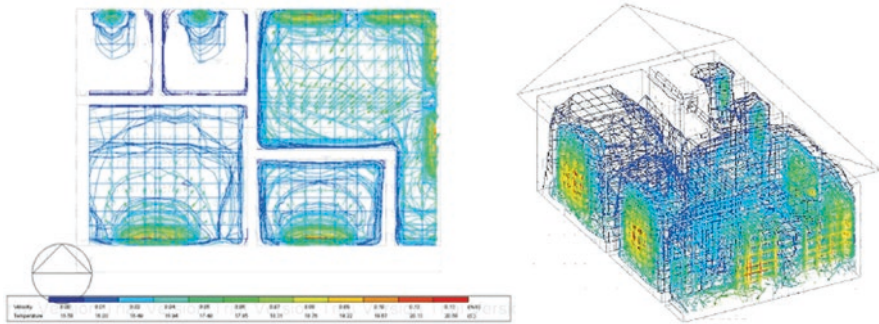
Fig. 6 H = 70 cm
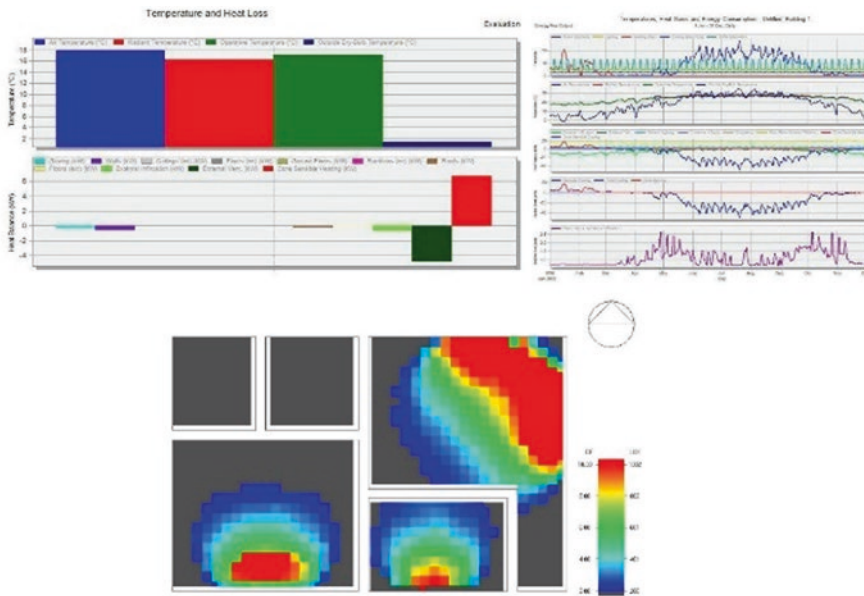
Fig. 7 Thermal exchange (heating and cooling) of the building by using Design Builder software, H = 90 cm/entrance of light and brightness into the building, by using Design Builder, H = 90 cm

According to Fig. 7, the thermal exchange of the opening with H = 90 cm is −0.35 KW. In winter, due to the opening and closing of openings, a lot of cold air enters the building. To have thermal convenience, the interior of the building can be divided into cold and warm parts. Hence, those parts of the building that are used less, can be parted from others so that thermal convenience can be provided by consuming less energy. However, the permanent residential rooms need not be at the same temperature. Brightness in an opening with H = 90 cm is lesser than openings with H = 70 cm.
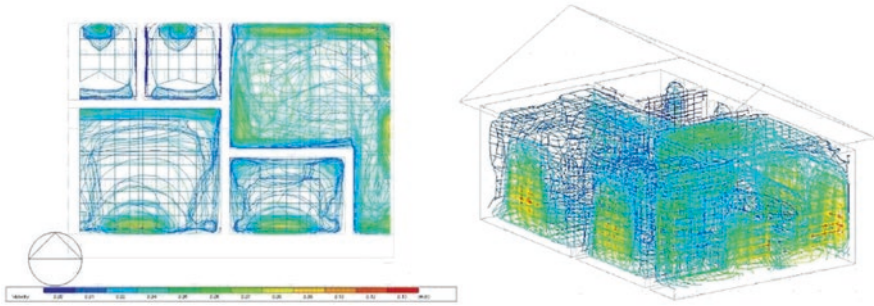
Fig. 8 H = 90 cm

Thermal exchange in the distance between the window frame and floor with 90 cm is 0.35 KW (Table 2), which has better natural ventilation in comparison to the distance between the window frame and floor with 70 cm (Fig. 8). Also, as shown in Fig. 8, airflow affects more interior space of buildings. In a way, when air enters the interior space of a building, its speed decreases, and then, it flows into the corner of interior space, and as a consequence air passes slowly through the corners. Therefore, when high-pressure airflow enters a building, the low-pressure airflow exits from the opening. In this simulated model, due to more distance of the opening from the floor, airflow has more penetration to the corners.

The results of changing the distance between window frames and the floor on façade are shown in Table 2. Energy dissipation changes by changing the distance between window frames and floor. Energy dissipation in the distance between the window frame and floor of 70 cm is more than the distance between window frames and floor of 70 cm or 110 cm. Therefore, energy dissipation in windows with the distance between the window frame and floor of 110 cm is lesser than the others. The location of windows is one of the most important factors in absorbing sunlight. A window located south of the building acts like an effective sunlight absorber. Disregarding the color and the form of the internal crust, the radiations which enter the room are unlikely to be reflected (Fig. 9). As a result, regarding the sun radiations to the openings, the lighting level in this model is lesser than in other designed models.

Thermal exchange in openings with a distance between the window frame and floor of 110 cm is −0.35 KW (Table 2), and its thermal exchange and airflow are equal to the opening with a distance between the window frame and floor of 90 cm (Fig. 10). By increasing the distance between the window frame and floor, the airflow level does not notably change and thermal exchange, also, remains constant. It means that thermal comfort in a building with the distance between the window frame and floor of 90 cm is the same as in a building with the distance between the window frame and floor of 110 cm.
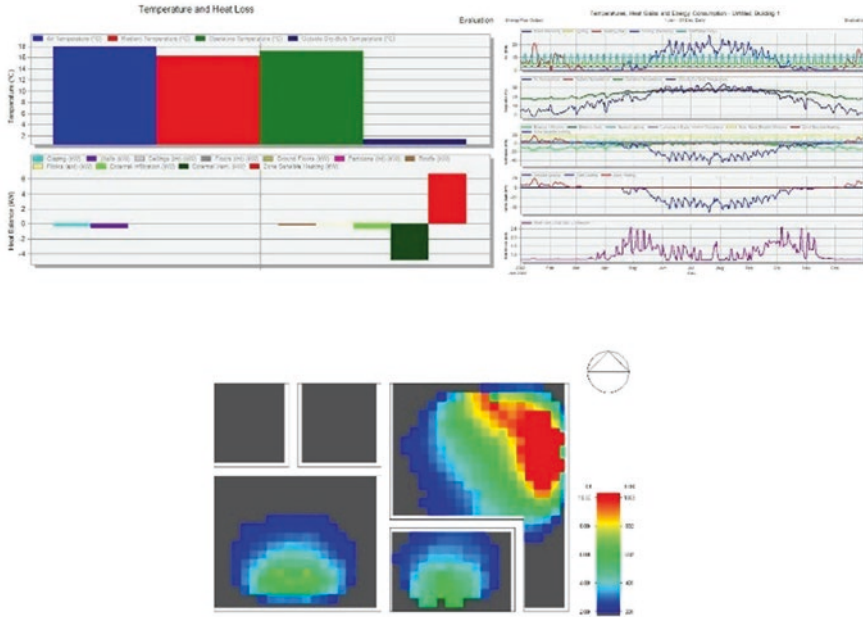
Fig. 9 Thermal exchange (heating and cooling) of the building by using Design Builder software, H = 110 cm/entrance of light and brightness into the building, by using Design Builder, H = 110 cm
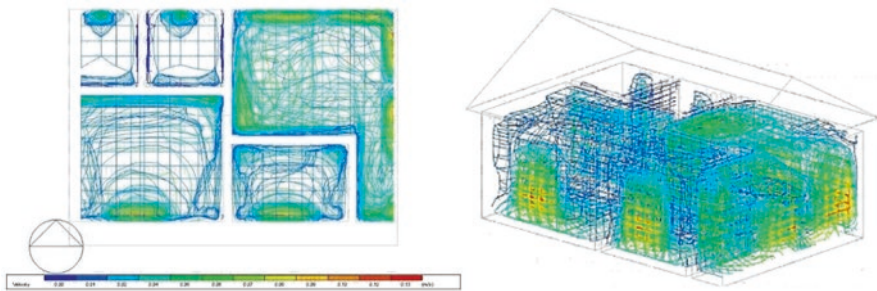

Fig. 10   H = 110 cm

5   Findings and Simulations

In the simulation, after entering primary data, an exact result has been achieved that allows tracking the window's behavior and thermal exchange. In accordance with these results, an appropriate technique for the size of the distance between window frames and the floor can be chosen to achieve desired thermal efficiency during a year. The important key point of using simulation is that this software evaluates only the considered situation and then it is the designer's duty to choose the most appropriate technique in designing according to all critical points of the results.

According to the simulation results, when natural ventilation occurs, air flows circularly in every room and moves parallel to walls when entering the rooms. According to results acquired from Design Builder and a comparison of three types of openings with distance between window frames and floor with 70 cm, 90 cm, and 110 cm, airflow level, natural ventilation, and thermal comfort of residents in openings with a distance between window frame and floor with 70 cm is less than other types of openings. Provided airflow in openings with a higher distance between window frames and the floor is more than others. As a result, airflow and thermal exchange increase by increasing the distance between window frames and the floor. Hence, thermal comfort increases, but after a specific distance between window frames and the floor, natural ventilation does not change and remains constant.

In relation to comparing the results of this study to previously conducted literature in this field, it can be stated that previous studies have especially been focused on influential factors of occupant window-opening behavior [31], CFD simulation of cross-ventilation [27], window opening model [32, 33], actual validation of energy simulation [34], multi-objective optimization methodology for window design [35], the effect of building shape, orientation, window to wall ratios [36], the impact of glazing ratio and window configuration on occupants' comfort [37] on openings. Although the previous studies have been mainly conducted on the dimensions and angle of the windows, the distance between window frames and the floor has been paid less attention to.

In the understudied building, the least energy dissipation is for the window with distance between window frame and floor with 70 cm, which is –0.37 km. The most energy dissipation is for the window with distance between window frame and floor with 110 cm, which is –0.35 km. Therefore, by increasing the distance between window frames and floor, the lighting of the interior and thermal exchanges is decreased. In this article, the effects of the window's structure on total energy consumption have been evaluated. However, it is obvious that other parameters such as neighbors, materials, use of the building, etc. affect energy consumption, which can be considered a limitation of the study. Therefore, the considered factor is a parameter in order to evaluate the effects of other parameters in future studies.

References

1. Olabi, A.G., Wilberforce, T., Abdelkareem, M.A.: Fuel cell application in the automotive industry and future perspective. Energy. **214**, 118955 (2021). https://doi.org/10.1016/j.energy.2020.118955
2. Korsavi, S.S., Zomorodian, Z.S., Tahsildoost, M.: Energy and economic performance of rooftop PV panels in the hot and dry climate of Iran. J. Clean. Prod. **174**, 1204–1214 (2018). https://doi.org/10.1016/j.jclepro.2017.11.026
3. Li, L., Sun, W., Hu, W., Sun, Y.: Impact of natural and social environmental factors on building energy consumption: Based on bibliometrics. J. Build. Eng. **37**(June), 2021 (2020). https://doi.org/10.1016/j.jobe.2020.102136

4. Naderi, E., Sajadi, B., Behabadi, M.A., Naderi, E.: Multi-objective simulation-based optimization of controlled blind specifications to reduce energy consumption, and thermal and visual discomfort: Case studies in Iran. Build. Environ. **169**(November 2019), 106570 (2020). https://doi.org/10.1016/j.buildenv.2019.106570

5. Khaksar, A., Tabadkani, A., Mofidi Shemirani, S.M., Hajirasouli, A., Banihashemi, S., Attia, S.: Thermal comfort analysis of earth-sheltered buildings: The case of meymand village, Iran. Front. Archit. Res. **11**(6), 1214–1238 (2022). https://doi.org/10.1016/j.foar.2022.04.008

6. Ansari, D., Holz, F.: Between stranded assets and green transformation: Fossil-fuel-producing developing countries towards 2055. World Dev. **130**, 104947 (2020). https://doi.org/10.1016/j.worlddev.2020.104947

7. Azari, R., Abbasabadi, N.: Embodied energy of buildings: A review of data, methods, challenges, and research trends. Energy Build. **168**, 225–235 (2018). https://doi.org/10.1016/j.enbuild.2018.03.003

8. Yazdi Bahri, S., Alier Forment, M., Sanchez Riera, A.: Thermal comfort improvement by applying parametric design panel as a second skin on the facade in building refurbishment in moderate climate. ACM Int. Conf. Proc. Ser. **no. Teem 2021**, 763–767 (2021). https://doi.org/10.1145/3486011.3486535

9. D'Agostino, D., Mazzarella, L.: What is a Nearly zero energy building? Overview, implementation and comparison of definitions. J. Build. Eng. **21**(September 2018), 200–212 (2019). https://doi.org/10.1016/j.jobe.2018.10.019

10. Yazdi Bahri, S., Alier Forment, M., Sanchez Riera, A., Bagheri Moghaddam, F., Casañ Guerrero, M.J., Llorens Garcia, A.M.: A literature review on thermal comfort performance of parametric façades. Energy Reports. **8**, 120–128 (2022). https://doi.org/10.1016/j.egyr.2022.10.245

11. Yazdi-Bahri, S., Alier Forment, M., Sanchez Riera, A., Askarizad, R.: Assessing the impact of double-skin façades on social activities of people in urban spaces using empirical and syntactical analysis. J. Asian Archit. Build. Eng. (2023). https://doi.org/10.1080/13467581.2023.2238042

12. Li, Y., Kubicki, S., Guerriero, A., Rezgui, Y.: Review of building energy performance certification schemes towards future improvement. Renew. Sustain. Energy Rev. **113**(June) (2019). https://doi.org/10.1016/j.rser.2019.109244

13. Cannavale, A., Martellotta, F., Cossari, P., Gigli, G., Ayr, U.: Energy savings due to building integration of innovative solid-state electrochromic devices. Appl. Energy. **225**(February), 975–985 (2018). https://doi.org/10.1016/j.apenergy.2018.05.034

14. Kosonen, A., Keskisaari, A.: Zero-energy log house – Future concept for an energy efficient building in the Nordic conditions. Energy Build. **228**, 110449 (2020). https://doi.org/10.1016/j.enbuild.2020.110449

15. Stein, R. (ed.): Building Physics of the Envelope Principles of Construction, Berlin

16. Liu, Y., Liu, T., Ye, S., Liu, Y.: Cost-benefit analysis for Energy Efficiency Retrofit of existing buildings: A case study in China. J. Clean. Prod. **177**, 493–506 (2018). https://doi.org/10.1016/j.jclepro.2017.12.225

17. Casini, M.: Active dynamic windows for buildings: a review. Renew. Energy. **119**, 923–934 (2018). https://doi.org/10.1016/j.renene.2017.12.049

18. Bere, J.: An Introduction to Passive House. RIBA Publishing, London (2019). https://doi.org/10.4324/9780429347696

19. Jian, Y., et al.: Individual-based insight into occupants' interaction with windows in apartments in Beijing. J. Build. Eng. **56**(100), 104795 (2022). https://doi.org/10.1016/j.jobe.2022.104795

20. Fino, R., Tadeu, A., Simões, N.: Influence of a period of wet weather on the heat transfer across a wall covered with uncoated medium density expanded cork. Energy Build. **165**, 118–131 (2018). https://doi.org/10.1016/j.enbuild.2018.01.020

21. Uzar, U.: Political economy of renewable energy: does institutional quality make a difference in renewable energy consumption? Renew. Energy. **155**, 591–603 (2020). https://doi.org/10.1016/j.renene.2020.03.172

22. Chaudhuri, T., Zhai, D., Soh, Y.C., Li, H., Xie, L.: Random forest based thermal comfort prediction from gender-specific physiological parameters using wearable sensing technology. Energy Build. **166**, 391–406 (2018). https://doi.org/10.1016/j.enbuild.2018.02.035

23. Shan, X., Xu, W., Lee, Y.K., Lu, W.Z.: Evaluation of thermal environment by coupling CFD analysis and wireless-sensor measurements of a full-scale room with cooling system. Sustain. Cities Soc. **45**(October 2018), 395–405 (2019). https://doi.org/10.1016/j.scs.2018.12.011

24. Sharmin, T., Steemers, K., Humphreys, M.: Outdoor thermal comfort and summer PET range: a field study in tropical city Dhaka. Energy Build. **198**, 149–159 (2019). https://doi.org/10.1016/j.enbuild.2019.05.064

25. Amirifard, F., Sharif, S.A., Nasiri, F.: Application of passive measures for energy conservation in buildings – a review. Adv. Build. Energy Res. **13**(2), 282–315 (2019). https://doi.org/10.1080/17512549.2018.1488617

26. Hachem-Vermette, C.: Solar Buildings and Neighborhoods: Design Considerations for High Energy Performance. Springer, Cham (2020)

27. Montazeri, H., Montazeri, F.: CFD simulation of cross-ventilation in buildings using rooftop wind-catchers: impact of outlet openings. Renew. Energy. **118**, 502–520 (2018). https://doi.org/10.1016/j.renene.2017.11.032

28. Moosavi, L., Zandi, M., Bidi, M.: Experimental study on the cooling performance of solar-assisted natural ventilation in a large building in a warm and humid climate. J. Build. Eng. **19**(April), 228–241 (2018). https://doi.org/10.1016/j.jobe.2018.04.026

29. Lu, H., Zhang, Z., Yang, L.: A review on airflow distribution and management in data center. Energy Build. **179**, 264–277 (2018). https://doi.org/10.1016/j.enbuild.2018.08.050

30. Schieweck, A., et al.: Smart homes and the control of indoor air quality. Renew. Sustain. Energy Rev. **94**(May), 705–718 (2018). https://doi.org/10.1016/j.rser.2018.05.057

31. Pan, S., et al.: A study on influential factors of occupant window-opening behavior in an office building in China. Build. Environ. **133**(November 2017), 41–50 (2018). https://doi.org/10.1016/j.buildenv.2018.02.008

32. Markovic, R., Grintal, E., Wölki, D., Frisch, J., van Treeck, C.: Window opening model using deep learning methods. Build. Environ. **145**(July), 319–329 (2018). https://doi.org/10.1016/j.buildenv.2018.09.024

33. Daemei, A.B., Limaki, A.K., Safari, H.: Opening performance simulation in natural ventilation using design builder (case study: a residential home in Rasht). Energy Proc. **100**, 412–422 (2016). https://doi.org/10.1016/j.egypro.2016.10.196

34. Fathalian, A., Kargarsharifabad, H.: Actual validation of energy simulation and investigation of energy management strategies (case study: an office building in Semnan, Iran). Case Stud. Therm. Eng. **12**(March), 510–516 (2018). https://doi.org/10.1016/j.csite.2018.06.007

35. Zhai, Y., Wang, Y., Huang, Y., Meng, X.: A multi-objective optimization methodology for window design considering energy consumption, thermal environment and visual performance. Renew. Energy. **134**, 1190–1199 (2019). https://doi.org/10.1016/j.renene.2018.09.024

36. Pathirana, S., Rodrigo, A., Halwatura, R.: Effect of building shape, orientation, window to wall ratios and zones on energy efficiency and thermal comfort of naturally ventilated houses in tropical climate. Int. J. Energy Environ. Eng. **10**(1), 107–120 (2019). https://doi.org/10.1007/s40095-018-0295-3

37. Ashrafian, T., Moazzen, N.: The impact of glazing ratio and window configuration on occupants' comfort and energy demand: the case study of a school building in Eskisehir, Turkey. Sustain. Cities Soc. **47**(February), 101483 (2019). https://doi.org/10.1016/j.scs.2019.101483

Optimization of Window-to-Wall Ratio in a Transfer Hall of an Urban Integrated Transportation Hub

Nan Yu, Zheng Shen, Xiaona Zheng, Peng Gao, Jinshun Wu, and Xuan Liu

1 Introduction

The urban integrated transport hub has developed rapidly with the acceleration of China's urbanization process. According to the Beijing Municipal Commission of Transport planning, by 2038, Beijing will have nearly 40 new, reconstructed and expanded comprehensive transport hubs. As a result, building energy consumption has grown daily, reaching one-third of the total national energy consumption [1]. As a large public building, an urban integrated transport hub is a significant energy consumer. Among them, the energy consumption of air conditioning and lighting in transfer halls, which is ample space, accounts for 40–60% and 20–35%, respectively, with tremendous energy saving potential [2, 3].

The natural light source introduced into the exterior window can reduce the energy consumption of lighting but also introduced solar radiation to increase the energy consumption of building air conditioning [4–7]. Therefore, the proportion of external windows and exterior walls (referred to as window-wall-ratio) directly affects the lighting quality and air-conditioning cooling and heating load of buildings, and the changing trend of both is opposite with the increase (or decrease) of the window-to-wall ratio [8–13]. Lu Libing et al. [14] theoretically calculated the heat consumption of enclosure structures in severe cold regions and concluded that it increases rapidly with the increase of window wall ratio. Fu Sujuan et al. [15]

N. Yu (✉) · J. Wu
North China Institute of Science and Technology, Sanhe, China
e-mail: yunan@ncist.edu.cn

Z. Shen · X. Zheng · X. Liu
Beijing General Municipal Engineering Design & Research Institute Co., Ltd., Beijing, China

P. Gao
Technical Center of North China Company China Construction Industrial & Energy Engineering Group Co., Ltd., Beijing, China

simulated that the natural room temperature in North China decreased with the increase in window-to-wall ratio. Jian Yiwen et al. [16] concluded that the increase in the ratio of East (West) to North windows and walls in Shanghai led to an increase in the total energy consumption of air conditioning in buildings throughout the year. Long Enshen et al. [17] concluded that the window-to-wall ratio in Chongqing has a much more significant impact on the air-conditioning cooling consumption index than on the heating heat consumption index. Danny H.W.I [18] took a comprehensive office building with different lighting designs as the test object. By changing the architectural design parameters that affect the lighting effect, and recording the total electricity consumption of the building when artificial lighting is controlled, the results show that a good lighting design can save a lot of energy consumption. A. Zain-Ahwed [19] systematically analyzed the influence of the window area of a building on energy consumption in a hot climate zone, and the results showed that increasing the window area could not only obtain natural lighting but also reduce energy consumption. Joseph C. Lam [20], Ivan Korolijaa [21], J. W. Lee [22] carried out simulation calculations on the impact of natural lighting on energy consumption of lighting, air conditioning and heating in different regions. The influence of window ratio, light transmittance and other factors on energy consumption of lighting, air conditioning and heating was analyzed.

However, presently, domestic and foreign studies mainly focus on the impact of the window-to-wall ratio on building cooling and heating energy consumption or lighting energy consumption without considering the impact of the window-to-wall ratio on the total energy consumption of the two. At the same time, there is less research on the sensitivity analysis of building energy consumption of window wall ratio with different orientations. Therefore, according to the architectural characteristics of the transfer hall of an urban transport hub, this chapter takes the transfer hall of an actual transport hub in Beijing as the research object and uses the dynamic simulation method to study the cooling. Furthermore, the impact law of heating and lighting system energy consumption aims to provide a reference for optimizing the window-to-wall ratio of urban transport hub buildings and achieving the carbon reduction goal by passive energy saving.

2 Materials and Methods-Building Model

2.1 Project Overview

This project was a comprehensive transportation hub in Beijing (39°54′ North latitude, 116°25′ East longitude), which is mainly a transfer hub for the subway, aboveground public transport and long-distance transport vehicles. The total building area was 90381 m^2, and the aboveground building area was 51990 m^2. According to different functions, it was divided into three individual blocks: East, North, and South (Figs. 1 and 2). Among them, the first floor of the East building was the

Fig. 1 Aerial view of the building

transfer hall and waiting hall, with a floor height of 15.3 m, which belongs to the tall space and is the research object of this study. The window-to-wall ratio of the transfer hall was 0.55. The South building had six floors above the ground, including car arrival, business, office, etc. The North building had four floors above the ground; the first floor was the departure area, and the rest was the office area. The East, North and South floors were connected underground, and the two underground floors were mainly underground parking garage and equipment room. It can be seen from Fig. 1 that there were many glass curtains on the East and West sides of the East building transfer hall, which increased the energy consumption of air conditioning while making full use of natural lighting to reduce lighting energy consumption.

2.2 Computational Model

The building model was built with DesignBuilder software, as shown in Fig. 3. EnergyPlus energy consumption simulation software was used to dynamically simulate the building energy consumption of the transfer hall of the transport hub for 8760 h throughout the year. The calculation process strictly follows the Heat Balance Method [23–25]. In the simulation process, only the window-to-wall ratio of each direction was considered a variable, and other conditions remained unchanged. The influence of the window-to-wall ratio of each orientation on the building energy system was analyzed, assuming that the indoor illuminance met the standard value of 150 lx specified in the relevant code [26] as the premise.
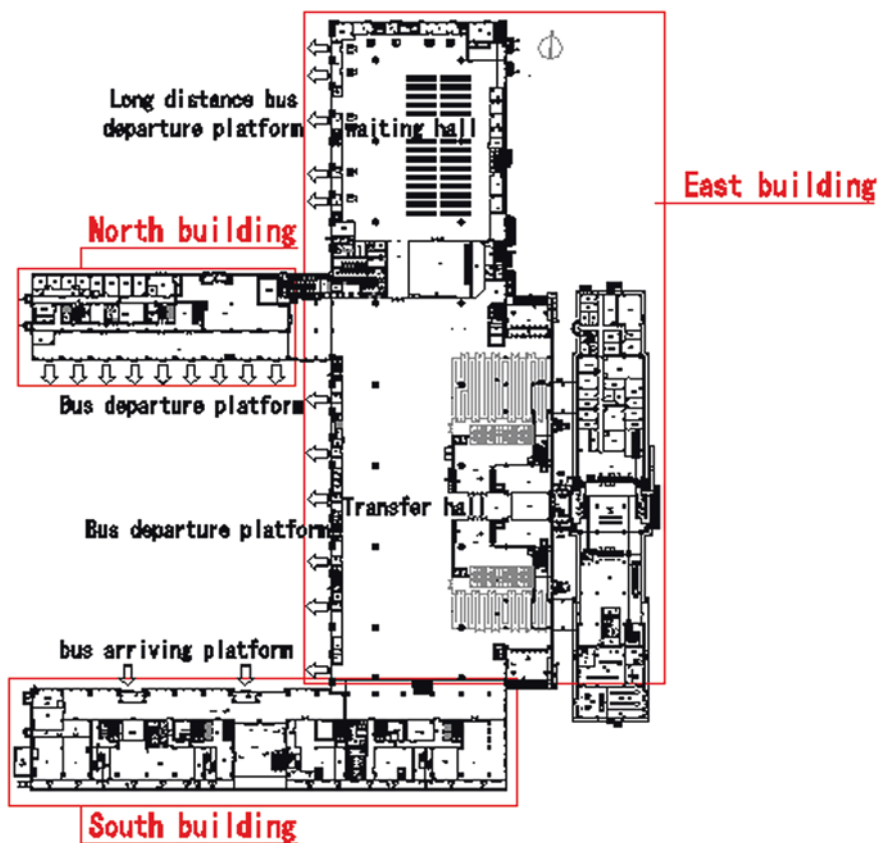
Fig. 2 First-floor building plan
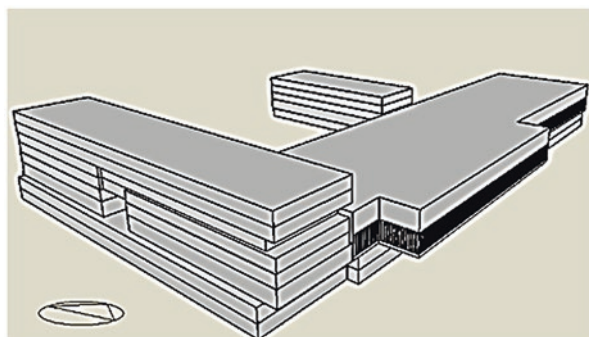
Fig. 3 Building model drawing
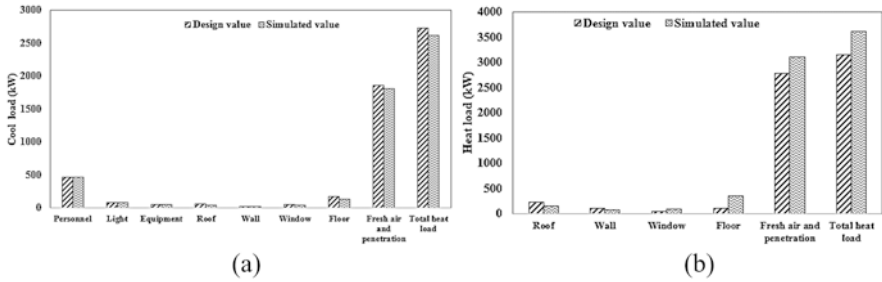
Fig. 4 Load comparison—(**a**) cooling load comparison; (**b**) heating load comparison

2.3 Model Validation

Figure 4 compares the design calculated and simulated value of building cooling and heating loads. It can be seen from the figure that the difference in total cooling load was slight, and the relative error was 4.16%. On the other hand, the total heating load differed significantly, and the simulation value was 13.6% larger than the design value. This was mainly because the floor load and fresh air load were designed and calculated using the steady indoor and outdoor temperature difference method. On the other hand, EnergyPlus used the dynamic outdoor temperature calculation method, resulting in the high simulation value of this load part.

3 Results and Discussions

3.1 Heating Load Comparison

Figure 5 shows the influence of the window-to-wall ratio on various energy use systems of buildings. It can be seen from Fig. 5a, b that the solar radiation heat gain through the window and the energy consumption of air-conditioning cooling were linear with the window-to-wall ratio. With the window-to-wall ratio increase, the solar radiation heat gain and the energy consumption of air-conditioning cooling also increased gradually. Figure 5c, d show that building heating energy consumption and lighting energy consumption was nonlinearly related to the window-to-wall ratio and decreased with the increase of the window-to-wall ratio. This is because the larger the window area was, the more solar radiation heat and natural lighting obtained indoors, the more energy consumption for cooling, and the less energy consumption for heating and lighting. It can be seen that the window-to-wall ratio directly affected the energy consumption of the building's cooling, heating and lighting systems (referred to as "three annual total energy consumption").
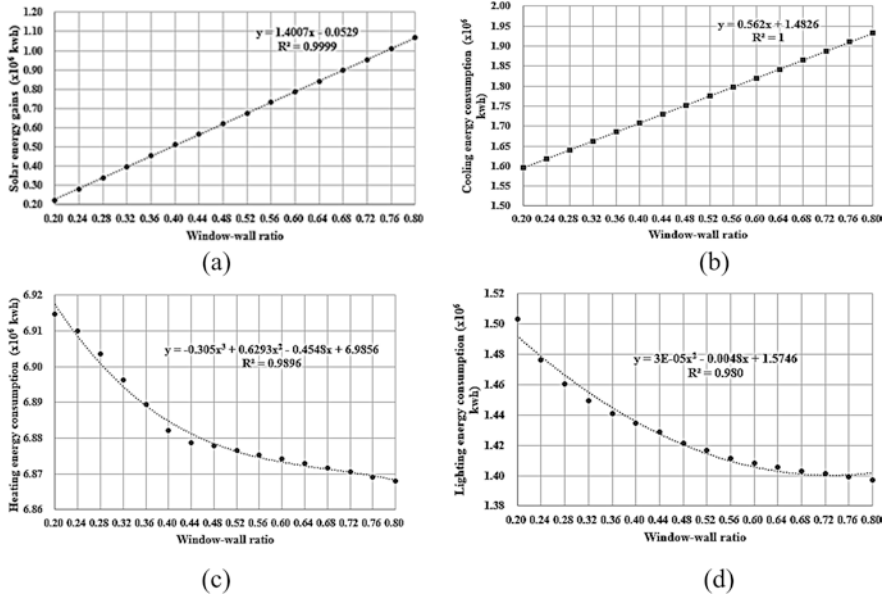
Fig. 5 Effect of window-to-wall ratio on energy consumption of buildings—(**a**) solar radiation heat gain; (**b**) cooling energy consumption; (**c**) heating energy consumption; (**d**) lighting energy consumption

3.2 Determination of Optimal Window Wall Ratio

According to the analysis in Section 3A, the window-to-wall ratio directly affected the three energy consumption items of the building. Therefore, the transfer hall's optimal window-to-wall ratio should take the three items' minimum total energy consumption as the objective function to ensure standard indoor illuminance. To facilitate unified calculation, all three energy consumption items were converted into primary energy calculation. The three annual total energy consumption expressions in Fig. 6 were obtained by function fitting, and the fitting result R2 was more significant than 0.99. It can be seen that with the increase in the window-to-wall ratio, the annual total energy consumption of the three items decreased first and then increased. When the window-to-wall ratio was 0.28, the annual total energy consumption of the three items was the lowest, which was 80322 kWh less than that of the actual building transfer hall (the window-to-wall ratio was 0.55). When the window-to-wall ratio was more significant than 0.28, for every 0.04 increase in the window-to-wall ratio, the total annual energy consumption of the three items per unit building area increased by 0.36–1.55 kWh.

The graph displays:
$$y = 0.5051x^2 - 0.1664x + 10.015$$
$$R^2 = 0.9943$$

Y-axis: Total energy consumption ($\times 10^6$ kwh), ranging from 10.00 to 10.20

X-axis: Window-wall ratio, ranging from 0.20 to 0.80
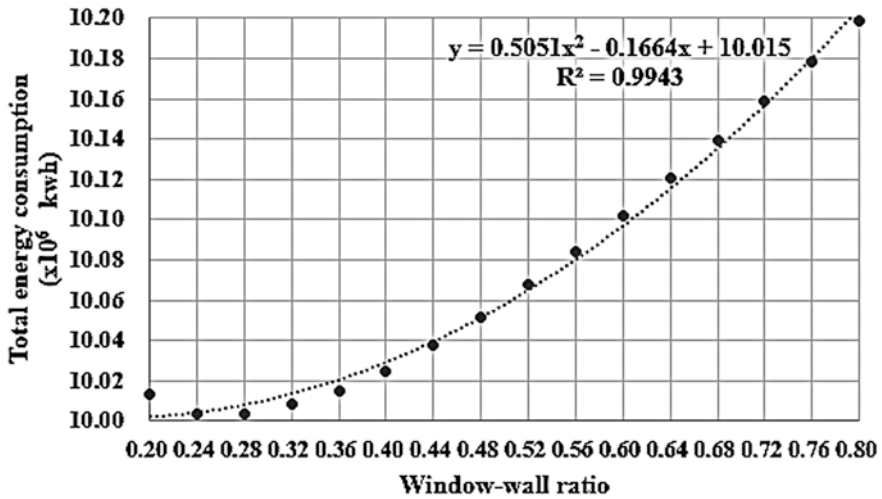
Fig. 6 The total energy consumption of the three items varies with the window-to-wall ratio

3.3 Sensitivity Analysis of Three Annual Total Energy Consumption for Window-to-Wall Ratios in Different Orientations

As the South side of the transfer hall was the South building, the sensitivity of the window-to-wall ratio to the three total energy consumption was further studied from the East, West and North directions. When the window-to-wall ratio of each orientation changed from 0.20 to 0.40, the window-to-wall ratio of a certain orientation was changed, and the window-to-wall ratio of other orientations remained unchanged at 0.28. The total energy consumption of the three items of the building is shown in Fig. 7. When the window-to-wall ratio changed from 0.20 to 0.28, the total energy consumption decreased by 2806 kwh, increased by 907 kwh, and increased by 1251 kwh for each increase of 0.04 in the East, West, and North-facing window-to-wall ratios. The window-to-wall ratio had the most significant impact on the energy consumption of the three items, and the East-facing windows were opened as much as possible. When the window-to-wall ratio changed from 0.28 to 0.40, the total energy consumption of the three items increased with the increase of the window-to-wall ratio in each direction. The total energy consumption increased by 553 kwh, 3485 kwh and 1318 kWh for every 0.04 increase in the East, West and North-facing window-to-wall ratios. It can be seen that the ratio of west-facing window-to-wall ratio had the most significant impact on the three total energy consumption items, and the East-facing windows had the most negligible impact. Therefore, West-facing windows were reduced as much as possible.
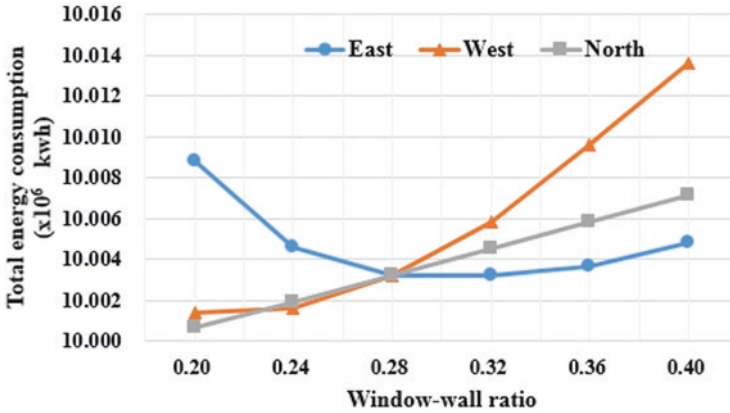
Fig. 7 Variation of window-to-wall ratio for each orientation

4   Conclusion

The solar radiation heat gain and air-conditioning cooling energy consumption in the Beijing transport hub transfer hall were linearly related to the window-to-wall ratio, which increased with the increase of the window-to-wall ratio. On the other hand, building heating and lighting energy consumption was nonlinearly related to the window-to-wall ratio and decreased with the increase of the window-to-wall ratio. Therefore, the window-to-wall ratio directly affected the energy consumption of buildings' cooling, heating and lighting systems.

The total energy consumption of the three items in the transfer hall throughout the year decreased first and then increased with the window-to-wall ratio, and the optimal window-to-wall ratio was 0.28. Compared with the actual building transfer hall (the window-to-wall ratio was 0.55), the annual total energy consumption of the three items was reduced by 80322 kWh. For every 0.04 increase in the window-to-wall ratio, the annual total energy consumption of the three items per unit building area will increase by 0.36–1.55 kWh. From the perspective of reducing building energy consumption, the most suitable window orientation for transfer halls was East, and West-facing windows were minimized. This chapter studied the influence of the win-dow-to-wall ratio on building energy consumption in the transfer hall of an urban transport hub.

Since the South side of the transfer hall is an office building, this research object lacks South-facing exterior windows. Therefore, future research should combine other building models to study further the impact of the ratio of South-facing exterior windows on the energy consumption of the transfer hall.

References

1. China Building Energy Conservation Association: Research report on China building energy consumption in 2019 [J]. Building. **07**, 30–39 (2020)
2. Yan, X., Wang, X., Li, D.: Compliance check of window wall area ratio during Revit modelling [J]. Graph. News. **40**(4), 761–765 (2019)
3. Wang, X.: Optimal design of window wall ratio and sunshade control method consid-ering lighting and air-conditioning energy consumption [D]. Xi'an University of Architecture and Technology, Xi'an (2020)
4. Jiang, H., He, C., Dai, X.: Simulation and analysis the influence of window-wall ratio on building energy consumption based on PKPM software [J]. J. Anhui Jianzhu Univ. **(1)**, 69–72 (2015)
5. TU, F.: Building sunshade is an important method for building energy efficien-cy [J]. Arch. Technol. **42**(10), 875–876 (2011)
6. Liu, L., Liu, C., Wu, D., et al.: Energy saving analysis and optimization of space de-sign factors of Tianjin office buildings [J]. J. Harbin Univ. Technol. **50**(4), 181–187 (2018)
7. Xie, J., Li, Q., Wang, J., et al.: The impact of building window wall ratio on air conditioning energy consumption of the island reef hotel [J]. J. Harbin Univ. Technol. **50**(8), 88–94 (2018)
8. Xu, S., Jiang, H., Wang, J.: Parametric study on the impact of building window wall ratio on building energy consumption under five climatic conditions [J]. Build. Sci. **35**(4), 91–95 (2019)
9. Marino, C., Nucara, A., Pietrafesa, M.: Does window-to-wall ratio have a significant effect on the energy consumption of buildings? A parametric analysis in Italian climate conditions [J]. J. Build. Eng. **13**, 169–183 (2017)
10. Alghoul, S.K., Rijabo, H.G., Mashena, M.E.: Energy consumption in buildings: a correlation for the influence of window-to-wall ratio and window orientation in Tripoli, Libya [J]. J. Build. Eng. **11**, 82–86 (2017)
11. Luke, T., Robert, P., Matthew, J.E., David, F.: Effect of window-to-wall ratio on measured ener-gy consumption in US office buildings [J]. Energy Build. **203** (2019)
12. Gao, M., Chen, S., Cheng, Y., et al.: Study on the natural lighting quality and energy saving potential of translucent photovoltaic windows in cold regions [J]. Renew. Energy. **36**(5), 682–689 (2018)
13. Maureen, D.G., Andrea, E.P.: Window energy efficiency in Argentina-Determining factors and energy savings strategies [J]. J. Cleaner Prod. **247** (2020)
14. Lu, L., Wang, Y., Gao, M., et al.: Study on window-wall ratio on heat transfer of enclosure structure [J]. Low Temp. Arch. Technol. **33**(10), 105–106 (2011)
15. Fu, S., Liu, H., Hao, Y.: Analysis of the influence of window-wall ratio on the indoor temperature in rural residential [J]. Building Energy Effic. **7**, 55–58 (2015)
16. Ian, Y., Jiang, Y.: Influence of window wall ratio on annual energy consumption for heating and air conditioning in residential buildings [J]. HV&AC. **36**(6), 1–5 (2006)
17. Long, E., Fu, X.: Effect of area ratio of window to wall on cooling and heating energy consumption on index and energy efficient rate for residential buildings [J]. HV & AC. **37**(2), 46–50 (2007)
18. Li, D.H.W., Lam, J.C.: Evaluation of lighting performance in office buildings with daylighting controls [J]. Energy Build. **33**(8) (2001)
19. Zain-Ahmed, A., Sopian, K., Othman, M.Y.H., Sayigh, A.A.M., Surendran, P.N.: Day lighting as a passive solar design strategy in tropical buildings: a case study of Malaysia [J]. Energy Convers. Manage. **43**(13) (2002)
20. Lam, J.C., Tsang, C.L., Yang, L.: Impacts of lighting density on heating and cooling loads indifferent climats in China [J]. Energy Convers. Manage. **47**(13) (2005)
21. Korolija, I., Marjanovic-Halburd, L., Zhang, Y., Hanby, V.I.: UK office buildings archetypal model as method logical approach in development of regression models for predicting building energy consumption from heating and cooling de-mands [J]. Energy Build. **60**, 152–162 (2013)

22. Lee, J.W., Jung, H.J., Park, J.Y., Lee, J.B., Yoon, Y.: Optimization of building window system in Asian regions by analyzing solar heat gain and daylighting elements [J]. Renew. Energy. **50**, 522–531 (2013)
23. Feng, J., Ding, Y., Wu, H.: Energyplus energy simulation software and its application tools [J]. Build. Energy Effic. **40**(1), 64–67 (2012)
24. Zhou, X., Yan, D., Hong, T., et al.: Comparison and research on HVAC system simulation part for different building energy modeling Programs [J]. HV&AC. **4**, 113–122 (2014)
25. Zhu, D., Yan, D., Wang, C., et al.: Comparison of building energy simu-lation programs: DeST'Energyplus and DOE- 2 [J]. Build. Sci. **28**(S2), 213–222 (2012)
26. The standard for Lighting Design of Buildings; GB50034-2013

Forecasting Future Climate with a Neural Network Trained on Monitored Data: An Analysis of the Energy Demand of a Detached House

Valentino Festa, Rosa Francesca De Masi, Antonio Gigante, Michele Parrotta, Silvia Ruggiero, and Alessandro Russo

1 Introduction

Climate change is caused by human activities such as burning fossil fuels and deforestation. As a result of climate change, the air temperature increases, changing precipitation, wind patterns and sea levels. Moreover, extreme events often occur, causing biodiversity loss [1]. Actions to reduce global greenhouse gas emissions are needed, for instance, on economic resources and local administrations sensitivity [2]. Mathematical models are used to create projected climate files for 2050 or 2080 and make long-term predictions for energy demand [3]. Yassaghi et al. [4], using stochastic methods and the morphing technique, find that the energy demand in three office buildings decreases between 29.6% and 20.5% for the heating and increases between 25.5% and 41.6% for the cooling period. Liu et al. [5] evaluated the impact of climate change with future weather data using downscaled data. The results showed that for a residential user located in Hong Kong, annual energy demand for cooling will increase by 278.8% by the end of this century. Chakraborty et al. [6] exploited eXplainable, an artificial intelligence model. They noted an increase of 87% in cooling demand between 2020 and 2010 for a warm, humid climate. Wang and Chen [7] used the HadCM3 model to generate weather data for typical years (2020, 2050 and 2080) for 15 US cities based on three CO_2 emission scenarios. For each location, two residential buildings and seven commercial activities were simulated. As regards cooling demand, an increase of $10\% \div 100\%$ of annual energy consumption is shown for all 15 cities, and this increase grows as the level of greenhouse gas emissions. As regards the heating need, for all cities, there is an energy reduction demand greater than 180%, while, for Miami this reduction is almost zero. Narowski et al. [8], with the WYEC2 procedure, implemented an

V. Festa · R. F. De Masi · A. Gigante · M. Parrotta · S. Ruggiero (✉) · A. Russo
Department of Engineering – DING, University of Sannio, Benevento, Italy
e-mail: sruggiero@unisannio.it

atypical year (UMY). Four buildings and four different exposures were simulated and compared with the typical year. They found a maximum difference for heating needs of 24% and for cooling demand of 46%.

The present paper aims to investigate short-term climate forecasting to evaluate the future energy demand of the HVAC-building system in a reference building in Italy. The focus is on the immediate future because the performance of building components and systems decreases dramatically over time; they usually become obsolete after 20–30 years of useful life [9]. The novelty of this paper is the simultaneous application of neural networks (NN) and dynamic energy simulations.

2 Methodology

NN can be used to predict the behavior of non-linear systems without fixing a mathematical model. They can be used in multiple areas, such as price forecasting [10] and so on, but also in the predictions of climate change [11, 12]. A NN is an algorithm that tries to imitate the functioning of the human brain [13, 14]. NN consists of many "neurons" organized in layers: each neuron receives a certain amount of input from outside and returns an output. Neurons are connected through synapses, associated with weight being the relative importance of each input for the neuron. NN can be divided into two main categories:

- Feedforward networks
- Recurrent networks

Feedforward networks are NN in which neurons are organized in layers, and the connections between neurons only go in one direction, from the input layer to the output layer. Recurrent networks are NN in which neurons can receive input from neurons of earlier or later layers. NN can be trained on a large dataset using a process called "supervised learning" in which the correct answers are given for each input so that the NN can "learn" to produce correct answers for similar inputs in the future. NN can be trained to make predictions on a local scale or to make forecasts at different time scales. Furthermore, NN can be easily updated with new data, which makes them suitable for use in situations where the input data may change rapidly.

In this paper, NN is used in MATLAB environment to predict future short-term temperatures from monitored in-field data. The NN is trained based on the temperature monitored from 1/1/2016 to 31/12/2022 at the climatic station in the laboratory of the engineering department of the University of Sannio, in Benevento city. The sampling rate of the source data is six samples per hour, but due to the onerousness of the operation, the average daily temperature value is then considered. After that, these forecasts are implemented in dynamic energy simulations of a single-family building to calculate the variation in primary energy demand for heating and cooling. The building numerical model is developed in the EnergyPlus engine.
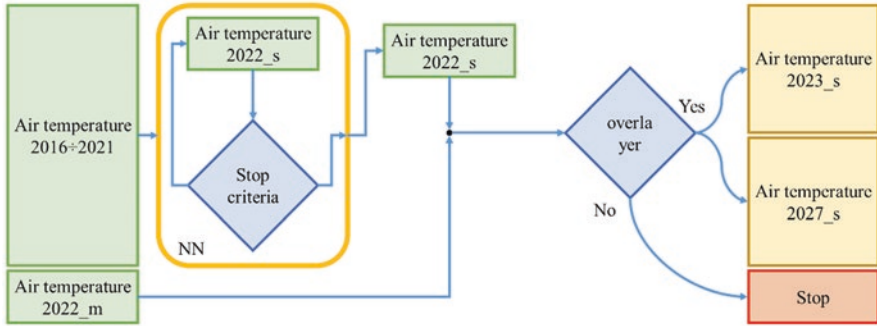
Fig. 1 Methodological approach developed

Figure 1 shows the methodological approach used. The dataset of daily mean temperatures from 2016 to 2021 is used as input to the NN to train the network. When a stop criterion occurs, the NN returns a list of values for the year 2022, called 2022_s (simulated). Various stopping criteria can be chosen, i.e., Mean Absolute Error (MAE) or Root Mean Square Error (RMSE). In this paper, the Mean Square Error (MSE) is used. The 2022_s list is compared with the monitored data of 2022, called 2022_m (monitored). If the year 2022 measured and simulated could be overlayered, then the forecast for 2023 and 2027 is carried out.

To use the NN, these steps have been followed:

- Collection of air temperature data
- Data preparation:
  - Remove any outlier values
  - Normalize the data to make the variables comparable to each other
  - Split the data into two parts, the first to be used for training and the second for testing
- Creation of the NN
- Training the NN using a supervised learning process
- Validation of the NN, it is important to test the network on test data to verify that it can make accurate predictions
- Using the NN to make predictions

The algorithm, Fig. 2, starts from the standardization of the input data to speed up the calculation operations. The data is organized into two groups: input and target data. The input data consists of an array of dimensions lag x n-lag where:

- Lag is the number of data points that are used to make a future prediction.
- *n* is the total number of data points monitored.

While target data is the latest lag+1 values from the temperature dataset. The input data is divided into three families:
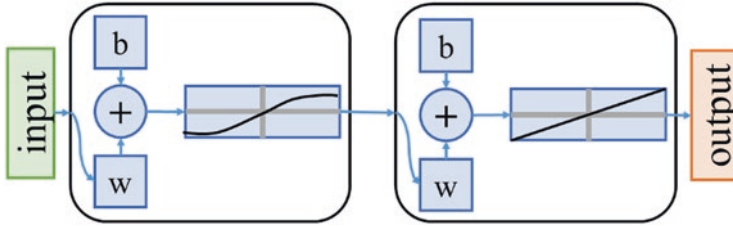
Fig. 2 Neural network used

- Train data is used to train the NN, i.e., to make it gain the ability to recognize patterns and make predictions on new data. During the training process, the NN changes the weights.
- Validation data is used to evaluate the performance of the NN during the training process.
- Unlike validation data, test data are used at the end of the training process to supply an assessment of the NN performance on unseen data.

Bias (b) is a value that shifts the activation function of a neuron; it allows the NN to output a non-zero value even when all inputs are zero, and it helps to prevent overfitting. The weights (w) are the values that determine the importance of the synapses and are adapted during training to improve the performance of the NN. The activation function is applied to each neuron in a NN to determine its output and allows the NN to learn non-linear relationships.

A temperature vector of length equal to n-lag+1, called window, is cyclically given as input. NN returns a value that occupies the last position in the window, and the first value in the list is deleted. By repeating this operation, the air temperature for Benevento is predicted up to 2027.

The data monitored in Fig. 3 with a blue solid line show an annual seasonality and a slightly increasing trend. The seasonality is respected by the results of the NN both for the simulation of 2023, orange solid line, and for the projection to 2027, green solid line. The growing trend has been correctly included in the output data.

Table 1 reports the maximum and minimum values of the air temperature for each year (T_{max} and T_{min} respectively). The increasing trend of the maximum air temperature can be observed. This behavior is also observable for the minimum temperature but in a less evident way.

3 Case Study

The case study is a detached house built in 1985, developed in TABULA project to be a reference building [15]. The structure consists of three floors, one of which is semi-underground and used as a garage. In total there are 198 m^2 of heated surface with a surface-to-volume ratio of 0.65 m^{-1}. The table in Fig. 4a summarizes the
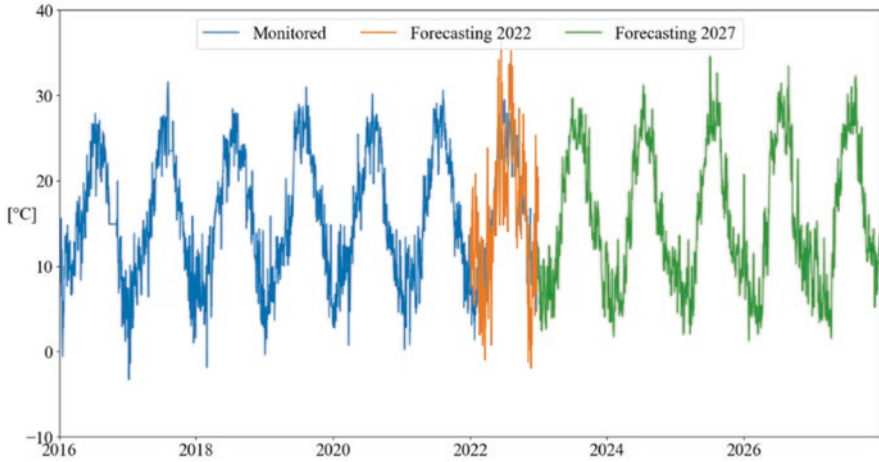
Fig. 3 Monitored data, forecast to 2023 and forecast to 2027

thermophysical properties of the building envelope. A natural gas boiler in the garage is used for heating and DHW, with a total efficiency equal to 0.73. Radiators are used as the system terminal for each room, fueled with water at 80 °C. A DX multi-split system with a nominal EER of 3.45 is present for the cooling service. The indoor set point temperature is 20 °C for the heating period and 26 °C for the cooling one. The render view of the building in its "base case" configuration could be seen in Fig. 4b. In addition, a "refurbished" case is also developed. The refurbishment involves the external wall insulation through 2 cm of vacuum insulation panels (VIP) that reduces their transmittance to 0.26 W/m²K.

4 Results

The histogram in Fig. 5 reports the results of the primary energy for cooling for all analyzed years. With respect to the 2016_m year, an increase could be seen over time, with values between 22% and 59%, for the base case and between 20% and 54% for the refurbished case. The difference between the base case and the refurbished case is about 6% ÷ 10% considering all years. Analyzing the 2022_m and 2022_s, the percentage difference in primary energy needs is 10% for both cases. The increase in primary energy for cooling is due to the rise in air temperature obtained from NN developed.

Figure 6 shows the results in terms of primary energy demand for the heating period. First of all, for both monitored years (2016_m and 2022_m) and the simulated years (2022_s, 2023_s and 2027_s), the base case has a primary energy demand that is approximately 40% higher than the refurbished case. There is an increase in the primary energy demand for both the base case and the refurbished

Table 1 Maximum and minimum temperature for each year

	2016_m	2017_m	2018_m	2019_m	2020_m	2021_m	2022_m	2022_s	2023_s	2024_s	2025_s	2026_s	2027_s
T_{max} [°C]	27.9	31.6	28.4	31.0	30.2	30.6	29.5	36.6	29.7	31.2	34.5	33.4	32.2
T_{min} [°C]	−0.6	−3.3	−1.9	−0.3	0.7	0.3	1.4	−1.9	2.5	1.8	2.0	1.3	1.6
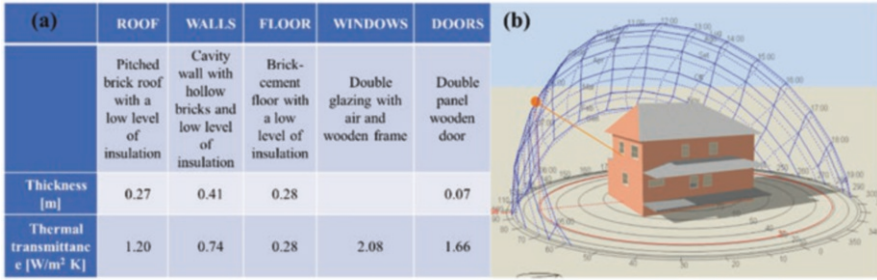
Fig. 4 Envelope thermo-physics characteristics (**b**) and render view (**a**) of the case study
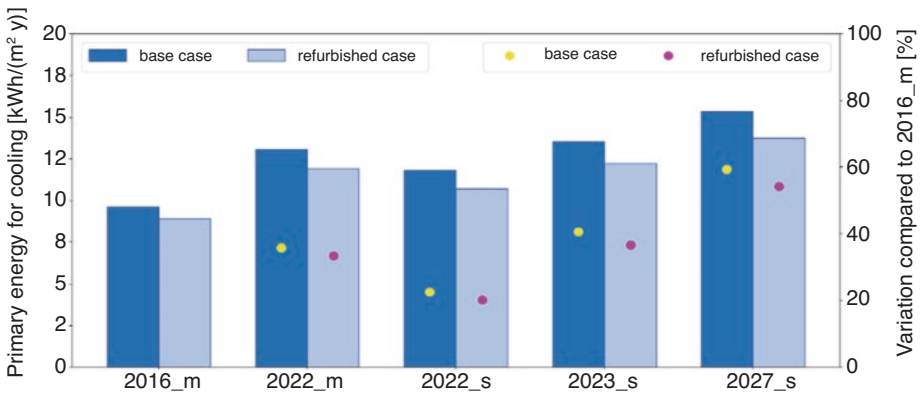
Fig. 5 Primary energy for cooling
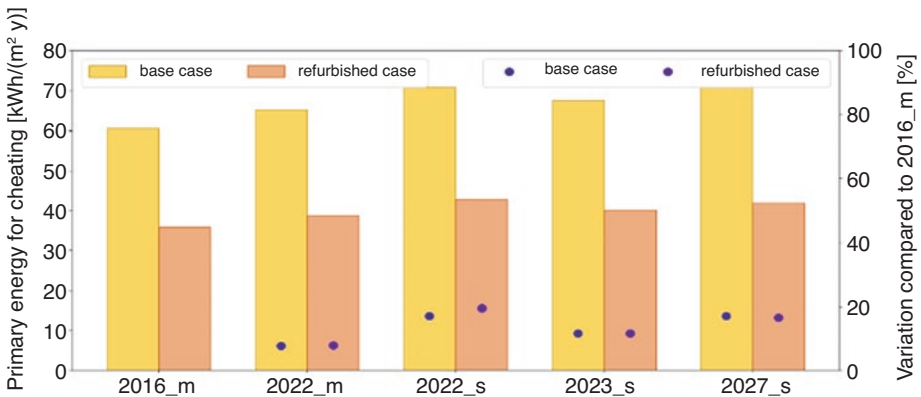
Fig. 6 Primary energy for heating

case with respect 2016_m. For instance, the base case demand increases between 8% and 17%, while the refurbished case between 8% and 20%. On the other hand, the year 2022 has been analyzed for both monitored and simulated cases. It shows a deviation of 9% and 11% for the base and refurbished case, respectively. The increase in primary energy demand for heating is linked to the future temperature reaching lower minimum values.

5   Conclusions

The developed work made it possible to take Benevento city's outside temperature through a neural network in MATLAB engine. Starting from 6 years of in-field monitoring, the forecast to 2027 has been carried out. Using a reference building case study, the following conclusions could be drawn:

- The error in the proposed method to predict the cooling or heating energy demand is about 10%, considering that the year 2022 has been both simulated and measured.
- With respect to 2016, the cooling energy demand in 2027 increases by 59% considering a building with poor insulation level and 54% with a well-insulated building envelope.
- Considering the heating demand, with respect to the 2016 year also increases, due to the reduction of minimum values of temperatures obtained over the years. In this case the increase reaches a maximum 17% in 2027 for both refurbished and base case building configurations.

The limitations of this work lie in the fact that to know the real energy need of the building in the future, the evaluation of other climatic parameters (such as radiation, wind speed, rain etc.) is needed. Moreover, the aging of materials and thermal systems should also be evaluated. These issues will be investigated in a future development.

References

1. Coderoni, S., Pagliacci, F.: The impact of climate change on land productivity. A micro-level assessment for Italian farms. Agric. Syst. **205**, 103565 (2023)
2. Guglielmo, R., Ellena, M., Barbato, G., Giugliano, G., Schiano, P., Leporati, S., Traina, C., Mercogliano, P.: Climate change adaptation cycle for pilot projects development in small municipalities: the northwestern Italian regions case study. City Environ. Interact. **17**, 100097 (2023)
3. De Masi, R.F., Gigante, A., Ruggiero, S., Vanoli, G.P.: Impact of weather data and climate change projections in the refurbishment design of residential buildings in cooling dominated climate. Appl. Energy. **303**, 117584 (2021)

4. Yassaghi, H., Gurian, P.L., Hoque, S.: Propagating downscaled future weather file uncertainties into building energy use. Appl. Energy. **278**, 115655 (2020)
5. Liu, S., Kwok, Y.T., Ka-Lun Lau, K., Wai Tong, H., Chan, P.W., Edward, N.G.: Development and application of future design weather data for evaluating the building thermal-energy performance in subtropical Hong Kong. **209** (2020)
6. Chakraborty D., Alam A., Chaudhuri S., Başağaoğlu H., Sulbaran T., Langar S.: Scenario-based prediction of climate change impacts on building cooling energy consumption with explainable artificial intelligence, 291, 1 June 2021
7. Wang, H., Chen, Q.: Impact of climate change heating and cooling energy use in buildings in the United States. Energ. Buildings. **82**, 428–436 (2014)
8. Narowski, P., Janicki, M., Heim, D.: Comparison of untypical meteorological years (UMY) and their influence on building energy performance simulations, Building Simulation, 2013, Chambéry, France
9. Official Journal of the European Union, 19.4.2012, C 115/1, Guidelines accompanying Commission Delegated Regulation (EU) No 244/2012 of 16 January 2012 supplementing Directive 2010/31/EU of the European Parliament and of the Council on the energy performance of buildings by establishing a comparative methodology framework for calculating cost-optimal levels of minimum energy performance requirements for buildings and building elements (2012/C 115/01)
10. Bouteska A., Hajek P., Fisher B., Abedin M.Z.: Nonlinearity in forecasting energy commodity prices: Evidence from a focused time-delayed neural network
11. Moghanlo, S., Alavinejad, M., Oskoei, V., Saleh, H.N., Mohammadi, A.A., Mohammadi, H., Derakhshan Nejad, Z.: Using artificial neural networks to model the impacts of climate change on dust phenomenon in the Zanjan region, north-west Iran
12. Jung, D., Kim, H.S., Jhin, C., Kim, H., Park, S.H.: Time-serial analysis of deep neural network models for prediction of climatic conditions inside a greenhouse
13. Long, N.K., Sgarioto, D., Garratt, M., Sammut, K.: Response component analysis for sea state estimation using artificial neural networks and vessel response spectral data
14. Jain, A.K., Mao, J., Mohiuddin, K.M.: Artificial Neural Networks: a Tutorial (1996). https://doi.org/10.1109/2.485891
15. De Masi, R.F., Ruggiero, S., Vanoli, G.P.: Multi-layered wall with vacuum insulation panels: results of 5-years in-field monitoring and numerical analysis of aging effect on building consumptions. Appl. Energy. **278**, 115605 (2020)

Part VIII
Environmental Impact Assessment and Management of Different Power Generation Technologies

Solar Photovoltaic End-of-Life Waste Management Policies in Leading Countries and the Lessons Learned for the Kingdom of Saudi Arabia

Abdulrahman Aleid, Amjad Ali, and Md Shafiullah

1 Introduction

The development and implementation of renewable energy sources are accelerating as the effect of greenhouse gases becomes more prominent. Solar photovoltaic is the world's third-largest renewable technology for generating electricity [1]. Therefore, the deployment of SPV has grown dramatically during the last decade (2011 to 2021), reaching a cumulative global installed capacity of 843 GW at the end of 2021 as depicted in Fig. 1 [2].

Based on the literature China, Japan, India, and Germany are leading in solar PV accumulative installation globally. As the leading countries are racing to implement PV technology on substantial scales, it has been anticipated that after one decade there will be a huge solar PV wastage at the end of their life. However, the development and implementation of policies that manage the waste and handling of PV panels are lacking globally as given in Table 1.

As the Kingdom of Saudi Arabia announced that one of its Vision 2030 objectives is to increase domestic generation capacity from renewable energy to 50% by 2030 [7]. Most of this increase is set to be achieved by solar PV energy. However, Saudi Arabia currently has no specific policies for PV waste management. Therefore, policy assessments for PV end-of-life disposal are needed to achieve the objective of Saudi Arabia effectively and safely.

A. Aleid
Department of Mechanical Engineering, King Fahd University of Petroleum and Minerals, Dhahran, Saudi Arabia

A. Ali (✉) · M. Shafiullah
Interdisciplinary Research Center for Renewable Energy and Power Systems (IRC-REPS), King Fahd University of Petroleum and Minerals, Dhahran, Saudi Arabia
e-mail: Amjad.ali@kfupm.edu.sa

Solar PV cumulative global installed capacity
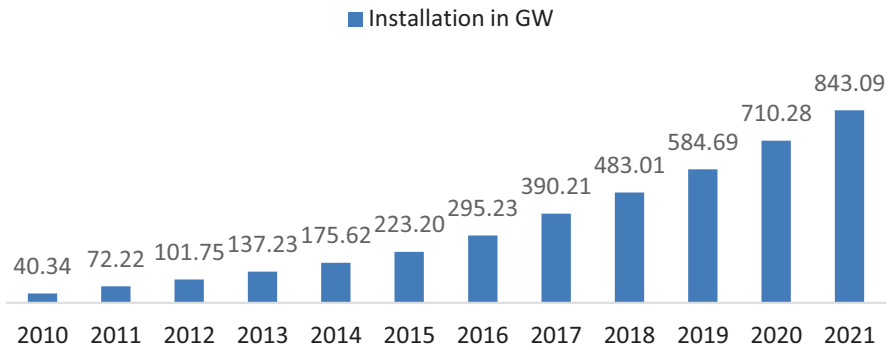
Fig. 1 2010–2021 solar PV cumulative global installed capacity

Table 1 Overview of the solar PV end-of-life policies in the top countries by projected cumulative PV waste in 2050

Country	China	Japan	India	Germany
PV cumulative capacity 2021 (GW) [3]	306.4	74.19	49.34	58.46
Regulator agency/party [4, 5]	State Council of the People's Republic of China	Ministry of Economy Ministry of the Environment	Ministry of Environment, Forest and Climate Change	National Register for Waste Electrical Equipment (Stiftung EAR)
Specific PV waste policy	X	x	x	✔
Regulatory framework	X	The Waste Management and Public Cleansing Act [5] The Construction Waste Recycling Law [5]	Solid Waste Management Rules and the Hazardous and Other Wastes Rules [6]	The Electrical and Electronic Equipment Act [5]
Plans and initiatives	The National High-Tech R&D Programme [4, 5]. PV Recycling and Safety Disposal Research	NEDO and several other R&D activities	"PV Waste Management in India" report at Solar India Summit [6]	R&D initiatives that aim to decrease recycling costs and increase the potential revenue from recovered materials [5]

2   Germany

Germany is one of the leading countries in terms of installed PV panels. Germany has the highest installed solar energy capacity in the EU, with a capacity of around 58GW [3]. As a member of the European Union (EU), Germany must follow the EU directives or must develop its policies for solar PV end-of-life waste management. Solar PV waste falls under category 4 in the WEEE Directive 2012/19/EU. Therefore, the recovery and recycling target for PV waste is 85% and 80%, respectively. The German policy concerning financial responsibility over the PV life cycle is based on the extended-producer responsibility (EPR) principle. The focus of the policy is on how to place the responsibility for managing PV waste logistically and financially. The two main financing mechanism types enforced in Germany are business-to-consumer (B2C) and business-to-business (B2B) [5].

2.1   Business-to-Business (B2B)

Based on the quantities and size of a PV consumer, it can be classified as a business (B) instead of a regular consumer (C). This type of transaction allows the producer and the consumer to have a more flexible and efficient process between them. The buyer is permitted through this scheme to have contractual agreements on the responsibility and handling of PV waste, where the owner of the project (buyer) has the right to have a contract for handling waste with the producer or with another third-party handler. B2B transaction ensures a preferred and more efficient method between large-scale consumers and producers provided that the WEEE directive regulations are followed. Furthermore, the policy encourages a competitive market for financial models that funds the collection and recycling of PV for large projects [5].

2.2   Business-to-Consumer (B2C)

The type of transaction between private households and PV producers is classified as a B2C mechanism. The scheme ensures that producers take full responsibility for financing handling and recycling costs of present and future PV waste generated from consumers (households). The scheme consists of two levels of financing.

Level 1 of Operation and Financing   Level 1 obligates producers to provide the financing for immediate recycling and handling of their products, along with products that were put on the market before including it in the law. The required financing is provided through a joint-and-several liability format. The amount of financing that is distributed among producers is determined by the overall volume collected; moreover, the share of volume for each producer is determined by their market

share of registered products. If a producer leaves the market, the volume share of the producer is distributed among the remaining producers. All running systems should be paid for their handling by the producers (pay-as-you-go system). Producers are required to report the collected and recycled volumes to a clearing house, along with reports of their registered products on the market [5].

Level 2 of Operation and Financing Level 2 covers the future costs of collection and recycling, ensuring that producers provide the required financing in advance according to the regulator. The share of financing responsibility for each producer is determined by their market share, assumed return rate of PV panels, and assumed disposal costs. Producers are not allowed to put their products on the market unless they declare to a clearing house that they are responsible for level 2 costs. If all producers withdrew from the market, the costs would be covered by last-man-standing insurance [5].

3 Japan

Japan is one of the pioneers in solar PV technology. It is the third largest country in the world in terms of installed PV capacity, with a capacity of 74 GW [3]. Although Japan has no PV-specific regulatory framework, PV waste falls under the Waste Management and Public Cleansing Act. The act focuses on industrial waste and the responsibilities of waste generators and handlers. The Ministry of Economy and the Ministry of the Environment have jointly promoted R&D in PV technology, and schemes for managing and handling PV waste through their introduced roadmap in 2015. In 2017, guidelines for the disposal of end-of-life PV were published by The Japan Photovoltaic Energy Association (JPEA) [8]. Although the guidelines were highly recommended by the JPEA, they are not enforceable by the law [4, 5].

3.1 Japan's Waste Management Law

Since Japan has no specific PV waste management laws, PV waste is regulated through the Waste Management and Public Cleansing Act (WMPCA). WMPCA implements the extended producer responsibility principle. PV waste is classified as industrial waste; thus, the waste generator is responsible for managing the waste materials. The generator can hire a licensed disposal business to handle the materials. The waste generator must oversee the waste disposal process if it was commissioned to another party. The process of transporting, handling, treatment, and disposal is monitored and should be reported to the governor by all responsible parties. Intermediate treatment disposal facilities should be permitted to be installed. To be permitted, the firm should comply with the standards and requirements imposed by prefectural or designated city governments. Authorities conduct spot

inspections to ensure the standards and requirements are met by businesses permitted to operate on industrial waste. In general, the Japanese legal framework concerning waste management law is focused on the responsibility of waste generators with specific laws that apply the EPR principle [9].

4 China

China has a solar PV cumulative capacity higher than the United States, Japan, Germany, and India combined. China has a solar capacity of 306 GW in 2021 [3]. Since China has the highest usage of PV panels in the world, the amount of waste generated is going to be the highest among other countries by far. However, China has no specific waste policies for PV waste. There are specific and extensive regulations for e-waste through the Waste Electrical and Electronic Product Recycling Management Regulation; however, PV waste is not included in this regulatory framework. The National High-tech R&D Programme PV Recycling and Safety Disposal Research recommended solutions for the problems of PV waste and its challenges. Technical requirements for the recycling of PV modules were issued by The China Photovoltaic Industry Association in 2017; however, it lacks clear guidance and plans for handling the waste [5, 10].

4.1 China's Waste Management Law

China has no specific PV waste management laws; thus, PV waste is categorized as general waste [5]. The implemented laws for managing catalogued e-waste are a specific, advanced, and possible model for PV waste management policies. The recovery and disposal of e-waste are subsidized by the state through a treatment fund. The extended producer responsibility system was formed in 2020 with plans for the development of relevant recycling systems in the upcoming years. Features of the e-waste law in China include supporting enterprises to develop their recycling systems to meet the required standards and plans for waste management development. Waste collecting encouragement is practiced through a monetary bonus or goods purchase bonus system for the recycling of e-waste. The collection of waste is supported by self-service recycling bins that track the waste information using barcodes [11].

5 India

India has a solar PV cumulative capacity of almost 50 GW in 2021 [3]. About 80% of the current installed capacity was installed in the last 5 years. However, India has no specific PV waste management laws. PV waste in India is managed by the

Ministry of Environment, Forest, and Climate Change [5]. However there exist no major plans or initiatives to categorize PV waste as a distinct category, nor does the government have plans for R&D in policy development concerning PV waste. PV waste does not fall under e-waste, nor does it pass the hazard tests and sampling that are covered by the government for products that comply with Hazardous Waste Management Rules (RoHS). Currently, PV waste is not specifically regulated, and it is up to the owner to dispose of it or store it for different uses. The disposal of PV modules in India could include illegal or uncontrolled landfill practices; moreover, the responsibility of financing the management of the waste is not well defined; thus, confusion and randomness are the themes of handling PV waste. The most recent initiative concerning PV end-of-life policies is the "PV Waste Management in India" report at Solar India Summit [6].

6 Saudi Arabia

One of the goals of Saudi Arabia's Vision 2030 is to transform its energy production to be less reliant on fossil fuel and instead utilize solar power to feed its energy needs [7]. Thus, many substantial projects were launched to build PV power plants across Saudi Arabia. In 2019–2020 a total of 2670 MW of ten pre-developed projects were tendered [2]. Such plans mean that Saudi Arabia should have an effective and ready legal infrastructure for developing policies that achieve its desired goals. PV waste is an important concern that needs to be considered by the government while developing its PV market and projects. Currently, Saudi Arabia has no specific laws of PV waste management, nor initiatives or plans to develop any.

6.1 Saudi Arabia Waste Management Law

On 15th September 2021, Saudi Arabia announced its new "Waste Management Law." The law aims to regulate the safe disposal of waste, segregation, transport, storage, export, import, and all other related activities. According to the law, institutions must ensure that the disposal and recycling of waste are done safely through environmentally sound methods [12].

7 Recommendations and Proposals for a General Initial Framework

- EPR system is the most likely scenario for PV waste management in Saudi Arabia. Considering the current legal environment and the articles of the KSA Waste Management Law, EPR could be the guiding principle for developing PV waste management policies. The responsibilities under EPR and their implica-

tions should be established. While a basic model could be introduced in the next 5 years, a more precise and compact system should be developed along with effective communication and connection between all involved parties in the system.

- Since PV modules are not readily available to small consumers and households, the initial plans and systems in the upcoming years should focus on a B2B approach. The need for a B2C system would become more prominent in the future when PV systems spread to households and small-scale consumers.
- A roadmap that outlines the goals of the competent authorities, private service providers, and producers is necessary. The roadmap could outline goals and plans like the minimum percentage of recovered materials from PV waste, the R&D initiatives for policies and technologies in PV waste management, and the expected outcomes from each involved party.
- A well-coordinated plan between ministries, provinces, and municipalities is necessary for a smooth implementation of the system.

8   Conclusion

The paper has given a general review of the PV end-of-life waste management policies in the top countries globally in terms of accumulative PV installation. The findings of the paper showed that PV waste management is lacking globally; however, based on the initiatives and plans of multiple countries, there is a rapid and clear trend for developing and implementing PV waste management policies. The benchmarking of Saudi Arabia Waste Management Law has shown that the law is currently ineffective in dealing with the anticipated amounts of PV waste resulting from the plans of Vision 2030.

The Saudi environmental law has many shortcomings when it comes to PV waste management; however, the PV market in Saudi Arabia is still relatively new. Therefore, the experiences from advanced examples of other countries would significantly help and accelerate the R&D and implementation of an effective legal framework that covers all aspects of PV production, distribution, and end-of-life management. Currently, there is no published work on the assessment of PV waste management with a benchmark for Saudi Arabia Law. Therefore, further extensive research is needed to investigate the details and complications of Saudi's legal environment, social environment, and economics, concerning the development of new PV waste management laws. Furthermore, the implementation of PV end-of-life policies requires an analysis of the different levels of PV waste management. A micro-level and macro-level distinction for the waste management processes should be considered when investigating new PV end-of-life policies in Saudi Arabia.

References

1. Solar PV – Analysis – IEA.: https://www.iea.org/reports/solar-pv. Accessed 14 Feb 2023
2. Ali, A., Irshad, K., Alam Malik, S.: Solar photovoltaic end-of-life disposal policy assessment for the Kingdom of Saudi Arabia. [Online]. Available: https://www.researchgate.net/publication/368247815. "Statistical Review of World Energy 2022"
3. I. PVPS Task et al.: End-of-Life Management of Photovoltaic Panels: Trends in PV Module Recycling Technologies End-of-Life Management of Photovoltaic Panels: Trends in PV Module Recycling Technologies Operating Agent (2018)
4. IRENA and IEA-PVPS: End-of-Life Management: Solar Photovoltaic Panels (2016)
5. EU and India launch 'PV Waste Management in India' Report | EEAS Website: *Delegation of the European Union to India and Bhutan* (2021). https://www.eeas.europa.eu/delegations/india/eu-and-india-launch-%E2%80%9Cpv-waste-management-india%E2%80%9D-report_en. Accessed 23 Jan 2023
6. Saudi Green Initiative - Vision 2030.: https://www.vision2030.gov.sa/v2030/v2030-projects/saudi-green-initiative/. Accessed 11 Mar 2023
7. Japan issues guidelines on 'proper disposal' of used solar modules - PV Tech.: https://www.pv-tech.org/japan-issues-guidelines-on-proper-disposal-of-used-solar-modules/. Accessed 23 Jan 2023
8. Japan Industrial Waste Information Center: Waste Management in Japan ~Rules and Figures~ (2018). Accessed 11 Mar 2023. [Online]. Available: https://www.jwnet.or.jp/assets/pdf/en/20190322133536.pdf
9. Wang, C., Feng, K., Liu, X., Wang, P., Chen, W.Q., Li, J.: Looming challenge of photovoltaic waste under China's solar ambition: a spatial–temporal assessment. Appl. Energy. **307**, 118186 (2022). https://doi.org/10.1016/J.APENERGY.2021.118186
10. Tan, Q.: EPR for e-waste management in China. Accessed 11 Mar 2023. [Online]. Available: https://www.itu.int/en/ITU-D/Regional-Presence/AsiaPacific/SiteAssets/Pages/Events/2019/Policy-awareness-workshop-on-E-waste/China%20E-waste%20EPR.pdf
11. "تفاصيل النظام" https://laws.boe.gov.sa/BoeLaws/Laws/LawDetails/4d5bda56-cc0d-4b16-a025-ad9d00b281ab/1. Accessed 12 Mar 2023
12. Ali, A., Malik, S.: "Solar Photovoltaic End-of-Life Disposal Policy Assessment for the Kingdom of Saudi Arabia," in International Association for Energy Economics (IAEE), 2023

Electrification of the Portuguese Railway: Life Cycle Analysis of Current Scenario and Future Decarbonization Goals

Tiago Ramos da Silva, Bruna Moura, and Helena Monteiro

1 Introduction

Transportation and mobility services are one of the key areas to tackle in ensuring future global sustainability. Railway transport should be at the forefront of our efforts, considering it is the high-volume transportation service with the lowest environmental impact per transported passenger. It is also the only transport type to have lowered its global emissions in recent times, with a 2% decrease from 2000 to 2018 [1]. Railway transport represents 7% of total transported freight, and 8% of the total passenger market, but only emits 2% of the global sector emissions [2]. Considering that projections expect a doubling of transport demand by 2050, railway services have the possibility to greatly assist in the decarbonization of the transportation sector, in line with the Paris agreement and the European Union's efforts to combat climate change.

However, to the best of the authors' knowledge, the only available work on the life cycle environmental impacts of the Portuguese railway was published by Jones et al. [3], whereby a life cycle assessment of a prospective high speed rail line between Porto and Lisbon was conducted. The present work is, therefore, the first life cycle analysis of a conventional rail line in the Portuguese territory, with the caveat that this the only type of railway currently operating in the country. It intends to provide a point of reference on its environmental performance, for both the present scenario and the future prospects of the aforementioned decarbonization goals. To accomplish this, the Douro line was used as a representative case study. The environmental performance of building the necessary infrastructure and rolling stock for this line, maintaining it, and operating it was quantified.

T. Ramos da Silva (✉) · B. Moura · H. Monteiro
Low Carbon & Resource Efficiency, R&Di, Instituto de Soldadura e Qualidade, Grijó, Portugal
e-mail: tandsilva@isq.pt

Structure wise, Sect. 2 of this chapter will describe the case study and the applied methodology for the assessment. Section 3 will provide a brief description and analysis of the obtained results for the different scenarios. Section 4 will resume the main findings and provide the concluding observations.

2 Materials and Methods

Life cycle assessment (LCA) is an internationally accepted and widely used methodology, normalized through the ISO 14040 [4] and ISO 14044 [5] norms. For the purposes of this chapter, this methodology was employed to measure the environmental impact of the Portuguese conventional railway, using the Douro railway line as a case study.

To perform and translate the results of the assessment, the functional unit was defined as 1 passenger-kilometer (pkm). The system boundaries for the study include: the extraction and transportation of raw materials; infrastructure and rolling stock construction; its maintenance; and its operation. The end-of-life of the railway line components and the rolling material were not taken into account, as well as the particle emission from the train wheels, catenary lines, and brakes.

The alternative scenarios under analysis are presented below:

- Firstly, and serving as a baseline, the environmental performance of the Douro line in its present operating condition was assessed, with data gathered for the year 2019. In its current state, the Douro line has a mixed circulation of both diesel and electric trains, with only a third of the line being electrified.
- The second setting presents the results for a hypothetical complete electrification of the line and its rolling stock, considering the current Portuguese electricity mix.
- The third setting builds on the same hypothesis of the second but instead considers the public projections for the Portuguese electricity mix for the year 2030 [6].
- The fourth and last setting considers the same full electrification scenario and the projections of the electric mix for the year 2050 [6], the date by which carbon neutrality of the national electricity production is expected.

Sectorial life cycle assessment information provided by Tuchschmid et al. [7] was used as the main source of secondary data. The methodology proposed by Tuchschmid et al. was deemed the most transparent and versatile by the International Union of Railways in a comparison of several different railway life cycle assessment approaches [8], and has been applied in several recent studies on this topic [9–11].

A complete inventory was assembled with the quantities of each component in the Douro line, according to the categorization presented by Tuchschmid et al. Documents provided by Infraestuturas de Portugal were used as a data source for the line occupancy rates and the annual traveled pkm and tkm (train-kilometer), while annual reports from Comboios de Portugal were utilized to gather data on the

Table 1 Life cycle assessment indicators used for the analysis

Indicator	Unit	Impact method
Global Warming Potential (GWP)	kg CO_2-eq	ReCiPe 2016 v1.1 Midpoint (H) [14]
Cumulative Energy Demand (CED)	MJ	CED v1.11 [14]
PM_{10}	kg	Selected LCI results, additional v1.04 [14]
SO_2	kg	Selected LCI results v1.05 [14]
NO_X	kg	Selected LCI results v1.05
NMVOC	kg	Selected LCI results v1.05

rolling material currently in use. The power usage of the electrified rolling material was obtained from the ecoinvent 3.8 database [12].

In addition to Excel, SimaPro (version 9.3) [13] software was used to analyze the environmental flows of processes not included in the secondary data provided by Tuchschmid et al., specifically the adaptation to the different Portuguese electricity mixes and pollutant discharge from the diesel trains.

The same impact indicators utilized by Tuchschmid et al. were applied for this analysis. They are outlined in Table 1.

3   Results and Discussions

Figure 1 outlines the environmental results of the four scenarios for each indicator.

The comparative percentual emissions of each line element are also provided.

Most of the impact of the railway infrastructure is associated with the earthworks needed for line construction and the subsequent basic components of a railway line: the deposition of the ballast sub-layer, the installation of the sleepers on top of this ballast, and the laying of the rails on top of the sleepers.

The building and upkeep of tunnels and bridges/viaducts are also considerable contributors to GWP and PM_{10}. The catenary structure presents high impacts for PM_{10} and SO_2. Nevertheless, for the present setting, operation of the railway line has a much higher impact than its construction and maintenance. The biggest portion of pollutant emissions from operation come from the diesel powering the internal combustion trains, while electricity consumption for powering the infrastructure and the electric trains comes second. These two elements (diesel and electricity consumption) account for more than 70% of the global impact of every indicator but PM_{10}. In comparison, manufacturing and maintaining the rolling stock presents very modest emissions across the board.

Looking at the second setting (Diesel → electric transition), the increase in emissions from electricity is small when compared to the emissions being avoided from the diesel trains. Moreover, the gradual decarbonization of electricity production associated with the remaining scenarios showcases great reductions in total electricity emissions for the years 2030 and 2050, which leads to big overall environmental savings for the railway line.
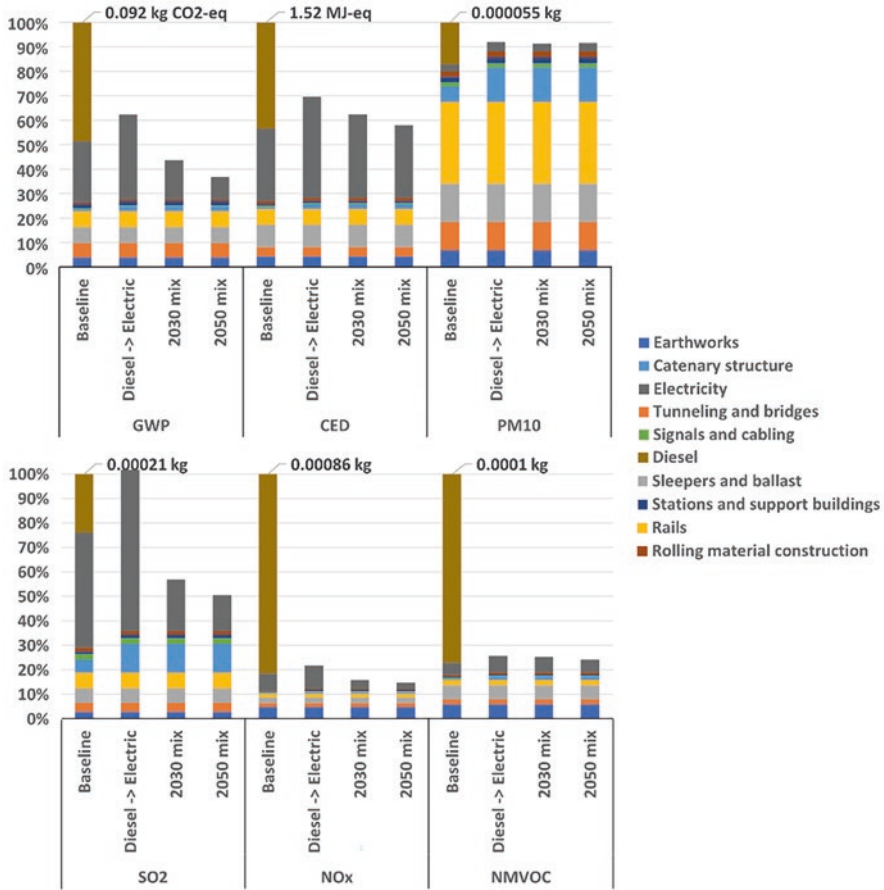
Fig. 1 Life cycle analysis results per pkm

With regard to GWP, the diesel to electric transition of the second scenario permits a reduction of 35 g in carbon footprint/pkm, or 38% of emissions. Furthermore, the transition from the current electric mix to the 2050 mix allows for a further saving of 24 g in carbon footprint/pkm, or an additional 41% decrease.

Save for an increase in PM_{10} and SO_2 emissions of the catenary structure in the full electrification scenarios (due to the additional catenary that needs to be installed), infrastructure construction and maintenance impact stays uniform across the different scenarios and indicators. Although the operation stage accounts for most of the impact in the present setting, the gradual emission reduction of operating the line throughout the different scenarios leads to the infrastructure having an also gradually increasing percentual contribution to the global emission total. From the present setting to the year 2050 setting, operation and maintenance of the line diminishes from 74% of the total to 27%. This means that by 2050 construction and maintenance of the infrastructure represents the majority of emissions.

A sensitivity analysis to determine the effect of the annual pkm on the carbon footprint of each passenger was also executed, for the three scenarios of complete electrification. If an increase from the currently traveled 1.81E8 annual pkm to 3.00E8 annual pkm is verified, a reduction of 10 g in carbon footprint/pkm is obtained, which amounts to an average decline of 24% among the three scenarios. This stresses the necessity of an increase in public acceptance and use of railway transportation.

4 Conclusions

This work intended to quantify the environmental impact of the Portuguese conventional railway, through a life cycle assessment of the Douro railway line. Railway and rolling stock operation, construction, and maintenance were assessed. The more relevant hotspots were signaled, and courses of action for improvement identified. Four distinct scenarios were assessed, permitting not just a quantification of the environmental performance in the present situation, but also in terms of future prospects, considering the projected Portuguese electricity mixes for the years 2030 and 2050, in line with the European Union's decarbonization objectives.

For the current setting, it was found that operation of the railway line accounts for the biggest portion of emissions for every indicator except PM_{10}, and specifically 74% of CO_2-eq output (GWP). This is owed mostly to the diesel burned to power the internal combustion trains, and in a smaller part to the electricity employed to power the infrastructure and electric trains. Building and maintaining the stations/support buildings and the rolling material has little impact on global emissions. It is the combination of the earthworks and the subsequent deposition of the ballast sublayer, the sleepers, and the laying of the rails that represent the biggest hotspots for infrastructure.

Analysis of the alternative scenarios showed that substituting the diesel trains with electric units shows great impact reductions for all the studied indicators, bar SO_2. Specifically, for GWP, a 38% decrease in carbon footprint can be immediately obtained with this switch, making it a priority for short-term action.

It was also found that the projected gradual decarbonization of the electricity mixes for 2030 and 2050 is fundamental in further lowering global railway emissions, given electricity use was identified as one of the main environmental hotspots of railway operation. To this point, the 2030 scenario enables a further reduction of 30% in GWP emissions, and the 2050 scenario of 41%. If we compare these scenarios to the present situation (operating diesel trains), decreases in carbon footprint are of 56% (2030 projection) and 63% (2050 projection). Results are also promising for the other impact indicators: per pkm, the scenario for the year 2050 displays a decrease from 1.52 MJ to 0.89 MJ in terms of cumulative energy demand, a reduction from 5.55E-05 to 5.08E-05 kg of PM_{10} particle emission, a drop from 0.00021 to 0.00011 kg of sulfur dioxide gases, as well as big declines from 0.00086 to 0.00013 kg of NOx and from 0.0001 to 0.000025 kg of non-methane-based volatile organic compounds.

Further reductions can also be obtained by strengthening the competitive positioning of railway transportation within the transport sector and encouraging its adoption by the mass public, as this leads to higher load factors for the rolling material and infrastructure, helping to offset their impacts against a higher number of users.

A research gap not covered by this work pertains to the end-of-life of the different railway and train components. Be it through recycling or reuse, there is still a significant opportunity for effective environmental impact reduction measures by smartly managing railway materials at the end of their useful life. Therefore, as a final note, the authors suggest further research is concentrated on these topics.

References

1. International Union of Railways (UIC): Sustainability, Sep. 23, 2021. https://uic.org/sustainability/. Accessed 25 Nov 2022
2. International Energy Agency: The Future of Rail – Opportunities for Energy and the Environment (2019). Accessed 25 Nov 2022. [Online]. Available: www.iea.org
3. Jones, H., Moura, F., Domingos, T.: Life cycle assessment of high-speed rail: a case study in Portugal. Int. J. Life Cycle Assess. **22**, 410–422 (2017). https://doi.org/10.1007/s11367-016-1177-7
4. ISO: 14040 – Environmental management – Life cycle assessment – Principles and framework. (2006)
5. ISO: 14044 – Environmental management – Life cycle assessment – Requirements and guidelines, (2006)
6. República Portuguesa and Agência Portuguesa do Ambiente: Roteiro para a Neutralidade Carbónica 2050. (2019)
7. Tuchschmid, M., Knörr, W., Schacht, A., Schmied, M.: Carbon Footprint and environmental impact of Railway Infrastructure, Heidelberg/Zürich/Berlin (2011)
8. International Union of Railways (UIC): Carbon Footprint of Railway Infrastructure. International Union of Railways (UIC), Paris (2016)
9. Kortazar, A., Bueno, G., Hoyos, D.: Environmental balance of the high speed rail network in Spain: a life cycle assessment approach. Res. Transp. Econ. **90** (2021). https://doi.org/10.1016/J.RETREC.2021.101035
10. Landgraf, M., Horvath, A.: Embodied greenhouse gas assessment of railway infrastructure: the case of Austria. Environ. Res. Infrastruct. Sustain. **1** (2021). https://doi.org/10.1088/2634-4505/ac1242
11. Gratzer, H.: Railway Infrastructure and its Environmental Effects in the Alps (1945-today) (2021)
12. Ecoinvent: Ecoinvent Database. https://ecoinvent.org/the-ecoinvent-database/. Accessed 9 Sept 2022
13. PRé Sustainability B.V.: SimaPro | LCA software for informed-change makers. https://simapro.com/. Accessed 9 Sept 2022
14. PRé Sustainability B.V.: SimaPro Database Manual – Methods Library (2020)

Environmental Impacts of Power Plants and Energy Conversion Systems

Moses Jeremiah Barasa Kabeyi and Oludolapo Akanni Olanrewaju

Acronyms

CAL	Ca-looping
CCS	Carbon capture and sequestration
eLCC	Electricity levelized cost
(ExLCA)	Exergetic life cycle assessment
GWP	Global Warming Potential
LCA	Life cycle assessment
LCC	Life cycle cost
MEA	Monoethanolamine
NMVOC	Non-methane volatile organic compounds
TWh	Terawatt hour

1 Introduction

Life cycle assessment (LCA) is an important decision support tool used to evaluate the environmental impacts of different products or processes from extraction to disposal of waste, i.e., cradle-to-grave or cradle-to-cradle. The lifecycle assessment has increasingly addressed environmental impacts of various technologies energy technologies [1]. Energy is an essential resource for modern society used for many applications like lighting, transport, communication, heating, air conditioning, and manufacturing, among others. The evaluation of energy production technologies considers all aspects such as energy and raw materials consumptions, energy efficiency, and environmental impacts. The environmental impact is an important factor in the evaluation of power generation technologies [2]. Electricity systems account for 38% of primary energy use globally and are set to rapidly grow as demand for

M. J. B. Kabeyi (✉) · O. A. Olanrewaju
Industrial Engineering Department, Durban University of Technology, Durban, South Africa
e-mail: mkabeyi@uonbi.ac.ke; oludolapoo@dut.ac.za

electricity-based services increases such as looking, lighting, sanitation, heating and cooling, and information and communications. The current global electricity mix is dominated by fossil fuels led by coal, natural gas, nuclear, and petroleum which are all nonrenewable [3].

Life cycle assessment (LCA) is a holistic approach applied in evaluating the environmental impacts of products and systems through their entire life. Life cycle analysis is needed to foster the development of energy technologies in a sustainable manner [4]. Life cycle assessment (LCA) is a decision support tool which assesses environmental burdens of products and processes right from materials extraction to disposal popularly referred to as cradle-to-grave or even cradle-to-cradle. For accuracy, the power generation life cycle assessments should better characterize spatial and temporal characteristics [1]. A life cycle assessment is regarded as an environmental assessment of all steps used in production and delivery whose goal is to present a holistic and inclusive picture of environmental impacts by considering all significant downstream and upstream activities and their impacts [5]. The commitment to reduce greenhouse gas emissions by reducing the consumption of fossil fuel sources of energy has driven many countries toward the increased use of low-carbon electricity systems. Nevertheless, reducing greenhouse gas emissions (GHG) may be achieved at the expense of other environmental impacts, like higher depletion of abiotic resources [6, 7].

Selection of generation technologies is coming complex and involves economic, operational, siting, social, and policy constraints [3]. Since the environmental impacts and benefits tend to occur at different phases of the power plant life cycle, it is very important to consider the entire lifecycle. When comparing two options, important phases may not be the same. Therefore, the life cycle approach, i.e., life cycle assessment (LCA) methodology, is preferred. The LCA is a methodology for the evaluation of environmental impact of a product, process, or an activity in the course of its life cycle by quantitatively and qualitatively identifying and describing energy and materials requirements, and associated emissions and wastes generated and released to the environment [8].

As a powerful decision support tool, life cycle assessment (LCA) evaluates the environmental burdens products cross the life cycle. LCA is increasingly being used to address environmental impacts of energy systems and technologies. A typical life cycle analysis is neither spatially explicit nor temporally resolved; hence, it represents a snapshot in space and time or with general data that is not representative of a location at a particular time. Occasionally, LCA results are impactful to the energy sector evolution through knowledge improvement of energy systems and influence policy decisions [1, 9]. LCAs are however challenged by economically powerful and highly innovative energy sectors, more so high regional and temporal variability of operations. These variabilities contribute to unresolved problems in LCA notably the highly diverse generation technologies, leading to different regional mixes which are highly influential in LCA results. Therefore, life cycle assessment for power generation should adequately characterize spatial and temporal characteristics for accuracy and reliability [1, 10].

This review assesses the state of the art of LCA applied in power generation technologies and systems with emphasis on areas like methodological issues, challenges associated with power generation technologies, quantitative results obtained from the literature, and improvement opportunities for LCA applied in power generation.

1.1   Problem Statement

Life cycle analysis for power generation technologies increasingly addresses the environmental impacts of energy technologies. As LCA's role continues to grow as a decision support tool for energy policy, lingering questions remain on how results can be applied in the face of uncertain assumptions in an ever-evolving energy sector. Typical LCA is neither spatially explicit nor temporally resolved and therefore it represents a snapshot in space and time or with general data that do not represent a location and particular time. Although the life cycle results are impactful to the evolution of the energy sector through enhanced knowledge of energy systems and influence policy, the assessments are challenged by economically powerful, fast-paced, and highly innovative energy sector mainly by high regional and temporal variability of operations. The variability contributes to unresolved problems in life cycle analysis. Different regions have different regional energy mixes since the power grid consists of highly diverse power generation technologies [1, 9].

1.2   Rationale of the Study

The transition to renewable energy sources and "green" technologies for power generation and storage should mitigate the climate change resulting from greenhouse gas emissions. The main sustainability challenge for the transition is the dependency on critical materials, processes, and other resources that have significant environmental impacts. Beyond global warming concerns, we have serious sustainability concerns such as loss of biodiversity, water scarcity, environmental pollution, and energy security that should equally be addressed during the transition [11, 12].

Energy and environment issues are seriously interconnected and need comprehensive analysis and understanding of resource management strategies and their consequences. As an example vital water resource depletion and contamination is related to possible shortages in power generation, distribution, and use while the supply of water needs energy [11].

Therefore, there is a need for a system perspective to locate and quantify the impact of human activities and processes on the environment. The life cycle assessment (LCA) is one of the most inclusive analytical techniques to analyze sustainability trade-offs and benefits resulting from complex energy and environmental systems [11, 13].

For accuracy, power generation LCA analysis should better characterize spatial and temporal characteristics [2]. The comparison of power generation technologies is considered generic because it presents a general overview of environmental and economic impacts that are generally expected. Specific impacts can be smaller or greater based on site-specific conditions or mitigation measures put in place [5]. The comparisons help decision makers as follows:

 (i) Policy decisions may be needed before site-specific information is available; hence, "generic" comparisons can be used in decision making.
 (ii) Many energy system analyses do not consider the impacts of entire energy systems from extraction and processing, operation and disposal.
(iii) Many assessments neglect sustainability and reliability aspects, yet they are important in sustainable development.
(iv) There is a need for generic data at the planning level for power generation technologies but is not a substitute for detailed and careful analysis of site-specific conditions. However it provides indication of impacts and choices that need more careful detailed consideration [5].

1.3 Potential Uses of Life Cycle Assessment

The life cycle assessment (LCA) is designed to fulfill different functions and objectives. The various applications include [5]:

 (i) Analysis of the performance of modern commercial technologies even when the performance of older technologies is totally different.
 (ii) LCA can be used to present short-term performance, not necessarily the long-term or expected future performance.
(iii) LCAs can effectively use typical conditions of region or technology [5].

2 Generation Options

Power generation systems do not have equal capability to provide energy services which are variable and time varying. Reliable power systems cannot rely on the "must-run" power systems such as geothermal and nuclear energy or on intermittent power systems like solar and wind alone, but rather an optimized mix of different sources. Energy sources like hydropower with storage can service all electricity needs and maintain system balance. Likewise is oil or diesel, or gas fired power plants which have desirable flexibility, due to the ability to store the energy resource for later use without loss. Intermittent sources constantly require a "backup" system to compensate for fluctuations and storage to store excess when generation for use during high electricity demand [5, 14].

Table 1 Classification based on expected service level

	Power plant technology	Application	Remarks
1	Hydropower with reservoir	Base and peak load	Very efficient and flexible systems
2	Runoff river plants	Base load	Less flexibility
3	Pumped storage	Peak load	Can enhance use of variable renewables
4	Diesel power plants	Base load and peak load	Expensive and polluting but highly flexible
5	Natural gas	Base load	Less flexible
6	Coal	Base load	Have some flexibility for peak and variable load supply
7	Heavy oil	Base load	Some flexibility and highly polluting
8	Biomass	Base load	Less flexibility
9	Nuclear	Base load	Very little flexibility

2.1 Analysis of Intermittent Sources

Two approaches can be applied for analysis of intermittent generation systems: for fair comparison.

 (i) The systems can be combined for analysis with a typical backup system, which provides the same reliability as other stand-alone systems. Though technically challenging, it can be done, adding wind energy to hydropower.
(ii) Where the system does not consider the required backup, then can be recognized clearly that the assessment is not at par with other "stand-alone" systems [5].

2.2 Main Types of Electricity Generation Systems

Power generation technologies vary greatly but can be grouped on their ability to meet fluctuating electricity demand. Electricity demand as shown in Table 1.

3 Life Cycle Inventory Analysis

LCI involves the compilation and quantification of natural resources consumed and substances released into the environment. In the life cycle inventory (LCI) analysis, the life cycle is drawn with all energy and material requirements such as air, water, soil, and land, as well as their environmental releases which are quantified. The steps in an LCI analysis are the development of a flow diagram, collection of data, multi-output processes, and results reporting [15]. Life cycle inventory (LCIs) are generally based on average data of energy and material inputs and outputs collected from the site or estimated from literature or from modeling studies. To construct an

LCI, all inputs and outputs for all processes should be identified and quantified. An LCI process should be at an industrial scale for the modeled system to be as close as possible to a real process. In the case of an ongoing development and low technology readiness level (TRL) of a new process, there should be a scale-up modeling to determine material and energy flows for the desired real scale [16].

3.1 Development of a Flow Diagram

A flow diagram is used to reflect processes making up the product system and the inputs and outputs of the processes within the system. The boundaries are defined by the scope and goal of the analysis. Almost all processes in a system involve a form of transport between processes which requires energy. Processes relate to flows of intermediate products while elemental flows are shown to and from the environment. The elemental flows are material or energy flows entering or leaving the system drawn from the environment or discarded to the environment. Therefore the elemental flows originate directly from the environment. e.g., energy and material resources and land use; or they are discharged directly to the environment like emissions, heat, radiation, and sound [15].

From Fig. 1, it is noted that a system has boundary with product inflow from other systems and direct elemental flow from the environment. Main processes in
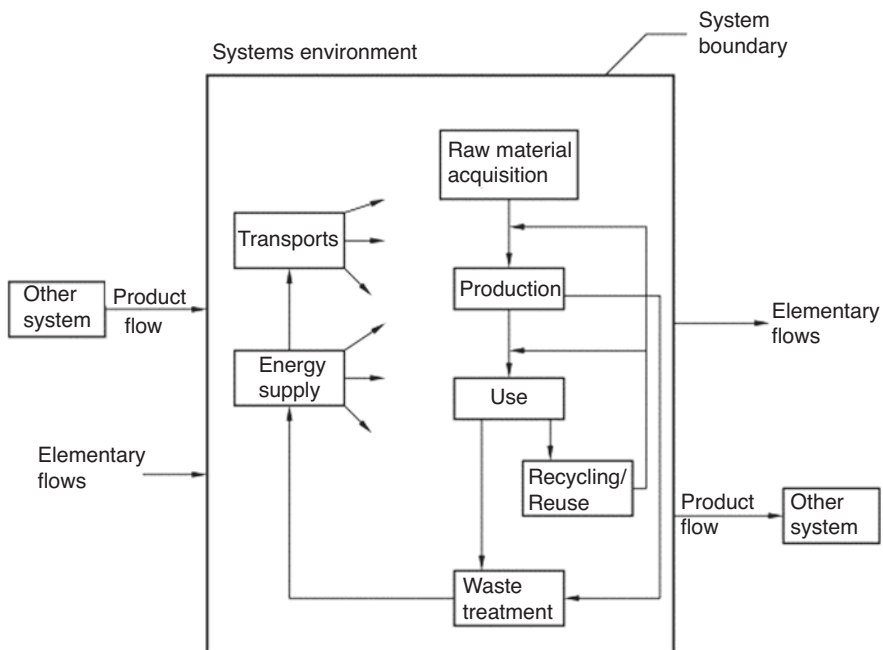
Fig. 1 A product system for life cycle inventory analysis
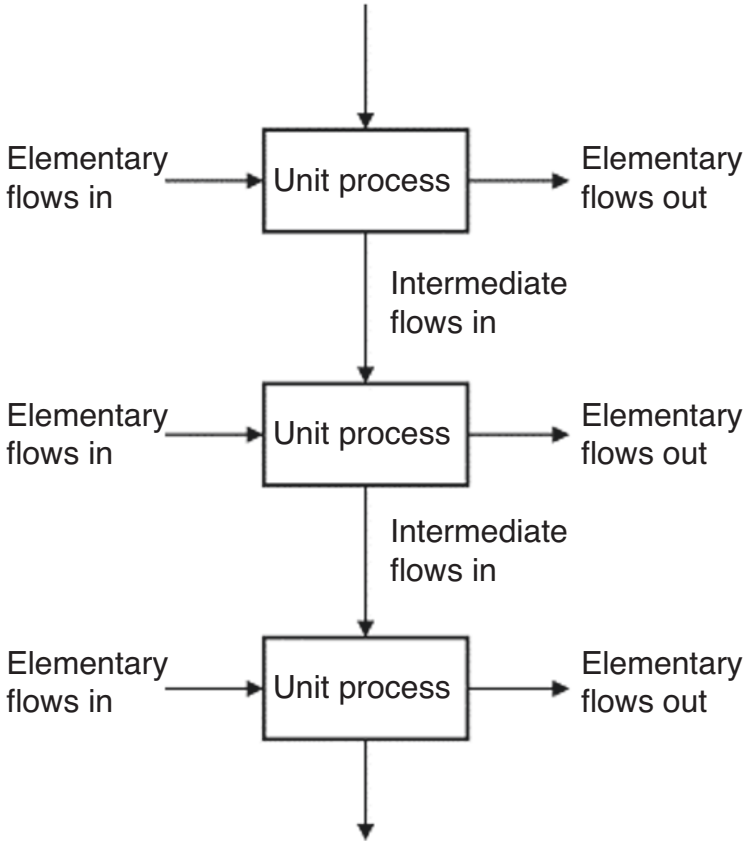
Fig. 2 Unit processes within a product system

the energy system are transportation, energy supply, waste treatment, production, acquisition of raw materials, material, recycling, and consumption. The system outputs include product flows to other systems, elementary flows to the environment.

The elementary flows originate from processes within the energy system boundary, as is shown in Fig. 2.

From Fig. 2, it is noted that there are elementary flow-specific unit processes that have their own elementary flows. Intermediate flows occur between various units in the system data collection.

The most time-consuming system in the life cycle inventory assessment is data collection. Data collected should be accurate and relevant for this purpose. Quite often, data is a mix of site-specific data which is obtained by measurements and calculations from measurement and generic, non-site-specific data which is obtained from databases or expert estimates [15].

3.2   Multi-output Processes

Energy systems have many processes that have a single useful output. In such multi-output processes, just one of the outputs may be used in the life cycle. The systems can also have outputs useful to other life cycles that are not under investigation. Material and energy inputs and the elementary flows of the processes under study are allocated among the useful outputs. An example of a multi-output process is cogeneration processes and products where fuel input in combined heat and power (CHP) plants is divided between electricity generation and heat production. In this case, the system can be extended by introducing reference technology for either product; e.g., for heat production, fuel input for heat production can be computed as the fuel required for heat production in a reference boiler. The fuel consumption for power generation is then determined by deducting the fuel input for heat production in the cogeneration system. The reverse can also be done where a reference electricity plant is introduced instead of a reference boiler and the process repeated. In another approach, physical properties of products like mass or energy content are applied as the allocation factor. Mass allocation may not however work for a CHP plant; instead energy content either on a heat/enthalpy basis or on an exergy basis is more realistic and is more meaningful. In the third approach, the economic value of the individual products can be applied for proper allocation factor. The three approaches have been widely used in LCAs [15].

3.3   Reporting

The LCI outcome is a list of all elementary flows to or from the environment for each energy system study resulting from the functional unit provided by the energy systems. They can be organized based on the life cycle stage and/or media like air, water, or land. These results can be used in further analysis like comparison of energy alternatives and identification of life cycle stages with significant environmental releases. These releases do not however express potential environmental impacts [15].

4   Life Cycle Impact Assessment Method

A life cycle impact assessment provides a more meaningful basis for comparisons; e.g., we may know that 8500 tons of carbon dioxide (CO_2) and 5000 tons of methane are released to the atmosphere; both being potentially harmful greenhouse gases, it is through a life cycle impact assessment (LCIA) we can determine that the

gases have a greater impact. In terms of smog formation? Or which is worse than the other? Or what are the potential impacts on global warming? The LCIA uses science-based characterization factors to determine the impacts of each emission to the environment [17].

Life cycle impact assessment (LCIA) is part of life cycle assessment (LCA) whose objective is to evaluate and understand the magnitude and significance of environmental impacts for a product system across its life cycle [18]. Life cycle impact assessment involves characterization of impacts and selection of impact assessment categories based on their contribution to normalized and weighted analysis results. There are two basic approaches that can be used to characterize environmental impacts:

 (i) The midpoint approach and midpoint indicators recommended by the EC Environment Footprint Guidelines [12, 13].
(ii) The endpoint approach and endpoint indicators.

These approaches are different in terms of objectives and robustness. A comprehensive LCA may display the results using both midpoint and endpoint approach and the endpoint and endpoint indicators approach; but the conclusions remain the same. The term "impact" is generally used as the shorthand for "potential impact," as it is defined in the ISO standards. Therefore, in the life cycle assessment (LCA), "impact-"associated terms like "impact assessment" or "impact category" is associated with the potential detrimental effects that a substance or a stress can leave on the environment, resources, or human health. Therefore, only potential environmental impacts are regarded as real impacts influenced by factors usually not included in the study. "The LCIA does not have to quantify any actual, specific impacts associated with a product, process, or activity, but seeks to establish a linkage between a system and potential impacts" [19].

Although much can be learned about a process through the life cycle inventory data. An impact assessment is used to provide a more informed basis to make comparisons. It is through an impact assessment we can establish environmental releases with greatest impact. A life cycle impact assessment is used to compute impacts of the environmental releases like global warming and smog [17]. In this regard, the LCI is converted in environmental impacts by category. The impact categories include toxicity, climate change, respiratory effects, acidifications, ozone layer depletion, acidification, eutrophication, natural resources depletion, etc. The substances in the life cycle impact assessment have one or more impact categories; e.g., NO_x is responsible for respiratory effects, acidification, and eutrophication [16]. Environmental models can be used to establish specific parameters that quantify the effects of a substance. The result of the impact is proportionally linked to the mass of the substance released to the environment [16]. The environmental gains of energy technology substitution can be determined through complete analyses of LCA and LCI using data from pilot and industrial–scale studies [16].

5   Exergetic LCA Studies

Exergetic life cycle assessment (ExLCA) can be used to quantify the environmental impacts associated with the exergy losses and exergy destruction in an energy system, process, or product. Environmental impact is reduced by increasing exergy efficiencies [20]. The framework of ExLCA is similar to LCA with main steps summarized in Table 3.

Figure 3 shows a flow diagram with inputs and outputs of matter, energy, and exergy at various steps in the life cycle of a product or process.

Exergy and its methodological advancements can be used in LCA studies. Exergy analysis is a multi-disciplinary and emerging field, with applications in resources used in both energetic and non-energetic resources. The exergy is applied in sustainability assessment for thermodynamic properties and parameters, which require less subjective choices as compared to fate, exposure, and effects models applied in most LCA methods. The measurement would make characterization independent of reference substances like carbon dioxide for global warming potential which enables a combination of the results of different impact categories into a cumulative value by using the same unit of exergy. Extensive application of exergy analysis to conventional LCA is done through a systematic and comprehensive determination of exergies which considers standard thermodynamic conditions, emissions, pure state of resources, and individual emission amounts [11].
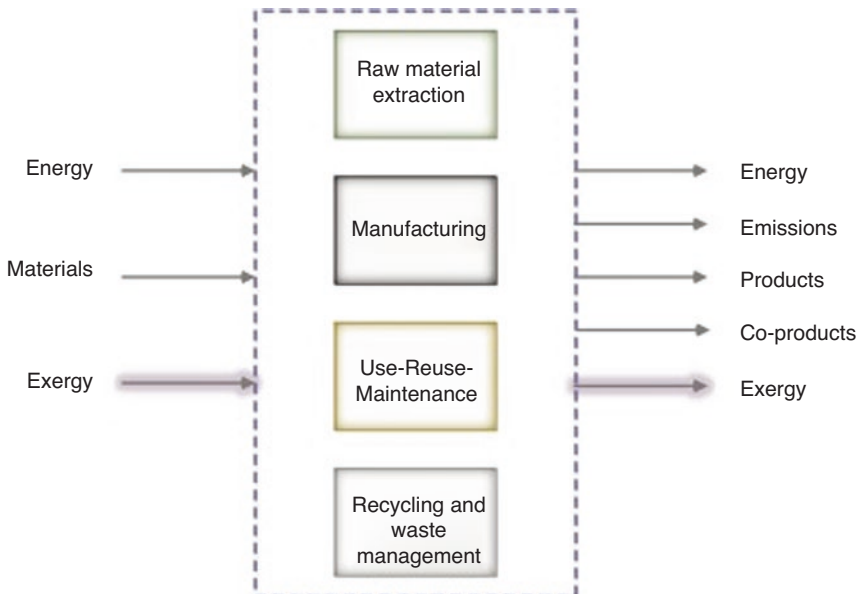
Fig. 3 The framework for ExLCA

6 Results of Life Cycle Assessments

Life cycle assessments are applied to analyze the environmental costs and benefits of climate mitigation measures which are usually static in nature and address specific power plants and technology. This study presents the general life cycle assessment of climate mitigation technologies [21].

6.1 Greenhouse Gas Emissions and Environmental Impacts

The following are the environmental impacts of greenhouse gas emissions and global warming:

  (i) More intense precipitation events cause flooding, landslides, avalanche, and mudslide damage.
 (ii) Increased summer drying over most mid-latitude continental interiors and associated risk of drought.
(iii) Increase in tropical cyclone peak wind intensities, mean, and peak precipitation intensities.
(iv) More intense droughts and floods associated with El Nino events in many different regions.
 (v) Rise in the sea level and an increase in the intensity cyclones which can displace millions of people in lowlands.

6.2 Understanding the Studies on Greenhouse Gas Emissions

The potential impacts of climate change have led to many studies focused on greenhouse gas emission assessment which have produced data on emissions of CO_2 equivalent; therefore, CO_2 and other greenhouse gases are captured in the assessment. Greenhouse gases have different effects on the climate with different life spans in the atmospheric. The global warming potential is used to assess the greenhouse effect of various substances and different substances have different greenhouse gas potential; e.g., a gram of CH_4 has a *global warming potential* of 23, relative to a gram of CO_2 assessed over a 100-year period [5, 22].

6.3 Main Findings Concerning Greenhouse Gas Emissions

Based on greenhouse gas emissions, run-of-river hydropower presents the best performance among all systems, followed by nuclear, reservoir-based hydropower and wind power. Run-of-river hydropower with no upstream reservoir and nuclear energy are less flexible, and wind power is intermittent. A backup system is needed

for these energy systems and maybe fossil fuel, which significantly increases the final emission factor of the overall electricity system. Coal has the highest emission factor which is about twice the emissions of natural gas combined cycle [5].

For hydropower, a common source of greenhouse gas emissions is the decay of flooded biomass whose assessment is site specific based on factors like reservoir per kWh which varies with topography. The amount of flooded biomass, per unit of area, varies by a factor of 5 (500 t/ha for tropical forest versus 100 t/ha for boreal climate. For average size reservoir per kWh, in boreal or mountain regions, the emission factor for hydropower is approximately 60 times lower than the modern coal-fired generation [5].

Greenhouse gas emissions from hydropower reservoirs resulting from decaying biomass in hydropower reservoirs have persistent uncertainties. Reservoirs in boreal or mountain regions have a small amount of flooded biomass, but reservoirs in tropical environments have higher emission factors, depending on many site-specific conditions [5].

6.4 Future Performance of Energy Systems Concerning Greenhouse Gas Emissions

The global expectations over issues like climate change are high since many studies target only one stage of the life cycle, yet life-cycle assessment may show different expectations since some technologies emit less greenhouse gas at one stage of their life cycle, only to emit more at another stage. Alternative fuels such as ethanol coming from crops may have lower emissions at combustion compared to oil, but crop production-related emissions offset these benefits. In another example, fuel cells have almost zero emissions, but hydrogen production has higher level than natural gas turbines. For carbon sequestration, scrubbing of CO_2 emissions from flue gas is complex and expensive. For sulfur, the benefits of scrubbing technologies are justifiable by the fact that the waste generated by these technologies are manageable, but for CO_2 emissions, it is complex because carbon is responsible for about 50% CO_2 emissions of the coal, while sulfur is 1% or 2% in coal. Capturing all this carbon and pumping it in deep underground reservoirs is energy intensive, polluting, expensive, and relatively fewer benefits. Therefore, the next few decades may not see major technologies to solve the climate change challenges. Therefore, energy efficiency measures and renewable energy technologies will remain the best options to reduce greenhouse gas emissions in the near future [5, 23].

6.5 Acid Precipitation

Environmental Issues Acid precipitation remains a major environmental concern. SO_2 and NO_x emissions acidify lakes, rivers, and forests and affect their productivity. It is, however, difficult to identify the direct link between ecosystem impacts and

atmospheric emissions. Additionally, vulnerability of forests varies based on soil types. It is generally difficult to establish a direct link between one specific emission and the ultimate environmental damage they cause. Therefore, emission factors may be considered as indicators of "potential" impacts [5].

For forest productivity, impacts of pollutants include the following:

(i) Acid will remove essential nutrients from soils like K, Ca, Mg.
(ii) Acid may mobilize toxic metals like aluminum which damage crops or plant roots.
(iii) Nitrogen from pollutants, although the main nutrient of plants, can create resource imbalance and make trees more vulnerable to frost and diseases.
(iv) Emissions cause photochemical smog which can cause damage.
(v) They contribute to climate change which can cause heat stress or intensity of droughts [5].

Sulphur dioxide leads to formation of sulfuric acid while NO_x leads to the formation of nitric acid before contributing to the formation of acid precipitation. NO_x also contributes to smog formation from related chemical reactions [5].

Fuels have different sulfur compositions with coal having sulfur content varying between 0.5% and 5% even more in exceptional cases. The average sulfur content for oil and diesel is about 0.2% for light oil/diesel and 2% for heavy fuel, but the percentages vary significantly from one region to another. Natural gas has virtually no sulfur content as it is removed in processing plants after extraction. Various technologies are available for the removal of sulfur dioxide with some capable of scrubbing as high as 90% of SO_2 emissions. Technologies that involve high pressure and temperature combustion like diesel engines generate high levels of NO_x emissions. Coal, which has significant amounts of nitrogen, is also part of the fuel, leading to high NOx emission factors.

Emission factors for hydropower and nuclear energy are hundreds of times lower than those of fossil fuel–based technologies like coal power generation systems without scrubbing. Therefore, based on SO_2 and NO_x emissions produced, coal, oil and diesel-based power generation systems are significant contributors to acid. Biomass has low SO_2 but a very high factor for NO_x, hence a significant source of acid precipitation. Natural gas is also a significant contributor to acid precipitation because of NOx emissions. Wind power can reduce the use of fossil fuel–fired plants by substituting them, leading to reduction in net emissions, although in some cases wind power may increase the use of oil-fired plants as backup.

Future Performance of Energy Systems Concerning Acid Precipitation The main source of SO_2 is fossil fuels, particularly coal and oil-fired power plants. Through scrubbing technologies, SO_2 emissions can be reduced by more than 90%, but the technologies are expensive and reduce the power plant efficiency. Burning low sulfur fuels is another option, but these fuels are costlier, needing longer transportation [5].

Land Requirements *Environmental Issues.* Emerging renewable energy technologies like wind and solar have large land requirements. Land demand continues to grow due to use in agriculture, cities, and industries, and land for other uses. The alternative sources of biofuels, like ethanol from crops, need large areas of farmland [5].

Understanding the Studies on Land Requirements For many countries including the United States, most reservoirs were built for irrigation and water supply. Several reservoirs are small or have no power generation function and would have even higher land use factors per TWh. Fossil fuels have less data available and hence some upstream activities are not considered; e.g., surface mining of coal requires more land than underground mining, but no data is available to distinguish them [5, 24].

Main Findings Concerning Land Requirements Nuclear power plants have the lowest land requirements, if the land required for long-term nuclear waste disposal is neglected. However, inclusion of disposal land requirements seriously increases the nuclear energy land requirements since less land is needed but over a very long time in many thousands of years e.g. 0.1 km/TWh is required for waste disposal, multiplied by 30,000 years, for 30 years of generation, the factor would increase from 0.5 km/TWh to 100 km/TWh) [5].

Renewable energy sources led by biomass plantation have the highest land requirements per unit of energy. This is followed by renewable sources, i.e., hydropower, wind power, and solar power, with almost similar requirements with significant variations based on site-specific conditions. Coal requires much less land than any renewable source of energy in an assessment based on direct land requirements only, i.e., power plants and mining activities. Land-related indirect use is not included in the data. Yet these areas are huge and can multiply the land use factors of energy sources [5].

6.6 Future Performance of Energy Systems Concerning Land Requirements

There is little likelihood that technological development will lead to significant land use reductions. No new technology may be needed to reduce areas affected by acid precipitation for coal and oil. For hydropower, the size of reservoir is important and reservoir areas are about five times smaller than existing ones per unit of energy. Future development of renewables could be significantly constrained by land requirements. Compatibility with existing land uses differ widely and is guided by factors like population density [5, 25].

Hydropower may have other water uses like irrigation, water supply, or flood control. In terms of competition with food production, many renewable energy

projects have little negative impacts on agriculture; e.g., land around windmills can still be used for agricultural production while solar energy can be developed on rooftops and over water masses like reservoirs as well as non-arable land. Hydropower can be developed in mountainous or rocky terrain while water from hydro reservoirs can be used for irrigation [5].

However, future energy options like biomass plantations for energy production through direct combustion or bio refinery and anaerobic digestion can be severely limited by the availability of land and hence feedstock [5, 6].

Energy Payback Ratio Energy payback ratio is the ration of energy produced during the power plants normal life span, divided by the energy required to pay for the construction, maintenance, and fuel for the power generation facility [5].

6.7 Environmental Issues and Payback Ratio

A system with a low payback ratio requires much more energy to maintain it, which generates more environmental impacts. The environmental impacts for fossil fuels are realized during extraction, transportation, and processing of fuels, while for renewable sources, the main impact is from building or facility construction. A payback ratio of close to one implies that the system consumes as much energy as it produces and hence does not need to be developed [5].

LCAs have focused mainly on greenhouse gas emissions from energy in the recent context of climate change commitments. The emissions vary dramatically based on factors like materials used and how they are produced, e.g., aluminum from smelters using hydropower as electricity and smelters using fossil fuels like natural gas and coal to produce the same [1, 5].

The main benefit of using energy payback ratios as a metric is that it is less affected by upstream choices of energy supply, which minimizes the fluctuation in the evaluation of greenhouse gas emissions energy payback ratio, one of the most reliable indicators of environmental performance. Energy payback ratio as an indicator minimizes fluctuations in the results of studies without eliminating them. Renewable energies can have very large variations in energy payback ratios. due to a wide variation of site-specific conditions, i.e., topography for the case hydro, quality of the wind for wind energy, and solar intensity of solar radiation for solar energy [5].

Payback Ratio of Energy Sources Various analyses show hydropower clearly has the highest performance, with energy payback ratios of 205 to 267 while fossil fuels have payback ratio of 5–7. The payback ratio value for hydropower with reservoir is 205 while the run-of-river has a payback ratio of 267. Best wind sites have payback ratio of about 80 without backup. Biomass has about 27 for power from forestry waste and 5 for planted trees due to higher energy inputs. The higher the distance of the power plants from biomass sources, the lower the payback ratio. Natural gas has a payback ratio of about 5 with some energy being spent on transportation over long

Table 2 Payback ratios for
generation technologies

	Technology	Payback ratio
1	Hydro with reservoir	205
2	Run-of-river hydro	267
3	Wind	80
4	Forestry biomass	27
5	Cultivated biomass	5
6	Natural gas	5
7	Coal	5

distances. The ratio for natural gas power plants located close to the source of natural gas is higher. With high investment on transportation, the payback ratio for coal is also low at about 5 as well as investment on scrubbing of SO_2, which requires lime and other resources that need transportation and other investment in production and delivery on site and disposal [5]. Table 2 shows the payback ratios for different generation technologies.

From Table 2, it is observed that hydro with reservoir has the highest payback ratio, followed by wind. Coal, natural gas, and cultivated biomass have the lowest payback ratios.

6.8 Future Performance of Energy Systems Concerning the Payback Ratio

Fossil fuel sources of energy have low energy payback ratios which continue to decline due to reasons like depletion of reserves which tend to be replaced by oil wells that have higher energy requirement like those wells located deep into the sea. Exploitation of fossil fuel resources like coal located far away from load centers and power stations increases transport costs by road and rail. Further investment in emission reduction technology like scrubbing of SO_2 can reduce the overall efficiency of coal generation and hence reduce payback ratio while capture and sequestration of CO_2 will require huge investment in capital and energy for the operation of scrubbing and disposal equipment while noting that sulfur is about 1% of coal and carbon is more than 50% of the coal. Therefore, mandatory investment in emission reduction technologies will reduce the overall efficiency and feasibility of coal and other fossil fuel power plants [5].

6.9 The Atmospheric Emissions

Health Issues Emission factors are mainly concerned with climate change and acid precipitation, while other types of air emissions have local and direct effects on health. They include particulate matter, toxic metals like mercury, and non-methane

Table 3 Other atmospheric emissions from power generation technologies (some data is not life cycle assessment)

	Technology	NMVOC emissions (t/TWh)	Particulate matter emissions (t/TWh)	Mercury emissions (kg Hg/TWh
1	Hydropower with reservoir		5	
2	Hydropower run-of-river		1-5	
3	Diesel	1570	122–213	
4	Natural gas c.c. turbines	72–164	1–10	0.3–1
5	Bituminous coal (modern)	18–29	30–663	1–360
6	Lignite: old plant		100–618	2–42
7	Heavy oil: no scrubbing	22		2–13
8	Biomass combustion	89	190–320	0.5–2
9	Nuclear		2	
10	Wind power		5–35	
11	Solar photovoltaic	70	12–190	

volatile organic compounds (NMVOC) which directly contribute to smog formation [5]. Table 3 shows other atmospheric emissions from power plants.

From Table 3, it is noted that different energy technologies have difference range of values for NMVOC emissions (t/TWh), particulate matter emissions (t/TWh), and mercury emissions (kg Hg/TWh). However, the limitation of the data is that some emissions represent direct emissions from power plants and not life cycle assessment values. The analysis shows hydropower, wind power, nuclear energy, and natural as energy sources and technologies with lowest emissions [5].

Comparing Mercury Contamination Some hydro reservoirs are known to release mercury in the food chain; the impact can be compared with that of coal or oil-fired mercury emissions, which contaminate the food chain of many lakes. On average, hydro reservoirs can generate 0.07 kg Hg/TWh can be calculated while coal is about 200 times more. However, further analysis shows that about half of mercury released by hydro reservoirs is mercury emitted by coal-fired plants and smelters [5].

7 Carbon Capture and Sequestration

There is continuing and increasing demand for clean coal technologies which are environmentally acceptabler since fossil fuel power plants have environmental impacts like formation of acid rains and photochemical smog formation.

Emissions that need control include particulates, NO_x and So_x, and trace elements, polycyclic aromatic hydrocarbons, and, importantly, CO_2. This has led to technologies that are more environmentally friendly, by reducing pollutant emissions, called clean coal technologies [2].

The two ways of reducing coal emissions are efficiency improvement which improves output and lower emissions per unit of energy output and application CCS technologies to reduce C_{O2} emissions by 80–90%. CCS is an arrangement between further use of fossil fuels to satisfy increasing energy demand and reduction in CO2 emissions. Carbon capture is not a single technology; instead it is a suite of technologies, some of which can be applied to existing coal-fired power stations, while other technologies are still new technologies and are evolving [2, 26].

There are different techniques used to capture CO_2 released by fossil fuel plants, especially coal plants, and to sequester it in storage sites. Three approaches used to integrate CO_2 capture technologies with power generation systems are post-combustion, pre-combustion, and oxy-fuel combustion [2].

In post-combustion technology, carbon dioxide is removed after the combustion of fossil fuel. This technology can be implemented as a retrofit option for operating or existing power plants. Technologies that could be employed with post-combustion CCS include adsorption, i.e., physical absorption, cryogenics separation, chemical absorption, and membranes technology [2].

Chemical absorption for CO_2 capture can be applied to post-combustion systems, due to low CO_2 partial pressure in the flue gas in coal power plants. The amine technology is generally dedicated for retrofitting of existing power plants. The major challenge remains minimizing the operation and investment costs related to the technologies [2]. The alternative chemical absorption in aqueous ammonia solutions can be used to selectively capture the CO_2 from the flue gases by the use of an ammonia-based solution at reduced temperature in an absorption column. The ammonia solution is regenerated in a desorption column, and the cycle is repeated. The advantages of ammonia-based technology include low reboiler regeneration energy, high CO_2-carrying capacity, low cost, and low power consumption in compression of carbon dioxide [2].

The Ca-looping (CaL) technology is post-combustion CO_2 capture technology suitable for integration in power plants and other large CO_2 emission industrial plants, e.g., cement industry and steel plants. CAL is based on the multi-cyclic carbonation/calcination of CaO at a high temperature range of 800–950 °C, whereas CO_2 in flue gases reacts with the solid sorbent (CaO) at about 500–650 °C, forming calcium carbonate formation. The carbonate product is then decomposed to produce CaO which is recycled back in the carbonator in order to absorb more CO, and a CO_2 stream which is dried and compressed for storage and the cycle process is repeated [27].

In the study by [28] focusing on supercritical pulverized coal, a natural gas combined cycle (NGCC), and an integrated gasification combined cycle (IGCC), with and without CCS, it was observed that for a 90% CO_2 capture efficiency, life cycle GHG emissions are reduced by 75–84% based on the technology applied, the global

warming potential reduced when MEA-based CO_2 capture is employed, and other air pollutants such as NO_x and NH_3 increase leads to higher eutrophication and acidification potentials.

In another study, the LCA study of three pulverized coal power plants with/without post-combustion CCS was undertaken. Two reference chains considered were subcritical and ultra-supercritical pulverized coal-fired electricity generation. In this study, it was observed that the global warming potential reduced by over 70% when CCS were applied, but notable environmental trade-offs encountered are increased—ozone layer depletion, human toxicity, and fresh water ecotoxicity potential. State-of-the-art power plants having no CCS perform better in eutrophication, acidification, and photochemical oxidation although we have deeper reduction in emissions in the form of SO_x and NO_x in the CCS power plant [2, 29].

In the study by [30], which compared fuel technologies, i.e. IGCC, NGCC, oxy-fuel, and pulverized coal (PC) coupled with CCS, it was observed that carbon capture and sequestration (CCS) results in a net reduction of the GWP by 65–84% by power plants in their life cycle, i.e., for (PC-CCS) the GWP is reduced by 68–87%, (IGCC-CCS), and the reduction is by 47–80% for (NGCC-CCS), and in (Oxyfuel) the GWP is reduced by 76–97%. However, the deployment of CCS technology in PC, IGCC, and NGCC leads to relative increases in eutrophication and acidification compared to power plants without CCS. The assessments of power plants with CCS should consider upstream emissions from coal mining, coal transport, and MEA production and downstream emissions from CO_2 transport and CO_2 storage for the accurate assessment of environmental performance of power plants with CCS [2, 10].

In the study by [31], post-combustion CO_2 capture combined with CO_2-enhanced oil recovery was investigated using lignite coal as the fuel and post-combustion CCS based on monoethanolamide (MEA). The results showed a significant reduction in global warming and air impact categories. Although some categories associated with soil and water increased, the broad distribution associated with atmospheric release was significantly reduced [32, 33].

Life cycle greenhouse gas emission evaluation of power plants with carbon capture and storage (CCS) is a critical factor in energy and policy analysis. Studies show that 90% carbon dioxide (CO_2) capture efficiency can be achieved with overall reduction in life cycle greenhouse gas emissions by 75–84% based on technology applied. IGCC technology is the most favorable compared to NGCC with CCS and can achieve GHG emissions of less than 170 g/kWh. IGCC technology is found to be favorable too. Through sensitivity analysis, it is established that coal power plants have varying CO_2 capture efficiency while the coal transport distance has a pronounced effect on life cycle GHG emissions compared to changing the length of carbon dioxide (CO_2) transport pipeline. Although the global warming potential is reduced when MEA-based CO_2 capture is applied, other pollutants like NOx and NH3 increase leading to higher impact in firm of eutrophication and acidification potentials [28, 34].

8   Results and Discussion

Life cycle assessments have identified hydropower, particularly the run-of-river and with reservoir, nuclear energy, and wind power, as most sustainable options for power generation. Although hydropower with storage or reservoir has high land requirements, the sustainability is enhanced by high-capacity factors and efficiency as well as multiple secondary applications like irrigation, domestic water supply, flood control and energy security, and high reliability as well as operational flexibility [5, 35].

Analyses show very attractive performance for nuclear energy in many parameters. However nuclear energy faces resistance in any many parts of the world due to radioactive waste and concerns about catastrophic accidents. However, it remains difficult for LCAs to adequately address such concerns [5, 36].

Natural gas is the cleanest fossil fuel for power generation compared to coal and oil-fired generation. However, natural gas has high emissions, compared to renewable sources of energy. Long distance delivery and exploitation of natural gas is however characterized by high upfront emissions which may be hard to account through LCA [5, 37–40].

Coal clearly emerges as the worst option in most criteria, i.e., emissions of greenhouse gases, emissions of SO_2, emissions of NO_x, volatile organic compounds, particulates emissions, toxicity, and land requirements. However, coal has a better energy payback ratio only if there is no scrubbing and the process has minimal transportation [5].

The study shows that LCA has numerous analysis tools and data challenges, hence the need to consider the development of spatial and temporal methods. Substantial gaps remain in LCA analysis that considers spatial and temporal factors. It is important for stakeholders, decision-makers, policy makers, and practitioners to have greater understanding of how broadly applicable LCA results are or whether they are just specific to a particular region or a snapshot in time. Life cycle assessments (LCAs) should be a strong basis for decision-making in power generation. Specifications that consider spatial and temporal dimensions would be valuable in making sustainable decisions and create an environmentally sound supply chain and with minimum risks [1, 5].

Life cycle cost (LCC) is not a financial accounting method, but instead a cost management tool meant to estimate and analyze all the costs associated with a product's existence. The life cycle cost (LCC) methodology has been in use since the 1960s for the assessment of economic issues related to products and systems. Today, interest has grown in combining economic and environmental elements in sustainability analysis through integrating LCC and life cycle assessment (LCA) meant to estimate the environmental impacts of the life cycle of a product or service [5, 41]. The coupling of LCA and LCC can be achieved by means of E*nvironmental LCC* (eLCC), which is an expansion of conventional LCC considering all direct costs incurred during the life cycle of the product to incorporate externalities having well-defined market price and are likely to be internalized soon. These externalities

include greenhouse gas emissions. The study is known as Full Environmental Life Cycle Cost if other environmental externalities are also monetized and incorporated into the analysis [41].

Although hydropower with reservoir has high land requirements, considering that it has secondary benefits and applications like provision of water for irrigation, industrial and domestic use, flood control, and above water solar power, it is possible to conclude hydro with reservoir has the highest performance.

Evaluation of life cycle greenhouse gas emissions for power plants with carbon capture and storage (CCS) is important for energy and policy analysis. Analysis shows that if 90% CO_2 is captured, life cycle greenhouse gas emissions (GHG) can be reduced by 75–84% depending on the type of technology applied. Life cycle greenhouse gas emissions for coal power plants can also be significantly changed by reducing the coal transport distance as well as the length of CO_2 transport pipeline. The global warming potential is also reduced when CO_2 capture is employed although this may increase other air pollutants such as NO_x and NH_3, leading to higher eutrophication and acidification potentials [28]. Investment in CO_2 removal is partially offset by an increase in greenhouse gas emissions in the up- and downstream processes caused by the CCS infrastructure. The most notable environmental trade-offs caused by CCS are the increase in human toxicity, ozone layer depletion, and fresh water ecotoxicity potential. Power plants without CCS are better in eutrophication, acidification, and photochemical oxidation potential although they are outperformed in So_x and NO_x by CCS power plants although the reductions can be offset by increased emissions in the life cycle, leading to energy penalty and a factor five increase in NH_3 emissions [29].

For power plants without CCS, the contribution to the global warming potential (GWP), acidification, and eutrophication comes from direct emissions, while for power plants with CCS, the main contribution to GWP, acidification, and human toxicity potential comes from indirect emissions. It is therefore important to consider emissions from upstream operations like coal mining, coal transport, and MEA production and downstream operations like transport of captured CO_2 and CO_2 storage for accurate assessment of the environmental performance of power plants [30].

9 Conclusion

The use of life cycle analysis (LCA) for power generation technologies has a promising future as the world seeks solutions for the growing global electricity demand while attaining emission and climate targets and sustainable development. Although use of LCAs have some limitations, the LCAs of power generation technologies can shed light on the life cycle energy, greenhouse gas emissions, air pollutant emissions, water consumption, and other environmental and sustainability concerns. The electricity grid consists of highly diverse conversion technologies from fossil fuels, nuclear, wind, and solar, leading to differences in mixes for

different regions. Life cycle assessments for power generation need to better characterize spatial and temporal characteristics for accuracy.

The application of LCAs shows that renewable power technology options compare favorably with conventional and fossil fuel–based generation technologies. Most renewable generation technologies outperform conventional technologies with respect to both life cycle primary energy use and air pollutant emissions. Conventional or traditional environmental analyses are often limited to operational impacts like power plant stack emissions and effluent discharge to the environment, but the LCA perspective considers both upstream and downstream issues in addition to operation- and maintenance-level impacts. Therefore, the LCA approach naturally increases the understanding of the potential environmental trade-offs between technologies and identify their competitive advantage. Carbon sequestration and scrubbing of CO_2 emissions from flue gas are complex and expensive. For sulfur, the benefits of scrubbing technologies are justifiable by the fact that the waste generated by these technologies are manageable, but for CO_2 emissions, it is complex because carbon is responsible for about 50% CO_2 emissions of the coal, while sulfur is 1% or 2% in coal, making capturing all this carbon and pumping it in deep underground reservoirs is energy intensive, polluting, and expensive, hence fewer relative benefits. Therefore, the next few decades may not see major technologies to solve the climate change challenges. Therefore, energy efficiency measures and renewable energy technologies will remain the best options to reduce greenhouse gas emissions in the power generation.

The global warming potential reduced by over 70% when CCS was applied but notable environmental trade-offs encountered are increased: ozone layer depletion, human toxicity, and fresh water ecotoxicity potential. State-of-the-art power plant having no CCS performs better in eutrophication, acidification, and photochemical oxidation potential although we have deeper reduction in emissions in the form of So_x and NO_x in the CCS power plant. It is therefore important to consider emissions from upstream operations like coal mining, coal transport, and MEA production and downstream operations like transport of captured CO_2 and CO_2 storage for the accurate assessment of the environmental performance of power plants.

References

1. Jordaan, S.M., Combs, C., Guenther, E.: Life cycle assessment of electricity generation: a systematic review of spatiotemporal methods. Adv. Appl. Energy. **3**, 100058 (2021). https://doi.org/10.1016/j.adapen.2021.100058
2. Petrescu, L., Bonalumi, D., Valenti, G., Cormos, A.-M., Cormos, C.-C.: Life cycle assessment for supercritical pulverized coal power plants with post-combustion carbon capture and storage. J. Clean. Prod. **157**, 10–21 (2017). https://doi.org/10.1016/j.jclepro.2017.03.225
3. Edenhofer, O., Seyboth, K., Creutzig, F., Schlömer, S.: On the sustainability of renewable energy sources. Annu. Rev. Environ. Resour. **38**(1), 169–200 (2013). https://doi.org/10.1146/annurev-environ-051012-145344

4. Paredes, M.G., Padilla-Rivera, A., Güereca, L.P.: Life cycle assessment of ocean energy technologies: a systematic review. J. Marine Sci. Eng. **7**(9). https://doi.org/10.3390/jmse7090322

5. Gagnon, L., Bélanger, C., Uchiyama, Y.: Life-cycle assessment of electricity generation options: the status of research in year 2001. Energy Policy. **30**(14), 1267–1278 (2002). https://doi.org/10.1016/S0301-4215(02)00088-5

6. Turconi, R., Tonini, D., Nielsen, C.F.B., Simonsen, C.G., Astrup, T.: Environmental impacts of future low-carbon electricity systems: detailed life cycle assessment of a Danish case study. Appl. Energy. **132**, 66–73 (2014). https://doi.org/10.1016/j.apenergy.2014.06.078

7. Kabeyi, M.J.B., Olanrewaju, O.A.: Bagasse electricity potential of conventional sugarcane factories. J. Energy. **2023**, 5749122 (2023). https://doi.org/10.1155/2023/5749122

8. Rentizelas, A., Georgakellos, D.: Incorporating life cycle external cost in optimization of the electricity generation mix. Energy Policy. **65**, 134–149 (2014). https://doi.org/10.1016/j.enpol.2013.10.023

9. Kabeyi, M.J.B., Oludolapo, A.O.: Characteristics and applications of geothermal wellhead powerplants in electricity generation. In: 31ST Annual Southern African Institution for Industrial Engineering Conference, South Africa, H. Teresa, Ed., 5th – 7th October 2020 2020, vol. 2020, No. 31, South Africa: South African Journal of Industrial Engineering, pp. 222–235 (2020). Available: https://www.saiie.co.za/system/files/2021-11/SAIIE31%20Conference%20Proceedings.pdf

10. Kabeyi, M.J.B.: Potential and challenges of bagasse cogeneration in the Kenyan sugar industry. Int. J. Creat. Res. Thoughts. **10**(4), 379–526 (2022). https://doi.org/10.1729/Journal.30042

11. Ciacci, L., Passarini, F.: Life Cycle Assessment (LCA) of environmental and energy systems. Energies. **13**(22). https://doi.org/10.3390/en13225892

12. Kabeyi, M.J.B., Olanrewaju, A.O.: Managing sustainability in electricity generation. In: 2020 IEEE International Conference on Industrial Engineering and Engineering Management (IEEM), 14–17 December 2020, pp. 530–536 (2020). https://doi.org/10.1109/IEEM45057.2020.9309994. Available: https://ieeexplore.ieee.org/abstract/document/9309994

13. Kabeyi, M.J.B., Olanweraju, O.A.: Sustainability assessment for non-combustible renewable power generation. In: Presented at the 12th Annual Istanbul International Conference on Industrial Engineering and Operations Management, Istanbul, Turkey, March 7–10, 2022, Paper 429 (2022). Available: https://ieomsociety.org/proceedings/2022istanbul/429.pdf

14. Kabeyi, M.J.B., Olanrewaju, O.A.: Review and design overview of plastic waste-to-pyrolysis oil conversion with implications on the energy transition. J. Energy. **2023**, 1821129 (2023). https://doi.org/10.1155/2023/1821129

15. Nieuwlaar, E.: Life cycle assessment and energy systems☆. In: Reference Module in Earth Systems and Environmental. Elsevier, Sciences (2013)

16. Angoy, A., et al.: Chapter 17: Microwave technology for food applications. In: Chemat, F., Vorobiev, E. (eds.) Green Food Processing Techniques, pp. 455–498. Academic (2019)

17. Curran, M.A.: Life-cycle assessment. In: Jørgensen, S.E., Fath, B.D. (eds.) Encyclopedia of Ecology, pp. 2168–2174. Academic, Oxford (2008)

18. Zhu, X., Wang, S., Wang, L.: Life cycle analysis of greenhouse gas emissions of China's power generation on spatial and temporal scale. Energy Sci. Eng. **10**(4), 1083–1095 (2022). https://doi.org/10.1002/ese3.1100

19. UNECE: Carbon Neutrality in the UNECE Region: Integrated Life-Cycle Assessment of Electricity Sources, vol. 2022. United Nations Economic Commission For Europe, Uni, 2021 (2022). Available: https://unece.org/sites/default/files/2022-04/LCA_3_FINAL%20March%202022.pdf

20. Dincer, I., Bicer, Y.: Chapter 7: Enhanced dimensions of integrated energy systems for environment and sustainability. In: Dincer, I., Bicer, Y. (eds.) Integrated Energy Systems for Multigeneration, pp. 403–440. Elsevier (2020)

21. Hertwich, E.G., et al.: Integrated life-cycle assessment of electricity-supply scenarios confirms global environmental benefit of low-carbon technologies. Proc. Natl. Acad. Sci. **112**(20), 6277–6282 (2015). https://doi.org/10.1073/pnas.1312753111

22. Burchart-Korol, D., Pustejovska, P., Blaut, A., Jursova, S., Korol, J.: Comparative life cycle assessment of current and future electricity generation systems in The Czech Republic and Poland. Int. J. Life Cycle Assess. **23**(11), 2165–2177 (2018). https://doi.org/10.1007/s11367-018-1450-z

23. Turconi, R., Boldrin, A., Astrup, T.: Life cycle assessment (LCA) of electricity generation technologies: overview, comparability and limitations. Renew. Sust. Energ. Rev. **28**, 555–565 (2013). https://doi.org/10.1016/j.rser.2013.08.013

24. Kabeyi, M.J.B., Olanrewaju, O.A.: The role of electrification of transport in the energy transition. In: Presented at the Fifth European Conference on Industrial Engineering and Operations Management, Rome, Italy, July 26–28, 2022, 426 (2022). Available: https://ieomsociety.org/proceedings/2022rome/426.pdf

25. Kabeyi, M., Olanrewaju, O.: Diesel powerplants: design and operation and performance enhancements. In: Presented at the Fifth European Conference on Industrial Engineering and Operations Management, Rome, Italy, July 26–28, 2022, 425 (2022). Available: https://ieomsociety.org/proceedings/2022rome/425.pdf

26. Toporov, D.D.: Chapter 2: coal combustion technologies. In: Toporov, D.D. (ed.) Combustion of Pulverised Coal in a Mixture of Oxygen and Recycled Flue Gas, pp. 5–22. Elsevier, Boston (2014)

27. Cormos, C.C.: Economic evaluations of coal-based combustion and gasification power plants with post-combustion CO_2 capture using calcium looping cycle. Energy. **78**, 665–673 (2014). https://doi.org/10.1016/j.energy.2014.10.054

28. Odeh, N.A., Cockerill, T.T.: Life cycle GHG assessment of fossil fuel power plants with carbon capture and storage. Energy Policy. **36**(1), 367–380 (2008). https://doi.org/10.1016/j.enpol.2007.09.026

29. Koornneef, J., van Keulen, T., Faaij, A., Turkenburg, W.: Life cycle assessment of a pulverized coal power plant with post-combustion capture, transport and storage of CO_2. Int. J. Greenh. Gas Control. **2**(4), 448–467 (2008). https://doi.org/10.1016/j.ijggc.2008.06.008

30. Corsten, M., Ramírez, A., Shen, L., Koornneef, J., Faaij, A.: Environmental impact assessment of CCS chains – lessons learned and limitations from LCA literature. Int. J. Greenh. Gas Control. **13**, 59–71 (2013). https://doi.org/10.1016/j.ijggc.2012.12.003

31. Manuilova, A., Koiwanit, J., Piewkhaow, L., Wilson, M., Chan, C.W., Tontiwachwuthikul, P.: Life cycle assessment of post-combustion CO_2 capture and CO_2- enhanced oil recovery based on the boundary dam integrated carbon capture and storage demonstration project in Saskatchewan. Energy Procedia. **63**, 7398–7407 (2014). https://doi.org/10.1016/j.egypro.2014.11.776. Available: https://www.scopus.com/inward/record.uri?eid=2-s2.0-84922896333&doi=10.1016%2fj.egypro.2014.11.776&partnerID=40&md5=30f8914abdf69e738457c978d001ccff

32. Restrepo, Á., Bazzo, E., Miyake, R.: A life cycle assessment of the Brazilian coal used for electric power generation. J. Clean. Prod. **92**, 179–186 (2015)

33. Tang, L., Yokoyama, T., Kubota, H., Shimota, A.: Life cycle assessment of a pulverized coal-fired power plant with CCS technology in Japan. Energy Procedia. **63**, 7437–7443 (2014). https://doi.org/10.1016/j.egypro.2014.11.780. Available: https://www.scopus.com/inward/record.uri?eid=2-s2.0-84922931962&doi=10.1016%2fj.egypro.2014.11.780&partnerID=40&md5=b3a15523815688296028ebb817b08e3e

34. Kabeyi, M.J.B., Oludolapo, A.O.: Development of a biogas plant with electricity generation, heating and fertilizer recovery systems. In: Presented at the 2nd African International Conference on Industrial Engineering and Operations Management, Harare, Zimbabwe, 5–7 December 2020, 082 (2020). Available: http://ieomsociety.org/harare2020/papers/82.pdf

35. M. J. B. Kabeyi, "Challenges of implementing thermal powerplant projects in Kenya,the case of Kipevu III 120MW power station,Mombasa Kenya," Masters, Department of Education Management, University of Nairobi, Nairobi, 2012. Available: http://erepository.uonbi.ac.ke:8080/xmlui/handle/123456789/11023

36. Kabeyi, M.J.B., Olanrewaju, O.A.: Energy and environment: oportunities and challenges for the energy transition. In: Presented at the Fifth European Conference on Industrial Engineering and Operations Management, Rome, Italy, July 26–28, 2022, 427 (2022). Available: https://ieomsociety.org/proceedings/2022rome/427.pdf

37. Kabeyi, M., Olanrewaju, O.: Diesel to gas engine power plant conversion: a review and preliminary design for an operating power plant. J. Energy Manag. Technol. (2022). https://doi.org/10.22109/jemt.2022.292982.1312

38. Kabeyi, M.J.B., Olanrewaju, O.A.: Conversion of diesel and petrol engines to biogas engines as an energy transition strategy. In: Presented at the 4th African International Conference on Industrial Engineering and Operations Management, Nsukka, Nigeria, April 5–7, 2022, 448 (2022). Available: https://ieomsociety.org/proceedings/2022nigeria/448.pdf

39. Kabeyi, M.J.B., Olanrewaju, O.A.: Performance analysis and evaluation of ethanol potential of Nzoia Sugar Company Ltd. Energy Rep. **8**(16), 787–799 (2022). https://doi.org/10.1016/j.egyr.2022.11.006

40. Kabeyi, M.J.B., Olanrewaju, O.A.: A techno-economic assessment of diesel to gas power plant conversion. In: Presented at the 12th Annual Istanbul International Conference on Industrial Engineering and Operations Management, Istanbul, Turkey, March 7–10, 2022, 406 (2022). Available: https://ieomsociety.org/proceedings/2022istanbul/406.pdf

41. Corona, B., Cerrajero, E., López, D., San Miguel, G.: Full environmental life cycle cost analysis of concentrating solar power technology: contribution of externalities to overall energy costs. Sol. Energy. **135**, 758–768 (2016). https://doi.org/10.1016/j.solener.2016.06.059

Hydrokinetic Turbine Impact Assessment on Fish

Marianela M. Macias ⓘ**, Rafael C. F. Mendes** ⓘ**, Taygoara F. Oliveira** ⓘ**, and Antonio C. P. Brasil Junior** ⓘ

1 Introduction

Renewable energy applications must adapt adequate solutions for each region or country to create an energetic hub based on its resources and possibilities. Brazil has vast hydro potential; over 70% of the electric energy produced comes from conventional hydroelectric plants. In recent years, the interest in hydrokinetic energy has grown as a solution based on hydro potential, contributing to the electric hub, providing electricity to isolated communities, or using the remaining energy in conventional hydroelectric plants.

Hydrokinetic devices, such as hydrokinetic turbines, employ kinetic energy in a flow to electricity production. The most common installation places for those devices are estuaries, rivers, or marine currents, where there are no major civil works such as reservoirs or dams, waterfalls, and diverting river beds. Thus, environmentally and socially, hydrokinetic energy presents advantages over conventional hydropower plants because it avoids human migrations, flooding areas, and methane gas emissions, among others [1].

However, the environmental impacts associated with the installation and operation of hydrokinetic turbines are still an open topic in the literature due to the incipience of the technology. The literature describes the main causes that can affect aquatic life after the installation of hydrokinetic devices such as sediment

M. M. Macias (✉)
Department of Mechanical Engineering and Industrial Design, Faculty of Engineering, University of Cadiz, Puerto Real, Cádiz, Spain
e-mail: marianela.machuca@uca.es

R. C. F. Mendes · T. F. Oliveira · A. C. P. Brasil Junior
Department of Mechanical Engineering, Laboratory of Energy and Environment, University of Brasilia, Brasilia, DF, Brazil
e-mail: rafael.mendes@unb.br; taygoara@unb.br; brasiljr@unb.br

suspension [2], alteration of the river's hydraulic regimes [3], noise [4], electromagnetic fields [1], fish collisions [5], flow conditions [6], toxicity from paints and other chemicals, and the installations the turbines in arrays [7].

Initially, research on the environmental impacts of hydrokinetic turbines focused on the problem of collisions between fish and rotors, based on the extrapolation of the knowledge acquired from the already well-established conventional hydroelectric turbines. Injuries, survival, and mortality rates have been evaluated from numerical simulations [6, 8] and laboratory experiments [9, 10], where the authors report high survival rates (>90%) for fish entering the rotor. Other works assess collision risks using probabilistic models based on empirical data on animal distribution, density, and behavior [11]. Field studies using acoustic techniques [12] and observation in situ [13] have also investigated the probability of fish meeting the turbine, evaluating collision risks and the fish's behavior in approaching and evading devices. The authors conclude that several factors influence the approach patterns, such as fish species, size, ambient light conditions, rotation speed, water turbidity, fish size, and whether they swim individually or in schools, influence the approach patterns.

On the other hand, fish could be affected by hydrodynamic flow alteration, predominantly in the wake region at the rotor downstream, highlighting drastic changing pressure, cavitation on blades, high level of shear stresses, and turbulent kinetic energy. Jacobson et al. [9] developed experiments in laboratory to propose a series of bio-criteria for rotor design and operation conditions to avoid dead risk in fish through the rotor. They reported minimum values to the pressure, around 50 kPa, avoiding high pressure gradients, and maximum values to shear stress rate levels, over 500/s, to not injure or damage fish. Zangiabadi et al. [6] carried out numerical simulations computing the pressure and the shear stress level in the vicinity of a tidal turbine, reporting a maximum value of shear rate equal to 12.7/s for a single turbine and smaller change pressure to conclude that the design and flow conditions carry out a fish-friendly turbine. Nonetheless, the impacts on fish caused by hydrokinetic turbines are much less aggressive than those from conventional hydropower turbines, because they generate very adverse conditions operating with high-speed waterfalls, abrupt changes in the flow direction, high rotational speeds, and high pressure.

Other authors have investigated fish swimming in perturbed flow to evaluate the influence of turbulent variables on their performance. In our problem, the wake rotor is a high-intensity turbulence region, and for that reason, a deep understanding of the effect on fish is a crucial issue from the environmental impact view. Odeh et al. [14] created turbulence conditions in a water tank to investigate the biological response of juvenile fish. They conclude that exposure to Reynolds shear stresses higher than 50 N/m^2 for 10 minutes may induce minor injury to some species but does not incur significant mortality over 48 h post-exposure period. Silva et al. [15] observed from experiments varying Reynolds shear stress values from 0.02 to 73.4 N/m^2 that fish was not damaged but suffered displacement and disorientation. In addition, Cotel and Webb [16] observed that fish swimming at higher turbulence levels increased tail beat frequency and amplitude, providing a direct response to the need for a greater impulse to control stability in more challenging flow

conditions, and having a clear impact on fish. Besides, the authors identified the vortex size as an essential parameter to define the quality of the interaction and the predictability of the flow in the vortex emission. They expose that vortices with sizes similar to the fish length could cause a higher impact because they could present difficulties managing these structures. On the other hand, smaller and larger vortices could not affect the fish. The first one could be not perceived by the fish, and the second one could understand as a large mass of fluid arriving without causing disorientation or a change of position.

In this work, flow characteristic and geometry configuration of the HK10 rotor are analyzed from numerical simulations to assess the impacts on fish around, computing pressure and shear stress field and discussing the vortical structure effects. The goal is to provide data on the flow variables that can affect fish for specific turbine geometry and operating conditions. The present chapter is organized as follows: Sect. 2 presents a rotor description and setup, and Sects. 3 and 4 show the results and conclusions, respectively.

2 Materials and Methods

2.1 HK-10 Turbine

Hydrokinetic turbine technology HK-10 presents a device capable of generating electricity sustainably. HK-10 is a propeller-type machine with four blades designed for installation on floating devices (see Fig. 1). These hydraulic machines provide electric energy from river or ocean currents with flexibility and low environmental impacts. The technology developed by the company AES-Tietê, in partnership with Brazilian universities and companies, allows its applicability in different situations, such as in the recovery of remaining potential in hydroelectric plants and supplying electricity to isolated communities (riverside or coastal), among many others.

Table 1 presents generic technical information about the turbine employed to assess the environmental impacts of a hydrokinetic device using computational numerical simulations. It is important to define the tip speed ratio (TSR) because it

Fig. 1 HK-10 turbine: front and lateral views of the conception model, photo and field assembly

Table 1 HK-10 turbine characteristics

Diameter	2.2 m	Weight	750 kg
Nominal power	10 kW	Generator	Permanent magnets with axial flow
Free flow velocity	2.5 m/s	Transmission	1:12 multiplication. Planetary gears
Nominal rotation	35 rpm	Power regulation	AC/DC rectification with converter
Nominal TSR	1.63	Nominal voltage	120/240/380 V
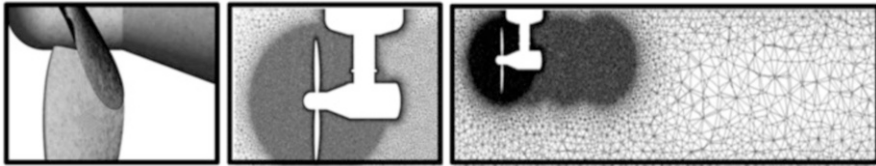
Fig. 2 HK-10 turbine model mesh details and numerical domain

is an important non-dimensional parameter in turbine studies described by the ratio between the tip speed of blade (ωR) and the free stream velocity (U).

2.2 Numerical Simulations

A computational fluid dynamics (CFD) study is carried out to solve the flow fields around the turbine, investigating environmental changes and the potential effect on fish. Simulations run in Ansys-CFX software employing the Unsteady Reynolds-averaged Navier–Stokes equations (URANS) approach in a framework of turbulence modeling. The numerical domain consists of a stationary rectangular prism with dimensions 2.5D × 2.5D× 8D, where the inlet flow surface is placed 1.5D upstream of the rotor, and D is the rotor diameter. A rotating cylindrical domain involving the rotor, with 1.4D of diameter and 0.5D m of length, represents the rotational movement of the rotor, considering the centripetal and Coriolis forces corresponding to a rotational reference frame, in the axial direction with an angular velocity.

On the inlet surface, the boundary condition is a uniform velocity profile, $U = 2.5$ m/s, and turbulence intensity, 5%. On the outlet surface, the imposed condition is the atmospheric pressure, and on the lateral walls, the boundary condition is free-slip flow. Finally, on the rotor (blades and hub), the boundary condition is the non-slip condition attributing a null velocity value on the surface. Figure 2 illustrates details of the numerical mesh, showing the tetrahedral elements and the spheres of influence employed to mesh refinement. The mesh convergence study is realized obtaining a mesh with 7.5 million nodes and y+ mean value in unit order as required by the turbulence model. The y+ parameter is a dimensionless parameter that evaluates the distance between the surface and the nearest element. Simulations run at operation conditions, characterized by rotations of 35 rpm and free flow

velocity equal to 2.5 m/s. For more details about HK-10 numerical simulations set-up and results, see the work of Brasil et al. [17].

3   Results

3.1   Bio-Criteria Assessment on HK-10 Turbine

The bio-criteria assessment on HK-10 turbine is realized from a CFD study, analyzing pressure, shear stress values, cavitation, mechanic design, and operation conditions, to evaluate the potential impacts on fish and characterize the machine as a fish-friendly turbine. Bio-criteria are described in Table 2 and recommended pressure levels at or above 50 kPa (around 50% of atmospheric pressure) to ensure that fish are not exposed to rapid pressure decreases. Figure 3a presents the absolute pressure field around the machine under design conditions (see Table 1). Simulations compute the lowest pressure (90 kPa) behind the blades, and the highest one (100 kPa) occurs on the front of the rotor and tip blades, without overcoming the minimum established value. In that region, the turbine causes a flow blockage. Inducing a high-pressure zone.

The imposition of the minimum pressure prevents cavitation phenomena, which could potentially damage the rotor mechanics and pose a risk of implosion from vapor bubbles, affecting fish. Complementing the pressure analysis, we analyze the manometric pressure evolution along the longitudinal axis in the center line at three different rotational velocities (and consequently, three TSR values), as shown in Fig. 4. It is observed that pressure increases in the front of the rotor and decreases to a minimum value behind it. The pressure is recovered in the wake at four diameters (y/D = 4) rotor far away. Consider how, under nominal conditions (TSR = 1.63), a higher pressure gradient occurs due to the maximum power extraction configuration. For TSR values higher or lower than the nominal TSR, the pressure performance on the centerline remains similar.

Shear stresses are unlikely to cause injury and mortality to fish swimming through hydrokinetic turbines. Fish could suffer disorientation and stress, becoming

Table 2 Bio-criteria [9] assessment on the HK-10 turbine

Injury mechanism	Suggested criteria	HK-10 data	Satisfied criteria
Absolute pressure	Minimum: 50 kPa	90 kPa	Yes
Shear stress rates	Maximum: 500/s	150/s	Yes
Cavitation	Cavitation free or at least minimum	No cavitation	Yes
Mechanical	Reducing the gap between components (stationary and rotating)	No significant gap	Yes
Blade strike	Strike velocities of less than 4.8 m/s	3.6 m/s	Yes

Pressure $[10^4 \times Pa]$ Shear rate $[10^2 \times s^{-1}]$
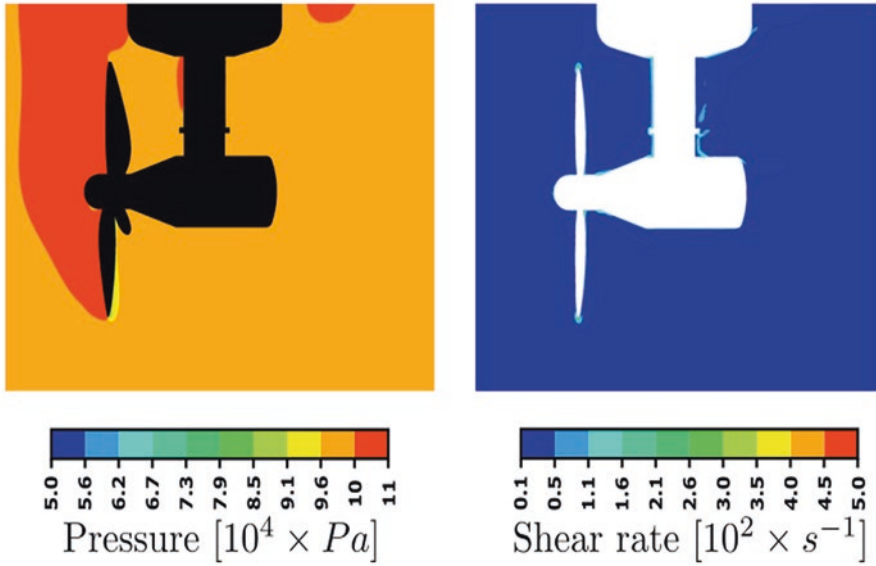
Fig. 3 (**a**) Absolute pressure field around the turbine; (**b**) shear rate levels
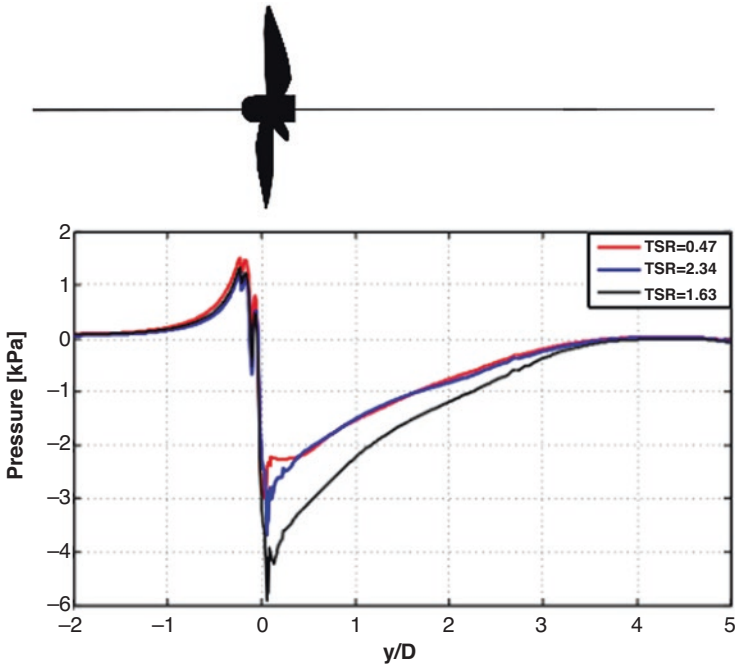
Fig. 4 Manometric pressure evolution at the central line in the wake at three different TSR

more vulnerable to predators. Based on the bio-criteria proposed in Table 2, a hydrokinetic turbine designed to shear stress rates lower than 500/s will not cause damage to fish. Figure 3b illustrates the shear stress rate field around the rotor, showing that the variable satisfied the proposed bio-criteria. The highest values to shear forces (150/s) are found along solid boundaries or at the leading edge of turbine blades. Even in conventional hydroelectric turbines, where intense changes in flow direction occur, strain rates are not a potential factor in fish mortality.

Finally, the mechanical design and blade strike probabilities are discussed. Figure 1 shows that the mechanical design of the rotor does not present a significant gap between stationary and rotating parts. In this sense, some critical configurations could require special attention by fish passage obstruction, such as an array of turbines or rotor assemblies with diffusers or stators requiring special attention. To minimize collisions and potential injuries and/or fish mortality, it is suggested that blade speed (strike velocity) was less than 4.8 m/s and that the leading-edge thickness of blades was big enough to avoid sharp designs. In the nominal conditions, the strike velocity at the tip blade is 3.6 m/s, less than the maximum suggested.

3.2 Flow Description

The horizontal axis turbine wake flow has characteristics well-defined, and therefore, the interaction between fish and turbine is an interesting subject to be studied. Figure 5 shows the velocity field induced by the HK-10 rotor and the vortical coherent structures in the near wake of a horizontal axis turbine, the blade tip vortex, and the nacelle vortex.

The nacelle vortex is oriented in the direction of flow along the x-axis and experiment a counterclockwise (positive) rotation, and the blade tip vortices present a three-dimensional orientation advancing along the x-axis. As proposed by Cotel and Webb [16], it is possible to evaluate the vortex influence on a specific fish computing the ratio L_e/L_f (being L_e the eddy diameter and L_f the body fish length). If $L_e/L_f \ll 1$, the vortexes are too small to create sufficient disturbance to affect the fish and if $L_e/L_f \gg 1$ the fish perceive flow as a linear because the vortex is big enough. On
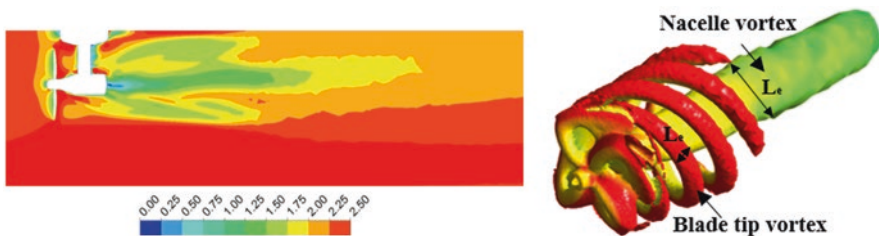
Fig. 5 (**a**) Near wake velocity field; (**b**) three-dimensional vortex structures in a horizontal axis turbine

the other hand, the authors report negative impacts on fish when the relative size is approximately 1. The vortexes diameter was determined with respect to some radial distance from the center of the eddy where vorticity is close to background levels. The nacelle vortex length is estimated at approximately 0.9 m and the blade tip vortex size in estimated at 0.45 m. In that case, fish with similar length could be affected by the flow, rotating in x-axis or translating the mass center.

Regarding the velocity field, it is observed that the flow decelerates abruptly when it passes through the rotor, which could be beneficial for the fish swimming in a more favorable environment. On the other hand, in the wake, the flow undergoes significant changes in velocity direction, requiring fish to adapt to this new condition. Therefore, it would be beneficial to study the fish's performance and energy production for executing evasive maneuvers or returning to the initially established position.

4   Conclusions

The present work assesses some potential HK-10 turbine environmental impacts on fish by running numerical simulations. Firstly, we measure the pressure field and the shear stress around the rotor verifying the bio-criteria reported by Jacobson et al. and concluding that, in this sense, the HK-10 turbine is a fish-friendly turbine. The minimum pressure value found was 90 kPa in a small region behind the blade and the shear rate levels (150/s) were smaller than the maximum bio-criteria (500/s). Finally, we present a flow description, presenting the velocity field and vorticity structures. The rotor wake presents a velocity decay which could be favorable to fish swimming. On the vortex issue, the rotor wake induced two main coherent vortical structures (nacelle and tip blade vortex) showing a spatio-temporal predictability that could allow the fish to recognize and act on these flow structures. Besides, we estimate the characteristic vortex length to compare with a specific fish (with a length Lf) and evaluate if the vortex size could influence fish swimming.

References

1. Laws, N.D., Eps, B.P.: Hydrokinetic energy conversion: technology, research, and outlook. Renew. Sust. Energ. Rev. **57**, 1245–1259 (2016)
2. Jordan, L.B., et al.: Laboratory study on the effects of hydrokinetic turbines on hydrodynamics and sediment dynamics. Renew. Energy. **129**, 271–284 (2018)

3. Daneshvar, F., Nejadhashemi, A.P., Woznicki, S.A., et al.: Applications of computational fluid dynamics in fish and habitat studies. Ecohydrol. Hydrobiol. **17**(1), 53–62 (2017)
4. Schramm, M.P., Bevelhimer, M., Scherelis, C.: Effects of hydrokinetic turbine sound on the behavior of four species of fish within an experimental mesocosm. Ocean Coast. Manag. **54**(1), 2–9 (2011)
5. Zhang, J., Kitazawa, D., Mizukami, Y.: Impact assessment of marine current turbines on fish behavior using an experimental approach based on the similarity law. J. Mar. Sci. Technol. **22**(2), 219–230 (2017)
6. Zangiabadi, E., Masters, I., Williams, A.J., et al.: Computational prediction of pressure change in the vicinity of tidal stream turbines and the consequences for fish survival rate. Renew. Energy. **101**, 1141–1156 (2017)
7. Musa, M., Hill, C., Sotiropoulos, F., Guala, M.: Performance and resilience of hydrokinetic turbine arrays under large migrating fluvial. Nat. Energy. **3**(10), 839–846 (2018)
8. Romero-Gomez, P., Richmond, M.C.: Simulating blade-strike on fish passing through marine hydrokinetic turbines. Renew. Energy. **71**, 401–413 (2014)
9. Jacobson, P.T., Amaral, T., Castro-Santos, D., et al.: Environmental Effects of Hydrokinetic Turbines on Fish: Desktop and Laboratory Flume Studies. Electric Power Research Institute. NTIS/13090078 (2012)
10. Yoshida, T., Zhou, J., Park, S., et al.: Use of a model turbine to investigate the high striking risk of fish with tidal and oceanic current turbine blades under slow rotational speed. Sustainable Energy Technol. Assess. **37**, 100634 (2020)
11. Rossington, K., Benson, T.: An agent-based model to predict fish collisions with tidal stream turbines. Renew. Energy. **151**, 1220–1229 (2020)
12. Bevelhimer, M., Scherelis, C., Colby, J., Andonizio, M.A.: Hydroacoustic assessment of behavioral responses by fish passing near an operating tidal turbine in the East River, New York. Trans. Am. Fish. Soc. **146**(5), 1028–1042 (2017)
13. Hammar, L., Anderson, S., Eggertsen, L., et al.: Hydrokinetic turbine effects on fish swimming behavior. PLoS One. **8**, 1–12 (2013)
14. Odeh, M., Noreika, J., Haro, A., Maynard, A., Castro-Santos, T., Cada, G.: Evaluation of the Effects of Turbulence on the Behaviour of Migratory Fish. Report by Oak Ridge National Laboratory (ORNL) No. DOE/BP-00000022-1) (2012)
15. Silva, A.T., Katopodis, C., Santos, J.M., Ferreira, M.T., Pinheiro, A.N.: Cyprinid swimming behaviour in response to turbulent flow. Ecol. Eng. **44**, 314–328 (2012)
16. Cotel, A.J., Webb, P.W.: Living in a turbulent world - a new conceptual framework for the interactions of fish and eddies. Integr. Comp. Biol. **55**(4), 662–672 (2015)
17. Brasil Junior, A.C.P., Mendes, R.C.F., Wirrig, T., et al.: On the design of propeller hydrokinetic turbines: the effect of the number of blades. J. Braz. Soc. Mech. Sci. Eng. **41**, 253 (2019)

Repurposing of the Industrial Hydrated Lime in Storing Carbon Dioxide and Producing Calcium Carbonate

Maisa El Gamal, Ameera F. Mohammad, and Abdel-Mohsen O. Mohamed

1   Introduction

Calcium carbonate obtained by the lime synthesis in the aqueous phase usually leads to rhombic (calcite), needle-like (aragonite), and polycrystalline spherical (vaterite) particles [1–3]. The phase transition temperature (from aragonite to calcite) depends on the impurity and water contents of the initial phase. For example, magnesium content has a significant effect in preventing the crystal growth transition from aragonite to calcite [4]. It was reported that aragonite particles were transformed into a calcite phase by heating the solids at high temperatures [5]. In addition, a low lime concentration promotes the formation of aragonite particles [6]. It was also observed that when a low residence time was used, no calcite particles were found, and by increasing the reaction time, more calcite particles were formed with smaller particles compared with aragonite particles. The least stable polycrystalline aggregate particles (vaterite) were obtained at a high pH level using the ammonia diffusion method, and the final morphology was a six-fold symmetry. The growth of vaterite crystals was reported to start from a spherical accumulation of nanoparticles with random orientation, followed by the formation of nano hexagonal (petal-like) platelets, and finally single (flower-like) crystals [3, 7]. It was described that characteristic morphologies of calcite crystals results from slaked

M. El Gamal (✉)
College of Natural and Health Sciences, Zayed University, Abu Dhabi, United Arab Emirates
e-mail: maisa.elgamal@zu.ac.ae

A. F. Mohammad
Collage of Engineering, UAE University, Al Ain, UAE

A.-M. O. Mohamed
Uberbinder Limited, Oxford, UK

EX Scientific Consultants, Abu Dhabi, United Arab Emirates

lime carbonation, where rhombohedral, scalenohedral, spheroidal, truncated prismatic, or chain-like agglomerates were generated by changing experimental carbonation conditions such as reaction temperature, gas flow rate, mixing rate, conductivity, and mass concentration of the suspended lime mixture [8]. It was indicated that calcite was the only polymorphic crystal structure in the final product and that the most significant factors affecting the morphology and size distribution are the initial conductivity of the lime mixture and the carbonation temperature. At a temperature range of 35–50 °C, calcite with a particle size of 0.3–1.5 μm and a rhombohedral morphology, mixtures of rhombohedral and truncated prismatic, or scalenohedral morphology is produced. At a lower temperature (20 °C) and low initial conductivity, crystalline and rhombohedral calcites are observed. In contrast, at high conductivities (high salt concentrations), nanometric spheroidal particles or submicrometric (chain-like) elongated agglomerates are observed. It was also reported that the presence of rhombohedral morphology or the predominantly scalenohedral structure is related to the percentage of dissolved calcium species [9] Thus, higher temperatures and conductivities result in the generation of scalenohedral crystals owing to the high concentration of the dissolved calcium hydroxide.

The preceding literature review indicates the significant effect of the process conditions of artificial lime carbonation on the resulting calcium carbonate structure. However, there is still limited information on the impact of carbonation conditions on calcium carbonate when industrial-hydrated lime is used as an alternative material for lime synthesis. Industrial hydrated lime is a major byproduct of acetylene synthesis through the hydrolysis of calcium carbide [3]. The byproduct is produced as an aqueous slurry and is composed mainly of calcium hydroxide, less than 10% calcium carbonate, and traces of unreacted carbon and silicates. The main characteristic of hydrated lime is a high pH level of >12 [3]. Utilizing hydrated lime as a source for CO_2 storing and producing calcium carbonate is considered a new attractive and sustainable method that has been recently invested. The effects of temperature, lime concentration, and conductivity on the calcite structure resulting from slaked lime were previously investigated [8]. However, this study investigated the effects of carbonation conditions such as carbonation reaction temperature and initial pH level on the morphological characteristics of the precipitated calcium carbonate products from hydrated lime.

2   Experimental Setup and Procedure

Hydrated lime samples were collected from Gulf Cryo Company, Abu Dhabi, UAE. The carbide sludge was filtered and then dried in an oven at 110 °C for 24 h. The solid samples were then grounded and prepared for testing. The schematic diagram and the flow chart for the carbonation system are shown in Fig. 1. In the contact system, hydrated lime and distilled water mixture was exposed to a continuous flow of carbon dioxide–air mixture (10% CO_2 and 90% air vol.%), the gas mixture was collected from Abu Dhabi Oxygen Company, UAE. A jacket surrounds the
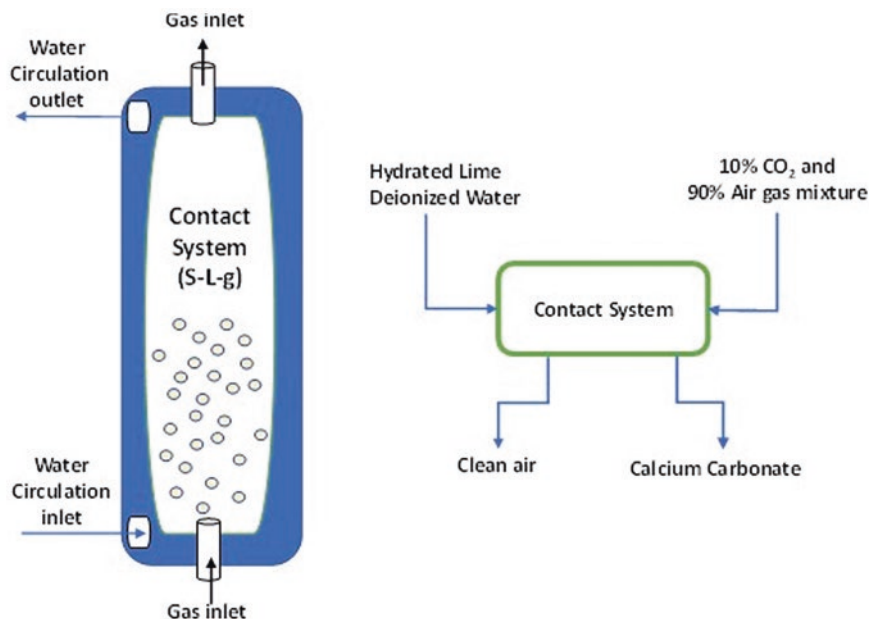
Fig. 1 Schematic diagram and flow chart of the hydrated lime carbonation system

Plexiglas vessel with a water bath circulation unit to control the carbonation reaction temperature. HACH portable pH meter (Model HQ11D53000000) was used to measure the pH level and temperature in the range of 0.00–14.00 ± 0.01 and 0.00–100.00 ± 0.01, respectively.

Two experimental parameters were investigated: reaction temperature and pH level. Different reaction temperatures of (20, 50, and 80 °C) were used at each experimental run and maintained constant during each run. The pH level was set at 10.9, 11.9, and 12.7 by controlling the hydrated lime-to-DW ratio to be 1:10, 1:500, and 1:1000 (mass-to-water volume ratios), respectively. After each run, the treated hydrated lime-DW mixture samples were collected after simple filtration and then dried in the oven at 110 °C for 24 h. Powder XRD, Raman spectroscopy, scanning electron microscopy (SEM), and TGA were used to identify the effects of pH and reaction temperature on the crystalline structure and morphological characteristics of the carbonated hydrated lime. The treated lime solids were characterized via SEM analysis, wherein the surface morphology, texture, and shape of the samples were characterized. The XRD analysis was conducted to study the structural properties of the samples with Cu Kα radiation (λ = 1.54 Å). The scanning range for 2θ values was set from 5° to 80° to cover all significant diffraction peaks with a scanning speed of 2°/min. In addition, Raman spectroscopy measurements were conducted to confirm the structure of the fresh and treated hydrated lime samples. Raman analysis was performed using a HORIBA XploRA at a power of 2 mW and an excitation wavelength of 532 nm. Finally, a thermogravimetric analyzer (Q500

series, TA Instruments) was used to conduct TGA analysis. The sample weight ranged from 2.0 to 5.0 mg, and a heating rate of 15 °C/min was used. Nitrogen gas was used as the carrier gas at a 20 ml/min flow rate.

3 Results and Discussion

3.1 *Reaction Temperature Effect on Morphology*

Three reaction temperatures were used and settled by the water circulation bath for the reaction between hydrated lime and DW mixture with the CO_2 gas. After completion of the carbonation process, the solid samples were filtered, dried, and prepared for the XRD, TGA, SEM, and Raman analyses. All solid products at different reaction temperatures exhibited calcite crystal structures, as confirmed by the XRD analysis shown in Fig. 2, which agrees well with the results reported in the literature [8]. The XRD analysis also indicated that the change in the carbonation temperature only affects the morphology and size distribution of the manufactured calcite crystals. This was indicated by the minor changes in the peak intensity at each reaction temperature [10].

Figure 3 shows the SEM results of the collected solids at 20 °C (Fig. 3a), 50 °C (Fig. 3b), and 80 °C (Fig. 3c). The formation of calcite with different morphological structures is visible in each case. For example, at 20 °C, calcite with a particle size
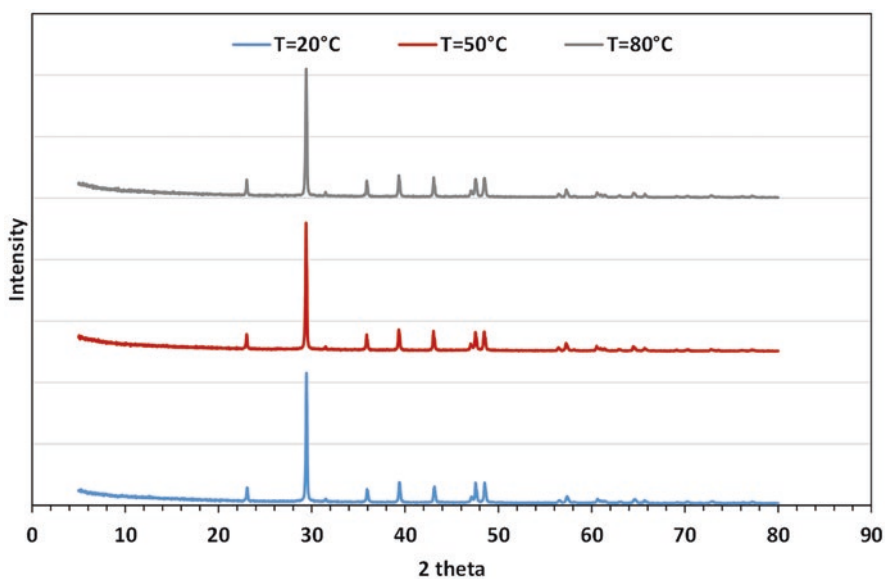
Fig. 2 X-ray diffraction patterns of treated hydrated lime material at different temperatures: 20 °C, 50 °C, and 80 °C
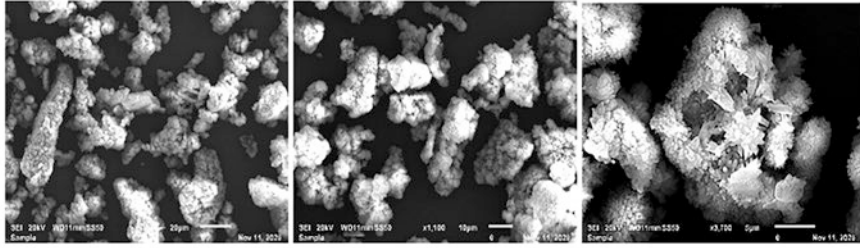
a. Cross-sectional SEM analysis of treated hydrated lime at 20°C.
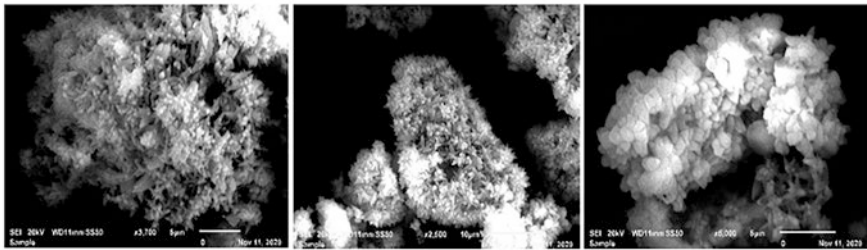
b. Cross-sectional SEM analysis of treated hydrated lime at 50°C.
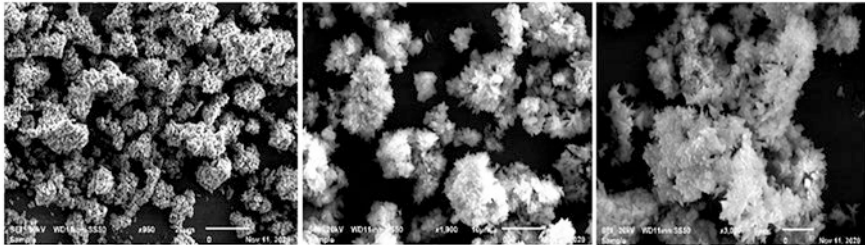
c. Cross-sectional SEM analysis of treated hydrated lime at 80°C.

Fig. 3 (**a**) Cross-sectional SEM analysis of treated hydrated lime at 20 °C. (**b**) Cross-sectional SEM analysis of treated hydrated lime at 50 °C. (**c**) Cross-sectional SEM analysis of treated hydrated lime at 80 °C

of 0.39–0.73 μm and a mixture of submicrometric (chain-like) elongated agglomerates and truncated prismatic morphology were observed. At higher temperatures (50 °C), calcite with a particle size of 0.59–1.31 μm and a mixture of scalenohedral and agglomerated spheroidal morphology were observed. A similar calcite particle size of 0.59–1.34 was observed at 80 °C but only with scalenohedral morphology and no spheroidal particles. These findings are in agreement with the results reported by Ukrainczyk et al. (2007) [8], in which higher temperatures resulted in calcite with a scalenohedral morphology. In addition, it was previously indicated that at a constant solid-to-liquid ratio of 1:10 (mass ratio), an initial pH of 12.7, and a conductivity of 8947 μs/cm while changing the reaction temperature [8]. This in turn
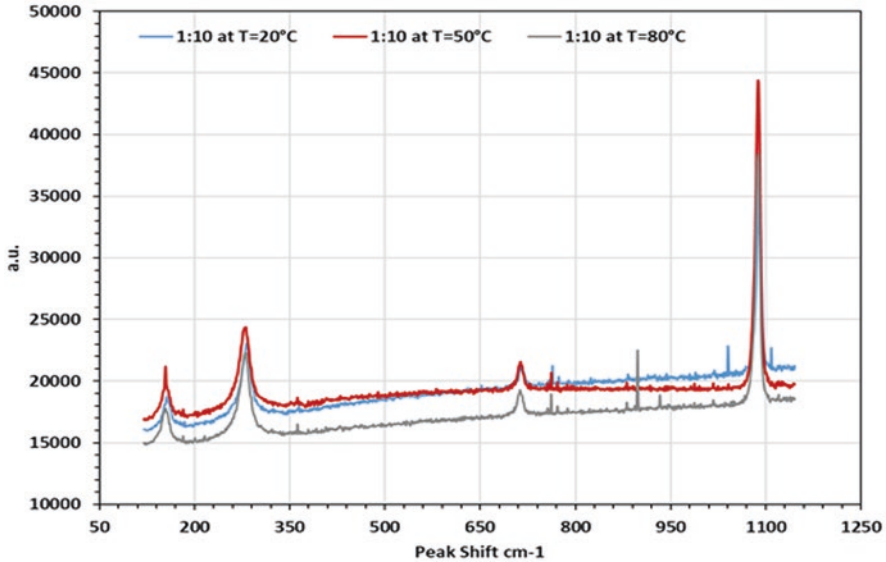
Fig. 4 Results of the Raman analysis of treated hydrated lime at different temperatures

indicates that the conductivity level may also have a significant effect on the morphological properties, which is discussed in the following sections.

Figure 4 shows the Raman analysis of treated hydrated lime at different temperatures. Similar recorded intensities for both samples collected at 50 °C and 80 °C and a noticeable deviation from the recorded intensity of the samples collected at 20 °C were obtained, confirming the differences in the morphological characteristics [11]. In addition, the TGA, represented in Fig. 5, indicates that a minimum calcite degradation temperature (20 °C) is associated with the minimum recorded particle size compared with higher carbonation temperatures [12].

3.2 pH Effect on Morphology

The initial hydrated lime-DW mixture pH was controlled by changing the solid-to-liquid ratio. Three pH values of 10.9, 11.75, and 12.7 were used at a constant carbonation temperature of 20 °C. As mentioned in Sect. 3.1, calcite particles with a particle size of 0.39–0.73 μm and a mixture of submicrometric elongated agglomerates and truncated prismatic morphology were obtained using an initial pH of 12.7. At a pH of 11.75, calcite particles with sizes ranging from 1.94 to 6.01 μm and a mixture of rhombohedral and agglomerates of small rhombohedral and spheroidal particles were obtained (Fig. 6a). At the lowest initial pH level of 10.9, calcite with maximum particle sizes ranging from 5.92 to 6.04 μm and only rhombohedral morphology was detected (Fig. 6b). Thus, decreasing the temperature and pH resulted
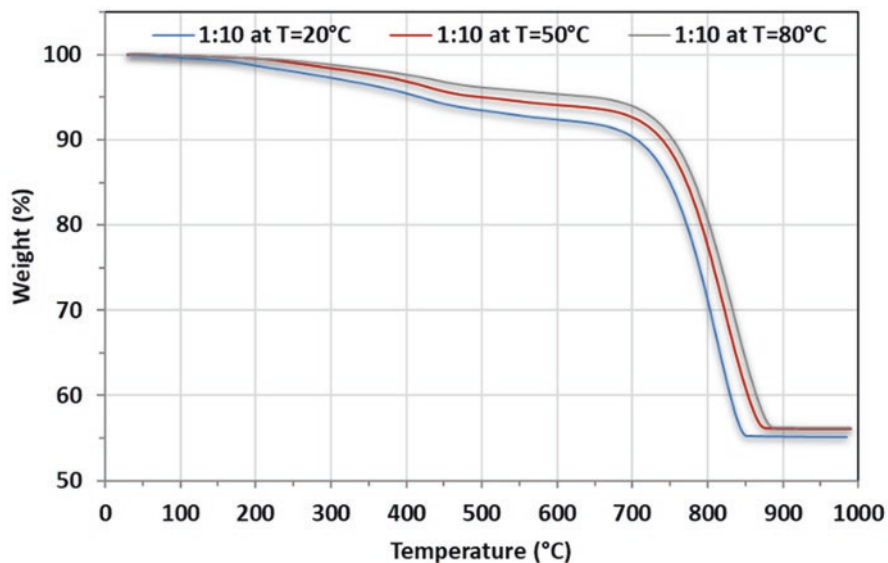
Fig. 5 Thermogravimetric analysis (TGA) of treated hydrated lime samples at different reaction temperatures
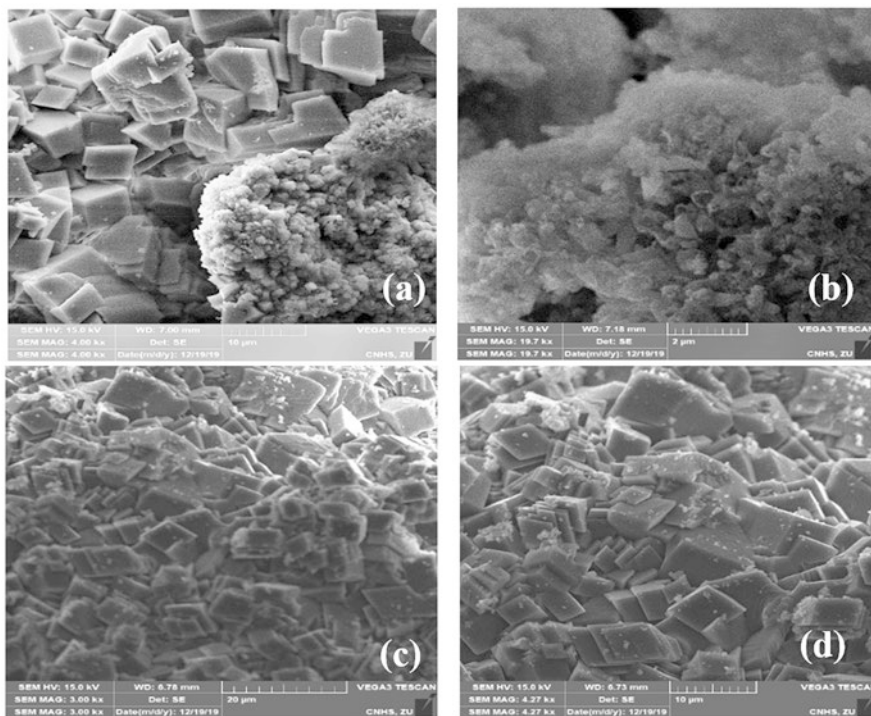
Fig. 6 Cross-sectional SEM analysis of treated hydrated lime samples (**a** and **b**) at pH = 11.7 at different magnifications, (**c** and **d**) at pH = 10.9, at different magnifications
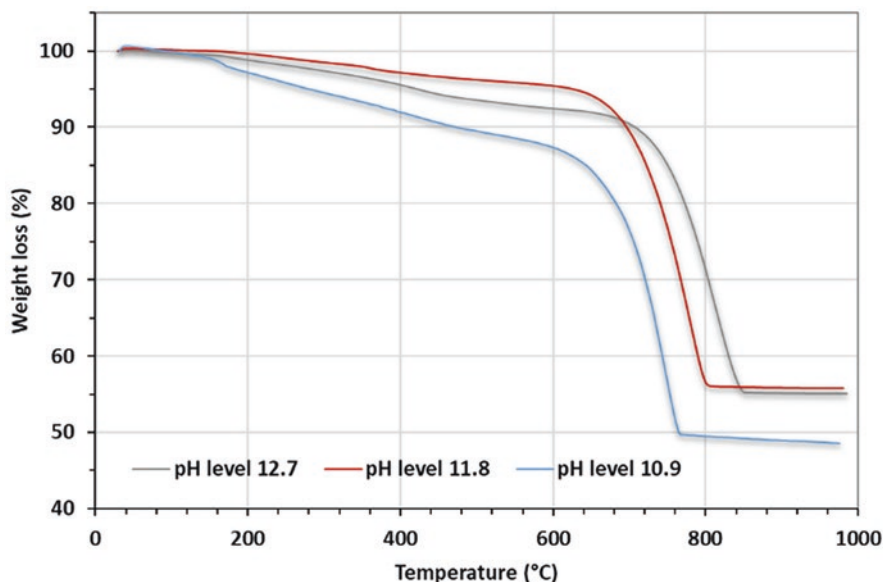
Fig. 7 TGA of treated hydrated lime samples at different pH levels

in a rhombohedral morphology, whereas increasing the temperature and initial pH promoted a scalenohedral morphology; confirming the results obtained by literature [8]. This could be attributed to the increase in the concentration of the total dissolved calcium species [9]. The results of the TGA analysis of the collected solids at the three pH levels (Fig. 7) indicate that the minimum calcite degradation temperature was that of the samples collected at a pH of 10.9, followed by those contained at pH of 11.75, and the highest calcite degradation temperature was obtained at the highest pH level. This can be attributed to the high cross-link density within the calcite crystals [12, 13].

4 Conclusion

The potential of using waste materials such as hydrated lime in a controlled CO_2 carbonation process to produce specific calcite morphology was investigated. Carbonated lime samples were characterized, identified, and compared under different carbonation reaction temperatures and pHs. These two parameters were highly significant, like the produced calcite morphologies and particle sizes. Scalenohedral morphology is dominant at high carbonation temperatures such as 80 °C, whereas the truncated prismatic morphology is dominant at low hydrated lime concentrations of 1:10 lime to DW mass-to-water volume ratio. The high initial pH value of 12.7 at ambient temperature resulted in the formation of the rhombohedral morphology. As a result, the effect of lime concentration, temperature, and initial

carbonation pH has a significant effect on the resulted morphology with specific characteristics; this could provide the ability to implement the carbonation controlling conditions in producing specific product's morphology and hence minimize the undesired characteristic associated with specific morphological structures. Further parametric analysis is recommended to optimize the carbonation conditions and enhance calcite morphology control.

References

1. Kezuka, Y., Kawai, K., Eguchi, K., Tajika, M.: Fabrication of single-crystalline calcite needle-like particles using the aragonite–calcite phase transition. Fortschr. Mineral. **7**(8), 133 (2017)
2. Jimoh, O.A., Ariffin, K.S., Hussin, H.B., Temitope, A.E.: Synthesis of precipitated calcium carbonate: a review. Carbonates Evaporites. **33**(2), 331–346 (2018)
3. Mohamed, A.-M.O., El-Gamal, M.M., Hameedi, S.: Sustainable Utilization of Carbon Dioxide in Waste Management. Elsevier, Moving Toward Reducing Environmental Impact. (2022)
4. De Choudens-Sanchez, V., Gonzalez, L.A.: Calcite and aragonite precipitation under controlled instantaneous supersaturation: elucidating the role of CaCO3 saturation state and Mg/Ca ratio on calcium carbonate polymorphism. J. Sediment. Res. **79**(6), 363–376 (2009)
5. Koga, N., Nishikawa, K.: Mutual relationship between solid-state aragonite–calcite transformation and thermal dehydration of included water in coral aragonite. Cryst. Growth Des. **14**(2), 879–887 (2014)
6. Swinney, L.D., Stevens, J.D., Peters, R.W.: Calcium carbonate crystallization kinetics. Ind. Eng. Chem. Fundam. **21**(1), 31–36 (1982)
7. Hu, Q., Zhang, J., Teng, H., Becker, U.: Growth process and crystallographic properties of ammonia-induced vaterite. Am. Mineral. **97**(8–9), 1437–1445 (2012)
8. Ukrainczyk, M., Kontrec, J., Babić-Ivančić, V., Brečević, L., Kralj, D.: Experimental design approach to calcium carbonate precipitation in a semicontinuous process. Powder Technol. **171**(3), 192–199 (2007)
9. Domingo, C., García-Carmona, J., Loste, E., Fanovich, A., Fraile, J., Gómez-Morales, J.: Control of calcium carbonate morphology by precipitation in compressed and supercritical carbon dioxide media. J. Cryst. Growth. **271**(1–2), 268–273 (2004)
10. Al-Gaashani, R., Radiman, S., Daud, A.R., Tabet, N., Al-Douri, Y.: XPS and optical studies of different morphologies of ZnO nanostructures prepared by microwave methods. Ceram. Int. **39**(3), 2283–2292 (2013)
11. Thongtem, T., Phuruangrat, A., Thongtem, S.: Characterization of MMoO4 (M= Ba, Sr and Ca) with different morphologies prepared using cyclic microwave radiation. Mater. Lett. **62**(3), 454–457 (2008)
12. Bennour, S., Louzri, F.: Study of swelling properties and thermal behavior of poly (N, N-dimethyl acrylamide-co-maleic acid) based hydrogels. Adv. Chem. **2014**, 1–10 (2014)
13. Safajou-Jahankhanemlou, M., Abbasi, F., Salami-Kalajahi, M.: Synthesis and characterization of thermally expandable PMMA-based microcapsules with different cross-linking density. Colloid Polym. Sci. **294**(6), 1055–1064 (2016)

Index